622.09
Un32mo
no.8295-8310
1978
copy 2
Inc.

BINDING POSTS CAN BE CUT

If too tightly bound to photocopy, please take to circulation desk so personnel can remove plastic posts.

622.09
Un33mo

RI 8295

Bureau of Mines Report of Investigations/1978

The Library of the
DEC 1 1978
University of Illinois
at Urbana-Champaign

Methane Drainage: Experience With Hydraulic Stimulation Through Slotted Casing

UNITED STATES DEPARTMENT OF THE INTERIOR

Report of Investigations 8295

Methane Drainage: Experience With Hydraulic Stimulation Through Slotted Casing

By Stephen W. Lambert and Michael A. Trevits

The person charging this material is responsible for its return to the library from which it was withdrawn on or before the **Latest Date** stamped below.

Theft, mutilation, and underlining of books are reasons for disciplinary action and may result in dismissal from the University.

UNIVERSITY OF ILLINOIS LIBRARY AT URBANA-CHAMPAIGN

APR 6 [illegible]

JAN 1 6 [illegible]

March 3 1849

UNITED STATES DEPARTMENT OF THE INTERIOR
Cecil D. Andrus, Secretary

BUREAU OF MINES

This publication has been cataloged as follows:

Lambert, Stephen W

Methane drainage : experience with hydraulic stimulation through slotted casing / by S. W. Lambert and M. A. Trevits. [Washington] : U.S. Dept. of the Interior, Bureau of Mines, 1978.

16 p. : maps, diagrs. ; 27 cm. (Report of investigations - Bureau of Mines ; 8295)

Bibliography: p. 14.

1. Methane. 2. Mine gases. 3. Mine drainage. I. Trevits, Michael A., joint author. II. United States. Bureau of Mines. III. Title. IV. Series: United States. Bureau of Mines. Report of investigations - Bureau of Mines ; 8295.

TN23.U7 no. 8295 622.06173

U.S. Dept. of the Int. Library

CONTENTS

Page

Abstract........ 1
Introduction........ 1
Drilling, completion, and production........ 2
Mine investigation........ 3
  Fracture survey........ 3
  Description of TW2........ 5
Discussion of results........ 7
  Drilling........ 7
  Cementing........ 7
  Logging........ 7
  Jet slotting........ 8
  Stimulation........ 9
  Production........ 12
Conclusions........ 13
References........ 14
Appendix.--History of test well No. 2 in the Mary Lee coalbed near Oak Grove, Jefferson County, Ala........ 15

ILLUSTRATIONS

1. Hydraulic stimulation pressure and fluid injection chart, TW2........ 3
2. Daily gas production from TW2........ 3
3. Survey stations dividing area of mine near TW2........ 4
4. Roof joint, cleat, and hydraulically induced channel directions near TW2........ 4
5. Position of mine face during underground examination of TW2........ 5
6. Sketch of mine face during underground examination of TW2........ 6
7. Portion of density log from TW2 compared with rock strata observed underground (log run before casing was slotted)........ 8
8. Comparison of density logs run before and after slotting........ 9
9. Comparison of roof joint and cleat directions in mine area with fractures induced or extended during drilling, cementing, and stimulation of TW1........ 10

Digitized by the Internet Archive
in 2018 with funding from
University of Illinois Urbana-Champaign Alternates

https://archive.org/details/reportofinvestig8295unit

METHANE DRAINAGE: EXPERIENCE WITH HYDRAULIC STIMULATION THROUGH SLOTTED CASING[1]

by

Stephen W. Lambert[2] and Michael A. Trevits[2]

ABSTRACT

The Bureau of Mines examined the wellbore of a vertical gas drainage well in the Mary Lee coalbed to determine the results of specific completion procedures in coal. A jet-slotting tool was used to cut four vertical slots through the casing about 1 ft below the coalbed. Even though stimulation treatment pressure was excessive, hydraulically induced channels were contained entirely within the target coal zone. Sand-filled, induced channels were horizontal, inclined, and vertical, and were propagated in directions similar to bedding planes, rock joint, and coal cleat directions measured in the mine. Variable gas flow rates, recorded during the productive life of the well, were attributed to chronic downhole pump malfunction and the slotted casing below the production zone.

INTRODUCTION

The purpose of this Bureau of Mines research was to test specific hydraulic stimulation procedures in coal by monitoring well production and to later inspect the results directly underground in the mine. A vertical degasification borehole that had been drilled in the Mary Lee coalbed and completed 600 ft ahead of active mining was intercepted on February 15, 1977. The borehole, referred to as test well No. 2 (TW2), is located in section 35, R 18 S R 6 W, near Oak Grove, Ala.; it is the second such borehole to be examined underground in the area.

A roller bit and foam were used to penetrate the coalbed to minimize wellbore damage. After the casing was set in the hole, the coalbed was exposed for stimulation using a jet-slotting tool. Density logs were used to identify slotted portions of casings and to identify zones within the coalbed that could have an influence on the geometry of hydraulically induced channels. The hydraulic forces used to stimulate the coalbed were diverted several times, resulting in numerous short channels. Horizontal channels were propagated when injection pressure exceeded effective overburden pressure.

---

[1] The work described in this report was performed by a component of the Bureau of Mines that was transferred to the Department of Energy on Oct. 1, 1977.

[2] Geologist.

It is indicated that because of the relative softness of coal, the principal mechanism leading to horizontal channel development is compression rather than the flexing and lifting of all the overburden. Also, there is a direct correlation between propagated vertical channel directions and the joint and cleat orientations, and a direct relationship between surface and underground fractures. These relationships can be used to determine the direction of the vertical channel before stimulation.

DRILLING, COMPLETION, AND PRODUCTION

TW2 was rotary-drilled using a 6-1/4-in-diam air-percussion bit to approximately 235 ft above the 5-ft-thick coal interval. To reduce the possibility of formation damage caused by drilling, a 6-1/8-in-diam roller bit was used to drill the remaining distance to 50 ft below the coalbed. TW2 was cased to total depth with 4-1/2-in-outside-diam (OD) pipe. The lower 500 ft of casing was set in place using 13.8 lb/gal cement.

A jet-slotting tool was positioned using a geophysical logging device. The design called for a water and sand slurry to cut four vertical slots, 90° apart, from the base of the coalbed to within 1 ft of the top. The coalbed was stimulated using 3,500 gal of a highly viscous fluid containing 4,000 lb of 10/30- and 20/40-mesh sand.

The hydraulic stimulation pressure averaged 2,400 lb/sq in gage with no apparent formation "breakdown," the fluid injection rate averaged 8 bbl/min, and the instantaneous shut-in pressure was 2,200 lb/sq in gage (fig. 1). After stimulation, water was circulated in the well removing approximately 200 lb of propping sand. The well was equipped with a pump to remove water and with meters to monitor production.[3]

TW2 was put on production November 13, 1976. During successful pumping periods, daily gas production averaged about 15,000 cu ft. Sand and other foreign material entering the downhole pump mechanism caused chronic malfunction and resulted in overall poor gas production (fig. 2). This malfunction made it necessary to dismount the pump and remove the material before water production could be resumed. Immediately after servicing the downhole pump and after removal of usually less than 5 bbl of water, temporary gas flow rates in excess of 80,000 cu ft/day were measured on several occasions. Such high gas flows appear to have brought significant amounts of propping sand into the wellbore.

---

[3] For details of drilling and completion of TW2, see the appendix.

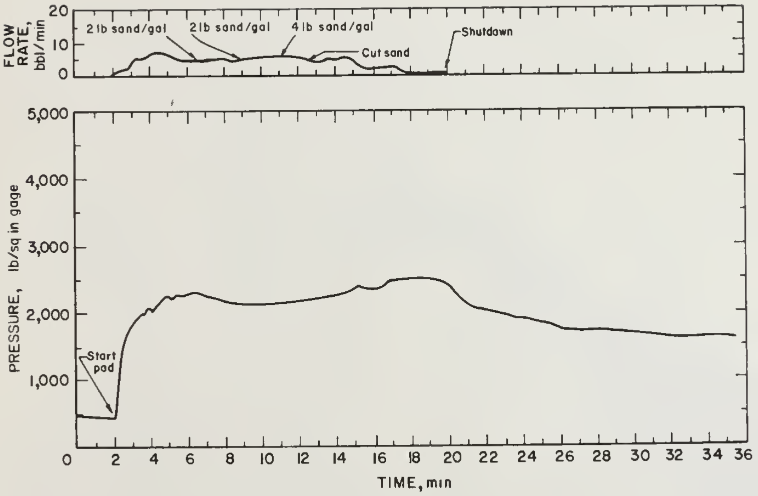

FIGURE 1. - Hydraulic stimulation pressure and fluid injection chart, TW2.

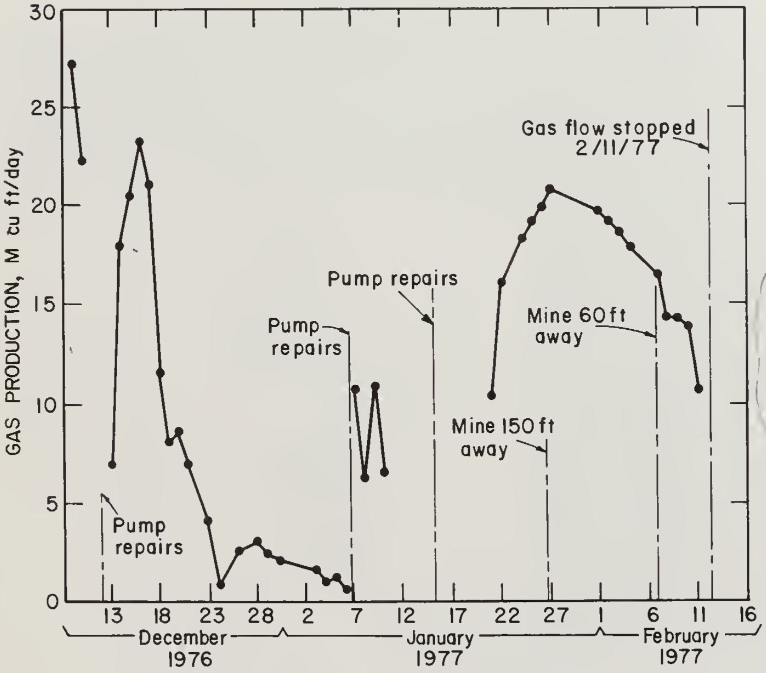

FIGURE 2. - Daily gas production from TW2.

MINE INVESTIGATION

A survey of fracture orientations in the coal and roof rock was conducted within an area of the mine near TW2. Physical characteristics of the coal and associated rock strata were noted during the survey. After borehole interception, the physical condition of the casing and wellbore and the geometry and orientation of hydraulically induced partings were studied in detail.

Fracture Survey

A mine survey was conducted to determine if hydraulically induced fractures had propagated in directions parallel to existing natural fracture trends. In an earlier study, at test well No. 1 (TW1), a correlation was made between cleat and joint directions and fractures believed to have been induced or extended by drilling, cementing, and stimulation.[4]

The area of the mine near TW2 is divided into seven stations (fig. 3). A compass was used to measure the direction of all visible roof joints and at least 15 coal cleats within each station. Directions of all observed hydraulically induced fractures containing prop sand were also measured. All measurements were adjusted for magnetic declination and then plotted on rose diagrams (fig. 4).

---

[4] TW1, completed approximately 500 ft from active mining, was hydraulically stimulated Nov. 23, 1975, using 5,000 gal of fluid and 2,500 lb of sand.

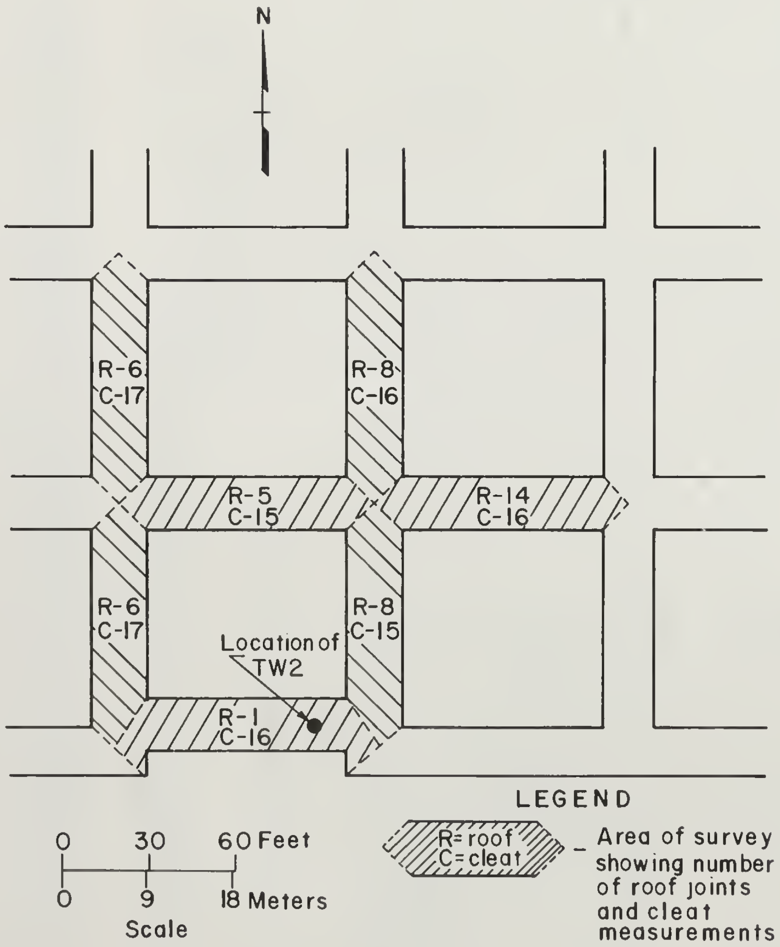
N
R-6
C-17
R-8
C-16
R-5
C-15
R-14
C-16
R-6
C-17
R-8
C-15
Location of
TW2
R-1
C-16
LEGEND
R=roof
C=cleat
Area of survey showing number of roof joints and cleat measurements
0
30
60 Feet
0
9
18 Meters
Scale

FIGURE 3. - Survey stations dividing area of mine near TW2.

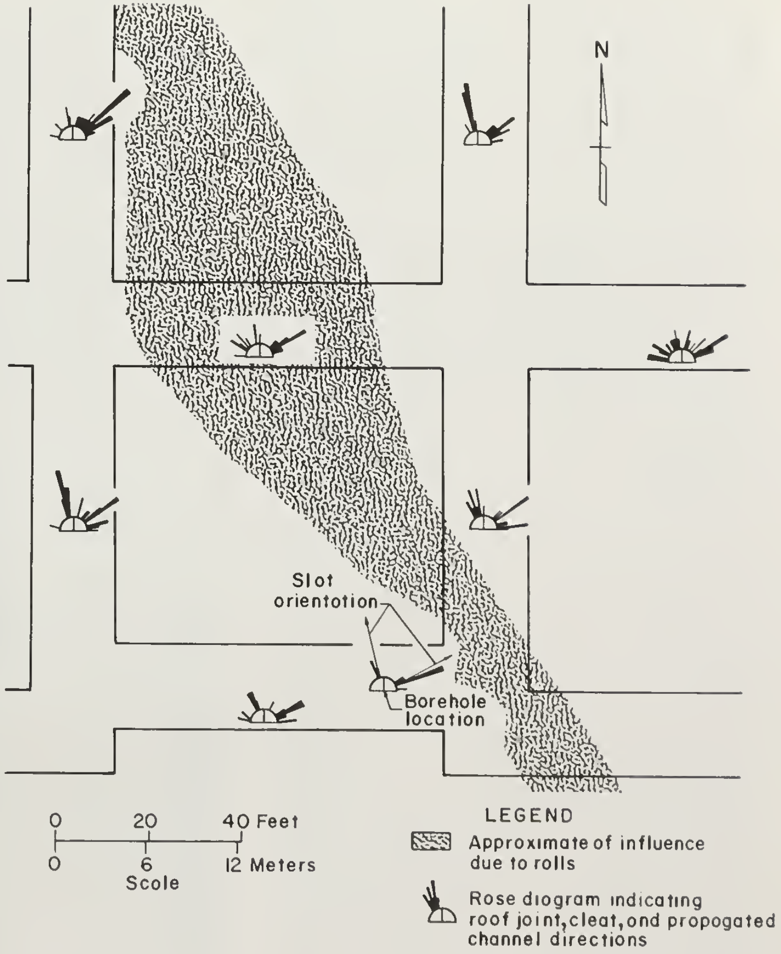
N
Slot
orientotion
Borehole
location
0
20
40 Feet
0
6
12 Meters
Scole
LEGEND
Approximate of influence due to rolls
Rose diogram indicating roof joint, cleat, and propogated channel directions

FIGURE 4. - Roof joint, cleat, and hydraulically induced channel directions near TW2.

Prominent linear features commonly called "rolls" are present in the mine approximately 20 ft northeast of TW2 trending roughly N 35° W. These rolls are expressed in the roof rock as troughlike features where the underlying coal thins abruptly. Coal and roof rock within and along the flanks of the rolls are highly slickensided with badly distorted bedding planes.

The upper 3-ft portion of the coalbed in the area studied, including the borehole site, was highly sheared and appeared to be generally friable and soft. The lower 2 ft of coal was considerably harder with well-developed, closely spaced cleat.

Description of TW2

TW2 and induced sand channels were exposed by a continuous-mining machine extracting coal eastward. Coal was removed to approximately 4 ft beyond the borehole location where there were very wide, short, vertical channels and longer, thin, horizontal, sand-packed channels. After bolting the roof, the site was studied in detail and measurements were made with the coal face in the position shown in figure 5; the borehole site and coal face at that time are shown in figure 6.

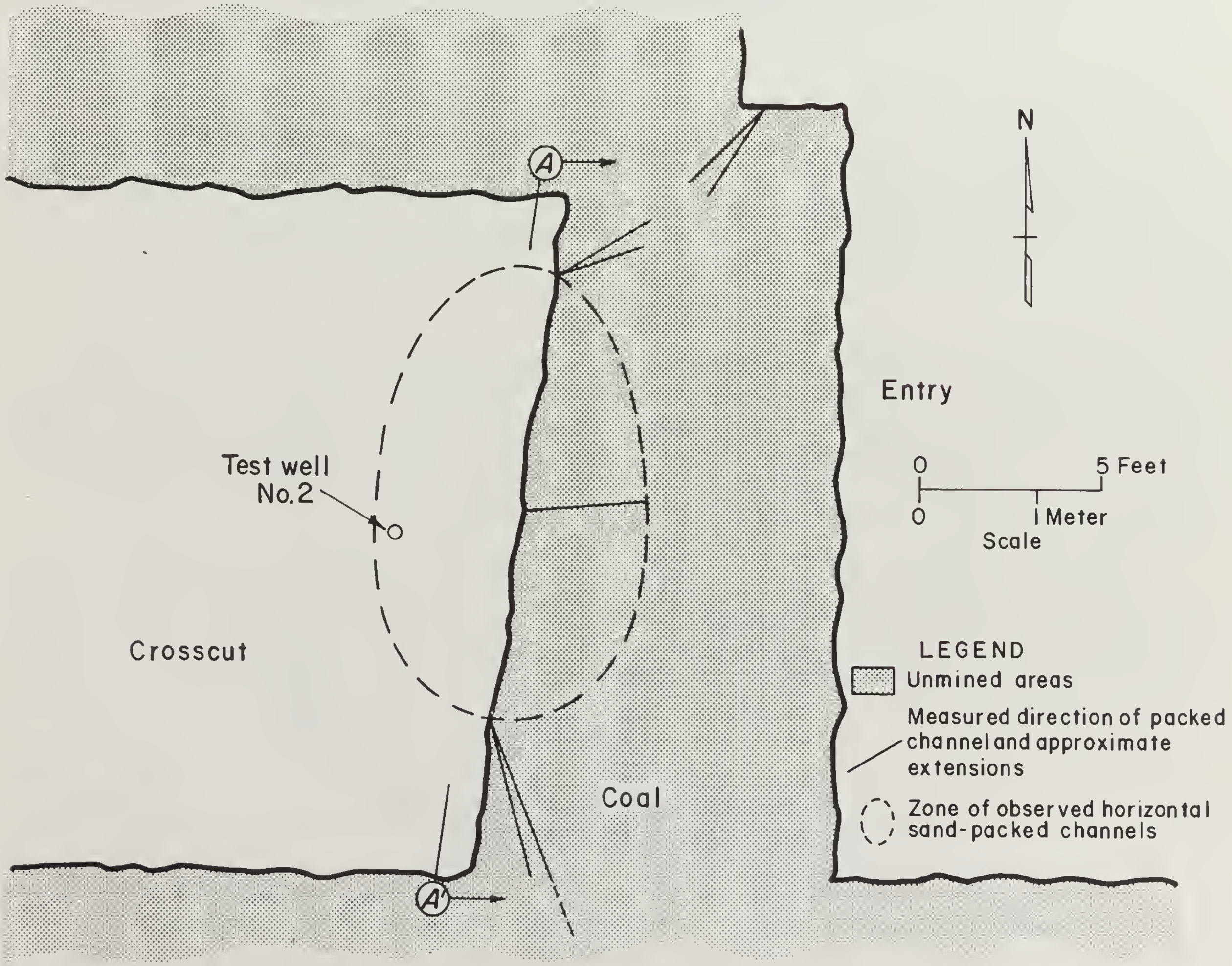
A
N
Entry
Test well No. 2
Crosscut
0
5 Feet
0
1 Meter
Scale
LEGEND
Unmined areas
Measured direction of packed channel and approximate extensions
Zone of observed horizontal sand-packed channels
Coal
A'

FIGURE 5. - Position of mine face during underground examination of TW2.

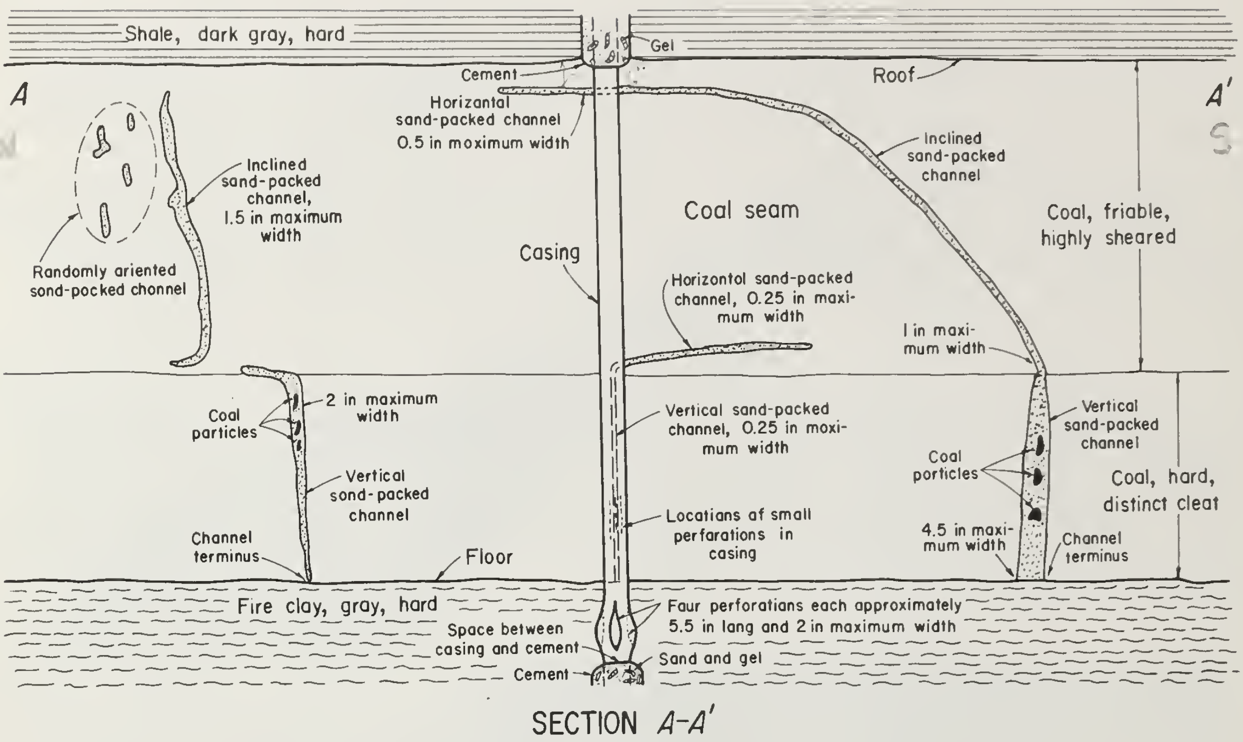
Shale, dark gray, hard
Gel
Cement
Roof
A
N
A'
S
Horizontal sand-packed channel 0.5 in maximum width
Inclined sand-packed channel, 1.5 in maximum width
Randomly oriented sand-packed channel
Inclined sand-packed channel
Coal seam
Coal, friable, highly sheared
Casing
Horizontal sand-packed channel, 0.25 in maximum width
1 in maximum width
Coal particles
2 in maximum width
Vertical sand-packed channel
Channel terminus
Floor
Vertical sand-packed channel, 0.25 in maximum width
Locations of small perforations in casing
Coal particles
Vertical sand-packed channel
4.5 in maximum width
Channel terminus
Coal, hard, distinct cleat
Fire clay, gray, hard
Space between casing and cement
Cement
Four perforations each approximately 5.5 in long and 2 in maximum width
Sand and gel
SECTION A-A'

FIGURE 6. - Sketch of mine face during underground examination of TW2.

Wellbore Observations: Hard cement was observed to fill the northern half of the 1-in space between the casing and the drill hole in the roof and floor. No cement was found in the southern half of the wellbore; instead prop sand and/or gel filled this annular space at both the floor and the roof.

The casing was expanded outward, where it was pierced by four roughly diamond-shaped slots about 5.5 in long and 2 to 2.5 in wide. Five holes (0.3-in maximum diameter) in the casing were 5 to 9 in above the slots. The tops of the slots were about 4 in below the base of the coalbed, and directions of the slots were N 60° E and N 15° W. No cement could be found on either side of the casing exposed within the coal interval.

Induced Hydraulic Channels: Three well-defined vertical channels at the borehole site were contained in the lower third of the coalbed, and they were completely filled with propping sand. The channel sides appeared smooth and unabraded, and they followed local vertical fracture planes in the coal. The widest channel (4.5 in), located south of TW2, tapered upward gradually; a 2.0-in-thick channel, north of the borehole, tapered sharply to the floor; the remaining vertical channel, located directly behind the exposed casing, was 0.3 in throughout. All three channels terminated at the base of the coalbed with no evidence of fracture continuation into the floor rock.

Two channels sloped downward to the south and were contained entirely in a more friable, soft, and highly slickensided portion of the coalbed. Their sides were smooth and unabraded but somewhat irregular; they appeared to follow local shear fracture planes in the coal, with minor vertical development along cleat planes. The shape and downward extension of these channels indicate direct or inferred continuation with the vertical channels described earlier.

Four horizontal channels appeared at the coal face as extensions of either vertical or inclined channel development; all four occurred along bedding planes. Three of the channels were present approximately one-third of the distance up from the floor near the line of contact between hard, distinctly cleated coal and soft, friable, sheared coal. The fourth horizontal channel ran along a line 6 in below the coal-roof-rock interface; coal immediately surrounding the horizontal channels was very soft and appeared crushed.

Four small, separate, randomly oriented, sand-filled channels were in the upper portion of the coal face north of the wellbore. Their locations indicate close association with a system of larger channels trending approximately N 65° E. These channels were along shear, cleat, and bedding planes, and thus possessed characteristics of all three channel types described earlier.

DISCUSSION OF RESULTS

Drilling

There was no evidence that drilling adversely affected the coalbed or surrounding rock strata. Except for hydraulically induced partings in the coal, the only opening in rock leading directly from the wellbore was a well-developed roof joint which was believed to have opened sometime after TW2 was completed because it did not contain cement or propping sand.

Cementing

The lightweight, low-fluid-loss cement mixture, together with the low injection rates used to stabilize casing in the borehole (see appendix), prevented excessive permeability damage to the coalbed. No evidence of cement infiltration was found in the floor, coal, or roof rock.

The cement bond to casing was generally poor. For example, the mining machine which exposed the borehole never came in direct contact with the casing or cement, so the cement, if ever present, must have been pulled from the casing leaving no residue as coal surrounding the test well fell away under its own weight. The lack of cement within approximately one-half of the wellbore annulus in the roof also indicates poor cementing.

Logging

A comparison of density logs with underground observations shows the logs to be an important tool for predicting coalbed characteristics. All density logs clearly indicate two major density zones within the coalbed (fig. 7).

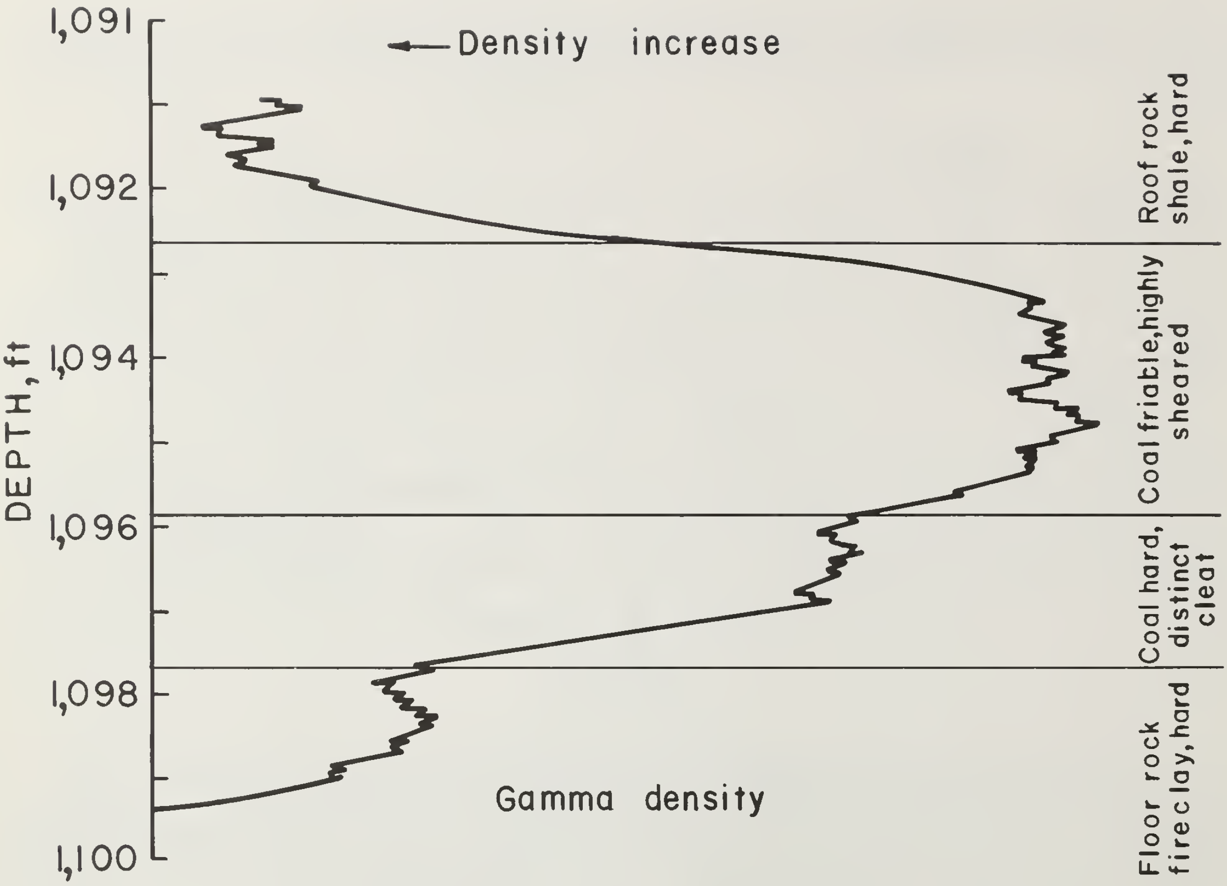

FIGURE 7. - Portion of density log from TW2 compared with rock strata observed underground (log run before casing was slotted).

The upper, less dense zone correlates precisely with the friable, highly sheared portion of the coalbed containing all induced channels that were inclined or horizontal. The denser, lower zone on the log locates the interval of hard, distinctly cleated coal containing induced, vertical channels.

Jet Slotting

Using density log information, the base of the coalbed was determined to be 1,099.2 ft deep, and four vertical slots, each 48 in long, were to be cut at that depth. Subsequent logging revealed that the base of the coalbed was actually 1,098.4 ft deep, and that jet slotting had begun below the coal.

If the casing had been cut throughout the prescribed length, the fact that the slots began several inches below the coalbed would have been of little consequence. However, as observed underground, the casing had not been penetrated throughout the entire coal interval. Factors that may have contributed to poor slotting results include insufficient time allowed to cut the casing; slight rotation or twisting of the tool could have occurred as it was raised and lowered through the prescribed interval (at least two heavily abraded, vertically oriented "tracks" were noted along inner surfaces of casing exposed to each jet nozzle), and the very soft, friable nature of the coal could have absorbed much of the cutting "energy" (all perforations through casing occurred either in the hard floor rock or in the hard lower portion of the coalbed).

Close examination of density logs taken before and after slotting operations indicated that the small section of pipe successfully cut could have been recognized before actual underground observations. Logs taken after slotting show a significant density decrease along the interval of borehole directly exposed to rock strata (fig. 8).

Stimulation

The treatment used to stimulate TW2 was designed to induce vertical, 1-in-wide, sand-filled channels in two directions from the wellbore. Each channel was to be approximately 150 ft long and just under 5 ft high. Based on prior underground observation at the TW1 site, channels were expected to propagate in directions similar to existing natural fractures in the coal.

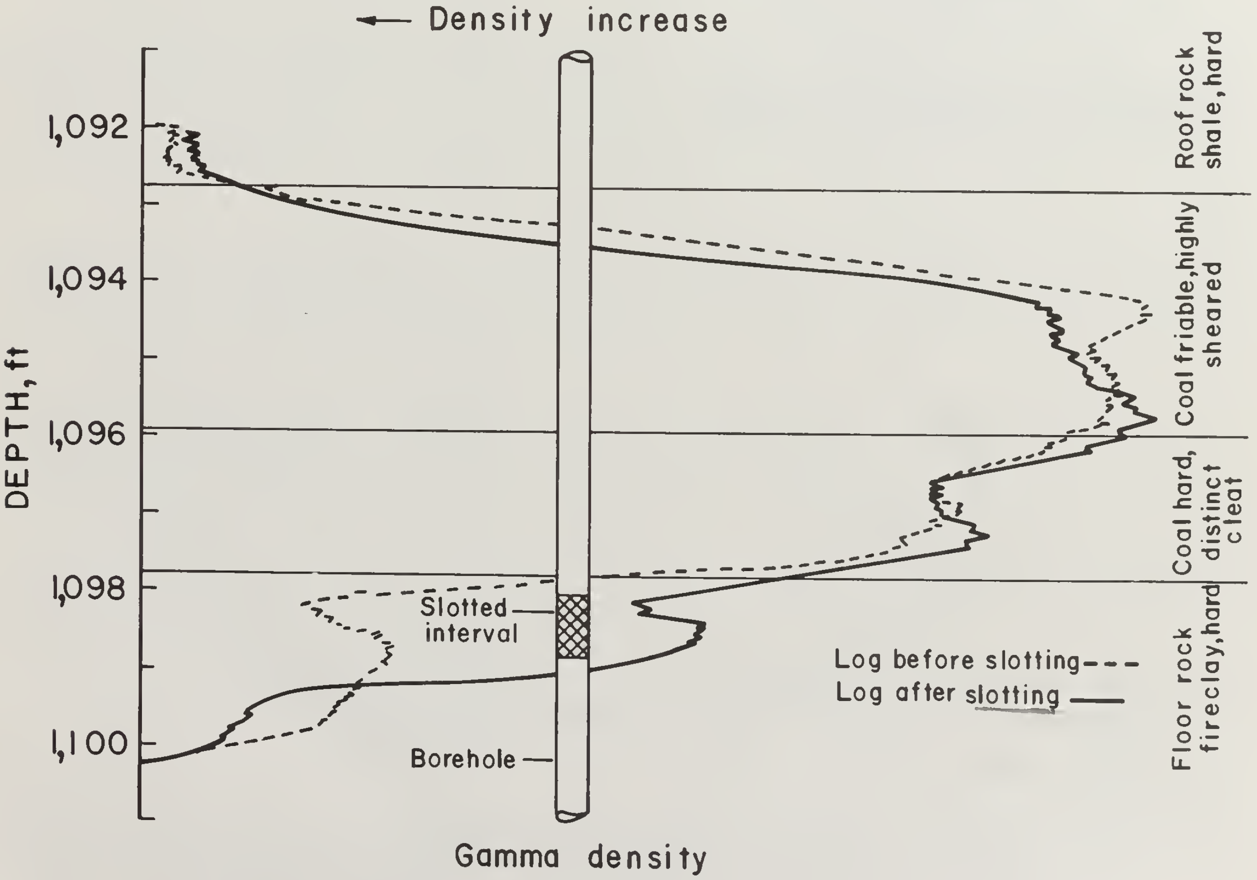

FIGURE 8. - Comparison of density logs run before and after slotting.

Previous work on stimulating the Mary Lee coalbed (1)[5] indicated that formation breakdown could be expected to occur below 900 lb/sq in.

The sand channels hydraulically induced into the coalbed were horizontal, inclined, and vertical, making it difficult to determine the complete dimensions of each. However, figure 5 indicates that the maximum length of propagation from the wellbore was 50 ft or less, rather than the maximum 300 ft calculated in the original design.

The underground channels, especially the wide vertical channels, were generally composed of several smaller induced sand channels. The number of slightly different directions measured along the channel walls; the coal particles contained in these channels; and the number of small, randomly oriented, sand-filled channels all indicate a complex system of propagated channels along closely spaced vertical planes (as cleat planes). Instead of one or two extended directions, the hydraulic force used to propagate fractures in the coal is believed to have been diverted several times in slightly different directions during high-pressure pumping. This apparently resulted in numerous short channels rather than in one or two continuous long channels as predicted in the design.

Results of the underground vertical fracture (fig. 4) show a direct correlation between propagated channel direction and joint and cleat orientation. Findings from a previous underground study at TW1 yielded similar results which are shown in figure 9. Although sand-filled channels were not observed at TW1, there is sufficient evidence to indicate that partings, in the coal and roof rock had been opened during drilling, cementing, and early stages of stimulation.

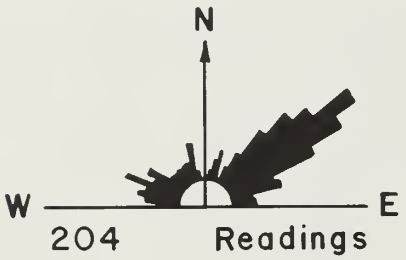

Roof joint and cleat direction in mine area of No.1 Test Well.

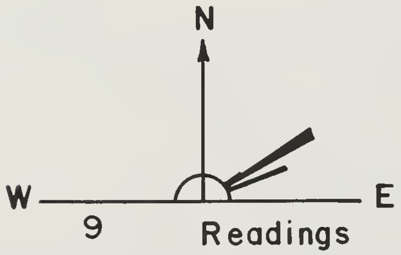

Partings, induced or extended from Test Well No.1 during drilling, cementing, and stimulation.

FIGURE 9. - Comparison of roof joint and cleat directions in mine area with fractures induced or extended during drilling, cementing, and stimulation of TW1.

---

[5] Underlined numbers in parentheses refer to items in the list of references preceding the appendix.

Surface rock joint and coal cleat directions measured in an area overlying both test well locations (3) indicate a close correlation between the surface and underground fracture orientations of figures 4 and 9. Given the observed relationship of induced channel direction with existing underground and surface fracture orientation, it may be concluded that the direction of induced channel development can be predetermined, thus aiding future placement of coal gas wells in the area.

The most obvious explanation for the initial high treatment pressure during stimulation is that fluid was first exposed to hard fireclay, rather than to relatively soft coal. The high pressure that was maintained throughout the treatment is attributed primarily to the high viscosity of the treating fluid, and second, to the flow resistance created by the small openings in the casing.

When injection pressures exceed the overburden pressure horizontal channels may develop. Given a mean specific gravity of 2.5, the overburden pressure gradient should be about 1.06 lb/sq in/vertical ft (2). Since the depth to the coalbed at TW2 is 1,093 ft, horizontal channels could be expected to develop when injection pressures exceeded 1,160 lb/sq in. Treating pressures maintained throughout stimulation of TW2 were in excess of 2,200 lb/sq in gage (fig. 1).

Horizontally oriented sand-filled channels can result from one of two types of rock movement: The compression of rock in the vicinity of the fracture or the flexing and lifting of all or a portion of the overburden (4). The crushed appearance of coal surrounding the horizontal channels suggests that, in this case, compression of rock was the principal mechanism.

The loss of treatment fluid during propagation resulting in the premature drop of sand proppant is believed to have remained at a minimum during stimulation of TW2. Such "sand-outs" are not indicated on the treatment chart (fig. 1). Low fluid loss to the formation is also indicated by the extremely high pressures maintained in the wellbore after pumps were shut down.

Although injection pressures were as high as 2,500 lb/sq in during the stimulation treatment, there was no evidence of induced fractures in the roof or floor rock. Sand proppant and gel found in the wellbore annulus in the floor indicate direct exposure to treatment fluid under high pressure. In preference to fracturing the harder floor rock, fluid moved upward, near the casing, and into the coal zone before extending outward. A roof joint extending directly from the wellbore was believed to have opened sometime after stimulation since it contained no sand or gellike material.

The stimulation design provided for an enzyme-type breaker to considerably reduce the treatment fluid viscosity within a few days. Gel, however, was found around the casing in the roof and floor. The gel in the roof contained no sand and therefore must have been included in the initial fluid pad before the proppant was added. The gel around the bottom of the casing did contain sand and could have been placed there anytime during treatment.

Gel presence may be explained in two ways: Either the breaker was not added to the stimulation fluid as planned, or the breaker was added throughout treatment but chemical factors in both roof and floor prevented gel breakdown. The first explanation is unlikely; the second is more probable considering temperature variation, possible reaction with pipe, cement, etc.

Production

Two major factors responsible for the poor production at TW2 are heavy grease used to preserve downhole water production equipment was not completely removed before installation and repeatedly clogged the pump, and the position of slots below the production zone allowed water to drain from the coalbed but was not conducive to gas drainage. Since water drains to lower horizons of the coalbed, free gas is believed to have accumulated in the upper portions of the coal against the overlying impervious roof rock (shale).

During the first 3 days of successful pumping, TW2 produced no gas, although a significant volume of gas is thought to have accumulated in upper portions of the coalbed around the wellbore. On the fourth day the pump clogged with grease and was dismounted for servicing. The water level rose in the borehole as formation pressures partially recovered. Based on previous Bureau of Mines studies,[6] it may be assumed that free gas pressure equilibrated with the increasing hydraulic head.

The pump was repaired and water production resumed on the eighth day, and after removing approximately 4.3 bbl of water and measuring no flow through gaslines, the well "unloaded," suddenly producing gas at more than 80,000 cu ft/day. This indicates that the free gas pressure around the wellbore had built up during the previous 8 days and that it was suddenly released when pumping caused a disequilibrium pressure state between the coalbed and the wellbore. This sequence of events was repeated several times during the productive life of the well because the pump became inoperative following each unloading.

Gas production stabilized slightly during a 2-week interval prior to underground interception. Given the position of slots in the casing, stabilized gas production could not have been possible while significant amounts of water continued to flow through the coalbed. Waterflow from the well did, in fact, decrease during this period. Since experience with other coal gas wells in the Mary Lee indicates relatively stable waterflow over extended periods (1), it is believed that pumping did not significantly "dewater" the coalbed around the wellbore and that the reduction of water production rate was due to drainage of water into the approaching mine opening.

---

[6] Recent laboratory experiments show conclusively that gas desorption from Mary Lee coal will continue at pressures in excess of 120 lb/sq in gage. Field studies indicate Mary Lee coalbed gas will continue to flow from new wells until a static water level is achieved.

CONCLUSIONS

1. Rotary drilling using roller bit and foam is an effective technique to avoid extensive wellbore and/or coalbed damage.

2. A lightweight, low-fluid-loss cement mixture can reduce cement infiltration into the floor, coal, and roof rock.

3. Density logs may be used to identify zones within coalbeds which may have a substantial influence on the geometry of hydraulically induced channels. Density logs may also be used to identify successfully slotted portions of casing.

4. The hydraulic forces used to stimulate coal may be diverted several times, resulting in numerous short channels rather than one or two continuous long channels. Horizontal channels may be propagated when injection pressure exceeds effective overburden pressure, but because of the relative softness of coal, the principal mechanism leading to horizontal channel development is compression rather than flexing and lifting of the overburden.

5. Underground fracture studies indicate a direct correlation between propagated vertical channel directions and the joint and cleat orientations. There is also a direct relationship between surface and underground fractures which can be used to determine the vertical induced channel direction before stimulation.

6. Gel may not break down sufficiently near the wellbore, because of low temperatures or adverse chemical reaction with casing materials.

7. Highly variable gas flow rates may be attributed to downhole water pump malfunction and/or to the positioning of production openings (slots or perforations) below the productive coal zone.

REFERENCES

1. Elder, C. H., and M. Deul. Degasification of the Mary Lee Coalbed Near Oak Grove, Jefferson County, Ala., by Vertical Boreholes in Advance of Mining. BuMines RI 7968, 1974, 21 pp.

2. Hubbert, M. K., and D. G. Willis. Mechanics of Hydraulic Fracturing. Pres. at Ann. Fall Meeting, Soc. Petrol. Eng., AIME, Los Angeles, Calif., Oct. 14-17, 1956, SPE Reprint No. 5, 1970, pp. 241-256.

3. Murrie, G. W., W. P. Diamond, and S. W. Lambert. Geology of the Mary Lee Group of Coalbeds, Black Warrior Coal Basin, Alabama. BuMines RI 8189, 1976, 49 pp.

4. Perkins, T. K., and L. R. Kern. Widths of Hydraulic Fractures. Pres. at 36th Ann. Fall Meeting, Soc. Petrol. Eng., AIME, Dallas, Tex., Oct. 8-11, 1961, SPE Reprint No. 5, 1970, pp. 265-277.

APPENDIX.--HISTORY OF TEST WELL NO. 2 IN THE MARY LEE COALBED NEAR OAK GROVE, JEFFERSON COUNTY, ALA.

DRILLING

Drilling depth, ft	Bit type	Bit diameter, in	Circulation medium
0 to 10.0	Tricone	8.75	Air.
10 to 857.0	Air percussion	6.25	Air-foam.
857 to 1,150.6	Tricone	6.13	Do.

CASING

Casing, ft	Casing type	Weight, lb/ft	Casing diameter, in
0 to 10.0	Surface pipe	13.0	6.63
0 to 1,150.0	K-55	9.5	4.50

NOTE.--The lower bench of the Mary Lee coalbed is from 1,093.4 to 1,098.4 ft deep. TW2 is in section 35, T 18 S, R 6 W. Drilling was started September 26, 1976, and it was completed October 20, 1976, to a total depth of 1,150.5 ft. The total depth of the casing was 1,150.0 ft.

Cement

Date	October 21, 1976.
Zone cemented	650 to 1,150.5 ft.
Number of sacks	35.
American Petroleum Institute class	A.
Yield	1.44 cu ft per sack.
Mixed weight	13.8 lb/gal.
Additives	2 pct gel.
Do	10 lb gilsonite.
Do	4 lb salt.
Do	2 pct calcium chloride.
Circulating pressure	100 lb/sq in gage.
Displacement pressure	150 lb/sq in gage.
Maximum pressure	150 lb/sq in gage.
Treating rate	1 bbl/min.
Displacement rate	1 bbl/min.
Cement left in casing	15 ft.

Geophysical Logging

Date	October 23, 1976.
Type of log	Natural gamma, gamma density.
Interval logged	0 to 1,132 ft.
Do	1,012 to 1,130 ft.
Do	1,062 to 1,130 ft.
Date	October 27, 1976.
Type of log	Gamma density.
Interval logged	1,080 to 1,106 ft.
Do	1,066 to 1,105 ft.
Do	1,084 to 1,101 ft.
Do	1,082 to 1,105 ft.
Do	1,078 to 1,105 ft.

Slotting the Casing

Date	October 24, 1976.
Type of tool used	Jet slotting.
Abrasive medium	20- to 40-mesh sand.
Interval treated	1,094.4 to 1,098.4 ft.
Perforations, type, spacing	4 slots, 90° apart.

Hydraulic Stimulation

Date	October 24, 1976.
Propping sand	20- to 40-mesh sand, 1,000 lb.
Do	10- to 20-mesh sand, 3,000 lb.
Treatment fluid	Gelled water, 3,500 gal.
Surfactant concentration	3 gal/1,000 gal.
Fluid-loss additive concentration	50 lb/1,000 gal.
Gelling agent concentration	66.7 lb/1,000 gal.
Breaker concentration	2 lb/1,000 gal.
Complexer concentration	0.4 gal/1,000 gal.
Maximum pressure	2,500 lb/sq in gage.
Average pressure	2,400 lb/sq in gage.
Treatment rate, average	8 bbl/min.
Hudraulic horsepower	1,000 hp.

Well Life

Date production equipment installed	November 12, 1976.
Date production began	November 13, 1976.
Date production equipment removed	February 14, 1977.
Date underground interception	February 15, 1977.

☆U.S. GOVERNMENT PRINTING OFFICE: 1978-703-103/58

INT.-BU.OF MINES,PGH.,PA. 23146

622.09
Un3&mo

RI 8297

Bureau of Mines Report of Investigations/1978

Mechanical Properties of Cores Obtained From the Unleached Saline Zone, Piceance Creek Basin, Rio Blanco County, Colo.

DEPOSITORY
NOV 17 1978
UNIV. OF ILL. LIBRARY
AT URBANA-CHAMPAIGN

UNITED STATES DEPARTMENT OF THE INTERIOR

Bureau of Mines

Report of Investigations 8297

MECHANICAL PROPERTIES OF CORES OBTAINED FROM THE UNLEACHED SALINE ZONE, PICEANCE CREEK BASIN, RIO BLANCO COUNTY, COLO.

by

Frank G. Horino and Verne E. Hooker

ERRATA

Please replace pages 13 and 19 with the attached versions.

TABLE 8. - Average physical properties for design purposes for horizons of interest

Horizon	Roof					Pillar				
	σ_c, psi	E × 10^6, psi	S.G.	T_o, psi	Poisson's ratio	σ_c, psi	E × 10^6, psi	S.G.	T_o, psi	Poisson's ratio
R4B:										
Average	11,921	0.88	2.020	1,230	0.29	12,107	0.93	2.068	1,191	0.38
Number of samples	17	14	15	12	14	61	61	61	33	59
Standard deviation	±2,574	±0.36	±0.10	±294	±0.09	±2,167	±0.34	±0.09	±356	±0.11
L4B:										
Average	21,798	2.38	2.220	655	0.37	10,056	1.17	2.220	NCT	0.37
Number of samples	1	1	1	1	1	2	2	2	-	2
Standard deviation	-	-	-	-	-	±556	±0.13	±0.02	-	±0.0
R3A:										
Average	15,177	1.67	2.247	1,098	0.26	11,059	1.47	2.134	1,084	0.33
Number of samples	32	32	32	30	33	86	80	84	29	79
Standard deviation	±3,573	±0.71	±0.13	±330	±0.10	±2,886	±0.81	±0.09	±341	±0.13
L3:										
Average	11,214	0.60	2.080	1,061	0.16	15,895	1.44	2.168	1,241	0.32
Number of samples	2	2	2	3	2	28	28	28	25	26
Standard deviation	±492	±0.09	±0.05	±463	±0.12	±4,508	±0.69	±0.15	±244	±0.09

NCT No core tested.

TABLE 9. - Average compressive strengths for the horizons of interest at the various holes based on geologic depths

Hole	R3A	R4B	L4B	L3
29	NCT	NCT	$\overline{x}$ = 13,970, s = 6,791, n = 3	NCT
30	$\overline{x}$ = 7,287, s = 992, n = 4	NCT		NCT
33	$\overline{x}$ = 11,608, s = 513, n = 4	$\overline{x}$ = 9,878, s = 1,000, n = 4	NCT	NCT
34	$\overline{x}$ = 14,410, s = 2,188, n = 7	$\overline{x}$ = 12,566, s = 238, n = 2	NCT	NCT
35	NCT	$\overline{x}$ = 12,237, s = 751, n = 9	NCT	$\overline{x}$ = 14,829, s = 2,260, n = 4
36	$\overline{x}$ = 9,631, s = 3,944, n = 2	$\overline{x}$ = 12,738, s = 1,451, n = 8	NCT	NCT
37A	$\overline{x}$ = 11,290, s = 1,291, n = 7	$\overline{x}$ = 13,105, s = 1,141, n = 6	NCT	NCT
38	$\overline{x}$ = 9,667, s = 1,746, n = 8	$\overline{x}$ = 12,993, s = 1,844, n = 4	NCT	NCT
39	NCT	$\overline{x}$ = 11,351, s = 846, n = 7	NCT	$\overline{x}$ = 16,220, s = 2,959, n = 6
40	$\overline{x}$ = 15,123, s = 1,093, n = 3	NCT	NCT	$\overline{x}$ = 18,584, s = 4,721, n = 12
41	$\overline{x}$ = 13,134, s = 2,979, n = 9	$\overline{x}$ = 13,181, s = 922, n = 6	NCT	NCT
42	$\overline{x}$ = 11,200, s = 2,911, n = 5	NCT	NCT	NCT
43	$\overline{x}$ = 10,510, s = 889, n = 3	NCT	NCT	NCT
44	NCT	NCT	NCT	$\overline{x}$ = 10,904, s = 783, n = 6
45	$\overline{x}$ = 11,443, s = 2,337, n = 13	$\overline{x}$ = 12,822, s = 3,105, n = 6	NCT	NCT
46	$\overline{x}$ = 9,391, s = 1,178, n = 11	$\overline{x}$ = 12,383, s = 4,210, n = 3	NCT	NCT

Where $\overline{x}$ = average compressive strength in psi; s = standard deviation in psi; n = number of samples; NCT = no core tested.

TABLE 13. - Constants for creep equation for samples loaded greater than 35% anticipated ultimate stress

Sample	E, kip/in^2	B, in^3/in kip day	α	C, in^3/in kip day	γ	β
38-120............	2.08×10^3	2.5×10^{-9}	3.17	8.69×10^{-6}	1.0	0.171
38-121............	2.03×10^3	9.7×10^{-9}	3.17	7.89×10^{-6}	1.0	.171
45-177-2..........	1.40×10^3	2.6×10^{-9}	3.17	24.69×10^{-6}	1.0	.171
45-177-5..........	1.32×10^3	21.4×10^{-9}	3.17	19.42×10^{-6}	1.0	.171
45-178-4..........	1.44×10^3	11.1×10^{-9}	3.17	20.19×10^{-6}	1.0	.171

TABLE 14. - Constants for creep equation for samples loaded less than or equal to 35% anticipated ultimate stress

Sample	E, kip/in^2	B, in^3/in kip day	α	C, in^3/in kip day	γ	β
38-120............	2.08×10^3	2.5×10^{-9}	3.17	7.76×10^{-5}	1.0	0.09
38-121............	2.03×10^3	9.7×10^{-9}	3.17	3.98×10^{-6}	1.0	.09
45-177-2..........	1.40×10^3	2.6×10^{-9}	3.17	10.70×10^{-6}	1.0	.09
45-177-5..........	1.32×10^3	21.4×10^{-9}	3.17	2.43×10^{-6}	1.0	.09
45-178-4..........	1.44×10^3	11.1×10^{-9}	3.17	13.7×10^{-6}	1.0	.09

TABLE 15. - Theoretical strain values for sample 45-177-2

t, days	B, $\sigma_0^{3.17} t$ in/in $\times 10^{-6}$	C, $\sigma_0 t^{0.171}$ in/in $\times 10^{-6}$	E, σ_0 in/in $\times 10^{-6}$	ϵ, in/in $\times 10^{-6}$	Displacement, mils	Experimental curve value, mils
0....	0	0	5,053	5,053	9.40	9.40
2....	3	2,051	5,053	7,107	13.22	13.17
4....	6	2,309	5,053	7,368	13.70	13.66
6....	9	2,474	5,053	7,536	14.02	13.95
10....	15	2,700	5,053	7,768	14.45	14.48
18....	26	2,986	5,053	8,068	15.01	15.15
30....	44	3,258	5,053	8,355	15.54	15.58
42....	62	3,451	5,053	8,566	15.93	16.01
50....	73	3,556	5,053	8,682	16.15	16.15
54....	79	3,603	5,053	8,735	16.25	16.20
66....	97	3,729	5,053	8,879	16.51	16.49
70....	103	3,766	5,053	8,922	16.59	16.57
78....	114	3,837	5,053	9,004	16.75	16.67
90....	132	3,932	5,053	9,117	16.96	16.81

Using the highest load level and the largest creep rate of 14.0 μin/in/day from table 12, a 1:1 pillar 20 ft high, loaded at 60% of breaking strength, would have a total displacement of 24.5 in in a time span of 20 years as shown in the following:

$$\text{displacement} = 14.0 \times 10^{-6} \times (20 \times 12) \times (20 \times 365) = 24.5 \text{ in.}$$

Report of Investigations 8297

Mechanical Properties of Cores Obtained From the Unleached Saline Zone, Piceance Creek Basin, Rio Blanco County, Colo.

By Frank G. Horino and Verne E. Hooker

March 3 1849

UNITED STATES DEPARTMENT OF THE INTERIOR
Cecil D. Andrus, Secretary

BUREAU OF MINES

The work upon which this report is based was done under a cooperative agreement with the Bureau of Mines, U.S. Department of the Interior, and The Superior Oil Company.

This publication has been cataloged as follows:

Horino, Frank G

Mechanical properties of cores obtained from the unleached saline zone, Piceance Creek Basin, Rio Blanco County, Colo. / by Frank G. Horino and Verne E. Hooker. [Washington] : U.S. Dept. of the Interior, Bureau of Mines, 1978.

21 p. : ill., diagrs., maps ; 27 cm. (Report of investigations - Bureau of Mines; 8297)

Based on work done in cooperation with The Superior Oil Company.

Bibliography: p. 21.

1. Oil-shales - Colorado - Piceance Creek Basin. 2. Rock mechanics. 3. Creep of rocks. I. Hooker, Verne E., joint author. II. United States. Bureau of Mines. III. Title. IV. Series: United States. Bureau of Mines. Report of investigations - Bureau of Mines ; 8297.

TN23.U7 no. 8297 622.06173

U.S. Dept. of the Int. Library

CONTENTS

Page

Abstract........ 1
Introduction........ 1
Location........ 2
Physiography and stratigraphy........ 2
Experimental procedure........ 5
    Sample preparation........ 6
    Equipment used........ 6
Tests conducted........ 7
    Uniaxial tests........ 7
    Triaxial tests........ 8
    Brazilian tests........ 8
Analysis of data........ 8
    Statistical analyses........ 8
    Creep data........ 14
Summary........ 20
References........ 21

ILLUSTRATIONS

1. Topographic location of exploratory holes........ 3
2. Approximate area of study in the Piceance Creek Basin--northwestern Colorado........ 4
3. NX cores of solid oil shale and nodular nahcolite........ 6
4. Instrumented NX-size oil shale core........ 7
5. Typical time-dependent curve for oil shale........ 15
6. Dependence of final steady-state creep rate on stress level for L:D ratios of 1:1 and 0.5:1........ 16
7. Elements of creep equation........ 18

TABLES

1. Correlation coefficient, R, of regression analyses........ 9
2. Correlation coefficients for density versus yield with and without 1% nahcolite........ 9
3. Variation of compressive strength with yield variation of 5 gpt........ 10
4. Variation of compressive strength with yield divided into two groups--less than 25 gpt and greater than 25 gpt........ 10
5. Variation of elastic parameters for samples with less than 10% nahcolite and greater than 10% nahcolite........ 11
6. Variation of elastic parameters for samples with less than 3% dawsonite and greater than 3% dawsonite........ 11
7. Average compressive strengths for the horizons of interest using the indicated percentages of nahcolite and dawsonite........ 12
8. Average physical properties for design purposes for horizons of interest........ 13
9. Average compressive strengths for the horizons of interest at the various holes based on geologic depths........ 13

TABLES--Continued

Page

10. Average physical properties of proposed adit based on geologic depths........ 14
11. Average shear strength and coefficient of internal friction for horizons of interest........ 14
12. Creep rates for samples tested........ 17
13. Constants for creep equation for samples loaded greater than 35% anticipated ultimate stress........ 19
14. Constants for creep equation for samples loaded less than or equal to 35% anticipated ultimate stress........ 19
15. Theoretical strain values for sample 45-177-2........ 19

MECHANICAL PROPERTIES OF CORES OBTAINED FROM THE UNLEACHED SALINE ZONE, PICEANCE CREEK BASIN, RIO BLANCO COUNTY, COLO.

by

Frank G. Horino[1] and Verne E. Hooker[2]

ABSTRACT

Drill cores from 18 exploratory holes that were drilled into the unleached saline beds were tested for mechanical properties by the Bureau of Mines. Test cores were primarily selected from zones L4B, R4B, L3, and R3A in the Piceance Creek Basin, Rio Blanco County, Colo. Regression analysis techniques were tried in an attempt to relate kerogen yield or apparent specific gravity to the parameters compressive strength, Young's modulus, and Poisson's ratio. Correlation coefficients were very poor, indicating that this type of analysis was not amenable to these data. Analysis of variance techniques were tried using a division of either greater than or less than 10% nahcolite together with the requirement of less than 3% dawsonite. Results showed that a larger percentage of nahcolite tended to lower the compressive strength and to increase Young's modulus. A second analysis was made using a division of less than 3% dawsonite and greater than 3% dawsonite together with the requirement of less than 1% nahcolite. For this analysis, a larger percentage of dawsonite tended to increase compressive strength, Young's modulus, and Poisson's ratio. Mean compressive strength values were determined for the mining horizons of interest. Average physical properties for design purposes were also determined for the horizons of interest and for a proposed adit based only on logged geologic depths to these horizons. No consideration was given to percentages of nahcolite and dawsonite. Creep data obtained from nahcolite- and dawsonite-rich oil shales provides a best fit to a modified power equation.

INTRODUCTION

The evaluation of resources and development of satisfactory mining systems require knowledge and information on critical rock mechanics parameters. One of these is physical properties of the materials in the proposed mining zones.

---

[1] Geophysicist.

[2] Supervisory geophysicist.

Both authors are with the Denver Mining Research Center, Bureau of Mines, Denver, Colo.

Since very little is known at this time about the properties of the materials in the saline-rich zones of the Piceance Basin, the Bureau of Mines entered into a cooperative agreement with The Superior Oil Company to obtain this information relative to their proposed development and mining location. Rock properties were determined on drill cores obtained from 18 exploratory holes to assist in the development of preliminary mine design criteria. The selection of test cores included dawsonite- and nahcolite-rich oil shale rock materials. The physical properties that were determined and analyzed, and that are presented in this report, include uniaxial compressive strength, triaxial strength, Young's modulus (E), Poisson's ratio, apparent specific gravity, indirect tensile strength, and creep characteristics.

LOCATION

Surface locations of the 18 exploratory holes from which drill core was tested are shown in figure 1. All of these holes lie in T 1 N, R 96 W, and R 97 W, Rio Blanco County, Colo. The approximate area of study lies in the north-central edge of the Piceance Creek Basin as shown in figure 2.

PHYSIOGRAPHY AND STRATIGRAPHY

The Piceance Creek Basin lies in the northwestern part of Colorado in Rio Blanco and Garfield Counties. It covers an area of approximately 1,600 sq mi with the axis of the basin trending northwest-southeast. The plateaus are as much as 1,000 to 4,000 ft above the lowlands. Elevations range from about 6,000 to 9,400 ft above sea level with the greatest relief being shown in the south margin of the area which the Roan Cliffs tower above the valley of the Colorado River (3).[3]

Late Cretaceous to Tertiary beds are exposed in the area. The Mesaverde Group of Late Cretaceous Age is represented by sandstones, shales, and coalbeds. The Mesaverde Group forms prominent benches, ridges, and cliffs. Overlying the Mesaverde Group is the Ohio Creek conglomerate of Paleocene Age and the Fort Union Formation of late Paleocene and early Eocene Age. The Fort Union Formation is composed primarily of a sequence of massive brown and gray, poorly consolidated sandstone beds; gray and brown clay and shale beds; and a few thin coal lenses. Above the Fort Union Formation is the Wasatch Formation of Eocene Age. The Wasatch Formation is composed of bright-colored clays and shales with some sandstones and coalbeds. Above the Wasatch Formation lies the Green River Formation of middle Eocene Age. The Green River Formation is composed largely of kerogen-rich magnesium marlstones, sandstones, siltstones, limestones, and oolite. It is divided into four members, with the Douglas Creek Member being the oldest, followed by the Anvil Points Member, Garden Gulch Member, and finally by the Parachute Creek Member. The Douglas Creek Member is made up of sandstone, limestone, and small amounts of gray shale. This member has only been found in the southern, western, and central parts of the basin. The Douglas Creek Member attains a maximum thickness of 800 ft in the southwestern part of the basin.

---

[3] Underlined numbers in parentheses refer to the items in the list of references at the end of this report.

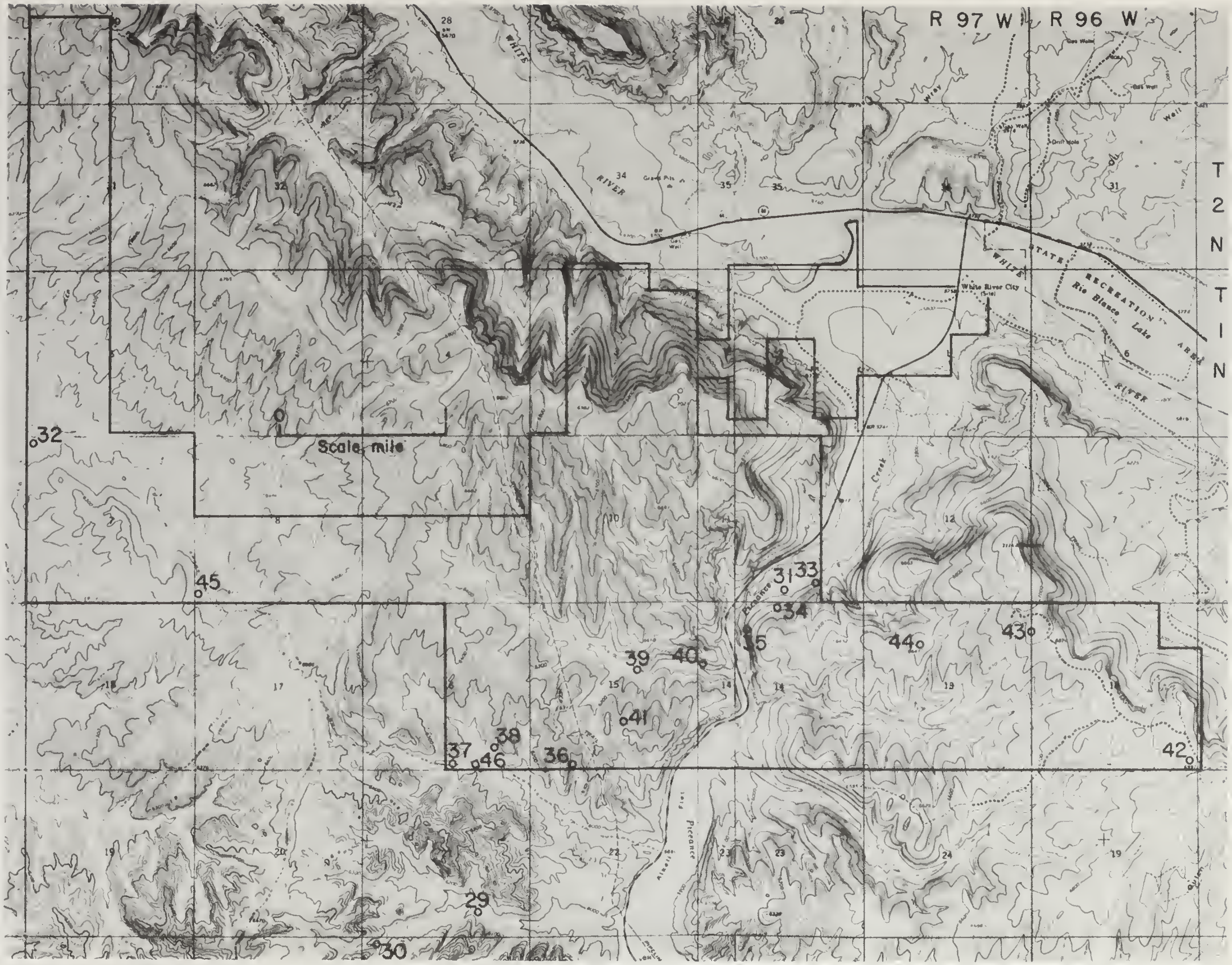
R 97 W
R 96 W
T 2 N
T 1 N
WHITE
RIVER
STATE
RECREATION AREA
Rio Blanco Lake
White River City
Piceance
Creek
Scale, mile
0
32
45
31
33
34
35
39
40
41
36
37
38
46
44
43
42
29
30

FIGURE 1. - Topographic location of exploratory holes.

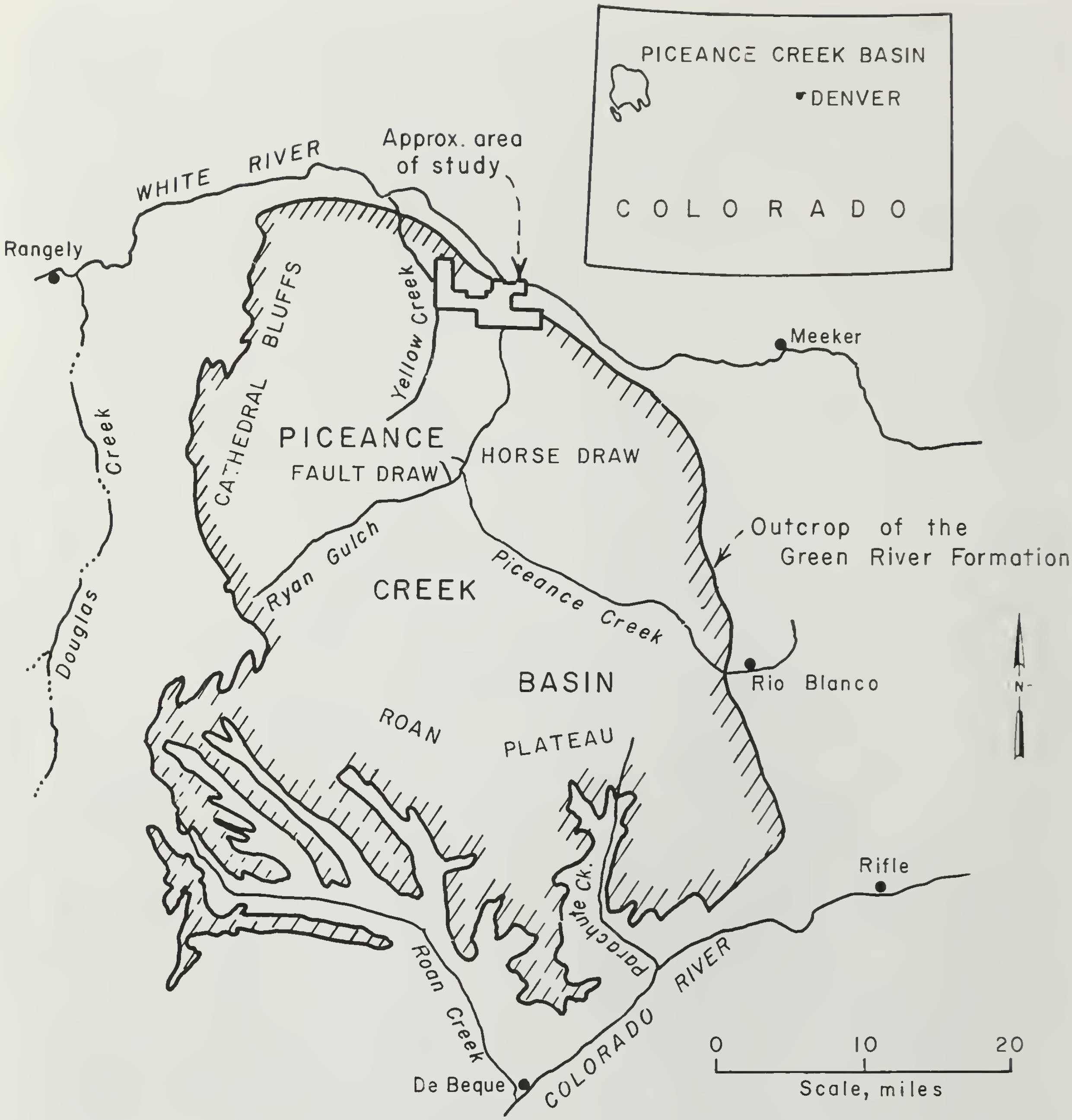
PICEANCE CREEK BASIN
DENVER
COLORADO
Approx. area of study
WHITE RIVER
Rangely
Meeker
Douglas Creek
CATHEDRAL BLUFFS
Yellow Creek
PICEANCE
FAULT DRAW
HORSE DRAW
Ryan Gulch
CREEK
Piceance Creek
Outcrop of the Green River Formation
BASIN
Rio Blanco
N
ROAN
PLATEAU
Parachute Ck.
Roan Creek
Rifle
COLORADO RIVER
De Beque
0
10
20
Scale, miles

FIGURE 2. - Approximate area of study in the Piceance Creek Basin—northwestern Colorado.

The clastic facies of the Douglas Creek, Garden Gulch, and lower Parachute Creek Members are designated as the Anvil Points Member. It is very heterogeneous and is composed of gray shale, gray shale interbedded with brown and gray sandstones, marlstone, siltstone, and limestone. It ranges from 0 to 1,870 ft thick and it is found only in the eastern and southern part of the basin.

The Garden Gulch Member is predominantly made up of shales and marlstones; the marlstones are generally barren of oil. The Garden Gulch Member attains a thickness of 900 ft in the northwestern part of the basin. The lower and upper contacts of the Garden Gulch Member are well-defined on resistivity logs and are known as the Orange and Blue markers. Resistivity logs show these two contacts as low resistivity zones. The Blue marker marks the contact between the Garden Gulch Member and the overlying Parachute Creek Member.

The Parachute Creek Member is the most important member of the Green River Formation as it contains the richest and thickest beds of oil shale. The thickness ranges from over 2,000 ft in the north-central part of the basin to 500 ft around the margins. The Parachute Creek Member also contains numerous thin, analcime-rich tuff beds, finely disseminated dawsonite, nodular nahcolite, and beds of halite and nahcolite (4). The Parachute Creek Member can be divided into zones, ledges, beds, and groups of beds on the basis of yield or weathering characteristics. The Mahogany zone is the richest in kerogen content, and it is the most widespread. The upper boundary of the Mahogany zone is marked by the "A" groove, a 10- to 15-ft-thick sequence of marlstone and lean oil shale. This "A" groove sequence is less resistant to erosion than the kerogen-rich beds below, and it will form slopes on outcrops which resemble grooves. The thickness of the Mahogany zone will range from 100 to 215 ft depending upon whether the section measured is near the margin or in the north-central part of the basin. The lower limit of the Mahogany zone is defined by the "B" groove, a lean oil shale zone. Below the "B" groove, a series of rich zones (R zones) and lean zones (L zones) have been identified by Donnell and Blair. These zones can also be divided into the leached and unleached zones on the basis of whether nahcolite and/or halite have been removed by dissolution or leaching by ground water. The unleached zone or saline zone contains very probable economic deposits of nahcolite and dawsonite (6). The unleached zone ranges from 500 to 1,100 ft thick in the central part of the basin.

The Uinta Formation, which was formerly the Evacuation Creek Member, is composed of marlstones, shales, siltstones, and sandstones which overlie most of the basin. The Uinta Formation, for the most part, rests, conformably on the Parachute Creek Member (3).

EXPERIMENTAL PROCEDURE

Cores were selected by Federal Bureau of Mines personnel and W. I. Duvall, consultant to The Superior Oil Company. Core selection was based primarily on the stratigraphic locations of potential roof rock, pillar rock, and floor rock of the nahcolite- and dawsonite-rich beds in the unleached saline zone. Primary emphasis was placed upon the L4B, R4B, L3, and R3A beds because these were deemed the prospective horizons of interest. Core samples were also obtained in the zone of a proposed pilot adit incline.

In general, specific strength tests were determined from zones relevant to their potential application. For instance, indirect tensile strengths were obtained by the Brazilian technique from roof rock and, where possible, triaxial data were obtained for rock located in potential pillar zones. Apparent specific gravity or weight-volume relationship was determined for each test piece of core. Fischer assays to determine kerogen content and percentages of nahcolite and dawsonite were determined by The Superior Oil Company on all tested cores, and these were provided to the Bureau for use in data analyses. Fischer assay and mineral analyses were made on the actual sample tested and not on a split sample taken over a 1-ft interval.

Sample Preparation

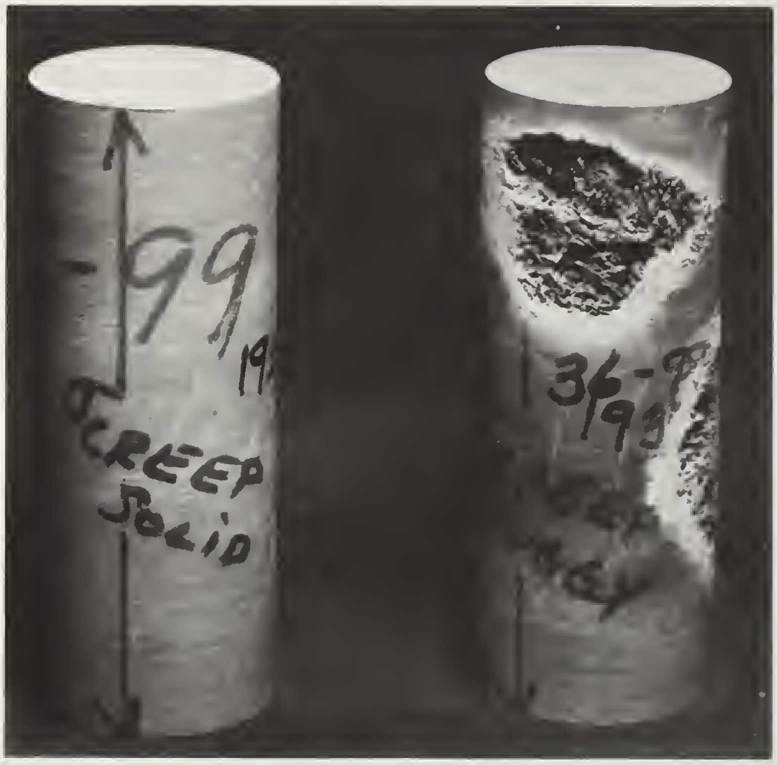

FIGURE 3. - NX cores of solid oil shale and nodular nahcolite.

Samples were cut to the desired lengths and the ends were surface finished with a grinder. End planes were made parallel within a 0.001-in tolerance. Lengths of the cores were kept within a length tolerance of 0.1 in for the length-to-diameter (L:D) ratio specified. Perpendicular tolerance of the end planes to the axis of the specimen was less than 1°. Figure 3 shows NX cores of solid oil shale and nodular nahcolite.

Equipment Used

A materials test system (MTS)[4] stiff testing machine was used for the testing of the cores. This is a closed loop, servocontrolled hydraulic system with a rated capacity of 600,000 lb. This machine can be programed for a constant load rate or constant strain rate.

Linear variable differential transformers (LVDT) were used as the readout device to measure axial as well as lateral deformation under uniaxial tests as shown in figure 4. This physical arrangement allows a determination of Young's modulus (E) and Poisson's ratio (ν).

Triaxial tests were completed using a triaxial cell originally designed by Obert (12), but modified so that LVDT's could be used as the axial deformation readout device.

---

[4] Reference to specific brands is made for identification only and does not imply endorsement by the Bureau of Mines.

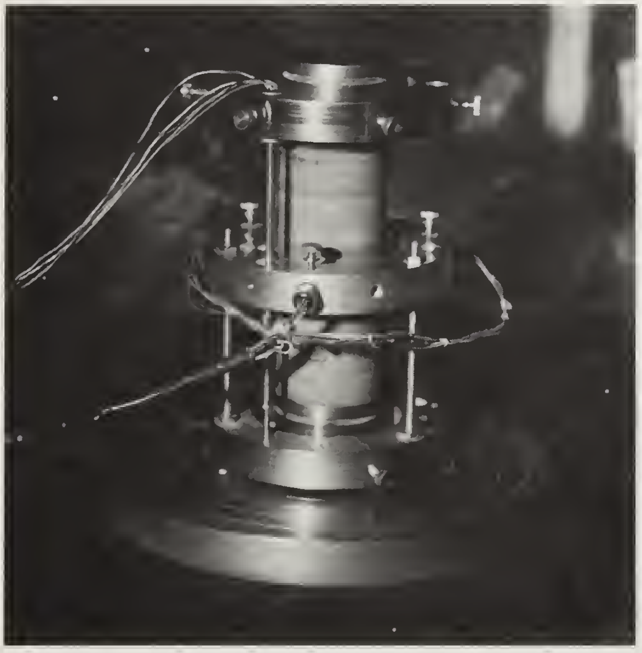

FIGURE 4. - Instrumented NX-size oil shale core (2.125 in diameter X 5.313 in length) with LVDT's to measure both axial and lateral displacements.

TESTS CONDUCTED

Uniaxial Tests

Samples with L:D values of 1:1, 2:1, and 2.5:1 were selected as desirable for these tests. The 2.5:1 samples were tested to reduce the end constraint effects from steel platens. Thus, it was on these specimens that Young's modulus and Poisson's ratio values were determined under uniaxial conditions. L:D ratios of 2:1 and 1:1 were tested to evaluate whether the following formula (13) was applicable:

$$C_o = \frac{C_p}{0.778 + 0.222\left(\frac{D}{L}\right)},$$

where C_o = compressive strength of sample with L:D = 1:1

and C_p = compressive strength of sample with $2 > L:D > 1/3$.

The results indicate that the strength results are valid only if the kerogen yield is the same for samples with different L:D ratios. This would also have to be true for samples containing nahcolite and dawsonite, because the testing indicated that the mechanical properties are dependent upon the percentages of these two minerals. Thus, the effect of the difference in L:D ratio cannot be measured unless a very large number of samples are tested.

The value of Young's modulus and Poisson's ratio were determined between an overburden stress level and a selected stress value of approximately 7,500 psi. This stress value was found to be within the linear portion of the stress-strain curve for the specimen tested. Thus, those elastic parameters are secant values up to approximately 7,500 psi for this rock material.

Triaxial Tests

Triaxial testing was conducted using lateral pressures of 250, 500, 750, 1,000, and 2,000 psi. Values of shear strength (S_o) and the coefficient of internal friction (μ_m) were determined by obtaining a Mohr's envelope using the maximum shear stress (τ_m) and mean normal stress (σ_m) technique that has been described elsewhere (7). It is important to note that the validity of the Mohr's envelope generated and the resulting shear strength and coefficient of internal friction values are dependent upon tests being performed on samples with the same or nearly the same kerogen yield or apparent specific gravity.

Brazilian Tests

Cylindrical specimens were loaded across the diameter with the axis of the core horizontal between the platens of the compression machine. A minimum L:D ratio of 1:2 was used with the ends of the specimen cut perpendicular to the axis; the ends were not finished by grinding. A small 3- by 5-in cardboard was inserted between the specimen and upper platen which contained a spherical seat, and another was placed between the bottom platen and the specimen (11).

This tensile strength, calculated by the following equation gives a value which is usually greater than the direct tensile strength and less than the flexural strength:

$$T_o = \frac{2\ F_c}{\pi DL},$$

where F_c = the failure load,

and D and L are the diameter and length of the specimen.

ANALYSIS OF DATA

Statistical Analyses

Earlier studies of the mechanical properties of oil shale by authors such as East and Gardner (5), Sellers, Haworth, and Zambas (14) at the Anvil Points mine, Garfield County, Colo.; Agapito (1), Horino and Hooker (8) at the Colony mine, Garfield County, Colo.; Horino and Hooker (9) on the Union Oil Co.'s property, Garfield County, Colo.; and Horino and Hooker (10) on White River Oil Shale Corp.'s property in Uintah County, Utah; all clearly indicate a dependence of mechanical properties on the yield in gallons per ton (gpt) for Mahogany zone rock materials. There is an apparent one-to-one correspondence between kerogen yield and apparent specific gravity. The mechanical properties can also be predicted by knowing the apparent specific gravity. Therefore, statistical treatment of the Mahogany zone data can produce predictive equations relating kerogen yield or apparent specific gravity to compressive strength, Young's modulus, and Poisson's ratio.

Selection of The Superior Oil Company's samples was primarily based on the determination of physical properties on the nahcolite and dawsonite zones. Regression analyses were run, but the correlation coefficients were very poor for the saline zone tests as shown in table 1. No acceptable relationships between the control parameters can be concluded.

TABLE 1. - Correlation coefficient, R, of regression analyses

Control parameters	Number of data points	Correlation coefficient, R
Density versus yield..............................	439	0.66
Compressive strength versus density............	184	.39
Compressive strength versus yield..............	173	.21
Compressive strength versus percent-nahcolite...	185	.37
Compressive strength versus percent-dawsonite...	185	.49

An assumption was made that high percentages of nahcolite or dawsonite in the samples may affect the density subsequently giving poor correlation coefficients. Therefore, all samples containing a nahcolite percentage greater than 1% were then excluded and the regression analyses were rerun on data from holes 29, 36, 38, 39, and 45. T-tests performed on the two regressions for each of the five holes showed that there was not a significant difference in the correlation coefficients with nahcolite and without nahcolite; the results are shown in table 2.

TABLE 2. - Correlation coefficients for density versus yield with and without 1% nahcolite

Hole	Sample size	Correlation coefficient with nahcolite	Sample size	Correlation coefficient without nahcolite
29..........	32	0.778	27	0.784
36..........	15	.682	10	.784
38..........	40	.253	31	.274
39..........	41	.712	35	.691
45..........	41	.917	36	.931

Analysis of variance techniques (2) were used to determine if yield, percent-nahcolite, and percent-dawsonite had any effect on the compressive strength, Young's modulus, and Poisson's ratio for the saline zone materials.

The following tabulation shows the format used to show the F-statistics with a high significance level by asterisks.

	Indicated by:[1]
$0.01 < \text{significance level} \leq 0.05$	*
$.001 < \text{significance level} \leq .01$	**
$\text{significance level} \leq .001$	***

---

[1] No asterisks are printed for significance levels > 0.05.

The higher the "F" ratio, the lower the probability that an error will be made in accepting the hypothesis that the two variances came from the same population. Thus, three asterisks would indicate that the two variances came from different populations.

For the effect of kerogen yield, the samples were grouped as indicated in table 3. Only samples with less than 3% dawsonite and less than 10% nahcolite were used. The values of these percentages were determined by trial and error until it became apparent that these percentages represented significant changes for the parameters sought. The results of table 3 with an F ratio of only 1.92 would indicate no significant difference with the yield divided as given. However, if the yield is divided into only two divisions, less than 25 gpt and greater than 25 gpt, a significant difference is obtained as shown in table 4.

TABLE 3. - Variation of compressive strength with yield variation of 5 gpt

Yield, gpt	Average compressive strength, psi	Standard deviation, psi	Number of samples
Less than 15............	13,202	3,814	14
15 to 20................	14,871	4,476	11
20 to 25................	13,472	2,955	15
25 to 30................	12,942	3,022	17
30 to 35................	10,885	2,167	11
35 to 40................	11,458	2,394	10
Greater than 40.........	12,989	1,155	6

NOTE.--F ratio for one-way analysis of variance = 1.92 and significance level = 0.09.

TABLE 4. - Variation of compressive strength with yield divided into two groups--less than 25 gpt and greater than 25 gpt

Yield	Average compressive strength, psi	Standard deviation, psi	Number of samples
Less than 25 gpt........	13,762	3,690	40
Greater than 25 gpt.....	12,097	2,590	44

NOTE.--F ratio for one-way analysis of variance = 5.82 and significance level = 0.018*.

Nahcolite was grouped as indicated in table 5 for samples with less than 3% dawsonite and regardless of kerogen yield. There is a significant difference in the means of the two groups for the compressive strengths and Young's modulus, but not for Poisson's ratio. A greater percentage of nahcolite in the sample tended to give a lower compressive strength and a larger Young's modulus.

TABLE 5. - Variation of elastic parameters for samples with less than 10% nahcolite and greater than 10% nahcolite

Elastic parameter	Less than 3% dawsonite		Analysis of variance	
	Less than 10% nahcolite	Greater than 10% nahcolite	F ratio	Significance level
Average compressive strength...psi..	12,702	9,379	21.80	0.00001 ***
Standard deviation............psi..	3,164	1,599		
Number of samples..................	94	21		
Average Young's modulus x 10^6..psi..	1.06	2.38	67.77	0.00000 ***
Standard deviation............psi..	0.52	1.03		
Number of samples..................	87	20		
Average Poisson's ratio............	0.33	0.32	0.08	1.00000
Standard deviation.................	0.14	0.10		
Number of samples..................	87	19		

Dawsonite was grouped as indicated in table 6. The nahcolite content for all data values was less than 1%. Analysis of variance indicated a significant difference in the means of the two groups for all three elastic parameters. A higher dawsonite content in the sample tended to give a greater compressive strength, greater Young's modulus, and a greater Poisson's ratio.

TABLE 6. - Variation of elastic parameters for samples with less than 3% dawsonite and greater than 3% dawsonite

Elastic parameter	Less than 1% nahcolite		Analysis of variance	
	Less than 3% dawsonite	Greater than 3% dawsonite	F ratio	Significance level
Average compressive strength...psi..	12,821	15,398	18.75	0.0000 ***
Standard deviation............psi..	3,245	3,819		
Number of samples..................	86	57		
Average Young's modulus x 10^6..psi..	1.10	1.47	11.99	0.00072 ***
Standard deviation............psi..	0.54	0.69		
Number of samples..................	79	57		
Average Poisson's ratio............	0.33	0.37	5.0	0.02700 *
Standard deviation.................	0.13	0.14		
Number of samples..................	79	57		

Further refinement of the data using various restrictions on the percent of nahcolite and dawsonite have been tabulated and these values are shown in table 7 for the horizons of interest.

TABLE 7. - Average compressive strengths for the horizons of interest using the indicated percentages of nahcolite and dawsonite

Horizon	Less than 1% nahcolite		Less than 3% dawsonite	
	Less than 3% dawsonite	Greater than 3% dawsonite	Less than 10% nahcolite	Greater than 10% nahcolite
R4B:				
Average compressive strength..psi..	12,065	12,975	11,764	NCT
Standard deviation............psi..	1,216	2,157	1,169	-
Number of samples.................	6	23	8	-
L3:				
Average compressive strength..psi..	13,185	18,517	13,185	NCT
Standard deviation............psi..	2,768	4,849	2,768	-
Number of samples.................	11	13	11	-
R3A:				
Average compressive strength..psi..	12,207	14,012	11,805	9,671
Standard deviation............psi..	2,767	2,126	3,411	1,508
Number of samples.................	19	4	21	11

NCT No core tested.

To establish the average values of compressive strength, Young's modulus (E), apparent specific gravity, indirect tensile strength (T_o), and Poisson's ratio (ν) for design purposes for the horizons of interest, test values were grouped on the basis of logged geologic depths alone and table 8 was determined. It is to be noted that large standard deviations are evident. This is to be expected in the light of the previous conclusion that physical property values are dependent on percentages of nahcolite and dawsonite. Table 9 is included here to verify that, based on logged geologic depths alone, large differences in compressive strengths for a given horizon do exist and consequently, large standard deviations can be expected. Therefore, design values in table 8 are to be taken as good first approximations only.

The average physical properties of a proposed adit were also determined based only on depth of intersection in certain holes and these results are given in table 10.

TABLE 8. - Average physical properties for design purposes for horizons of interest

Horizon	Roof					Pillar				
	σ_c, psi	E x 10^6, psi	S.G.	T_o, psi	Poisson's ratio	σ_c, psi	E x 10^6, psi	S.G.	T_o, psi	Poisson's ratio
R4B:										
Average	11,921	0.88	2.020	1,230	0.29	12,107	0.93	2.068	1,191	0.38
Number of samples	17	14	15	12	14	61	61	61	33	59
Standard deviation	±2,574	±0.36	±0.10	±294	±0.09	±2,167	±0.34	±0.09	±356	±0.11
L4B:										
Average	21,798	2.38	2.220	655	0.37	10,056	1.17	2.220	NCT	0.37
Number of samples	1	1	1	1	1	2	2	2	-	2
Standard deviation	-	-	-	-	-	±556	±0.13	±0.02	-	±0.0
R3A:										
Average	15,177	1.67	2.247	1,098	0.26	11,059	1.47	2.134	1,084	0.33
Number of samples	32	32	32	30	33	86	80	84	29	79
Standard deviation	±3,573	±0.71	±0.13	±330	±0.10	±1,286	±0.81	±0.09	±341	±0.13
L3:										
Average	11,214	0.60	2.080	1,061	0.16	15,895	1.44	2.168	1,241	0.32
Number of samples	2	2	2	3	2	28	28	28	25	26
Standard deviation	±492	±0.09	±0.05	±463	±0.12	±4,508	±0.69	±0.05	±244	±0.09

NCT No core tested.

TABLE 9. - Average compressive strengths for the horizons of interest at the various holes based on geologic depths

Hole	R3A	R4B	L4B	L3
29	NCT	NCT	$\overline{x}$ = 13,970, s = 6,791, n = 3	NCT
30	$\overline{x}$ = 7,287, s = 992, n = 4	NCT		NCT
33	$\overline{x}$ = 11,608, s = 513, n = 4	$\overline{x}$ = 9,878, s = 1,000, n = 4	NCT	NCT
34	$\overline{x}$ = 14,410, s = 2,188, n = 7	$\overline{x}$ = 12,566, s = 238, n = 2	NCT	NCT
35	NCT	$\overline{x}$ = 12,237, s = 751, n = 9	NCT	$\overline{x}$ = 14,829, s = 2,260, n = 4
36	$\overline{x}$ = 9,631, s = 3,944, n = 2	$\overline{x}$ = 12,738, s = 1,451, n = 8	NCT	NCT
37A	$\overline{x}$ = 11,290, s = 1,291, n = 7	$\overline{x}$ = 13,105, s = 1,141, n = 6	NCT	NCT
38	$\overline{x}$ = 9,667, s = 1,746, n = 8	$\overline{x}$ = 12,993, s = 1,844, n = 4	NCT	NCT
39	NCT	$\overline{x}$ = 11,351, s = 846, n = 7	NCT	$\overline{x}$ = 16,220, s = 2,959, n = 6
40	$\overline{x}$ = 15,123, s = 1,093, n = 3	NCT	NCT	$\overline{x}$ = 18,584, s = 4,721, n = 12
41	$\overline{x}$ = 13,134, s = 2,979, n = 9	$\overline{x}$ = 13,181, s = 922, n = 6	NCT	NCT
42	$\overline{x}$ = 11,200, s = 2,911, n = 5	NCT	NCT	NCT
43	$\overline{x}$ = 10,510, s = 889, n = 3	NCT	NCT	NCT
44	NCT	NCT	NCT	$\overline{x}$ = 10,904, s = 783, n = 6
45	$\overline{x}$ = 11,443, s = 2,337, n = 13	$\overline{x}$ = 12,822, s = 3,105, n = 6	NCT	NCT
46	$\overline{x}$ = 9,391, s = 1,178, n = 11	$\overline{x}$ = 12,383, s = 4,210, n = 3	NCT	NCT

Where $\overline{x}$ = average compressive strength in psi; s = standard deviation in psi; n = number of samples; NCT = no core tested.

TABLE 10. - Average physical properties of proposed adit based on geologic depths

	Compressive strength, psi	Young's modulus x 10^6, psi	Apparent specific gravity	Indirect tensile strength, psi	Poisson's ratio
Adit roof:					
Average..................	17,497	1.95	2.328	1,239	0.33
Number of samples........	10	10	10	11	10
Standard deviation.......	3,220	0.29	0.04	306	0.09
Adit walls:					
Average..................	13,357	1.46	2.155	1,188	0.35
Number of samples........	18	18	18	8	16
Standard deviation.......	2,538	0.79	0.12	273	0.13

The average shear strength values and coefficient of internal friction values are given in table 11 for the horizons of interest from a limited number of tests.

TABLE 11. - Average shear strength and coefficient of internal friction for horizons of interest

Horizon	Shear strength, psi	Coefficient of internal friction
R4B:		
Average........................	3,620	0.420
Number of samples..............	11	11
Standard deviation.............	1,234	0.201
L3:		
Average........................	3,350	0.660
Number of samples..............	7	7
Standard deviation.............	601	0.303
R3A:		
Average........................	3,138	0.406
Number of samples..............	8	8
Standard deviation.............	748	0.123

Creep Data

A series of tests was conducted on core samples from the saline zone with L:D ratios of either 1:1 or 0.5:1 at several stress levels that may be anticipated in the prototype structures.

Because it was recognized that the strain rate is stress-dependent, the same sample was tested at various stress levels. The same sample had to be used to obtain meaningful results because of the ever-changing nature of the bedded materials in a vertical direction. Samples were loaded to a selected load level to simulate the in situ field condition. Deformation of samples was monitored mechanically by three precision dial gages, and an average of the three readings was then used. The testing equipment was kept in an air-conditioned room in which the temperature was kept constant at 74° F. Humidity controls were not available. The gages were read daily and the load was adjusted to offset the creep and the resulting load decrease of approximately 100 to 200 lb daily.

At the outset of the creep testing program, tests were run for only 7 days under a constant load. It appeared as though the sample had reached the secondary creep rate stage. This was later shown to be wrong when a long-term, 90-day test was run on nodular nahcolite. Thus, all subsequent tests were at least 45 days long, or until it was quite apparent that the creep rate was constant. A typical plot is shown in figure 5. Similar curves will be generated if this same sample is retested at different load levels. The only difference will be that the creep rate will be larger as the stress is increased. The results of the testing of some samples are shown in table 12. If the final steady-state creep rate of table 12 is plotted against the stress level for the two L:D ratios of 1:1 and 0.5:1, as shown by figure 6, the larger creep rate with the larger stress level becomes evident. The five samples tested in table 12 (45-178-4, 45-177-5, 45-177-2, 38-120, and 38-121) at three different load levels were analyzed to see if the data would fit the Burger's equation as follows:

$$\epsilon = \frac{\sigma_o}{E} + B\ \sigma_o^{\alpha}\ t + C\ \sigma_o (1 - e^{-\beta t}),$$

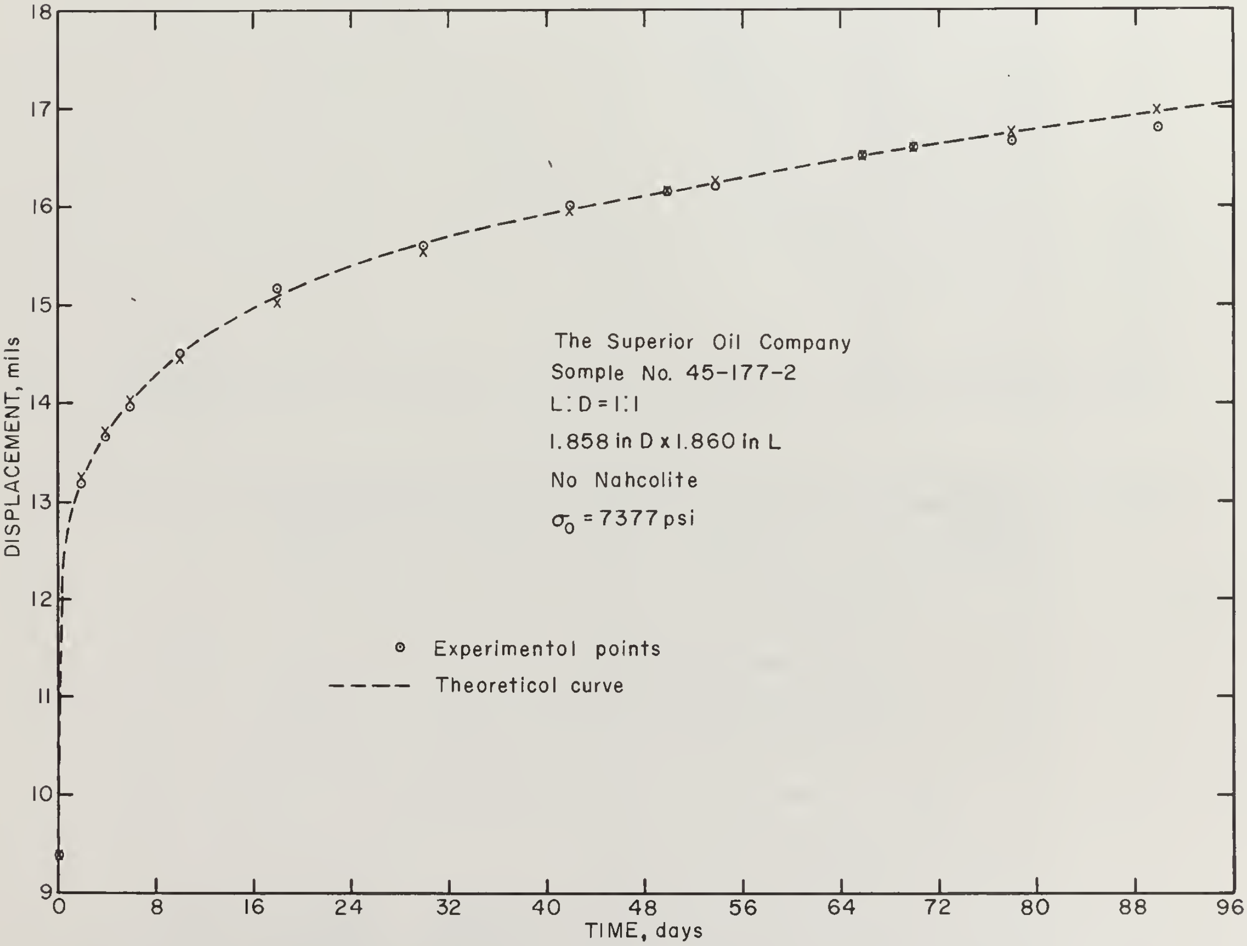

FIGURE 5. - Typical time-dependent curve for oil shale.

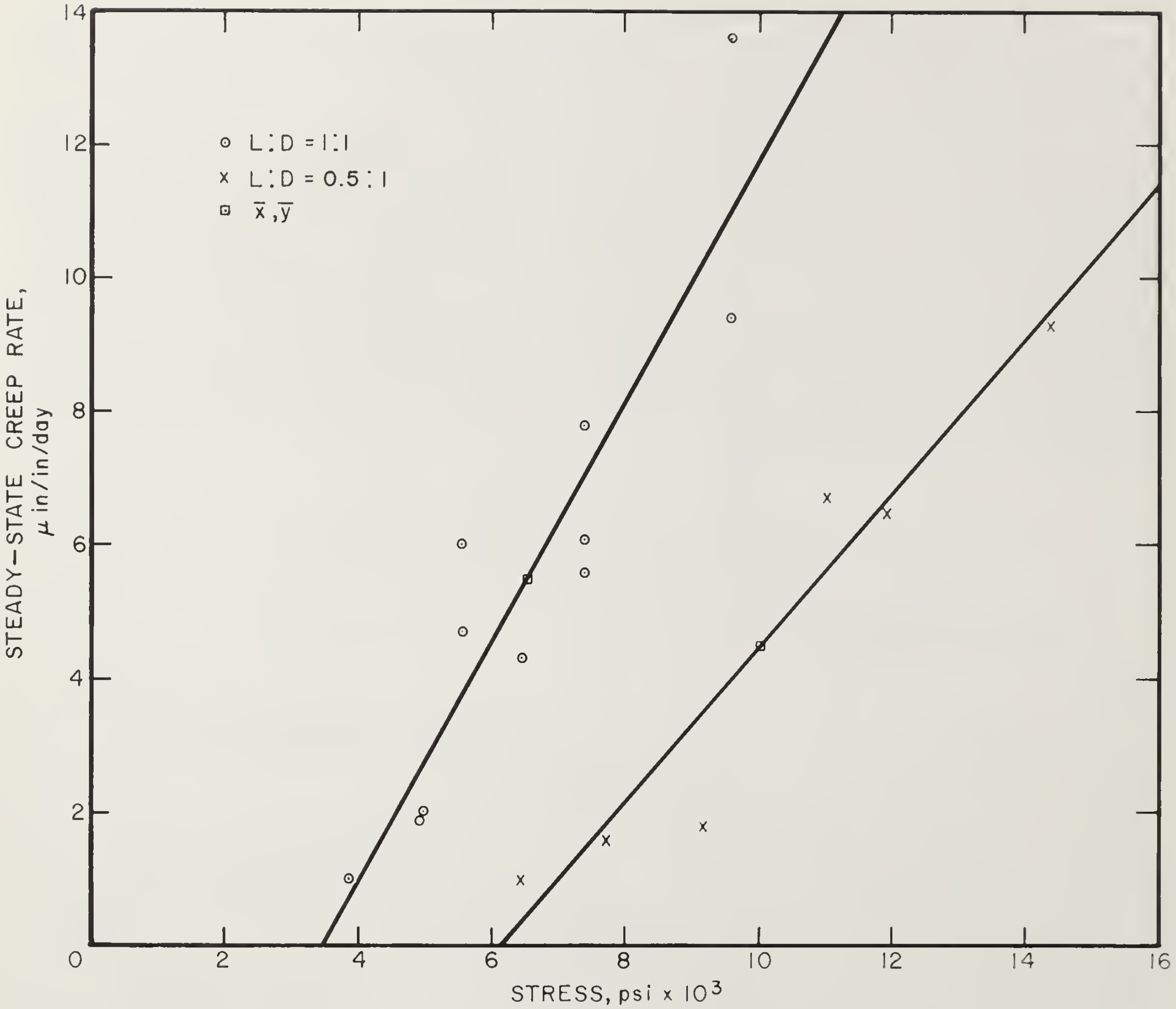

FIGURE 6. - Dependence of final steady-state creep rate on stress level for L:D ratios of 1:1 and 0.5:1.

where ε = strain,

σ_o = constant stress,

t = time of stress application,

$\frac{\sigma_o}{E}$ = instantaneous elastic strain,

$B\,\sigma_o^{\alpha}\,t$ = steady-state creep,

and $C\,\sigma_o(1 - e^{-\beta t})$ = initial or transient creep.

The initial or transient creep term did not conform too well to the curves.

TABLE 12. - Creep rates for samples tested

Sample	Depth, ft	Length of test, days	L:D ratio	Stress, psi	Ultimate stress, percent	Nahcolite, percent	Dawsonite, percent	Final steady-state creep rate, μin/in/day
45-176-2.....	2,408.3 to 2,408.5	90	1:1	5,543	50.8	27.19	2.37	3.5
45-176-4.....	2,408.5 to 2,409.1	90	1:1	6,467	46.4	9.10	1.91	4.3
45-178-2.....	2,412.0 to 2,412.2	90	1:1	5,543	51.2	12.93	2.48	4.7
45-175-2.....	2,405.8 to 2,406.0	90	1:1	7,399	46.5	.38	3.86	7.8
45-178-4.....	2,412.4 to 2,412.65	45	1:1	4,985	29.9	26.34	2.51	2.0
45-178-4.....	2,412.4 to 2,412.65	90	1:1	7,386	44.2	26.34	2.51	5.6
45-178-4.....	2,412.4 to 2,412.65	45	1:1	9,601	57.5	26.34	2.51	9.4
45-177-5.....	2,410.1 to 2,410.3	45	1:1	3,880	33.5	12.53	2.56	1.0
45-177-5.....	2,410.1 to 2,410.3	90	1:1	5,543	47.9	12.53	2.56	6.0
45-177-5.....	2,410.1 to 2,410.3	45	1:1	7,021	60.7	12.53	2.56	13.9
45-177-2.....	2,409.5 to 2,409.7	45	1:1	4,980	31.7	3.51	3.49	1.9
45-177-2.....	2,409.5 to 2,409.7	90	1:1	7,377	46.9	3.51	3.49	6.1
45-177-2.....	2,409.5 to 2,409.7	45	1:1	9,591	61.0	3.51	3.49	13.6
38-120.......	2,000.5 to 2,000.6	45	0.5:1	7,729	30.8	.88	3.22	1.6
38-120.......	2,000.5 to 2,000.6	45	0.5:1	11,042	44.1	.88	3.22	6.7
38-120.......	2,000.5 to 2,000.6	45	0.5:1	14,354	57.3	.88	3.22	9.3
38-121.......	1,002.4 to 1,002.5	32	0.5:1	6,441	25.2	33.37	2.88	1.0
38-121.......	1,002.4 to 1,002.5	45	0.5:1	9,201	36.0	33.37	2.88	1.8
38-121.......	1,002.4 to 1,002.5	45	0.5:1	11,962	46.8	33.37	2.88	6.5

A simple power law decay with time equation $\varepsilon = B\sigma^m t^n$ was tried, but this also did not fit the data too well. Therefore, a modified power equation was then tried as follows:

$$\varepsilon = \frac{\sigma_o}{E} + B\,\sigma_o^{\alpha}\,t + C\,\sigma_o^{\gamma}\,t^{\beta}.$$

The first term is the instantaneous elastic strain, the second term is the steady-state creep, and the third term is the initial or transient creep; σ_o and E must be in kip per square inch, t must be in days, and ε must be in inches per inch. These components of the final strain are shown in figure 7.

The proper analytical treatment of the equation and subsequent log-log plots will determine the constants of the equation. Pooling techniques were tried, and division had to be made for samples loaded at greater than 35% anticipated ultimate stress and less than 35% anticipated ultimate stress. The results are given in tables 13-14.

To test the validity of the equations generated, the values of the constants of sample 45-177-2, table 13, with the stress value of 7.377 kip/in^2, were used to calculate the resulting strains and are shown as the theoretical curve in figure 5. Thus, using the following formula, table 15 was generated:

$$\varepsilon = \frac{7.377}{1.40 \times 10^{3}} + (2.6 \times 10^{-9})(7.377)^{3.17}t + (24.69 \times 10^{-5})(7.377)^{1}\;t^{0.171}.$$

The curve fit of the theoretical to the experimental as shown by figure 5 is excellent. A very cursory examination of the data of table 12 would indicate that the higher the percentage of nahcolite, the less will be the strain rate for like stress levels.

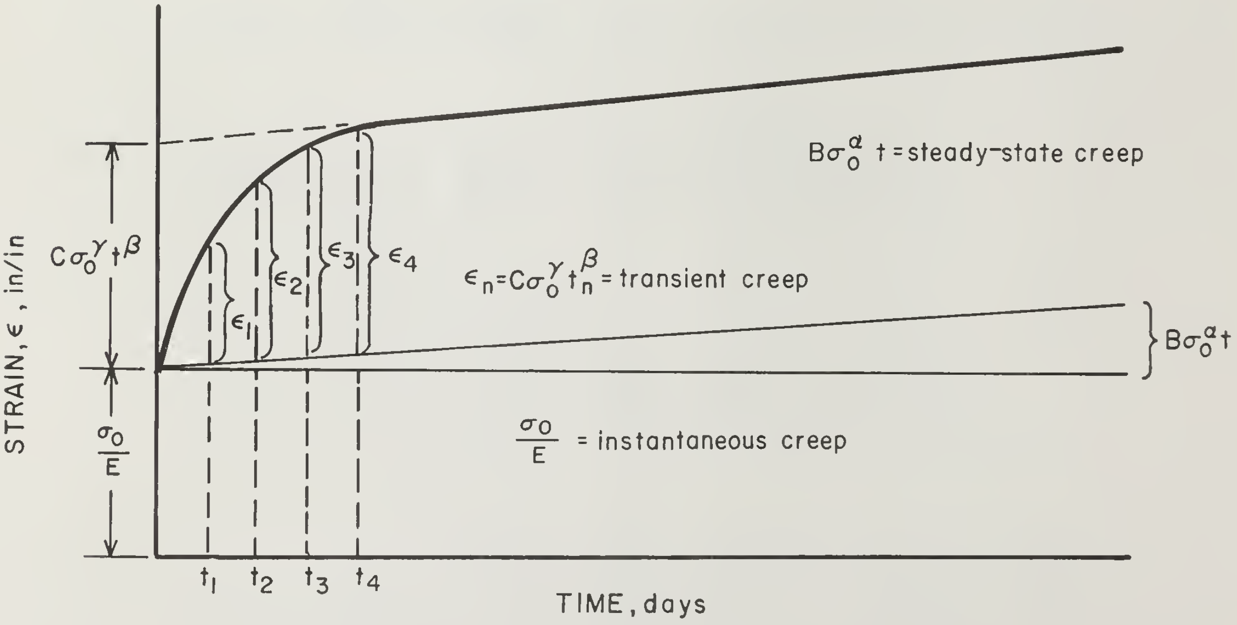
$B\sigma_0^{\alpha}t$ = steady-state creep
$C\sigma_0^{\gamma}t^{\beta}$
ϵ_1
ϵ_2
ϵ_3
ϵ_4
$\epsilon_n = C\sigma_0^{\gamma}t_n^{\beta}$ = transient creep
$B\sigma_0^{\alpha}t$
$\frac{\sigma_0}{E}$
$\frac{\sigma_0}{E}$ = instantaneous creep
STRAIN, ϵ, in/in
t_1
t_2
t_3
t_4
TIME, days

FIGURE 7. - Elements of creep equation.

TABLE 13. - Constants for creep equation for samples loaded greater than 35% anticipated ultimate stress

Sample	E, kip/in^2	B, in^3/in kip/day	α	C, in^3/in kip/day	γ	β
38-120............	2.08×10^3	2.5×10^{-9}	3.17	8.69×10^{-5}	1.0	0.171
38-121............	2.03×10^3	9.7×10^{-9}	3.17	7.89×10^{-5}	1.0	.171
45-177-2..........	1.40×10^3	2.6×10^{-9}	3.17	24.69×10^{-5}	1.0	.171
45-177-5..........	1.32×10^3	21.4×10^{-9}	3.17	19.42×10^{-5}	1.0	.171
45-178-4..........	1.44×10^3	11.1×10^{-9}	3.17	20.19×10^{-5}	1.0	.171

TABLE 14. - Constants for creep equation for samples loaded less than or equal to 35% anticipated ultimate stress

Sample	E, kip/in^2	B, in^3/in kip/day	α	C, in^3/in kip/day	γ	β
38-120............	2.08×10^3	2.5×10^{-9}	3.17	7.76×10^{-5}	1.0	0.09
38-121............	2.03×10^3	9.7×10^{-9}	3.17	3.98×10^{-5}	1.0	.09
45-177-2..........	1.40×10^3	2.6×10^{-9}	3.17	10.70×10^{-5}	1.0	.09
45-177-5..........	1.32×10^3	21.4×10^{-9}	3.17	2.43×10^{-5}	1.0	.09
45-178-4..........	1.44×10^3	11.1×10^{-9}	3.17	$13.7\ \times10^{-5}$	1.0	.09

TABLE 15. - Theoretical strain values for sample 45-177-2

t, days	B, $\sigma_o^{3.17}t$ in/in $\times 10^{-6}$	C, $\sigma_o t^{0.171}$ in/in $\times 10^{-6}$	E, σ_o in/in $\times 10^{-6}$	ϵ, in/in $\times 10^{-6}$	Displacement, mils	Experimental curve value, mils
0....	0	0	5,053	5,053	9.40	9.40
2....	3	2,051	5,053	7,107	13.22	13.17
4....	6	2,309	5,053	7,368	13.70	13.66
6....	9	2,474	5,053	7,536	14.02	13.95
10....	15	2,700	5,053	7,768	14.45	14.48
18....	26	2,986	5,053	8,068	15.01	15.15
30....	44	3,258	5,053	8,355	15.54	15.58
42....	62	3,451	5,053	8,566	15.93	16.01
50....	73	3,556	5,053	8,682	16.15	16.15
54....	79	3,603	5,053	8,735	16.25	16.20
66....	97	3,729	5,053	8,879	16.51	16.49
70....	103	3,766	5,053	8,922	16.59	16.57
78....	114	3,837	5,053	9,004	16.75	16.67
90....	132	3,932	5,053	9,117	16.96	16.81

Using the highest load level and the largest creep rate of 14.0 μin/in/day from table 12, a 1:1 pillar 20 ft high, loaded at 60% of breaking strength, would have a total displacement of 24.5 in in a time span of 20 years as shown in the following:

$$\text{displacement} = 14.0 \times 10^{-6} \times (20 \times 12) \times (20 \times 365) = 24.5 \text{ in.}$$

SUMMARY

In an effort to predict behavioral characteristics of new potential mining materials, static and time-dependent property tests were conducted on NX-size drill cores from 18 exploratory holes located in the northern portion of the Piceance Creek Basin, Colo.

Emphasis during the core sampling and testing was on the saline-rich beds of the Green River Formation, namely R4B and R3A and the accompanying roof horizons L4B and L3. Regression analyses techniques were used in an attempt to relate gpt or apparent specific gravity to compressive strength, Young's modulus, and Poisson's ratio; these correlation coefficients were very poor.

Statistical treatment of the data for samples with less than 3% dawsonite and with a division of less than 10% nahcolite and greater than 10% nahcolite showed that there is a significant difference in the means of the two groups for the compressive strengths and Young's modulus. A greater percentage of nahcolite tends to lower the compressive strength and to increase Young's modulus.

Analysis of data using less than 1% nahcolite and with a division of less than 3% dawsonite and greater than 3% dawsonite showed a significant difference in the means of two groups for all three elastic parameters. A higher percentage of dawsonite tends to increase compressive strength, Young's modulus, and Poisson's ratio.

Average physical properties for design purposes for the horizons of interest and for the proposed adit are given based only on the logged geologic depths. No consideration is given for the percentages of nahcolite and dawsonite and thus, large standard deviations are the result. However, the values should be useful for first approximations for preliminary mine design.

Creep tests indicated that the amount of creep is stress-dependent and that the larger stress levels produce the greater creep rate. Attempts were made to fit the data to both the Burger's equation and the simple power law equation. The data did not fit these models; therefore, a modified power equation was used and constants of this equation were determined. These data should be useful in preliminary mine design criteria and in the evaluation of rock structure problems.

REFERENCES

1. Agapito, J. F. T. Pillar Design in Competent Bedded Formations. Ph. D. Thesis 1485, Colorado School of Mines, Golden, Colo., 1972, 195 pp.

2. Dixon, W. J., and F. J. Massey. Introduction to Statistical Analysis. McGraw-Hill Book Co., Inc., New York, 2d ed., 1957, pp. 209-220.

3. Donnell, J. R. Tertiary Geology and Oil Shale Resources of Piceance Creek Basin Between the Colorado and White Rivers, Northwestern Colorado. U.S. Geol. Survey Bull. 1082-L, 1961, pp. 834-891.

4. Donnell, J. R., and R. W. Blair, Jr. Resource Appraisal of Three Rich Oil-Shale Zones in the Green River Formation, Piceance Creek Basin, Colorado, and Uinta Basin, Utah. Colorado School of Mines Quarterly, v. 65, No. 4, 1970, pp. 73-87.

5. East, J. H., Jr., and E. D. Gardner. Oil-Shale Mining, Rifle, Colo., 1944-56. BuMines Bull. 611, 1964, p. 40.

6. Hite, R. J., and J. R. Dyni. Potential Resources of Dawsonite and Nahcolite in the Piceance Creek Basin, Northwest Colo. Colorado School of Mines Quarterly, v. 62, No. 3, July 1967, pp. 591-604.

7. Horino, F. G., and M. L. Ellickson. A Method for Estimating Strength of Rock Containing Planes of Weakness. BuMines RI 7449, 1970, 29 pp.

8. Horino, F. G., and V. E. Hooker. The Mechanical Properties of Oil Shale and In Situ Stress Determinations Colony Mine. Denver Mining Research Center, Denver, Colo., Prog. Rept. 10001, December 1971, 17 pp.

9. _____. The Mechanical Properties of Oil Shale, Union Oil Co. of Calif., Garfield County, Colo. Denver Mining Research Center, Denver, Colo., Prog. Rept. 10015, April 1976, 14 pp.

10. _____. The Mechanical Properties of Oil Shale, White River Oil Shale Corp., Uintah County, Utah. Denver Mining Research Center, Denver, Colo., Prog. Rept. 10014, June 1976, 15 pp.

11. Mitchell, N. B. The Indirect Tension Test for Concrete. Mater. Res. Std., v. 1, No. 10, 1961, pp. 780-788.

12. Obert, L. An Inexpensive Triaxial Apparatus for Testing Mine Rock. BuMines RI 6332, 1963, 10 pp.

13. Obert, L., and W. I. Duvall. Rock Mechanics and the Design of Structures in Rock. John Wiley & Sons, Inc., New York, 1967, p. 232.

14. Sellers, J. B., G. R. Haworth, and P. G. Zambas. Rock Mechanics on Oil Shale Mining. Trans. AIME, v. 252, June 1972, pp. 222-232.

INT.-BU.OF MINES,PGH.,PA. 23162

U.S. GOVERNMENT PRINTING OFFICE: 1978-703-103/50

622.09
Un32mo

RI 8298

Bureau of Mines Report of Investigations/1978

The Library of the
NOV 21 1978
University of Illinois
at Urbana-Champaign

Effects of Time Between Exposure and Support on Mine Roof Stability, Bear Coal Mine, Somerset, Colo.

UNITED STATES DEPARTMENT OF THE INTERIOR

Report of Investigations 8298

Effects of Time Between Exposure and Support on Mine Roof Stability, Bear Coal Mine, Somerset, Colo.

By Daryl E. Radcliffe and Raymond M. Stateham

March 3 1849

UNITED STATES DEPARTMENT OF THE INTERIOR
Cecil D. Andrus, Secretary

BUREAU OF MINES

This publication has been cataloged as follows:

Radcliffe, Daryl E
Effects of time between exposure and support on mine roof stability, Bear coal mine, Somerset, Colo. / by Daryl E. Radcliffe and Raymond M. Stateham. [Washington] : U.S. Dept. of the Interior, Bureau of Mines, 1978.

13 p. ; 27 cm. (Report of investigations - Bureau of Mines ; 8298)

Bibliography: p. 13.

1. Coal mines and mining - Safety measures. 2. Mine timbering. 3. Rock mechanics. I. Stateham, Raymond M., joint author. II. United States. Bureau of Mines. III. Title. IV. Series: United States. Bureau of Mines. Report of investigations - Bureau of Mines ; 8298.

TN23.U7 no. 8298 622.06173
U.S. Dept. of the Int. Library

CONTENTS

Page

Abstract.... 1
Introduction.... 1
Acknowledgments.... 2
General considerations.... 2
Instrumentation.... 3
Procedures.... 7
Data.... 8
    Data acquisition.... 8
    Data treatment.... 8
Results.... 9
Continuing study.... 12
References.... 13

ILLUSTRATIONS

1. Mine location map.... 3
2. Bear mine plan.... 4
3. Test area plan.... 4
4. Vertical-displacement gage.... 5
5. Horizontal-strain indicator.... 6
6. Typical gage station.... 7
7. Stations with zero- to 2-hour delay.... 10
8. Stations with 2- to 4-hour delay.... 10
9. Stations with 4- to 12-hour delay.... 10
10. Stations with 12- to 88-hour delay.... 10
11. Average deflection for all time groups.... 10
12. Average deflection, by location.... 11

TABLE

1. Station time delays.... 8

EFFECTS OF TIME BETWEEN EXPOSURE AND SUPPORT ON MINE ROOF STABILITY, BEAR COAL MINE, SOMERSET, COLO.

by

Daryl E. Radcliffe[1] and Raymond M. Stateham[2]

ABSTRACT

The Bureau of Mines studied the displacement of the roof in a portion of the Bear coal mine near Somerset, Colo. Horizontal- and vertical-displacement gages were installed in a five-entry section during normal room-and-pillar mining procedures. Monitoring of the roof continued until this section was mined out. Displacement measurements in combination with known time lapses between mining and bolting operations indicate that once support is achieved, the length of unsupported time does not appear to affect long-term roof stability in the mine under investigation.

INTRODUCTION

Roof falls are responsible for about one-half of all coal mine fatalities. The question of how long a roof can be left unsupported after exposure without influencing the overall stability of the roof is important to both mine planning and safety. It is generally accepted that increasing the time between exposure of the roof by mining operations and installation of permanent support increases the probability of falls of ground from the roof. Currently, the coal mining industry follows a practice of supporting the roof immediately or as soon as possible (within the constraint of practical mining procedures) after mining is complete. In many cases, temporary support is installed and left in place until permanent support is installed in the form of roof bolts. The reported investigation was made as part of the Bureau of Mines ongoing study in ground control and was designed to evaluate the effect of time lapse on the roof of a working section in the Bear mine near Somerset, Colo.

The authors acknowledge that the most valid evidence for a study of this nature would be a statistical investigation of all known roof falls with their respective time intervals between exposure and support. However, it is not feasible to gather enough data in one mine or mining district by recording time lapses for comparison with roof falls in other mines, because few falls occur in any one mine. Therefore, many years would be required to gather enough data for statistical significance. For this reason, it is necessary to make certain basic assumptions regarding roof behavior so that the relationship of stability to time lapse can be evaluated.

---

[1] Civil engineer.
[2] Geophysicist.
Both authors are with the Denver Mining Research Center, Bureau of Mines, Denver, Colo.

The authors have assumed displacement (roof sag) to be indicative of roof failure and realize that the magnitude of this sag can vary from mine to mine without roof falls. It is also realized that in unique situations such as jointed, blocky roofs, sag may increase the stability of the roof (2).[3] However, it is believed that in most coal mines, roof sag can be used as an indicator of impending failure. The validity of this concept has been demonstrated by Stahl (4) in using sag measurements to predict roof falls. Also sag and convergence measurements are commonly used in the industry to indicate instability. Based on these observations, measured roof displacements are used as the basis of failure criteria in this investigation.

Vertical-displacement gages and horizontal-strain indicators were placed in the inside entries and connecting crosscuts of a five-entry section. These gages were read at scheduled intervals from October 1976 to February 1977, at which time the section was mined out. Displacement rates developed from these readings are used as indicators of stability or instability for comparison with known time lapses at the gage locations.

ACKNOWLEDGMENTS

The authors express their gratitude to the Bear Coal Co. and to the supervisory personnel of that mine for the use of the mine and services supplied to the Bureau of Mines during the investigation. Special thanks are extended to William A. Bear, General Superintendent, Bear Coal Co.

GENERAL CONSIDERATIONS

The Bear coal mine is located about 10 miles east of Paonia, Colo., and about 1 mile east of Somerset, Colo., along the North Fork of the Gunnison River and just off Colorado Highway 135 (fig. 1). The mine is in coal seam C of the Somerset coalfield at an elevation of about 5,000 feet above sea level. The C seam, in the region of the Bear mine, ranges in thickness from 4-1/2 to 8-1/2 feet. In the test area, the opening averaged about 7 feet high. The C seam is part of the younger mesaverde coals in the Bowie shale member and is of fair- to good-coking quality. Overlying the coal seam is a layer of shale from 3 to 6 feet thick with numerous slickensided fractures (1). Above the shale is a massive sandstone ranging from 150 to 200 feet thick. The Bear coalbed dips from 3° to 4° to the northeast, and the dominant joint set in the test area strikes northeast-southwest. The face cleat in the coal strikes at about N 69° E and dips 88° to the northwest.

---

[3] Underlined numbers in parentheses refer to items in the list of references at the end of this report.

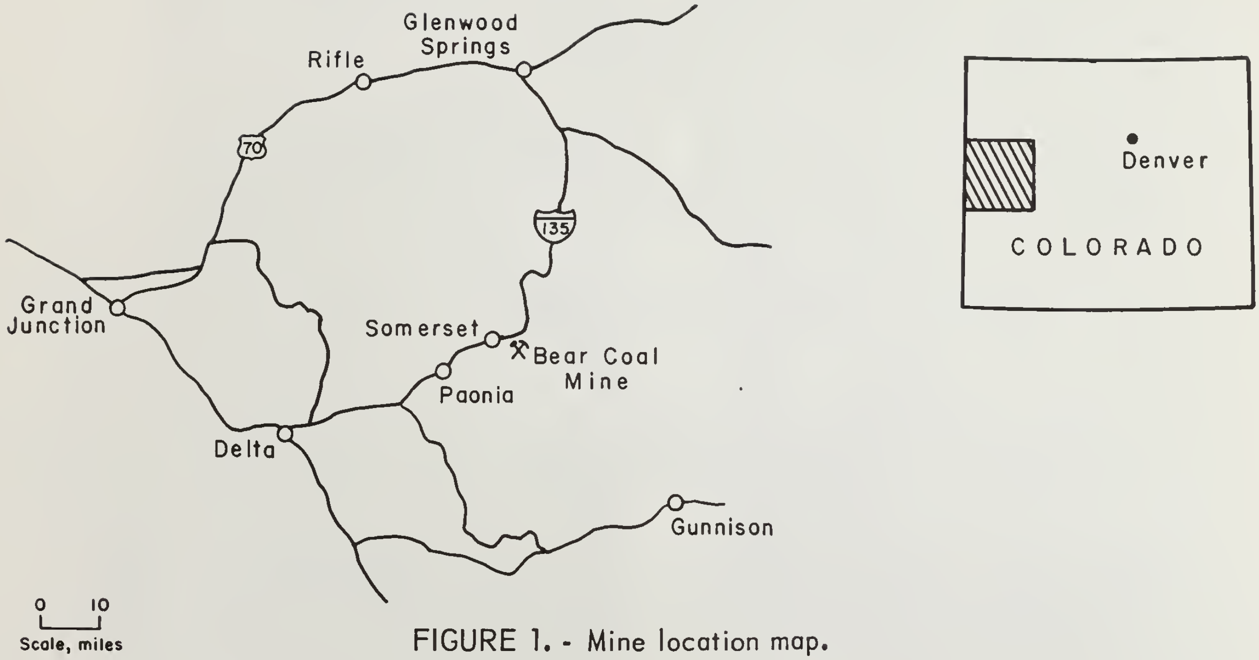

FIGURE 1. - Mine location map.

A plan of the Bear mine as it looked at the time of this investigation is shown in figure 2. The test area was in work section 6 East. The test followed room-and-pillar operations through the section from the time it was opened until it was mined out. Figure 3 is a plan view of the test area. Roof support was achieved by 3/4-inch-diameter by 6-foot resin-grouted bolts at 4 feet on center, with the exception of instrument location A, which was supported with mechanical anchor bolts.

INSTRUMENTATION

Several types of instruments were used in this investigation to determine the extent and location of roof movement. Vertical-displacement gages were installed to measure differential roof displacement during and after mining and support operations. Horizontal-strain indicators were used to determine the existence of horizontal-stress fields that might influence roof stability. In addition to the two types of instruments installed in the roof, a drill hole was provided at each station for use with a stratascope to determine locations and widths of roof separations.

The vertical-displacement gage (fig. 4) consists of four spring clips used to anchor high-strength, prestretched wire at selected depths in a 1-3/8-inch-diameter hole drilled into the roof. The upper spring clip must be placed in an unmoving layer to be used as a reference base for displacement measurements. For this investigation, a hole depth of 7 feet was used. This depth was determined from conversations with mine personnel on the maximum heights of roof falls near the test area. The uppermost spring clip is placed at maximum depth in the hole, and the attached wire will register maximum sag

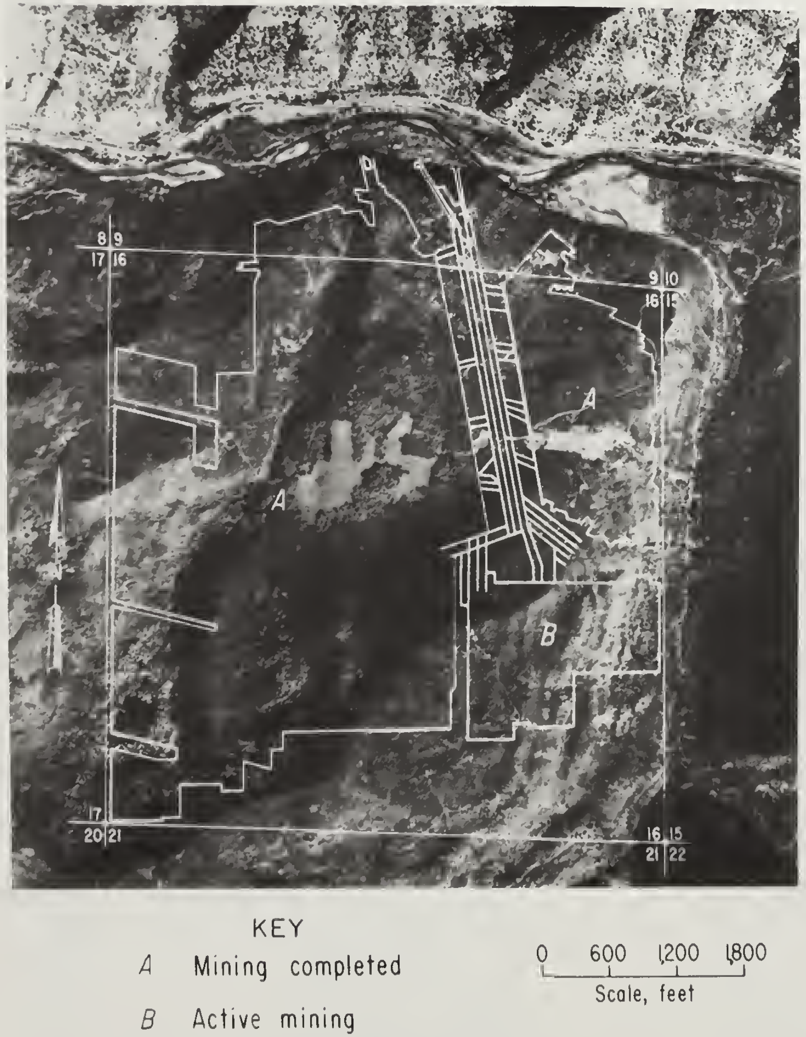
8 9
17 16
9 10
16 15
17
20 21
16 15
21 22
A
A
B
KEY
A Mining completed
B Active mining
0 600 1,200 1,800
Scale, feet

FIGURE 2. - Bear mine plan.

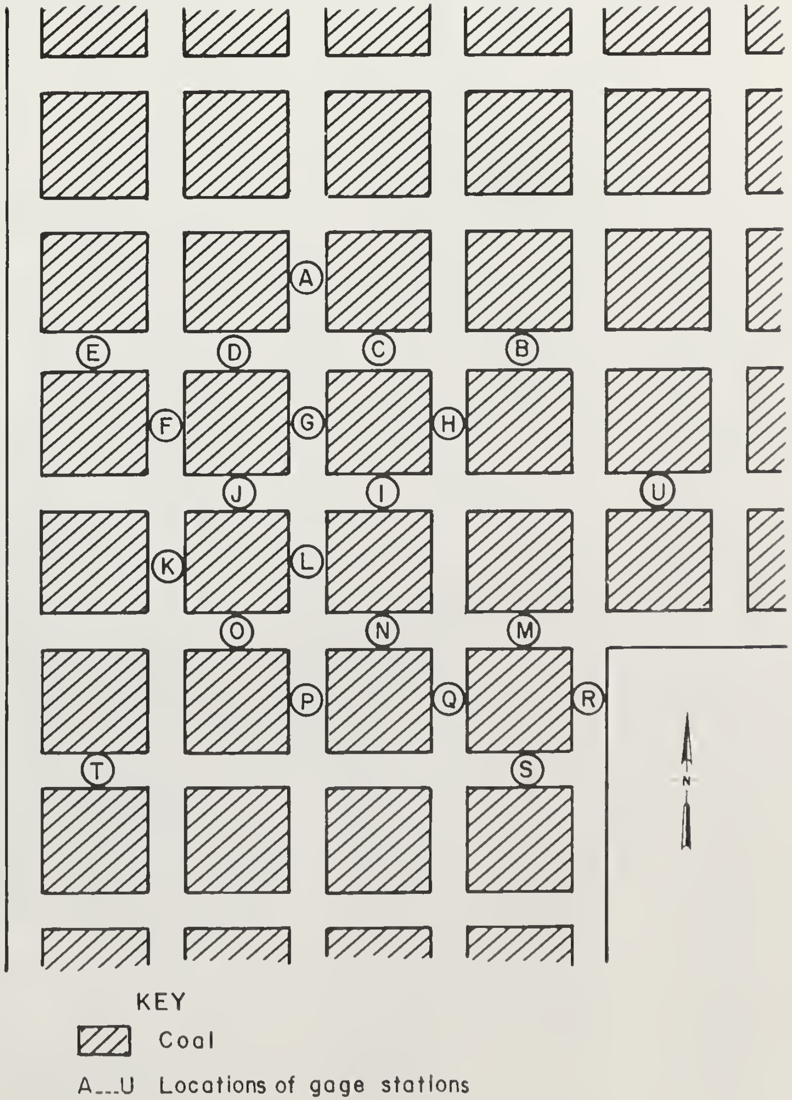
A
B
C
D
E
F
G
H
I
J
K
L
M
N
O
P
Q
R
S
T
U
N
KEY
▨ Coal
A---U Locations of gage stations

FIGURE 3. - Test area plan.

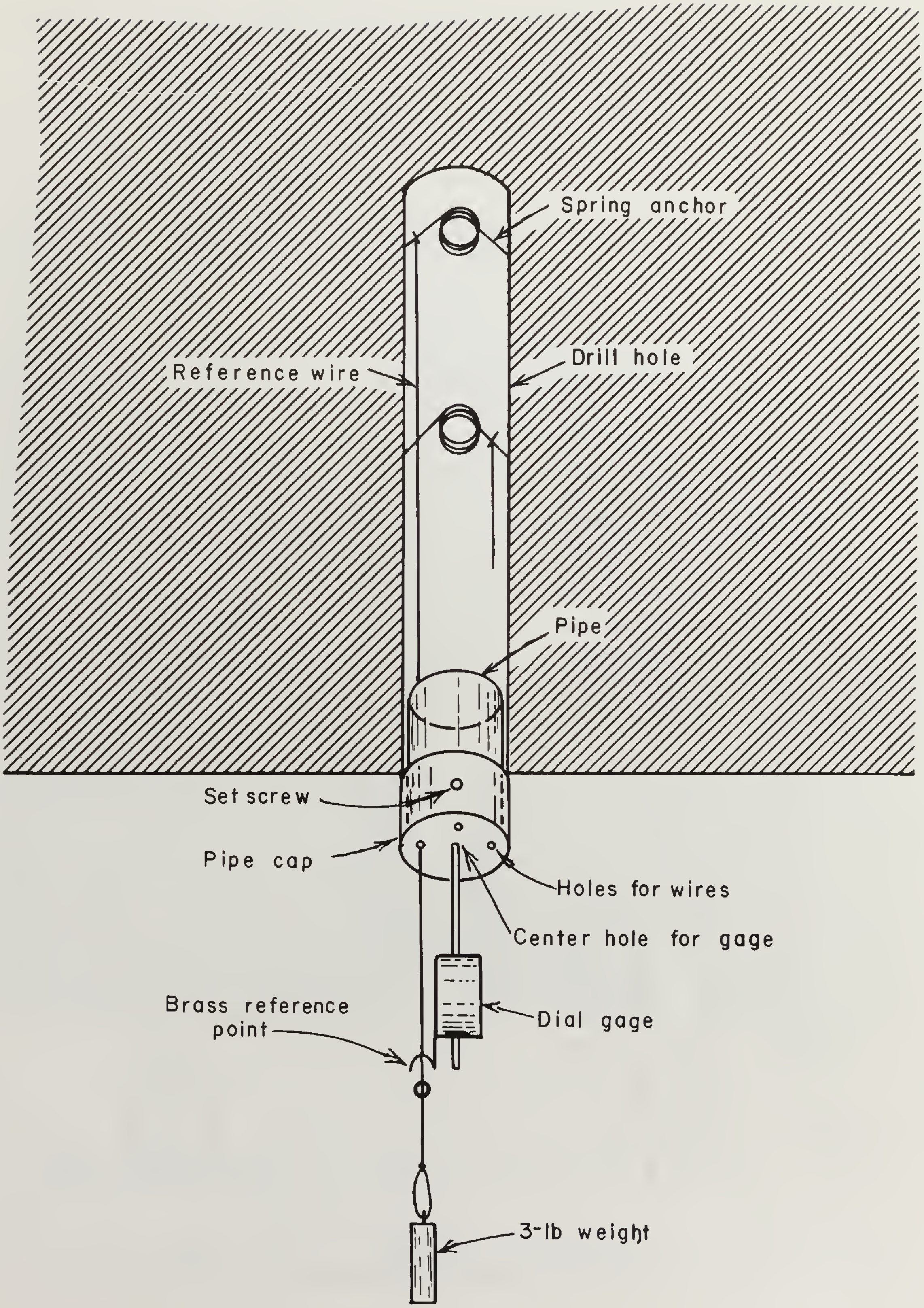
Spring anchor
Reference wire
Drill hole
Pipe
Set screw
Pipe cap
Holes for wires
Center hole for gage
Brass reference point
Dial gage
3-lb weight

FIGURE 4. - Vertical-displacement gage.

for each location. The remaining three spring clips are placed at even intervals or above and below suspected layers if separations are expected. The clips in all gage stations used in this test were placed at 84 inches, 54 inches, 36 inches, and 18 inches into the roof. The wires from the four spring clips run through a 10-inch-long tube anchored in the collar of the drill hole. The wires go through numbered holes in a brass cap on the end of the tube and have small brass fittings that are used as reference points. A loop is made at the end of each wire so that a weight can be attached to maintain constant tension on the wire while readings are taken. Readings are made with a dial indicator placed between the cap and the reference point on each wire.

A horizontal-strain indicator (HORSI) was used to measure horizontal roof strain at most of the instrument stations. A detailed discussion of this instrument has been presented by Panek (3), but for clarity a brief description is presented here. The HORSI gage is shown in figure 5. Two 10-inch-long pipes are anchored into 1-inch-diameter by 8-inch-deep holes in the roof approximately 4 feet apart. Caps are attached to each pipe, and piano wire is run from a solid post on one cap to a plunger on the other. Horizontal movement of one pipe with respect to the other causes the plunger to move in or out, and differential displacement of the roof surface can be measured by placing a dial indicator into the plunger fitting.

Typical instrumentation stations consisted of three vertical-displacement gages, one or two horizontal-strain indicators, and a stratascope hole. Configuration of a typical station is shown in figure 6. A total of 21 gage stations were instrumented for this investigation.

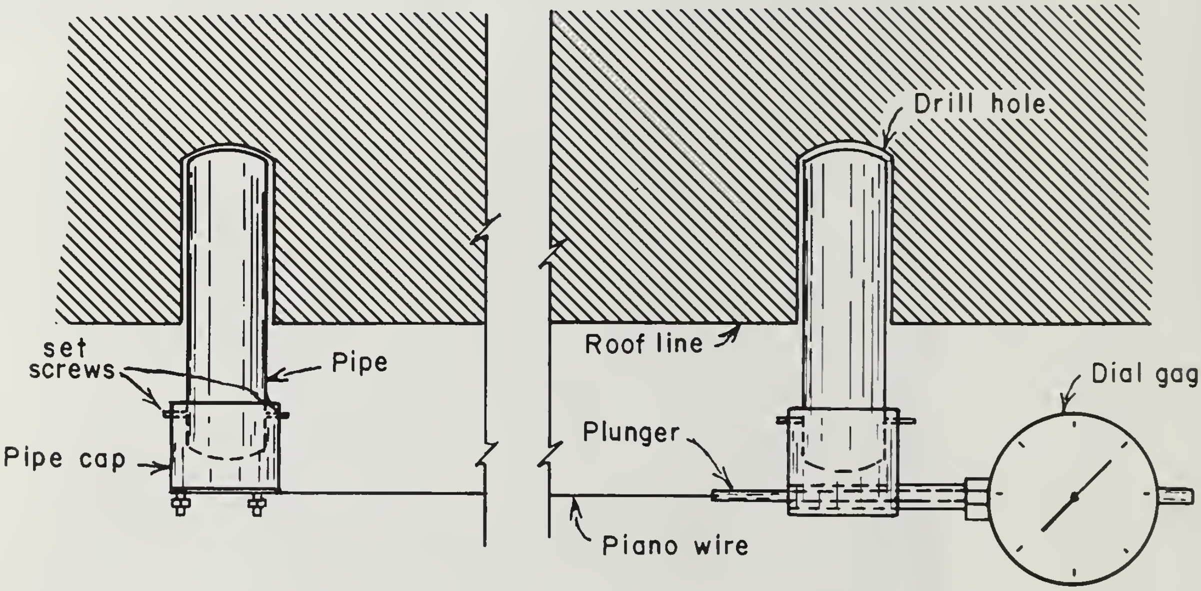

FIGURE 5. - Horizontal-strain indicator (HORSI).

PROCEDURES

Instrument stations were located near the center of the room in both crosscuts and entries to eliminate the effects of intersections on stability. The first displacement gage of each station was placed at the face in the first cut past an intersection. After mining and bolting operations were completed, two holes were drilled as close to the face as possible and past the last row of roof bolts. One hole was for the stratascope and the other for the vertical-displacement gage. This gage was installed and an initial base reading was taken. After the second cut was made into the room, a time delay to support was requested. The length of delay was often dependent on the mining schedule; therefore, a specific time lapse was not always possible if it tended to interfere with the overall mining operation. The length of time to first support ranged from about 15 minutes after mining to 88 hours (table 1). Location of the first displacement gage at each station made it possible to monitor roof deflection of the unsupported area during mining and the subsequent time delay to support.

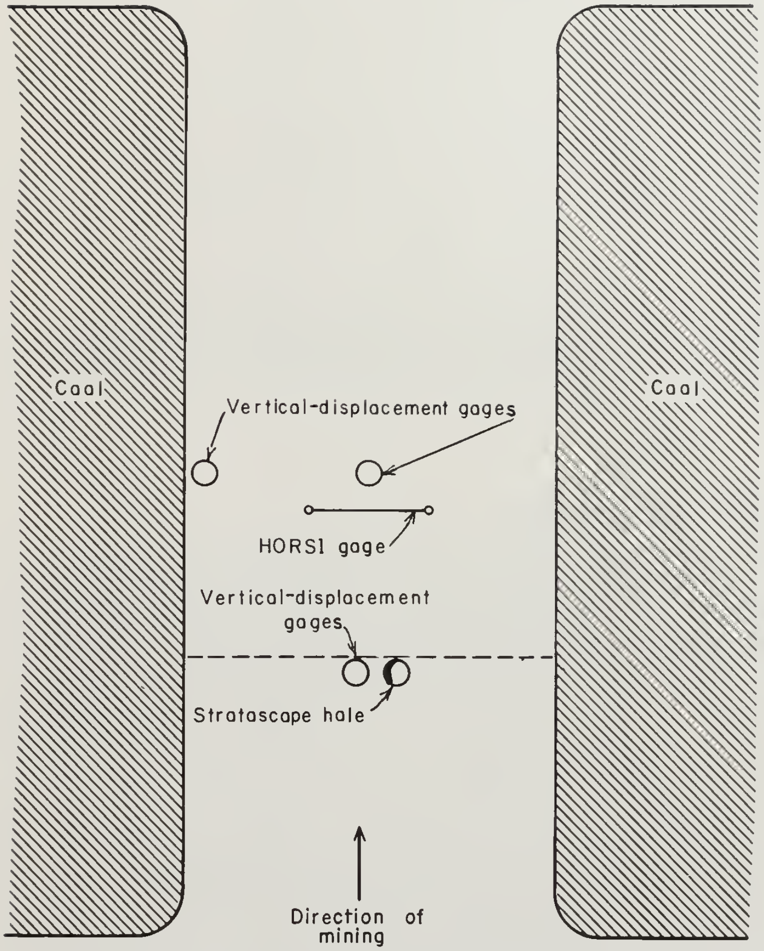

FIGURE 6. - Typical gage station. Dashed line indicates face location when the first gage was installed.

After the second cut was bolted, holes were drilled in the center of the long direction of the cut (this would become the center of the room) for two vertical-displacement gages and one horizontal-strain gage. These gages were to monitor displacement-related roof stability for each time delay. One of the vertical gages and the horizontal gage were located near the center of the narrow dimension (width) of the opening. The other vertical gage was located near the rib to measure any displacement taking place at the sides of the room.

TABLE 1. - Station time delays

Station	Time delay, hours	Station	Time delay, hours
A...........	2.00	L...........	25.00
B...........	88.00	M...........	75.00
C...........	4.00	N...........	2.00
D...........	11.00	O...........	1.00
E...........	4.00	P...........	1.00
F...........	10.00	Q...........	.50
G...........	4.00	R...........	.25
H...........	9.00	S...........	6.00
I...........	7.00	T...........	2.00
J...........	.25	U...........	7.50
K...........	60.00		

Similar procedure was repeated for each station. Stratascope readings were made after installation of the first gage and intermittently through the remainder of the test for each instrument station.

DATA

Data Acquisition

Displacement values are based on differential measurements for each gage from the time of installation to the conclusion of the tests. A data base was established by making daily readings of each station over a 5-week period. This initial data block reflects roof movement as influenced by the various time delays to support and mining activity in adjacent openings. Additional data were collected by making intermittent readings for approximately 3 months after establishment of the data base, at which time the section was mined out.

Readings for both horizontal and vertical displacement were made to the nearest 0.001 inch, with excellent reproducibility of measurements to ±0.002 of an inch. Values of total change in vertical displacement ranged from 0.023 to 1.325 inches, with an average maximum deflection of 0.257 inch. Horizontal-strain gages showed changes from 5 to 125 microinches per inch. (One microinch equals 1×10^{-6} inches.) The average strain value was 84 microinches per inch of roof surface. Because of the low values measured with the horizontal-strain-indicator gages, it was determined that horizontal movement was too low to influence roof stability in this area, and, therefore, these measurements are not used in further analysis.

Data Treatment

For comparison with each of the various time lapse intervals, displacement values for individual gages were plotted as a function of time from installation. Plots of the first gage installed at the working face of each test location allowed comparison of displacement rates from mining to the end of the test. Each wire was plotted separately to show differential settlement of the four anchor points in the roof.

Maximum displacement values for individual instrument stations were then grouped because data tended to fall into four representative time-lapse intervals. The groups of time from exposure to support were zero to 2 hours, 2 to 4 hours, 4 to 12 hours, and 12 to 88 hours. Averages were computed from the readings of the six gages in each of the first three groups and the three gages in the last time group. Plots of the average data values from these sets are shown in figures 7 through 10. Figure 11 shows a combined plot of these values taken from 10 days after installation for comparison of the displacement with initial time effects removed. The displacement value at day 10 was set to zero so that long-term displacement could be evaluated. This breakdown of lapsed time allows comparison of roof movement for individual stations with a common unsupported time interval and also comparison of the combined roof displacement values as affected by the different time-interval sets. Only measurements from the longest reference wire, giving total displacement, were used in averages for these plots.

For comparison of roof stability at the various gage locations in each opening, total displacement data were listed for each gage in each time-interval group. Average values were then combined in plots for face gages (those installed initially at the face), center gages, and gages at the rib (fig. 12).

RESULTS

Analysis of displacement values measured by the different gages yields a similarity in overall trends. In general, the displacement-per-unit time (rate of sag) was high immediately after mining and before bolting took place. After bolting operations, the rate of sag fell to a much slower value and eventually reached a stabilized rate of very little or no increase in displacement.

Comparison of figures 7 through 10 shows that the foregoing trend in roof displacement activity occurred for all of the representative time-lapse intervals. As would be expected, the average amount of total displacement during the unsupported time was greater for the longer time lapses. Gages installed at the working face where the next cut was left unsupported for zero to 2 hours showed an average initial displacement (before bolting) of 0.046 inch. Gages installed where the opening was left unsupported for 2 to 4 hours showed an average initial displacement of 0.058 inch. Gages at openings left unsupported for 4 to 12 hours showed an average initial displacement of 0.127 inch. The greatest average initial displacement of 0.218 inch was measured in gages installed where the opening was left unsupported for more than 12 hours. Even though test areas with longer lengths of unsupported time had more total displacement, no unusual instability was noted in these areas once roof bolting was completed. The rate of sag leveled off to essentially zero in all time-lapse groups within 10 to 20 days after full support. (See fig. 11.)

Gages installed in the test openings after bolting generally showed very little displacement. Plots of the average-displacement rates for center gages and rib gages (fig. 12) show that the test rooms were fairly stable after support.

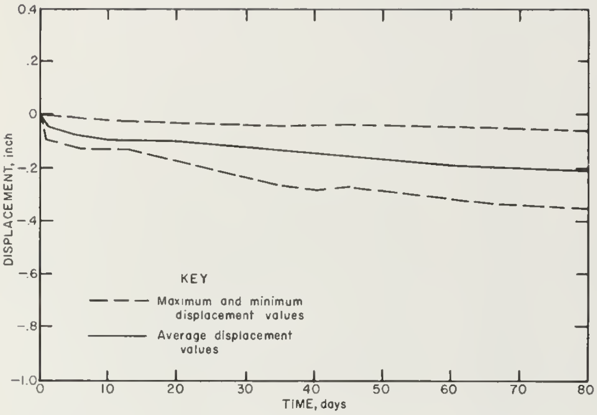

FIGURE 7. - Stations with zero- to 2-hour delay.

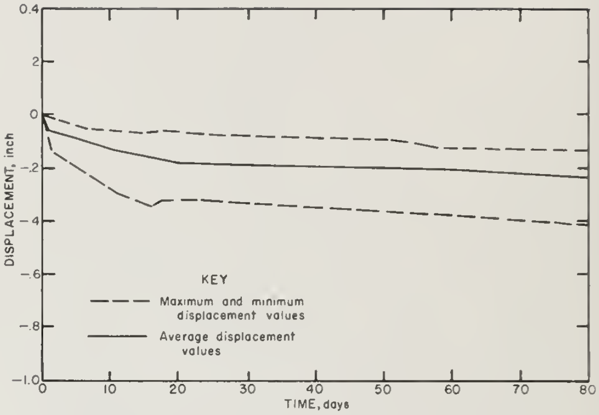

FIGURE 8. - Stations with 2- to 4-hour delay.

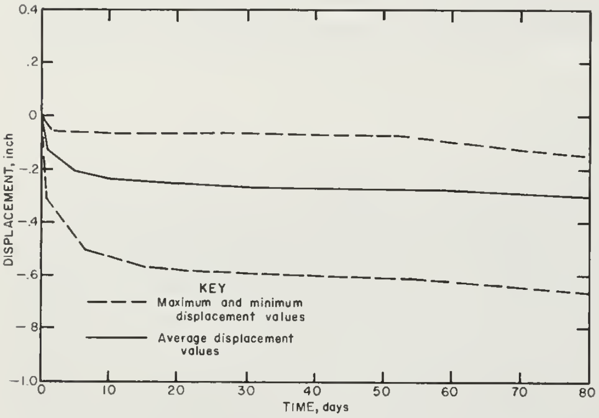

FIGURE 9. - Stations with 4- to 12-hour delay.

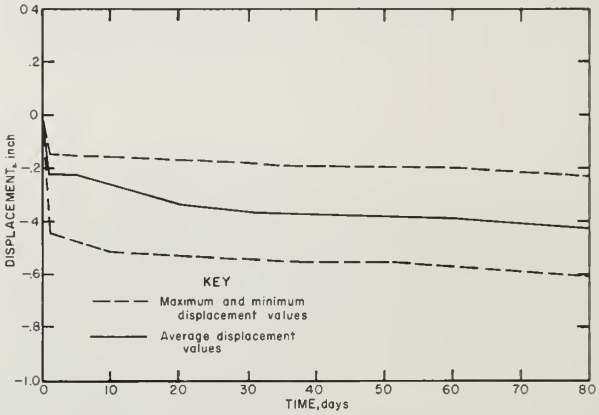

FIGURE 10. - Stations with 12- to 88-hour delay.

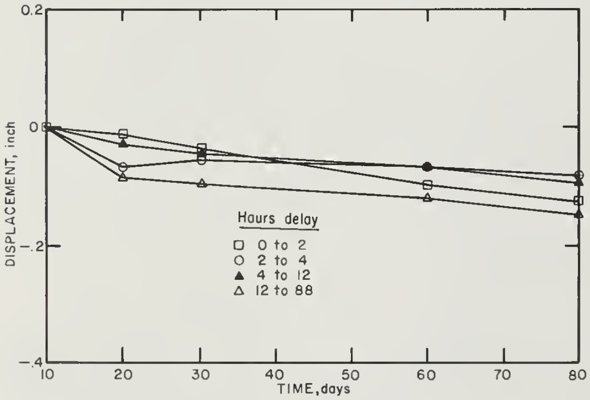

FIGURE 11. - Average deflection for all time groups.

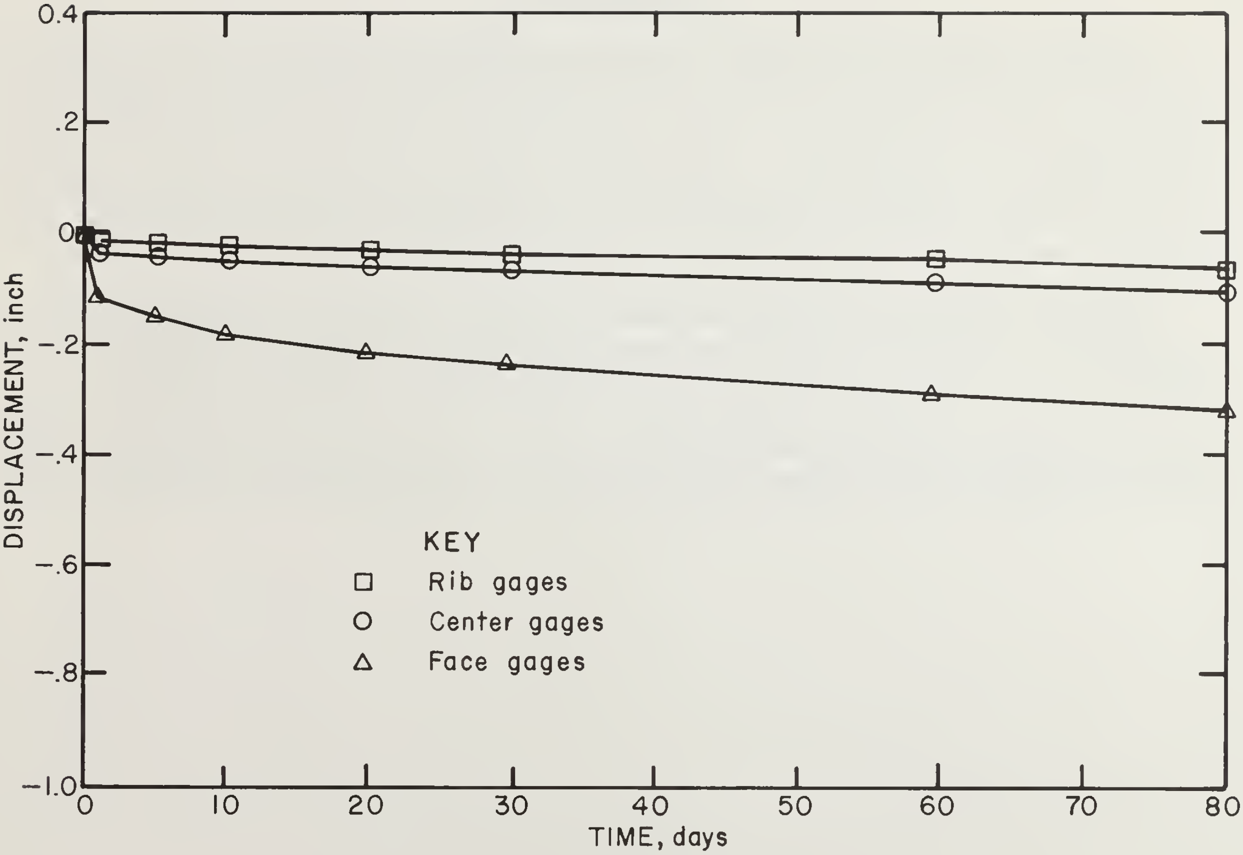

FIGURE 12. - Average deflection, by location.

However, a few of the gages installed after the rooms were bolted did show an unusually large amount of differential displacement from the time of installation. Gage stations A, F, I, L, and P showed more roof sag than average. Station A was left unsupported for 2 hours, but was the only station in the test area using mechanical anchor bolts rather than resin-grouted bolts. This difference in bolt anchoring systems would appear to be an influencing factor in the high deflection of this area. Station F was left unsupported for 10 hours, station I for 7 hours, station L for 25 hours, and station P for 1 hour. Because these stations are from different time-lapse groups, the high rate of deflection does not appear to be related to the time the roof was left unsupported. Further investigation of geology and other factors will be required before the high rate of sag in these areas can be explained.

The largest differential sag measured in the test area was between the 18- and 37-inch roof levels. Stratascope observations near the test stations indicated that differential roof movements were consistent with gage readings. A hairline fracture was noted at the 33-inch level, and a larger separation of 0.06 to 0.25 inch wide was observed at the 19-inch level. A fracture at about the 19-inch level was found to exist throughout most of the test area, widening to a measurable separation near the locations with large displacement values. Other hairline fractures were observed at the 12- and 52-inch levels in some of the test holes.

CONTINUING STUDY

As part of the continuing research associated with the study described in this report, an additional 80 instruments have been installed in the roof of a coal mine. These instruments consist of resin-grouted roof bolts fitted with three pairs of strain gages. Strain measurement readings were made daily for 3 weeks after installation and currently are made at 30-day intervals. Also, 88 pressure pads have been installed in a coal mine roof, and changes in load have been measured for correlation with time lapse.

Perhaps the most significant phase of the study, which is now in progress, involves the widening of rooms and entries in a work section. This phase requires that records be kept for time lapse between exposure and support of each cut in the section. After room-and-pillar mining is completed, all rooms will be widened an additional 20 feet. It is expected that the widening will induce controlled roof falls. The roof falls will be compared with the original time lapse of the room to determine the correlation.

REFERENCES

1. Dunrud, C. R. Some Engineering Geologic Factors Controlling Coal Mine Subsidence in Utah and Colorado. U.S. Geol. Survey Prof. Paper 969, 1976, p. 27.

2. Maher, J., and G. H. Bennett. Resin Bolting Developments at the White Pine Mine. Skillings' Min. Rev., v. 64, 1975, pp. 6-9.

3. Panek, L. A. Evaluation of Roof Stability From Measurements of Horizontal Roof Strain. Paper in Ground Control Aspects of Coal Mine Design. Proceedings: Bureau of Mines Technology Transfer Seminar, Lexington, Ky., Mar. 6, 1973. BuMines IC 8630, 1974, pp. 92-96.

4. Stahl, R. W. Survey of Practices in Controlling Roof at Intersections and Junctions in Underground Coal Mines. BuMines IC 8113, 1962, 13 pp.

☆U.S. GOVERNMENT PRINTING OFFICE: 1978-703-103/51

INT.-BU.OF MINES,PGH.,PA. 23168

622.09
Un32mo

RI 8299

Bureau of Mines Report of Investigations/1978

Wood Precharring: A Novel Fire-Retardancy Technique

The Library of the
NOV 21 1978
University of Illinois
at Urbana-Champaign

UNITED STATES DEPARTMENT OF THE INTERIOR

Report of Investigations 8299

Wood Precharring: A Novel Fire-Retardancy Technique

By Calvin K. Lee, Robert F. Chaiken, and Joseph M. Singer

UNITED STATES DEPARTMENT OF THE INTERIOR
Cecil D. Andrus, Secretary

BUREAU OF MINES

This publication has been cataloged as follows:

Lee, Calvin K

Wood Precharring: A novel fire-retardancy technique / by Calvin K. Lee, Robert F. Chaiken, and Joseph M. Singer. [Washington] : U.S. Dept. of the Interior, Bureau of Mines, 1978.

22 p. ; ill., diagrams ; 27 cm. (Report of investigations - Bureau of Mines ; 8299)

Bibliography: p. 21-22.

1. Fireproofing of wood. 2. Fireproofing agents. 3. Fire-resistant materials. 4. Mine timbering. I. Chaiken, Robert F., joint author. II. Singer, Joseph M., joint author. III. United States. Bureau of Mines. IV. Title. V. United States. Bureau of of Mines. Report of investigations - Bureau of Mines ; 8299.

TN23.U7 no. 8299 622.06173

U.S. Dept. of the Int. Library

CONTENTS

Page

Abstract.. 1
Introduction.. 1
Acknowledgments... 2
Concept and technique of wood precharring................... 2
Fire tests on precharred wood and discussion................ 5
    Laser irradiation test.................................. 6
    ASTM E-162 Radiant Panel Test........................... 8
    ASTM E-84 Tunnel Test................................... 10
    Bureau of Mines model fire-tunnel test.................. 11
Commentary on tests... 18
Conclusions... 19
References.. 21

ILLUSTRATIONS

1. Experimental pyrolysis rate of maple at surface heat flux $\dot{q}_i'' = 2$ cal/cm^2 sec.............................. 2
2. Theoretical pyrolysis rate of maple at surface heat flux $\dot{q}_i'' = 2$ cal/cm^2 sec as a function of prechar-layer thickness (d_c).. 3
3. Schematic of Automatic Wood Precharring Apparatus (AWPA).......... 4
4. Photograph of wood being precharred in air using AWPA............. 5
5. Photograph of virgin and precharred wood.......................... 5
6. Schematic of laser irradiation experiment......................... 7
7. Surface temperature of virgin oak ($d_c = 0$) and wood temperature immediately below the prechar layer of precharred oak........... 7
8. Burning rate in air and pyrolysis rate in nitrogen of oak at surface heat flux $\dot{q}_i'' = 2$ cal/cm^2 sec......................... 8
9. Maximum distance of flame spread (x_{max}) and corresponding time (t) for spruce during ASTM Radiant Panel Test.................. 9
10. Exhaust gas temperature of virgin and precharred oak during ASTM Radiant Panel Test... 9
11. Flame spread of virgin and precharred white pine during ASTM Tunnel Test.. 10
12. Schematic of Bureau of Mines model fire tunnel.................. 12
13. Instrumentation of Bureau of Mines model fire tunnel............ 13
14. Photograph showing virgin oak in ignition section of Bureau of Mines fire tunnel.. 14
15. Flame spread of virgin and precharred oak during Bureau of Mines fire-tunnel test.. 15
16. Mass flow rates of virgin and precharred oak during Bureau of Mines fire-tunnel test....................................... 16
17. Normalized fuel-to-air ratio of virgin and precharred oak during Bureau of Mines fire-tunnel test............................ 17
18. Molar concentration of carbon monoxide in tunnel exhaust gas during tests in Bureau of Mines fire tunnel.......................... 17
19. Temperature of tunnel exhaust gas during tests in Bureau of Mines fire tunnel... 17

ILLUSTRATIONS--Continued

Page

20. Optical transmission at wavelength λ = 0.63 μm of tunnel exhaust gas during tests in Bureau of Mines fire tunnel.................. 18
21. Flame spread of virgin oak in ASTM Radiant Panel Test (E-162), ASTM Tunnel Test (E-84), and Bureau of Mines fire-tunnel test.... 19

TABLES

1. Flame-spread indices of ASTM Radiant Panel Test on virgin and fire-retardant-treated wood.. 10
2. Results of ASTM Tunnel Test on virgin and precharred white pine.... 11
3. Flame-spread ratios between precharred and virgin wood for fire tests.. 19

WOOD PRECHARRING: A NOVEL FIRE-RETARDANCY TECHNIQUE

by

Calvin K. Lee,[1] Robert F. Chaiken,[2] and Joseph M. Singer[2]

ABSTRACT

This Bureau of Mines report describes a simple fire-retardant treatment for wood. The treatment involves preheating the wood surface at high heat flux (~0.6 cal/cm^2 sec) to form an in situ surface char layer (~3 mm thick) on the wood. Laboratory-scale fire tests show that the precharring technique improves the fire-resistance of virgin wood by decreasing and delaying generation of volatile gases through thermal insulation effect of the surface prechar layer.

INTRODUCTION

Various fire-retardant treatments for wood have been developed in the past in an effort to reduce the potential fire hazards of wood used in underground mines (10).[3] Most of these treatments involve either impregnation of chemicals into virgin wood to modify the wood pyrolysis process upon heating, or coating of the wood surface with paints to form a thermal barrier, between the oxidizing air and the surface of the wood (13). These treatments by chemicals and paints are generally effective under standard fire test conditions, but they are often expensive to apply and some of them liberate toxic gases at high temperatures (12). In the present work, we describe a relatively simple technique for improving the fire-resistance of wood by prepyrolyzing the exterior surface of the wood at high surface heat flux. This treatment results in a discrete layer of in situ char on the wood surface, which imparts a resistance to ignition and burning of the precharred wood in a fire environment. The prechar layer effectively decreases the pyrolysis rate of the underlying virgin wood thereby delaying or inhibiting flaming ignition and combustion of the precharred wood. These fire-retardant effects of the precharring technique have been confirmed by standard ASTM flammability tests and laboratory-scale fire tests.

---

[1] Mechanical engineer.

[2] Research chemist.

All authors are with the Pittsburgh Mining and Safety Research Center, Bureau of Mines, Pittsburgh, Pa.

[3] Underlined numbers in parentheses refer to items in the list of references at the end of this report.

ACKNOWLEDGMENTS

The authors are thankful to the following people for their assistance to the present work: C. Bennett, K. Cashdollar, L. Dalverny, A. Damick, R. Diehl, F. Donnelly, M. Harris, W. Hoffman, and E. Kansa of the Pittsburgh Mining and Safety Research Center, Pittsburgh, Pa. (laser and tunnel tests); J. Gallagher of the Mine Safety and Health Administration, Pittsburgh, Pa. (E-162 Test); T. Chestnut of Factory Mutual Research Corp., Norwood, Mass. (E-84 Test); and M. Sibulkin and K. Annamalai of Brown University, Providence, R.I. (design of ionization flame detector).

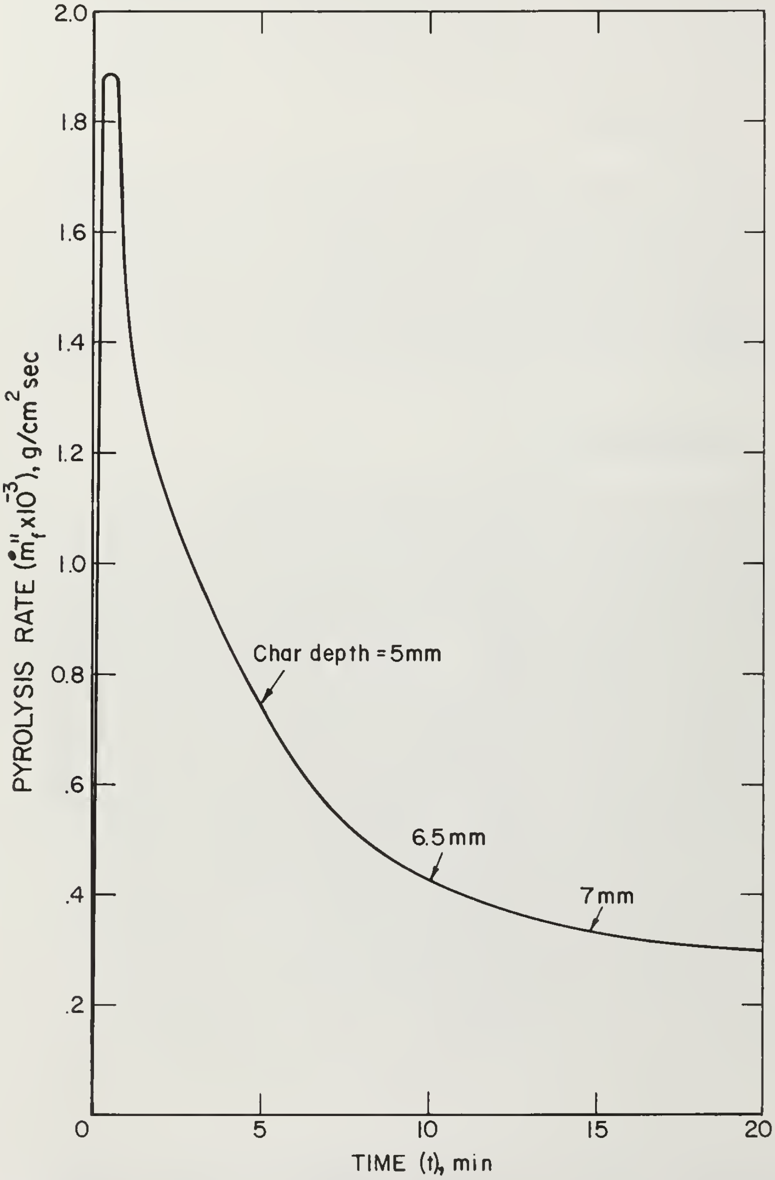

FIGURE 1. - Experimental pyrolysis rate of maple at surface heat flux $\dot{q}_i'' = 2$ cal/cm² sec.

CONCEPT AND TECHNIQUE OF WOOD PRECHARRING

Previous studies of wood pyrolysis at the Bureau of Mines (9) have shown that the pyrolysis rate $\dot{m}_f''$ at fire-level surface heat flux typically increases from zero to a maximum value during an initial heating period, and subsequently decreases with time as a surface char layer builds up (fig. 1). For flaming combustion to occur at the wood surface a certain threshold pyrolysis rate $\dot{m}_{f\,t}''$ has to be maintained; typically, $\dot{m}_{f\,t}''$ ranges from 0.1×10^{-3} to 2.2×10^{-3} g/cm^2 sec (8).

Figure 1 suggests that if surface heating begins with a wood that already has a char layer on its surface, the initial high peak value of $\dot{m}_f''$ could be eliminated, resulting in less opportunity for flaming ignition to occur as compared with virgin wood. The resultant lower evolution rates of volatile gas would not only delay flaming ignition, but also should decrease the rate of flame spread.

The decrease in pyrolysis rate by the prechar layer is due to the following:

First, thermal insulation effect--the prechar layer is a poor thermal conductor [its thermal conductivity is about two to three times less than that of virgin wood (9)] and an excellent black-body radiant-heat emitter [reradiation as high as 80% of the incident heat flux $\dot{q}_i'' = 2$ cal/cm^2 sec by the char surface was measured (9)]. Thus, heat transfer from an external source to the underlying virgin wood is partially blocked by the prechar layer. Second, pregasification effect--the prechar layer consists mainly of carbon with relatively little volatile matter content. Therefore, the prechar layer can sustain relatively high temperatures without emitting flammable gases. Flaming combustion would occur only when the pyrolysis gases are generated from heating the virgin wood beneath the prechar layer.

Recognizing the fire-retardant mechanism of a prechar layer, one would expect its effectiveness to depend on the thickness of the prechar layer d_c. This was studied theoretically using a one-dimentional wood pyrolysis model (7); analytical results are shown in figure 2. It is seen that the decrease in pyrolysis rate is proportional to the char depth d_c, and at d_c = 5 mm, the lower limit of the threshold pyrolysis rate for ignition is approached; that is, 0.1×10^{-3} g/cm^2 sec. As will be shown later, these theoretical results are in good qualitative agreement with the experimental results, differing primarily in the absolute value of the pyrolysis rate, the experimental value being a factor of 2 to 3 higher.

Due to the low thermal conductivity of virgin wood, a rather discrete char layer can be conveniently formed on a wood surface by preheating the wood surface with a high-intensity heat source, such as a gas-fired radiant-heating panel or an electric filament heater, in the presence or absence of oxygen.

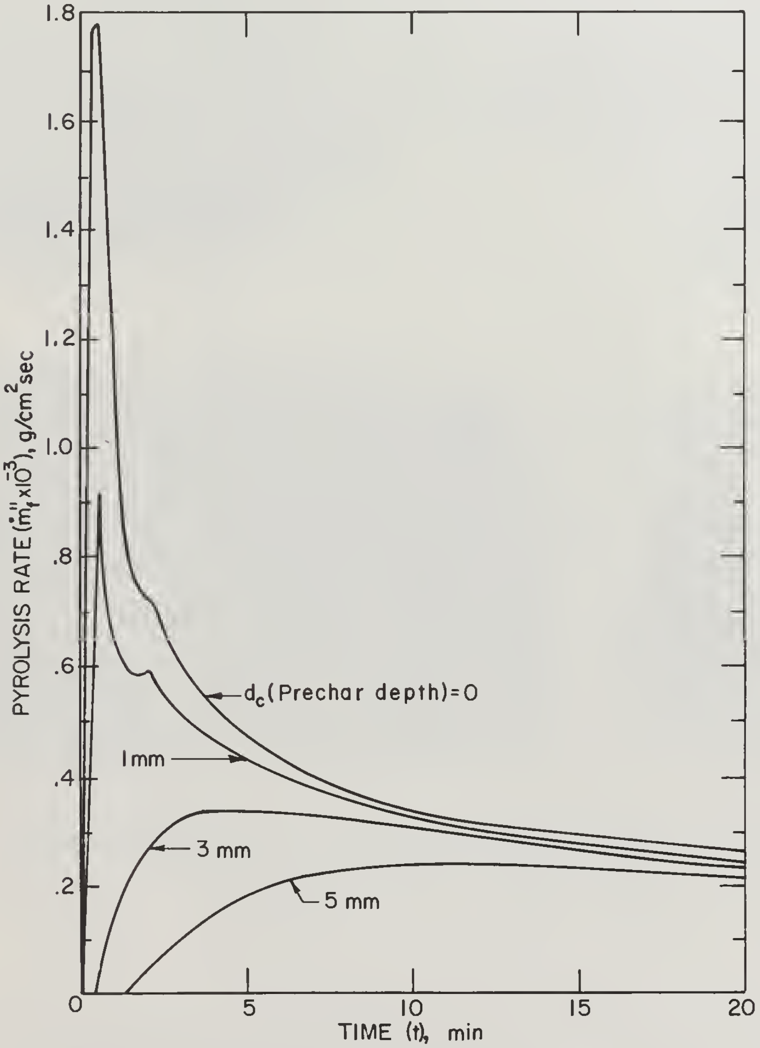

FIGURE 2. - Theoretical pyrolysis rate of maple at surface heat flux $\dot{q}_i'' = 2$ cal/cm^2 sec as a function of prechar-layer thickness (d_c).

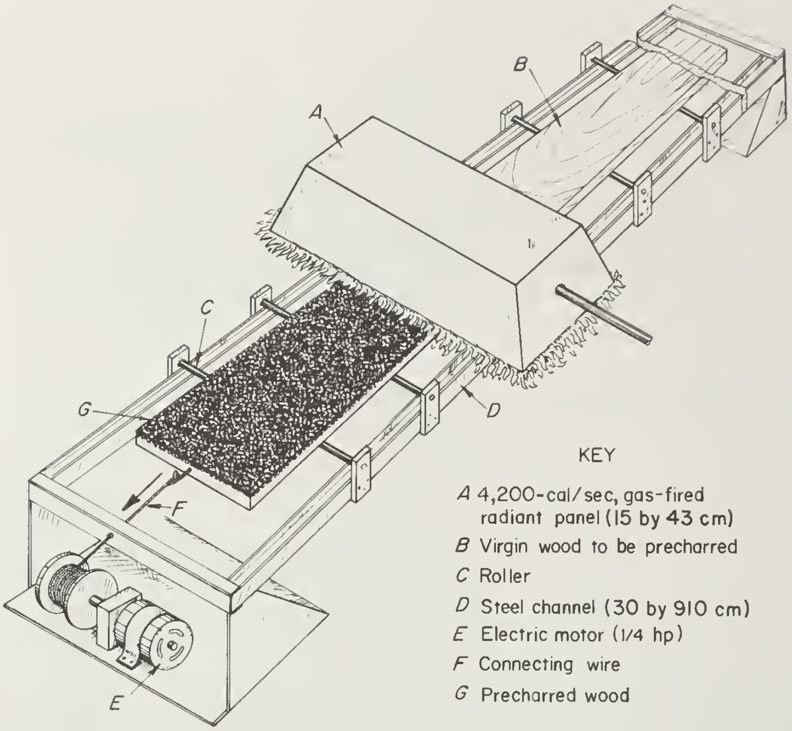
A
B
C
D
E
F
G
KEY
A 4,200-cal/sec, gas-fired radiant panel (15 by 43 cm)
B Virgin wood to be precharred
C Roller
D Steel channel (30 by 910 cm)
E Electric motor (1/4 hp)
F Connecting wire
G Precharred wood

FIGURE 3. - Schematic of Automatic Wood Precharring Apparatus (AWPA).

The important factor here is that a high surface heat flux (for example, $\gtrsim 0.5$ cal/cm^2 sec) will allow for charring of the surface layer without significant heating of the wood underlying the char layer. At much lower surface heat flux, the rate of char buildup is accompanied by smaller temperature gradients in the wood; therefore, the underlying wood is exposed to more heat. Figure 3 shows a schematic of an Automatic Wood Precharring Apparatus (AWPA) that was used in the present study (4). It consists of a stationary gas-fired radiant heat panel with its heat flow directed vertically downward onto the surface of the virgin wood that is being precharred. The virgin wood is supported and transported horizontally on a metal channel by an electric motor. A photograph of the AWPA in operation is shown in figure 4. For the present investigation, it was convenient to perform the precharring process in air, although it could obviously also be carried out under inert gas conditions. A char depth of 2 to 3 mm without flaming combustion (that is, without forming large quantities of ash) of the wood was obtained with the following conditions:

Natural gas flow rate	cm^3/sec..	425
Distance between heater and wood surface	cm..	15
Surface heat flux	cal/cm^2 sec..	0.6
Wood translational velocity	cm/min..	3
Prechar-layer thickness	cm..	0.2-0.3

Presumably, thicker char depths could be formed by precharring in an inert atmosphere (9). The typical precharred wood in figure 5 clearly shows the rather discrete char layer on the wood surface. Since the underlying wood was not exposed to significantly high temperatures, it is reasonable to expect that its structural properties were not altered by the precharring process.

It was measured that the char-layer density was about 20% of the virgin wood (9), resulting from an ~80% loss of volatile matter. This high percentage of mass loss during precharring apparently gives rise to the numerous cracks that are formed in the char layer (fig. 5).

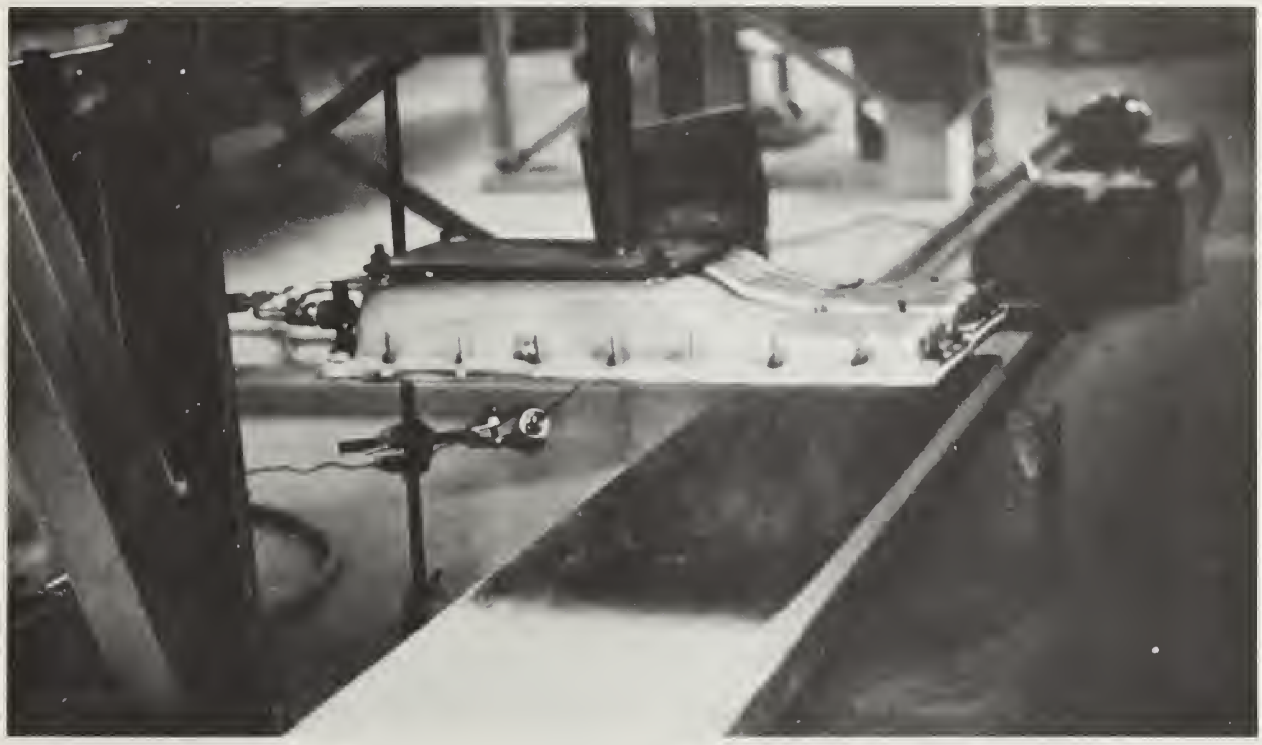

FIGURE 4. - Photograph of wood being precharred in air using AWPA.

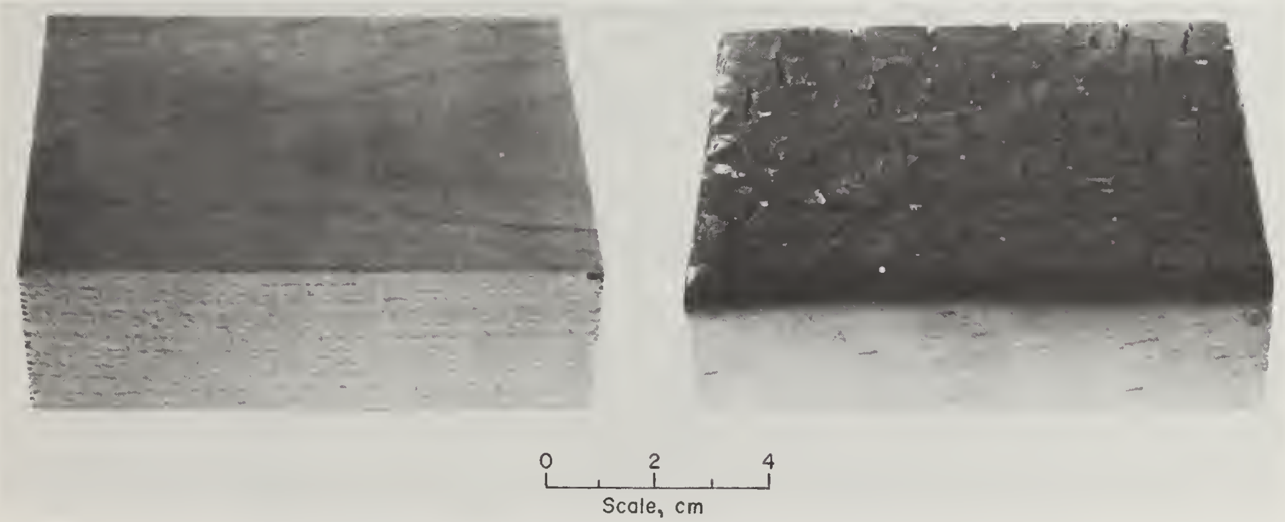

FIGURE 5. - Photograph of virgin and precharred wood.

FIRE TESTS ON PRECHARRED WOOD AND DISCUSSION

Currently, there are several standard flammability tests (6) for comparing the burning characteristics of materials under laboratory test conditions. These tests are generally used for initial screening purposes rather than for predicting burning characteristics in a large fire (3). As an initial evaluation of the precharring technique, the commonly used ASTM E-162 Radiant Panel Test (2) and the E-84 Tunnel Test (1) were used for comparing surface burning characteristics of virgin and precharred wood. The laser irradiation technique (9) and the model fire tunnel (5) developed by the Bureau of Mines were used for detailed comparison in ignition, mass loss, fire buildup, heat release, and generation of toxic gases and smoke between virgin and precharred wood. Results of these four tests are as follows.

Laser Irradiation Test

An experimental setup employing a 250-watt, continuous CO_2 laser as an ignition source was developed for wood combustibility studies. Details of the setup have been reported elsewhere (9). Basically, the CO_2 laser supplies a radiation beam (~2 cm diameter) of fire-level surface heat flux (up to 4 cal/cm^2 sec), which is directed onto the top surface of an insulated wood cylinder that stands upright on a weighing cell. (See fig. 6.) Numerous measuring devices are employed during the pyrolysis process to determine total mass loss, temperature, internal gas pressure, gas composition, and local wood density.

For the present study, solid temperature T and mass loss rate $\dot{m}''$ of virgin and precharred oak in air and in nitrogen were measured at surface heat flux $\dot{q}_i'' = 2$ cal/cm^2 sec. Prechar-layer depth $d_c = 2$ mm and 4 mm were chosen to investigate the effect of depth d_c on mass loss rate $\dot{m}''$. Surface temperature measurements of the virgin oak and the oak immediately below the prechar layer are shown in figure 7. The difference in the temperature rise of the two woods clearly reflects the thermal insulation effect of the prechar layer, which is seen to increase with depth d_c. The temperatures measured under the air environment are higher than those under the nitrogen environment, which is apparently due to exothermic surface oxidation of the char.

The effect of the prechar layer on mass loss rate is shown in figure 8, which shows that during the first 5 min of heating, precharred oak generates volatiles at lower rates than virgin oak, and the amount of decrease in the rate of mass loss is proportional to the char depth. It is noted that the maximum rate of mass loss occurred later for precharred oak than for virgin oak. Although flaming ignition occurred within 15 sec after exposure for virgin oak, only occasional small flames were observed a few minutes after exposure for precharred oak due to the decrease and delay in mass loss rate. At about 5 min, the char layer (formed during laser irradiation) of the virgin oak built up to such a degree that the rate of mass loss for both virgin and precharred oak were about the same. The higher rate of mass loss in air as opposed to nitrogen was apparently due to carbon oxidation in the char layer. The theoretical results of the effect of char depth on the rate of mass loss shown in figure 2 are in general agreement with the experimental measurements.

In a real fire situation, the decrease and delay in the volatile evolution rate, even in the initial burning stage, would mean a less intense and slower fire buildup, which is advantageous to fire fighting. These fire-retardant effects of precharring are confirmed in the Bureau of Mines model fire-tunnel test, which is discussed later.

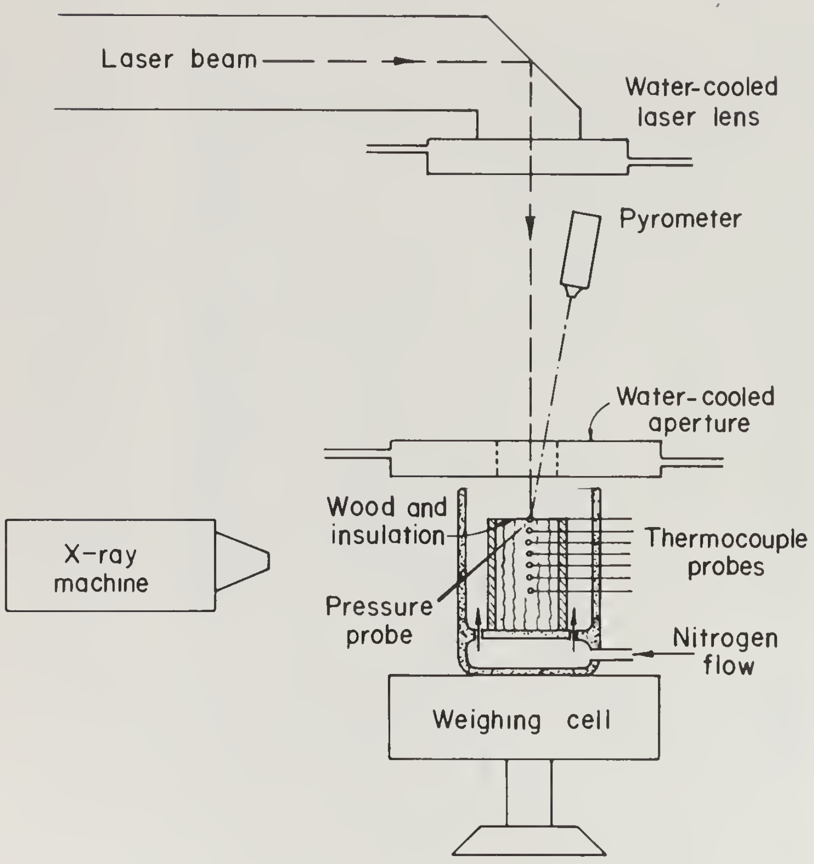
Laser beam
Water-cooled laser lens
Pyrometer
Water-cooled aperture
Wood and insulation
Thermocouple probes
Pressure probe
Nitrogen flow
X-ray machine
Weighing cell

FIGURE 6. - Schematic of laser irradiation experiment.

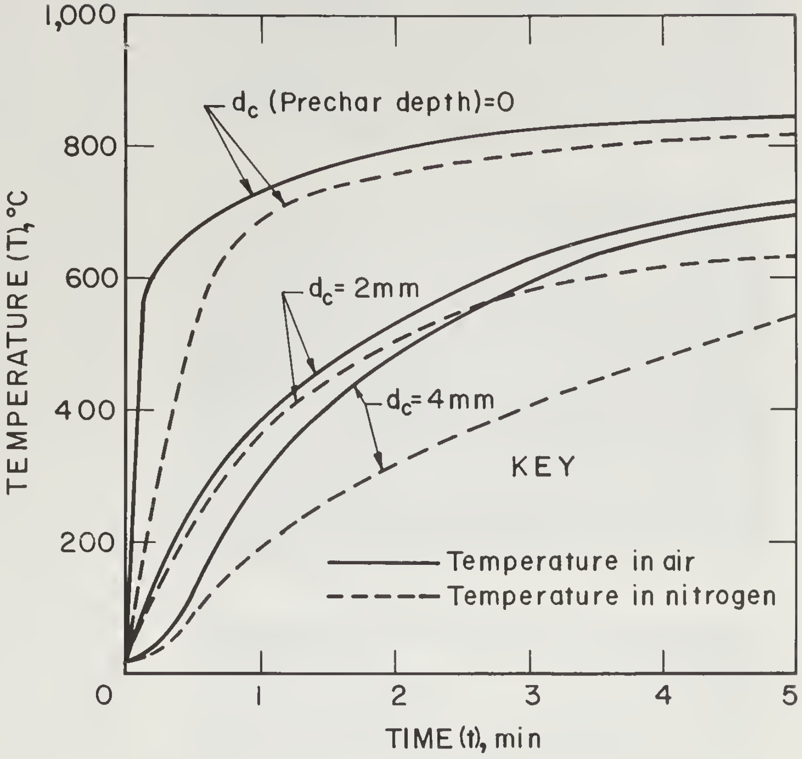

FIGURE 7. - Surface temperature of virgin oak ($d_c = 0$) and wood temperature immediately below the prechar layer of precharred oak.

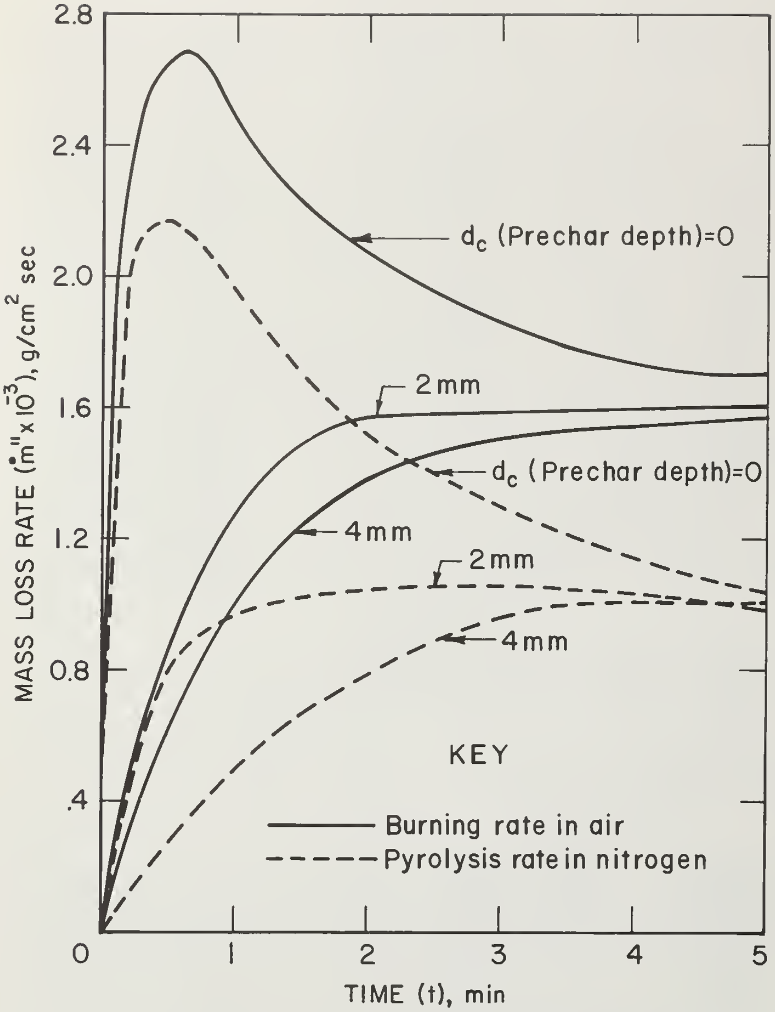

FIGURE 8. - Burning rate in air and pyrolysis rate in nitrogen of oak at surface heat flux $\dot{q}_i''$= 2 cal/cm^2 sec.

ASTM E-162 Radiant Panel Test

The ASTM E-162 Radiant Panel Test is a test of surface flammability of materials in terms of a flame-spread index I_s as compared with the standards of red oak (I_s = 100) and asbestos (I_s = 0)(2). In the test, the sample is held in open air at 60° downward from horizontal, heated by a gas-fired radiant panel, and pilot-ignited at the top by a gas flame. (See fig. 9.) A defined flame-spread index I_s is calculated based on the downward flame-spread rate and the exhaust-gas temperature above the test sample.

Flame-spread characteristics of virgin and precharred (d_c = 3 mm) spruce, beech, and oak were compared using this test. In addition, virgin wood coated with fire-retardant chemicals of intumescent paint, sodium silicate, and zinc chloride were also tested for comparison with the precharred woods. It was noted that during tests (1) all virgin woods showed rapid downward surface flame-spread rates, (2) the sodium silicate and zinc chloride coating decreased the flame-spread rate somewhat, and (3) flame did not spread on the precharred and intumescent-paint-coated woods. These phenomena are depicted in figure 9, which shows the maximum distance of flame spread and the corresponding time. Although the precharred wood did not show downward flame spread, the slow burning that is normal to the wood surface near the pilot flame did occur, causing a slowly increasing exhaust temperature as compared to the fast rising and higher exhaust temperatures for virgin wood. The comparison of the two temperature histories is shown in figure 10.

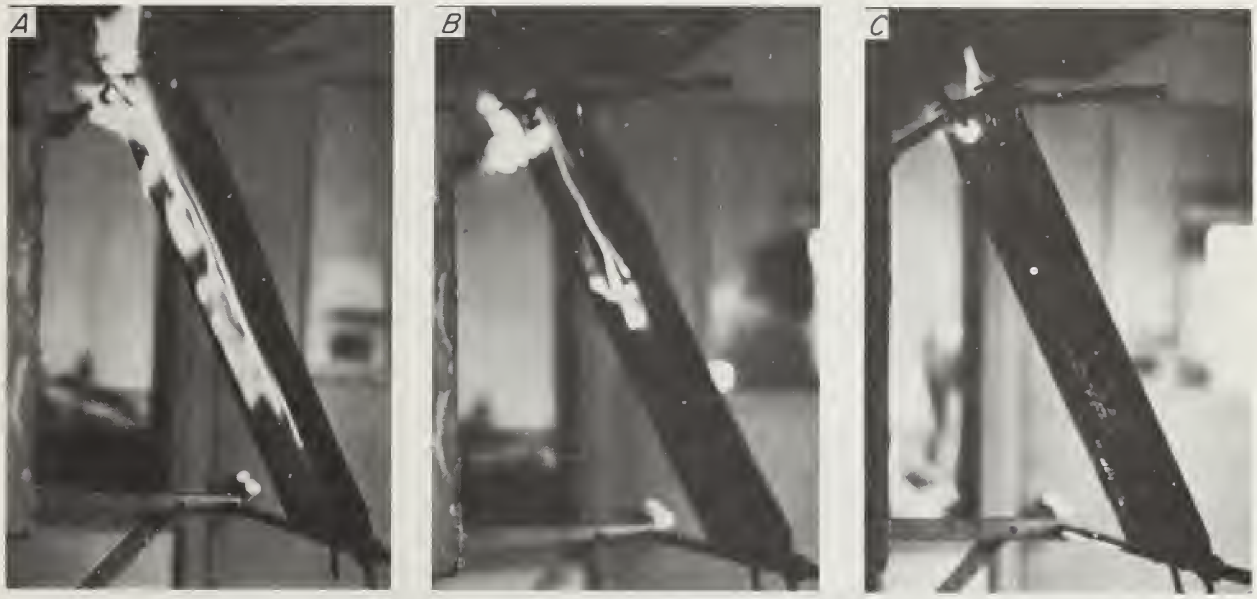

$x_{max} = 3.8$ cm; t = 2.4 min

$x_{max} = 2.3$ cm; t = 3.0 min

$x_{max} = 0$; t = 15 min

FIGURE 9. - Maximum distance of flame spread (x_{max}) and corresponding time (t) for spruce during ASTM Radiant Panel Test. *A*, Virgin; *B*, sodium silicate coated; and *C*, precharred.

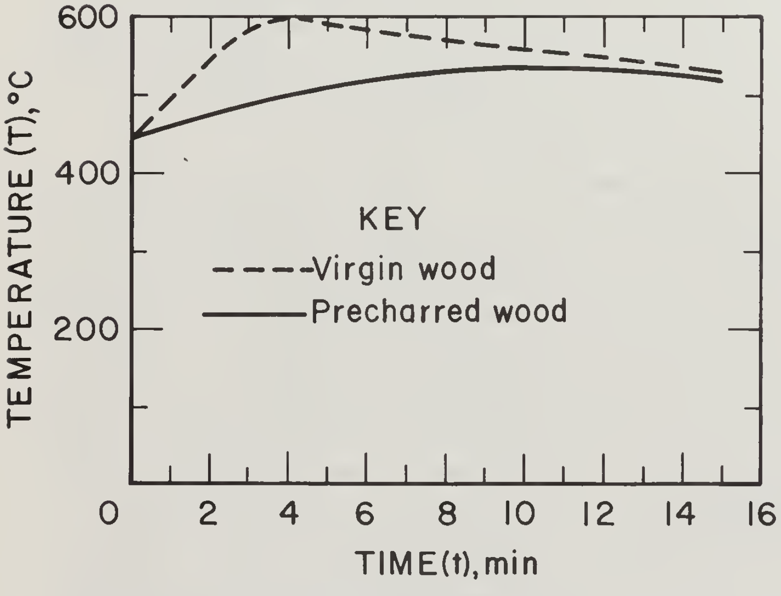

FIGURE 10. - Exhaust gas temperature of virgin and precharred oak during ASTM Radiant Panel Test.

The resultant flame-spread indices for the virgin and treated woods are tabulated in table 1. Test results show that precharred and intumescent-paint-coated woods have similar flame-spread indices, and zinc chloride and sodium silicate are not as effective under the Radiant Panel Test conditions. The last column of table 1 shows the flame-spread index for double fire-retardant treatment of zinc chloride coating on a prechar layer. As expected, the flame-spread index for the double treatment is lower than each individual treatment, implying that the effectiveness of the precharring technique can be further improved by additional treatment of the prechar layer, such as coating with chemicals. It is of interest to note that the present maximum allowable flame-spread index for a material used in an underground mine is $I_s = 25$.

TABLE 1. - Flame-spread indices of ASTM Radiant Panel Test on virgin and fire-retardant-treated wood

	Spruce	Beech	Oak[1]
Untreated	110	120	80
Precharred	11	10	8
Coated with intumescent paint	14	20	-
Coated with zinc chloride	30	-	-
Coated with sodium silicate	47	61	-
Zinc chloride coating on prechar layer	5	-	-

[1] Standard flame-spread index (I_s) for red oak is 100 (2).

ASTM E-84 Tunnel Test

The ASTM E-84 Tunnel Test is a test of surface burning characteristics of materials in terms of ratings of flame spread, fuel contribution, and smoke development as compared with the standards of red oak and asbestos (1). In the test, the sample, with its burning surface facing downward and positioned on the top of a horizontal, ventilated tunnel, is heated and pilot-ignited by a series of gas burners at the tunnel entrance. Ratings of flame spread, fuel generation, and smoke development are computed based on surface flame-spread rate, tunnel exhaust temperature and light transmission.

Burning characteristics of virgin and precharred white pine (d_c = 2-3 mm) were examined in this test. Test results showed that flaming ignition occurred on the virgin wood 30 sec after exposure to the gas burners, and on the precharred wood 1 min after exposure. At the end of the 10-min test, flame propagated to 6.7 m on the virgin wood and 4.4 m on the precharred wood. Allowing the initial 1.7 m on the wood for the flame from the gas burners, the actual distances covered by the flame were 5.0 and 2.7 m for the virgin and precharred wood, respectively. These results are shown in figure 11.

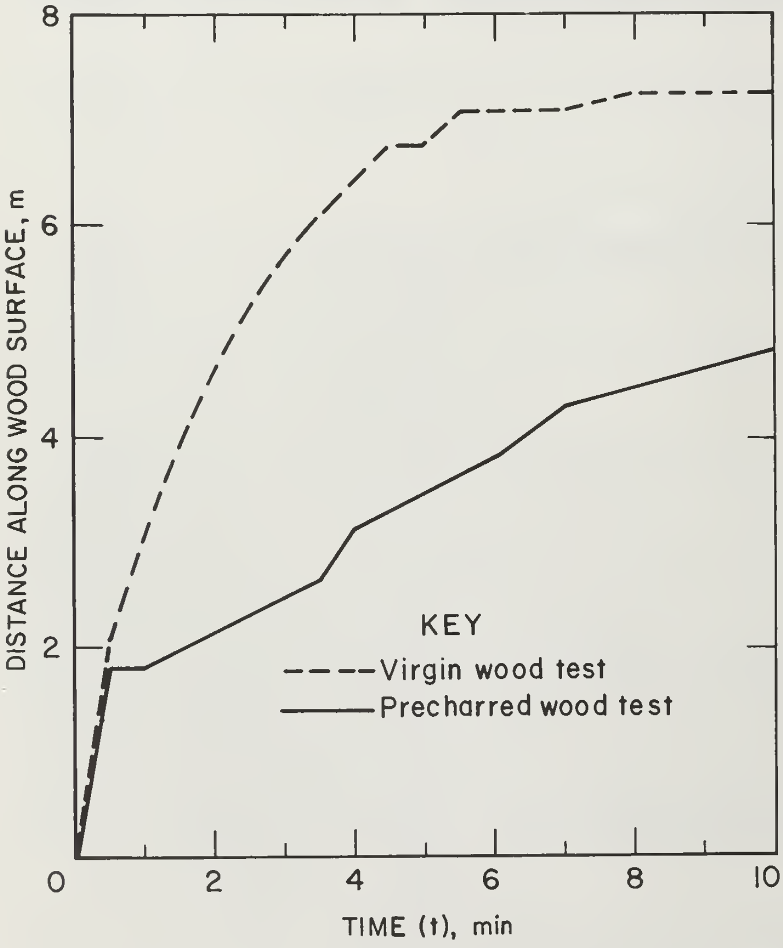

FIGURE 11. - Flame spread of virgin and precharred white pine during ASTM Tunnel Test.

Flame-spread rates calculated from figure 11 indicate that the initial flame-spread rate of the virgin wood is about seven times higher than that for precharred wood, and there is an overall higher flame-spread resistance for the precharred wood than for virgin wood.

Ratings of flame spread, fuel contribution, and smoke developed for the virgin and precharred white pine are shown in table 2. These ratings support the fire-retardant effect of the precharring technique.

TABLE 2. - Results of ASTM Tunnel Test on virgin and precharred white pine

Wood	Flame spread	Fuel contributed	Smoke developed
Virgin white pine........	73	45	0
Precharred white pine....	46	43	0
Red oak[1]	100	100	100

[1] Standard rating index is 100 (1).

Bureau of Mines Model Fire-Tunnel Test

A laboratory-scale fire tunnel was constructed to study small-scale tunnel wood fires and to simulate large-scale mine timber fires. A schematic of the tunnel layout and the associated instrumentation are shown in figures 12 and 13. [Details of tunnel design and construction have been reported elsewhere (5).] The tunnel mainly consists of four parts: flow control, ignition, test, and cooling sections. Numerous measuring devices are employed in each section to follow the course of the fire, as shown in figure 13.

Two fire tests were performed, one with a virgin oak lining and one with a precharred oak lining (d_c = 2-3 mm) on the ceiling and on two side walls of the test section. For both tests, the exhaust fan was set at a constant speed that ventilated the room air in the tunnel at a velocity of 1.5 m/sec. Virgin oak was used as the ignition source in the ignition section. (See fig. 14.) During the tests, the entrance gate between the ignition and test sections was first closed, and the exhaust gate in the stack of the ignition section was opened. (See fig. 12.) The virgin wood in the ignition section was then ignited by a multiport, gas-fired lance. The lance was withdrawn when burning became self-sustained throughout the ignition section by natural convective flow. Finally, exact time exposure of the wood lining in the test section to the ignition source (burning wood) was accomplished by rapidly maneuvering the entrance and exhaust gates to direct the hot ventilated flow into the test section. Unfortunately, flaming combustion in the ignition section was partially quenched owing to the sudden increase in air flow from natural convection to forced ventilation. This resulted in a heat flow of about 42 kw into the test section for both tests, which is about half of the heat release rate of the gas burners used in the ASTM Tunnel Test. (The ignition section was subsequently modified to avoid flame quenching.)

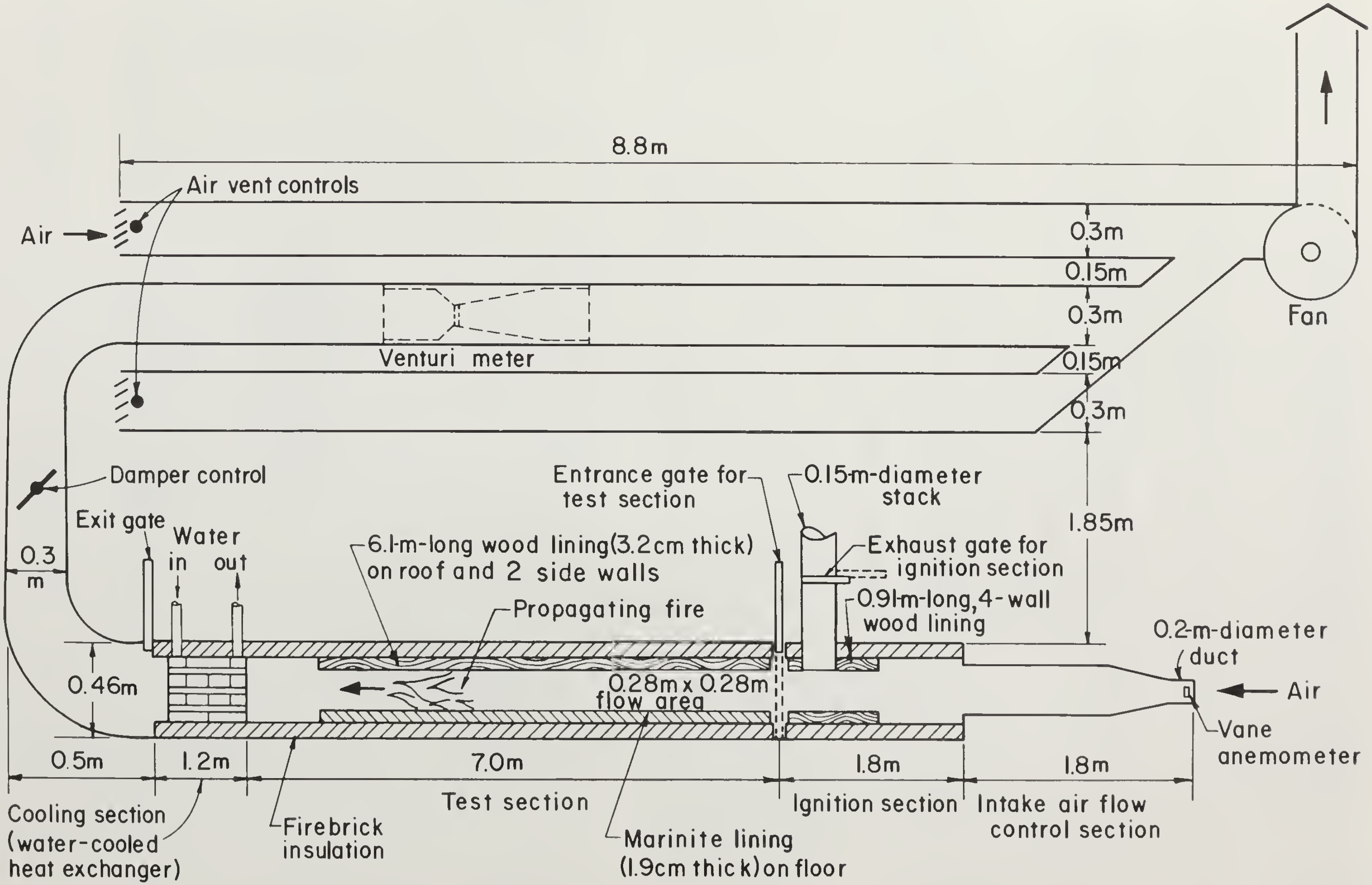
8.8m
Air vent controls
Air
0.3m
0.15m
0.3m
0.15m
0.3m
Fan
Venturi meter
Damper control
Exit gate
Water
in
out
0.3
m
0.46m
Entrance gate for test section
0.15-m-diameter stack
Exhaust gate for ignition section
0.91-m-long, 4-wall wood lining
1.85m
6.1-m-long wood lining (3.2cm thick) on roof and 2 side walls
Propagating fire
0.28m x 0.28m flow area
0.2-m-diameter duct
Air
Vane anemometer
0.5m
1.2m
7.0m
1.8m
1.8m
Cooling section (water-cooled heat exchanger)
Firebrick insulation
Test section
Marinite lining (1.9cm thick) on floor
Ignition section
Intake air flow control section

Note.-For detailed tunnel instrumentation, see figure 13.

FIGURE 12. - Schematic of Bureau of Mines model fire tunnel.

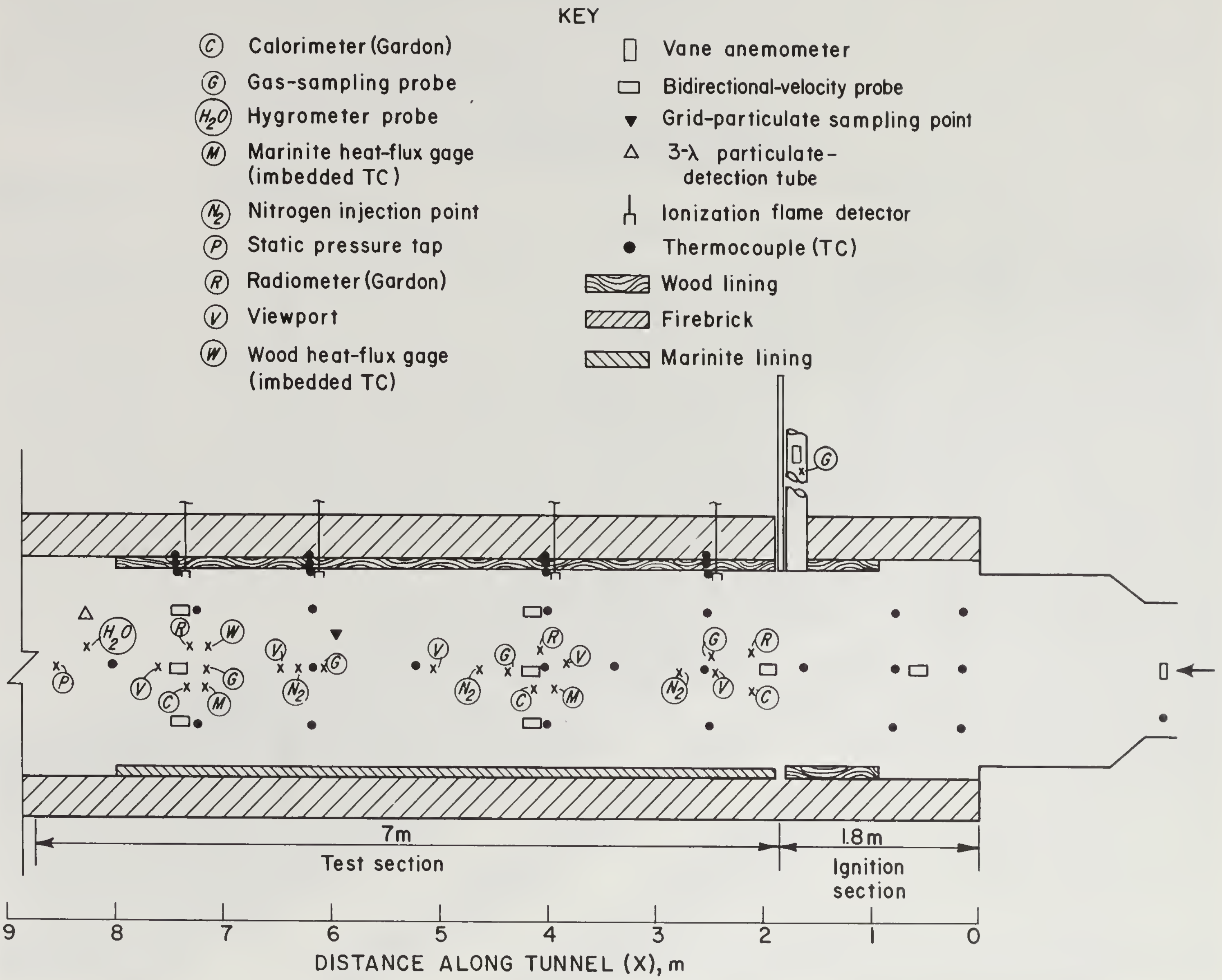
KEY
C Calorimeter (Gardon)
G Gas-sampling probe
H2O Hygrometer probe
M Marinite heat-flux gage (imbedded TC)
N2 Nitrogen injection point
P Static pressure tap
R Radiometer (Gardon)
V Viewport
W Wood heat-flux gage (imbedded TC)
Vane anemometer
Bidirectional-velocity probe
Grid-particulate sampling point
3-λ particulate-detection tube
Ionization flame detector
Thermocouple (TC)
Wood lining
Firebrick
Marinite lining
7m
Test section
1.8m
Ignition section
9
8
7
6
5
4
3
2
1
0
DISTANCE ALONG TUNNEL (X), m

FIGURE 13. - Instrumentation of Bureau of Mines model fire tunnel.

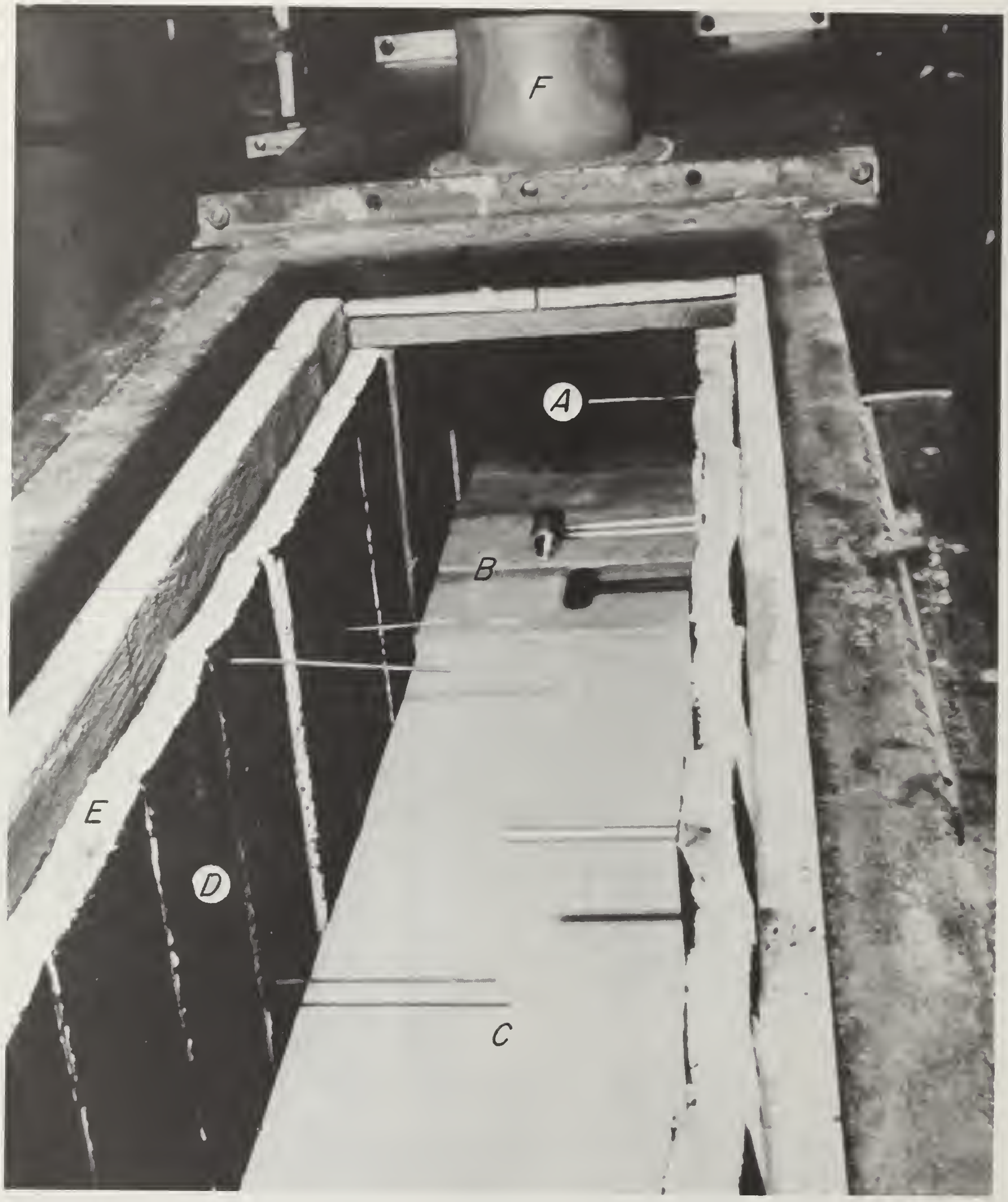

FIGURE 14. - Photograph showing virgin oak in ignition section of Bureau of Mines fire tunnel. *A*, Ignition section; *B*, virgin wood; *C*, marinite; *D*, precharred wood; *E*, fire bricks; and *F*, exhaust chimney for ignition section.

The foregoing tunnel arrangement and operation were designed to compare the ignition delay, flame spread, and subsequent fire buildup of the virgin and precharred oak. However, flame spread on the virgin wood occurred in a way that presented difficulties in comparing the two tests. Eighteen seconds after the virgin wood was exposed to the ignition source, flame was detected at the 2.4-m flame detection station; the precharred wood took 3.75 min. However, in the virgin wood test, the initial flame spread apparently ceased and did not propagate again until several minutes later; on the other hand, the flame spread for the precharred wood was continuous. This phenomenon is depicted in figure 15. This peculiarity in flame spread could be due to the large temperature drop experienced in the ignition zone at $t > 0$ (fig. 15); in any case, it throws doubt on any comparison between the two tests with regard to the delay time and flame spread. However, once continuous flame spread did occur, the data on fire buildup appear to be interpretable and significant.

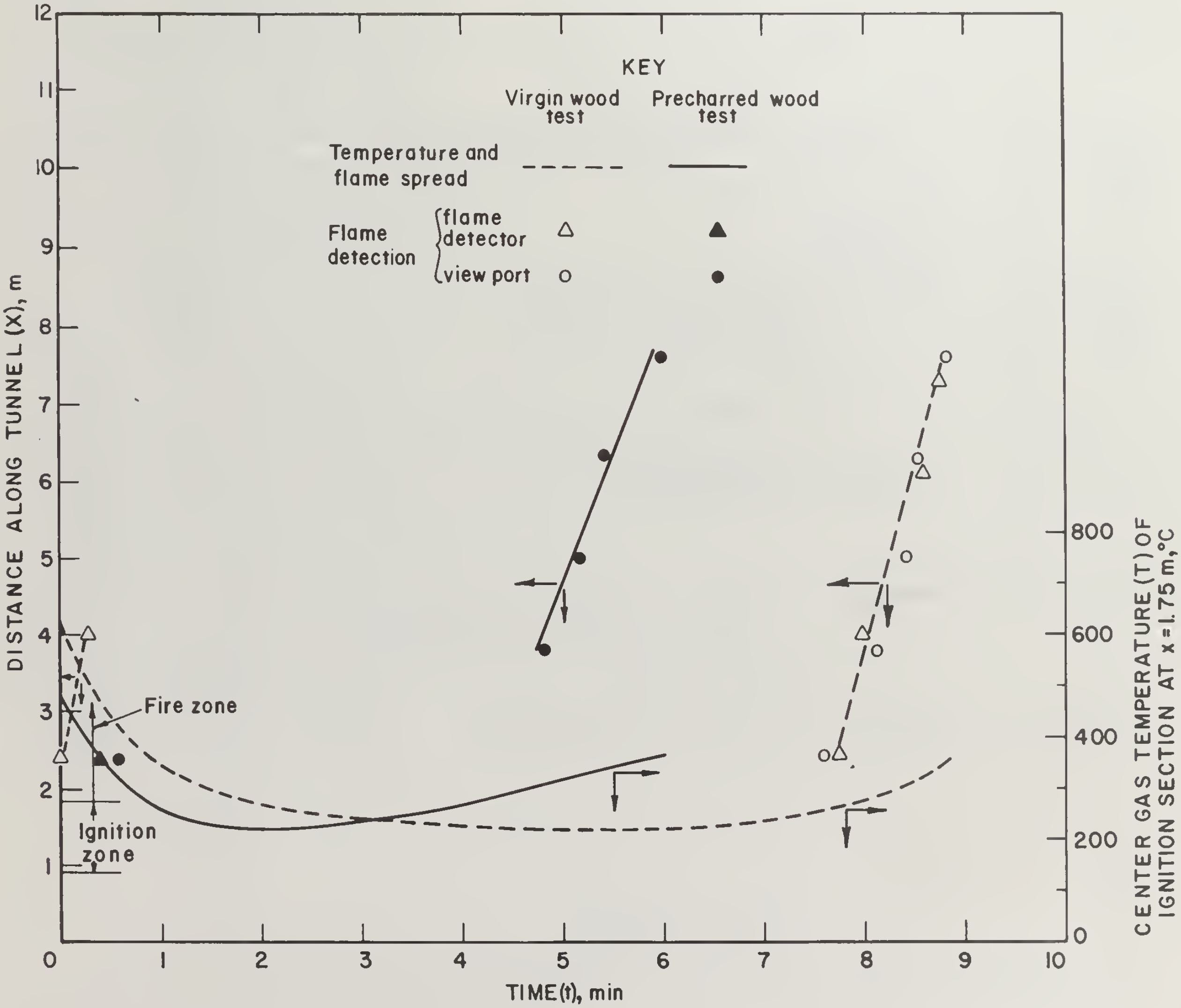

FIGURE 15. - Flame spread of virgin and precharred oak during Bureau of Mines fire-tunnel test.

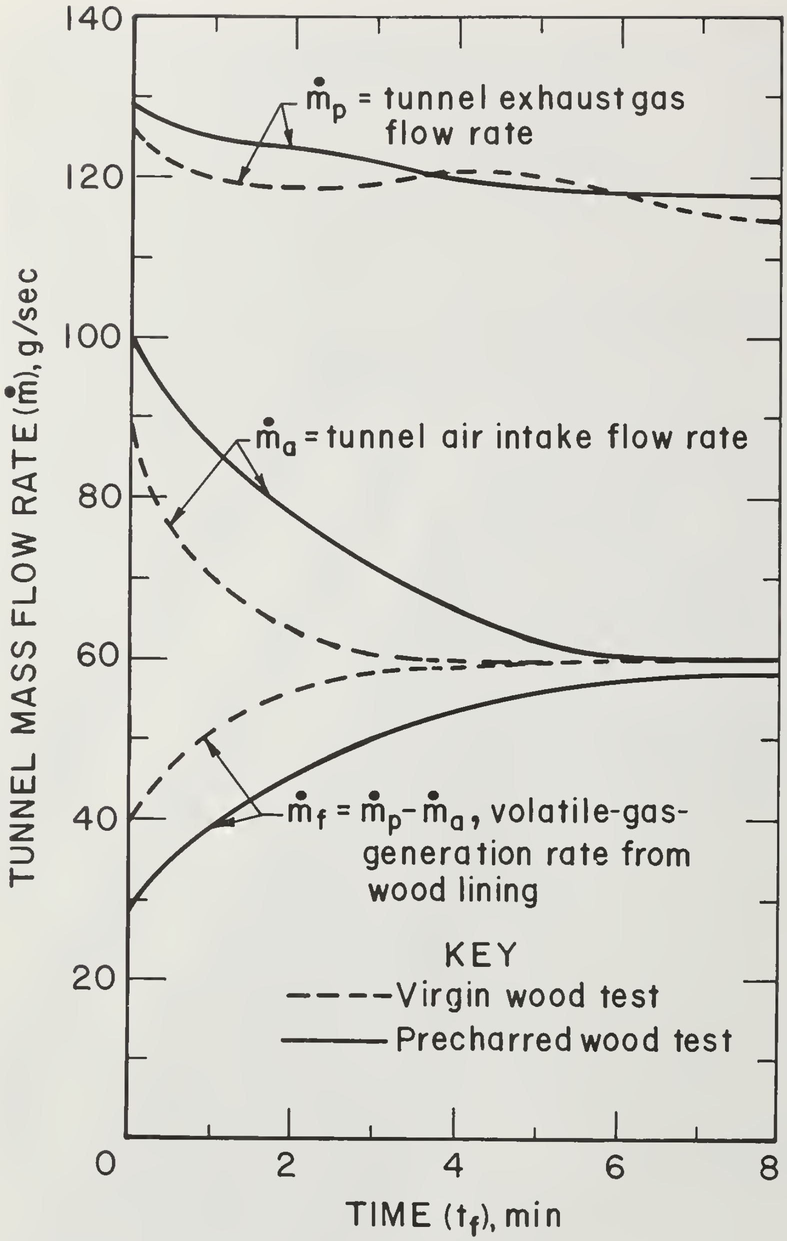

FIGURE 16. - Mass flow rates of virgin and precharred oak during Bureau of Mines fire-tunnel test.

During the continuous flame propagation, the fire spread rates were 8.2 m/sec and 5.4 m/sec for the virgin and precharred oak, respectively.

Figure 16 shows the measured combustion product flow rate $\dot{m}_p$, the air intake flow rate $\dot{m}_a$, and the calculated volatile gas generation rate $\dot{m}_f$ ($\dot{m}_f = \dot{m}_p - \dot{m}_a$) from the wood lining of the two tests immediately following flame detection at the end of the tunnel. Measurement of time t_f in figure 16 begins when the flame arrives at the end of the test section. The mass flow rate measurements show a delay in fire buildup for the precharred wood relative to the virgin wood in terms of the gas generation rate, and less fire throttling (decrease in air flow rate) for the precharred wood in terms of intake air flow rate. The delay in fire buildup is further verified by figures 17 through 20, which show the time histories of the fuel-to-air ratio (11), CO concentration, temperature, and optical transmission of the tunnel exhaust gas for both tests. A delay in these fire hazards by the precharred wood is evident from these experimental results.

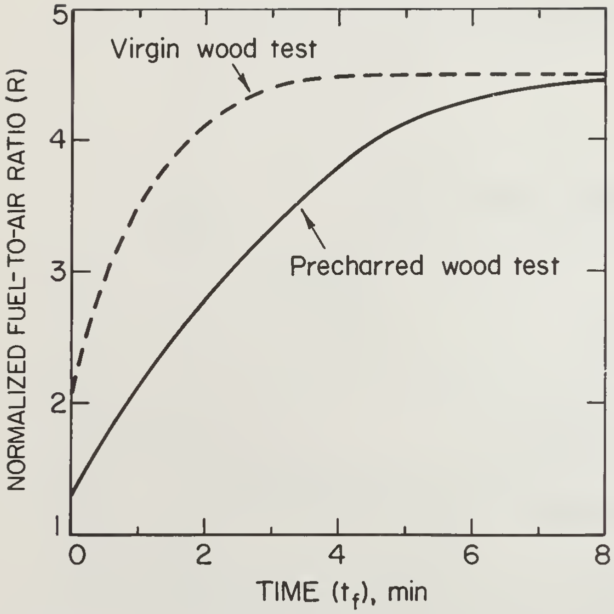

FIGURE 17. - Normalized fuel-to-air ratio of virgin and precharred oak during Bureau of Mines fire-tunnel test.

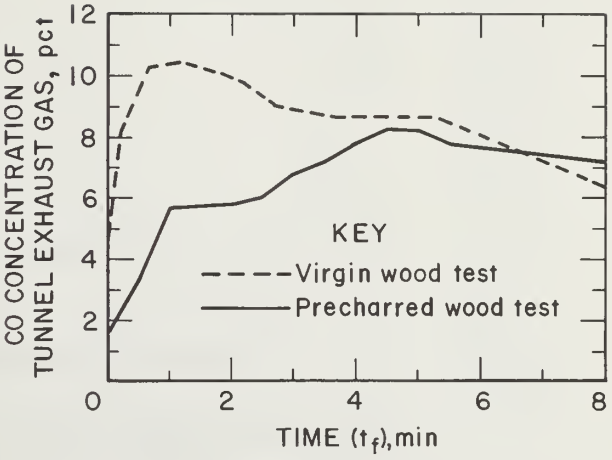

FIGURE 18. - Molar concentration of carbon monoxide in tunnel exhaust gas during tests in Bureau of Mines fire tunnel.

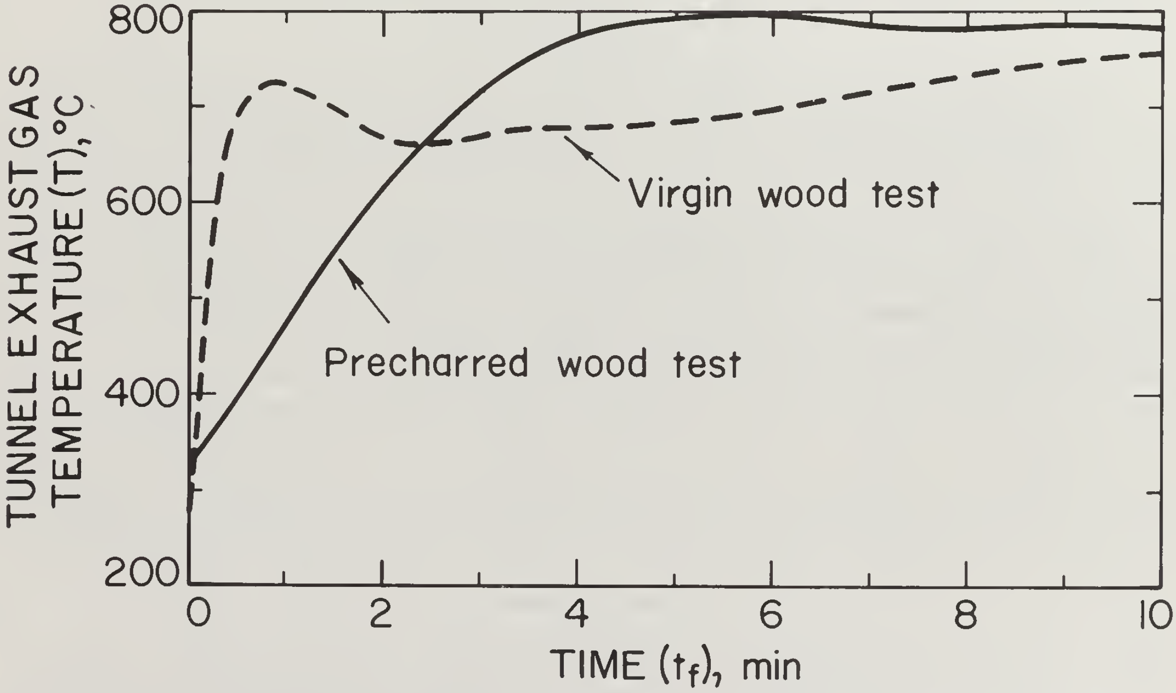

FIGURE 19. - Temperature of tunnel exhaust gas during tests in Bureau of Mines fire tunnel.

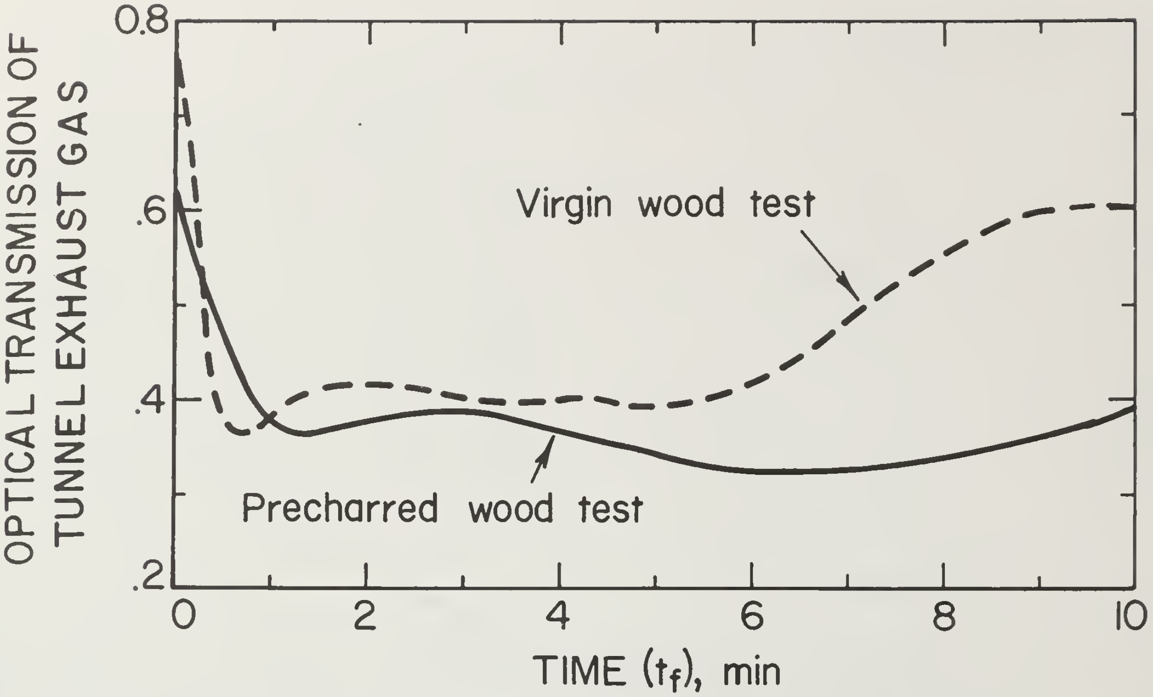

FIGURE 20. - Optical transmission at wavelength $\lambda = 0.63$ µm of tunnel exhaust gas during tests in Bureau of Mines fire tunnel.

COMMENTARY ON TESTS

It is constructive to compare the test conditions of the ASTM Radiant Panel Test, the ASTM Tunnel Test, and the Bureau of Mines fire-tunnel test in order to gain some insight into the implication of the results on flame-spread rate. It is known that the rate of flame spread on a solid surface depends on the rate of energy transfer to the unburned fuel ahead of the propagating flame (assuming there is sufficient oxygen for combustion). In the Radiant Panel Test, where flame spread is downward, the wood sample is heated primarily by radiation from the radiant panel. Because of surface reradiation loss to the surroundings at ambient temperature, only a small percentage of this radiant energy is absorbed into the wood. In the ASTM Tunnel Test, the wood is heated by both convection and radiation owing to the confined tunnel geometry and ventilation, but there is less radiation loss from the wood surface. In the Bureau of Mines fire-tunnel test, practically all the radiant and convective input energy is transferred to the wood lining and contributes to flame spread. Therefore, the flame-spread rate for virgin oak was higher in the Bureau of Mines tunnel than in the ASTM tunnel (1) (fig. 21) although the heat input from the ignition source in the Bureau tunnel was only half that of the ASTM tunnel. As might be expected, the Radiant Panel Test shows a much lower flame-spread rate as compared with the other two tunnel tests. In this respect, the Bureau of Mines tunnel test is the most severe of the three tests employed. This is shown quantitatively in table 3, in which the flame-spread index ratio $I_{s,p}/I_{s,v}$ and flame velocity ratio U_p/U_v of precharred and virgin oak are listed. These data confirm the general finding that fire-retardant treatments become less effective as the fire environment becomes more severe (13).

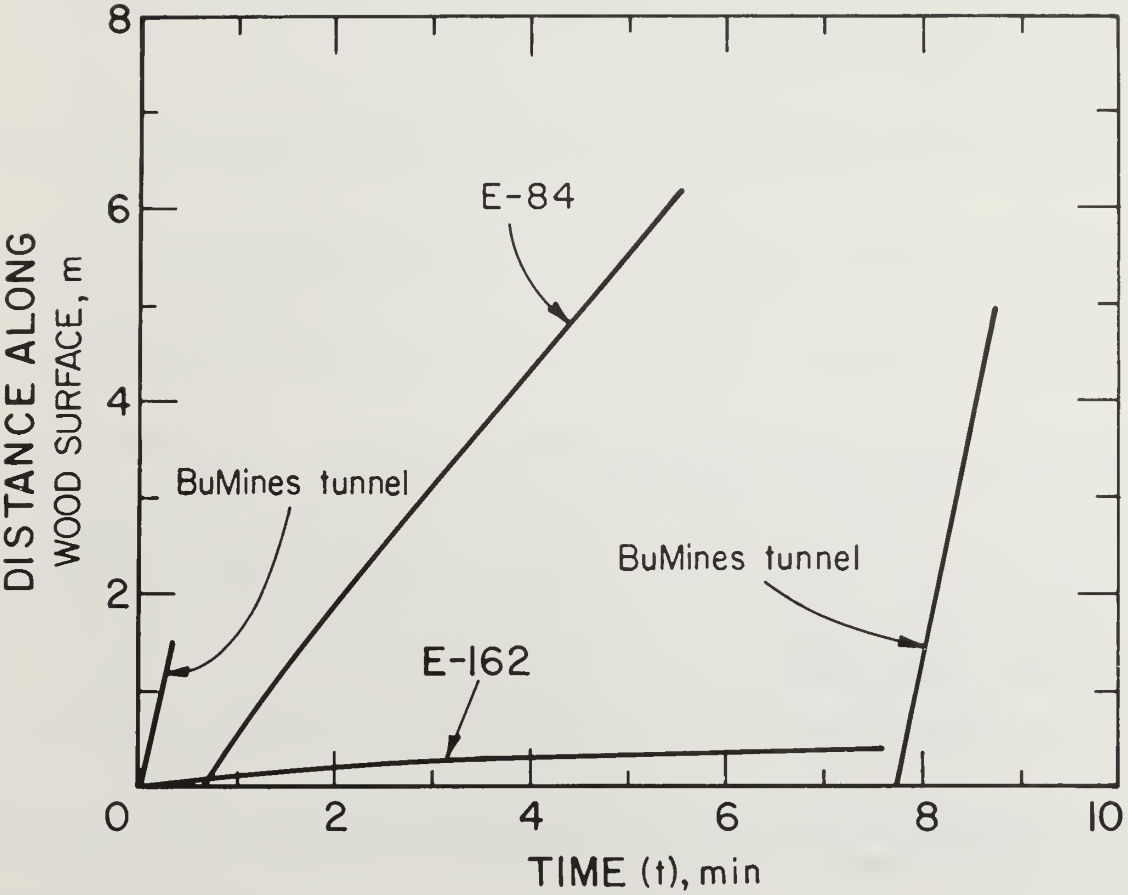

FIGURE 21. - Flame spread of virgin oak in ASTM Radiant Panel Test (E-162), ASTM Tunnel Test (E-84), and Bureau of Mines fire-tunnel test.

TABLE 3. - Flame-spread ratios between precharred and virgin wood for fire tests

Test	Flame-spread index ratio ($I_{s,p}/I_{s,v}$)	Flame-spread velocity ratio (U_p/U_v)
ASTM Radiant Panel (E-162).........	0.1	0
ASTM Tunnel (E-84)..................	.63	0.575
Bureau of Mines tunnel.............	NAp	.659

NAp Flame-spread index ratio is applicable to standard tests only.

CONCLUSIONS

Based on the results of the four fire tests performed on virgin and precharred woods, it can be concluded that the precharring technique decreases the flammability of wood by delaying the ignition, decreasing the surface flame-spread rate, decreasing the heat release rate, and lowering the generation rate of smoke particulates and toxic gases. Although only limited comparisons between the precharring technique and other fire-retardant treatments were made, there are several obvious advantages of the precharring technique over the existing treatments:

1. The present technique is simple and perhaps less expensive to employ since elaborate high-pressure chemical-impregnation processes are not required, and coatings of relatively expensive fire-retardant paints are eliminated.

2. Chemical and paint additives to the wood are eliminated; thereby avoiding such problems as skin allergies and the evolution of toxic gases.

3. Natural structure and integrity of the virgin wood beneath the prechar layer is preserved.

4. The prechar layer should be relatively stable and insensitive to environmental changes such as humidity and waterleaching.

A potential advantage of the prechar technique that requires further development relates to the fact that the char layer has cracks and is porous. Such characteristics enable the prechar layer to absorb and retain rot-resistant agents or other nontoxic chemical agents to further improve the effectiveness of the prechar layer.

Some drawbacks of the prechar technique that may limit its utility are as follows:

1. The prechar layer is not as structurally strong as virgin wood and can be partially removed by abrasion.

2. Warping of thin wood pieces would occur during one-sided precharring due to the high internal thermal gradient. This might be avoided by simultaneous two-sided precharring.

In conclusion, the wood precharring technique shows promise as a convenient treatment for improving the fire-retardancy of wood for certain applications such as mine timbers and structural members. Further development of the technique is warranted.

REFERENCES

1. American Society for Testing and Materials. Surface Burning Characteristics of Building Materials. ASTM Test E-84-76a in 1976 Annual Book of ASTM Standards: Part 18, Thermal and Cryogenic Insulating Materials; Building Seals and Sealants; Fire Tests; Building Constructions; Environmental Acoustics. Philadelphia, Pa., 1976, p. 652.

2. _____. Surface Flammability of Materials Using a Radiant Heat Energy Source. ASTM Test E-162-76 in 1976 Annual Book of ASTM Standards: Part 18, Thermal and Cryogenic Insulating Materials; Building Seals and Sealants; Fire Tests; Building Constructions; Environmental Acoustics. Philadelphia, Pa., 1976, p. 751.

3. Benjamin, I. A. Problems in the Correlation of Small and Large Scale Tests. Proc. Internat. Symp. on Fire Safety of Combustible Materials. Center for Industrial Consultancy and Liaison, University of Edinburgh, Edinburgh, Scotland, 1975, p. 141; available upon request from C. K. Lee, Bureau of Mines, Pittsburgh, Pa.

4. Chaiken, R. F., and C. K. Lee. Automatic Wood Precharring Apparatus. Bureau of Mines Report of Invention MIN-2800, Pittsburgh Mining and Safety Research Center, Pittsburgh, Pa., Dec. 4, 1977, 8 pp.; available upon request from C. K. Lee, Bureau of Mines, Pittsburgh, Pa.

5. Chaiken, R. F., and J. M. Singer. Experimental Coal Mine Fire Research. Arch. Thermodynamics and Combustion Processes (Warsaw, Poland), v. 7, 1976, p. 529; available upon request from C. K. Lee, Bureau of Mines, Pittsburgh, Pa.

6. Hilado, C. J. The Multicapability Fire Test Method. J. Fire and Flammability, v. 7, 1976, p. 248.

7. Kansa, E. J., H. E. Perlee, and R. F. Chaiken. Mathematical Model of Wood Pyrolysis Including Internal Forced Convection. Combustion and Flame, v. 29, 1977, p. 311.

8. Koohgar, A. N., J. R. Welker, and C. M. Sliepievich. The Irradiation and Ignition of Wood by Flame. Fire Technol., v. 4, No. 4, 1968, p. 284.

9. Lee, C. K., R. F. Chaiken, and J. M. Singer. Charring Pyrolysis of Wood in Fires by Laser Simulation. 16th Symp. (Internat.) on Combustion. MIT, Cambridge, Mass., Aug. 15-20, 1976. The Combustion Institute, Pittsburgh, Pa., 1977, p. 1459.

10. Lyons, J. W. Cellulose: Chemistry, Wood, Paper and Forest Fire Control. Ch. in The Chemistry and Uses of Fire Retardants. John Wiley & Sons, Inc., New York, 1970, pp. 133-143.

11. Roberts, A. F. The Propagation of Fires in Passages Lined With Flammable Materials. Combustion and Flame, v. 11, 1967, p. 365.

12. Uehara, Y., and E. Yanai. Smoke, CO and CO_2 From Cellulosic Materials Treated With DAP in a Fire Environment. Paper in Fire and Flammability Series, ed. by C. J. Hilado. Technomic Co., Westport, Conn., v. 2, 1973, p. 116.

13. Wilde, D. G. Fire-Retardant Treatments for Mine Timbers. Min. Eng., v. 131, No. 138, 1972, p. 281.

U.S. GOVERNMENT PRINTING OFFICE: 1978-703-103/52 INT.-BU.OF MINES,PGH.,PA. 23169

622.09
Un32mo

RI 8300

Bureau of Mines Report of Investigations/1978

A Flexible Helical Rock Bolt

The Library of the
NOV 21 1978
University of Illinois
at Urbana-Champaign

UNITED STATES DEPARTMENT OF THE INTERIOR

Report of Investigations 8300

A Flexible Helical Rock Bolt

By Clarence O. Babcock

March 3 1849

UNITED STATES DEPARTMENT OF THE INTERIOR
Cecil D. Andrus, Secretary

BUREAU OF MINES

This publication has been cataloged as follows:

Babcock, Clarence O

A flexible helical rock bolt / by Clarence O. Babcock. [Washington] : U.S. Dept. of the Interior, Bureau of Mines, 1978.

26 p. : diagrams ; 27 cm. (Report of investigations - Bureau of Mines ; 8300)

Bibliography: p. 24.

1. Rock bolts. I. United States. Bureau of Mines. II. Title. III. Series: United States. Bureau of Mines. Report of investigations - Bureau of Mines ; 8300.

TN23.U7 no. 8300 622.06173

U.S. Dept. of the Int. Library

CONTENTS

Page

Abstract.......... 1
Introduction.......... 1
Acknowledgments.......... 3
Theory.......... 3
Manufacture and laboratory testing of helical coils.......... 4
Manufacture and laboratory testing of helical rock bolts.......... 10
Preliminary field testing of helical rock bolts and vibrating-wire load gages.......... 17
Summary and conclusions.......... 22
References.......... 24
Appendix.--Deformation behavior of an elastic helical coil loaded in tension.......... 25

ILLUSTRATIONS

1. Theoretical flexibility of an elastic helical coil.......... 3
2. Experimental changes in coil geometry with increasing load.......... 4
3. Two-dimensional projection of experimental helical coil shape versus maximum tensile force applied.......... 5
4. Change in coil length as a function of the maximum tensile force applied.......... 6
5. Radius and outside diameter of coil as a function of the maximum tensile force applied.......... 6
6. Pitch of coil as a function of the maximum tensile force applied.......... 7
7. Elastic, plastic, and total average strains for coil as a function of the maximum tensile force applied.......... 8
8. Flexibility ratio of the helical coil to a straight rod of the same length for a given maximum tensile force applied.......... 9
9. Relative bolt flexibilities and elastic work capabilities of coil geometries tested.......... 9
10. Relative work capabilities of loading and unloading helical coils.......... 10
11. Flexible helical bolts and other hardware tested in the York Canyon mine.......... 11
12. Change in helical bolt length as a function of the maximum tensile force applied.......... 12
13. Radius and outside diameter of helical bolt as a function of the maximum tensile force applied.......... 12
14. Pitch of helical bolt as a function of the maximum tensile force applied.......... 13
15. Elastic, plastic, and total average strains for helical bolts as a function of the maximum tensile force applied.......... 14
16. Flexibility ratio of the helical bolt to a straight rod of the same length for a given maximum tensile force applied.......... 15
17. Work done by helical bolt during manufacture with increasing tensile load compared with the elastic work done by a straight bolt.......... 16
18. Plan map of York Canyon mine panel 5N.......... 17

ILLUSTRATIONS--Continued

Page

19. Bolt patterns used in the York Canyon mine........................ 18
20. Bolt loads measured by vibrating-wire load gage for helical and straight bolts in York Canyon mine crosscut 1S................... 19
21. Bolt loads measured by vibrating-wire load gage for helical and straight bolts in York Canyon mine crosscut 2S................... 20
22. Bolt loads measured by vibrating-wire load gage for helical and straight bolts in York Canyon mine crosscut 3S................... 21
23. Bolt loads measured by vibrating-wire load gage for helical and straight bolts in York Canyon mine crosscut 4S................... 22

A FLEXIBLE HELICAL ROCK BOLT

by

Clarence O. Babcock[1]

ABSTRACT

This report describes the results of Bureau of Mines laboratory and preliminary field tests on a rock bolt of helical shape. The flexible construction allows the bolt to maintain a more stable load level than is possible with a straight bolt. Bolt load changes resulting from anchor slippage, blasting shock, or changes in mine geometry with mining advance are minimized.

Preliminary field tests were performed at the Kaiser Steel York Canyon mine where the load changes of straight and helical bolts were measured using a vibrating-wire load gage. The field tests were performed to establish the viability of the concept of a helical bolt. The practical usefulness in terms of performance and economics remains to be shown. The change in bolt load for the flexible bolts was one-third that for the straight bolts. There were no malfunctions of the gage, and the bolts maintained a more uniform load than the straight bolts used as controls.

INTRODUCTION

The use of over 90 million rock bolts in the United States every year indicated their importance to mining. Recently, the shift has been away from conventional expansion shell- or wedge-type anchor bolts to resin-grouted bolts. This has occurred because the resin-grouted bolts have been more effective in supporting the roof, even though the conventional bolts are less expensive. Different bolting innovations have been tried over the years and a few recent ones with promise will be mentioned in this report. Ortlepp and Reed (6)[2] describe a yieldable rock bolt (also referred to as a yielding rock bolt) that uses a circular die to plastically deform a rolled, threaded portion of the bolt. Based on tests in South African mines, Ortlepp and Reed conclude that a fully grouted rock bolt placed and grouted immediately after rock excavation, even though untensioned initially, should be several times more effective than a tensioned but ungrouted bolt in preventing rock dilatation.

---

[1] Mining engineer. Denver Mining Research Center, Bureau of Mines, Denver, Colo.

[2] Underlined numbers in parentheses refer to items in the list of references preceding the appendix.

A modification of this bolt was studied in the laboratory by Conway and was patented in July 1976 (3). These tests show that the bolt can maintain a nearly stable load over an elongation of about 8 inches. Harrell (5) used 30-inch-long, hydraulically driven steel pins to join rock layers at the Orient No. 6 mine of the Freeman Coal Mining Corp., Waltonville, Ill. He concludes that roof-pinning is still in the experimental stage and will require more testing and time before it is a proven roof-control system. In a 1975 report on a pumpable polymeric roof bolt, Thompson and Bates conclude that "the results to date show that the ground support characteristics of the pumpable bolt are comparable with those of resin grouted steel bolts." The placing of such bolts is too complicated for general use at the present time. The polyester resin used was made in Japan and was no longer available. The most promising new bolt appears to be the friction rock stabilizer for which Scott (7) received two U.S. patents, 3,922,867 (December 2, 1975) and 4,012,913 (March 22, 1977). In an article describing these inventions he concludes, "the simplicity of the system, the reproducibility of the data in both the laboratory and field test program, coupled with the ease of manufacture and economy all would seem to dictate that the mining industry should take a hard look at this system to solve many of its ground control problems." In another article, Chaiko and Scott (2) conclude, "the results are encouraging, but much work remains to be done. While key performance benefits have been demonstrated, superior economics and operational installation equipment are yet to be shown." This bolt which has the trade name Split Set is a steel tube split lengthwise. The bolt is forced into a drill hole and support is provided through friction or a change in shape plastically so that the tube more nearly matches the hole shape. Performance and cost are equal to those of a resin-grouted bolt. In a private conversation, Scott indicated that 60,000 of these bolts had been made at that time (April 1977) and that greater quantities were expected.

While there is an increased interest in resin-grouted bolts, the biggest part of the bolting market is still bolts of conventional design with an expansion or split-wedge anchor. In addition to their lower cost, they supply the full bolt load over the length of the bolt. The weakest link appears to be the anchorage capacity of the expansion-anchor rock system. Although a 5/8-inch nominal-diameter rock bolt can support a load of 17,000 pounds and more if a high-strength or extra-high-strength bolt is used, the anchor may slip at loads of 8,000 to 10,000 pounds (8). Since the elongation of the bolt is only 0.077 inch (1/13 inch) for a 6-foot bolt loaded to 8,000 pounds, such anchor slippage seriously decreases the bolt load. The anchor can supply more nearly the full strength of the bolt if a displacement of 0.1 or 0.2 inch is possible before the bolt unloads. The usual remedy is to tighten the bolts a number of times during use. If anchor slippage was not so critical to bolt load, this would not be necessary.

A possible solution to the problem is the use of a flexible bolt of helical shape described in this report. Patent 3,942,329, assigned by the author to the Department of the Interior, was granted on the bolt on March 9, 1976. A helical bolt can be made many times as flexible as the straight bolt, depending on the geometry used, and can maintain bolt loads when the straight bolts cannot. For example, if a straight bolt loses 50% of its load from anchor slippage, a helical bolt with a flexibility of five would lose only 10% of its load. This means that if a straight bolt load decreased from 8,000 pounds to 4,000 pounds, the flexible bolt load would change from 8,000 to 7,200 pounds. Conversely, if the load change increases 50%, the 8,000 pounds on the straight bolt would become 12,000 pounds and the load for the flexible bolt would increase to 8,800 pounds. Stated another way, the straight bolt load would be in the range of 4,000 to 12,000 pounds, while the helical bolt with a flexibility of five would be in the range of 7,200 to 8,800 pounds, If greater flexibility can be produced, the load would be more stable. In addition, if a bolt geometry that produces plastic flow in the bolt during use is used, it can also provide a more uniform-loading behavior. The flexible bolt can tolerate loading or unloading, while the yieldable rock bolt (3) works well only as long as the load is increasing. In decreasing bolt loads it should perform almost the same as a straight conventional bolt. The bolt loads were determined during the field testing by means of a vibrating-wire load gage, which (1) was assigned U.S. patent 3,942,329.

ACKNOWLEDGMENTS

The author wishes to thank the following: Ed Moore, mine manager, and Bill Sikes, mining engineer, for the use of the Kaiser Steel York Canyon coal mine for field tests. Don Gentry, professor, and Carlos Alves, graduate student, both of the Colorado School of Mines who were in charge of the field tests and load gage readings. David Wisecarver, supervisory mining engineer, and Frank Popich, engineering technician, both of the Federal Bureau of Mines, cooperated in arranging and helping with the field tests.

Minimum hole diameters required to place helical bolts made from 9/16-inch straight bolts

R	0	0.5	0.6	0.7	0.8	0.9	1.0	1.1	1.2	1.3	1.4	1.5	1.6
D	1	2.0	2.2	2.4	2.6	2.8	3.0	3.2	3.4	3.6	3.8	4.0	4.2
D, inches	9/16	1.1	1.3	1.4	1.5	1.6	1.7	1.8	1.9	2.0	2.2	2.3	2.4

$$F_r = \frac{\left\{1263R^4 + 16R^2\,p^2 + p^2\right\}}{p\sqrt{39.5R^2 + p^2}}$$

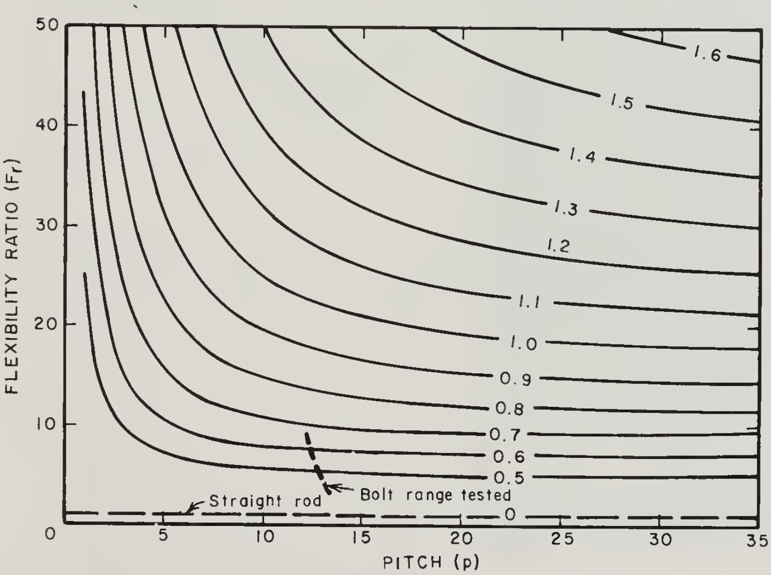

FIGURE 1. - Theoretical flexibility of an elastic helical coil. Theoretical flexibility of an elastic helical coil in terms of its pitch, p, and radius, R, expressed in rod diameter units, d.

THEORY

The elongation behavior of a helical elastic coil (given in the appendix as equation 8) is plotted in figure 1. In this figure, the flexibility ratio, F_r, is the elongation of a helical coil loaded in tension divided by the elongation of a straight rod of the same length, materials and cross-sectional area and loaded with the same tensile force. An F_r value of 5, for example, indicates that the coil stretches five times as much as the straight rod of the same length at any force value as long as the unloaded bolt geometry is unchanged. In figure 1, the variables R and p are the radius and pitch of the coil, respectively, in units of rod diameters, d, for the rod from which the coil is made. D is the outside diameter of the coil. The curve R = 0.5d represents a coil wound around and touching a straight line so that the coil has no center hole. The F_r value decreases rapidly with an increase in the applied force, and extremely flexible coils cannot be manufactured for the loads applied to small bolt diameters such as those used in mining; that is, the helical bolts change their geometry as the tensile force is increased, becoming less flexible at force values applied to rock bolts. The table in figure 1 relates the R and D values for the helical bolts made from 5/8-inch-diameter straight bolts. R is given in d units, and D is given in both d units and inches. The outside diameter of the coil, D, is the smallest hole diameter into which the bolt would fit. In practice, the smallest hole size of 1-3/8 inches is dictated by the anchor diameter.

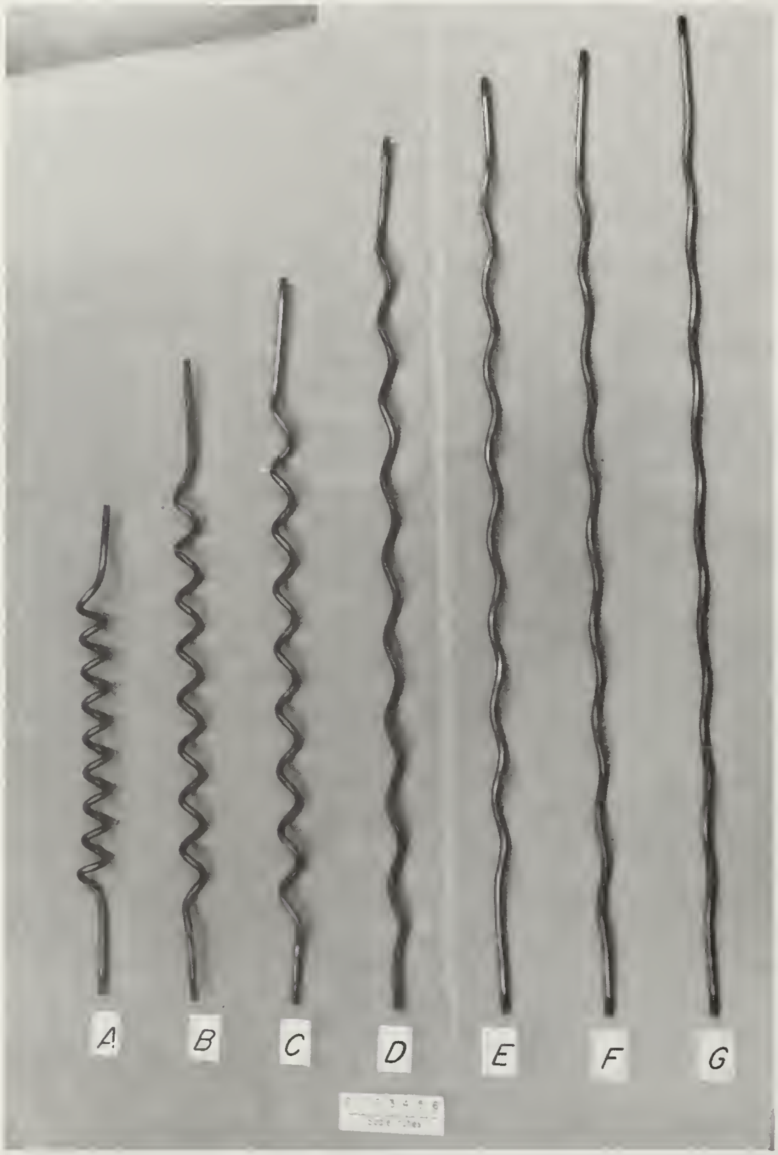

FIGURE 2. - Experimental changes in coil geometry with increasing load (pounds). A–2,000; B–3,000; C–4,000; D–6,000; E–9,000; F–10,000; G–13,000.

MANUFACTURE AND LABORATORY TESTING OF HELICAL COILS

Helical coils were made by a spring manufacturer from rods of 4140 steel, 0.5 inch in diameter, and 5 feet long, as shown in figure 2A. This steel was chosen because many coiled springs are made from this material. Although the coils tested were not hardened, this could have been done had it been desirable or necessary. As the tensile force was increased, the coil geometry changed from A to B to C, etc., in sequence. The geometry changes in figure 2 correspond to maximum tensile force applied, in pounds. The changes in shape with an increasing maximum force resulted from plastic flow. The helical shapes of these coils in two dimensions are shown as sine or cosine waves in figure 3. The experimental values of F_r for these geometries are given by numbers preceded by X. In figure 3A, the coil was 82 times as flexible as a straight rod of the same length for a tensile force of 2,000 pounds or less. By the time the tensile force was 9,000 pounds, the coil was only six times the flexibility of the straight rod of the same length, size, and force.

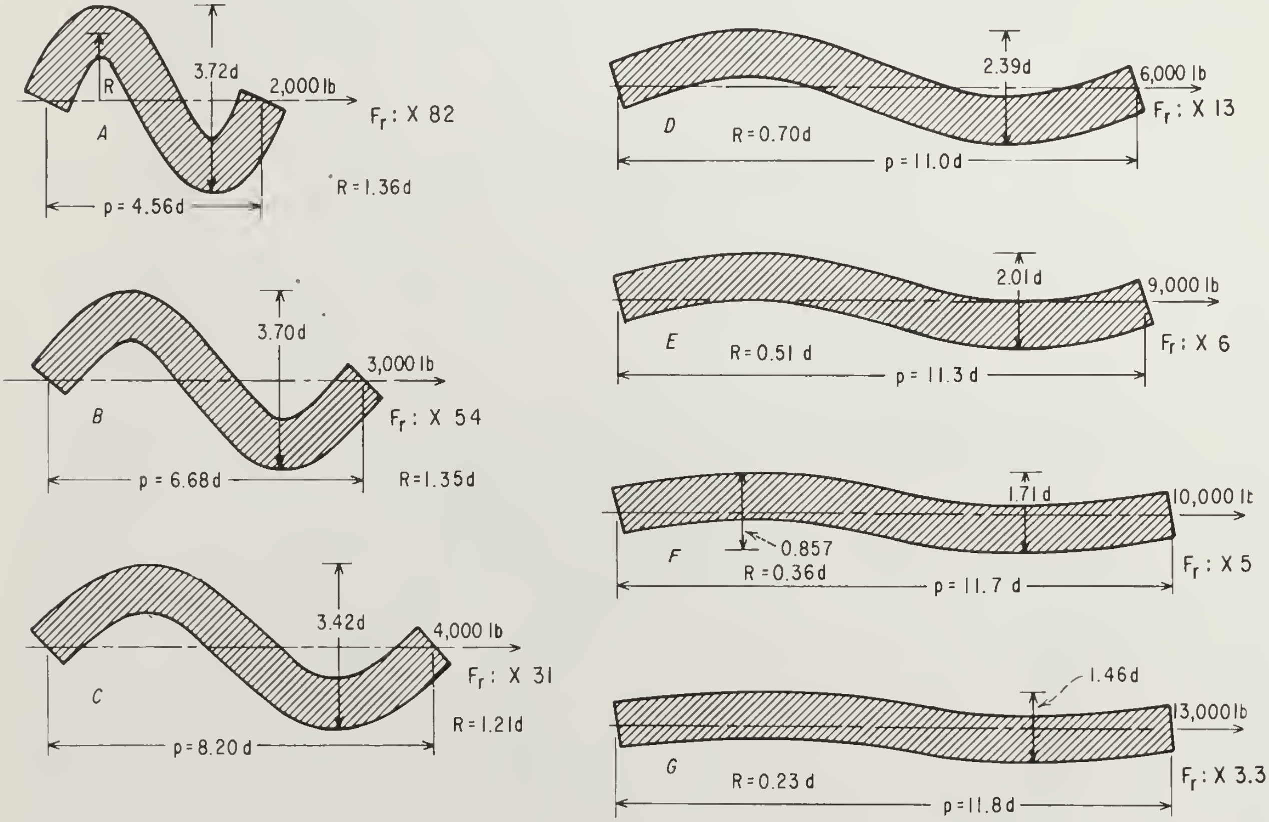
R
3.72d
2,000 lb
F_r: X 82
A
R = 1.36d
p = 4.56d
3.70d
3,000 lb
B
F_r: X 54
p = 6.68d
R = 1.35d
3.42d
4,000 lb
F_r: X 31
C
R = 1.21d
p = 8.20 d
2.39d
6,000 lb
F_r: X 13
D
R = 0.70d
p = 11.0d
2.01d
9,000 lb
E
F_r: X 6
R = 0.51 d
p = 11.3 d
1.71d
10,000 lt
0.857
F
R = 0.36d
p = 11.7 d
F_r: X 5
1.46d
13,000 lb
G
R = 0.23 d
F_r: X 3.3
p = 11.8 d

FIGURE 3. - Two-dimensional projection of experimental helical coil shape versus maximum tensile force applied.

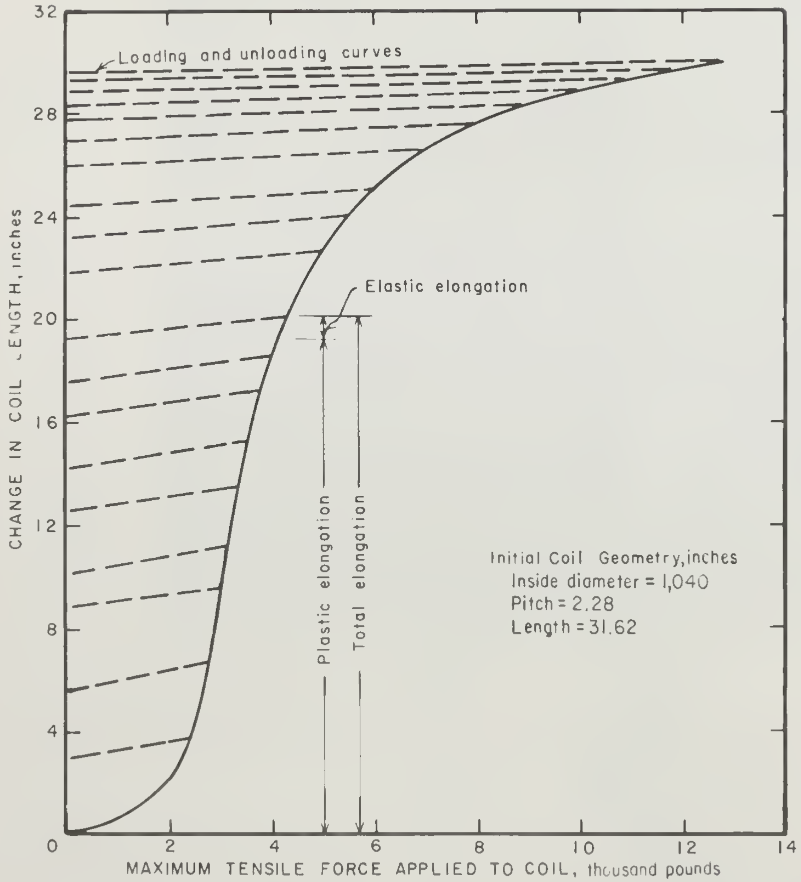

FIGURE 4. - Change in coil length as a function of the maximum tensile force applied.

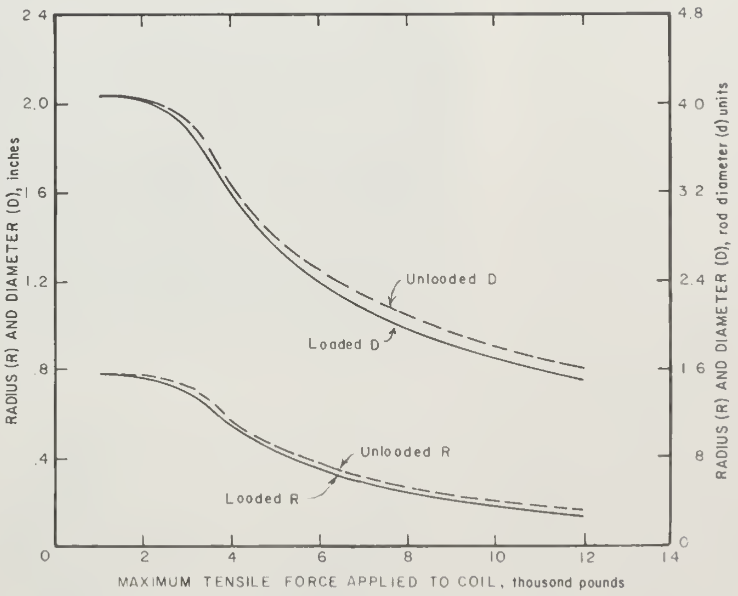

FIGURE 5. - Radius and outside diameter of coil as a function of the maximum tensile force applied.

In figure 4, the change in coil length is plotted against the maximum tensile force applied. After each increase in load above the previous maximum, the load was removed to establish how much of the elongation was plastic and how much was elastic. The broken lines represent both the loading and unloading curves. The change in length of the unloaded coil, from the initial shape A in figure 2, is given by the y-axis intercept with the broken line. The difference between the y = 0 length and this value resulted from the plastic flow; most of the elongation from shape A was plastic.

In figure 5, the change in coil radius, R, and the outside diameter of the coil, D, in inches and in rod diameter units, d, are given as functions of the maximum tensile force applied. The loaded and unloaded R and D values are nearly the same.

In figure 6, the change in coil pitch, p, in inches and in rod diameter units is given as a function of the maximum tensile force applied. The difference in the loaded and unloaded p values is not large.

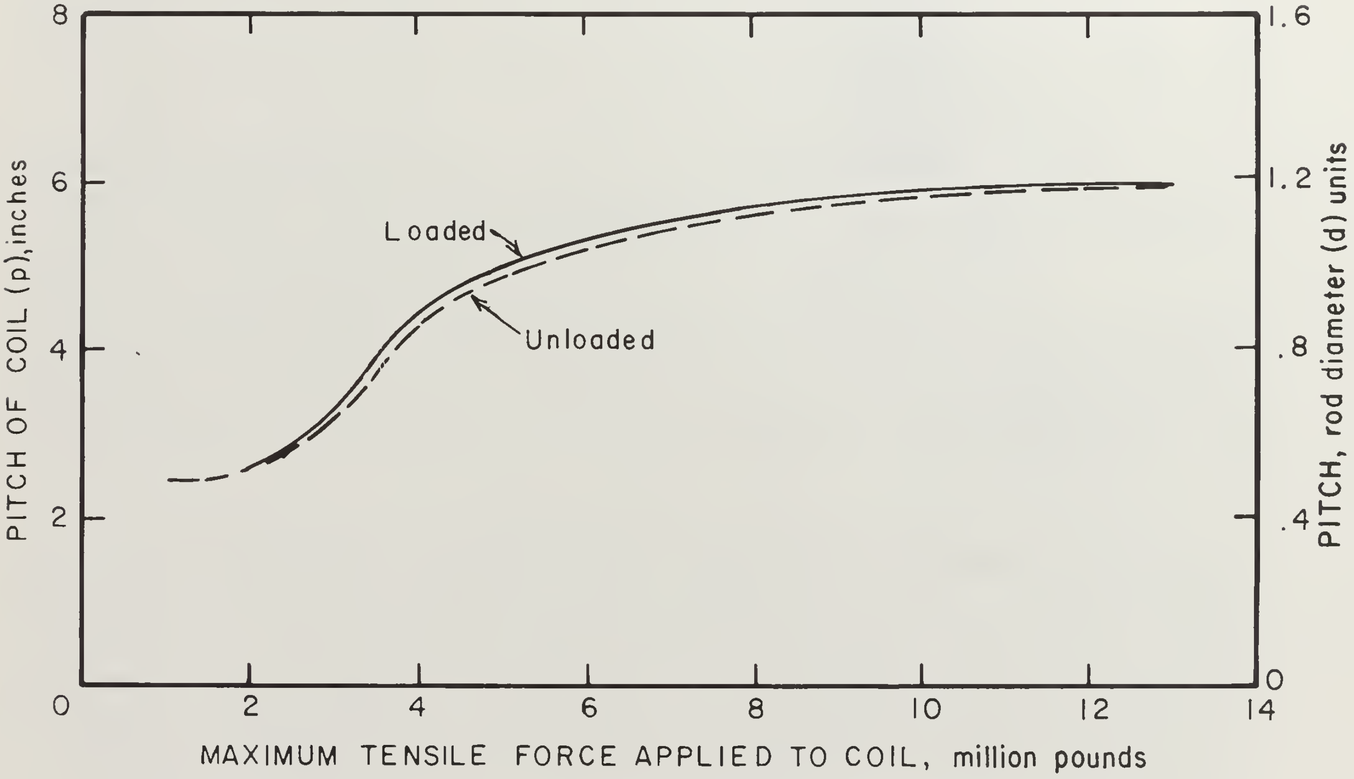

FIGURE 6. - Pitch of coil as a function of the maximum tensile force applied.

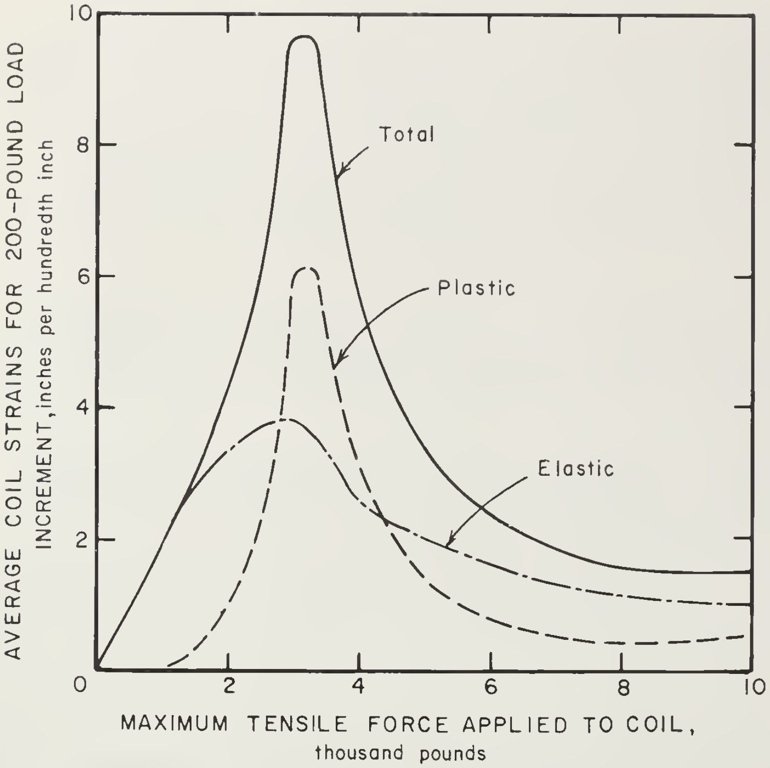

FIGURE 7. - Elastic, plastic, and total average strains for coil as a function of the maximum tensile force applied.

In figure 7, the results of cyclically loading and unloading the helical coil by increasing the force of each successive loading cycle in 200-pound increments above the previous maximum is shown as average total, plastic, and elastic strains occurring for that 200-pound-load increment at each loading level. These were obtained by dividing the total, plastic, and elastic elongations by the bolt length at that time. The elastic strains are important throughout the force range, especially for the high and low force values. The plastic strains are more restricted, occurring mostly for forces that are 20% to 50% of the maximum force applied. The most rapid change in coil length for a 200-pound-force increment occurred at about 3,200 pounds of force; the maximum total, plastic, and elastic strains occurred at about this value. This is 25% of the total force applied to the coil, which implies that if this extreme behavior is desired for a particular support application, the rod size should be loaded to 25% of its straight-rod-strength value.

In figure 8, the flexibility of the helical coil relative to that of a straight rod of the same length and material is given by the ratio, F_r, for maximum applied tensile force loads. This is compared with what is predicted by equation 8 for $r = 0.25$ inch when the experimental values of R and p are used. Considering the extensive plastic flow that has occurred in the coil, the theory and experimental results nearly agree with one another. Figure 8 indicates that the flexibility of a helical coil decreases rapidly as the load is initially applied, when torsion produces most of the change in the coil length. At larger loads, the relative importance of bending and tension increases.

In figure 9, the ratio of work that can be done by a stretched helical coil compared with the work that can be done by a stretched straight rod is given as F_r or A/A', which is called the flexibility ratio. The work ratios for the coil geometries given in figure 1 are tabulated in figure 9. For example, a coil with geometry C has 31 times as much recoverable elastic work

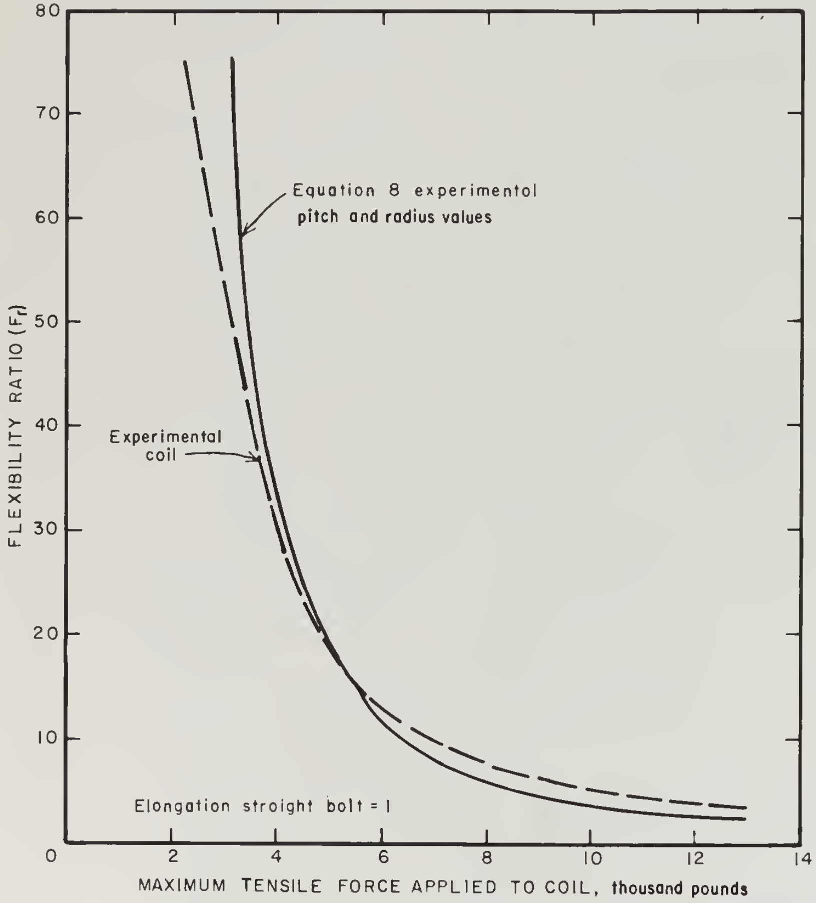

FIGURE 8. - Flexibility ratio of the helical coil to a straight rod of the same length for a given maximum tensile force applied.

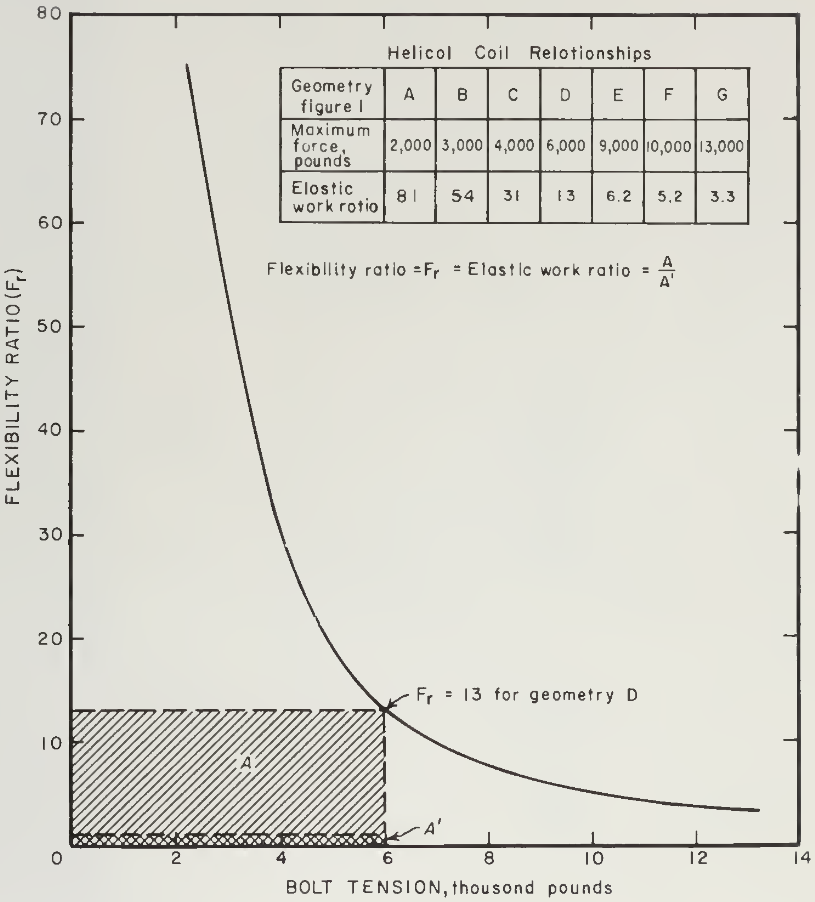

Geometry figure 1	A	B	C	D	E	F	G
Maximum force, pounds	2,000	3,000	4,000	6,000	9,000	10,000	13,000
Elostic work rotio	81	54	31	13	6.2	5.2	3.3

Flexibility ratio = F_r = Elastic work ratio = $\frac{A}{A'}$

FIGURE 9. - Relative bolt flexibilities and elastic work capabilities of coil geometries tested.

stored in it as a straight rod with the same length of coil and with the same applied force.

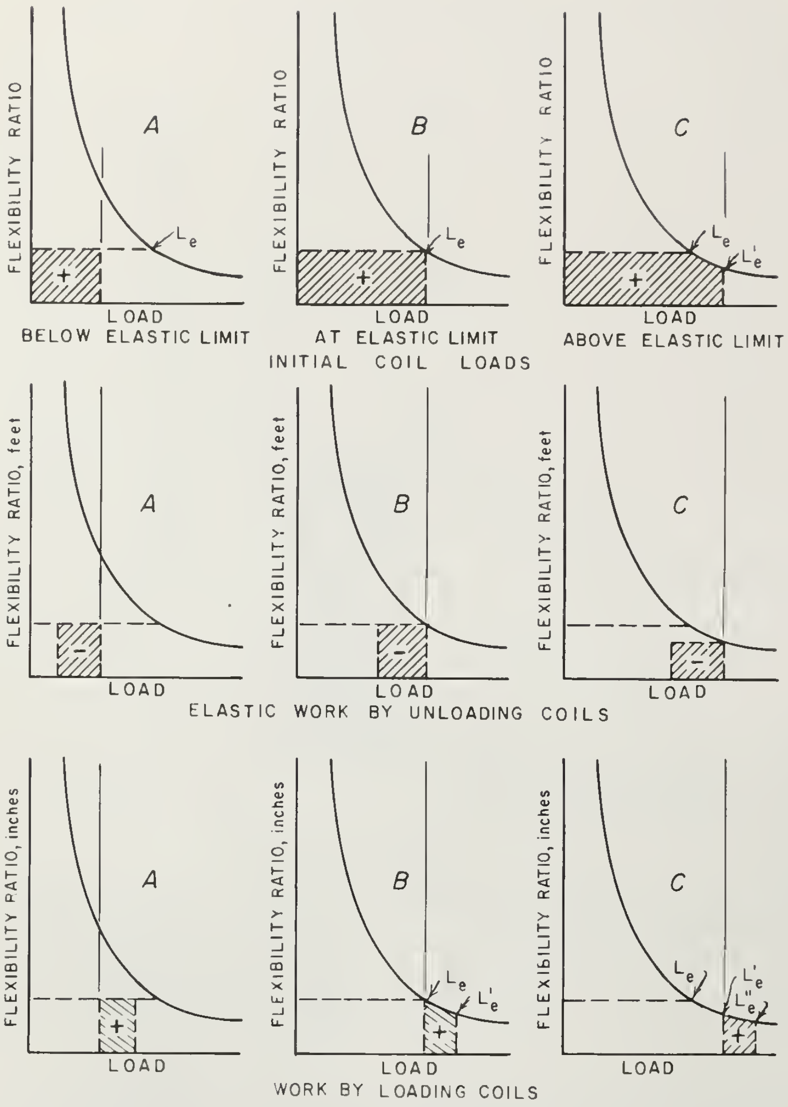

FIGURE 10. - Relative work capabilities of loading and unloading helical coils.

The helical coil exhibits either elastic or elastic-plastic behavior, depending upon the load conditions as described semiquantitatively in figure 10. In figure 10, L_e denotes the elastic limit established during the coil-manufacturing process. If this limit is not exceeded, the coil behaves in an entirely elastic manner. If the previous force used to establish the coil geometry is exceeded, a new elastic limit, L_e', is established. In this process, the flexibility of the coil is reduced and the coil elongates plastically. The total work done in loading the coil, both elastic and plastic, is applied to the structure when the load is increasing. However, only the elastic work is available to do work on the structure when the coil is unloading. The amount of elastic work that can be recovered is reduced if the new elastic limit, L_e', is replaced with still another ratio L_e'' by an increasing tensile force. Because plastic flow occurs at nearly constant force, this aspect of behavior can be used to advantage to help maintain a more nearly constant coil load when in use. Because of the geometry and combined state of stress (torsion, bending, and tension), instead of only tension for straight rod, plastic flow can be produced at loads well below those needed for straight rods. By choosing the coil geometry-load conditions, a wide variety of coil behaviors is possible.

MANUFACTURE AND LABORATORY TESTING
OF HELICAL ROCK BOLTS

The next laboratory testing was on helical rock bolts constructed from 5/8-inch nominal diameter (9/16-inch actual) Colorado Fuel and Iron expansion-anchor-shaped rock bolts of 6 foot-length. These bolts (shown in fig. 11) along with some other hardware were later tested in an operating mine. In figure 11, the letter A denotes straight bolts of the kind made into helical bolts by a spring manufacturer. The initial geometry used is not shown but resembled A of figure 2. A coil with a 2-5/8-inch pitch was wound on a 1-1/4-inch mandrel in a lathe. For commercial use, the method of manufacturing would be different and less expensive. The letters B, C, D, and E in figure 11 denote bolts that were loaded during manufacture with maximum forces of 10,000 pounds, 12,000 pounds, 14,000 pounds, and 16,000 pounds, respectively. All of these forces were above the intended bolt installation loads, and, therefore, the bolt behavior was expected to be elastic. If smaller values had been used, some plastic flow would have occurred during bolt use and would have helped the bolts to maintain their installed loads. Tests with bolts that deform plastically during use remain to be run. Note that all helical bolts retain some of their helical shape and flexibility for the load range that may result in mine use. The letters F, G, and H in figure 11 denote vibrating-wire load gages used to measure the bolt loads in field use, bearing plates, and 1-5/8-inch expansion anchors. None of the bolts was hardened.

In figure 12, the change in bolt length of a 40.75-inch-long helical bolt is plotted against the maximum tensile force applied. After each 200-pound

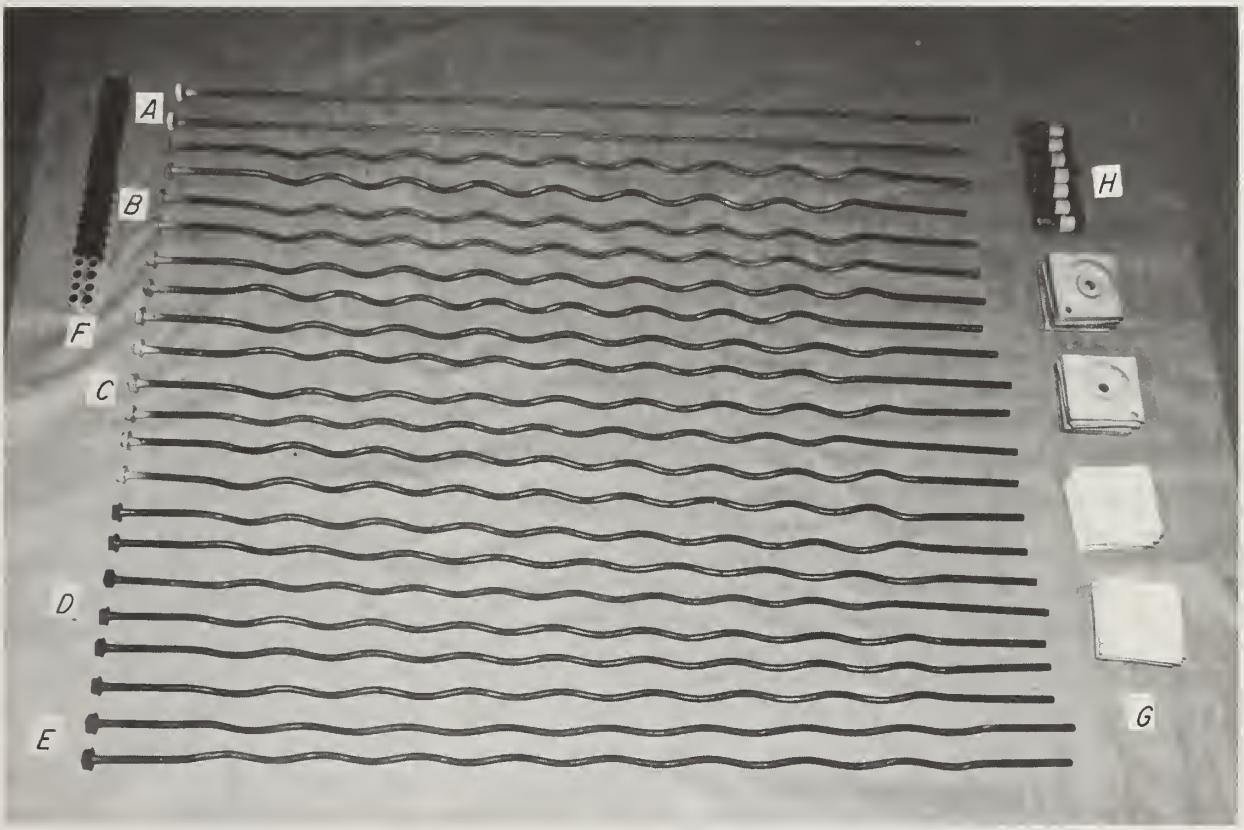

FIGURE 11. - Flexible helical bolts and other hardware tested in the York Canyon mine.

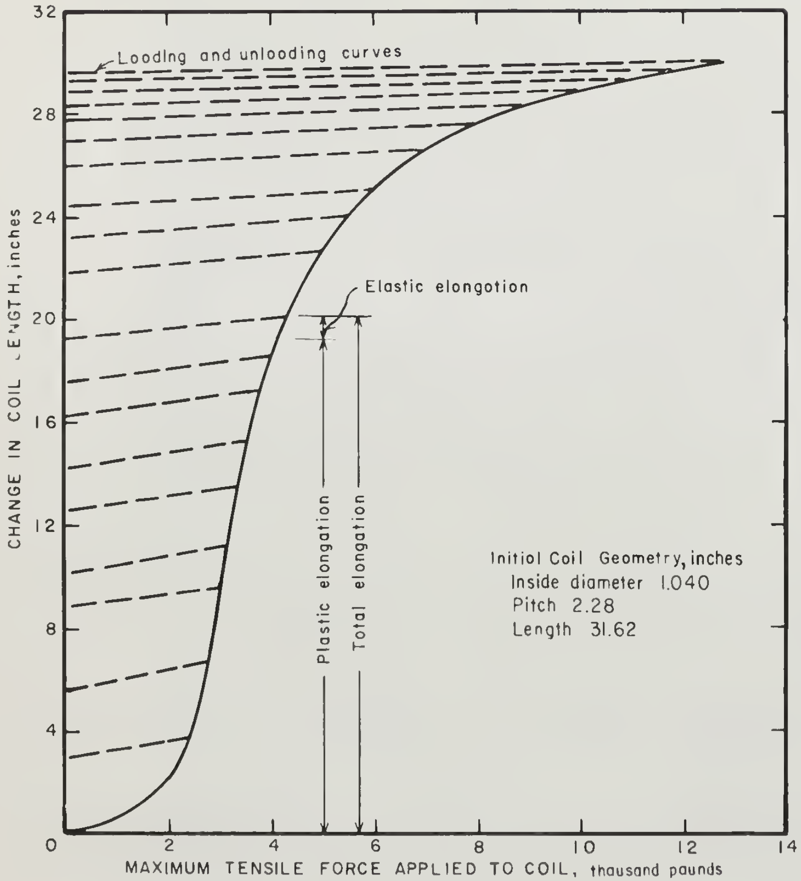

FIGURE 12. - Change in helical bolt length as a function of the maximum tensile force applied.

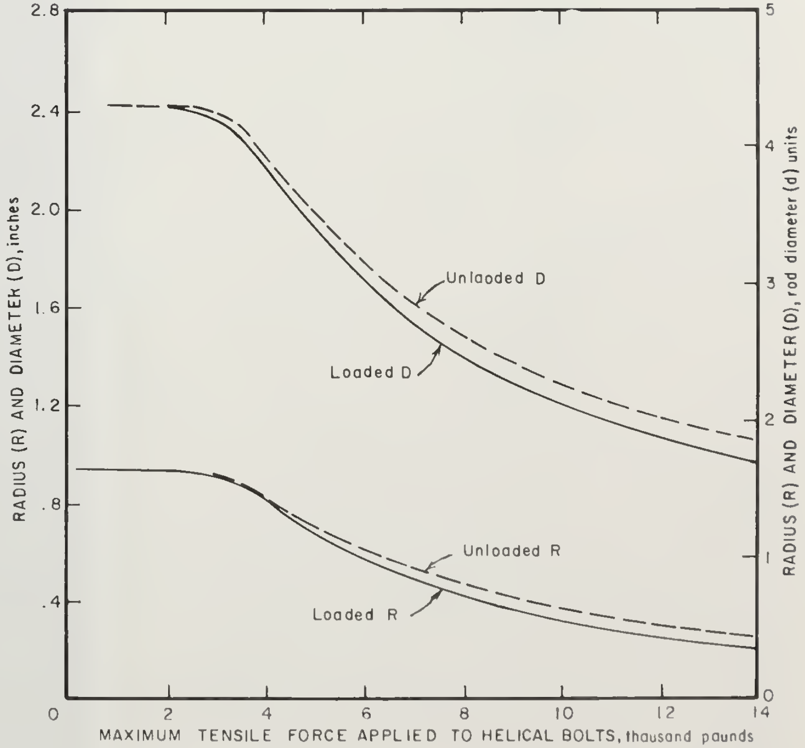

FIGURE 13. - Radius and outside diameter of helical bolt as a function of the maximum tensile force applied.

increase in load above the previous maximum, the load was removed to establish how much of the elongation was plastic and how much was elastic. The unloading and reloading curves, which are represented by the broken lines, show that most of the elongation was plastic.

In figure 13, the change in bolt radius, R, and in the outside diameter of the bolt, D, in inches and in rod-diameter units, are given as functions of the maximum tensile force applied. The hole diameter required to place a helical bolt can be obtained from the unloaded D, which should be 1.63 inches for the anchor size used.

In figure 14, the change in bolt pitch, p, in inches and in rod diameter units is given as a function of the maximum tensile force applied. The loaded and unloaded pitch values are nearly the same.

In figure 15, the results of cyclic loading and unloading the helical bolt between zero and a maximum force that was increased by 200-pound increments is shown in terms of the average total strains, the average plastic strains, and the average elastic strains. These were obtained by dividing the total, plastic, and elastic-bolt elongations by the bolt length before that loading cycle. The elastic strains are important throughout the force range, but the elastic strains are relatively more important for high force values. The plastic strains are more restricted, contributing most for forces between 20% and 50% of the largest force applied. The most rapid change in bolt length for a 200-pound-force increment occurred at about 3,200 pounds. These curves appear to have a log-normal shape.

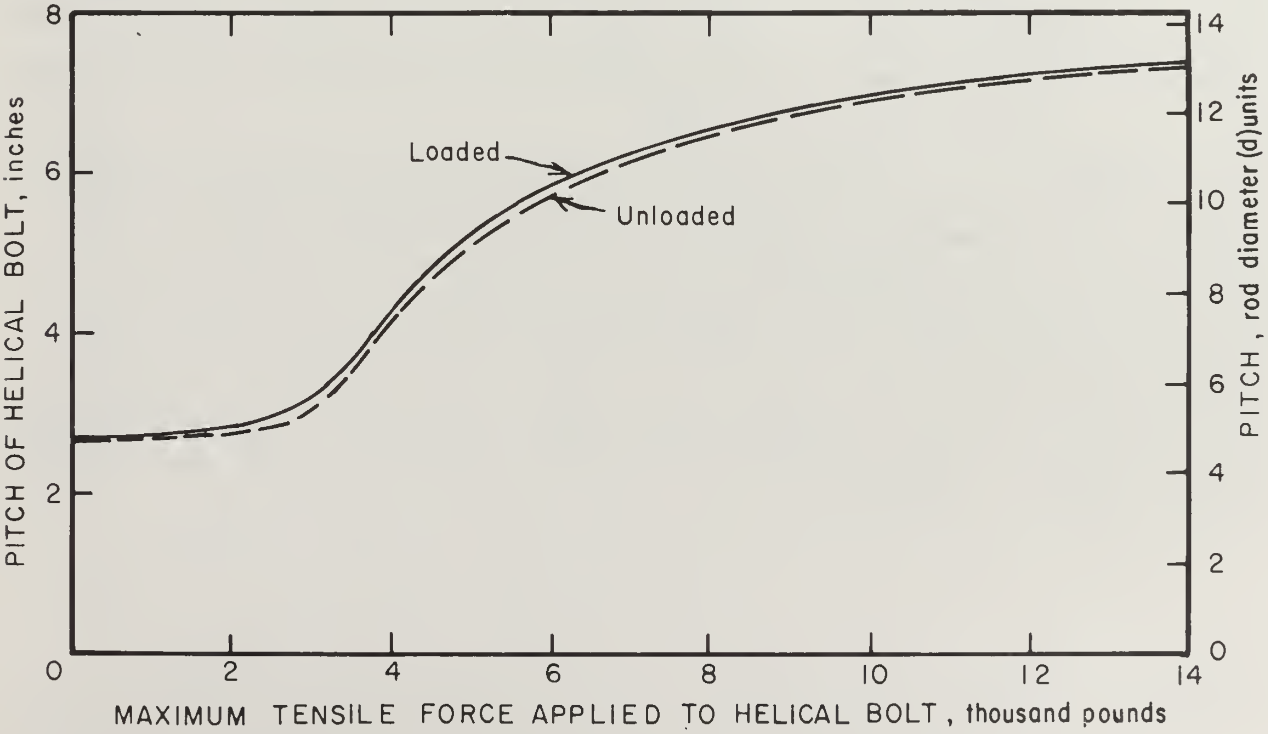

FIGURE 14. - Pitch of helical bolt as a function of the maximum tensile force applied.

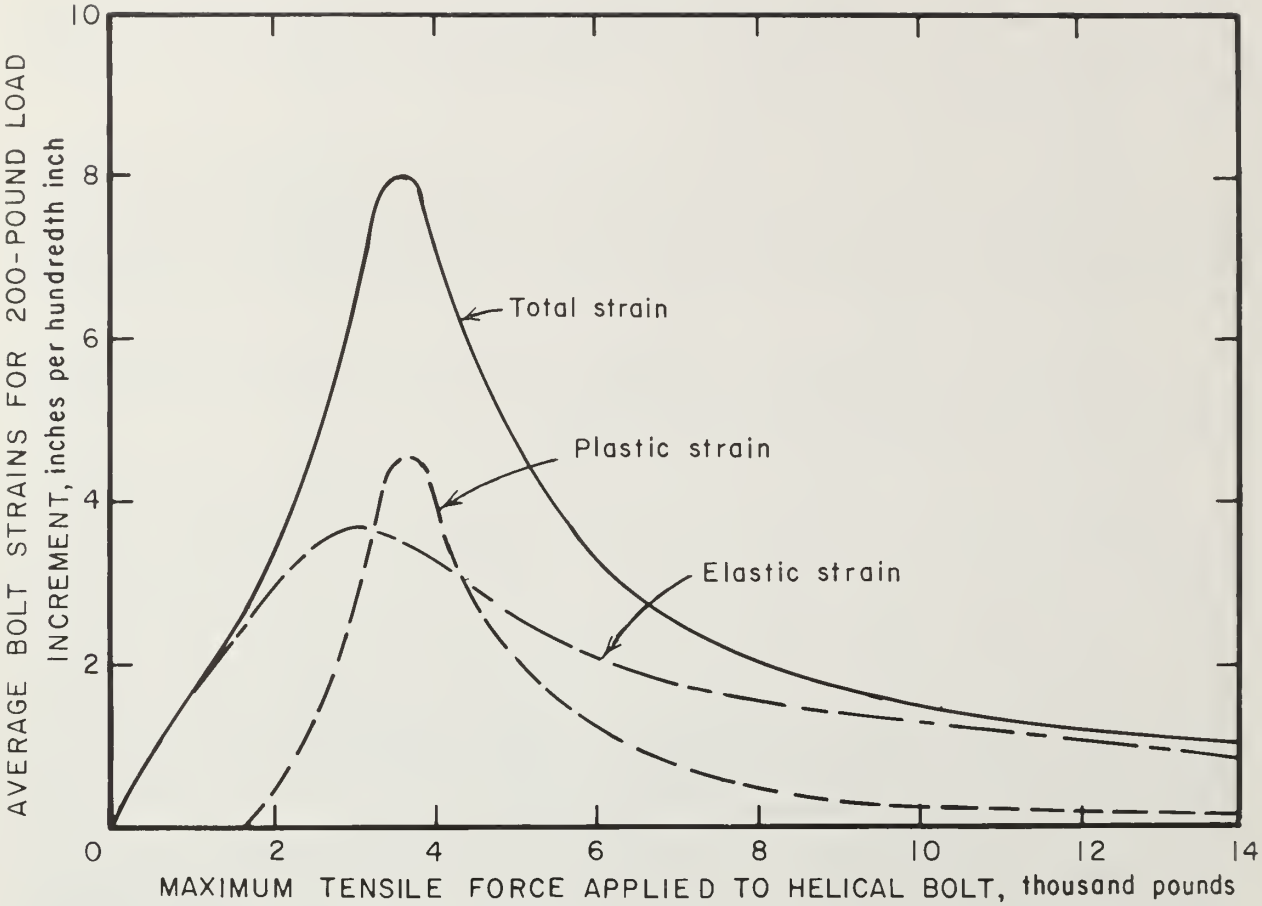

FIGURE 15. - Elastic, plastic, and total average strains for helical bolts as a function of the maximum tensile force applied.

In figure 16, the flexibility of the helical bolt relative to that of a straight bolt is given by the ratio, F_r, for maximum applied tensile force loads. This is compared with what is predicted by equation 8 for r = 0.281 inch when the experimental values of R and p are used. Considering the extensive plastic flow that has occurred in the coil, the elastic estimate of behavior is fairly good. This figure indicates that the flexibility of a helical bolt decreases rapidly as the load is initially applied and when torsion is the most important component of stress. The bolt becomes stiffer when the bending and tension stresses become equally important. Figures 12 through 16 show that the behavior of helical bolts is almost the same as that of coils shown by figures 4 through 8.

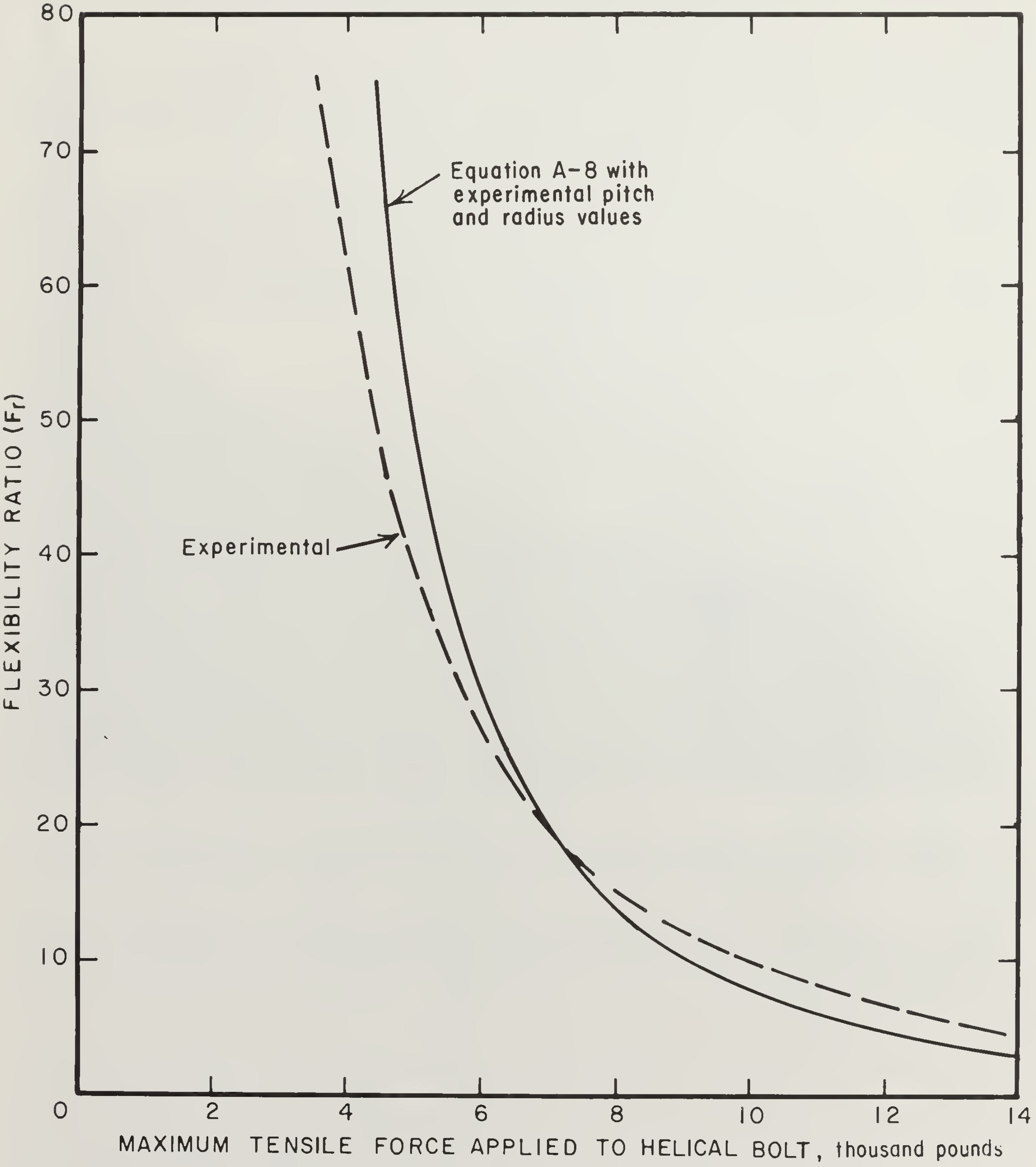

FIGURE 16. - Flexibility ratio of the helical bolt to a straight rod of the same length for a given maximum tensile force applied.

In figure 17, the total work done on the bolt by increasing the tension from the initial coiled shape to 10,000, 12,000, and 14,000 pounds of force is shown. This work was 14,350 foot-pounds for the 14,000-pound load. In comparison, the work done on a straight bolt was 79 foot-pounds for the

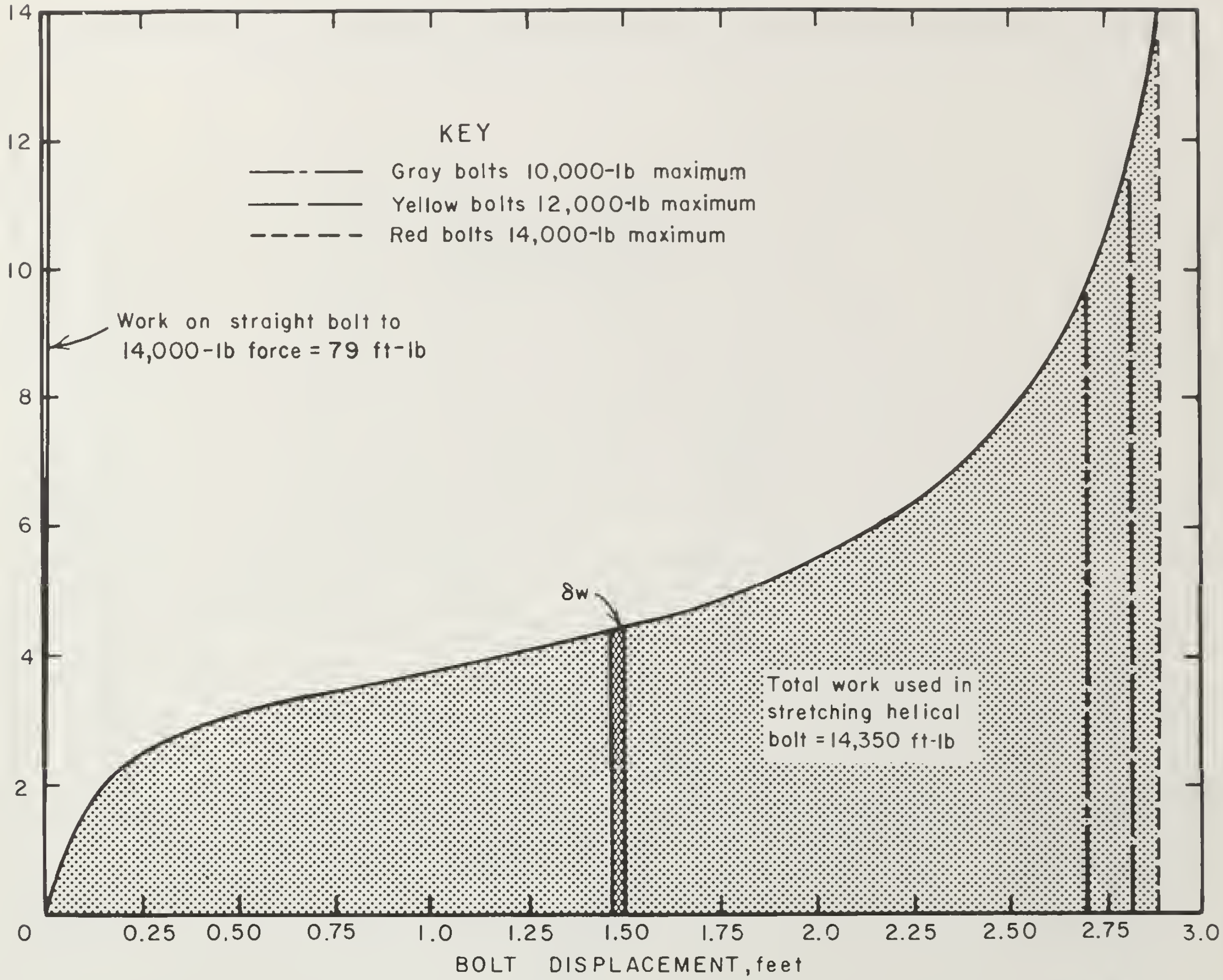

FIGURE 17. - Work done by helical bolt during manufacture with increasing tensile load compared with the elastic work done by a straight bolt.

14,000-pound load. An increment of work is denoted by δw. Most of the work done on the helical bolt was plastic and could not be recovered when the bolt was unloaded.

PRELIMINARY FIELD TESTING OF HELICAL ROCK BOLTS AND VIBRATING-WIRE LOAD GAGES

Some preliminary field tests were conducted at the Kaiser Steel Co.'s York Canyon coal mine, near Raton, N. Mex., to verify that both helical bolts and vibrating-wire load gages (1) behaved as expected in mine use. Eighteen

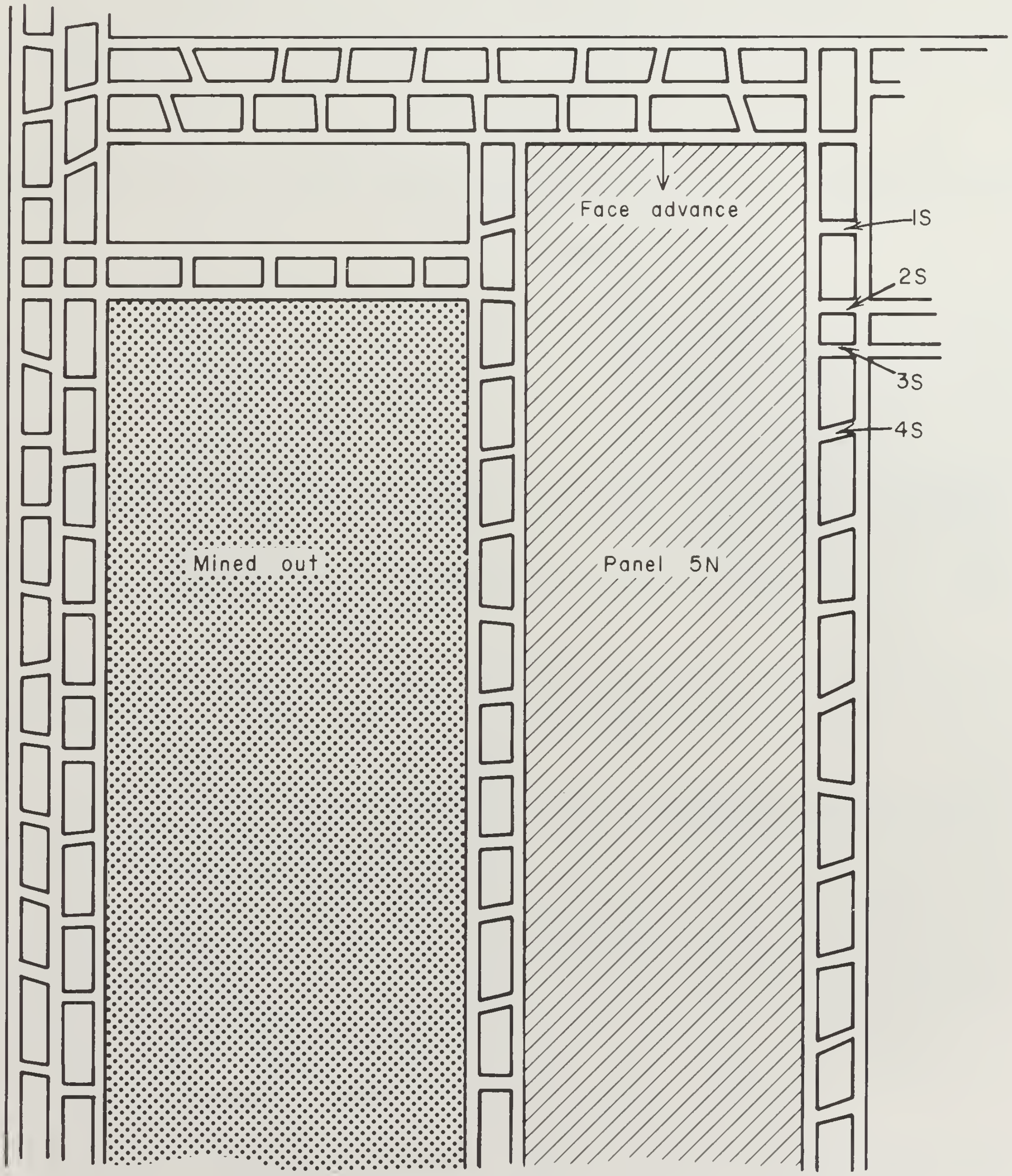
Face advance
1S
2S
3S
4S
Mined out
Panel 5N

FIGURE 18. - Plan map of York Canyon mine panel 5N.

helical and ten straight bolts with load gages were installed with a torque wrench with 150 foot-pounds of torque in four crosscuts on the headgate side between double entries of a longwall-mining panel (as shown in fig. 18). The bolts were installed in crosscuts marked 1S, 2S, 3S, and 4S next to coal panel 5 North, which was mined using Hemscheidt shields. The mining height of the coal was about 10 feet. Overbolting of an existing Mining Enforcement and Safety Administration (MESA)[3] approved resin-grouted bolt pattern was used because the use of an experimental bolt alone would have required much more time and effort than was available for this preliminary test. The test served the intended purpose of showing that the helical bolts do carry loads well, and it showed that the gages perform as expected in mine conditions.

Each grouted bolt is indicated by an X in figure 19. These bolts were placed through a sheet-metal strip about 12 inches wide. The straight bolts with expansion anchors are shown as open circles and are numbered 1 through

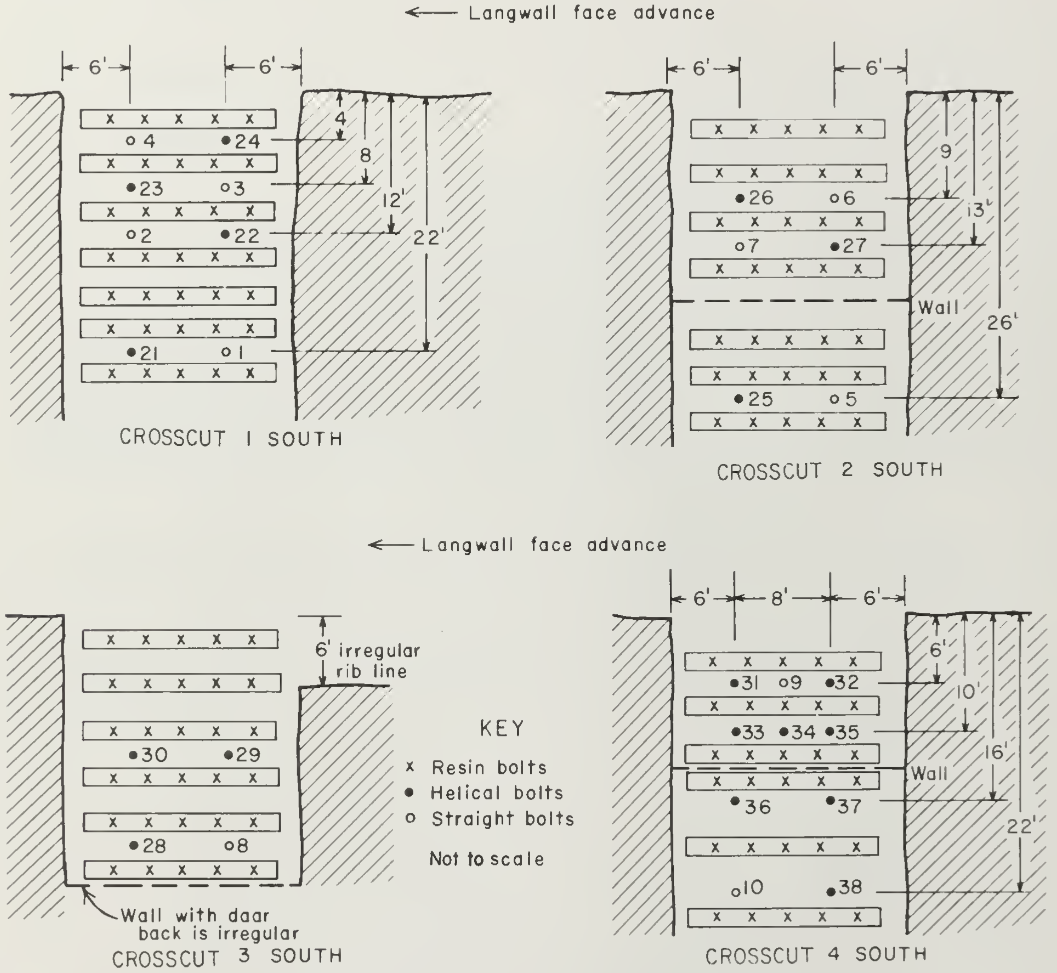
← Langwall face advance
6'
6'
4
8
12'
22'
o4 •24
•23 o3
o2 •22
•21 o1
CROSSCUT 1 SOUTH
6'
6'
9
13'
26'
•26 o6
o7 •27
Wall
•25 o5
CROSSCUT 2 SOUTH
← Langwall face advance
6' irregular rib line
•30 •29
•28 o8
Wall with daar back is irregular
CROSSCUT 3 SOUTH
KEY
x Resin bolts
• Helical bolts
o Straight bolts
Not to scale
6'
8'
6'
6'
10'
16'
22'
•31 o9 •32
•33 •34 •35
Wall
•36 •37
o10 •38
CROSSCUT 4 SOUTH

FIGURE 19. - Bolt patterns used in the York Canyon mine.

---

[3] MESA became the Mine Safety and Health Administration (MSHA), U.S. Department of Labor, on March 9, 1978.

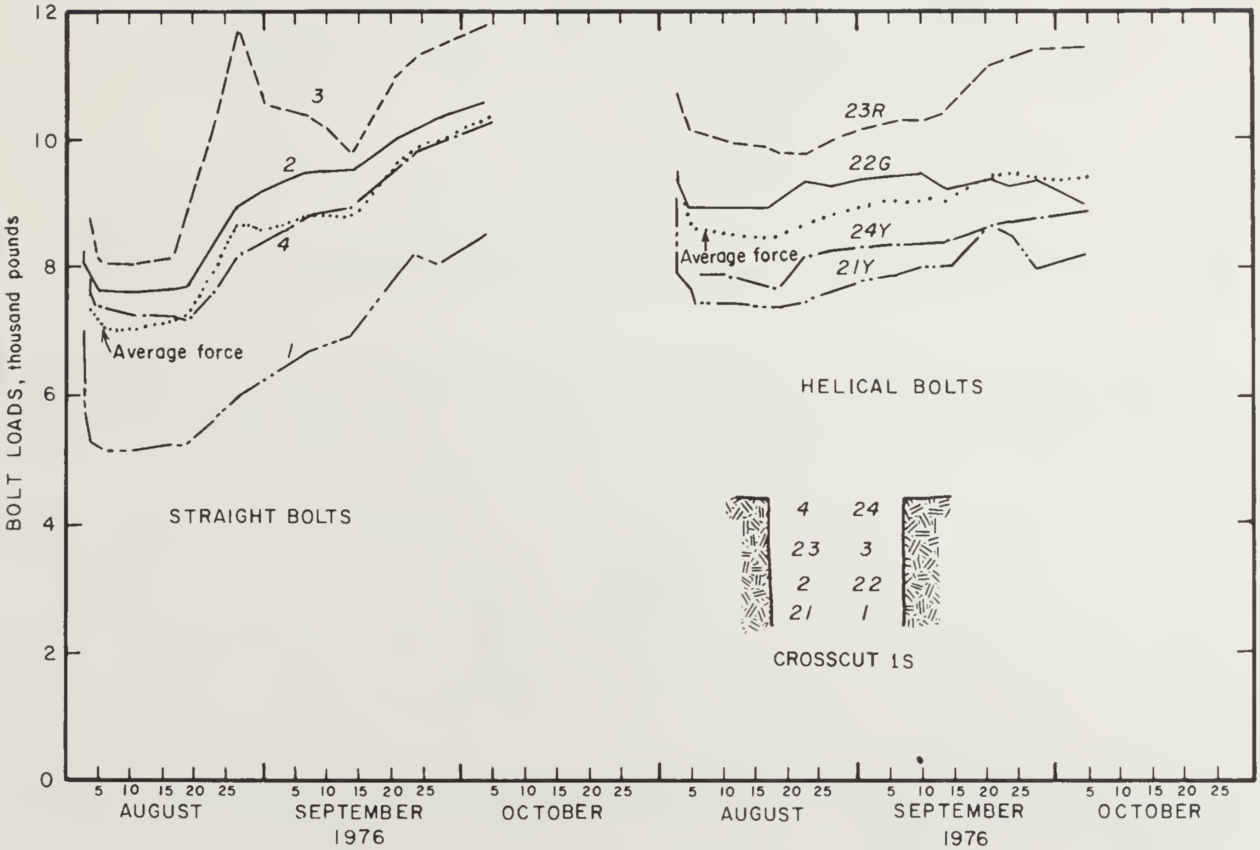

FIGURE 20. - Bolt loads measured by vibrating-wire load gage for helical and straight bolts in York Canyon mine crosscut 1S.

10. The helical bolts with expansion anchors are shown as solid circles and are numbered 21 through 38. The straight and helical bolts are used with equal distribution left to right and front to back in each crosscut to produce average results over the test locations.

The bolt loads were read during the mining sequence for 2 months, and after which the crosscuts were barricaded off by mine personnel. Neither gages nor bolts were recovered.

The experimental results for the bolts tested in the York Canyon mine are presented in figures 20 through 23. The gages performed well during this period without any gage malfunction. In crosscut 1S (fig. 20), the four straight bolts (1, 2, 3, and 4) increased their load during the test period. The four helical bolts (21Y, 22G, 23R, and 24Y) also increased in load, but only about one-third as much as the straight bolts. Bolt load stability is one of the features expected with the flexible bolt. The bolts subjected to previous maximum loads are shown in the following tabulation:

Letters	Colors used to code the bolt heads	Maximum loads used to manufacture bolts, pounds
G...............	Gray...............	10,000
Y...............	Yellow.............	12,000
R...............	Red................	14,000
LG..............	Light green........	16,000

Straight bolt 3 (fig. 20) had anchor slippage about August 27, 1976. Note that all bolts tested had a sudden drop in load during the first 2 days of use.

In crosscut 2S (fig. 21) all of the bolts failed to provide adequate support, with the exception of 26R. This bolt, which is near the cave line, had a high installation load, and this load increased to 14,150 pounds at the end of the test period. Tension losses of the other bolts indicate that either the

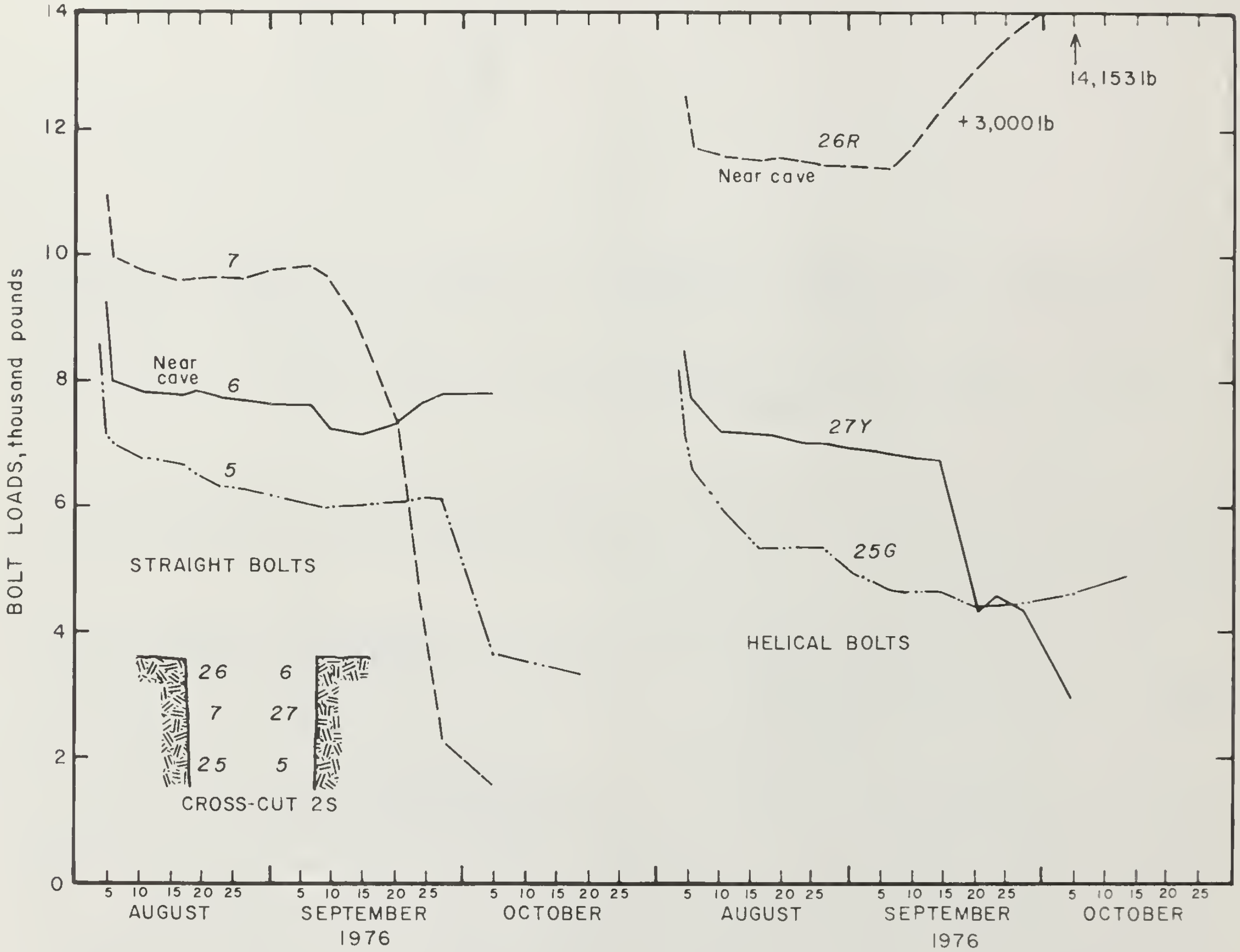

FIGURE 21. - Bolt loads measured by vibrating-wire load gage for helical and straight bolts in York Canyon mine crosscut 2S.

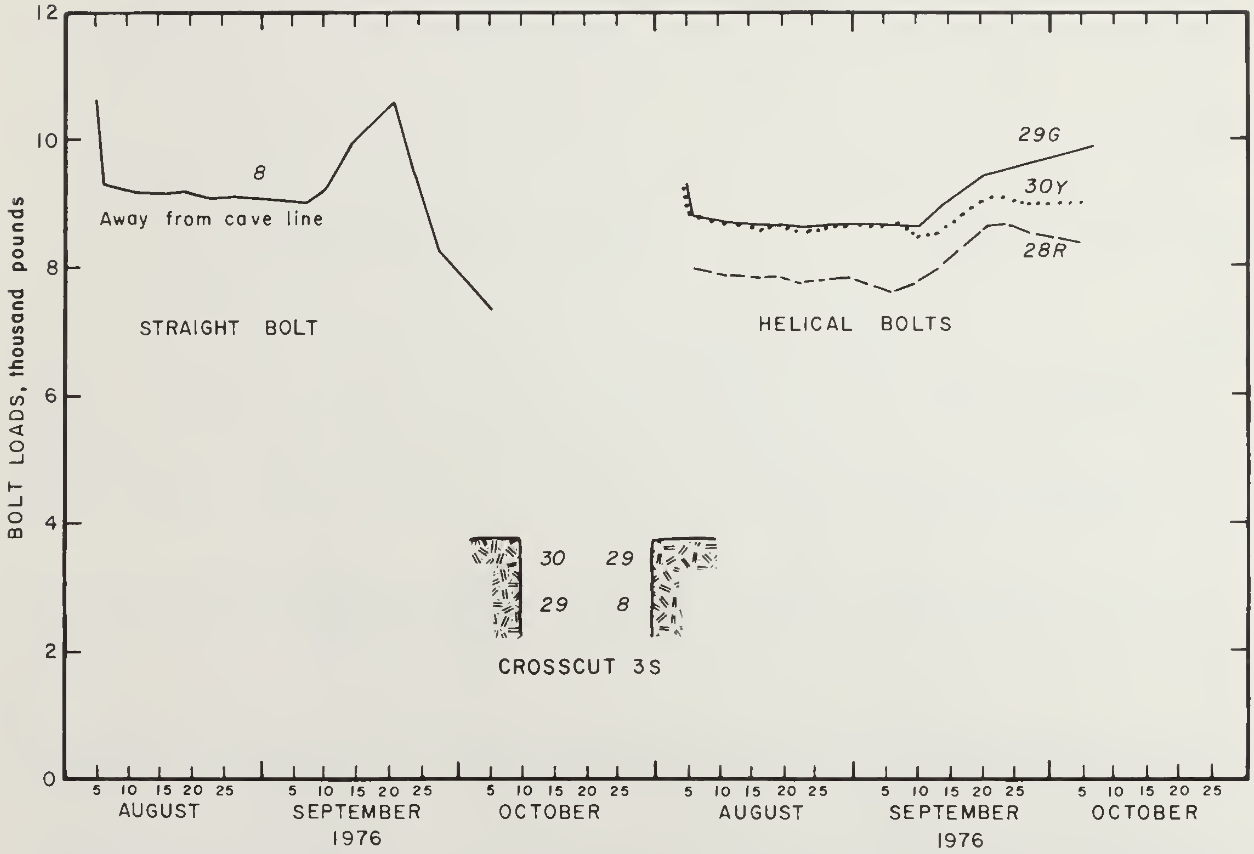

FIGURE 22. - Bolt loads measured by vibrating-wire load gage for helical and straight bolts in York Canyon mine crosscut 3S.

bolted beds were compressed as mining progressed, or the bolt anchors slipped due to poor anchorage capacity.

In crosscut 3S (fig. 22) the three helical bolts 28R, 29G, and 30Y gave stable support to the roof, but bolt 8, the single straight bolt away from the cave line, did not.

In crosscut 4S (fig. 23) six of the helical bolts gave stable support; bolt 31Y near the cave line increased in load suddenly, and bolt 23LG near the cave line decreased in load suddenly during the last week of the test. Bolt 10 away from the cave line had a stable, slightly increasing load, but bolt 9 near the cave line lost its load completely during the last week of the test.

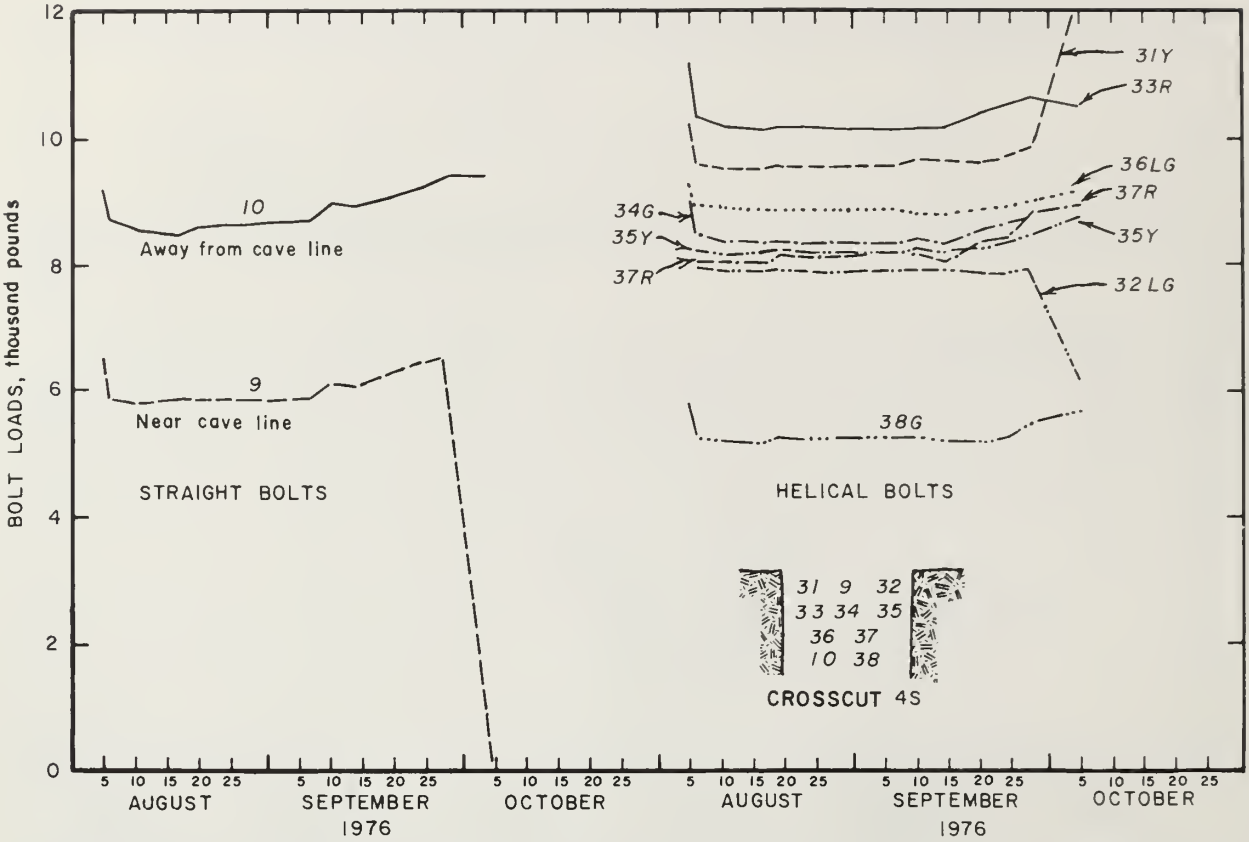

FIGURE 23. - Bolt loads measured by vibrating-wire load gage for helical and straight bolts in York Canyon mine crosscut 4S.

SUMMARY AND CONCLUSIONS

Helical coils were made, by a spring manufacturer, from 0.5-inch-diameter rod made of 4140 steel that was 5 feet long. They were stretched in the laboratory using a tensile-testing machine to define their elastic-plastic behavior and changes in geometry with an increasing applied tensile force. The elastic behavior conformed with theoretical considerations with regard to coil flexibility for a given geometry even though the stress distribution was appreciably different because of the plastic flow. As expected, the coils exhibited much greater flexibility than the straight rods from which the coils were made, even for loads up to 13,000 pounds (66,250 psi).

Next, helical rock bolts were manufactured from 5/8-inch nominal diameter Colorado Fuel and Iron expansion-anchor-type bolts, 6 feet long. These helical rock bolts were tested in the same way as the helical coils; however, the emphasis was on the behavior of the bolts that were loaded to a maximum force of 10,000 pounds, 12,000 pounds, 14,000 pounds, and 16,000 pounds, respectively, during manufacture. The behavior was very similar to that observed for the smaller helical coils. Results of the laboratory tests showed that the bolts were 5 to 10 times as flexible as a straight bolt.

Finally, 18 helical bolts with vibrating-wire load gages were compared, in the Kaiser Steel York Canyon mine, Raton, N. Mex., with the behavior of 10 straight bolts of the same brand with load gages. An existing grouted-bolt pattern was overbolted to establish that the helical bolts would maintain a more nearly stable load, and this was the case. The load changed only about one-third as much as for the straight bolts. All the helical bolts carried a load for the entire test period but this was not the case during the test period for the straight bolts. The test results were somewhat surprising in that the bolt loads changed as much as they did, increasing when the roof was already bolted with resin-grouted bolts. A flexibility of 5 to 10 was expected; however, only a flexibility of about 3 was realized. The straight bolt benefited relatively more from the softening provided by the anchor and bearing plate assemblies. Other bolt geometries with greater flexibilities or bolts with plastic flow during the loading phase should emphasize the better performance of the helical bolts over the straight bolts. When bolt loads are difficult to maintain or when the bolt assembly is softened by using wooden blocks under the bolt head, the helical bolt should work to advantage.

The concept of the helical bolt has been established as sound, but much testing remains before the bolt is established as a viable means of roof support.

REFERENCES

1. Babcock, C. O. Sensitive Vibrating Wire Rock Bolt Load Gage. Trans. AIME, v. 262, December 1977, pp. 293-299.

2. Chaiko, W. M., and J. J. Scott. Roof Support Experience With Friction Rock Stabilizer. Min. Cong. J., v. 63, No. 3, March 1977, pp. 36-41.

3. Conway, J. P., S. M. Dar, J. H. Stears, P. C. McWilliams, and K. G. Hoge. Laboratory Studies of Yielding Rock Bolts. BuMines RI 8058, 1975, 40 pp.

4. Faupel, J. H. Strength Under Combined Stress. Ch. in Engineering Design. John Wiley & Sons, Inc., New York, ch. 3, 1964, pp. 212-213.

5. Harrell, M. V. Roof Control With Hydraulic Driven Pins. Min. Cong. J., July 1971, pp. 27-31.

6. Ortlepp, W. D., and J. J. Reed. Yieldable Rock Bolts for Shock Loading and Grouted Bolts for Faster Rock Stabilization. The Mines Magazine, March 1970, pp. 12-17.

7. Scott, J. J. Friction Rock Stabilizers--A New Rock Reinforcement Method. Site Characterization. 17th U.S. Symp. on Rock Mech., Univ. of Utah, Snowbird, Utah, Aug. 25-27, 1976, pp. 5E5-1 to 5E5-8.

8. Stefanko, R. New Look at Long Term Anchorage; Key to Roof Bolt Efficiency. Trans. AIME, v. 226, 1963, pp. 197-201.

9. Thompson, R. R., and R. C. Bates. Field Testing the Pumpable Polymeric Roof Bolt. First Symp. on Underground Min., Nat. Coal Assoc./Bituminous Coal Res. Coal Conf. and Expo II, Louisville, Ky., Oct. 21-23, 1975. National Coal Association, Washington, D.C., 1975, v. 2, pp. 80-89.

APPENDIX.--DEFORMATION BEHAVIOR OF AN ELASTIC HELICAL COIL LOADED IN TENSION

Theory

Equation 3.274 in reference 4 for the elastic elongation, δ_h, of a spring with an open helical coil can be written as

$$\delta_h = \frac{4PR^2L}{\pi r^4 E}(1 + \cos^2\alpha). \qquad \text{(A-1)}$$

This equation contains the effects of bending and torsion, but not of tension because $\delta_h = 0$ for a straight rod when $R = 0$ and $\cos^2\alpha = 0$. The elongation of the coil length of L' from the tensile force P is

$$\delta_{h\,t} = \int_0^{L'} \epsilon_t \, \delta \ell' = PL'/A'E, \qquad \text{(A-2)}$$

so that the total elongation for bending, torsion, and tension becomes

$$\delta_h = 4PR^2L\,(1 + \cos^2\alpha)/\pi E r^4 + PL'/A'E, \qquad \text{(A-3)}$$

where $A' = A/\sin\alpha$, for $P \geq d$,

ϵ_t = strain in direction of coil length, not rod length,

$\delta\ell'$ = increment of coil length,

and $L' = n\sqrt{4\pi^2R^2 + p^2}\,\sin\alpha = L\sin\alpha.$

In these equations, P is the force in pounds; L, r, and A are the length, radius, and cross-sectional areas, respectively, of the rod from which the coil is made; L', R, and A' are the length of the coil, radius of the coil, the area of a section perpendicular to the center line of the coil, respectively; α is the angle between the areas A and A'; n and p are the number of turns and pitch of the coil; and E is Young's modulus of the rod material.

Equation A-3 can be written

$$\delta_h = \frac{PL}{\pi r^2 E}\left\{\frac{4R^2}{r^2}(1 + \cos^2\alpha) + \sin^2\alpha\right\} \qquad \text{(A-4)}$$

for the elongation of the helical coil.

The elongation of a straight rod of length, L, is

$$\delta_s = PL/AE = PL/\pi r^2 E. \qquad \text{(A-5)}$$

The relative displacement per unit length of the helical coil and the straight rod are δ_h/L' and δ_s/L, where L' and L are the lengths of the helical coil and the straight rod, respectively. The flexibility ratio, F_r, of the coil to the straight rod is, therefore,

$$F_r = \frac{L\delta_h}{L'\delta_s} = \frac{1}{\sin\alpha}\{4R^2\ (1 + \cos^2\alpha)/r^2 + \sin^2\alpha\}, \tag{A-6}$$

$$= \frac{\sqrt{4\pi^2 R^2 + p^2}}{p}\left\{\frac{4R^2}{r^2}\left(1 + \frac{4\pi^2 R^2}{4\pi R^2 + p^2}\right) + \frac{p^2}{4\pi^2 R^2 + p^2}\right\},$$

$$= \{4R^2\ (79\ R^2 + p^2)/r^2 + p^2\}/p\sqrt{39.5\ R^2 + p^2}\ \text{(approximately).} \tag{A-7}$$

If $d = 1 = 2r$, equation A-7 becomes,

$$F = \{1263\ R^4 + 16\ R^2p^2 + p^2\}\ /\ p\sqrt{39.5\ R^2 + p^2}. \tag{A-8}$$

This result with the flexibility, F_r, normalized to the rod diameter, d, taken as unity is plotted in figure 1; R and p are expressed in d units.

☆U.S. GOVERNMENT PRINTING OFFICE: 1978-703-103/53

INT.-BU.OF MINES,PGH.,PA. 23175

22.09
In32mo

RI 8300r

Bureau of Mines Report of Investigations/1978

A Flexible Helical Rock Bolt

DEPOSITORY

FEB [illegible] 1979

UNIV. OF ILL. LIBRARY
URBANA-CHAMPAIGN

UNITED STATES DEPARTMENT OF THE INTERIOR

Report of Investigations 8300 r

A Flexible Helical Rock Bolt

By Clarence O. Babcock

March 3 1849

UNITED STATES DEPARTMENT OF THE INTERIOR
Cecil D. Andrus, Secretary

BUREAU OF MINES

This publication has been cataloged as follows:

Babcock, Clarence O
A flexible helical rock bolt / by Clarence O. Babcock. [Washington] : U.S. Dept. of the Interior, Bureau of Mines, 1978.

26 p. : diagrams ; 27 cm. (Report of investigations - Bureau of Mines ; 8300r)

Bibliography: p. 24.

1. Rock bolts. I. United States. Bureau of Mines. II. Title. III. Series: United States. Bureau of Mines. Report of investigations - Bureau of Mines ; 8300r.

TN23.U7 no. 8300r 622.06173

U.S. Dept. of the Int. Library

CONTENTS

Page

Abstract........ 1
Introduction........ 1
Acknowledgments........ 3
Theory........ 3
Manufacture and laboratory testing of helical coils........ 4
Manufacture and laboratory testing of helical rock bolts........ 10
Preliminary field testing of helical rock bolts and vibrating-wire load gages........ 16
Summary and conclusions........ 22
References........ 24
Appendix.--Deformation behavior of an elastic helical coil loaded in tension........ 25

ILLUSTRATIONS

1. Theoretical flexibility of an elastic helical coil........ 3
2. Experimental changes in coil geometry with increasing load........ 4
3. Two-dimensional projection of experimental helical coil shape versus maximum tensile force applied........ 5
4. Change in coil length as a function of the maximum tensile force applied........ 6
5. Radius and outside diameter of coil as a function of the maximum tensile force applied........ 6
6. Pitch of coil as a function of the maximum tensile force applied.... 7
7. Elastic, plastic, and total average strains for coil as a function of the maximum tensile force applied........ 8
8. Flexibility ratio of the helical coil to a straight rod of the same length for a given maximum tensile force applied........ 9
9. Relative bolt flexibilities and elastic work capabilities of coil geometries tested........ 9
10. Relative work capabilities of loading and unloading helical coils... 10
11. Flexible helical bolts and other hardware tested in the York Canyon mine........ 11
12. Change in helical bolt length as a function of the maximum tensile force applied........ 12
13. Radius and outside diameter of helical bolt as a function of the maximum tensile force applied........ 12
14. Pitch of helical bolt as a function of the maximum tensile force applied........ 13
15. Elastic, plastic, and total average strains for helical bolts as a function of the maximum tensile force applied........ 14
16. Flexibility ratio of the helical bolt to a straight rod of the same length for a given maximum tensile force applied........ 15
17. Work done by helical bolt during manufacture with increasing tensile load compared with the elastic work done by a straight bolt........ 16
18. Plan map of York Canyon mine panel 5N........ 17

ILLUSTRATIONS--Continued

Page

19. Bolt patterns used in the York Canyon mine........................ 18
20. Bolt loads measured by vibrating-wire load gage for helical and straight bolts in York Canyon mine crosscut 1S.................. 19
21. Bolt loads measured by vibrating-wire load gage for helical and straight bolts in York Canyon mine crosscut 2S.................. 20
22. Bolt loads measured by vibrating-wire load gage for helical and straight bolts in York Canyon mine crosscut 3S.................. 21
23. Bolt loads measured by vibrating-wire load gage for helical and straight bolts in York Canyon mine crosscut 4S.................. 22

A FLEXIBLE HELICAL ROCK BOLT

by

Clarence O. Babcock [1]

ABSTRACT

This report describes the results of Bureau of Mines laboratory and preliminary field tests on a rock bolt of helical shape. The flexible construction allows the bolt to maintain a more stable load level than is possible with a straight bolt. Bolt load changes resulting from anchor slippage, blasting shock, or changes in mine geometry with mining advance are minimized.

Preliminary field tests were performed at the Kaiser Steel York Canyon mine where the load changes of straight and helical bolts were measured using a vibrating-wire load gage. The field tests were performed to establish the viability of the concept of a helical bolt. The practical usefulness in terms of performance and economics remains to be shown. The change in bolt load for the flexible bolts was one-third that for the straight bolts. There were no malfunctions of the gage, and the bolts maintained a more uniform load than the straight bolts used as controls.

INTRODUCTION

The use of over 90 million rock bolts in the United States every year indicated their importance to mining. Recently, the shift has been away from conventional expansion shell- or wedge-type anchor bolts to resin-grouted bolts. This has occurred because the resin-grouted bolts have been more effective in supporting the roof, even though the conventional bolts are less expensive. Different bolting innovations have been tried over the years and a few recent ones with promise will be mentioned in this report. Ortlepp and Reed (6)[2] describe a yieldable rock bolt (also referred to as a yielding rock bolt) that uses a circular die to plastically deform a rolled, threaded portion of the bolt. Based on tests in South African mines, Ortlepp and Reed conclude that a fully grouted rock bolt placed and grouted immediately after rock excavation, even though untensioned initially, should be several times more effective than a tensioned but ungrouted bolt in preventing rock dilatation.

---

[1] Mining engineer, Denver Mining Research Center, Bureau of Mines, Denver, Colo.

[2] Underlined numbers in parentheses refer to items in the list of references preceding the appendix.

A modification of this bolt was studied in the laboratory by Conway and was patented in July 1976 (3). These tests show that the bolt can maintain a nearly stable load over an elongation of about 8 inches. Harrell (5) used 30-inch-long, hydraulically driven steel pins to join rock layers at the Orient No. 6 mine of the Freeman Coal Mining Corp., Waltonville, Ill. He concludes that roof-pinning is still in the experimental stage and will require more testing and time before it is a proven roof-control system. In a 1975 report on a pumpable polymeric roof bolt, Thompson and Bates (9) conclude that "the results to date show that the ground support characteristics of the pumpable bolt are comparable with those of resin grouted steel bolts." The placing of such bolts is too complicated for general use at the present time. The polyester resin used was made in Japan and was no longer available. The most promising new bolt appears to be the friction rock stabilizer for which Scott (7) received two U.S. patents, 3,922,867 (December 2, 1975) and 4,012,913 (March 22, 1977). In an article describing these inventions he concludes, "the simplicity of the system, the reproducibility of the data in both the laboratory and field test program, coupled with the ease of manufacture and economy all would seem to dictate that the mining industry should take a hard look at this system to solve many of its ground control problems." In another article, Chaiko and Scott (2) conclude, "the results are encouraging, but much work remains to be done. While key performance benefits have been demonstrated, superior economics and operational installation equipment are yet to be shown." This bolt which has the trade name Split Set is a steel tube split lengthwise. The bolt is forced into a drill hole and support is provided through friction or a change in shape plastically so that the tube more nearly matches the hole shape. Performance and cost are equal to those of a resin-grouted bolt. In a private conversation, Scott indicated that 60,000 of these bolts had been made at that time (April 1977) and that greater quantities were expected.

While there is an increased interest in resin-grouted bolts, the biggest part of the bolting market is still bolts of conventional design with an expansion or split-wedge anchor. In addition to their lower cost, they supply the full bolt load over the length of the bolt. The weakest link appears to be the anchorage capacity of the expansion-anchor rock system. Although a 5/8-inch nominal-diameter rock bolt can support a load of 17,000 pounds and more if a high-strength or extra-high-strength bolt is used, the anchor may slip at loads of 8,000 to 10,000 pounds (8). Since the elongation of the bolt is only 0.077 inch (1/13 inch) for a 6-foot bolt loaded to 8,000 pounds, such anchor slippage seriously decreases the bolt load. The anchor can supply more nearly the full strength of the bolt if a displacement of 0.1 or 0.2 inch is possible before the bolt unloads. The usual remedy is to tighten the bolts a number of times during use. If anchor slippage was not so critical to bolt load, this would not be necessary.

A possible solution to the problem is the use of a flexible bolt of helical shape described in this report. Patent 3,942,329, assigned by the author to the Department of the Interior, was granted on the bolt on March 9, 1976. A helical bolt can be made many times as flexible as the straight bolt, depending on the geometry used, and can maintain bolt loads when the straight bolts cannot. For example, if a straight bolt loses 50% of its load from anchor slippage, a helical bolt with a flexibility of five would lose only 10% of its load. This means that if a straight bolt load decreased from 8,000 pounds to 4,000 pounds, the flexible bolt load would change from 8,000 to 7,200 pounds. Conversely, if the load change increases 50%, the 8,000 pounds on the straight bolt would become 12,000 pounds and the load for the flexible bolt would increase to 8,800 pounds. Stated another way, the straight bolt load would be in the range of 4,000 to 12,000 pounds, while the helical bolt with a flexibility of five would be in the range of 7,200 to 8,800 pounds. If greater flexibility can be produced, the load would be more stable. In addition, if a bolt geometry that produces plastic flow in the bolt during use is used, it can also provide a more uniform-loading behavior. The flexible bolt can tolerate loading or unloading, while the yieldable rock bolt (3) works well only as long as the load is increasing. In decreasing bolt loads it should perform almost the same as a straight conventional bolt. The bolt loads were determined during the field testing by means of a vibrating-wire load gage, which (1) was assigned U.S. patent 3,914,992.

ACKNOWLEDGMENTS

The author wishes to thank the following: Ed Moore, mine manager, and Bill Sikes, mining engineer, for the use of the Kaiser Steel York Canyon coal mine for field tests. Don Gentry, professor, and Carlos Alves, graduate student, both of the Colorado School of Mines who were in charge of the field tests and load gage readings. David Wisecarver, supervisory mining engineer, and Frank Popich, engineering technician, both of the Federal Bureau of Mines, cooperated in arranging and helping with the field tests.

Helical Coil Relationships

R, d units	0	0.5	0.6	0.7	0.8	0.9	1.0	1.1	1.2	1.3	1.4	1.5	1.6
D, d units	1	2.0	2.2	2.4	2.6	2.8	3.0	3.2	3.4	3.6	3.8	4.0	4.2
D, inches	9/16	1.1	1.3	1.4	1.5	1.6	1.7	1.8	1.9	2.0	2.2	2.3	2.4

$$Fr = \frac{\{1263R^4+16R^2p^2+p^2\}}{p\sqrt{39.5R^2+p^2}}$$

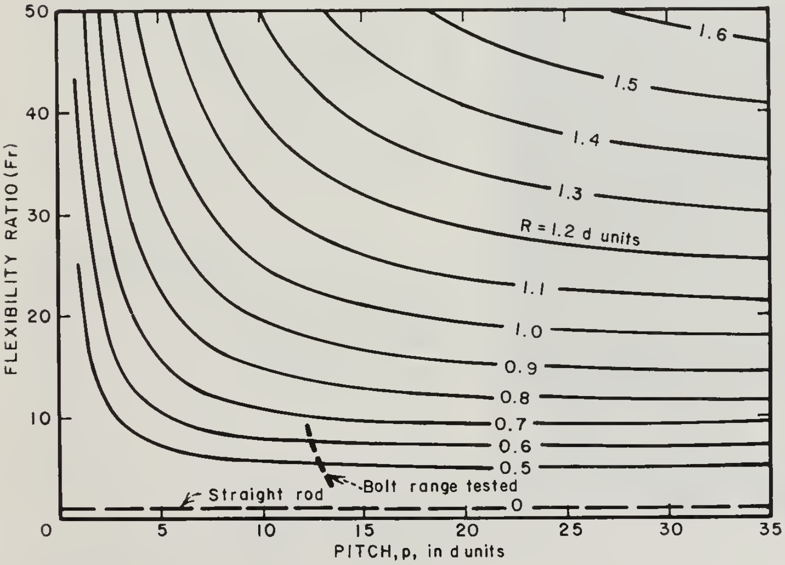

FIGURE 1. - Theoretical flexibility of an elastic helical coil in terms of its pitch, p, and radius, R, expressed in rod diameter units, d.

THEORY

The elongation behavior of a helical elastic coil (given in the appendix as equation 8) is plotted in figure 1. In this figure, the flexibility ratio, F_r, is the elongation of a helical coil loaded in tension divided by the elongation of a straight rod of the same length, materials and cross-sectional area and loaded with the same tensile force. An F_r value of 5, for example, indicates that the coil stretches five times as much as the straight rod of the same length at any force value as long as the unloaded bolt geometry is unchanged. In figure 1, the variables R and p are the radius and pitch of the coil, respectively, in units of rod diameters, d, for the rod from which the coil is made. D is the outside diameter of the coil. The curve R = 0.5d represents a coil wound around and touching a straight line so that the coil has no center hole. The F_r value decreases rapidly with an increase in the applied force, and extremely flexible coils cannot be manufactured for the loads applied to small bolt diameters such as those used in mining; that is, the helical bolts change their geometry as the tensile force is increased, becoming less flexible at force values applied to rock bolts. The table in figure 1 relates the R and D values for the helical bolts made from 5/8-inch-diameter straight bolts. R is given in d units, and D is given in both d units and inches. The outside diameter of the coil, D, is the smallest hole diameter into which the bolt would fit. In practice, the smallest hole size of 1-3/8 inches is dictated by the anchor diameter.

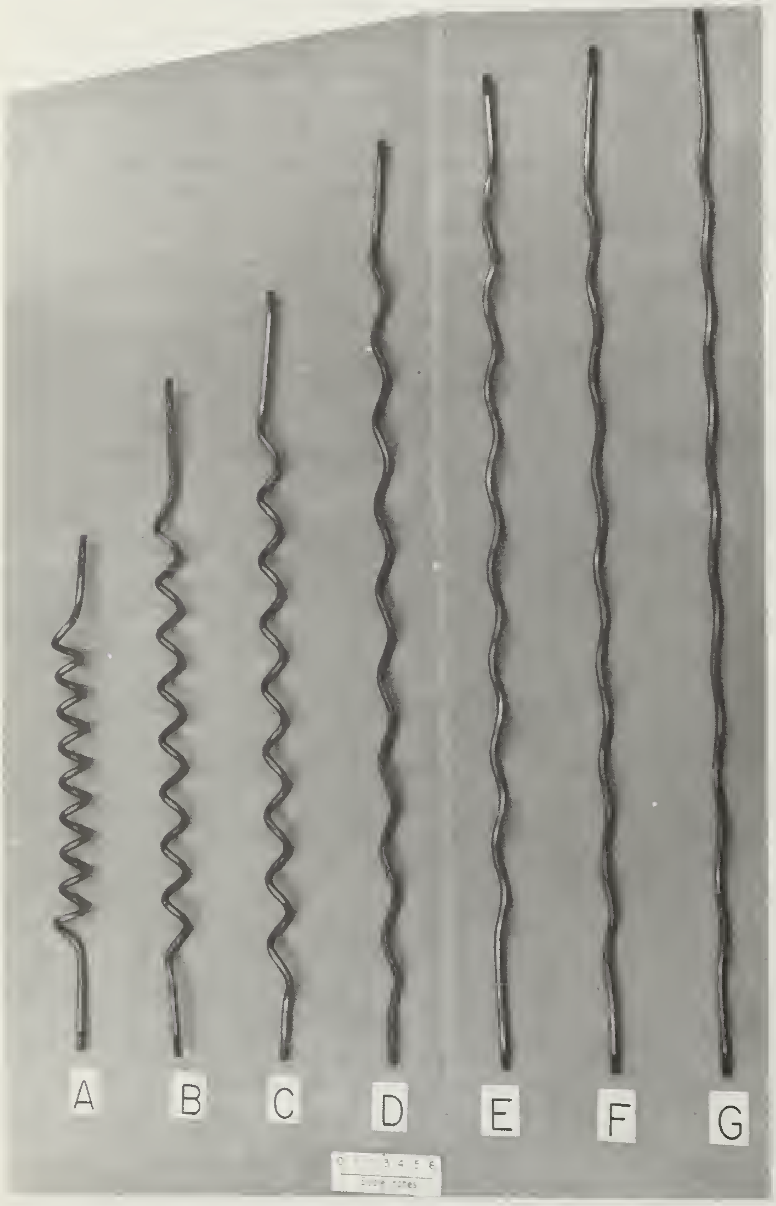

FIGURE 2. - Experimental changes in coil geometry with increasing load (pounds). *A*–2,000; *B*–3,000; *C*–4,000; *D*–6,000; *E*–9,000; *F*–10,000; *G*–13,000.

MANUFACTURE AND LABORATORY TESTING OF HELICAL COILS

Helical coils were made by a spring manufacturer from rods of 4140 steel, 0.5 inch in diameter, and 5 feet long, as shown in figure 2A. This steel was chosen because many coiled springs are made from this material. Although the coils tested were not hardened, this could have been done had it been desirable or necessary. As the tensile force was increased, the coil geometry changed from A to B to C, etc., in sequence. The geometry changes in figure 2 correspond to maximum tensile force applied, in pounds. The changes in shape with an increasing maximum force resulted from plastic flow. The helical shapes of these coils in two dimensions are shown as sine or cosine waves in figure 3. The experimental values of F_r for these geometries are given by numbers preceded by x. In figure 3A, the coil was 82 times as flexible as a straight rod of the same length for a tensile force of 2,000 pounds or less. By the time the tensile force was 9,000 pounds, the coil was only six times the flexibility of the straight rod of the same length, size, and force.

In figure 4, the change in coil length is plotted against the maximum tensile force applied. After each increase in load above the previous maximum, the load was removed to establish how much of the elongation was plastic and how much was elastic. The broken lines represent both the loading and unloading curves. The change in length of the unloaded coil, from the initial shape A in figure 2, is given by the y-axis intercept with the broken line. The difference between the y = 0 length and this value resulted from the plastic flow; most of the elongation from shape A was plastic.

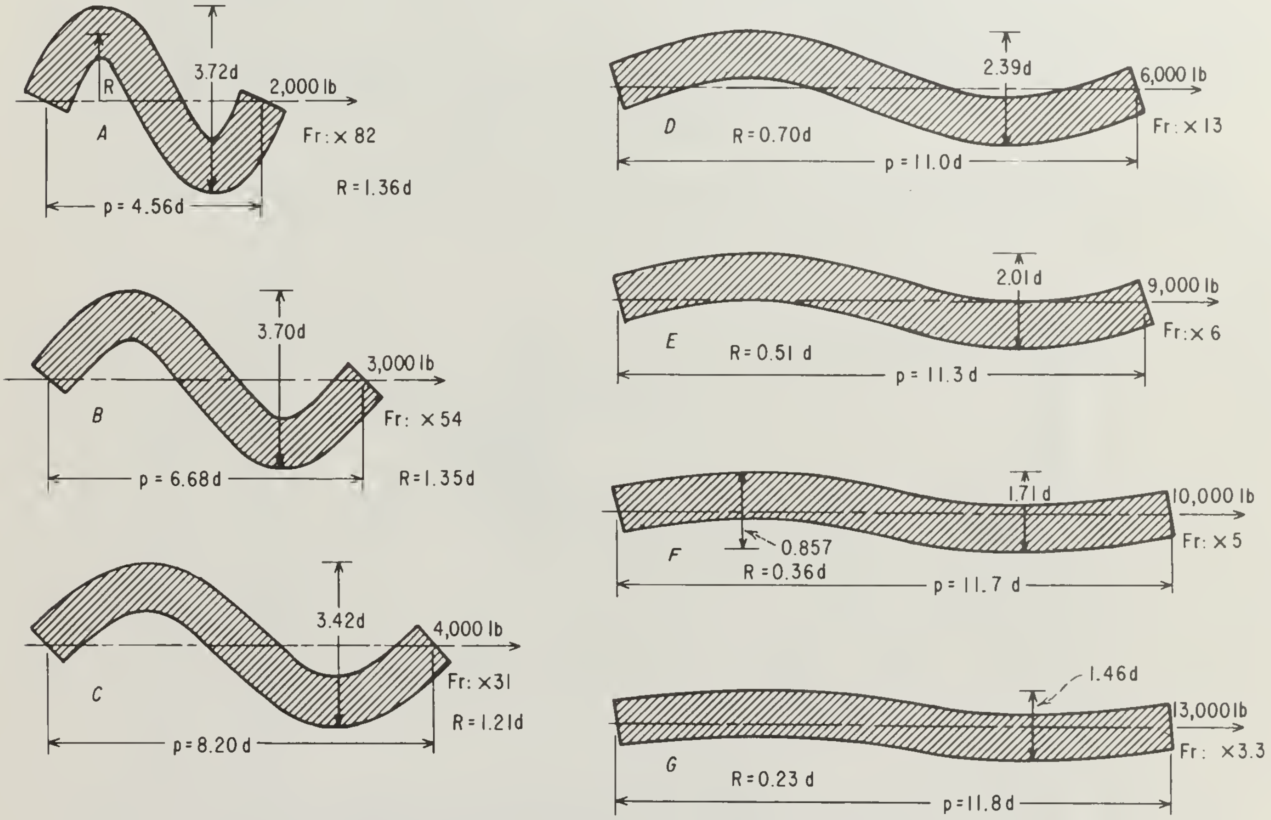
A
R
3.72d
2,000 lb
Fr: x 82
R = 1.36d
p = 4.56d
B
3.70d
3,000 lb
Fr: x 54
R = 1.35d
p = 6.68d
C
3.42d
4,000 lb
Fr: x31
R = 1.21d
p = 8.20 d
D
2.39d
6,000 lb
Fr: x 13
R = 0.70d
p = 11.0d
E
2.01d
9,000 lb
Fr: x 6
R = 0.51 d
p = 11.3 d
F
1.71 d
10,000 lb
Fr: x 5
0.857
R = 0.36d
p = 11.7 d
G
1.46d
13,000 lb
Fr: x3.3
R = 0.23 d
p = 11.8d

FIGURE 3. - Two-dimensional projection of experimental helical coil shape versus maximum tensile force applied.

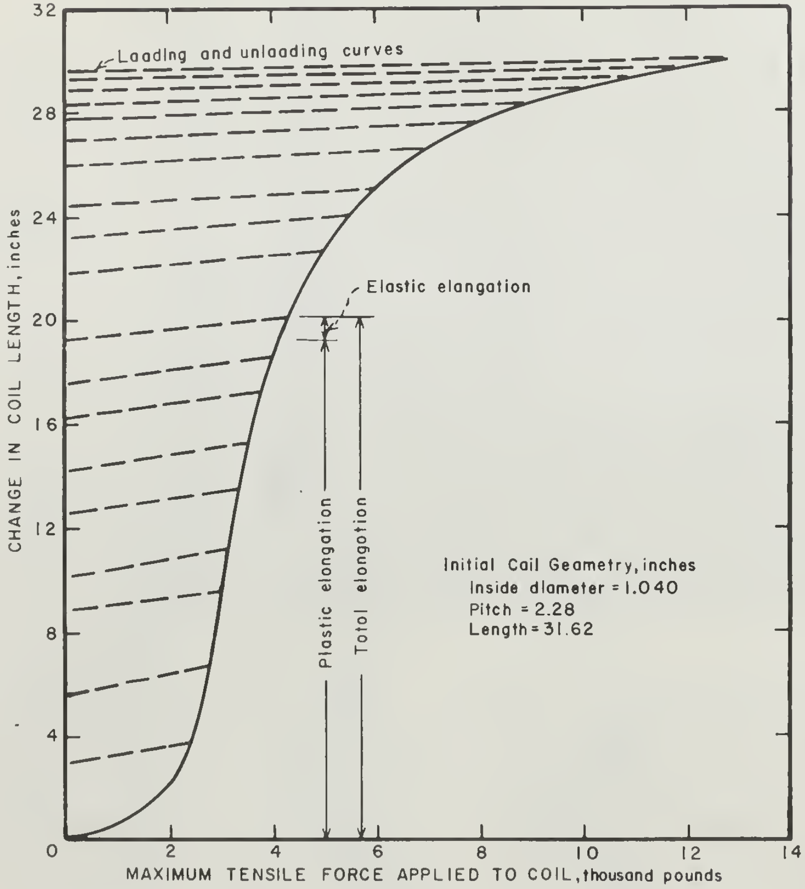

FIGURE 4. - Change in coil length as a function of the maximum tensile force applied.

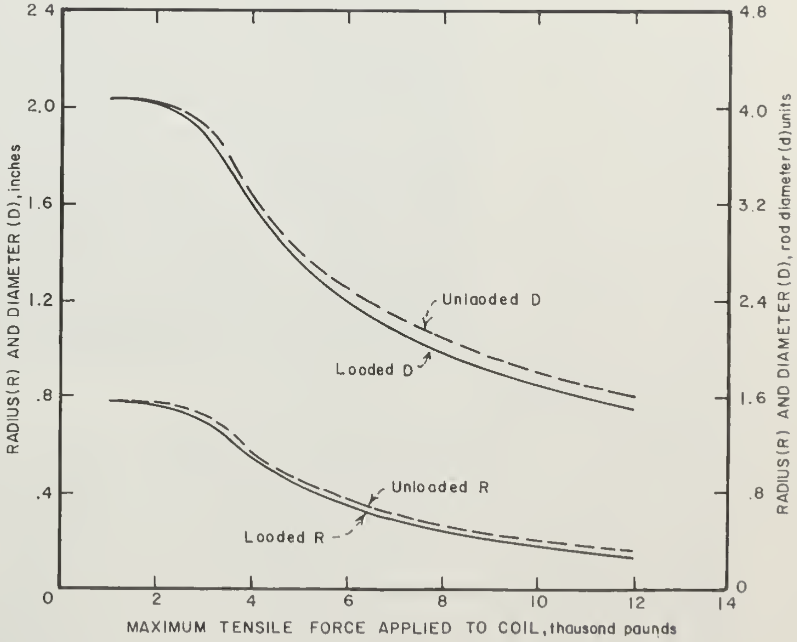

FIGURE 5. - Radius and outside diameter of coil as a function of the maximum tensile force applied.

In figure 5, the change in coil radius, R, and the outside diameter of the coil, D, in inches and in rod diameter units, d, are given as functions of the maximum tensile force applied. The loaded and unloaded R and D values are nearly the same.

In figure 6, the change in coil pitch, p, in inches and in rod diameter units is given as a function of the maximum tensile force applied. The difference in the loaded and unloaded p values is not large.

In figure 7, the results of cyclically loading and unloading the helical coil by increasing the force of each successive loading cycle in 200-pound increments above the previous maximum is shown as average total, plastic, and elastic strains occurring for that 200-pound-load increment at each loading level. These were obtained by dividing the total, plastic, and elastic elongations by the bolt length at that time. The elastic strains are important throughout the force range, especially for the high and low force values. The plastic strains are more restricted, occurring mostly for forces that are 20% to 50% of the maximum force applied. The most rapid change in coil length for a 200-pound-force increment occurred at about 3,200 pounds of force; the maximum total, plastic, and elastic strains occurred at about this value. This is 25% of the total force applied to the coil, which implies that if this extreme behavior is desired for a particular support application, the rod size should be loaded to 25% of its straight-rod-strength value.

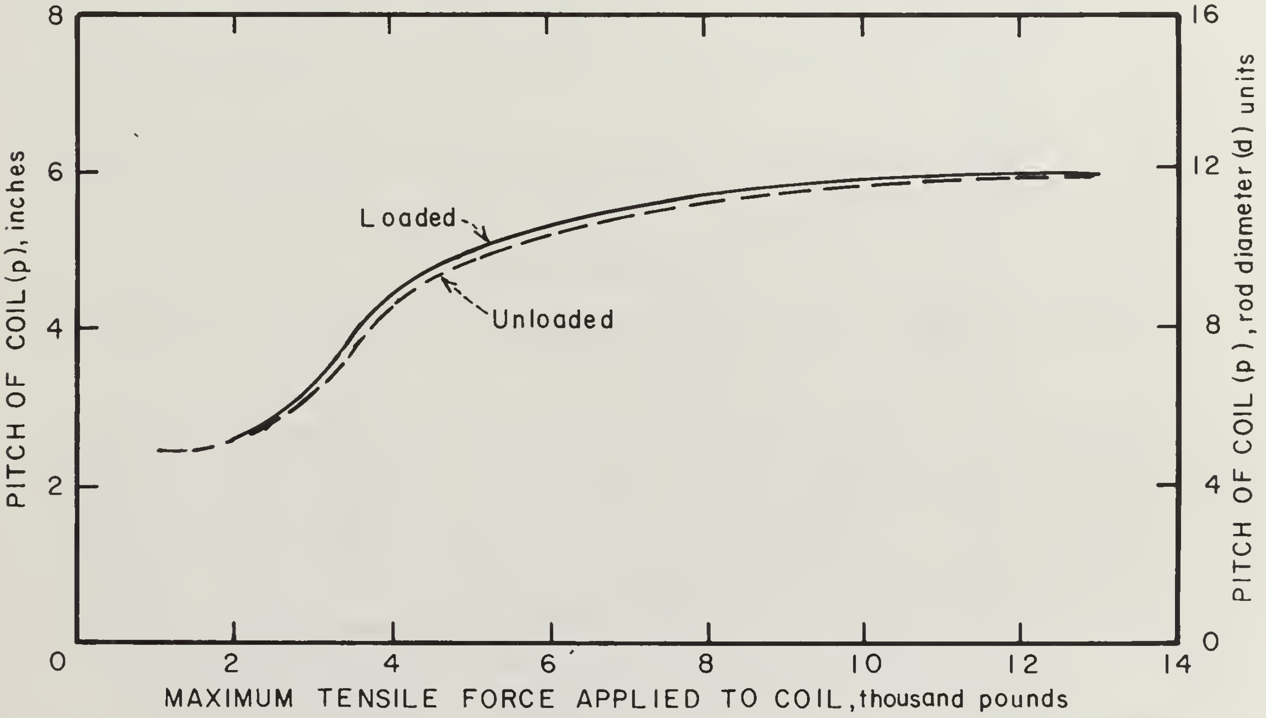

FIGURE 6. - Pitch of coil as a function of the maximum tensile force applied.

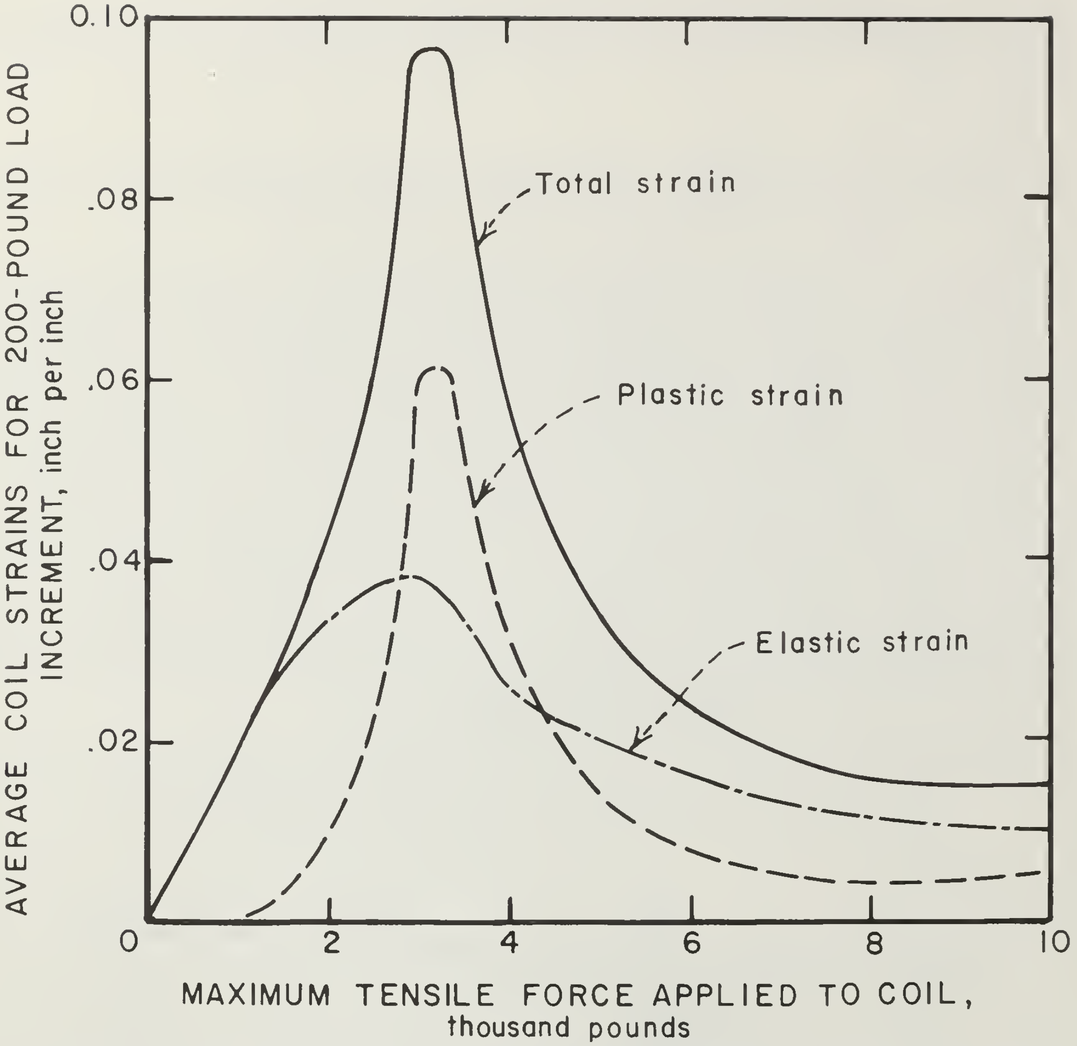

FIGURE 7. - Elastic, plastic, and total average strains for coil as a function of the maximum tensile force applied.

In figure 8, the flexibility of the helical coil relative to that of a straight rod of the same length and material is given by the ratio, F_r, for maximum applied tensile force loads. This is compared with what is predicted by equation 8 for r = 0.25 inch when the experimental values of R and p are used. Considering the extensive plastic flow that has occurred in the coil, the theory and experimental results nearly agree with one another. Figure 8 indicates that the flexibility of a helical coil decreases rapidly as the load is initially applied, when torsion produces most of the change in the coil length. At larger loads, the relative importance of bending and tension increases.

In figure 9, the ratio of work that can be done by a stretched helical coil compared with the work that can be done by a stretched straight rod is given as F_r or A/A', which is called the flexibility ratio. The work ratios

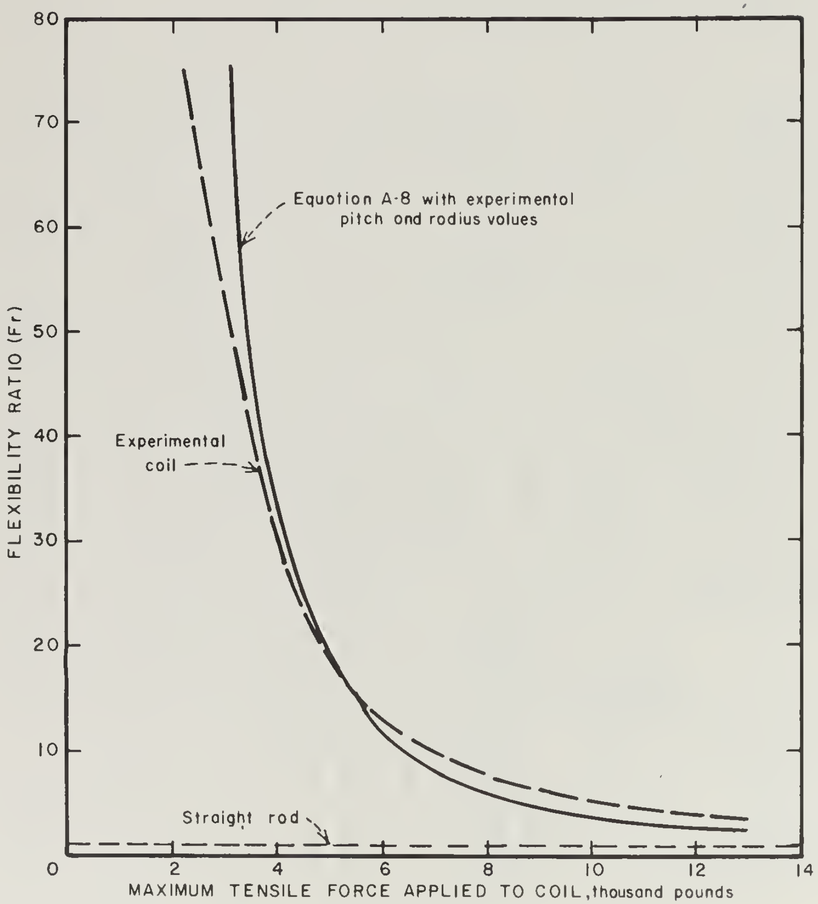

FIGURE 8. - Flexibility ratio of the helical coil to a straight rod of the same length for a given maximum tensile force applied.

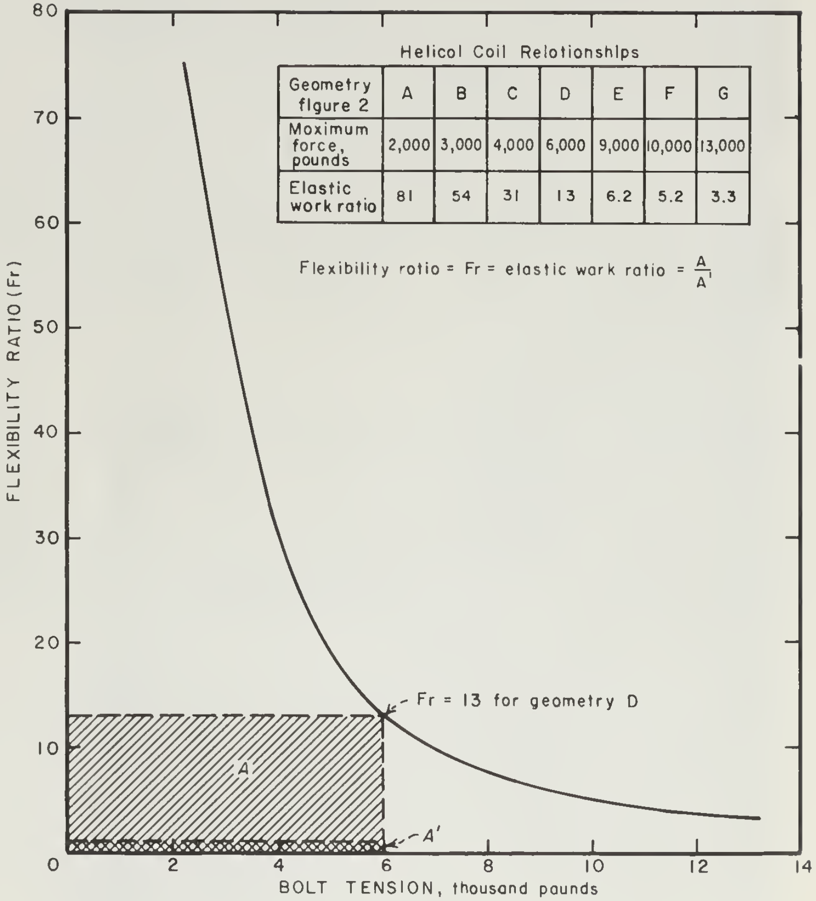

Helicol Coil Relotionships

Geometry figure 2	A	B	C	D	E	F	G
Moximum force, pounds	2,000	3,000	4,000	6,000	9,000	10,000	13,000
Elastic work ratio	81	54	31	13	6.2	5.2	3.3

Flexibility rotio = Fr = elostic work ratio = $\frac{A}{A'}$

FIGURE 9. - Relative bolt flexibilities and elastic work capabilities of coil geometries tested.

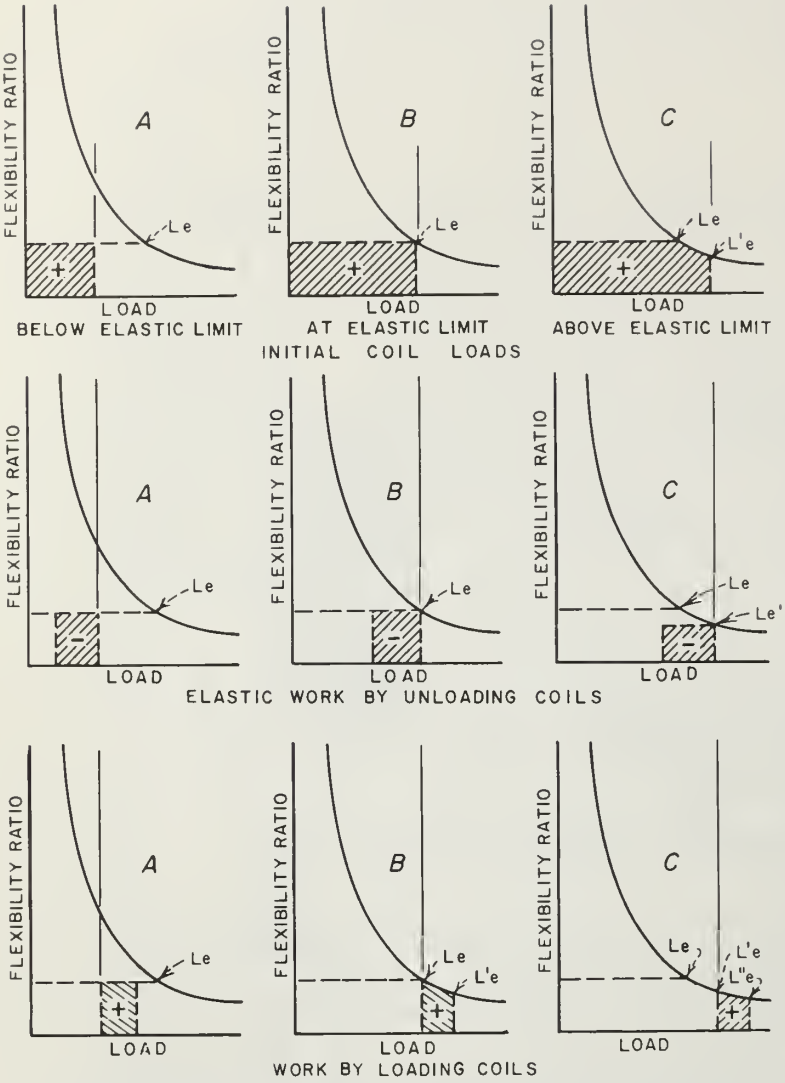

FIGURE 10. - Relative work capabilities of loading and unloading helical coils.

for the coil geometries given in figure 2 are tabulated in figure 9. For example, a coil with geometry C has 31 times as much recoverable elastic work stored in it as a straight rod with the same length and material and with the same applied force.

The helical coil exhibits either elastic or elastic-plastic behavior, depending upon the load conditions as described semiquantitatively in figure 10. In figure 10, L_e denotes the elastic limit established during the coil-manufacturing process. If this limit is not exceeded, the coil behaves in an entirely elastic manner. If the previous force used to establish the coil geometry is exceeded, a new elastic limit, L_e', is established. In this process, the flexibility of the coil is reduced and the coil elongates plastically. The total work done in loading the coil, both elastic and plastic, is applied to the structure when the load is increasing. However, only the elastic work is available to do work on the structure when the coil is unloading. The amount of elastic work that can be recovered is reduced if the new elastic limit, L_e'', is replaced with still another ratio L_e'' by an increasing tensile force. Because plastic flow occurs at nearly constant force, this aspect of behavior can be used to advantage to help maintain a more nearly constant coil load when in use. Because of the geometry and combined state of stress (torsion, bending, and tension), instead of only tension for straight rod, plastic flow can be produced at loads well below those needed for straight rods. By choosing the coil geometry-load conditions, a wide variety of coil behaviors is possible.

MANUFACTURE AND LABORATORY TESTING OF HELICAL ROCK BOLTS

The next laboratory testing was on helical rock bolts constructed from 5/8-inch nominal diameter (9/16-inch actual) Colorado Fuel and Iron expansion-anchor-type rock bolts of 6 foot-length. These bolts (shown in fig. 11) along

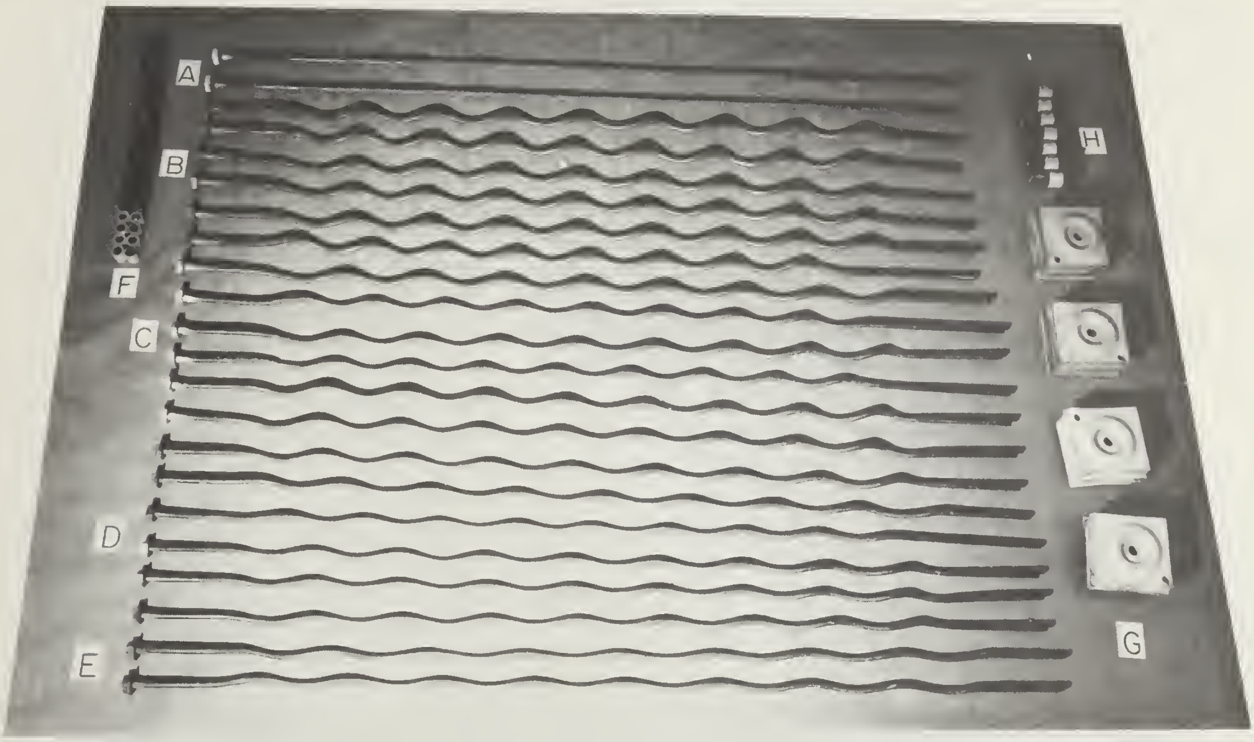

FIGURE 11. - Flexible helical bolts and other hardware tested in the York Canyon mine.

with some other hardware were later tested in an operating mine. In figure 11, the letter A denotes straight bolts of the kind made into helical bolts by a spring manufacturer. The initial geometry used is not shown but resembled A of figure 2. A coil with a 2-5/8-inch pitch was wound on a 1-1/4-inch mandrel in a lathe. For commercial use, the method of manufacturing would be different and less expensive. The letters B, C, D, and E in figure 11 denote bolts that were loaded during manufacture with maximum forces of 10,000 pounds, 12,000 pounds, 14,000 pounds, and 16,000 pounds, respectively. All of these forces were above the intended bolt installation loads, and, therefore, the bolt behavior was expected to be elastic. If smaller values had been used, some plastic flow would have occurred during bolt use and would have helped the bolts to maintain their installed loads. Tests with bolts that deform plastically during use remain to be run. Note that all helical bolts retain some of their helical shape and flexibility for the load range that may result in mine use. The letters F, G, and H in figure 11 denote vibrating-wire load gages used to measure the bolt loads in field use, bearing plates, and 1-5/8-inch expansion anchors. None of the bolts was hardened.

In figure 12, the change in bolt length of a 40.75-inch-long helical bolt is plotted against the maximum tensile force applied. After each 200-pound increase in load above the previous maximum, the load was removed to establish how much of the elongation was plastic and how much was elastic. The unloading and reloading curves, which are represented by the broken lines, show that most of the elongation was plastic.

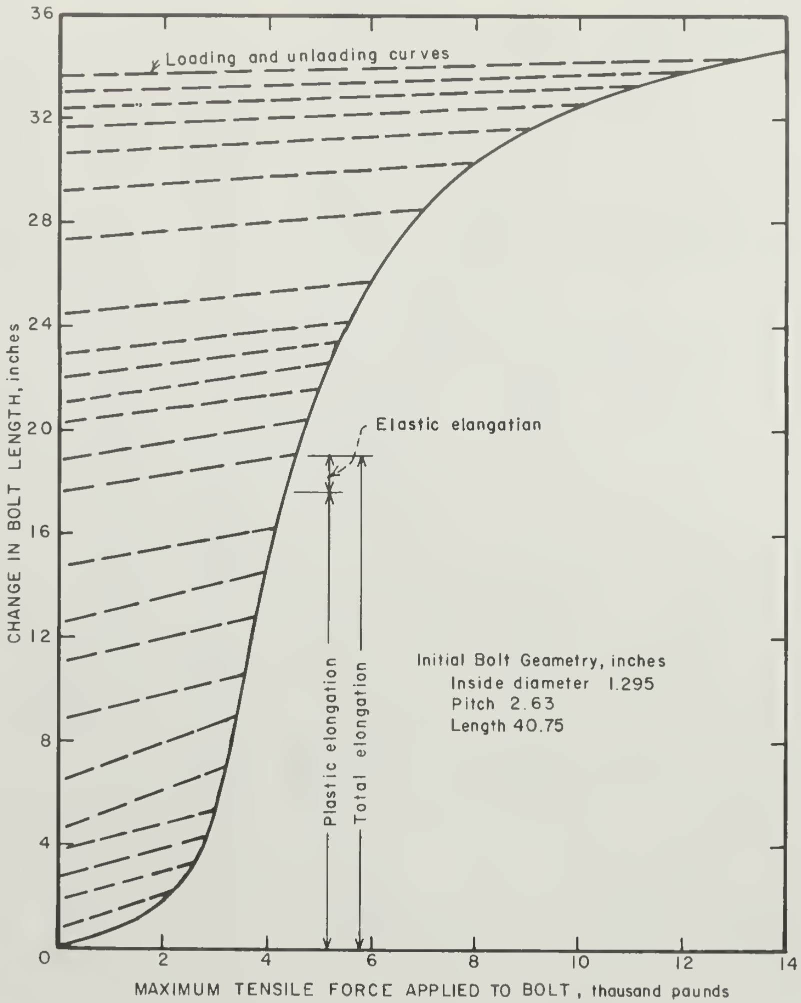

FIGURE 12. - Change in helical bolt length as a function of the maximum tensile force applied.

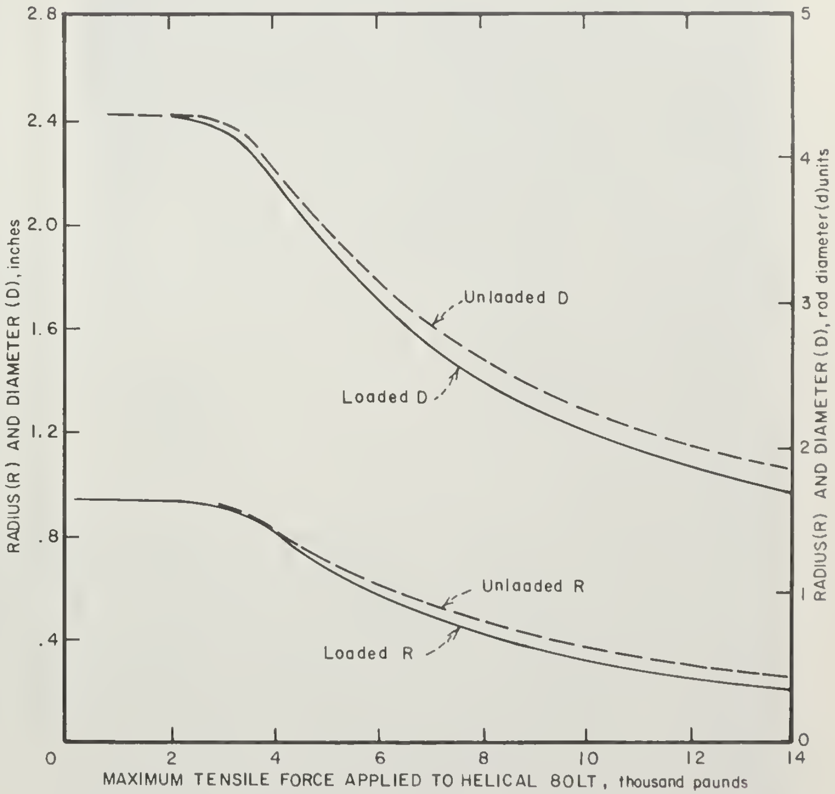

FIGURE 13. - Radius and outside diameter of helical bolt as a function of the maximum tensile force applied.

In figure 13, the change in bolt radius, R, and in the outside diameter of the bolt, D, in inches and in rod-diameter units, are given as functions of the maximum tensile force applied. The hole diameter required to place a helical bolt can be obtained from the unloaded D, which should be 1.63 inches for the anchor size used.

In figure 14, the change in bolt pitch, p, in inches and in rod diameter units is given as a function of the maximum tensile force applied. The loaded and unloaded pitch values are nearly the same.

In figure 15, the results of cyclic loading and unloading the helical bolt between zero and a maximum force that was increased by 200-pound increments is shown in terms of the average total strains, the average plastic strains, and the average elastic strains. These were obtained by dividing the total, plastic, and elastic-bolt elongations by the bolt length before that loading cycle. The elastic strains are important throughout the force range, but the elastic strains are relatively more important for high force values. The plastic strains are more restricted, contributing most for forces between 20% and 50% of the largest force applied. The most rapid change in bolt length for a 200-pound-force increment occurred at about 3,800 pounds. These curves appear to have a log-normal shape.

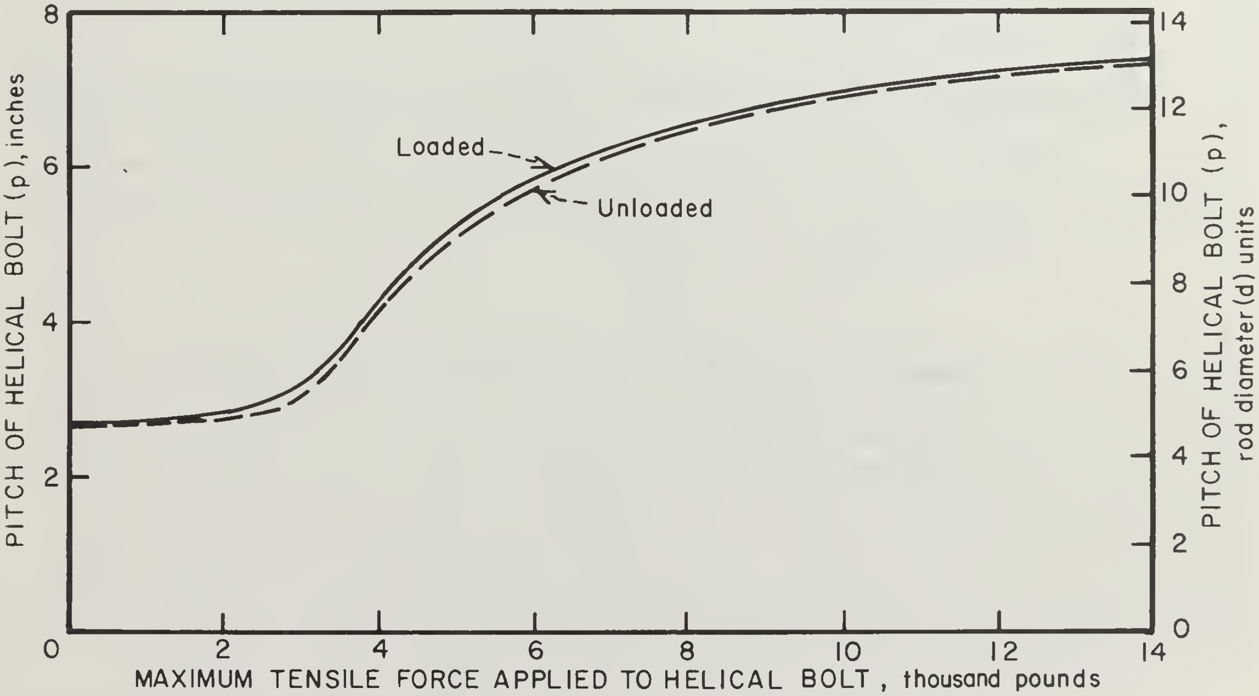

FIGURE 14. - Pitch of helical bolt as a function of the maximum tensile force applied.

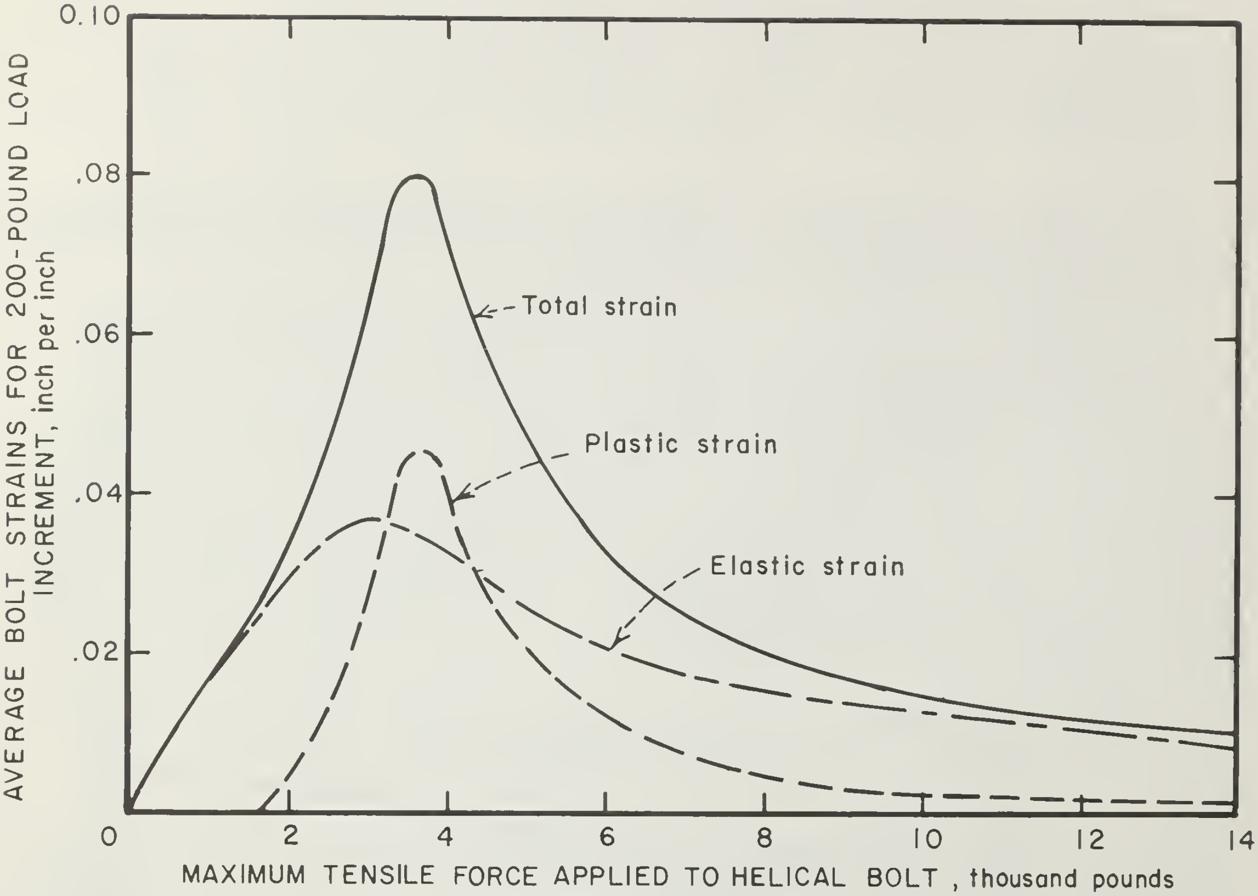

FIGURE 15. - Elastic, plastic, and total average strains for helical bolts as a function of the maximum tensile force applied.

In figure 16, the flexibility of the helical bolt relative to that of a straight bolt is given by the ratio, F_r, for maximum applied tensile force loads. This is compared with what is predicted by equation 8 for r = 0.281 inch when the experimental values of R and p are used. Considering the extensive plastic flow that has occurred in the coil, the elastic estimate of behavior is fairly good. This figure indicates that the flexibility of a helical bolt decreases rapidly as the load is initially applied and when torsion is the most important component of stress. The bolt becomes stiffer when the bending and tension stresses become equally important. Figures 12 through 16 show that the behavior of helical bolts is almost the same as that of coils shown by figures 4 through 8.

In figure 17, the total work done on the bolt by increasing the tension from the initial coiled shape to 10,000, 12,000, and 14,000 pounds of force is shown. This work was 14,350 foot-pounds for the 14,000-pound load. In comparison, the work done on a straight bolt was 79 foot-pounds for the 14,000-pound load. An increment of work is denoted by δw. Most of the work done on the helical bolt was plastic and could not be recovered when the bolt was unloaded.

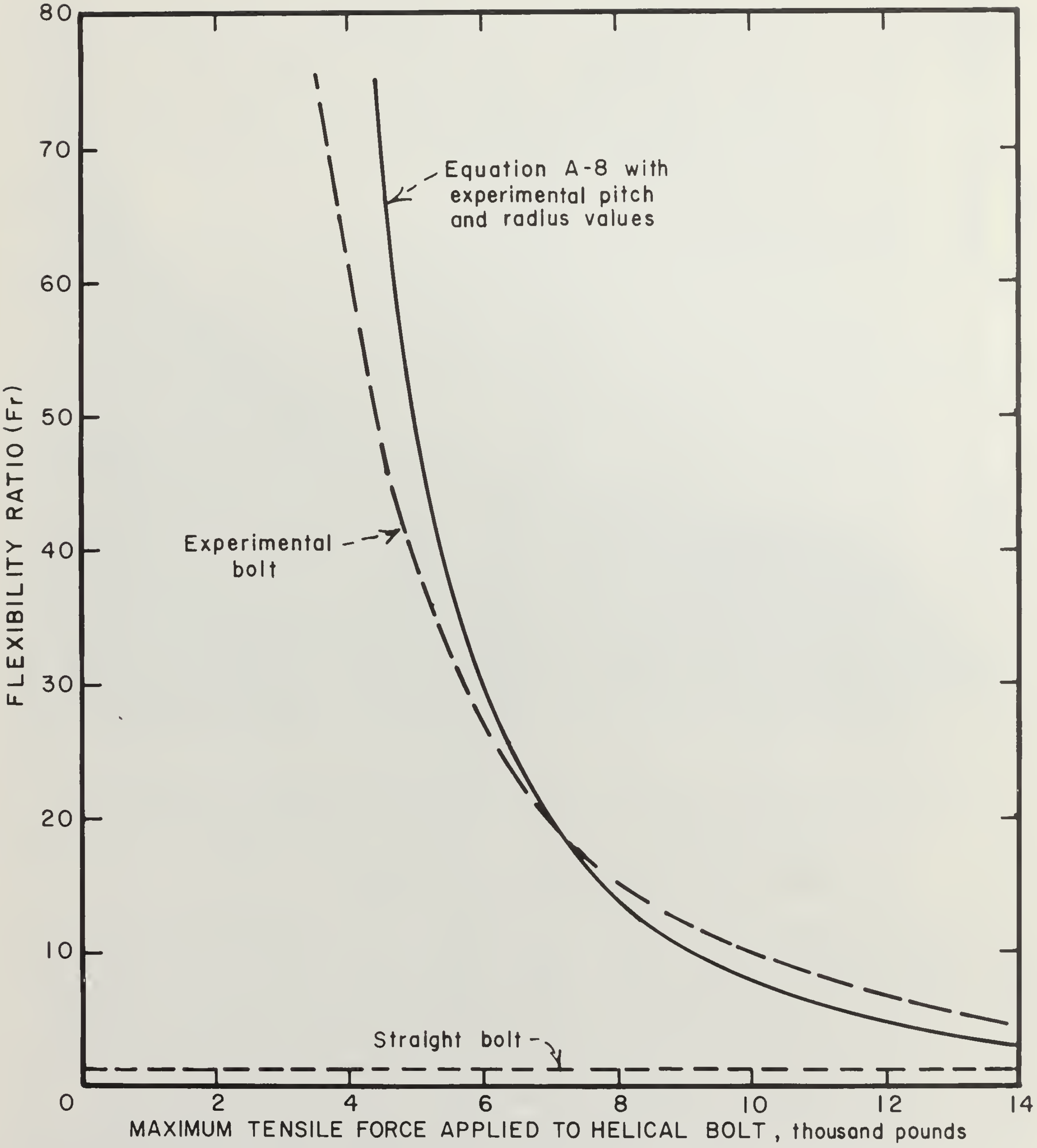

FIGURE 16. - Flexibility ratio of the helical bolt to a straight rod of the same length for a given maximum tensile force applied.

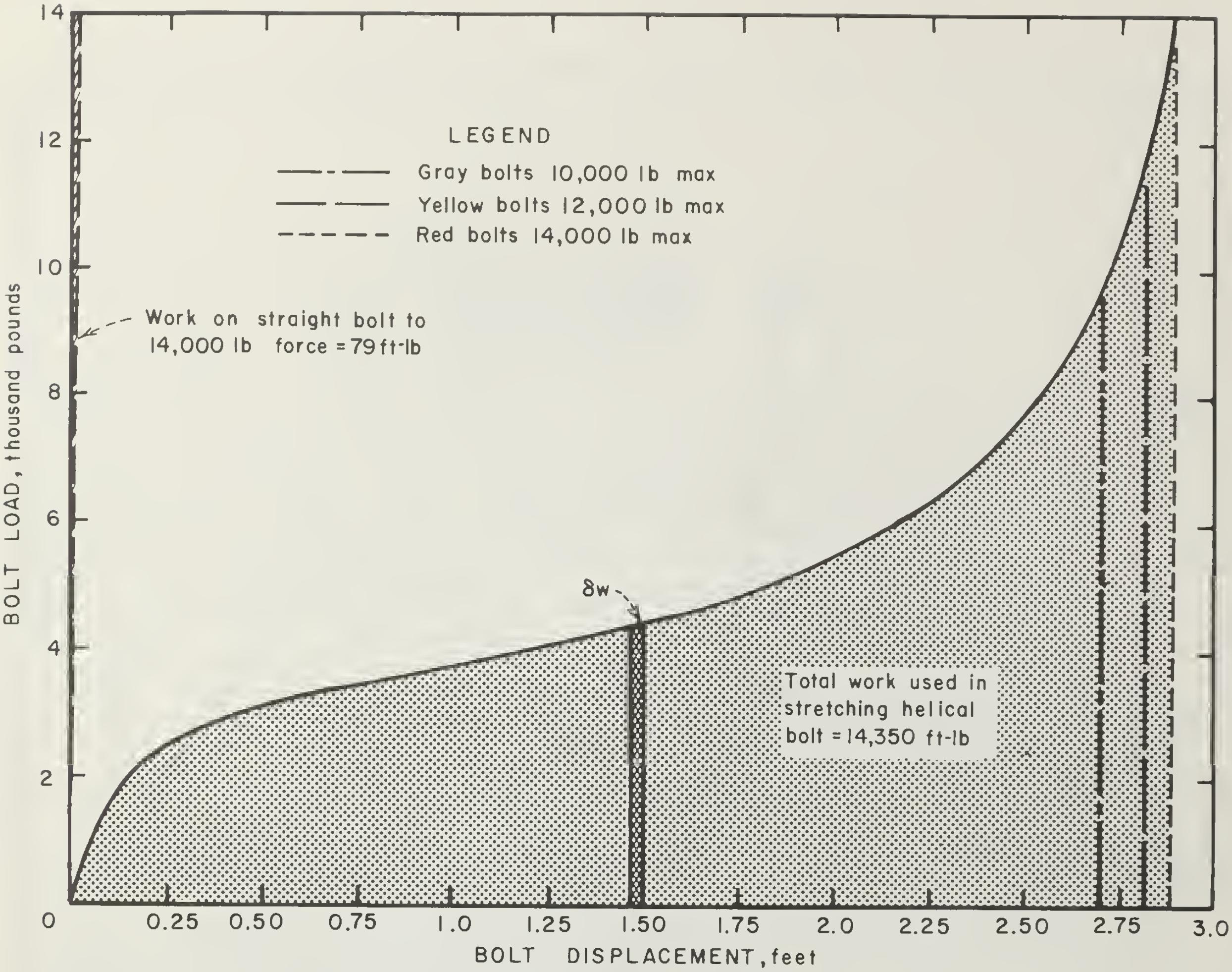

FIGURE 17. - Work done by helical bolt during manufacture with increasing tensile load compared with the elastic work done by a straight bolt.

PRELIMINARY FIELD TESTING OF HELICAL ROCK BOLTS AND VIBRATING-WIRE LOAD GAGES

Some preliminary field tests were conducted at the Kaiser Steel Co.'s York Canyon coal mine, near Raton, N. Mex., to verify that both helical bolts and vibrating-wire load gages (1) behaved as expected in mine use. Eighteen helical and ten straight bolts with load gages were installed with a torque wrench with 150 foot-pounds of torque in four crosscuts on the headgate side between double entries of a longwall-mining panel (as shown in fig. 18). The bolts were installed in crosscuts marked 1S, 2S, 3S, and 4S next to coal panel 5 North, which was mined using Hemscheidt shields. The mining height of the coal was about 10 feet. Overbolting of an existing Mining Enforcement and Safety Administration (MESA)[3] approved resin-grouted bolt pattern was used

---

[3] MESA became the Mine Safety and Health Administration (MSHA), U.S. Department of Labor, on March 9, 1978.

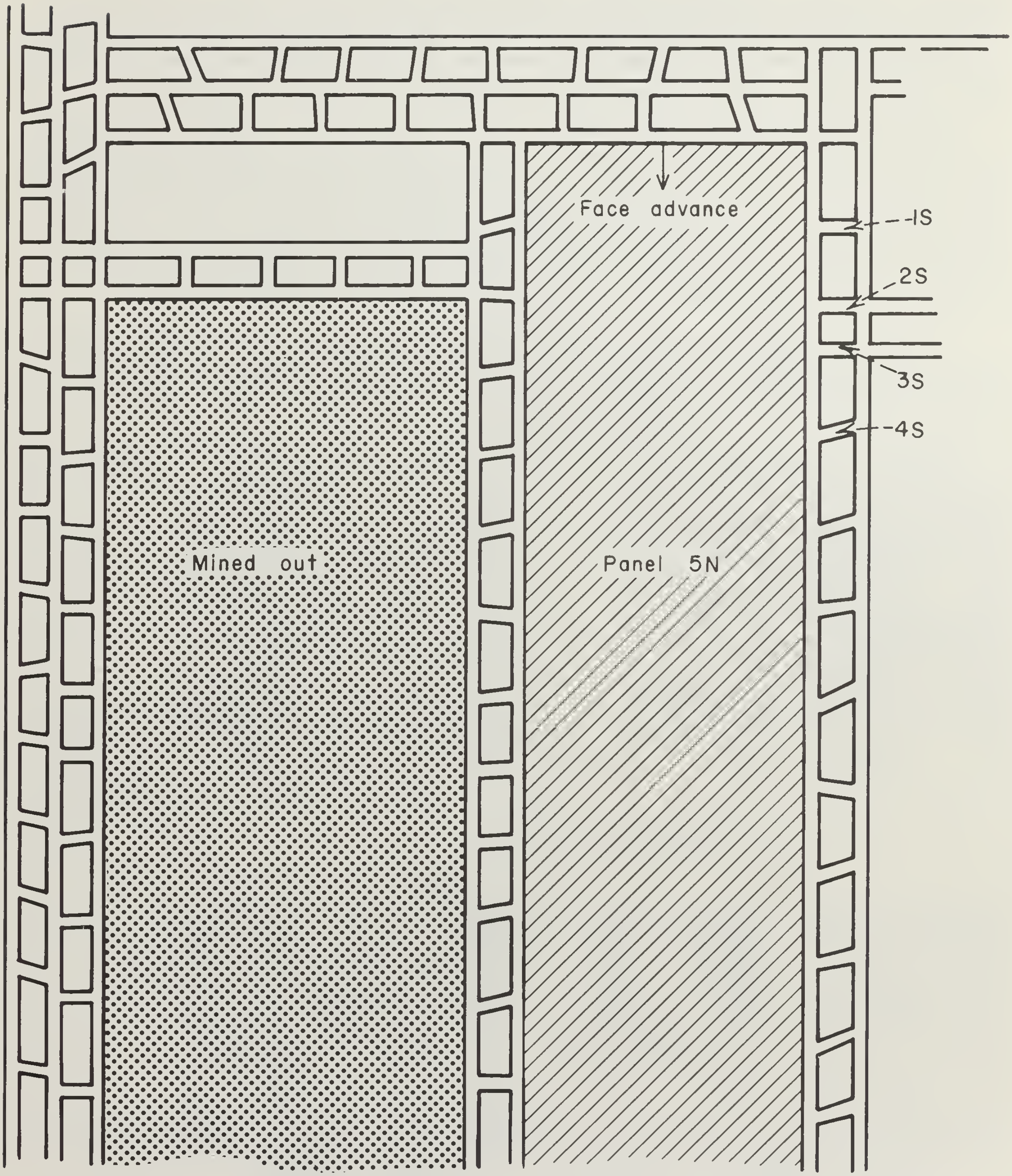
Face advance
-1S
2S
3S
-4S
Mined out
Panel 5N

FIGURE 18. - Plan map of York Canyon mine panel 5N.

because the use of an experimental bolt alone would have required much more time and effort than was available for this preliminary test. The test served the intended purpose of showing that the helical bolts do carry loads well, and it showed that the gages perform as expected in mine conditions.

Each grouted bolt is indicated by an x in figure 19. These bolts were placed through a sheet-metal strip about 12 inches wide. The straight bolts with expansion anchors are shown as open circles and are numbered 1 through 10. The helical bolts with expansion anchors are shown as solid circles and are numbered 21 through 38. The straight and helical bolts are used with equal distribution left to right and front to back in each crosscut to produce average results over the test locations.

The bolt loads were read during the mining sequence for 2 months, and after which the crosscuts were barricaded off by mine personnel. Neither gages nor bolts were recovered.

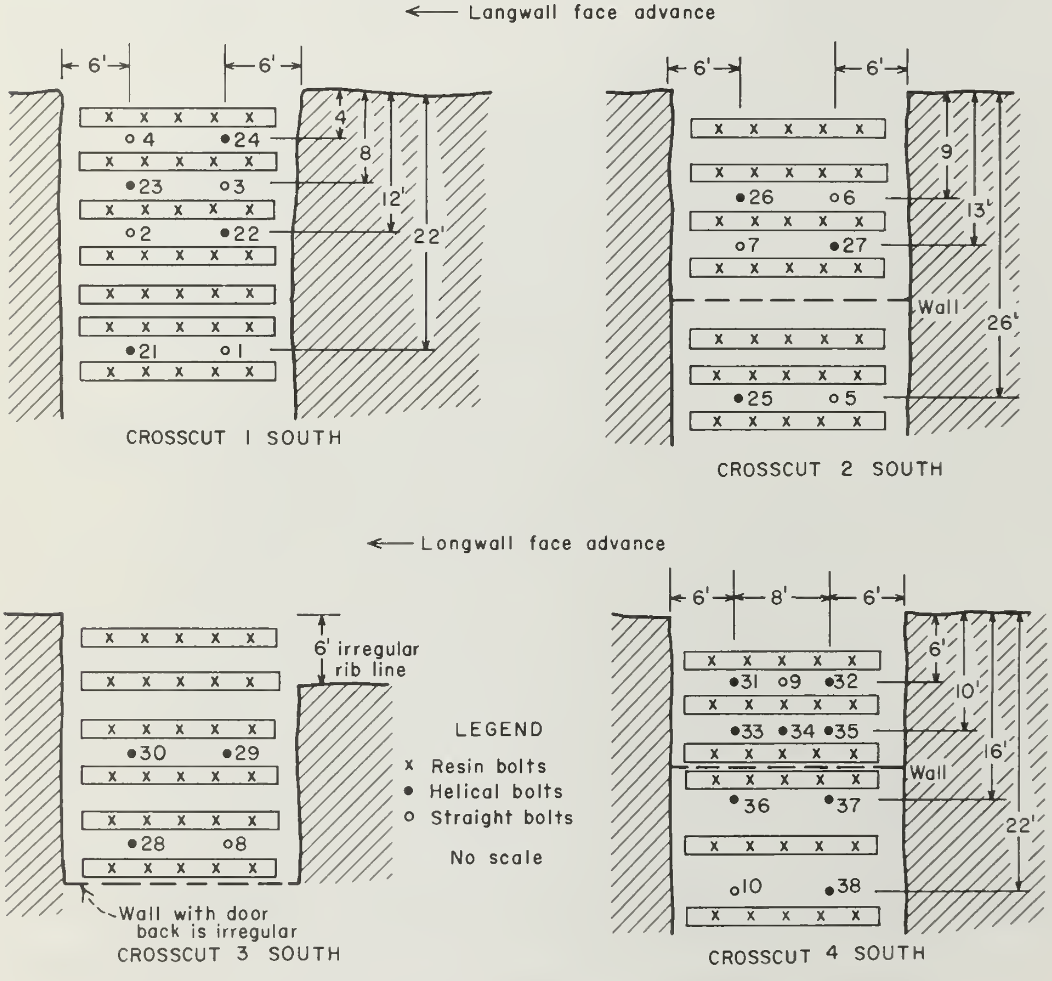

Longwall face advance
6'
6'
4
8
12'
22'
○4 ●24
●23 ○3
○2 ●22
●21 ○1
CROSSCUT 1 SOUTH
6'
6'
9
13'
26'
●26 ○6
○7 ●27
Wall
●25 ○5
CROSSCUT 2 SOUTH
Longwall face advance
6' irregular rib line
●30 ●29
●28 ○8
Wall with door
back is irregular
CROSSCUT 3 SOUTH
LEGEND
x Resin bolts
● Helical bolts
○ Straight bolts
No scale
6'
8'
6'
6'
10'
16'
22'
●31 ○9 ●32
●33 ●34 ●35
Wall
●36 ●37
○10 ●38
CROSSCUT 4 SOUTH

FIGURE 19.—Bolt Patterns Used in the York Canyon Mine

FIGURE 19. - Bolt patterns used in the York Canyon mine.

The experimental results for the bolts tested in the York Canyon mine are presented in figures 20 through 23. The gages performed well during this period without any gage malfunction. In crosscut 1S (fig. 20), the four straight bolts (1, 2, 3, and 4) increased their load during the test period. The four helical bolts (21Y, 22G, 23R, and 24Y) also increased in load, but only about one-third as much as the straight bolts. Bolt load stability is one of the features expected with the flexible bolt. The bolts subjected to previous maximum loads are shown in the following tabulation:

Letters	Colors used to code the bolt heads	Maximum loads used to manufacture bolts, pounds
G...............	Gray...............	10,000
Y...............	Yellow............	12,000
R...............	Red................	14,000
LG..............	Light green........	16,000

Straight bolt 3 (fig. 20) had anchor slippage about August 27, 1976. Note that all bolts tested had a sudden drop in load during the first 2 days of use.

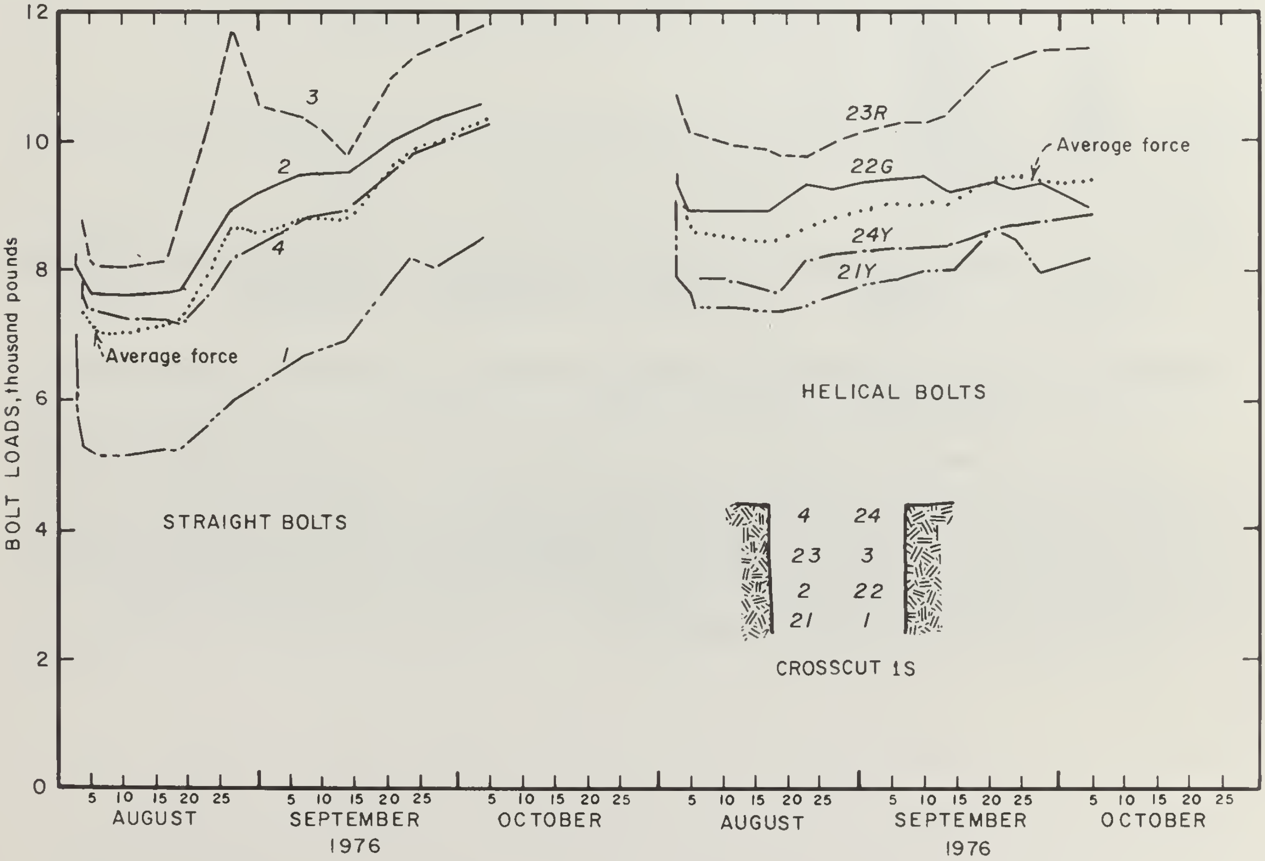

FIGURE 20. - Bolt loads measured by vibrating-wire load gage for helical and straight bolts in York Canyon mine crosscut 1S.

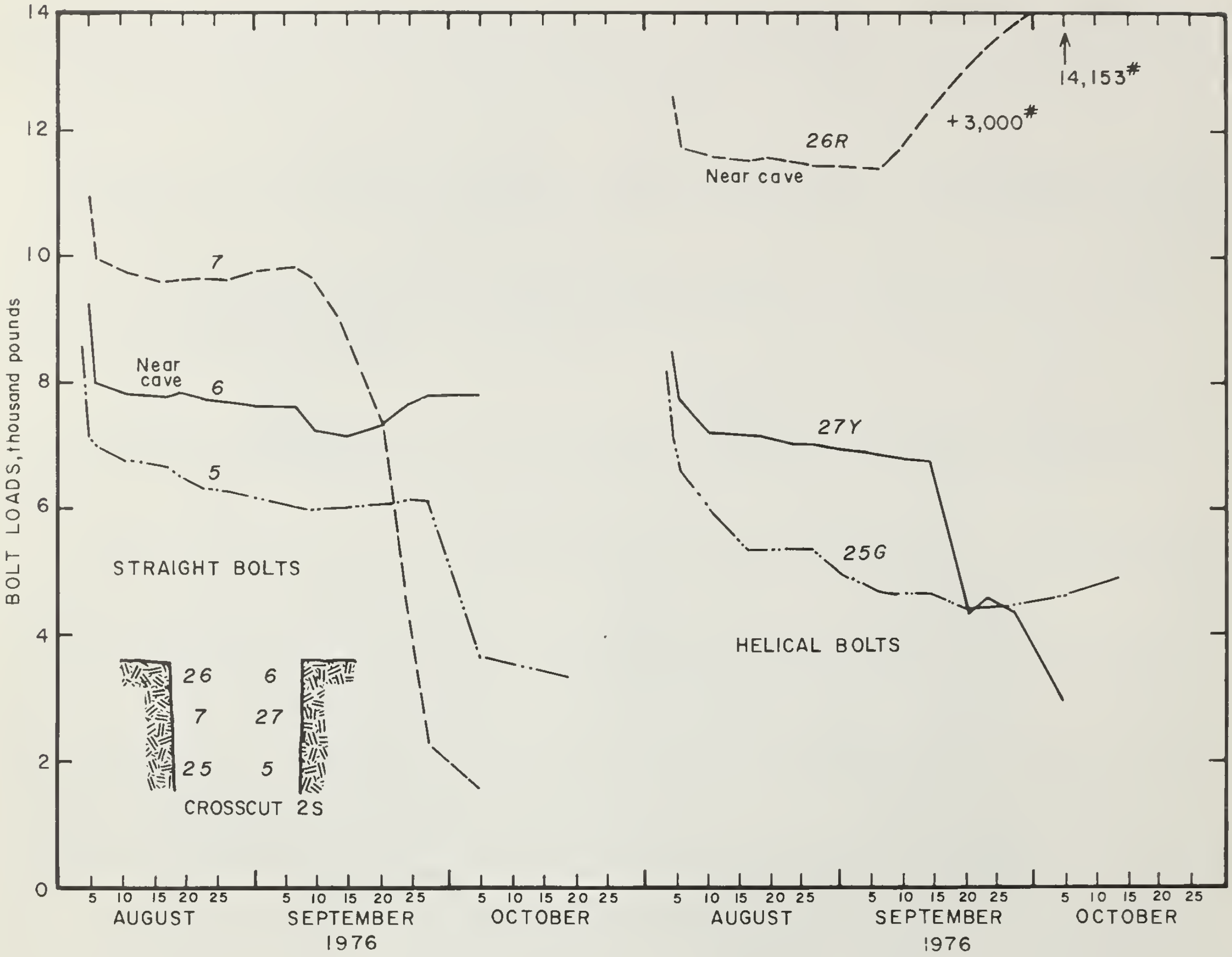

FIGURE 21. - Bolt loads measured by vibrating-wire load gage for helical and straight bolts in York Canyon mine crosscut 2S.

In crosscut 2S (fig. 21) all of the bolts failed to provide adequate support, with the exception of 26R. This bolt, which is near the cave line, had a high installation load, and this load increased to 14,150 pounds at the end of the test period. Tension losses of the other bolts indicate that either the bolted beds were compressed as mining progressed, or the bolt anchors slipped due to poor anchorage capacity.

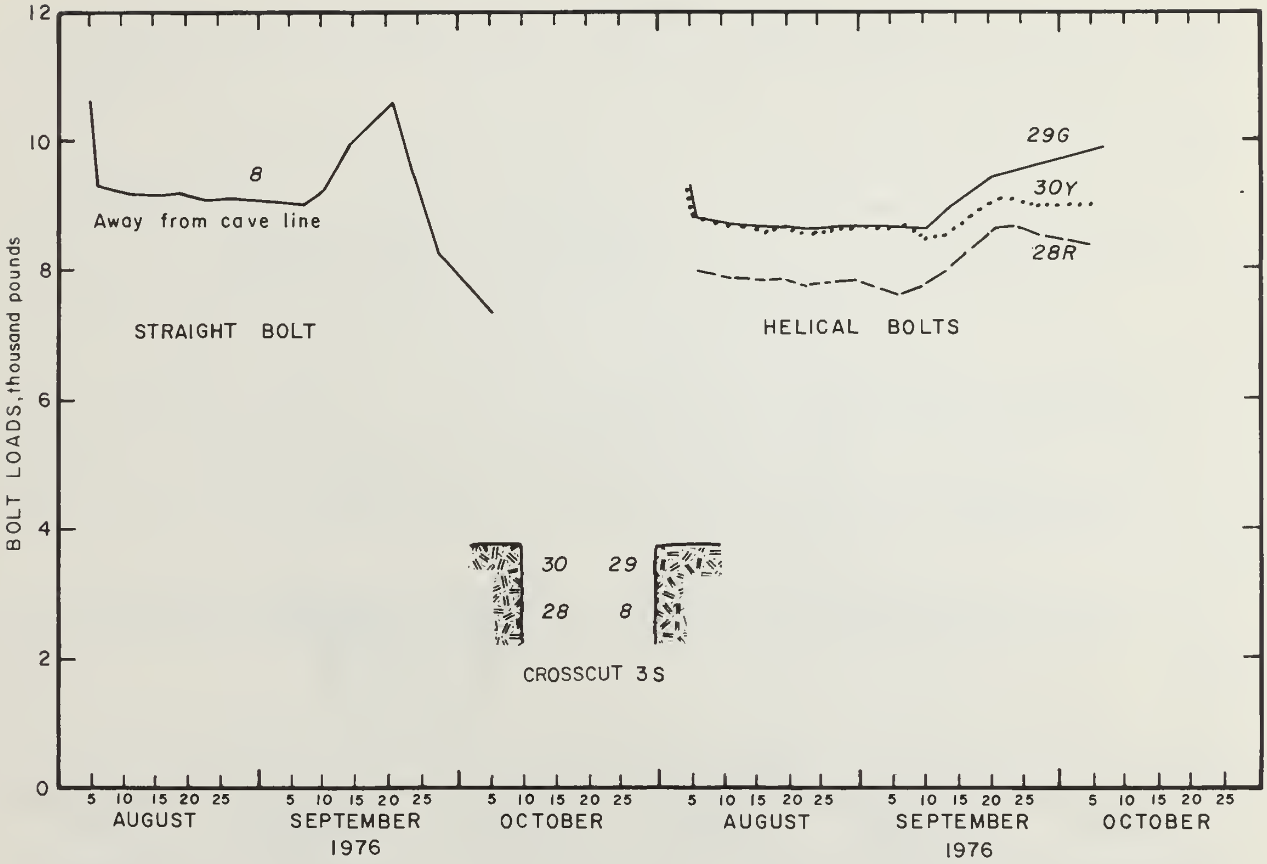

FIGURE 22. - Bolt loads measured by vibrating-wire load gage for helical and straight bolts in York Canyon mine crosscut 3S.

In crosscut 3S (fig. 22) the three helical bolts 28R, 29G, and 30Y gave stable support to the roof, but bolt 8, the single straight bolt away from the cave line, did not.

In crosscut 4S (fig. 23) six of the helical bolts gave stable support; bolt 31Y near the cave line increased in load suddenly, and bolt 23 LG near the cave line decreased in load suddenly during the last week of the test. Bolt 10 away from the cave line had a stable, slightly increasing load, but bolt 9 near the cave line lost its load completely during the last week of the test.

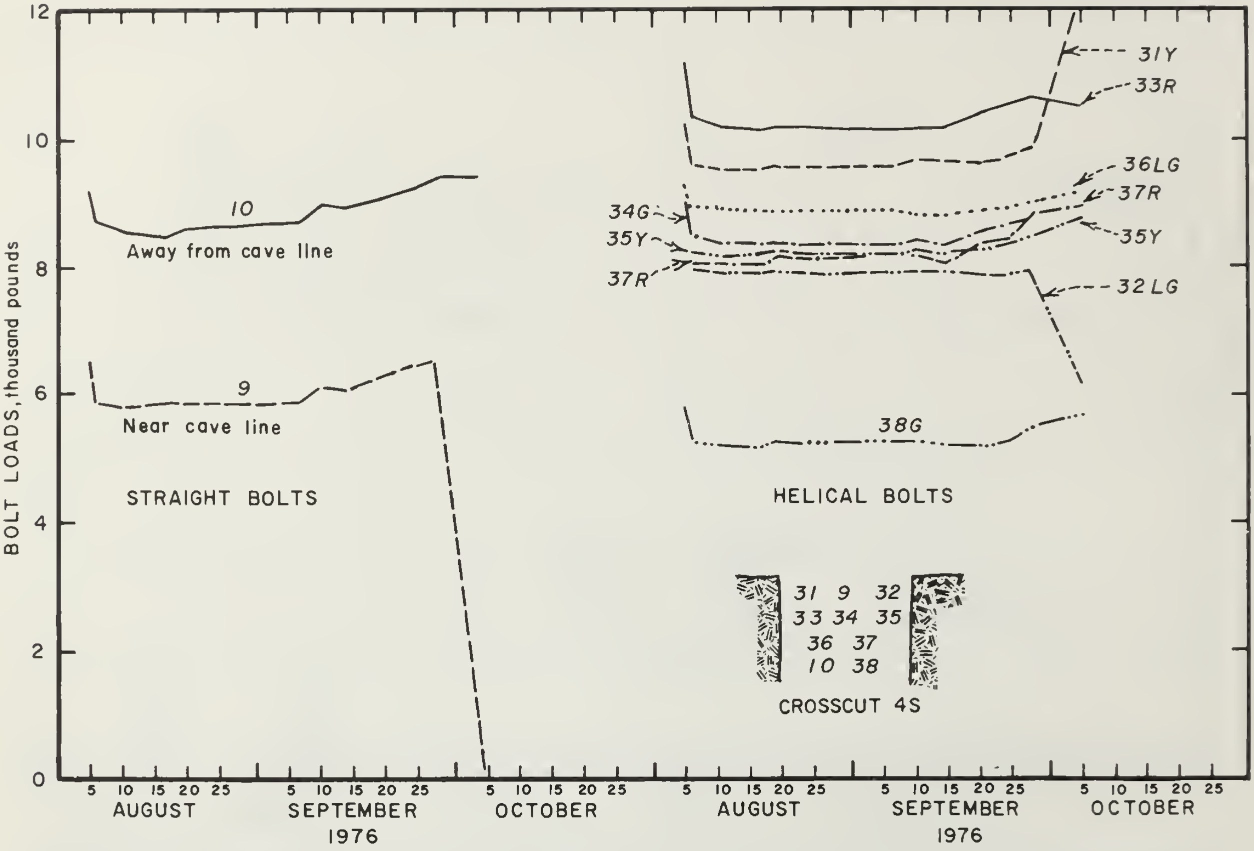

FIGURE 23. - Bolt loads measured by vibrating-wire load gage for helical and straight bolts in York Canyon mine crosscut 4S.

SUMMARY AND CONCLUSIONS

Helical coils were made, by a spring manufacturer, from 0.5-inch-diameter rod made of 4140 steel that was 5 feet long. They were stretched in the laboratory using a tensile-testing machine to define their elastic-plastic behavior and changes in geometry with an increasing applied tensile force. The elastic behavior conformed with theoretical considerations with regard to coil flexibility for a given geometry even though the stress distribution was appreciably different because of the plastic flow. As expected, the coils exhibited much greater flexibility than the straight rods from which the coils were made, even for loads up to 13,000 pounds (66,250 psi).

Next, helical rock bolts were manufactured from 5/8-inch nominal diameter Colorado Fuel and Iron expansion-anchor-type bolts, 6 feet long. These helical rock bolts were tested in the same way as the helical coils; however, the emphasis was on the behavior of the bolts that were loaded to a maximum force of 10,000 pounds, 12,000 pounds, 14,000 pounds, and 16,000 pounds, respectively, during manufacture. The behavior was very similar to that observed for the smaller helical coils. Results of the laboratory tests showed that the bolts were 5 to 10 times as flexible as a straight bolt.

Finally, 18 helical bolts with vibrating-wire load gages were compared, in the Kaiser Steel York Canyon mine, Raton, N. Mex., with the behavior of 10 straight bolts of the same brand with load gages. An existing grouted-bolt pattern was overbolted to establish that the helical bolts would maintain a more nearly stable load, and this was the case. The load changed only about one-third as much as for the straight bolts. All the helical bolts carried a load for the entire test period but this was not the case during the test period for the straight bolts. The test results were somewhat surprising in that the bolt loads changed as much as they did, increasing when the roof was already bolted with resin-grouted bolts. A flexibility of 5 to 10 was expected; however, only a flexibility of about 3 was realized. The straight bolt benefited relatively more from the softening provided by the anchor and bearing plate assemblies. Other bolt geometries with greater flexibilities or bolts with plastic flow during the loading phase should emphasize the better performance of the helical bolts over the straight bolts. When bolt loads are difficult to maintain or when the bolt assembly is softened by using wooden blocks under the bolt head, the helical bolt should work to advantage.

The concept of the helical bolt has been established as sound, but much testing remains before the bolt is established as a viable means of roof support.

REFERENCES

1. Babcock, C. O. Sensitive Vibrating Wire Rock Bolt Load Gage. Trans. AIME, v. 262, December 1977, pp. 293-299.

2. Chaiko, W. M., and J. J. Scott. Roof Support Experience With Friction Rock Stabilizer. Min. Cong. J., v. 63, No. 3, March 1977, pp. 36-41.

3. Conway, J. P., S. M. Dar, J. H. Stears, P. C. McWilliams, and K. G. Hoge. Laboratory Studies of Yielding Rock Bolts. BuMines RI 8058, 1975, 40 pp.

4. Faupel, J. H. Strength Under Combined Stress. Ch. in Engineering Design. John Wiley & Sons, Inc., New York, ch. 3, 1964, pp. 212-213.

5. Harrell, M. V. Roof Control With Hydraulic Driven Pins. Min. Cong. J., July 1971, pp. 27-31.

6. Ortlepp, W. D., and J. J. Reed. Yieldable Rock Bolts for Shock Loading and Grouted Bolts for Faster Rock Stabilization. The Mines Magazine, March 1970, pp. 12-17.

7. Scott, J. J. Friction Rock Stabilizers--A New Rock Reinforcement Method. Site Characterization. 17th U.S. Symp. on Rock Mech., Univ. of Utah, Snowbird, Utah, Aug. 25-27, 1976, pp. 5E5-1 to 5E5-8.

8. Stefanko, R. New Look at Long Term Anchorage; Key to Roof Bolt Efficiency. Trans. AIME, v. 226, 1963, pp. 197-201.

9. Thompson, R. R., and R. C. Bates. Field Testing the Pumpable Polymeric Roof Bolt. First Symp. on Underground Min., Nat. Coal Assoc./Bituminous Coal Res. Coal Conf. and Expo II, Louisville, Ky., Oct. 21-23, 1975. National Coal Association, Washington, D.C., 1975, v. 2, pp. 80-89.

APPENDIX.--DEFORMATION BEHAVIOR OF AN ELASTIC HELICAL COIL LOADED IN TENSION

Theory

Equation 3.274 in reference 4 for the elastic elongation, δ_h, of a spring with an open helical coil can be written as

$$\delta_h = \frac{4PR^2L}{\pi r^4 E}(1 + \cos^2\alpha). \qquad \text{(A-1)}$$

This equation contains the effects of bending and torsion, but not of tension because $\delta_h = 0$ for a straight rod when $R = 0$ and $\cos^2\alpha = 0$. The elongation of the coil length of L' from the tensile force P is

$$\delta_{h\,t} = \int_0^{L'} \epsilon_t\, \delta\ell' = PL'/A'E, \qquad \text{(A-2)}$$

so that the total elongation for bending, torsion, and tension becomes

$$\delta_h = 4PR^2L(1 + \cos^2\alpha)/\pi E r^4 + PL'/A'E, \qquad \text{(A-3)}$$

where $A' = A/\sin\alpha$, for $P \geq d$,

ϵ_t = strain in direction of coil length, not rod length,

$\delta\ell'$ = increment of coil length,

and $L' = \sqrt{4\pi^2R^2 + p^2}\,\sin\alpha = L\sin\alpha$.

In these equations, P is the force in pounds; L, r, and A are the length, radius, and cross-sectional areas, respectively, of the rod from which the coil is made; L', R, and A' are the length of the coil, radius of the coil, the area of a section perpendicular to the center line of the coil, respectively; α is the angle between the areas A and A'; n and p are the number of turns and pitch of the coil; and E is Young's modulus of the rod material.

Equation A-3 can be written

$$\delta_h = \frac{PL}{\pi r^2 E}\left\{\frac{4R^2}{r^2}(1 + \cos^2\alpha) + \sin^2\alpha\right\} \qquad \text{(A-4)}$$

for the elongation of the helical coil.

The elongation of a straight rod of length, L, is

$$\delta_s = PL/AE = PL/\pi r^2 E. \qquad \text{(A-5)}$$

The relative displacement per unit length of the helical coil and the straight rod are δ_h/L' and δ_s/L, where L' and L are the lengths of the helical coil and the straight rod, respectively. The flexibility ratio, F_r, of the coil to the straight rod is, therefore,

$$F_r = \frac{L\delta_h}{L'\delta_s} = \frac{1}{\sin\alpha} \{4R^2 \ (1 + \cos^2\alpha)/r^2 + \sin^2\alpha\}, \qquad \text{(A-6)}$$

$$= \frac{\sqrt{4\pi^2R^2 + p^2}}{p} \left\{ \frac{4R^2}{r^2} \left(1 + \frac{4\pi^2R^2}{4\pi R^2 + p^2} \right) + \frac{p^2}{4\pi^2R^2 + p^2} \right\},$$

$$= \{4R^2 \ (79\ R^2 + p^2)/r^2 + p^2\}/p\sqrt{39.5\ R^2 + p^2} \ \text{(approximately)}. \qquad \text{(A-7)}$$

If $d = 1 = 2r$, equation A-7 becomes,

$$F = \{1263\ R^4 + 16\ R^2p^2 + p^2\} / p\sqrt{39.5\,R^2 + p^2}. \qquad \text{(A-8)}$$

This result with the flexibility, F_r, normalized to the rod diameter, d, taken as unity is plotted in figure 1; R and p are expressed in d units.

☆U.S. GOVERNMENT PRINTING OFFICE: 1978-603-002/108

INT.-BU.OF MINES,PGH.,PA. 23549

622.09
Un32mo

RI 8301

Bureau of Mines Report of Investigations/1978

Electrochemical Determination of the Gibbs Energy of Formation of Sphalerite (ZnS)

NOV 17 1978
UNIV. OF ILL. LIBRARY
AT [illegible] CHAMPAIGN

UNITED STATES DEPARTMENT OF THE INTERIOR

Report of Investigations 8301

Electrochemical Determination of the Gibbs Energy of Formation of Sphalerite (ZnS)

By Seth C. Schaefer

March 3 1849

UNITED STATES DEPARTMENT OF THE INTERIOR
Cecil D. Andrus, Secretary

BUREAU OF MINES

This publication has been cataloged as follows:

Schaefer, Seth C

Electrochemical determination of the Gibbs energy of formation of sphalerite (ZnS) / by Seth C. Schaefer. [Washington] : U.S. Dept. of the Interior, Bureau of Mines, 1978.

16 p. ; ill., diagrs. ; 27 cm. (Report of investigations - Bureau of Mines ; 8301)

Bibliography: p. 15-16.

1. Sphalerite. I. United States. Bureau of Mines. II. Title. III. Title: Gibbs energy. IV. Series: United States. Bureau of Mines. Report of investigations - Bureau of Mines ; 8301.

TN23.U7 no. 8301 622.06173

U.S. Dept. of the Int. Library

CONTENTS

Page

Abstract.. 1
Introduction.. 2
Experimental work... 3
    Materials... 3
    Apparatus and procedure....................................... 4
Results and discussion.. 6
Summary and conclusions... 14
References.. 15

ILLUSTRATIONS

1. High-temperature galvanic cell................................ 5
2. Electromotive force versus temperature for cell reaction (1)......... 10
3. Plot of log pO_2 versus temperature for Zn-S-O system................ 12
4. Standard Gibbs energy of formation of sphalerite and wurtzite........ 13

TABLES

1. Analyses of reagents.. 4
2. Electromotive force of cell Pt, Cu + Cu_2O // ZrO_2 // O_2 = 0.21 atm, Pt 7
3. X-ray diffraction analyses of reagents and electrode mixtures........ 8
4. Electromotive force of cell Pt, ZnS + ZnO, SO_2 = 1 atm // ZrO_2 // Cu_2O + Cu, Pt.................... 9
5. Effect of temperature and pO_2 on pSO_2 for reaction $SO_3(g) = SO_2(g) + 1/2\ O_2(g)$.............. 12
6. Coefficients in linear Gibbs energy equation $\Delta Gf° = \Delta Hf° - T\Delta Sf°$(cal)........................ 14

ELECTROCHEMICAL DETERMINATION OF THE GIBBS ENERGY OF FORMATION OF SPHALERITE (ZnS)

by

Seth C. Schaefer[1]

ABSTRACT

As part of the Bureau of Mines, U.S. Department of the Interior, effort to provide thermodynamic data for the advancement of minerals technology, the Gibbs energy of formation of sphalerite (zinc sulfide) was investigated with a high-temperature galvanic cell employing stabilized zirconia as the electrolyte. In the temperature range 948 to 1,210 K, potential measurements were obtained for the cell

$$\mathrm{Pt,\ ZnS + ZnO,\ SO_2 = 1\ atm\ //\ ZrO_2\ //\ Cu_2O + Cu,\ Pt,}$$

with the overall cell reaction

$$\mathrm{ZnS(c) + 3\ Cu_2O(c) = ZnO(c) + 6\ Cu(c) + SO_2(g).} \qquad (1)$$

These results, combined with the best available values of $\Delta Gf°$ for ZnO, SO_2, and Cu_2O from the literature, give the Gibbs energy of formation of zinc sulfide for the reaction

$$\mathrm{Zn(l,v) + 1/2\ S_2(g) = ZnS(c)} \qquad (2)$$

$$\Delta Gf° = -64.223 + 24.02 \times 10^{-3} T \pm 0.650 \text{ kcal/mole} \qquad (3)$$

(948-1,180 K; standard states - pure liquid zinc and S_2 gas at 1 atm),

and $$\Delta Gf° = -92.720 + 48.17 \times 10^{-3} \pm 0.650 \text{ kcal/mole}$$

(1,180-1,210 K; standard states - pure zinc vapor and S_2 gas at 1 atm).

A third law analysis yields for the formation reaction

$$\mathrm{Zn(l) + 1/2\ S_2(g) = ZnS(c),} \qquad (5)$$

---

[1] Metallurgist, Albany Metallurgy Research Center, Bureau of Mines, Albany, Oreg.

a standard enthalpy of formation as follows:

$$\Delta Hf^\circ_{298.15} = -63.64 \pm 0.700 \text{ kcal/mole.} \tag{6}$$

INTRODUCTION

The thermodynamic properties of sphalerite (cubic crystalline form of ZnS) have been investigated as part of a continuing study by the Federal Bureau of Mines to provide metallurgists with fundamental data that can be applied in existing or new metallurgical processes to maximize productivity and decrease energy requirements. Sphalerite is the major mineralogical source of primary zinc in the world (2).[2]

Pioneering work by Kiukkola and Wagner (12) demonstrated the usefulness of stabilized zirconia as selective oxygen anion electrolytes to determine the Gibbs energies for cell reactions involving metal-metal oxide systems at elevated temperatures. Within limitation of the ionic properties of stabilized zirconia electrolyte (21), any equilibrium involving oxygen may be investigated by this technique. The method is based on measurement of the difference in chemical potential between an electrode of unknown oxygen potential and a reference electrode of known potential. In this investigation, the method was modified to measure the difference in potential of a reference electrode (Cu and Cu_2O) and an electrode consisting of a mixture of ZnS and ZnO which was equilibrated with pure anhydrous SO_2 at approximately 1 atm. The transport number of oxygen anions through a fully stabilized zirconia membrane is essentially unity for the range of oxygen potentials of this investigation. The relationship between the open-circuit potential of the cell and the Gibbs energy change for the actual cell reaction is

$$\Delta G(\text{reaction}) = -nFE, \tag{7}$$

where ΔG is the change in Gibbs energy for the cell reaction, n is the number of electrochemical equivalents involved in the cell reaction, F is the Faraday constant (23.061 kcal/v equivalent), and E is the electromotive force in volts.

X-ray parametric measurements showed intersolubility of the condensed phases was negligible at the temperatures of this investigation. Consequently, the assumption of unit activity for the solid phases introduced no appreciable error in the Gibbs energy of formation of sphalerite. The equilibrium oxygen pressures were calculated directly from the measured potentials. Ionic properties of the stabilized zirconia limit the application of this method. The appropriate equilibrium metal oxide-metal sulfide phases in the anode mixtures were selected. Participating solids in the electrode mixtures were maintained essentially at unit activity and checked to determine contamination and intersolubility after the measurements were completed.

Earlier Bureau of Mines investigations (17, 22) provide high-temperature enthalpy and low-temperature heat capacity data for sphalerite and wurtzite.

---

[2] Underlined numbers in parentheses refer to items in the list of references at the end of this report.

An enthalpy of formation of wurtzite has been determined by hydrochloric acid solution calorimetry (1); however, attempts to dissolve sphalerite in this solvent were not successful. A value of 3.19 kcal/mole has been reported for the transformation of sphalerite to wurtzite at 1,293 K (7); however, high-temperature enthalpy measurements (17) did not detect this heat effect when sphalerite was heated above the transformation temperature. In view of these results, the heat of transformation (7) of sphalerite to wurtzite is questionable. Investigators (15-16), who have obtained enthalpies of formation of ZnS from vapor pressure measurements, reported mixtures of wurtzite and sphalerite (15) or only wurtzite (16) in their equilibrated samples. Only one investigation (19), involving hydrogen reduction of zinc sulfide and checked by a vapor pressure method, was conducted below the transformation temperature and reported that the data were applicable to ZnS(β) or sphalerite. An electromotive force investigation (14) showed the data were independent of the crystal structure of ZnS and the equilibrated sample contained wurtzite and sphalerite derived from the most reliable sources (1, 14, 17, 19-20, 22) are included in the discussion.

EXPERIMENTAL WORK

Materials

High-purity reagents were obtained from commercial sources and used without further purification. X-ray emission and chemical analyses of these reagents were confirmed by analytical procedures, and are presented in table 1. Anhydrous-grade sulfur dioxide and ultra-high-purity argon from Matheson Co., Inc.,[3] were used. The reference electrode consisted of 1:1 molar mixture of copper and cuprous oxide and the anode was a 1:1 molar mixture of zinc oxide and zinc sulfide. Sulfur dioxide was dried by passing through anhydrous calcium sulfate (Drierite) to provide an atmosphere of pure sulfur dioxide over the zinc sulfide and zinc oxide mixture. Argon was passed through magnesium perchlorate (Anhydrone) and purified of residual oxygen by passing over hot titanium-zirconium chips to provide an inert atmosphere in the cells for the reference electrode.

---

[3] Reference to specific manufacturers, brands of equipment, or trade names is made for identification only and does not imply endorsement by the Bureau of Mines.

TABLE 1. - Analyses of reagents

Reagent	Element[1]	Wt-pct or major component	Reagent	Element[1]	Wt-pct or major component
Cu	Al	<0.1	ZnS	Al	0.001
	Si	<.01		B	<.003
	O	.0913		Co	.03
	H	.0033		Cu	<.010
	Cu	(2)		Mg	.005
				Si	.11
Cu_2O	B	<.003		Ti	<.01
	Fe	<.01		Zn	(2)
	Ni	<.03			
	Cu	(2)	ZnO	Zn	(1 2)

[1] Impurities not detected by spectrochemical analyses except as noted in table were Ag, Al, As, B, Mg, Mn, Mo, Na, Ni, P, Pb, Pt, Sb, Sn, Sr, Ta, Ti, V, W, Zn, Zr, and Y.

[2] Major component.

Apparatus and Procedure

Internal arrangement of the cell components is shown in figure 1. The solid electrolyte was an impervious zirconia tube, closed at one end and stabilized with 7 1/2 wt-pct calcia. This tube was approximately 9.5 mm outside diameter (OD) and 609.6 mm long. The cell was contained in two high-density, recrystallized alumina crucibles, 18 mm OD by 26 mm high and 31 mm OD by 42 mm high. Approximately 2 to 3 g of a 1:1 mixture of Cu and Cu_2O was placed in the inner crucible, and 1 to 2 g of a 1:1 mixture of ZnS and ZnO was placed inside the closed-end zirconia tube. Electrical contact between the electrodes and the internal circuit was made with two 24-gage platinum wires, which were sheathed with alumina insulation tubes. The cell assembly was enclosed in a closed-end alumina tube 47.6 mm OD by 508 mm long. An air-cooled aluminum head with Teflon fittings to seal the electrode leads, electrolyte tube, pedestal rod, and a thermocouple protection tube (not shown in figure 1) was attached to the top of the tube. The ZnS and ZnO electrode (inside the zirconia tube) was covered with approximately 200 mm of fused granulated alumina. The assembled cell was heated in a vertically mounted resistance furnace which was 51 mm inside diameter (ID) by 305 mm long. Power was supplied by a silicon-controlled-rectifier power supply. A temperature gradient of ±3.8 K existed over a 12.5-mm zone. Temperatures were maintained to ±0.5 K by an Electromax current-limiting controller. Electrode samples were placed in the uniform temperature zone. Sample temperatures were measured with a platinum versus platinum-10 pct rhodium thermocouple that was protected by a 7-mm-OD quartz tube and was positioned in the vicinity of the cell. The thermocouple was standardized against the melting points of ice and gold using the International Practical Temperature Scale of 1968.

Assembled cells were purged with purified argon for approximately 2 hours to remove all air from the cell chambers. Argon flow was shut off to the inner chamber and replaced with pure anhydrous SO_2, which was permitted to

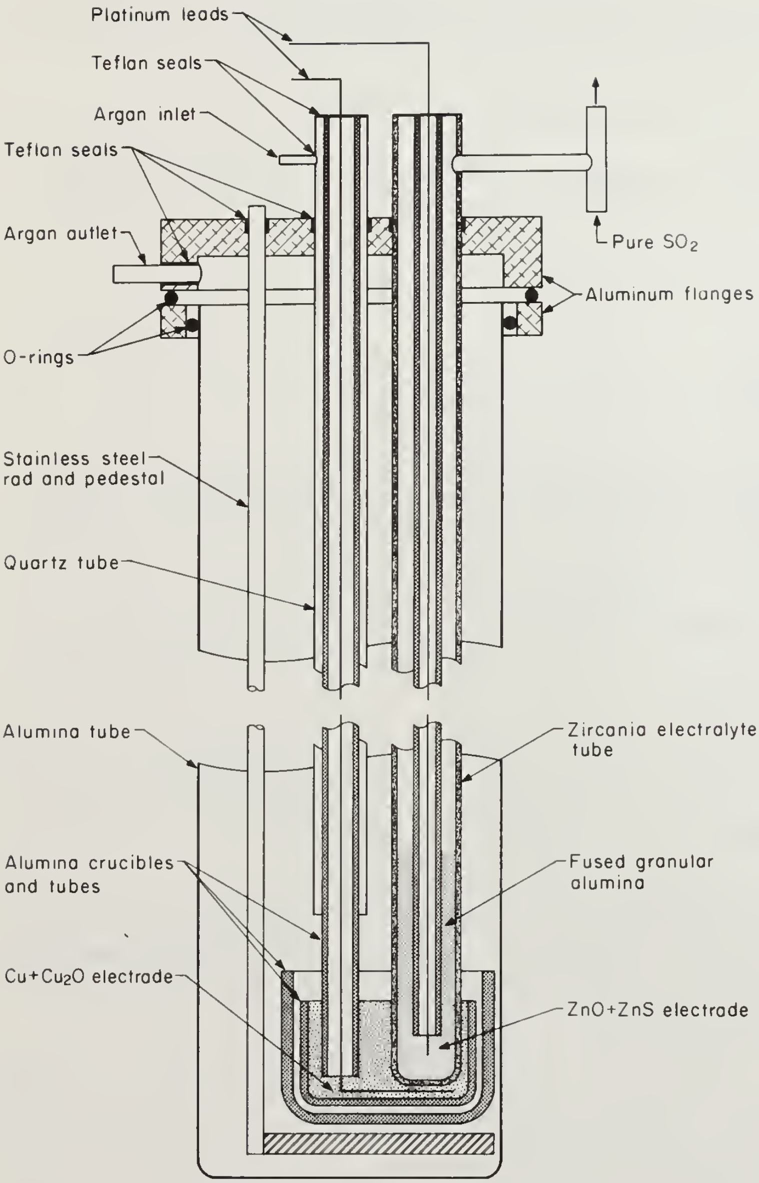
Platinum leads
Teflon seals
Argon inlet
Teflon seals
Argon outlet
O-rings
Stainless steel rod and pedestal
Quartz tube
Pure SO2
Aluminum flanges
Alumina tube
Alumina crucibles and tubes
Cu+Cu2O electrode
Zirconia electrolyte tube
Fused granular alumina
ZnO+ZnS electrode

FIGURE 1. - High-temperature galvanic cell.

flow through the chamber at approximately 7 ml/min and 1 atm of pressure for approximately 2 hours prior to heating the cell. A slight positive pressure of approximately 20 mm Hg maintained argon flow through the system at approximately 15 ml/min. Flow rates of argon and SO_2 were maintained in the two cell chambers throughout the experiment to provide the necessary stabilizing atmosphere for the two electrodes. After leaving the cell, all SO_2 was absorbed on sodium hydroxide pellets in a packed column. The cells were heated to approximately 1,040 K and permitted to stabilize for 12 hours. Electromotive force measurements were made with a Keithley model 630 high-input-impedance potentiometric electrometer, thereby reducing current flow to an absolute minimum and avoiding polarization of the source of the electromotive force. The cell was shielded from electric field effects in the high-impedance circuit by placing a grounded nickel sheet around the cell between two alumina crucibles. Measurements were completed during the first day following a 12-hour stabilization period. Reversibility of the cell reaction was checked by approaching equilibrium from above and below a specified temperature. Cell response to temperature change was rapid above 1,000 K and potentials stabilized within 1/2 hour after steady-state temperature was attained. Variation of flow rates from 5 to 23 ml/min of SO_2 and from 10 to 100 ml/min for argon did not affect the potential measurements. Potential measurements obtained from cells that were purged with argon prior to introducing anhydrous SO_2 into the inner chamber were in excellent agreement with those obtained from cells which were evacuated before backfilling with pure SO_2. Approximately 1 atm of SO_2 was maintained over the electrode containing ZnS and ZnO without sweeping the equilibrium gases away from the electrode. Experiments were repeated five or six times with each cell before the electrodes were removed and analyzed for phase identification.

RESULTS AND DISCUSSION

A preliminary experiment was conducted to calibrate and test the apparatus by measuring the open-circuit potential for the cell

$$\text{Pt, Cu + Cu}_2\text{O // ZrO}_2 \text{ // O}_2 = 0.21 \text{ atm, Pt,}$$

with the overall cell reaction

$$2\text{Cu(c)} + 1/2\text{O}_2 \text{ (g, 0.21 atm)} = \text{Cu}_2\text{O(c)}. \qquad (8)$$

An impervious closed-end zirconia tube stabilized with 7 1/2 wt-pct calcia served as the solid electrolyte and air was the reference electrode. Potential measurements from this cell may be expressed by the linear equation and a standard error of estimate as

$$E = 859.1896 - 0.39685\ T \pm 0.76 \qquad (9)$$

$$(1{,}038.7 - 1{,}169.9\ \text{K}),$$

where E is expressed in millivolts and the standard error of estimate, $S_{y \cdot x}$ is

$$S_{y \cdot x} = {}^1/_n \left[n\Sigma y^2 - (\Sigma y)^2 - \frac{(n\Sigma xy - \Sigma x \Sigma y)^2}{n\Sigma x^2 - (\Sigma x)^2} \right]^{1/2}.$$

The cell potentials and their corresponding smooth values, derived from equation 8 are given in columns 3 and 4 of table 2. A Gibbs energy of formation of cuprous oxide from the elements was deduced from the cell potential measurements and the following relationship

$$\Delta G(\text{reaction}) = -nFE = \Delta GF°(\text{Cu}_2\text{O}) - 1/2\ RT \ln pO_2\ (0.21\ \text{atm}). \qquad (10)$$

This equation gives

$$\Delta Gf°(\text{Cu}_2\text{O}) = -39.628 + 16.75 \times 10^{-3}T \pm 0.035\ \text{kcal/mole} \qquad (11)$$

$$(1{,}038.7 - 1{,}169.9\ \text{K}).$$

In the temperature range 900 to 1,210 K, the Gibbs energy of formation of cuprous oxide derived from a critical analysis of all published data (11) may be expressed as

$$\Delta Gf°(\text{Cu}_2\text{O}) = -40.062 + 17.15 \times 10^{-3}T \pm 0.200\ \text{kcal/mole}. \qquad (12)$$

In the temperature range 1,038.7 to 1,169.9 K, the standard Gibbs energy of formation of Cu_2O derived from equation 11 agrees within the assigned limit of error of ±0.200 kcal/mole, with the value obtained from equation 12.

TABLE 2. - Electromotive force of cell Pt, Cu + Cu_2O // ZrO_2 // O_2 = 0.21 atm (air), Pt

Experiment[1]	Temperature, K	E, mv	
		Measured[2]	Calculated[3]
6	1,038.7	445.82±0.009	446.98
8	1,039.9	447.47± .003	446.51
7	1,058.0	437.92± .021	439.32
9	1,062.0	438.50± .003	437.74
5	1,083.0	429.18± .017	429.40
10	1,084.0	429.50± .007	429.00
4	1,104.7	421.23± .017	420.79
3	1,124.8	413.41± .015	412.81
1	1,125.1	413.38± .010	412.69
11	1,127.7	411.50± .004	411.66
2	1,146.9	404.46± .015	404.04
13	1,149.0	402.63± .004	403.21
12	1,169.9	394.06± .006	394.92

[1] Chronological order of measurements.

[2] Average of two measurements taken at 20-minute intervals.

[3] Calculated from linear equation

$$E = 859.1896 - 0.39685\, T \pm 0.76.$$

The Gibbs energy of formation of ZnS (sphalerite) was investigated by measuring the Gibbs energy change for the reversible cell

$$\text{Pt, ZnS + ZnO, } SO_2 = 1 \text{ atm // } ZrO_2 \text{ // } Cu_2O + \text{Cu, Pt,}$$

with the overall cell reaction

$$ZnS(c) + 3Cu_2O(c) = ZnO(c) + 6Cu(c) + SO_2(g),$$

where zinc oxide, copper, zinc sulfide, and cuprous oxide are solids and sulfur dioxide is a gas at approximately 1 atm. Solubilities of oxygen in copper have been reported as 0.0018 and 0.0136 atomic pct at 1,073 and 1,250 K (18). Cuprous oxide is essentially of fixed composition (5). X-ray diffraction analyses of the electrode products are given in table 3. Parametric measurements showed no major change in the lattice parameter. The lattice parameter of a solid solution generally changes with composition up to the saturation limit and remains constant beyond that point. At 1,473 K, ZnS and ZnO form solid solutions (13) of the composition ZnS-1 mole pct ZnO and ZnO-0.3 mole pct ZnS. Consequently, the intersolubility is negligible and the assumption of unit activity for the reactants did not introduce appreciable error in the Gibbs energy of formation of sphalerite.

TABLE 3. - X-ray diffraction analyses of reagents and electrode mixtures

Sample designation	Phase identified	Crystal structure	Parametric measurements, A		Card No.[1]
			a_0	c_0	
ZnO........	ZnO(zincite).	Hexagonal....	3.250	5.207	5-664
ZnS........	Sphalerite...	Cubic........	5.4098	-	5-556
	Wurtzite[2]....	Hexagonal....	(3)	(3)	-
ZnO+.......	ZnO+.........	.....do......	3.250	5.207	5-664
ZnS........	Sphalerite...	Cubic........	5.4104	-	5-556
	Wurtzite[2]....	Hexagonal....	(3)	(3)	-
Cu+........	Cu...........	Cubic........	(3)	(3)	-
Cu_2O.......	Cu_2O.........	.....do......	(3)	(3)	-

[1] Powder diffraction file published by Joint Committee on Powder Diffraction Standards.

[2] Barely detectable trace.

[3] Not determined.

From the following relationships,

$$\Delta G(\text{cell reaction}) = -nFE = \Delta Gf°(ZnO) + \Delta Gf°(SO_2)$$

$$- \Delta Gf°(ZnS) - 3\ \Delta Gf°(Cu_2O) + RT\ \ln pSO_2, \qquad (13)$$

the standard Gibbs energy of formation of ZnS(c) was obtained.

Thirty-eight potential measurements were obtained from two cells that were designed to determine the Gibbs energy of formation of sphalerite. These results are summarized in table 4 and may be expressed as a function of temperature by the least-squares equation and standard error of estimate as follows:

$$E = -98.5039 + 0.23612T \pm 0.39 \qquad (14)$$

$$(948.7 - 1{,}209.4\ K),$$

where E is expressed in millivolts. The corresponding Gibbs energy change for the cell reaction is

$$\Delta G(\text{reaction}) = 13.630 - 32.67 \times 10^{-3}T \pm 0.054\ \text{kcal} \qquad (15)$$

$$(948.7 - 1{,}209.4\ K).$$

Smooth values of the cell potentials, derived from equation 14, are given in column 5 of table 4. Representative electromotive force versus temperature data are illustrated in figure 2.

TABLE 4. - Electromotive force of cell Pt, ZnS + ZnO, SO_2 = 1 atm // ZrO_2 // Cu_2O + Cu, Pt

Experiment		Temperature, K	E, mv	
Cell	COM[1]		Measured[2]	Calculated[3]
4	30	948.7	124.50±0.006	125.51
3	4	970.1	130.47± .001	130.56
3	8	971.7	130.35± .003	130.93
4	29	972.5	130.74± .003	131.12
3	3	993.6	136.62± .003	136.11
3	7	994.1	136.08± .002	136.22
4	28	995.6	136.40± .003	136.58
3	9	1,009.1	139.68± .002	139.76
4	31	1,009.1	140.04± .001	139.76
3	2	1,016.1	142.13± .002	141.42
3	6	1,017.1	141.57± .001	141.66
4	27	1,017.9	141.93± .001	141.85
3	1	1,038.8	147.57± .005	146.78
3	5	1,039.6	147.36± .002	146.97
4	26	1,040.2	147.24± .001	147.11
4	19	1,040.5	147.32± .005	147.18
4	32	1,040.6	147.25± .005	147.20
3	12	1,041.6	146.86± .003	147.44
4	33	1,062.9	152.65± .002	152.47
4	20	1,063.0	152.58± .001	152.49
3	13	1,064.0	152.43± .006	152.73
3	10	1,064.7	153.09± .006	152.89
4	21	1,084.7	158.08± .003	157.62
3	11	1,085.0	158.08± .005	157.69
4	34	1,085.0	158.19± .002	157.69
3	14	1,086.1	158.02± .003	157.95
4	22	1,106.4	162.97± .002	162.74
3	15	1,107.0	162.65± .003	162.88
4	23	1,127.8	167.84± .003	167.79
4	35	1,127.9	168.08± .002	167.82
3	16	1,128.8	167.92± .002	168.03
4	25	1,144.3	171.08± .002	171.69
3	18	1,161.7	174.96± .002	175.80
4	36	1,169.6	177.74± .002	177.67
4	24	1,170.4	177.56± .003	177.85
3	17	1,183.6	180.68± .002	180.97
4	38	1,189.0	182.28± .003	182.24
4	37	1,209.4	187.13± .002	187.06

[1] Chronological order of measurement.

[2] Average of two measurements taken at 20-minute intervals.

[3] Calculated from linear equation

$$E = -98.5039 + 0.23612\ T \pm 0.39.$$

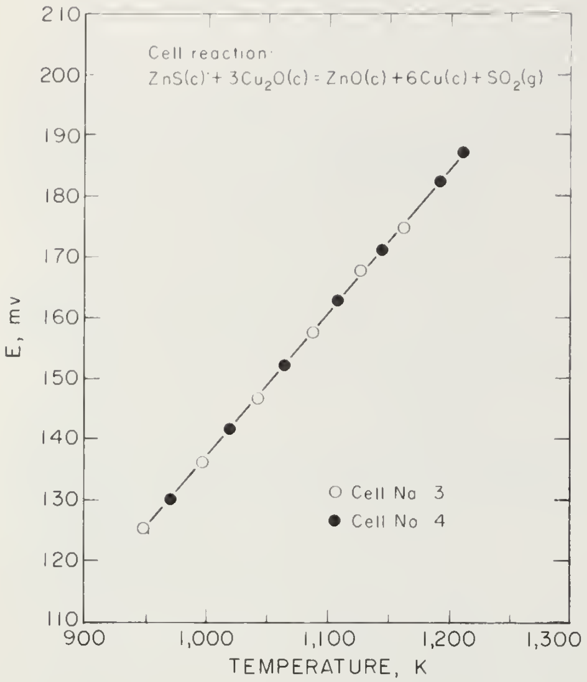

FIGURE 2. - Electromotive force versus temperature for cell reaction (1).

Gibbs energies of formation of ZnO (3) for the reactions

$$Zn(l) + 1/2\ O_2(g) = ZnO(c) \quad (16)$$

(900 - 1,180 K),

and

$$Zn(v) + 1/2\ O_2(g) = ZnO(c) \quad (17)$$

(1,180 - 1,210 K),

may be expressed by the following equations:

$$\Delta Gf^\circ(ZnO) = -84.274 + 25.36 \times 10^{-3}T \pm 0.200 \text{ kcal/mole} \quad (18)$$

(standard state - pure liquid zinc),

and

$$\Delta Gf^\circ(ZnO) = -112.760 + 49.50 \times 10^{-3}T \pm 0.200 \text{ kcal/mole} \quad (19)$$

(standard state - pure zinc vapor at 1 atm).

Gibbs energies of formation of Cu_2O (11) and SO_2 (3) for the temperature range 900 to 1,210 K may be expressed by equation 12 and the following least-squares equation

$$\Delta Gf^\circ(SO_2) = -86.506 + 17.44 \times 10^{-3}T \pm 0.150 \text{ kcal/mole.} \quad (20)$$

To calculate the Gibbs energy change for the cell reaction (equation 1), the partial pressure of SO_2 at the reaction site involves evaluation of the following equilibrium reaction and relationships:

$$SO_3(g) = SO_2(g) + 1/2\ O_2(g), \tag{21}$$

or

$$K(\text{equilibrium}) = \frac{pSO_2(pO_2)^{1/2}}{pSO_3} \tag{22}$$

and

$$P_{(total)} = pSO_3 + pSO_2 + pO_2, \tag{23}$$

where $P_{(total)} = P_{(atm)}$ and pSO_3, pSO_2, and pO_2 are the partial pressures of the gaseous components. At a given temperature, this univariant system (equation 1) becomes invariant if the total pressure is fixed. The oxygen pressure, pO_2, at the reaction site was determined from the potential measurements of the cell (reaction 1) and the relationship

$$\Delta G(\text{reaction 1}) = -nFE = RT\ \ln pO_2 - RT\ \ln pO_2'', \tag{24}$$

where pO_2'' is the oxygen pressure at the Cu-Cu_2O reference electrode, n=4, F is the Faraday constant, and E is the electromotive force in volts. Rearranging equation 24 and inserting values of pO_2'' derived from equations 9-10, 12 and of E from equation 14 yields the expression

$$\log pO_2(atm) = -15{,}525/T + 2.7361. \tag{25}$$

The pressure of SO_2, pSO_2, over the ZnS-ZnO electrode was calculated by combining equations 22 and 23 to yield the equation

$$pSO_2 = \frac{P_{(total)} - pO_2}{1 + (pO_2)^{1/2}/K(\text{equilibrium})}, \tag{26}$$

where K is the equilibrium constant (equation 22) as recommended by Kellogg (10), based on the study of Evans and Wagman (4). This constant is a function of temperature which may be expressed by the equation

$$\log K(\text{equilibrium}) = 8.8557 - 5{,}465.5/T - 1.21572 \log T. \tag{27}$$

Table 5 presents pressures of SO_2 as calculated from equation 26. These data, which are illustrated in figure 3, show the thermodynamic stability of a portion of the Zn-S-O system where ZnO and ZnS coexist in the temperature range 948 to 1,210 K at a constant pressure of SO_2 of approximately 1 atm. As noted in column 5, SO_2 is the predominant gaseous species at the reaction site. Consequently, in the temperature range of this investigation (948 to 1,210 K), the slight variation of SO_2 from standard-state conditions has no appreciable effect on the Gibbs energy of the cell reaction (equation 13).

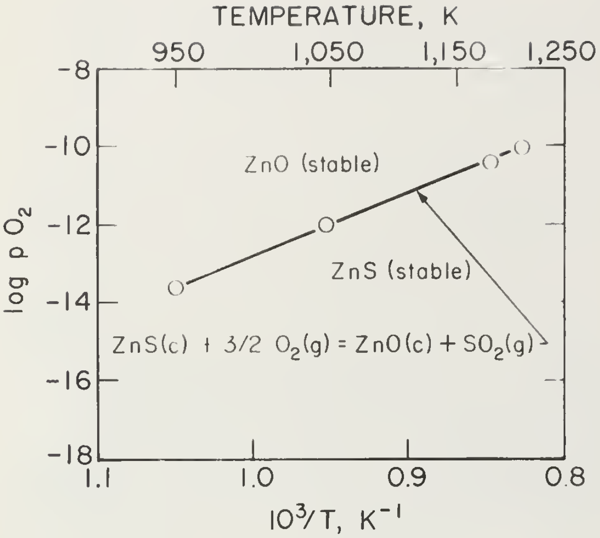

FIGURE 3. - Plot of log pO_2 versus temperature for Zn-S-O system.

TABLE 5. - Effect of temperature and pO_2 on pSO_2 for reaction $SO_3(g) = SO_2(g) + 1/2\ O_2(g)$

Temperature, K	K(equilibrium)[1]	Pressure, atm		SO_2, mole pct
		pO_2	pSO_2[2]	
950	0.3037134	2.478×10^{-14}	1.0009205	99.99995
1,050	.9496020	8.922×10^{-13}	1.0009201	99.99991
1,180	3.0858296	3.797×10^{-11}	1.0009191	99.99981
1,210	3.8990075	8.046×10^{-11}	1.0009187	99.99977

[1] $$K(\text{equilibrium}) = \frac{pSO_2\ (pO_2)^{1/2}}{pSO_3}$$

[2] $$pSO_2 = \frac{P_{(\text{total})} - pO_2}{1 + (pO_2)^{1/2}/K(\text{equilibrium})}\ ;\ P_{(\text{total})} = 1.000921 \text{ atm (av)}.$$

The standard Gibbs energy of formation of ZnS (sphalerite) for the reaction

$$Zn(l,v) + 1/2\ S_2(g) = ZnS(c).$$

was derived by rearranging equation 13 and substituting the Gibbs energy change for reaction 1 (equation 15) and the quantity, RT ln pSO_2, obtained from this investigation together with the standard Gibbs energies of formation for Cu_2O (11), ZnO (3), and SO_2 (3) from the literature as given by equations 12, 18, 19, and 20. Combining these data yields a standard Gibbs energy of formation of sphalerite for reaction 2 which may be expressed as

$$\Delta Gf°(ZnS) = -64.223 + 24.02 \times 10^{-3}T \pm 0.650 \text{ kcal/mole}$$

(948 - 1,180 K; standard states - pure liquid zinc and S_2 gas at 1 atm),

and $$\Delta Gf°(ZnS) = -92.720 + 48.17 \times 10^{-3}T \pm 0.650 \text{ kcal/mole}$$

(1,180 - 1,210 K; standard states - pure zinc vapor and S_2 gas at 1 atm).

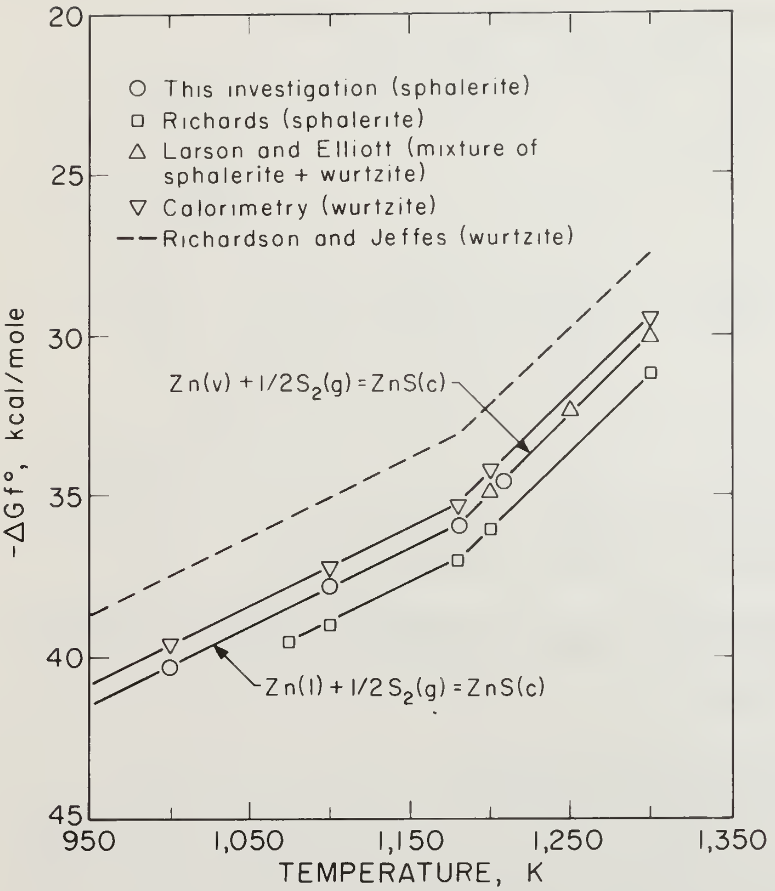

FIGURE 4. - Standard Gibbs energy of formation of sphalerite and wurtzite.

Gibbs energies of formation of ZnS (sphalerite) obtained from this investigation and results of previous investigations including some for wurtzite and mixtures of sphalerite and wurtzite are given in table 6 and representative data are illustrated in figure 4. Results of this investigation are approximately 1 kcal less negative than the only previously published experimental results for sphalerite (19) and are in close agreement with results reported for samples containing a mixture of sphalerite and wurtzite (14). Results reported for wurtzite (1, 17, 19-20, 22) are approximately 0.6 kcal more positive than those obtained for sphalerite in the present investigation. An estimate (20) for the Gibbs energy of formation of wurtzite (dashed line on figure 4) appears to be in error.

A third-law analysis, employing the present Gibbs energy of formation of sphalerite, entropy and enthalpy data for zinc (6), diatomic sulfur gas at 1 atm (8-9), and sphalerite (17, 22) yields for the formation reaction

$$Zn(l) + 1/2\ S_2(g) = ZnS(c),$$

a standard enthalpy of formation as follows:

$$\Delta Hf^\circ_{298.15} = -63.64 \pm 0.70 \text{ kcal/mole}.$$

This value is approximately 1 kcal more positive than the only previously reported value (-64.6 ± 1 kcal/mole) for sphalerite (19) and compares with -62.94 ± 0.20 kcal/mole that was reported for wurtzite (1). Comparison of the standard enthalpy of formation, $\Delta Hf^\circ_{298.15}$, of sphalerite, which was derived by a third-law analysis of the present data with that determined calorimetrically for wurtzite refutes the reported heat of transformation of 3.19 kcal/mole (7) of sphalerite to wurtzite. High-temperature enthalpy measurements (17) did not detect any heat effect when a sample of sphalerite was heated above the reported transformation temperature (7).

TABLE 6. - Coefficients in linear Gibbs equation $\Delta Gf^\circ = \Delta Hf^\circ - T\Delta Sf^\circ$(cal)

Reaction[1]	Temperature range, K	[2] ΔHf°	[2] $-\Delta Sf^\circ$	References
$Zn(l) + 1/2\ S_2(g) = ZnS(\beta)$.	948 to 1,180	-64,223	24.02	This investigation.
Do.	1,073 to 1,180	-65,667	24.34	19
$Zn(l) + 1/2\ S_2(g) = ZnS(\alpha)$.	692.7 to 1,180	-63,869	24.25	1, 17, 22
Do.	692.7 to 1,180	(-61,740)	(24.27)	20
$Zn(l) + 1/2\ S_2(g) = ZnS(\alpha$ and $\beta)$.	999 to 1,180	-65,690	25.36	14
$Zn(v) + 1/2\ S_2(g) = ZnS(\beta)$.	1,180 to 1,210	-92,720	48.17	This investigation.
Do.	1,180 to 1,302	-93,510	47.94	19
$Zn(v) + 1/2\ S_2(g) = ZnS(\alpha)$.	1,180 to 1,300	-91,354	47.54	1, 17, 22
Do.	1,180 to 1,500	(-89,165)	(47.50)	20
$Zn(v) + 1/2\ S_2(g) = ZnS(\alpha$ and $\beta)$.	1,180 to 1,379	-91,350	47.16	14

[1] $ZnS(\alpha)$ refers to wurtzite (hexagonal structure) and $ZnS(\beta)$ refers to sphalerits (cubic structure).

[2] Values in parentheses are estimates.

SUMMARY AND CONCLUSIONS

The standard Gibbs energy, enthalpy, and entropy of formation sphalerite (ZnS) were determined at elevated temperatures by a high-temperature galvanic cell employing stabilized zirconia as the electrolyte. Pertinent data required to calculate the Gibbs energy of formation of ZnS as a function of temperature are given in table 6 and illustrated in figure 4. A third-law analysis of the present data yields a standard enthalpy of formation, $\Delta Hf^\circ_{298.15}$ of -63.65 ± 0.70 kcal/mole of sphalerite. Results obtained from this investigation, combined with those obtained by references 1 and 17, refute the heat of transformation of sphalerite to wurtzite reported by reference 7. Equilibrium oxygen pressures were measured for that portion of the Zn-S-O system where ZnO coexists with ZnS in a SO_2 atm of approximately 1 atm, and in the temperature range of 948 to 1,210 K.

REFERENCES

1. Adami, L. H., and E. G. King. Heats and Free Energies of Formation of Sulfides of Manganese, Iron, Zinc, and Cadmium. BuMines RI 6495, 1964, 10 pp.

2. Cammarota, V. A., Jr., H. Babitzke, and J. M. Hague. Zinc. Ch. in Mineral Facts and Problems. BuMines Bull. 667, 1975, pp. 1223-1241.

3. Coughlin, J. P. Contributions to the Data of Theoretical Metallurgy. XII. Heats and Free Energies of Formation of Inorganic Oxides. BuMines Bull. 542, 1954, 80 pp.

4. Evans, W., and D. Wagman. J. Res. Nat. Bur. Std., v. 49, 1952, pp. 141-148.

5. Hansen, M., and K. Anderko. Constitution of Binary Alloys. McGraw-Hill Book Co., Inc., New York, 1958, pp. 604-606.

6. Hultgren, R., P. D. Desai, D. T. Hawkins, M. Gleiser, K. K. Kelley, and D. D. Wagman. Selected Values of the Thermodynamic Properties of the Elements. Am. Soc. Metals, Metals Park, Ohio, 1973, pp. 565-574.

7. Kapustinskii, A. F., and L. G. Chemtzova. Heats of Transformation in the System of Wurtzite-Sphalerite and Cinnabar-Metacinnabarite. Compt. Rend. Dokl. Acad. Sci., URSS, v. 30, 1941, pp. 489-490.

8. Kelley, K. K. Contributions to the Data on Theoretical Metallurgy. XIII. High-Temperature Heat-Content, Heat-Capacity, and Entropy Data for the Elements and Inorganic Compounds. BuMines Bull. 584, 1960, 232 pp.

9. Kelley, K. K., and E. G. King. Contributions to the Data on Theoretical Metallurgy. XIV. Entropies of the Elements and Inorganic Compounds. BuMines Bull. 592, 1961, 149 pp.

10. Kellogg, H. H. A Critical Review of Sulfation Equilibria. Trans. AIME, v. 230, 1964, p. 1623.

11. King, E. G., A. D. Mah, and L. B. Pankratz. INCRA Series on the Metallurgy of Copper. Monograph II. Thermodynamic Properties of Copper and Its Inorganic Compounds. The International Copper Research Association, Inc., New York, 1973, 257 pp.

12. Kiukkola, K., and C. Wagner. Measurements on Galvanic Cells Involving Solid Electrolytes. J. Electrochem. Soc., v. 104, No. 6, 1957, pp. 379-387.

13. Kroeger, F. A., and J. A. M. Dikhoff. The Function of Oxygen in Zinc Sulfide Phosphors. J. Electrochem. Soc., v. 99, No. 4, 1952, pp. 144-154.

14. Larson, H. R., and J. F. Elliott. The Standard Free Energies of Formation of Certain Sulfides of Some Transition Elements and Zinc. Trans. AIME, v. 239, 1967, pp. 1713-1720.

15. McCabe, C. L. Equilibrium Pressure Measurements Above ZnS From 610 to 825° C. J. Metals, v. 6, 1954, pp. 969-971. Trans. AIME, v. 200, 1954, pp. 969-971.

16. Munir, Z. A., and M. J. Mitchel. Studies on Sublimation of II B - VI A Compounds. I. The Sublimation Coefficient and Activation Energy for Sublimation of Single Crystalline Zinc Sulfide. High Temp. Sci., v. 1, 1969, pp. 381-387.

17. Pankratz, L. B., and E. G. King. High-Temperature Heat Contents and Entropies of Two Zinc Sulfides and Four Solid Solutions of Zinc and Iron Sulfides. BuMines RI 6708, 1965, 8 pp.

18. Pastorek, R. L., and R. A. Rapp. The Solubility and Diffusivity of Oxygen in Solid Copper From Electrochemical Measurements. Trans. AIME, v. 245, 1969, pp. 1711-1720.

19. Richards, A. W. The Heats of Formation and Dissociation of Zinc Sulphide. J. Appl. Chem., v. 9, 1959, pp. 142-145.

20. Richardson, F. D., and J. H. E. Jeffes. The Thermodyanics of Substances of Interest in Iron and Steel Making. III.--Sulphides. J. Iron Steel Inst., 1952, pp. 165-175.

21. Steel, B. C. H., and C. B. Alcock. Factors Influencing the Performance of Solid Oxide Electrolytes in High Temperature Thermodynamic Measurements. Trans. AIME, v. 233, 1965, pp. 1359-1367.

22. Stuve, J. M. Low-Temperature Heat Capacities of Sphalerite and Wurtzite. BuMines RI 7940, 1974, 8 pp.

☆U.S. GOVERNMENT PRINTING OFFICE: 1978-703-103/54

INT.-BU.OF MINES,PGH.,PA. 23198

622.09
Un32mo

RI 8302

Bureau of Mines Report of Investigations/1978

Electromagnetic Technique for Locating Boreholes

DEPOSITORY
NOV 17 1978
UNIV. OF ILL. LIBRARY
AT URBANA-CHAMPAIGN

UNITED STATES DEPARTMENT OF THE INTERIOR

Report of Investigations 8302

Electromagnetic Technique for Locating Boreholes

By H. Kenneth Sacks

March 3, 1849

UNITED STATES DEPARTMENT OF THE INTERIOR
Cecil D. Andrus, Secretary

BUREAU OF MINES

This publication has been cataloged as follows:

Sacks, H Kenneth

Electromagnetic technique for locating boreholes / by H. Kenneth Sacks. [Washington] : U.S. Dept. of the Interior, Bureau of Mines, 1978.

14 p. : ill., diagrs. ; 27 cm. (Report of investigations - Bureau of Mines ; 8302)

1. Mine rescue work - Equipment and supplies. 2. Boring. 3. Electromagnetic measurements. I. United States. Bureau of Mines. II. Title. III. Series: United States. Bureau of Mines. Report of investigations ; 8302.

TN23.U7 no. 8302 622.06173

U.S. Dept. of the Int. Library

CONTENTS

Page

Abstract.... 1
Introduction.... 1
Acknowledgments.... 2
Trapped miner location equipment.... 2
    Transmitter.... 5
    Null detection technique.... 5
    Field test.... 6
Conclusions.... 7
Appendix A.--Transmitter coil design.... 8
Appendix B.--Coil tilt errors.... 10

ILLUSTRATIONS

1. Trapped miner transmitter.... 3
2. Trapped miner receiver.... 3
3. Borehole transmitter.... 4
4. Transmitter disassembled.... 4
5. Plan view of transmitter in borehole and tunnel.... 5
6. Receiver coil mounted on transit.... 6
7. Results of field test at Ft. Ritchie, Md.... 7
B-1. Coordinate system with the transmitter at the origin.... 11
B-2. Plane view of the coil in the null direction.... 11
B-3. Effect of coil tilt on location accuracy.... 13
B-4. Effect of moving transmitter above and below tunnel center line on location accuracy.... 14

TABLE

1. Minimizing error by measuring above and below tunnel.... 13

ELECTROMAGNETIC TECHNIQUE FOR LOCATING BOREHOLES

by

H. Kenneth Sacks[1]

ABSTRACT

The Bureau of Mines has developed hardware for electromagnetic (EM) detection and location of miners trapped in underground coal mines. This report describes a technique for using the developed equipment for locating uncased boreholes underground. Results of several field and laboratory experiments are described.

INTRODUCTION

In many industrial situations, mining being a prime example, small-diameter holes are drilled from the surface to intersect an underground tunnel or room. The correct starting point on the surface is usually determined by standard surveying techniques. However, because of the tendency of small-diameter drill holes to drift, the true location of the bottom of a deep hole may be many feet from the expected coordinates. Often the true location will be determined by drilling small, horizontal pilot holes from within the underground opening in an effort to intersect the borehole. Depending on the diameter of the original borehole, the nature of the rock, and the luck of the driller, success may require considerable time and expense.

In previous work[2] a system was described for locating boreholes electromagnetically which depends upon a known receiver sensitivity and field strength. In practical situations, the field strength is a function of the electrical properties of the surrounding rock, which is generally unknown.

The technique to be described in this Bureau of Mines report eliminates this problem and it has proved to be accurate.

---

[1] Supervisory electrical engineer, Pittsburgh Mining and Safety Research Center, Bureau of Mines, Pittsburgh, Pa.

[2] Tervo, R. L., and L. Tirrul. Lost a Borehole Recently. Can. Min. J., 1973, pp. 56-58.

ACKNOWLEDGMENTS

Acknowledgment is expressed to Harry Dobroski, Jr., and Carl W. Ganoe of the Pittsburgh Mining and Safety Research Center, Pittsburgh, Pa., for their assistance in building and carrying out the field tests.

TRAPPED MINER LOCATION EQUIPMENT

Under the Bureau's post disaster rescue and survival program, hardware was developed for detecting and locating miners trapped in underground coal mines. Experiments by the Bureau have shown the equipment to be effective in overburden depths up to 1,000 feet.

The hardware is shown in figures 1-2. Reports describing the equipment and techniques are available.[3] For purposes of this report, a brief functional description will be given. Figure 1 is the trapped miner transmitter. It is powered by the miner's cap lamp battery and when connected to a 90-ft-long, horizontal wire loop, it generates a 0.1-sec-duration tone burst of low frequency (630 to 3,030 Hz) current of about 5 amp root mean square (RMS) with a repetition rate of once per second. The tone-burst frequency is crystal controlled and fixed. Experimentation and theory has shown that signals lying

---

[3] Collins Radio Group, Rockwell International. Waveform Generator for (EM) Location of Trapped Miners (Research Contract H0133045). BuMines Open File Rept. 9-75, 1974, 25 pp.; available from National Technical Information Service, Springfield, Va., PB 240 481/AS.

Farstad, A. J. Electromagnetic Location Experiments in a Deep Hardrock Mine (Research Contract H0242006). BuMines Open File Rept. 28-74, 1973, 54 pp.; available from National Technical Information Service, Springfield, Va., PB 232 808/AS.

Farstad, A. J., C. Fisher, R. F. Linfield, R. O. Maes, and B. Lindstrom. Trapped Miner Location and Communication System Development Program. Volume 1. Development and Testing of an Electromagnetic Location System (Research Contract H0220073). BuMines Open File Rept. 41(1)-74, 1973, 181 pp.; available from National Technical Information Service, Springfield, Va., PB 235 605/AS.

The preceding open file reports are available for consultation at the Bureau of Mines facilities in Denver, Colo., Twin Cities, Minn., Pittsburgh, Pa., and Spokane, Wash.; at the Department of Energy facility in Morgantown, W. Va.; and at the National Library of Natural Resources, U.S. Department of the Interior, Washington, D.C.

Powell, J. A. An Electromagnetic System for Detecting and Locating Trapped Miners. BuMines RI 8159, 1976, 15 pp.

Westinghouse Electric Corporation. Coal Mine Rescue and Survival. Volume 2. Communications/Location Subsystem. BuMines Open File Rept. 9(2)-72, 1972, 258 pp.; available for consultation at the Bureau of Mines facilities in Denver, Colo., Twin Cities, Minn., Pittsburgh, Pa., and Spokane, Wash.; at the Office of the Assistant Director--Mining, Columbia Plaza, Washington, D.C.; at the National Library of Natural Resources, U.S. Department of the Interior, Washington, D.C.; and from the National Technical Information Service, Springfield, Va., PB 208 267.

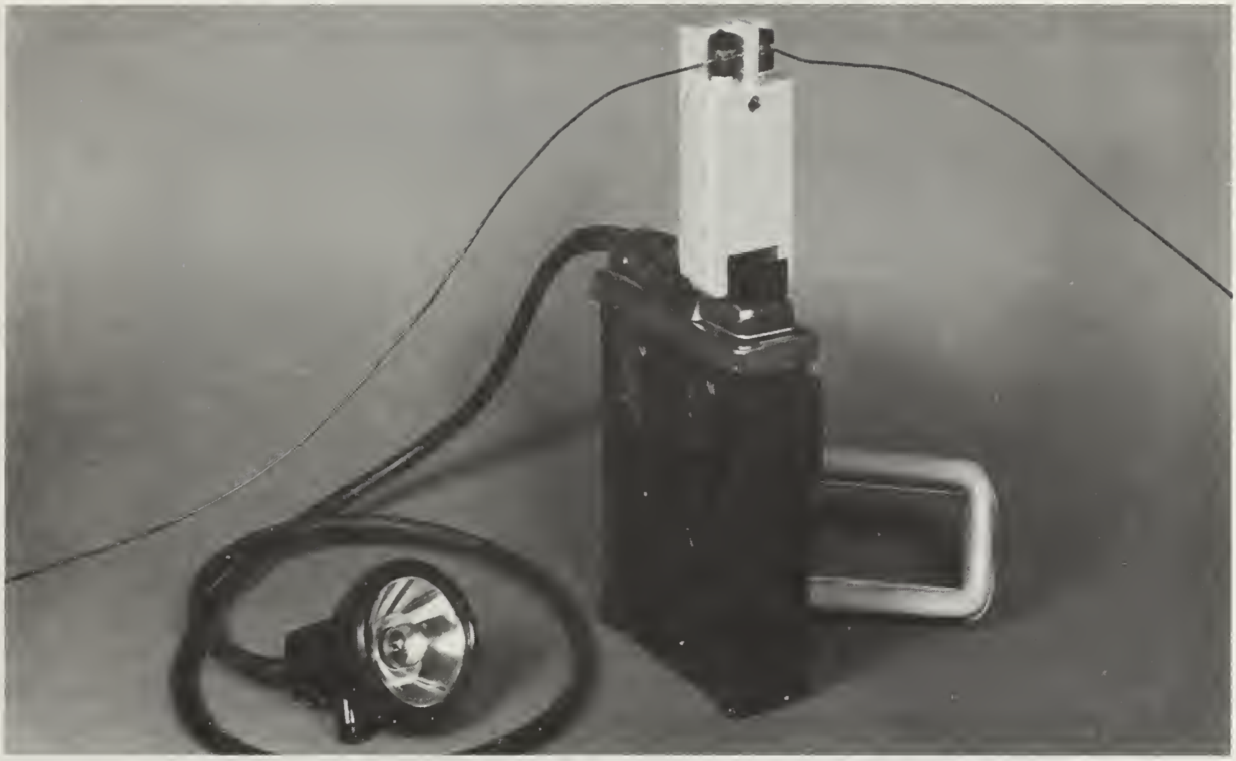

FIGURE 1. - Trapped miner transmitter.

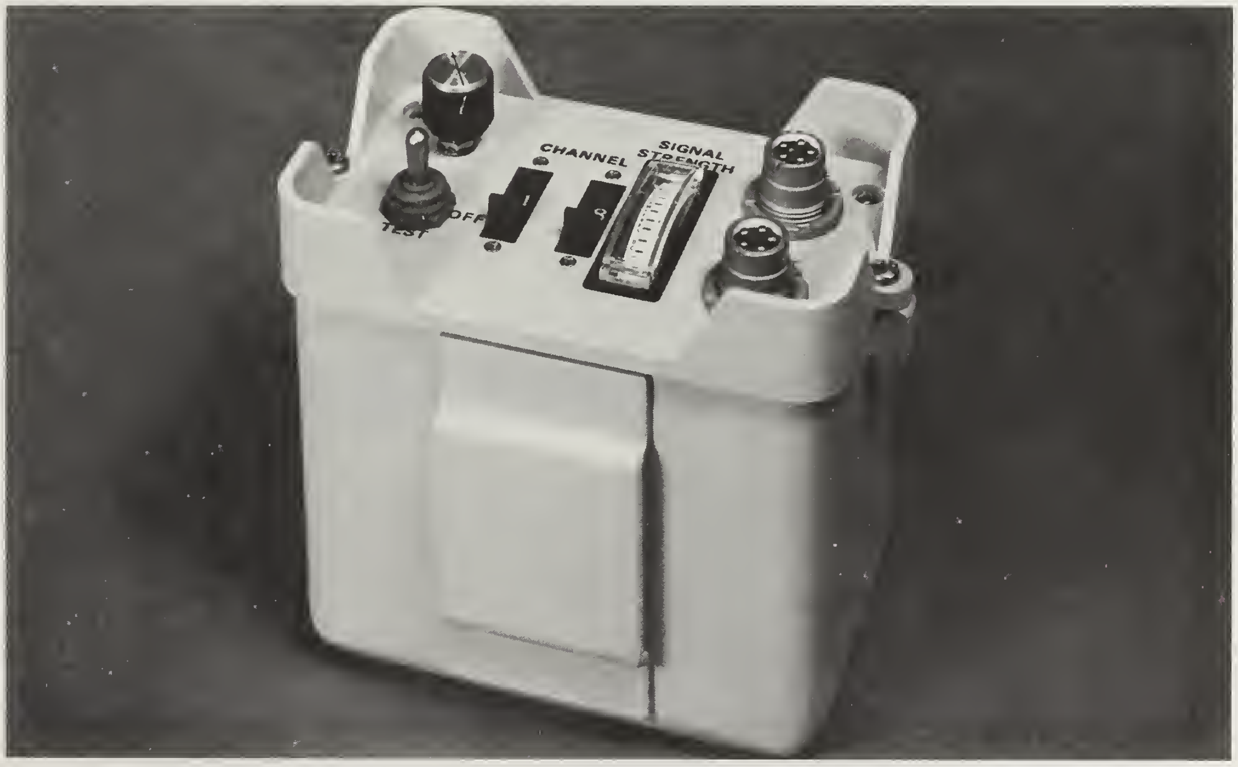
CHANNEL
SIGNAL STRENGTH
TEST
OFF
1
2

FIGURE 2. - Trapped miner receiver.

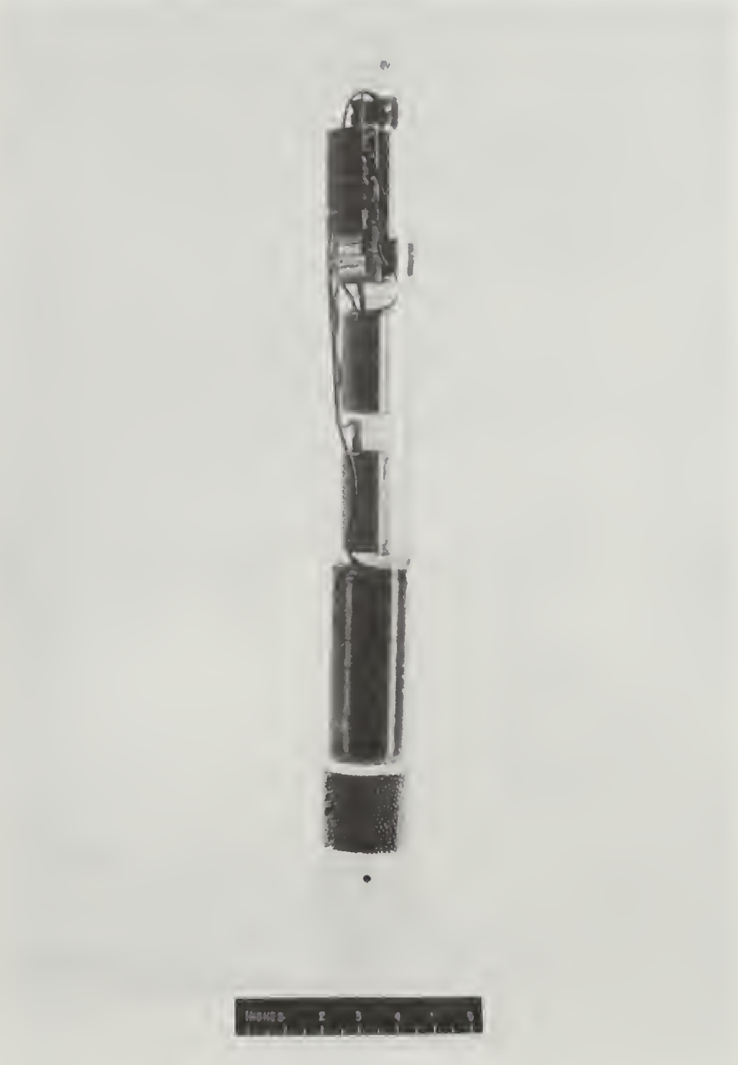
INCHES
2
3
4
5
6

FIGURE 3. - Borehole transmitter.

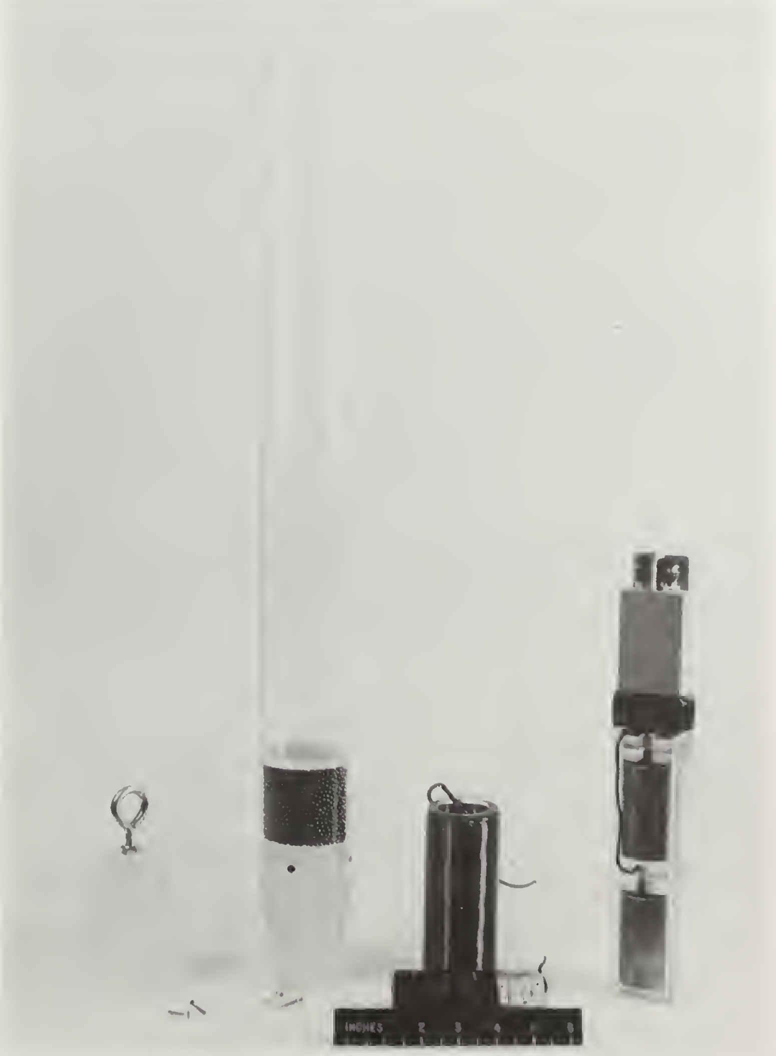
INCHES
2
3
4
5
6

FIGURE 4. - Transmitter disassembled showing from left to right, top seal, plastic case, coil and tuning capacitors, transmitter module, and batteries.

in the low audio range (<2,000 Hz) propagate best through the earth. By spacing the tone-burst frequencies midway between the harmonics of 60 Hz (that is, 810, 870, 930, 990, 1,050, etc.) interference from powerlines is greatly reduced.

The current in the wire loop produces a magnetic field that can be detected at the surface with the receiver shown in figure 2. The receiver can tune to any one of the predetermined frequencies produced by the transmitters. Its channel bandwidth is 25 Hz and it has a sensitivity of better than 0.1 microamp/m at 1,000 Hz. The narrow bandwidth and high sensitivity allows weak signals to be detected in the presence of background noise. These two units form the basic components of the borehole location technique.

Transmitter

An uncased borehole, for the purpose of this report, is any hole without a metallic casing in the vicinity of the underground opening. Holes cased in concrete or holes with metal linings that do not extend down to the underground opening are considered uncased.

For the borehole location system, the transmitter of figure 1 was packaged in a 2-3/4-in-diam plastic container as shown in figures 3-4. A nonconducting material must be used for the container to prevent electromagnetic shielding which greatly reduces the received field. The coil is tuned to the tone-burst frequency. Appendix A gives the details for the coil design. To conserve battery power, the battery is connected to the transmitter and the package is sealed just before the unit is lowered into the borehole. The 10-pct duty cycle of the transmitter (0.1 sec on, 1 sec off) allows a battery life in excess of 20 hr.

Null Detection Technique

Figure 5 is a plan view of the transmitter lowered down the hole. The magnetic field lines from the transmitter coil are radial. When the plane of

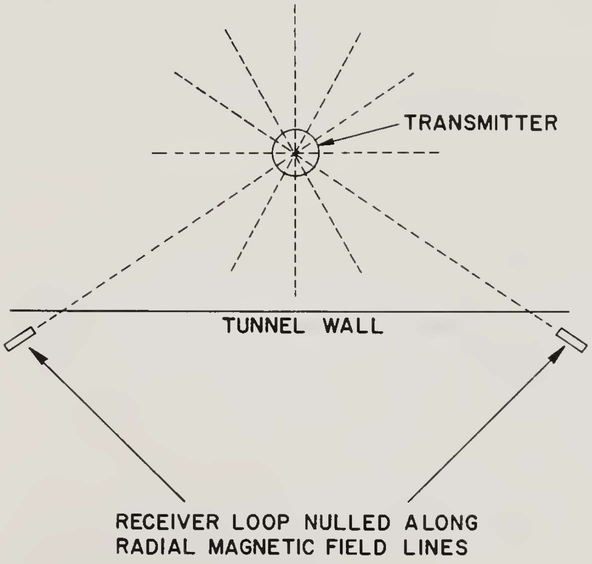

FIGURE 5. - Plan view of transmitter in borehole and tunnel.

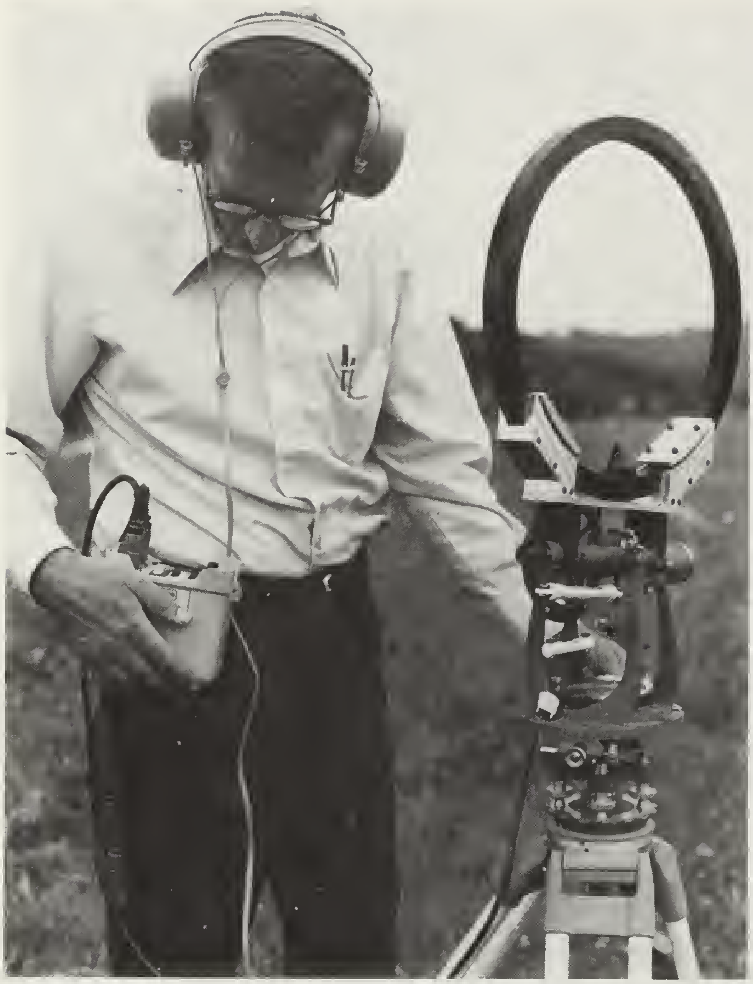

FIGURE 6. - Receiver coil mounted on transit.

the receiver coil is vertical and alined with the radial field lines, the received signal is a minimum or "nulled." This signal null is generally very sharp; that is, a slight change in the receiver coil azimuth gives a large signal increase. If the receiver coil is moved to another spot along the tunnel and nulled again, the position of the borehole can be found by triangulation. To aid in this scheme, the receiver coil is mounted on a surveyor's transit (fig. 6) which allows precise measurement of the coil angle with respect to a reference line for use in determining the hole location.

It is important for the transmitter coil not to be at the tunnel level, because the magnetic field will then have only a vertical component at the receiver and the received signal will be at a minimum for all azimuthal orientations. If the distance into the rock to the transmitter were known, then an optimum height above or below the tunnel would be equal to this distance (see appendix B).

Field Test

In the fall of 1975, the U.S. Army Corps of Engineers requested the Bureau's aid in locating a 10-in-diam fresh water well in the vicinity of an underground tunnel at Ft. Ritchie, Md. The Bureau used the equipment and techniques just described to accomplish the task. Figure 7 shows the layout of the tunnel and field results. A 50-ft baseline was laid out along the tunnel and null measurements were taken at six positions. Multiple readings were taken to increase the confidence of the results. The shaded area represents the most likely area of the hole.

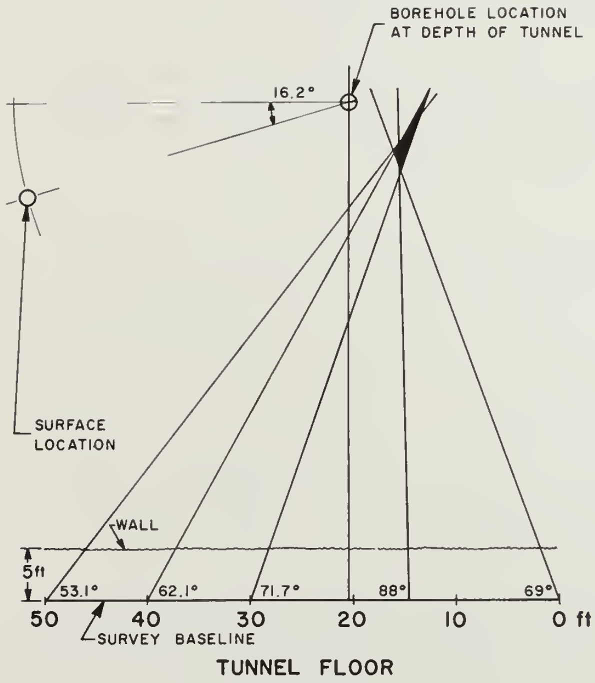

FIGURE 7. - Results of field test at Ft. Ritchie, Md.

The Corps of Engineers proceeded to drill a series of 2-in pilot holes on 8-in centers starting at the suggested location, and on the 11th hole, water was struck at the location shown. The location error of approximately 4.5 ft could have been caused by several factors including metal structures in the tunnel, a large diesel-electric generator 100 ft away, or tilt of the coil in the hole. The effect of core-tilt can be quite significant (see appendix B for analysis), but it can be minimized by using a small-diameter transmitter to insure that it hangs vertically and by taking two sets of readings--one with the transmitter above the tunnel and the other with the transmitter an equal distance below the tunnel. The area enclosed by the triangulation plot will include the borehole.

The effects of conducting bodies are generally impossible to predict, but they are not a problem unless they lie very close to the transmitter or receiver.

CONCLUSIONS

A technique has been described for locating boreholes in underground tunnels using equipment developed under the Bureau's trapped miner program. Theoretical calculations and field measurements have demonstrated that accuracies of the order of 1° are possible in the field.

The Bureau is presently working on an advanced technique using frequencies below 20 Hz in conjunction with a magnetometer. Preliminary results indicate the system will find cased holes at distances in excess of 100 ft. A complete description will be available when the contract is completed, possibly by late 1978.

APPENDIX A.--TRANSMITTER COIL DESIGN

The object of the transmitter coil design is to maximize the coil magnetic moment $M = INA$ for a given package size, weight, and available transmitter power. For convenience, the following terms are defined:

I = Coil current, RMS.

N = Coil turns.

A = Coil area, square meters.

D = Coil diameter, meters.

R_w = Wire resistance, ohms per meter.

α = Wire density, kilograms per cubic meters.

R_o = Transmitter internal resistance.

V_o = Transmitter open circuit voltage, root mean square.

R_c = Total coil resistance, ohms.

M = INA, ampere-square meter.

P_w = Wire resistivity, ohm-meters.

W = Coil weight, kilograms.

d = Wire diameter, meters.

If the coil is tuned to the transmitter frequency so that the coil current is limited only by its direct current (dc) resistance, the following results will be achieved:

$$I = \frac{V_o}{R_o + R_c}, \tag{A-1}$$

$$R_c = \pi D N R_w , \tag{A-2}$$

$$W = \pi D N \frac{\pi d^2 \alpha}{4}, \tag{A-3}$$

and

$$R_w = \frac{4 P_w}{\pi d^2} . \tag{A-4}$$

If the wire diameter from A-3 and A-4 is eliminated, a relationship between N and W will result

$$N = \frac{W R_w}{\pi D \alpha \ P_w}. \tag{A-5}$$

Using this expression for N in the equation for M the following is obtained:

$$M = \frac{\frac{V_o DWR_w}{\alpha \; P_w}}{4\left[R_o + \frac{WR_w}{\alpha P_w}\right]^2} . \qquad \text{(A-6)}$$

By differentiating A-6 with respect to R_w and setting equal to zero, the optimum wire resistance for a given coil weight and diameter is found. This procedure gives

$$R_w = \left[\frac{\alpha \; P_w R_o}{W}\right]^{1/2} . \qquad \text{(A-7)}$$

Using equations A-2 and A-5, these expressions can be rewritten as

$$R_c = R_o . \qquad \text{(A-8)}$$

That is, for a given weight, the best coil is one that matches the transmitter for optimum power transfer. The magnetic moment is given by

$$M = \frac{V_o D}{8R_w} . \qquad \text{(A-9)}$$

For the present transmitter and package No. 18 enameled wire was used which gives

R_o = 0.77 ohm,

V_o = 1.6 v,

for No. 18 copper wire,

P_w = 1.72×10^{-8} ohm-m,

α = 8,920 kg/m^3 ,

R_w = 0.02095 ohms/m,

and D = 0.064 m.

Then W = 0.27 kg (0.6 lb),

M = 0.61 A-m^2 ,

and N = 184 turns.

APPENDIX B.--COIL TILT ERRORS

The transmitter coil may not hang vertically in the borehole. Either the cylinder may be cocked in the hole or it may be resting against the side of the hole which is not vertical.

The purpose of this exercise is to calculate the probable effect of coil tilt on location accuracy as well as to minimize it. Consider a spherical coordinate system with the transmitter at the origin as shown in figure B-1.

The coil is tilted in the direction $\hat{R}$ and has a magnetic moment $\hat{M}$.

Assume the tunnel runs paralled to the $\hat{X}$ axis. The receiver coil is located at the coordinates x, y, z in the tunnel.

The problem is to find the direction of minimum magnetic field in the XY plane and determine the direction in which the coil will point. Figure B-2 shows a plane view of the coil in the null direction.

At null, the plane of the coil is alined with the component of the H field in the XY plane, or

$$\tan \Psi = \frac{H_y}{H_x} . \tag{B-1}$$

Therefore, to find the null direction the X and Y components of the magnetic field are found.

In the following analysis, it is assumed that rock conductivities are low enough to use the static fields of a magnetic dipole.

The tilted dipole can be represented as three dipoles alined with the X, Y, and Z axes as follows:

$$M_z = M \cos \theta_o , \tag{B-2}$$

$$M_x = M \sin \theta_o \cos \phi_o , \tag{B-3}$$

and

$$M_y = M \sin \theta_o \sin \phi_o , \tag{B-4}$$

where

$$M^2 = M^2_x + M^2_y + M^2_z . \tag{B-5}$$

The static fields due to each dipole component can be written as follows: At the receiver coil (x,y,z) it is found that

$$H_{m\,x} = \frac{M_x}{4\pi r^5} \left\{ 3\ x z \hat{z} + 3\ x y \hat{y} - (y^2 + z^2 - 2x^2)\ \hat{x} \right\} , \tag{B-6}$$

$$H_{m\,y} = \frac{M_y}{4\pi r^5} \left\{ 3\ xy\ \hat{x} + 3\ yz\ \hat{z} - (x^2 + z^2 - 2y^2)\ \hat{y} \right\} , \tag{B-7}$$

and

$$H_{m\,z} = \frac{M_z}{4\pi r^5} \left\{ 3\ xz\ \hat{x} + 3\ yz\ \hat{y} - (x^2 + y^2 - 2z^2)\ \hat{z} \right\} , \tag{B-8}$$

where $r^2 = x^2 + y^2 + z^2$.

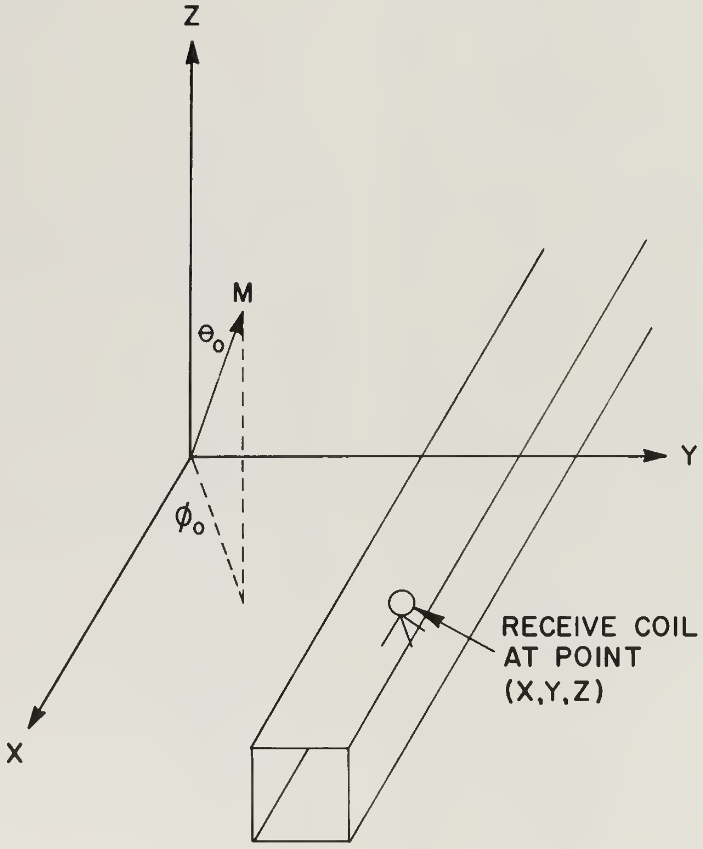
Z
M
θ_o
Y
ϕ_o
X
RECEIVE COIL
AT POINT
(X,Y,Z)

FIGURE B-1. - Coordinate system with the transmitter at the origin.

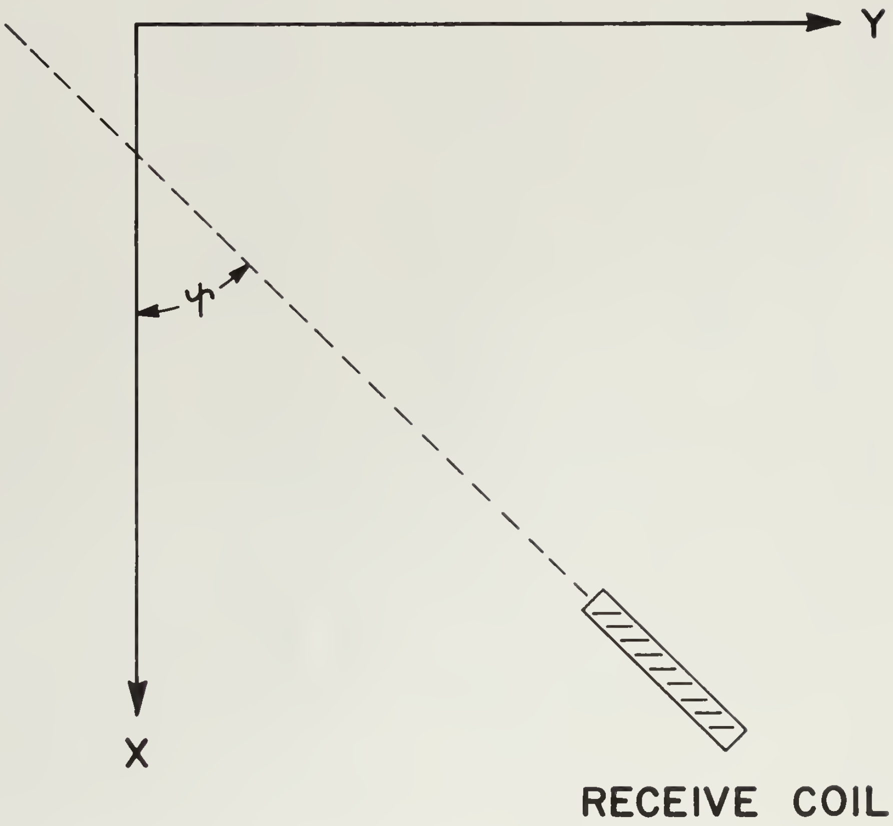
Y
ψ
X
RECEIVE COIL

FIGURE B-2. - Plane view of the coil in the null direction.

Each of these fields has x and y components.

By combining the x and y components, H_x and H_y are found as

$$H_x = \frac{1}{4\pi r^5}\left\{3\ M_z xz + 3\ M_y xy - M_x\ (z^2 + y^2 - 2x^2)\right\}, \qquad \text{(B-9)}$$

and

$$H_y = \frac{1}{4\pi r^5}\left\{3\ M_z yz + 3\ M_x xy - M_y\ (x^2 + z^2 - 2y^2)\right\}. \qquad \text{(B-10)}$$

Then from equation B-1,

$$\tan\Psi = \frac{H_y}{H_x} = \frac{3\ M_z yz + 3M_x\ xy - M_y\ (x^2 + z^2 - 2y^2)}{3\ M_z xz + 3M_y\ xy - M_x\ (y^2 + z^2 - 2x^2)}. \qquad \text{(B-11)}$$

It can be seen that if $\theta_o = 0$ then M_x and $M_y = 0$ (no tilt), and $\tan\Psi = \frac{y}{x} = \tan\phi$ as expected, where ϕ is the true angle.

If $\Psi = \phi + \delta\phi$ is allowed in equation B-11 where $\delta\phi$ is error in angle caused by coil tilt and convert to cylindrical coordinates by letting

$x = \rho\cos\phi$,

$y = \rho\sin\phi$,

$\rho^2 = x^2 + y^2$.

Then it can be shown that

$$\tan\delta\phi = \frac{(\rho^2 + z^2)\tan\theta_o\ \sin(\phi - \phi_o)}{3\rho z + (2\rho^2 - z^2)\tan\theta_o\ \cos(\phi - \phi_o)}. \qquad \text{(B-12)}$$

Figure B-3 shows the effect of coil tilt on location accuracy. The values of the tilt parameters were taken from the Ft. Ritchie, Md., experiment. Since the transmitter package diameter was nearly equal to the well diameter, we assumed the transmitter coil was alined with the wellhole; in addition, the wellhole is assumed to be straight. This gives $\theta_o = 3.08°$ and $\phi = +16.2°$. Figure B-3 shows reasonable agreement between the theoretical calculations and the measured data.

Minimizing the Error

Usually $\tan\theta_o \ll 1$, then the minimum value of the $\tan\delta\phi$ occurs when $z = \rho$. Since ρ is not known, this condition can be met only by using reasonable judgment when the transmitter is positioned in the hole.

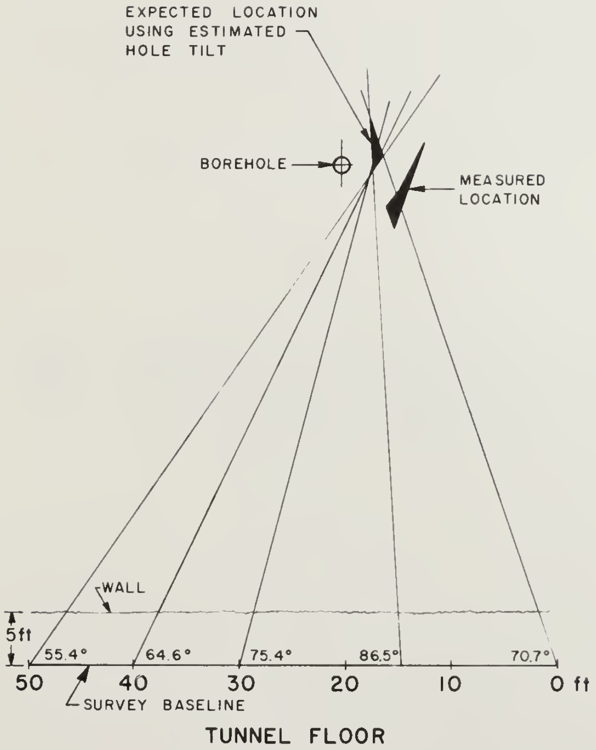
EXPECTED LOCATION USING ESTIMATED HOLE TILT
BOREHOLE
MEASURED LOCATION
WALL
5ft
55.4°
64.6°
75.4°
86.5°
70.7°
50
40
30
20
10
0 ft
SURVEY BASELINE
TUNNEL FLOOR

FIGURE B-3. - Effect of coil tilt on location accuracy.

When $\theta_o < \pm 6°$ and $1/2 < z/\rho < 4$ then equation B-12 can be written

$$\tan \delta \phi = \frac{\rho^2 + z^2}{3\rho z} \tan \theta_o \sin (\phi - \phi_o). \qquad \text{(B-13)}$$

Equation B-13 is odd in z. If the angle Ψ_1 is measured when the transmitter is z_1 ft above the tunnel and an angle Ψ_2 is measured at the same horizontal location when the transmitter is z_1 ft below the tunnel, then the true angle ϕ is found from the average of Ψ_1 and Ψ_2 as follows:

$$\phi = \frac{\Psi_1 + \Psi_2}{2} \qquad \text{(B-14)}$$

This is shown in table B-1 using the estimated hole tilt values of the field test.

TABLE B-1. - Minimizing error by measuring above and below tunnel

($\theta_o = 3.08°$, $\phi_o = 16.2°$, $x = 29.5$ ft, $y = 48$ ft, $\phi = 58.4°$)

Z_1, ft	Measured angle, degrees	Error, degrees	Average	Net error, degrees
+5	64.4	6.0	55.9	-2.5
-5	47.4	-11.0		
+50	59.8	1.4	58.4	.0
-50	57.0	-1.4		

In this case, the ideal value for z is approximately 50 ft, but it can be seen that over the range of 10 to 1, the error can be significantly reduced.

In any case, the measured angles bracket the true value so that the actual location will always be within the outlined quadrangle as long as

$$|z| > \rho \tan \theta_o ,$$

and $|z| < \rho / \tan \theta_o .$

An example of this is shown in figure B-4. The solid lines are the calculated null directions with the transmitter above and below the receiver. The dashed lines are derived from the arithmetic average of the two angular readings of each horizontal location and are virtually dead center.

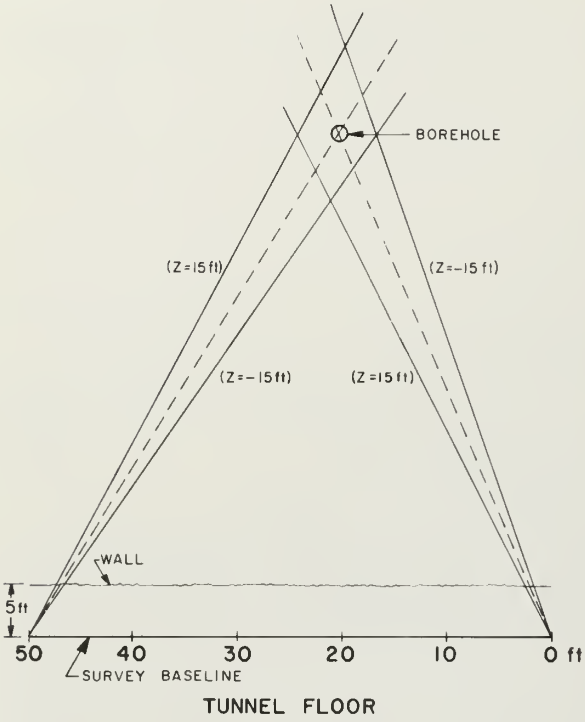
BOREHOLE
(Z=15 ft)
(Z=-15 ft)
(Z=-15 ft)
(Z=15 ft)
WALL
5 ft
50
40
30
20
10
0 ft
SURVEY BASELINE
TUNNEL FLOOR

FIGURE B-4. - Effect of moving transmitter above and below tunnel center line on location accuracy.

☆U.S. GOVERNMENT PRINTING OFFICE: 1978-703-103/55

22.09
In3amo

RI 8304

Bureau of Mines Report of Investigations/1978

Bureau of Mines Research on Trailing-Cable-Fault Locators

DEPOSITORY
NOV 17 1978
UNIV. OF ILL. LIBRARY
AT URBANA-CHAMPAIGN

UNITED STATES DEPARTMENT OF THE INTERIOR

622.09
Un32mo

Bureau of Mines
Report of Investigations 8304

BUREAU OF MINES RESEARCH ON TRAILING-CABLE-FAULT LOCATORS

by

George J. Conroy

ERRATA

On page 3, lines 4-6 should read as follows:

where R_1 is measured between A and C when A and B are shorted together and C and D are also shorted together,

R_2 is the measurement between A and B with the opposite end open-circuited,

and R_3 is the measurement between C and D with the opposite end open-circuited.

The Library of the
NOV 21 1978
University of Illinois
at Urbana-Champaign

Report of Investigations 8304

Bureau of Mines Research on Trailing-Cable-Fault Locators

By George J. Conroy

UNITED STATES DEPARTMENT OF THE INTERIOR
Cecil D. Andrus, Secretary

BUREAU OF MINES

This publication has been cataloged as follows:

Conroy, George J

Bureau of Mines research on trailing-cable-fault locators / by George J. Conroy. [Washington] : U.S. Dept. of the Interior, Bureau of Mines, 1978.

18 p. : ill., diagrams ; 27 cm. (Report of investigations - Bureau of Mines ; 8304)

Includes bibliographies.

1. Electric cables - Fault location. I. United States. Bureau of Mines. II. Title. III. Series: United States. Bureau of Mines. Report of investigations - Bureau of Mines ; 8304.

TN23.U7 no. 8304 622.06173

U.S. Dept. of the Int. Library

CONTENTS

Page

Abstract 1
Introduction 1
Establishing the character of the fault 2
Fault location by resistance measurement 2
Bridge methods 3
Continuous-high-voltage ac or dc 5
Pulse-echo methods 7
Tone generator plus probe 12
Infrared detection 16
Swept frequency method 17
Summary and conclusions 17

ILLUSTRATIONS

1. Instrument used to establish character of fault 2
2. Short-circuited cable 3
3. Numerical representation of short-circuited cable 3
4. Murray loop method of locating short-circuit fault in trailing cable 4
5. Cable with open-circuit fault 5
6. Theoretical representation of a capacitive bridge method of locating open-circuit fault 5
7. Biddle Co. impulse generator 6
8. Block diagram of TDR method of cable-fault locating 7
9. Bureau of Mines digital readout TDR 8
10. TDR logic diagram 9
11. TDR schematic diagram 10
12. Tektronix, Inc., TDR 11
13. Electromagnetic field probe method of locating short-circuit fault. 12
14. Low-cost tone generator-probe set for short-circuit location 13
15. Tone generator schematic diagram 13
16. Audioprobe schematic diagram 14
17. Low-cost set for open-circuit location 14
18. Tone generator modification for open-circuit location 15
19. Modified audioprobe schematic diagram 15
20. Bureau of Mines infrared probe 16

TABLE

1. Fault-location methods examined by the Bureau of Mines 18

BUREAU OF MINES RESEARCH ON TRAILING-CABLE-FAULT LOCATORS

by

George J. Conroy[1]

ABSTRACT

This Bureau of Mines publication describes several fault locators and methods, including time domain reflectometers, a frequency domain reflectometer, tone generators, an infrared method, the Murray loop method, and high-voltage "click" methods. The Bureau of Mines has been conducting research into these methods for several years, to improve mine safety and facilitate production through rapid, safe location of trailing-cable faults. The problems encountered in practical applications are discussed, and schematic diagrams of several instruments fabricated by the Bureau are presented. Since no present single method of locating trailing-cable faults is universally applicable, a kit composed of several of the more promising fault locators is advisable.

INTRODUCTION

At the Bureau of Mines, research into various methods of locating faults in trailing cables has been pursued for several years. The types of fault concerned are trailing-cable short circuits and open circuits which, either because of the nature of the fault or because of the rapid action of protective devices, do not at the time of occurrence discharge sufficient energy into the insulation to cause visual evidence such as a scorch mark, swelling, or blowout. The term "short circuit" as employed herein is not restricted to zero-resistance faults, but includes partial shorts with high values of shunt resistance. Similarly, the "open circuits" discussed here need not have infinite resistance. It is usually best to try to locate faults of this type quickly, with the cable right in place, because cooling, drying out, and mechanical movement can each have effects that tend to temporarily clear or cancel the fault. (Mechanical movement can also have the opposite effect, which is why it often pays to flex the cable at suspicious points when making tests.)

Table 1 at the end of the report summarizes fault-location methods examined by the Bureau of Mines.

---

[1] Supervisory electrical engineer, Pittsburgh Mining and Safety Research Center, Bureau of Mines, Pittsburgh, Pa.

ESTABLISHING THE CHARACTER OF THE FAULT

The first step in electrically locating a fault should be to obtain its resistance. If the cable can be physically disconnected at both ends, this isolation should be done; otherwise, the cable should be uncoupled at the power center and switched off, if possible, at the machine. An exception might occur when using an infrared probe detection method (to be discussed). Generally, however, the cable should be electrically isolated.

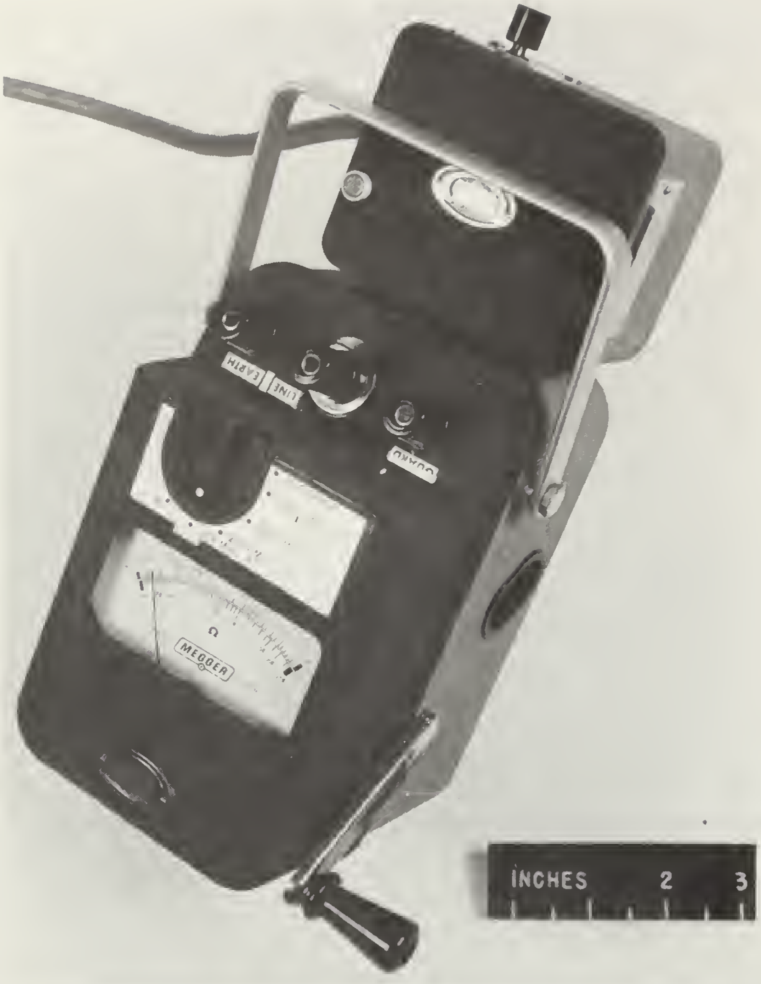

FIGURE 1. - Instrument used to establish character of fault.

Usually the first measurement is made with a Megger[2] tester (fig. 1). The "ohms" scale of the Megger can be used to check on conductor continuity to find an open circuit; the various ranges can be used to detect short circuits. A low insulation resistance between two conductors indicates a short. If the value using the "ohms" scale of the Megger is zero or very low, it pays to measure resistance with a battery-powered instrument such as a multimeter. The Megger tends to read low compared to such instruments, and since just a few ohms' resistance can render many fault location methods unusable, it is well to know from the beginning what to expect.

FAULT LOCATION BY RESISTANCE MEASUREMENT

Searching for the fault is easier if an approximate location can first be determined through measurements at the terminals of the cable. In theory, a series of simple resistance measurements could accomplish this. The problem here is the requirement for precision and sensitivity. Figure 2 is a representation of a short-circuited cable. With three measurements, the

---

[2] Trade names and company names are used to facilitate understanding, and their use does not imply endorsement by the Bureau of Mines.

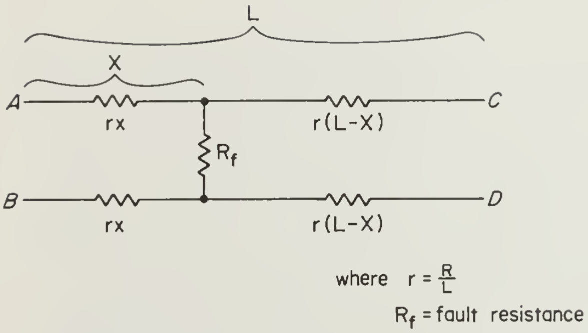

FIGURE 2. - Short-circuited cable.

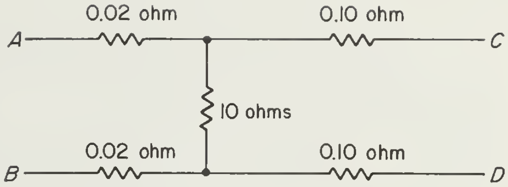

FIGURE 3. - Numerical representation of short-circuited cable.

value of the fault resistance cancels out, and the ratio of fault distance, X, to the total length, L, is found to be

$$\frac{X}{L} = \frac{1}{2} - \frac{(R_3 - R_2)}{8R_1},$$

where R_1 is measured between A and B when C and D are shorted together,

R_2 is the measurement between A and B,

and R_3 is the measurement between C and D.

As an example, in figure 3 if we measured $R_1 = 0.06$, $R_2 = 10.04$, and $R_3 = 10.20$ ohms:

$$\frac{X}{L} = \frac{1}{2} - \frac{(10.20 - 10.04)}{8\ (0.06)} = 0.5 - 0.33 = 0.167$$

$$\frac{X}{L} = \frac{1}{6}$$

The difficulty is that the resistance measurement must have much better than 1/2 percent precision, in order that the conductor resistances, on the order of hundredths of an ohm, can be distinguished in the presence of the 10-ohm fault resistance. If the fault had higher resistance, even more precise and sensitive resistance measurements would be required.

BRIDGE METHODS

A resistance method that avoids the problem of extremely precise measurement is the Murray loop method (fig. 4). It is drawn as shown to emphasize the bridge aspect. As the fault is not part of the bridge arms, it does not dictate the precision requirements. There is a limit as to how high the resistance can be without reducing sensitivity to below a practical level, and this limit depends on the kinds of current source and null detector used; however, with available apparatus, shorts with several thousand ohms can be located. The expression for locating the fault is

$$\frac{X}{L} = \frac{R_1}{R_{total}}.$$

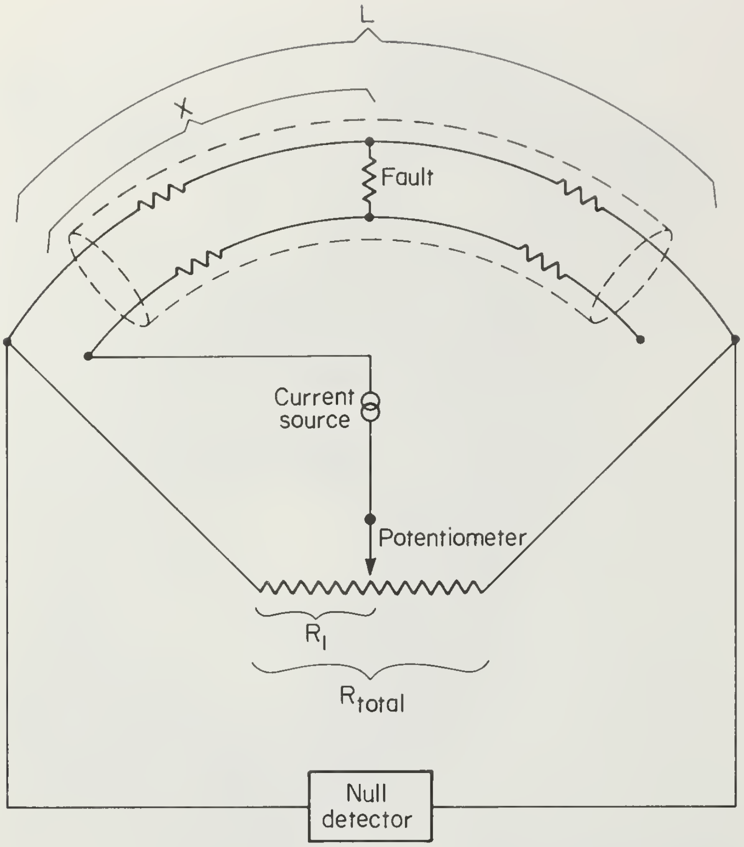

FIGURE 4. - Murray loop method of locating short-circuit fault in trailing cable.

If there are intact conductors in the cable in addition to the faulted ones, it may be possible to use them as connecting leads, with jumpers at the far end of the cable, to avoid problems of stretching wires to both ends. This only applies, of course, if the far-end terminations are accessible for connection.

The short-circuit-locating apparatus can be ac or dc. There are some advantages to low audiofrequency measurements, because interference can be better controlled. Also, since there are fewer problems in amplifying an ac signal than a dc one, highly sensitive null detection is easier to obtain. The apparatus utilized in recent Bureau of Mines tests at low frequency was laid out on a breadboard for the purpose; no commercial units have been evaluated for use in mine environments. The components consisted of a slidewire potentiometer prepared from a single strand of high-resistance wire about one-half meter long (5 ohms' total resistance), a machined-brass slider contact, terminals, a capacitor-isolated tone generator with added series resistance to limit overloading, and an oscilloscope to serve as a null detector. Trials with a 10-turn wire-wound potentiometer indicated that this might be a suitable replacement for the slidewire, provided a commercially available unit can be obtained that has a total resistance well below 50 ohms.

In analogy to the resistance method of locating short circuits, there is a capacitive method for open circuits. Figure 5 shows a representation of a cable with one conductor open-circuited. The capacitors in the sketch represent the distributed capacitance between conductors. An ac capacitive impedance method can be used to locate this fault, as shown in a simplified manner in figure 6. The circuit shown is academic and is not available in a commercial instrument. Available commercial devices utilize a Wier, Schering, or other bridge circuit incorporating resistances in the branches. Using the commercial devices, it would actually be necessary to independently measure the capacitances from each end of the cable. Finally, however, the expression for fault

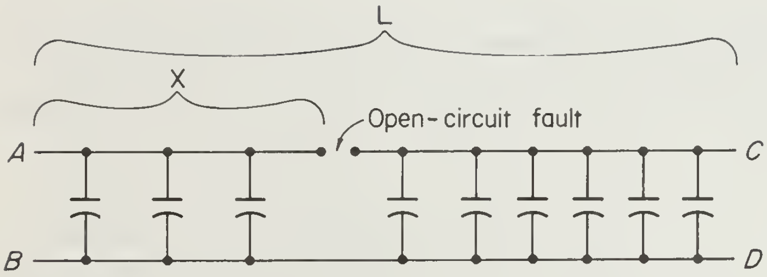

FIGURE 5. - Cable with open-circuit fault. Distributed capacitance per unit length is represented symbolically by lumped capacitances.

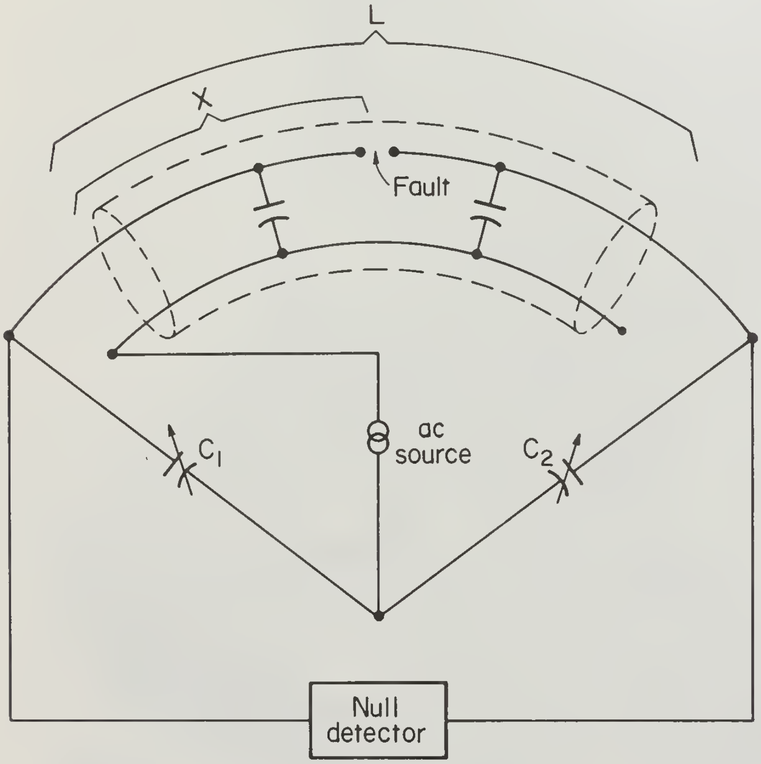

FIGURE 6. - Theoretical representation of a capacitive bridge method of locating open-circuit fault.

location would be the same as for the bridge circuit shown:

$$\frac{X}{L} = \frac{C_1}{C_1 + C_2}.$$

A problem that in many circumstances rules out the capacitive method, at least for unshielded trailing cables, is that the long cable length picks up radiated interference and makes it difficult or impossible to find a null. This problem does not occur so prominently with the resistance bridge method of locating short circuits because relatively high measurement currents are involved there, making interference less noticeable.

There are other bridge methods used for fault location. In some, applicable to cable manufacturing facilities, etc., a standard cable is compared with the faulted cable. This probably gives the highest accuracy since normal cable inductance, capacitance, series resistance, and insulation resistance will be balanced out simultaneously.

CONTINUOUS-HIGH-VOLTAGE AC OR DC

If a continuous high voltage in the range 10 to 40 kv is impressed across a faulted pair, there can occur a release of energy at the fault sufficient to permit detection either by visual or acoustic means or by detection of the magnetic field. Visual methods include observation of smoke, but a more reliable scheme requires that the cable be immersed in a water trough and observed for the occurrence of streams of bubbles. The acoustic method involves observing the cable to hear the crackling of an arc, usually using a probe containing a microphone and amplifier. A probe is also required for detecting the presence of a magnetic field caused by a current loop through the cable. The contribution made by the high voltage is to break down a high-resistance fault to a value low enough for the current to flow at least momentarily. High-voltage methods are much used in cable repair shops, because they can reveal insulation weaknesses as well as established faults. The high voltage itself, however, can have a weakening effect on good insulation. Also, a considerable personnel hazard is involved unless test conditions and test area are carefully controlled. An improvement over the continuously applied-voltage method employs "thumper" apparatus, as shown in figure 7; however, this method retains some of the personnel hazard aspects and is not presently recommended for inplace fault locating in underground mines. "Blowing" the fault by connecting the cable to a trolley line or other

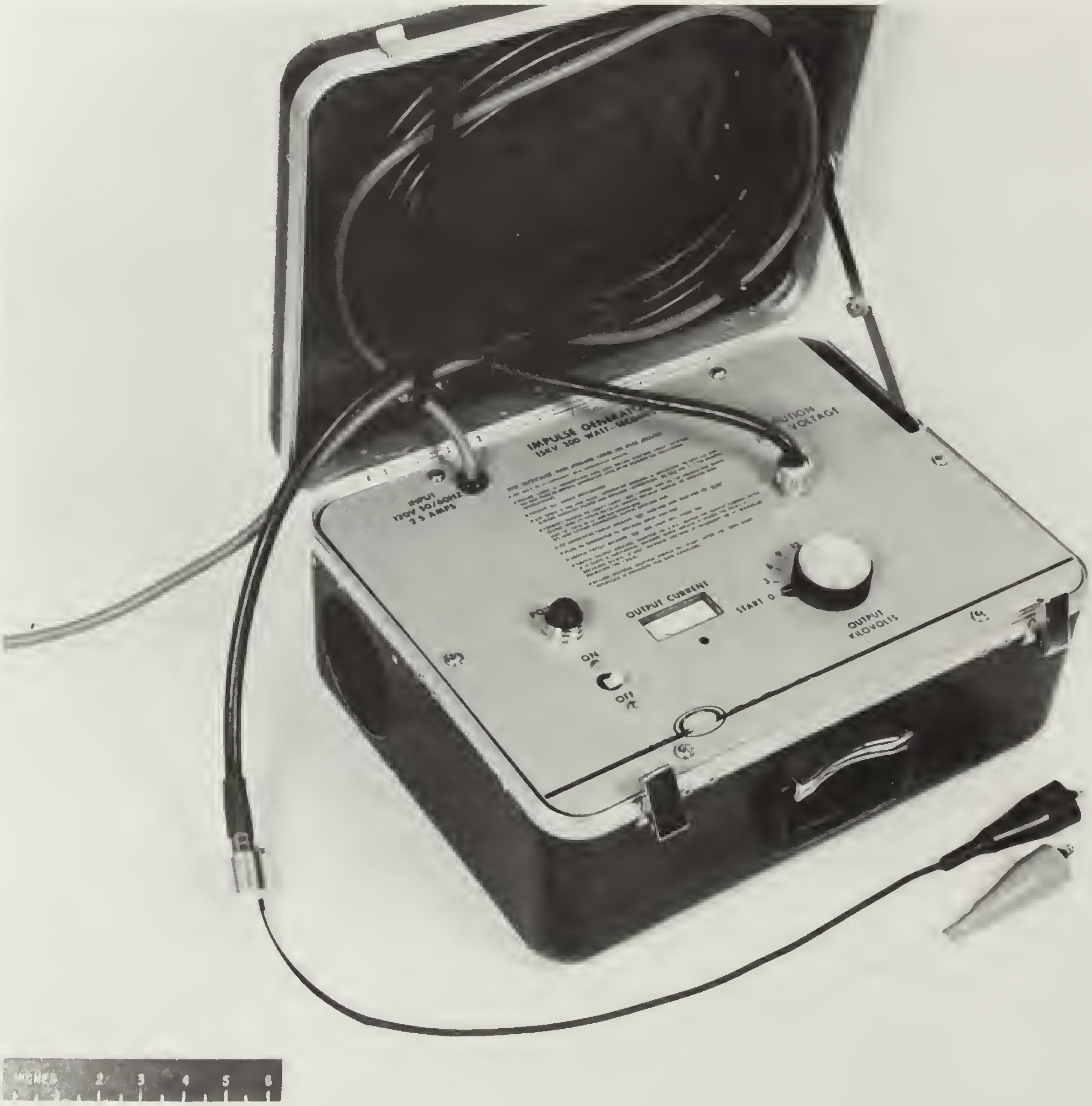
IMPULSE GENERATOR
15KV 300 WATT-SECONDS
INPUT
120V 50/60HZ
2.5 AMPS
VOLTAGE
OUTPUT CURRENT
START 0
OUTPUT KILOVOLTS
ON
OFF
INCHES 2 3 4 5 6

FIGURE 7. - Biddle Co. impulse generator.

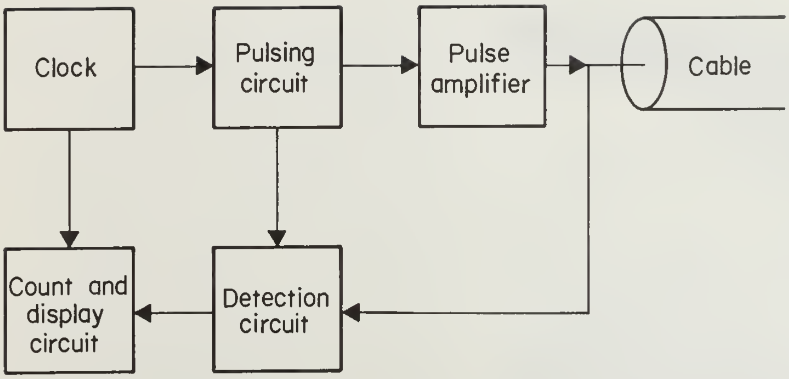

FIGURE 8. - Block diagram of TDR method of cable-fault locating.

high-power source is likewise not recommended, because of fire hazard and the possibility of injuring personnel.

PULSE-ECHO METHODS

Another category of pulse testing, the pulse-echo methods, has none of the danger of the high-voltage test and yet is an extremely versatile means of fault location for open circuits and low-resistance shorts. Any discontinuity in a conductor or the insulation in a cable will tend to reflect a pulse back to the origin. If the discontinuity is an open circuit, the echo will add to the amplitude of the pulse; if it is a short circuit, the echo will subtract. If an electronic circuit is built capable of distinguishing this amplitude effect and of measuring the time interval between the start of the pulse and the arrival of the echo, both the nature and the location of the fault can be established. Figure 8 is a simplified illustration of a pulse-echo system.

More than one basic system fits into this category. The amplitude or the frequency of the originating pulse may be varied, with corresponding selection of the detection circuitry. The system may rely on analog or digital processing. A cathode-ray oscilloscope is essential to some approaches but can be eliminated in others. The systems that have been the subject of Bureau of Mines development programs involve time domain reflectometers (TDR) and frequency domain reflectometers (FDR). A combination TDR and tone generator was built by FMC Corp. in 1973 under Bureau contract.[3] This unit locates short circuits that have resistance values no higher than several ohms and open circuits that have at least 100 ohms' resistance. An improved version was developed by Carnegie-Mellon Institute, Pittsburgh, Pa., again under Bureau contract, and was then the subject of a purchase contract with Preiser Co., Charleston, W. Va., under which four mine-duty models were built (fig. 9). These units can define and locate short circuits with resistance of 100 ohms or less and open circuits of 100 ohms or more. The logic diagram for the latest version is shown in figure 10, and its schematic diagram is presented in figure 11. Some minor research is continuing on this model, seeking to replace some of the TTL (transistor-transistor logic) integrated circuit modules with CMOS (complementary symmetry metal oxide semiconductor) modules, in order to reduce current drain and thereby extend the interval between battery charges.

---

[3] FMC Corp. Protection and Troubleshooting of Coal Mine Electrical Cables. 3. Summary Report. Cable Fault Locator Instrument for Period August 1971 to November 1972. BuMines Open File Rept. 42(3)-74, 1973, 133 pp.; available for consultation at the Bureau of Mines libraries in Denver, Colo., Pittsburgh, Pa., Spokane, Wash., and Twin Cities, Minn.; at the U.S. Department of Energy library, Morgantown, W. Va.; at the Central Library, U.S. Department of the Interior, Washington, D.C.; and from the National Technical Information Service, Springfield, Va. PB 235 641.

_____. Protection and Troubleshooting of Coal Mine Electrical Cables. 4. Final Report. BuMines Open File Rept. 42(4)-74, 1973, 113 pp.; available for consultation at the Bureau of Mines libraries in Denver, Colo., Pittsburgh, Pa., Spokane, Wash., and Twin Cities, Minn.; at the U.S. Department of Energy library, Morgantown, W. Va.; at the Central Library, U.S. Department of the Interior, Washington, D.C.; and from the National Technical Information Service, Springfield, Va. PB 235 642.

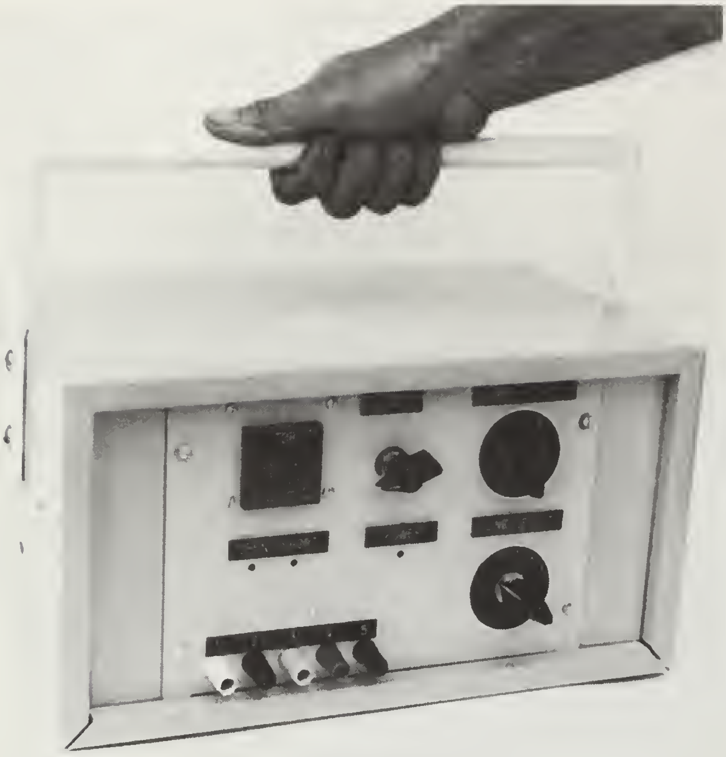

FIGURE 9. - Bureau of Mines digital readout TDR.

A third-generation system was also developed by Carnegie-Mellon, with field-test models being fabricated by Bendix Corp., Baltimore, Md., under Bureau contract. It includes a microprocessor programed to provide immunity from noise and other causes of inaccuracy, and a time-varying pulse detection concept by which a number of discontinuities can be located in one operation, if several are present along the cable. The Bendix model utilizes a single-card Intel 8080 microcomputer and incorporates an independent "gross fault" indicator intended to provide preliminary fault detection. Twelve units are currently being tested by the Bureau of Mines.

One of the most effective methods of utilizing a TDR has not yet been applied to inplace testing of underground mine cable. It involves direct comparison, on an oscilloscope screen, of the traces from a good and a faulted conductor pair. The anomalies provide fault location information. There is a high probability that the latest microprocessor TDR can be further improved to approximate this method of operation while retaining the advantages of a digital display, by including nonvolatile memory capability. This is one of the aspects being investigated by Carnegie-Mellon University under Bureau contract.

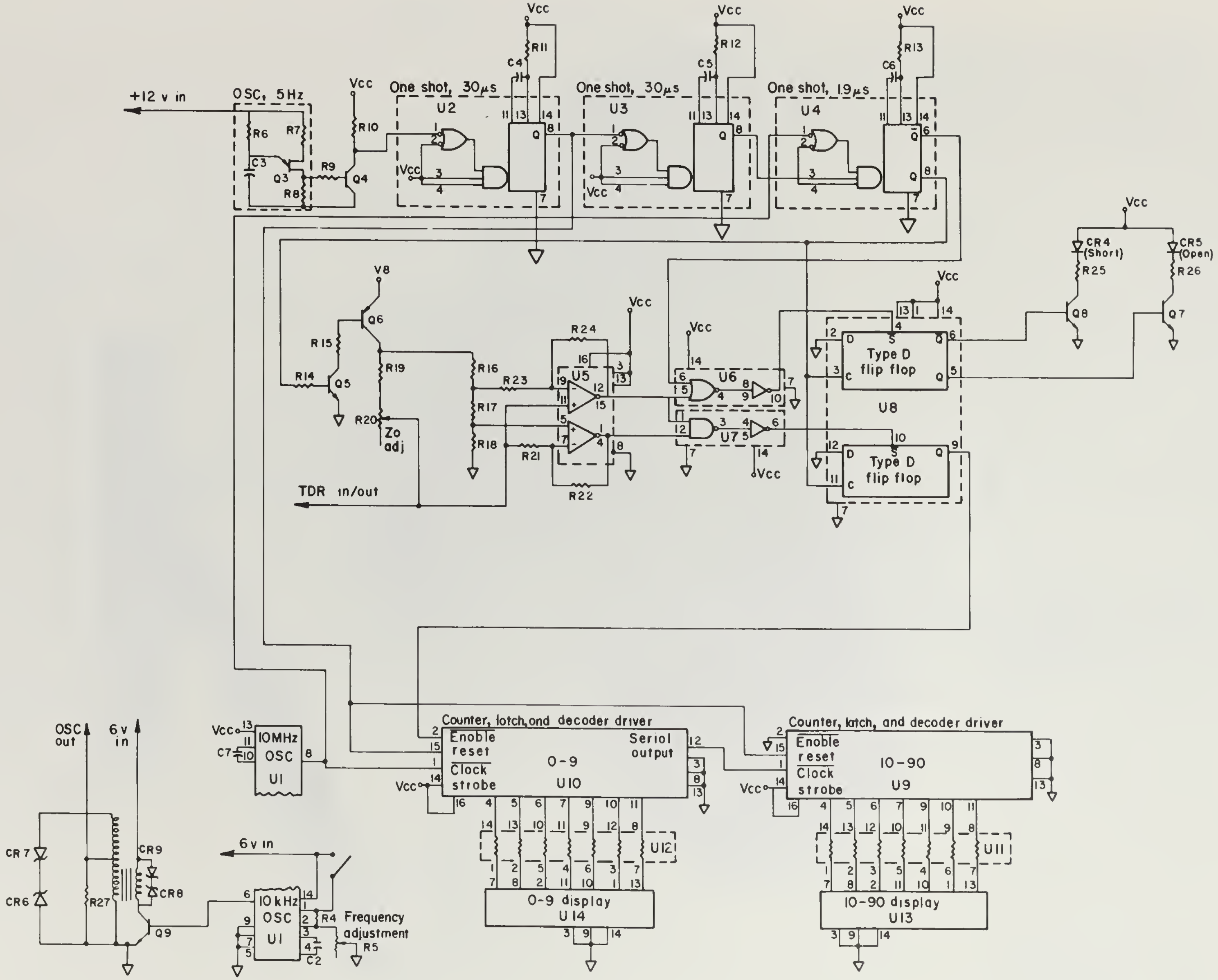
+12 v in
OSC, 5Hz
R6
R7
C3
Q3
R8
R9
Q4
Vcc
R10
One shot, 30μs
U2
One shot, 30μs
U3
One shot, 1.9μs
U4
C4
R11
C5
R12
C6
R13
CR4 (Short)
CR5 (Open)
R25
R26
Q8
Q7
V8
Q6
R15
R14
Q5
R19
R20
Zo adj
R16
R17
R18
R23
R21
R24
R22
U5
U6
U7
Type D flip flop
U8
Type D flip flop
TDR in/out
OSC out
6 v in
CR7
CR6
R27
CR9
CR8
Q9
10MHz OSC U1
C7
6 v in
10 kHz OSC U1
R4
Frequency adjustment
R5
C2
Counter, latch, and decoder driver
Enable reset
Clock strobe
0-9
U10
Serial output
Counter, latch, and decoder driver
Enable reset
Clock strobe
10-90
U9
U12
U11
0-9 display U14
10-90 display U13

FIGURE 10. - TDR logic diagram.

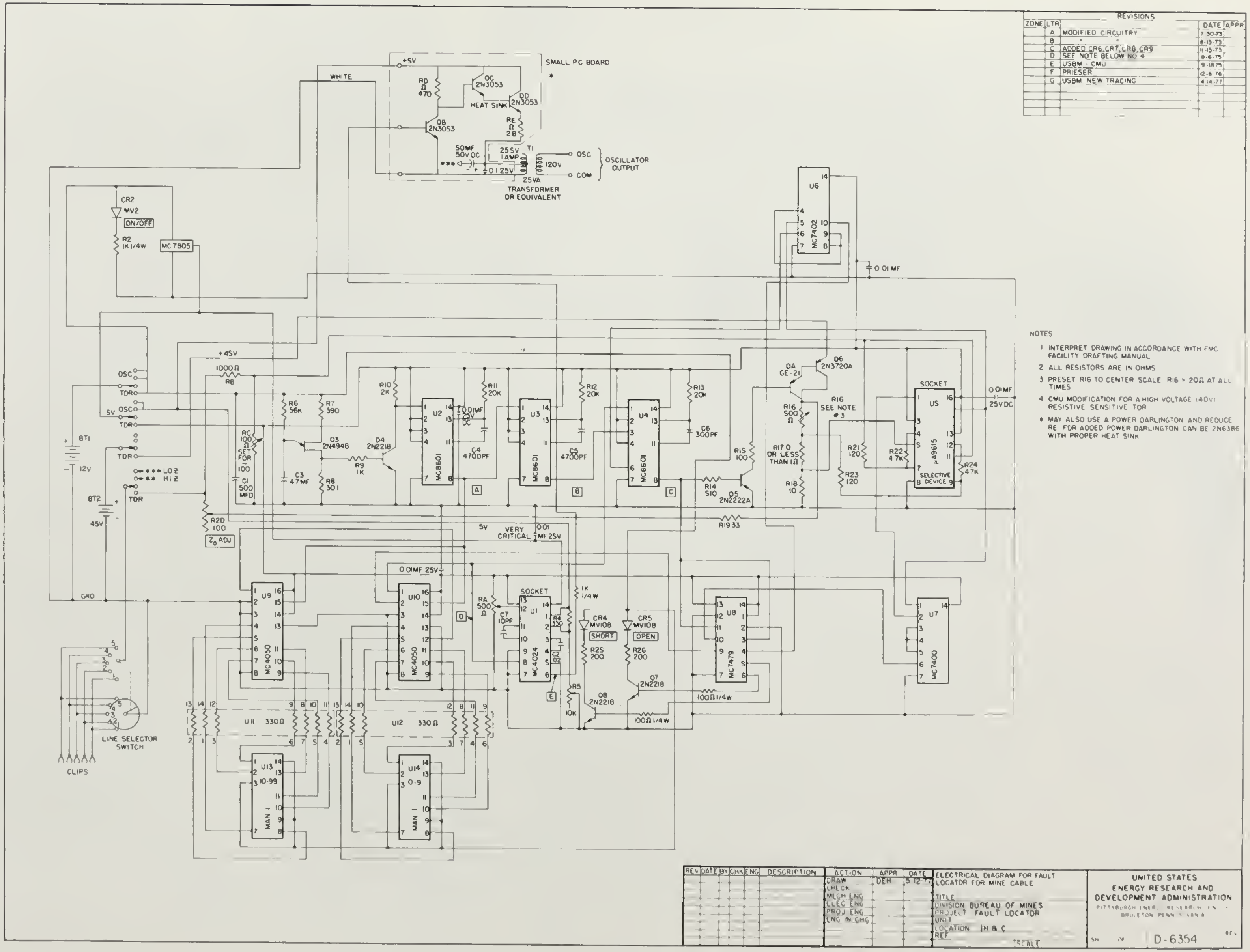
REVISIONS
ZONE LTR DATE APPR
A MODIFIED CIRCUITRY 7-30-73
B " 8-13-73
C ADDED CR6, CR7, CR8, CR9 11-13-73
D SEE NOTE BELOW NO 4 8-6-75
E USBM - CMU 9-18-75
F PRIESER 12-6-76
G USBM NEW TRACING 4-14-77
NOTES
1 INTERPRET DRAWING IN ACCORDANCE WITH FMC FACILITY DRAFTING MANUAL
2 ALL RESISTORS ARE IN OHMS
3 PRESET R16 TO CENTER SCALE R16 > 20Ω AT ALL TIMES
4 CMU MODIFICATION FOR A HIGH VOLTAGE (40V) RESISTIVE SENSITIVE TDR
* MAY ALSO USE A POWER DARLINGTON AND REDUCE RE FOR ADDED POWER DARLINGTON CAN BE 2N6386 WITH PROPER HEAT SINK
SMALL PC BOARD
+5V
WHITE
RD Ω 470
QC 2N3053
QD 2N3053
QB 2N3053
HEAT SINK
RE Ω 2.8
50MF 50VDC
25.5V 1AMP
0.125V
T1
120V
25VA TRANSFORMER OR EQUIVALENT
OSC
COM
OSCILLATOR OUTPUT
CR2 MV2
ON/OFF
R2 1K 1/4W
MC7805
U6 MC7402
0.01MF
+45V
1000Ω R8
R6 56K
R7 390
R10 2K
R11 20K
R12 20K
R13 20K
U2 MC8601
U3 MC8601
U4 MC8601
0.01MF 25V DC
C4 4700PF
C5 4700PF
C6 300PF
A
B
C
Q3 2N4948
D4 2N2218
R9 1K
C3 47MF
R8 301
RC 100 Ω SET FOR 100
C1 500 MFD
R15 100
R14 510
Q5 2N2222A
R19 33
QA GE-21
D6 2N3720A
R16 500 Ω
R16 SEE NOTE #3
R17 0 OR LESS THAN 1Ω
R18 10
R21 120
R22 4.7K
R23 120
R24 4.7K
SOCKET
U5 μA9615
SELECTIVE DEVICE
0.01MF 25VDC
OSC
TDR
5V
BT1 12V
BT2 45V
LO Z
HI Z
R20 100
Z0 ADJ
5V
VERY CRITICAL
0.01 MF 25V
GRD
0.01MF 25V
U9 MC4050
U10 MC4050
RA 500 Ω
D
C7 10PF
SOCKET
U1 MC4024
R4 330
1K 1/4W
CR4 MV108
SHORT
CR5 MV108
OPEN
R25 200
R26 200
Q7 2N2218
Q8 2N2218
R5 10K
E
100Ω 1/4W
100Ω 1/4W
U8 MC7479
U7 MC7400
U11 330Ω
U12 330Ω
U13 10-99 MAN 1
U14 0-9 MAN 1
LINE SELECTOR SWITCH
CLIPS
REV DATE BY CHK ENG DESCRIPTION
ACTION APPR DATE
DRAW DEH 5-12-77
CHECK
MECH ENG
ELEC ENG
PROJ ENG
ENG IN CHG
ELECTRICAL DIAGRAM FOR FAULT LOCATOR FOR MINE CABLE
TITLE
DIVISION BUREAU OF MINES
PROJECT FAULT LOCATOR
UNIT
LOCATION IH & C
REF
SCALE
UNITED STATES ENERGY RESEARCH AND DEVELOPMENT ADMINISTRATION
PITTSBURGH ENERGY RESEARCH CENTER
BRUCETON, PENNSYLVANIA
D-6354

FIGURE 11. - TDR schematic diagram.

There are TDR's on the market other than the Bureau of Mines items. Hewlett-Packard has had one for years. Tektronix currently supplies two models of an instrument (fig. 12) that includes a tiny chart recorder as well as a cathode ray tube. Biddle's "radar" unit employs pulse-echo principles. Furthermore, TDR's can be built up from a few integrated circuits and an oscilloscope. For underground mine use, the digital display is preferred to an oscilloscope pattern, because lower voltages are present in the apparatus and because less specialized skill is required for interpretation of results. Also, the simpler TDR circuits do not detect high-resistance short circuits. The use of the microprocessor promises to increase the upper limit to 10,000 ohms or higher.

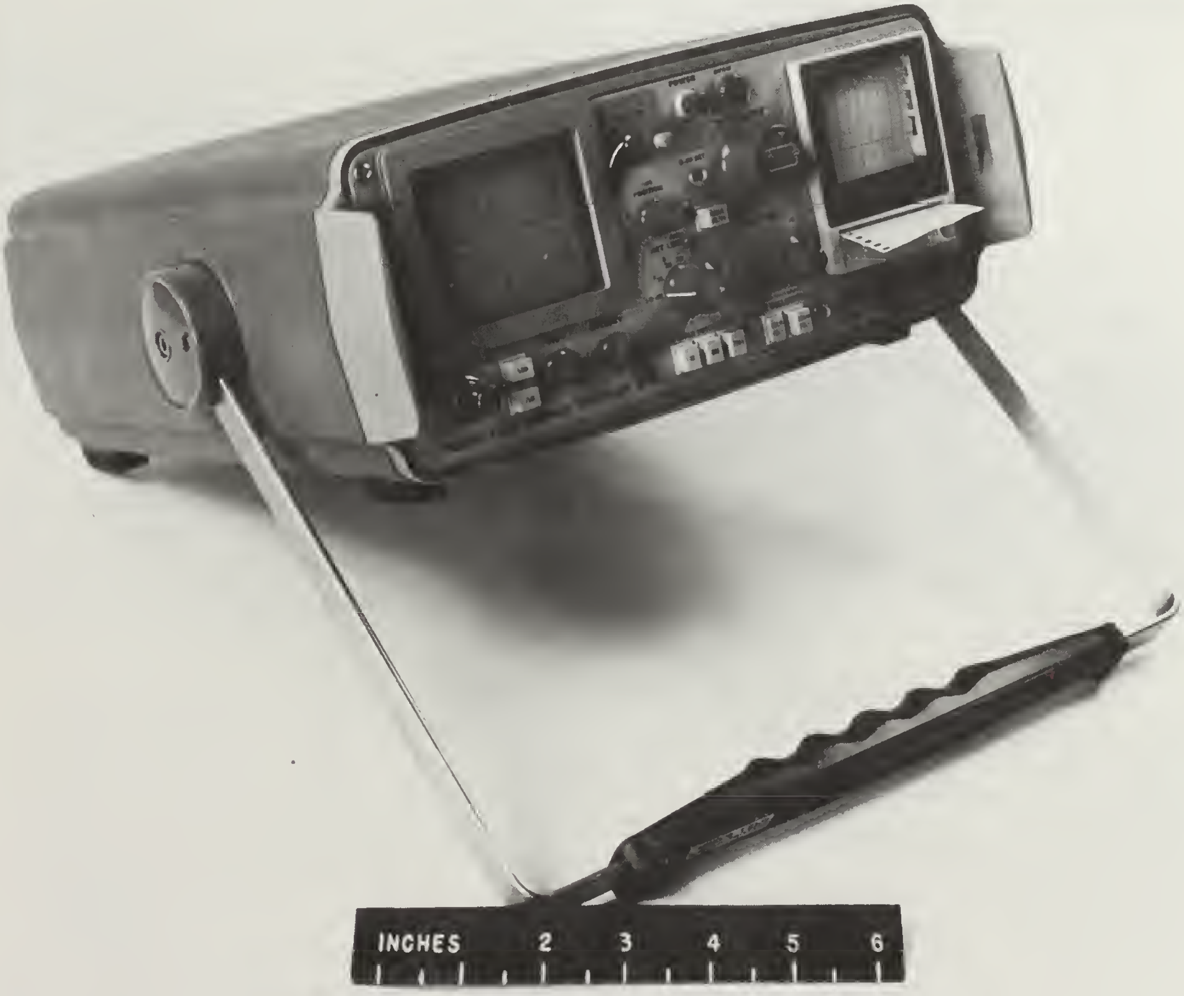

FIGURE 12. - Tektronix, Inc., TDR.

TONE GENERATOR PLUS PROBE

A limitation of the use of pulse methods such as the TDR is that, even assuming the electronic location is precise, the distance read must be associated in some way with distance along a real cable lying on the ground. It would take unusual confidence to pace off a stated distance and cut the cable at a particular spot, with no better evidence than the TDR reading. What is needed is a probe that provides an unequivocal indication when it is brought into the immediate vicinity of the fault.

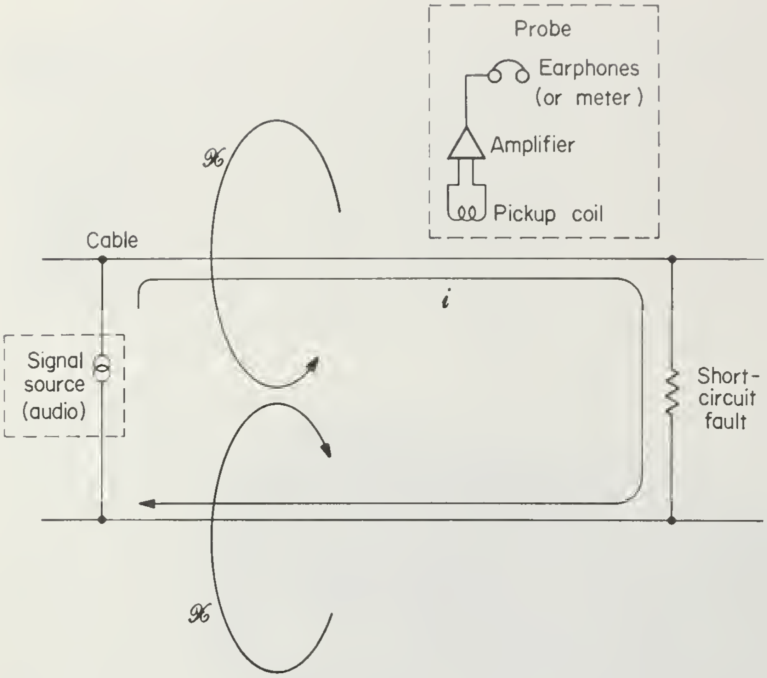

FIGURE 13. - Electromagnetic field probe method of locating short-circuit fault; H indicates the magnetic vector.

If an audiofrequency signal is applied to the end of a shorted pair, the current will flow as shown in figure 13. A magnetic field is produced by the current flow. If we consider current "i" at a particular instant, we see that while the electromagnetic fields from the two wires would cancel each other at any large distance from the cable, they do not balance out in its immediate vicinity. Therefore, if a probe with a loop of wire is brought close to the cable as shown, the net field will induce a current in the coil. This is amplified and yields meter deflection results.

This location method is very effective for low-resistance shorts, where the loop current is appreciable with low applied voltage, so that a fairly strong magnetic field is there to be sensed. A low applied voltage is advantageous for trailing-cable-short-circuit detection using a probe, because otherwise the potential on the conductor can provoke a response due to electrostatic coupling; sufficient potential may continue to be present at points beyond the short circuit so that this response is still provoked and the fault location is not therefore evident.

A higher resistance short may be detected by increasing the sensitivity of a probe; however, one other effect must be considered in some cases. If multiple short circuits exist, and one closer to the tone generator has higher resistance than the others, two or more branching-loop currents may be established, masking the location of the first short. It is then necessary to begin the location process at the far end of the cable, clearing each short circuit before proceeding to locate the next.

While the TDR finds the approximate location of short circuits with equal ease in shielded and unshielded cables, the precise location by the tone generator method is significantly more difficult in shielded cable. The shield severely attenuates the signal, and the generator must be capable of supplying a range of frequencies in order to provide a penetrating signal. The probe must have high sensitivity.

The tone generator utilized may be included in the same enclosure with the TDR, to provide immediate use without changing connections after the TDR's approximation has been obtained, or it may be a separate item to be used alone. Figure 14 shows a miniature, low-cost tone generator and probe combination

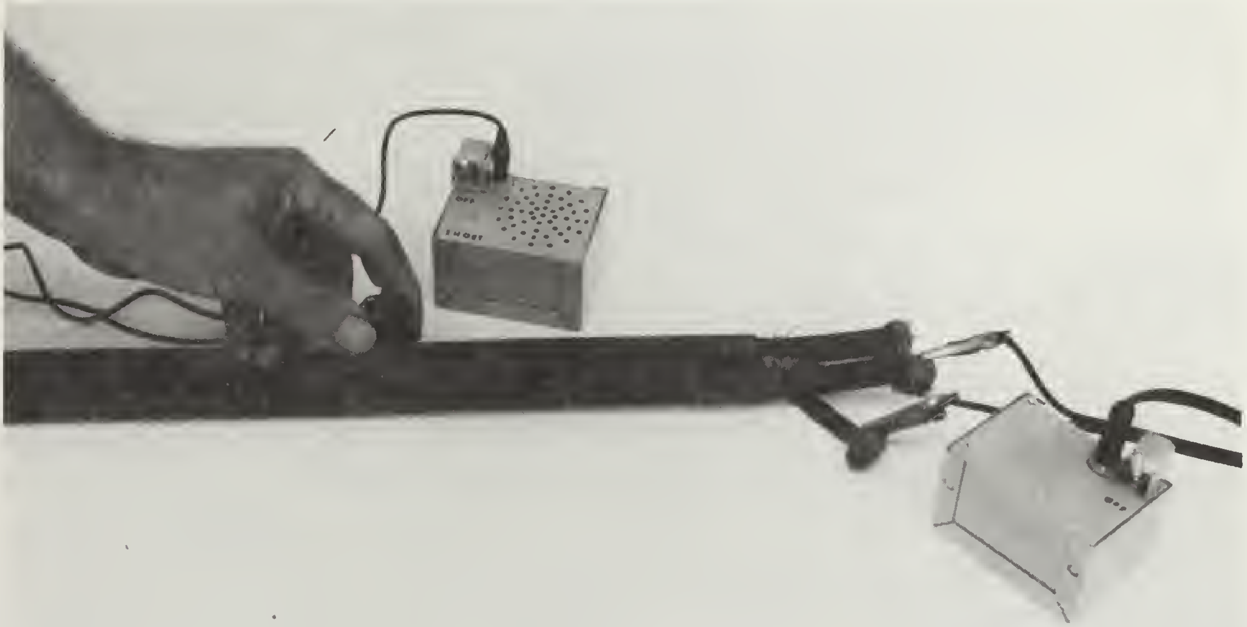

FIGURE 14. - Low-cost tone generator-probe set for short-circuit location.

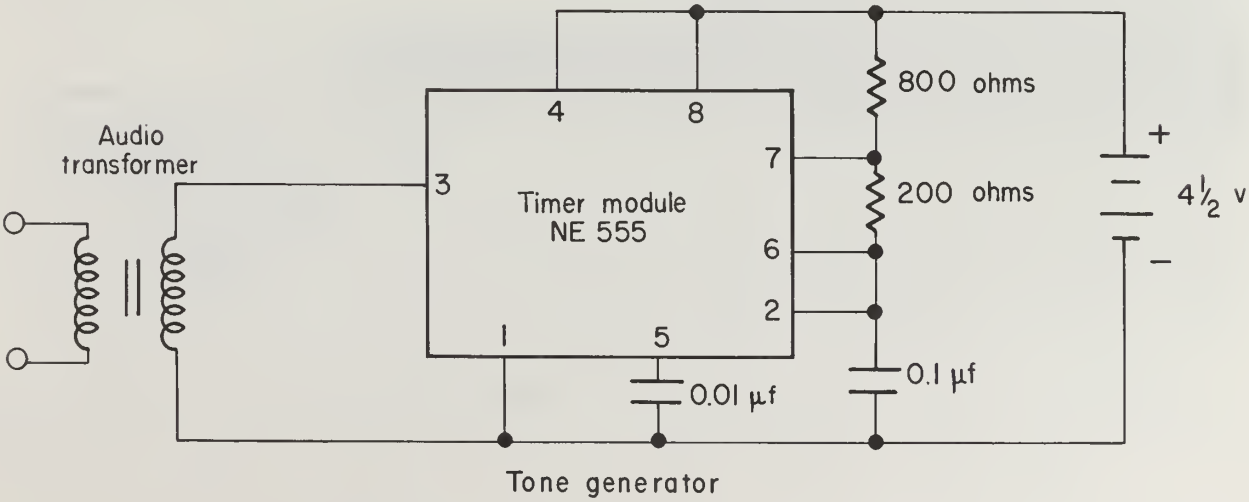
Audio transformer
Timer module NE 555
4
8
7
3
6
2
1
5
800 ohms
200 ohms
0.01 µf
0.1 µf
+
−
4½ v
Tone generator

FIGURE 15. - Tone generator schematic diagram.

designed by the Bureau for locating low-resistance short circuits. The schematic diagrams of the tone generator and the probe are presented in figures 15 and 16, respectively.

With a few modifications, the basic system can be adapted to locate open circuits through sensing the electrostatic field. The modified set is shown in figure 17, with schematics presented in figures 18 and 19.

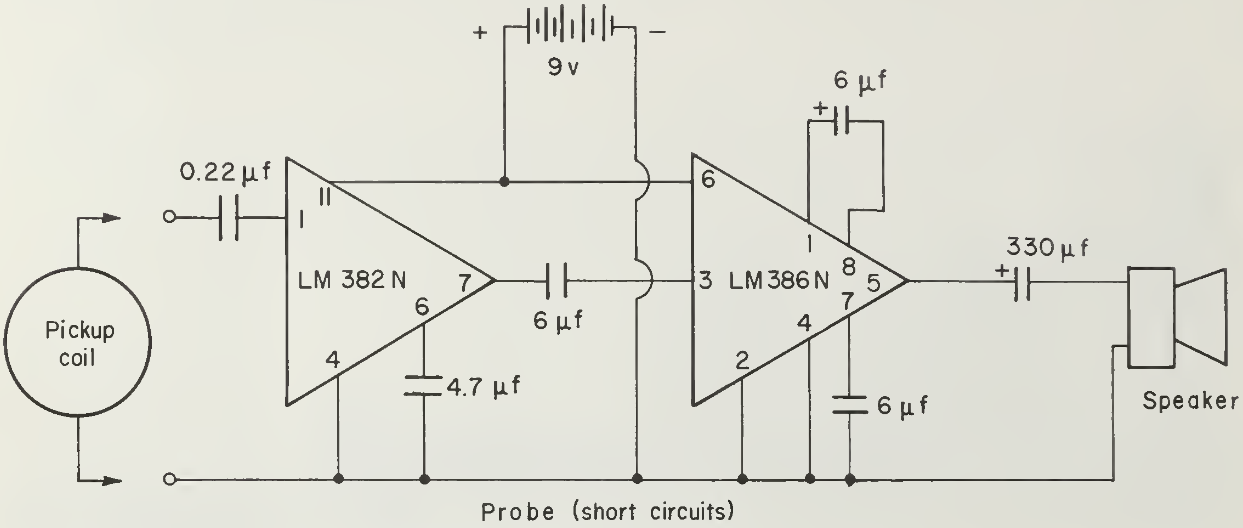
+
9v
−
6 µf
0.22 µf
LM 382 N
1
11
7
6
4
4.7 µf
6 µf
6
1
8
3
LM386N
5
7
4
2
6 µf
330 µf
Pickup coil
Speaker
Probe (short circuits)

FIGURE 16. - Audioprobe schematic diagram.

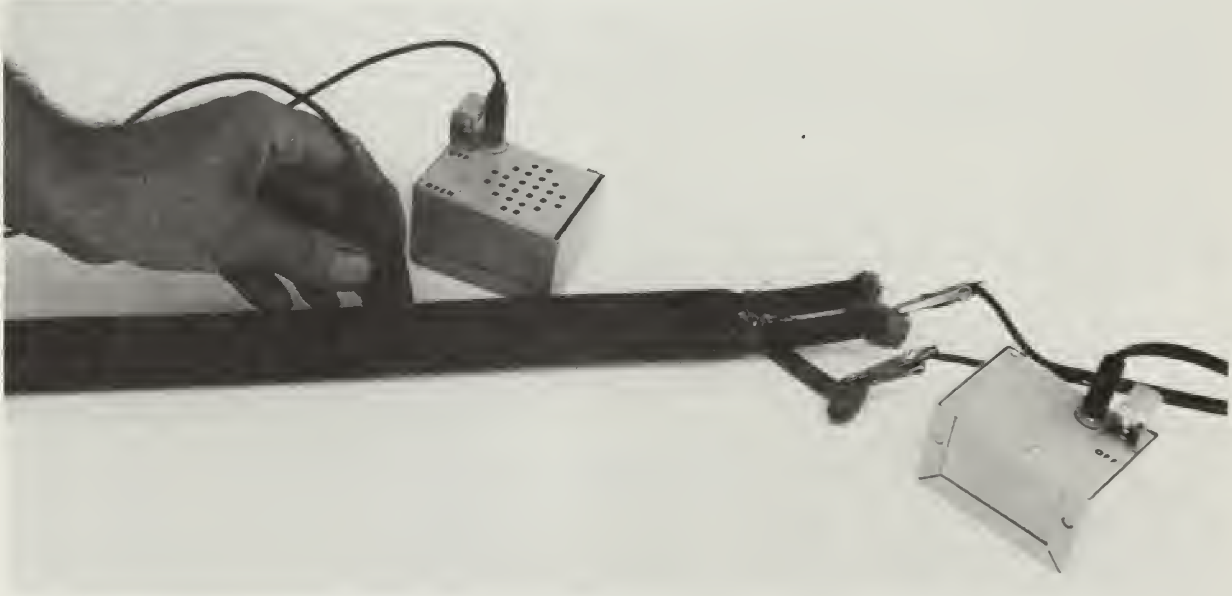

FIGURE 17. - Low-cost set for open-circuit location.

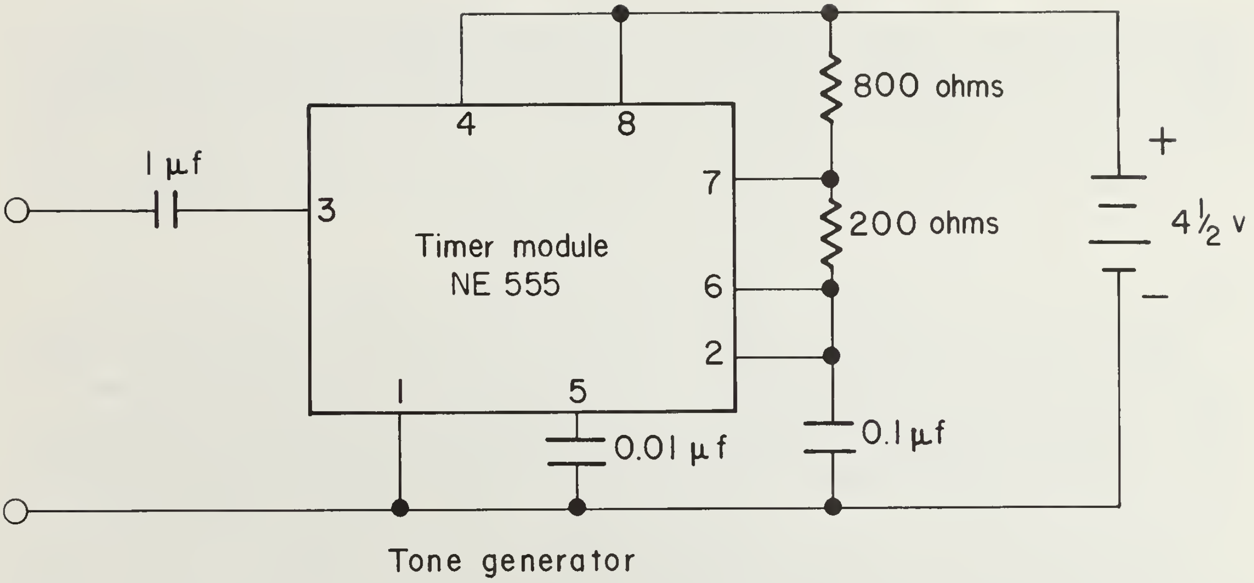
1 µf
3
4
8
7
Timer module
NE 555
6
2
1
5
0.01 µf
0.1 µf
800 ohms
200 ohms
+
4½ v
−
Tone generator

FIGURE 18. - Tone generator modification for open-circuit location.

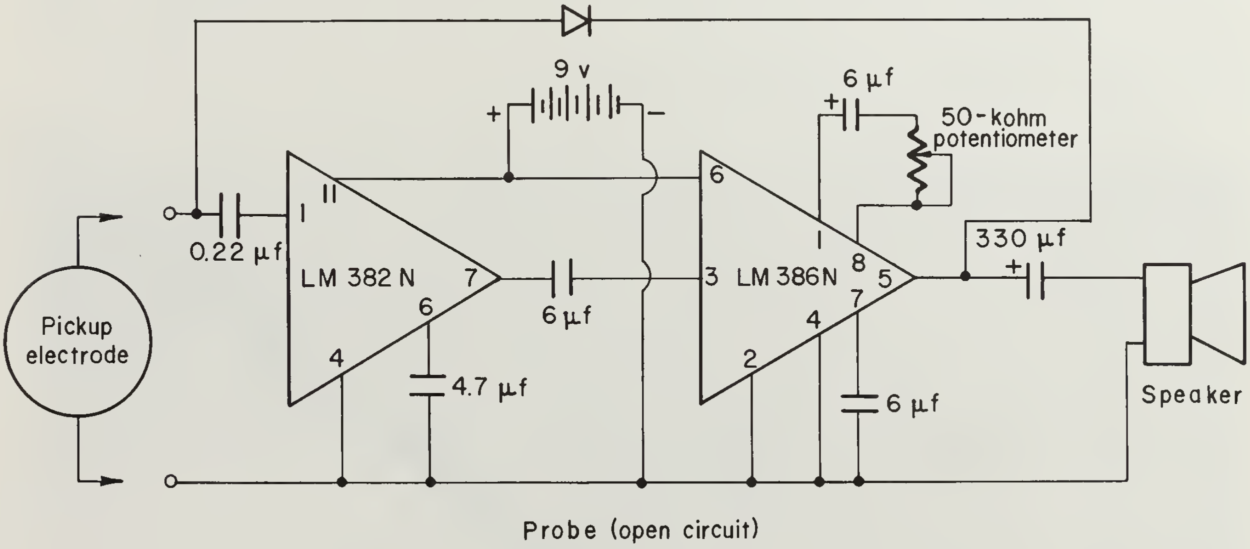
9 v
+
−
6 µf
+
50-kohm
potentiometer
0.22 µf
11
1
LM 382 N
7
6
4
4.7 µf
6 µf
6
3
LM 386N
1
8
5
7
4
2
6 µf
330 µf
+
Speaker
Pickup
electrode
Probe (open circuit)

FIGURE 19. - Modified audioprobe schematic diagram.

While a switching scheme has not yet been adopted for these particular units, there is little doubt that the changeover from short-circuit to open-circuit location mode could be accomplished by switching a single system, just as is done for the combination incorporated with the TDR, rather than having one complete circuit for open circuits and another for short circuits.

One apparent disadvantage of the method involving only a tone generator and probe--that of having to walk the entire length of a cable while holding the probe in contact--can be avoided to a large extent by using a bracketing technique. After listening for the tone at one end, spot-check every hundred feet or so along the length, and when a change in tone is experienced, go back half the distance from the last spot and listen again. Successively reduce the separation between readings until the cable length that must be continuously probed is a manageable distance.

Other methods of utilizing the tone-generator-plus-probe approach are currently under study at the Bureau of Mines.

INFRARED DETECTION

There might be one exception to the desirability of isolating the cable prior to fault location attempts. This would occur when an infrared detector probe is immediately available in the mine section just after a fault has occurred. Cable condition could then be explored before the heat dissipated in the fault has distributed itself over the cable and its surroundings.

The more common case of infrared fault detection, however, requires that the cable be isolated from source and machine, and connected to a high current-low voltage power supply. Only faults of resistance less than 70 ohms can be located in practice, and the ideal fault for the device is a "bolted" short created by a strand of wire that pierces the interconductor insulation. The infrared probe developed by the Bureau of Mines (fig. 20) is sensitive to a variation of 1° or 2° F, which can be obtained by dissipating about 30 watts at the fault for a few minutes of warmup time.

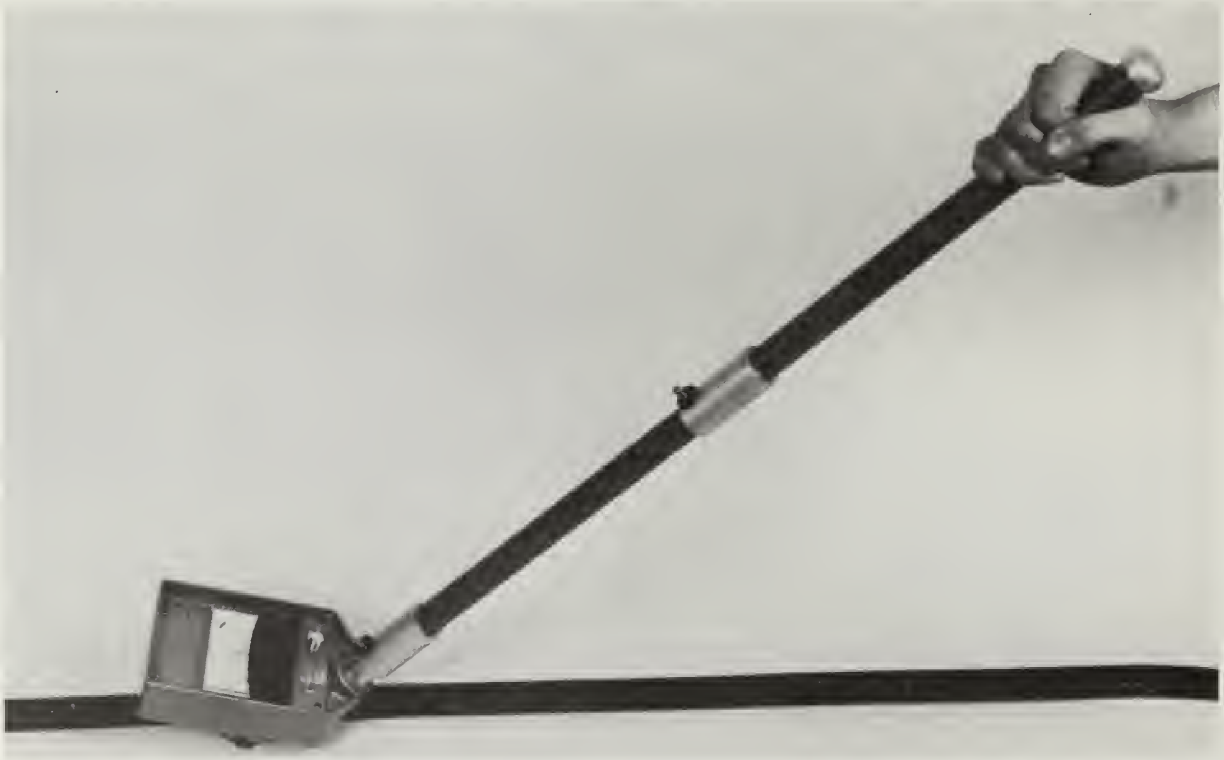

FIGURE 20. - Bureau of Mines infrared probe.

Despite its limitations, there is an important reason for using infrared detection. It is easily applied to shielded cable. Cable shielding strongly attenuates electric and magnetic fields but does not block the transmittal of heat. A useful combination of instruments for shielded-cable installations is a TDR, a high-current source, and an infrared probe.

SWEPT FREQUENCY METHOD

An approach strongly analogous to the TDR method is the frequency domain reflectometer (FDR) system, currently the subject of Bureau-sponsored research at Stanford Research Institute. In this system, connection is made to the faulted cable pair at the power center end, and the characteristic impedance is sounded by a signal whose frequency is swept from 10 MHz to 45 MHz at a sweep rate of 100 MHz per second. A directional coupler picks off the reflected signal, which is then mixed to produce low-frequency tones in which the tone frequency is given by the equation

$$f_{\tau} = \tau S,$$

where τ is the round-trip time to a reflecting discontinuity and S is sweep rate. The round-trip time is then related to the distance along the cable by digital circuitry.

An advantage this system has over the TDR is that relatively large energy can be directed into the cable without necessitating a high pulse voltage. Because of this and the frequency range utilized, the signal can penetrate shielding, and the precise location of a fault can be bracketed by placing a hand at various positions along the cable while the display is being observed to note location indications and relate them to that for the fault. Twelve field-test models of the FDR system will be fabricated by the contractor for evaluation in various mine and cable shop situations.

SUMMARY AND CONCLUSIONS

Table 1 lists the various fault-location methods examined during this research with a brief comment on each. The steps to locate a fault are, in general, as follows:

1. Isolate the cable, disconnecting from the power center, and if possible disconnecting or switching off at the machine.

2. Identify the character of the fault, using a Megger and, if necessary, an ohmmeter or multimeter to obtain a more precise reading for low resistance.

3. Approximately locate the fault using a terminal method such as the TDR.

4. More precisely locate the fault by exploring the suspected region of the cable with a probe responsive to an audio signal supplied by a source at the terminals. Short circuits in shielded cables are not in practice locatable by this audio signal but may be located by an infrared detector probe which responds to the temperature rise at the fault.

Several methods of trailing-cable-fault location have been described; none are universally applicable, but all have some possibility of application, depending on the individual circumstances. The easiest present method to use for open circuits and low-resistance short circuits in either unshielded or shielded cable is the time domain reflectometer with digital readout. At present the accuracy of this system is somewhat limited, and in any case the electrical reading must somehow be correlated with distance along the exterior of the cable. Therefore, a probe method of one type or another is usually employed after the approximate location is found by the TDR. For unshielded cable, an audiofrequency probe system is very effective for finding open circuits and low-resistance short circuits. An infrared probe system works well for low-resistance short circuits in shielded as well as unshielded cables.

Current research promises to extend the range of application of the TDR with regard to the fault resistance values that can be detected and to the precision of the location measurement. Research into FDR methods may eliminate the necessity for a separate electronic probe for relating the length information to an actual physical location, in shielded and unshielded cable, by reacting to the presence of a passive element such as a man's hand.

Meanwhile, as none of the above methods has been demonstrated to be completely effective in all situations, it is at present desirable to have a variety of instruments available for cable-fault locating, preferably assembled in kit form.

TABLE 1. - Fault-location methods examined by the Bureau of Mines

Method	Equipment used	Comment
Megger.............	Biddle Co. Major Megger (many others available).	Preliminary to fault locating.
Murray loop........	Breadboard (General Radio, Leeds & Northrop, etc., bridges may be used).	Short circuits only; low or high resistance.
Capacitance bridge..	General Radio Co. 1608A impedance bridge (smaller devices available).	Open circuits only.
Thumper............	Biddle Co. 650125 impulser with 40-kv dc test set.	Aboveground only.
Breakdown..........	Biddle Co. 40-kv test set, water bath.	Do.
TDR (time domain reflectometer).	FMC/Bureau, CMU/Bureau, Tektronix 1501.	Open circuits and up to 1,000-ohm short circuits, at present.
Tone generator plus probe.	FMC/Bureau, CMC/Bureau, Biddle HV tone generator, with cable route tracer.	Open circuits and low-resistance (4 ohms or less) short circuits; unshielded cable only.
155-v 60-kHz source plus probe.	Pyott-Boone Megatron, Biddle cable route tracer.	Short circuits only; unshielded cable only.
Infrared probe.....	FMC/Bureau, Barnes Engineering Co. PRT-10.	Short circuits only.

INT.-BU.OF MINES,PGH.,PA. 23226

☆U.S. GOVERNMENT PRINTING OFFICE: 1978-703-103/64

622.09
Un32mo

RI 8305

Bureau of Mines Report of Investigations/1978

Low-Temperature Heat Capacities and High-Temperature Enthalpies of Cuprous and Cupric Sulfides

DEPOSITORY
NOV 17 1978
UNIV. OF ILL. LIBRARY
AT URBANA-CHAMPAIGN

UNITED STATES DEPARTMENT OF THE INTERIOR

Report of Investigations 8305

Low-Temperature Heat Capacities and High-Temperature Enthalpies of Cuprous and Cupric Sulfides

By M. J. Ferrante, J. M. Stuve, G. E. Daut, and L. B. Pankratz

March 3 1849

UNITED STATES DEPARTMENT OF THE INTERIOR
Cecil D. Andrus, Secretary

BUREAU OF MINES

This publication has been cataloged as follows:

Low-temperature heat capacities and high-temperature enthalpies of cuprous and cupric sulfides / by M. J. Ferrante ... [et al.] [Washington] : U.S. Dept. of the Interior, Bureau of Mines, 1978.

22 p. : diagrs. ; 27 cm. (Report of investigations - Bureau of Mines ; 8305)

Bibliography: p. 19-22.

1. Copper - Thermal properties. 2. Copper compounds - Thermal properties. 3. Enthalpy. I. Ferrante, Michael J. II. United States. Bureau of Mines. III. United States. Bureau of Mines. Report of investigations - Bureau of Mines ; 8305.

TN23.U7 no. 8305 622.06173

U.S. Dept. of the Int. Library

CONTENTS

Page

Abstract.. 1
Introduction.. 1
Materials... 3
Experimental work and results..................................... 3
  Low-temperature heat capacities................................. 3
  High-temperature enthalpies..................................... 5
Standard enthalpies and Gibbs energies of formation............... 14
Discussion.. 16
References.. 19

ILLUSTRATIONS

1. Low-temperature heat capacities.............................. 4
2. High-temperature mean heat capacities........................ 12

TABLES

1. Experimental low-temperature heat capacities................. 6
2. Low-temperature thermodynamic properties of Cu_2S(c)........ 7
3. Low-temperature thermodynamic properties of CuS(c)........... 8
4. Experimental high-temperature enthalpies..................... 9
5. High-temperature thermodynamic properties of Cu_2S(c,l)..... 10
6. High-temperature thermodynamic properties of CuS(c).......... 11
7. Formation data for 2Cu(c) + S(c,l) = Cu_2S(c)................ 15
8. Thermodynamic data for the reaction 2Cu(c,l) + $1/2S_2$(g) = Cu_2S(c,l) 15
9. Formation data for Cu(c) + S(c,l) = CuS(c)................... 15
10. Thermodynamic data for the reaction Cu(c) + $1/2S_2$(g) = CuS(c)...... 16

LOW-TEMPERATURE HEAT CAPACITIES AND HIGH-TEMPERATURE ENTHALPIES OF CUPROUS AND CUPRIC SULFIDES

by

M. J. Ferrante,[1] J. M. Stuve,[1] G. E. Daut,[2] and L. B. Pankratz[1]

ABSTRACT

Low-temperature heat capacities and high-temperature enthalpies for synthetic Cu_2S and CuS were measured. This investigation is part of the Bureau of Mines goals to provide thermodynamic data essential to the more efficient processing of copper ores, and thereby minimize the current dislocations in energy, environment, and mineral supply. Heat capacities were measured with an adiabatic calorimeter from 5 to 310 K, and resulted in $S^\circ_{298} = 27.76$ for $Cu_2S(c)$ and $S^\circ_{298} = 16.05$ cal/deg mole for CuS(c). Low-temperature values are tabulated for Cp°, S°, $-(G^\circ-H^\circ_0)/T$, and $H^\circ-H^\circ_0$. Enthalpies were measured with a copper block calorimeter from 298.15 to 1,600 K for $Cu_2S(c,l)$ and 298.15 to 780 K for CuS(c). The thermal behavior of CuS showed no transitions or other significant anomalies for the low- or high-temperature investigations. Cu_2S showed reversible transitions at 376 K with an isothermal heat absorption of 0.865 kcal/mole, 720 K with an isothermal absorption of 0.280 kcal/mole, and approximately 1,400 K (congruent melting point) with a heat of fusion of 3.070 kcal/mole. High-temperature data are tabulated for $H^\circ-H^\circ_{298}$, Cp°, S°, and $-(G^\circ-H^\circ_{298})/T$. Enthalpies are also expressed in equation form. The low- and high-temperature data were combined with data from the literature to calculate and tabulate ΔHf°, ΔGf°, and log Kf as a function of temperature.

INTRODUCTION

The present investigation of the low-temperature heat capacities and high-temperature enthalpies of synthetic cuprous sulfide and cupric sulfide is one in a series of thermodynamic studies by the Bureau of Mines on metallurgically important copper compounds. Despite the importance of cuprous and cupric sulfides in the processing of copper, thermodynamic data for these substances are either incomplete or inadequate. Such thermodynamic properties are essential for more efficient extraction of copper from sulfide ores by roasting, and for the control of sulfur oxide pollutants that are formed during the roasting process. Thus, the thermodynamic data would foster

---

[1] Research chemist.

[2] Physical science technician.

All authors are with the Albany Metallurgy Research Center, Bureau of Mines, Albany, Oreg.

maximum productivity and minimum energy requirements in the processing of copper and related substances.

In this investigation, low-temperature heat capacities were measured with an adiabatic calorimeter, and high-temperature enthalpies with a drop calorimeter incorporating a copper block. Results from these calorimeters were combined with heats of formation at 298.15 K from the literature to provide tabulated values of the principal thermodynamic properties for cuprous sulfide (Cu_2S) and cupric sulfide (CuS).

This study of CuS (covellite) was undertaken: (1) To extend the low-temperature heat capacities of Anderson (2)[3] below 56 to near 0 K, and (2) to measure high-temperature enthalpies.

Thermodynamic studies on Cu_2S (chalcocite) were undertaken: (1) To extend Anderson's low-temperature data below 56 to near 0 K; (2) to extend the heat capacity values reported by Kubaschewski (26) and by Jost and Kubaschewski (20) above 823 K; (3) to measure high-temperature enthalpies, because values calculated by Kelley (22) from 350 to 1,400 K were based on the incomplete and scattered data reported by Bellati and Lussana (5) in 1888-89 for temperature between 273 and 463 K, by Bornemann and Hengstenberg (6) in 1920 for the range 273 to 1,373 K, and by White (47) in 1933 for 303 to 1,173 K; and (4) to measure enthalpies of the liquid state.

The present investigation established a transition temperature of 720 K for Cu_2S, which markedly differs from 623 K calculated by Kelley from the scattered data of investigators given previously. The transition temperatures of 376, 720, and 1,400 K of Cu_2S from the present investigation are in agreement with phase equilibria and thermodynamic studies reported in references listed later. Because such studies on copper sulfides have received considerable attention in recent years from scientists of different disciplines, publications related to phase transitions are widely dispersed in the literature of various fields. While it is beyond the scope of this paper to list all authors who have done work on Cu_2S and CuS, a listing of some publications provides a guide to the literature for locating original investigators. These references are King, Mah, and Pankratz (24), Craig and Scott (8), Roseboom (36), Yund and Kullerud (48), Hansen and Anderko (16), and supplements to the last by Elliott (11), and Shunk (38).

In recent investigations of thermodynamic properties of copper compounds by the Bureau of Mines, Stuve, Richardson, and King (39) measured low-temperature heat capacities and the standard enthalpy of formation of copper oxysulfate; Ko and Richardson (25) reported standard enthalpies of formation for cupric and cuprous bromides; Richardson and Brown (33) provided the enthalpy of formation for malachite; Ferrante (13) measured the high-temperature enthalpies of copper sulfate and oxysulfate; Taylor, Brown, and Taylor (40) obtained the heat of formation and low-temperature heat capacities of cuprous cyanide; Pankratz and King (32) investigated enthalpies above

---

[3] Underlined numbers in parentheses refer to items in the list of references at the end of the report.

298.15 K for chalcopyrite and bornite; Mah, Pankratz, Weller, and King (28) provided heat capacities, enthalpies, enthalpies of formation, and Gibbs energies of formation for cuprous and cupric oxides; Adami and King (1) reported the heat of formation for anhydrous copper sulfate; Weller (45) measured the low-temperature heat capacities of anhydrous copper sulfate; and Barany, Pankratz, and Weller (3) investigated the low-temperature heat capacities, high-temperature enthalpies, and standard enthalpies of formation of cuprous and cupric ferrites. In addition, a monograph on the thermodynamic properties of copper and its inorganic compounds was compiled by King, Mah, and Pankratz (24).

MATERIALS

Synthetic Cu_2S was prepared by reacting copper with appropriate amounts of sublimed sulfur. The copper was freshly prepared in the form of powder by converting a plate of 99.999 pct purity to cupric oxide powder, followed by hydrogen reduction at 800° C. The copper and sulfur were sealed in an evacuated Vycor[4] bulb and heated at 285° C for 1 day, and 685° C for 5 days. This product was ground, screened, analyzed, and adjusted for composition. The same heating cycle was then repeated. Chemical analyses of the sample showed 79.79 pct copper and 20.20 pct sulfur, compared with the theoretical 79.85 pct copper and 20.15 pct sulfur. Optical emission spectroscopy revealed that the sample contained less than 0.01 pct metallic impurities. An X-ray diffraction pattern of the product matched that given in the ASTM Catalog of X-ray Powder Data for orthohombic Cu_2S, which Evans (12) recently showed actually has a complicated monoclinic structure.

Synthetic CuS was prepared in the same manner as described for Cu_2S except for heating cycles. Reactants were heated at 285° C for 1 day, 500° C for 2 days, and 400° C for 6 days. After analyses, the composition of the product was adjusted and the same heating cycle repeated. Final chemical analyses showed 66.43 pct copper and 33.50 pct sulfur compared with the theoretical 66.46 pct copper and 33.54 pct sulfur. No metallic impurities were detected by optical emission spectroscopy. The X-ray diffraction pattern agreed with that given in the ASTM catalog for hexagonal CuS.

EXPERIMENTAL WORK AND RESULTS

Results of measurements from calorimetric investigations are expressed in terms of the thermochemical calorie (1 calorie = 4.1840 joules). Temperatures refer to the International Practical Temperature Scale of 1968 (7). Weighings were corrected to vacuum. The 1973 Table of Atomic Weights (17) gave molecular weights of 159.152 for Cu_2S and 95.606 for CuS.

Low-Temperature Heat Capacities

Heat capacity measurements of the samples were made from 5 to 310 K with an adiabatic calorimeter described by Stuve, Richardson, and King. Sample temperatures in the range of 16 to 310 K were measured with a platinum

---

[4] Reference to specific brand names is made for identification only and does not imply endorsement by the Bureau of Mines.

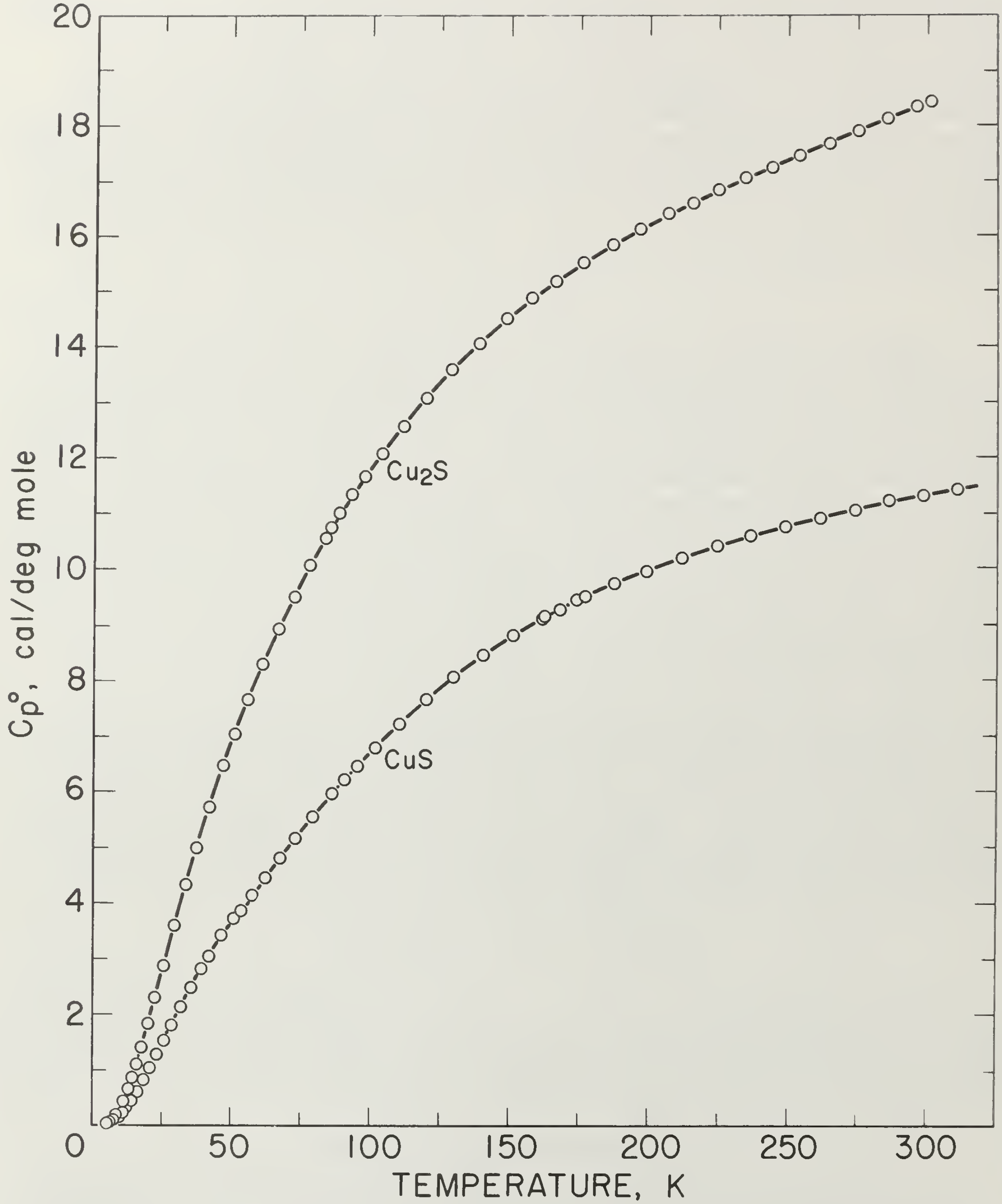

FIGURE 1. - Low-temperature heat capacities.

thermometer calibrated by the National Bureau of Standards. Temperatures below 16 K were measured with a calibrated germanium thermometer. Temperature changes in the calorimeter as small as ±0.0001 K were determined potentiometrically.

The calorimeter has a copper sample vessel with a capacity of 90 ml which was filled with a sample mass of 272.781 g Cu_2S or 109.468 g CuS. After the vessel was evacuated, it was backfilled with about 5.4×10^{-5} mole of helium gas for better thermal exchange with the powdered sample. Experimental measurements of heat capacity for both sulfides are listed in table 1 and shown graphically in figure 1. The overall uncertainty of measurements for either compound was estimated to be ±5 pct below 10 K, ±1 pct from 10 to 30 K, ±0.1 pct from 30 to 310 K. Measurements for Cu_2S generally had lower deviations from the smooth curve than those for CuS. Measured heat capacities of Cu_2S were a smooth function of temperature, whereas those for CuS had a very slight bump around 48 to 52 K. No transitions were encountered with either sulfide over the measured range of temperature.

Heat capacities of the sulfides were extrapolated to 0 K by plotting Cp/T versus T^2. These extrapolated data and experimental values were computer fitted with smooth curves by polynomial functions (21). These functions were then used to calculate the smooth heat capacities and related thermodynamic quantities at selected temperatures shown in tables 2-3.

High-Temperature Enthalpies

Enthalpies above 298.15 K were measured with a drop calorimeter described by Douglas and King (9). This isothermal-jacketed calorimeter has a copper block with a heat capacity of approximately 1.51 kcal/deg. The resistance thermometer was wound around the copper block and it was of the transposed bridge-type described by Maier (29). The apparatus was modified to incorporate a more sensitive potentiometer and null detector system. This system can resolve temperature changes equivalent to ±0.00005 K. The temperature of the sample in the furnace was measured with a platinum-10 pct rhodium versus platinum thermocouple, which was calibrated against the melting point of pure gold. Before and after enthalpy measurements of a substance, the calorimeter was calibrated electrically and the entire apparatus checked by measuring the enthalpy of pure magnesium oxide (periclase). The mass of a sample plus container was periodically checked for constancy during experimental measurements.

Sample containers for experimental measurements were pure silica-glass capsules; enthalpies for empty capsules were measured in separate experiments. Capsules were filled with powdered samples, evacuated, and fusion sealed with a flame while the portion of the capsule containing the sample was immersed in ice water. The sample mass of CuS was 7.79049 g. Sample masses for Cu_2S were 7.82646, 7.80144, 8.17838, and 8.84168 g. Extra Cu_2S samples were necessary to establish the curve of the enthalpy function in the liquid state, that is, above 1,400 K, because the glass capsules cracked in the calorimeter during measurements above the melting point.

TABLE 1. - Experimental low-temperature heat capacities

T, K	Cp°, cal/deg mole	T, K	Cp°, cal/deg mole	T, K	Cp°, cal/deg mole
			$Cu_2S(c)$		
5.84	0.063	46.85	6.474	148.58	14.519
6.43	.084	50.98	7.036	157.55	14.887
7.32	.123	55.74	7.653	166.03	15.19
8.48	.195	60.93	8.292	176.07	15.54
9.72	.303	66.58	8.929	186.57	15.86
11.15	.454	72.24	9.500	196.44	16.13
12.77	.653	77.97	10.060	206.48	16.40
14.28	.864	83.35	10.554	215.39	16.61
15.80	1.100	85.43	10.751	224.62	16.84
17.57	1.411	88.37	11.012	234.35	17.05
19.77	1.832	92.85	11.338	243.98	17.25
22.45	2.304	97.52	11.670	254.12	17.47
25.52	2.874	103.82	12.095	264.60	17.68
29.16	3.602	111.30	12.577	274.99	17.90
33.15	4.334	119.58	13.082	285.29	18.12
37.18	4.985	128.68	13.595	295.65	18.33
41.80	5.720	138.60	14.076	301.27	18.45
			CuS(c)		
5.16	0.034	31.70	2.125	140.22	8.455
5.41	.036	35.41	2.479	150.91	8.798
5.71	.041	39.13	2.815	161.71	9.107
6.31	.057	42.01	3.039	162.20	9.130
6.55	.063	46.25	3.429	167.86	9.258
7.05	.077	50.57	3.728	174.06	9.434
7.57	.094	53.40	3.859	176.96	9.490
8.16	.116	57.51	4.135	187.58	9.731
8.88	.145	62.15	4.453	198.94	9.958
9.85	.188	67.35	4.802	211.63	10.185
11.06	.252	72.93	5.155	224.32	10.406
12.46	.336	78.99	5.536	236.46	10.586
14.21	.456	86.04	5.956	248.80	10.749
16.20	.624	90.37	6.221	261.35	10.902
18.48	.831	95.06	6.460	273.78	11.041
20.68	1.035	101.48	6.799	286.05	11.202
23.14	1.277	110.17	7.218	298.25	11.289
25.75	1.538	119.91	7.653	310.43	11.411
28.43	1.804	129.73	8.055		

TABLE 2. - Low-temperature thermodynamic properties of $Cu_2S(c)$

T, K	Cp°, cal/deg mole	S°, cal/deg mole	$-(G°-H°_0)/T$, cal/deg mole	$H°-H°_0$, cal/mole
6	0.068	0.031	0.011	0.122
10	.328	.116	.033	.830
15	.976	.362	.097	3.973
20	1.849	.759	.210	10.982
25	2.803	1.274	.370	22.599
30	3.747	1.869	.569	38.992
35	4.632	2.514	.801	59.97
40	5.448	3.186	1.056	85.20
45	6.212	3.872	1.331	114.36
50	6.909	4.564	1.620	147.19
60	8.178	5.938	2.225	222.76
70	9.290	7.284	2.852	310.23
80	10.258	8.589	3.488	408.08
90	11.105	9.847	4.125	515.0
100	11.851	11.057	4.759	629.8
110	12.515	12.218	5.384	751.7
120	13.111	13.333	6.001	879.9
130	13.649	14.404	6.606	1,013.8
140	14.136	15.43	7.196	1,152.7
150	14.577	16.42	7.777	1,296.4
160	14.976	17.38	8.354	1,444.2
170	15.34	18.30	8.914	1,595.7
180	15.66	19.18	9.453	1,750.8
190	15.96	20.04	9.993	1,908.9
200	16.23	20.86	10.511	2,069.9
210	16.49	21.66	11.024	2,233.5
220	16.72	22.43	11.523	2,399.6
230	16.95	23.18	12.015	2,567.9
240	17.17	23.91	12.500	2,738.5
250	17.38	24.61	12.965	2,911.3
260	17.59	25.30	13.430	3,086.2
270	17.80	25.97	13.884	3,263.1
273.15	17.86	26.17	14.011	3,319.3
280	18.00	26.62	14.327	3,442.1
290	18.21	27.25	14.756	3,623.2
298.15	18.38	27.76	15.11	3,772.2

TABLE 3. - Low-temperature thermodynamic properties of CuS(c)

T, K	Cp°, cal/deg mole	S°, cal/deg mole	$-(G^\circ - H^\circ_0)/T$, cal/deg mole	$H^\circ - H^\circ_0$, cal/mole
6	0.052	0.014	0.001	0.077
10	.193	.069	.016	.527
15	.522	.204	.054	2.257
20	.968	.413	.116	5.942
25	1.466	.682	.201	12.018
30	1.962	.994	.308	20.595
35	2.433	1.332	.429	31.594
40	2.883	1.686	.564	44.893
45	3.316	2.051	.709	60.40
50	3.678	2.421	.862	77.97
60	4.325	3.147	1.182	117.91
70	4.972	3.863	1.514	164.42
80	5.593	4.568	1.852	217.26
90	6.179	5.261	2.193	276.15
100	6.723	5.940	2.533	340.70
110	7.222	6.605	2.874	410.46
120	7.675	7.253	3.211	484.99
130	8.081	7.884	3.547	563.8
140	8.444	8.496	3.878	646.5
150	8.769	9.090	4.206	732.6
160	9.060	9.665	4.529	821.7
170	9.321	10.222	4.847	913.7
180	9.559	10.762	5.161	1,008.1
190	9.775	11.285	5.470	1,104.8
200	9.974	11.791	5.774	1,203.5
210	10.157	12.282	6.072	1,304.2
220	10.326	12.759	6.365	1,406.6
230	10.482	13.221	6.653	1,510.7
240	10.628	13.671	6.937	1,616.2
250	10.764	14.107	7.214	1,723.2
260	10.893	14.532	7.488	1,831.5
270	11.016	14.945	7.756	1,941.0
273.15	11.054	15.07	7.833	1,975.8
280	11.134	15.35	8.022	2,051.8
290	11.244	15.74	8.279	2,163.7
298.15	11.324	16.05	8.485	2,255.6

Experimental enthalpies relative to 298.15 K for cuprous and cupric sulfides are listed in table 4. To obtain the best fit of smooth curves to these data, the values were fitted with polynomial functions with the aid of a computer. During this procedure, care was taken to merge the high-temperature enthalpies smoothly with the low-temperature data given in the previous section. The polynomial functions were then used to calculate smooth values of enthalpies and related properties of heat capacities, entropies, and Gibbs energy functions above 298.15 K. These thermodynamic quantities are listed in tables 5-6 at selected temperature intervals. Values at 298.15 and 300 K were taken from the low-temperature data. Enthalpies greater than 10 and less than 50 kcal/mole were rounded to the nearest 0.005 unit. Extrapolation of CuS values to 780 K from the last valid experimental measurement at 740.9 was based on reasonable projections of the smooth values. The constancy of the heat capacity data in the liquid state of Cu_2S permitted extrapolation of data to 1,600 K from the last valid measurement of 1,509.3 K. The standard error of measurement was 0.1 pct for CuS and 0.2 pct or less for Cu_2S. The latter excludes 0.9 pct for the three measurements below the 376 K transition, where the precision of measurements is significantly less than it is above 400 K. The enthalpies of tables 5-6 are estimated to have an absolute uncertainty of about ±0.4 pct.

TABLE 4. - Experimental high-temperature enthalpies

T, K	$H^\circ - H^\circ_{298}$, kcal/mole	T, K	$H^\circ - H^\circ_{298}$, kcal/mole	T, K	$H^\circ - H^\circ_{298}$, kcal/mole
		$Cu_2S(c,l)$			
350.7	0.990	628.7	8.115	747.9	10.901
360.3	1.184	639.2	8.347	800.1	11.932
370.2	1.391	686.5	9.356	846.8	12.858
380.2	2.462	700.5	9.671	895.4	13.822
399.4	2.910	710.3	9.870	1,004.6	15.963
399.4	2.928	719.5	10.165	1.084.1	17.540
453.5	4.197	719.7	10.059	1,109.6	18.001
497.3	5.192	720.5	10.212	1,205.5	19.888
548.3	6.343	720.9	10.283	1,304.4	21.816
595.9	7.402	726.0	10.480	[1]1,381.9	23.587
597.3	7.435	727.1	10.489	1,413.2	27.033
603.7	7.573	735.5	10.667	1,452.5	27.837
619.2	7.911	740.6	10.743	1,509.3	29.090
		CuS(c)			
402.0	1.214	580.7	3.454	713.0	5.221
421.0	1.445	590.1	3.578	722.3	5.345
456.0	1.878	600.6	3.715	732.6	5.491
506.6	2.507	618.7	3.959	740.9	5.603
540.8	2.942	637.6	4.207	[2]760.8	5.899
561.6	3.201	679.6	4.766	[3]779.4	6.241
569.7	3.308	700.3	5.044		

[1] Premelting.

[2] Probably decomposed.

[3] Decomposed.

TABLE 5. - High-temperature thermodynamic properties of $Cu_2S(c,l)$

T, K	Cp°, cal/deg mole	S°, cal/deg mole	$-(G^\circ-H^\circ_{298})T$, cal/deg mole	$H^\circ-H^\circ_{298}$, kcal/mole
298.15	18.38	27.76	27.76	0
300	18.42	27.88	27.77	.034
350	19.53	30.79	27.99	.981
[1]376	20.19	32.21	28.23	1.497
376	23.96	34.51	28.23	2.362
400	23.71	35.99	28.66	2.934
450	23.22	38.75	29.62	4.107
500	22.76	41.18	30.67	5.257
550	22.33	43.33	31.72	6.384
600	21.93	45.25	32.77	7.490
650	21.56	46.99	33.79	8.577
700	21.21	48.58	34.80	9.646
[1]720	21.09	49.17	35.18	10.070
720	19.83	49.56	35.18	10.350
750	19.81	50.37	35.78	10.945
800	19.77	51.65	36.73	11.935
850	19.73	52.85	37.65	12.920
900	19.70	53.97	38.52	13.905
950	19.66	55.04	39.37	14.890
1,000	19.62	56.04	40.17	15.875
1,050	19.59	57.00	40.95	16.855
1,100	19.55	57.91	41.70	17.830
1,150	19.52	58.78	42.42	18.810
1,200	19.48	59.61	43.12	19.785
1,250	19.44	60.40	43.80	20.755
1,300	19.41	61.16	44.44	21.730
1,350	19.37	61.90	45.09	22.695
[2]1,400	19.33	62.60	45.70	23.665
1,400	21.43	64.79	45.70	26.735
1,450	21.43	65.55	46.37	27.810
1,500	21.43	66.27	47.02	28.880
1,550	(21.43)	(66.98)	(47.66)	(29.950)
1,600	(21.43)	(67.65)	(48.26)	(31.025)

[1] Transition point of Cu_2S.

[2] Melting point of Cu_2S.

NOTE.--Values in parentheses are extrapolations.

TABLE 6. - High-temperature thermodynamic properties of CuS(c)

T, K	C_p°, cal/deg mole	S°, cal/deg mole	$-(G^\circ-H^\circ_{298})/T$, cal/deg mole	$H^\circ-H^\circ_{298}$, kcal/mole
298.15	11.324	16.05	16.05	0
300	11.339	16.12	16.05	.021
350	11.71	17.90	16.19	.599
400	12.02	19.49	16.51	1.192
450	12.31	20.92	16.92	1.800
500	12.58	22.23	17.39	2.422
550	12.85	23.44	17.88	3.058
600	13.10	24.57	18.39	3.707
650	13.35	25.63	18.91	4.368
700	13.60	26.63	19.43	5.042
750	13.84	27.57	19.93	5.728
780	(13.99)	(28.12)	(20.24)	(6.145)

NOTE.--Values in parentheses are extrapolations.

In addition to listing enthalpy values in tables 4-6 for Cu_2S and CuS, these data are shown graphically in figure 2 as $(H^\circ-H^\circ_{298})/(T-298.15)$ versus temperature. This expression is the mean heat capacity, and as such, is given in cal/deg mole. Although continuity was established down to 260 K during the merging of the high- and low-temperature data, the curves of figure 2 were extended only to the 300 K low-temperature value.

The curve of the mean heat capacity for CuS in figure 2 follows a regular course from 300 to 780 K. Decomposition of CuS was shown by the abnormally high thermal effect equivalent to 1.7 pct above the curve for the experimental measurement at 779.4 K, and by globular sulfur appearing on the interior wall of the glass capsule. The decomposition was also verified by X-ray diffraction analysis of the capsule contents, which showed that the sample contained a small amount of digenite ($Cu_{1.8}S$) and sulfur, in addition to CuS. However, a slight amount of decomposition probably occurred in the last reported measurement at 760.8 K. This measurement was 0.4 pct above the curve, whereas the previous seven measurements over a temperature range of 123 K varied only 0.04 pct or less from the curve. The decomposed sample would recombine to form CuS after heating at about 725 K for 2 hours in the sealed capsule. It was then found possible to reproduce enthalpy values previously obtained at lower temperatures. To test phase stability below 780 K, separate samples were cooled from 600 and 700 K to 298 K in the calorimeter in the same manner as for enthalpy measurements, and then subjected to X-ray diffraction analysis. In both cases, the diffraction patterns matched that of the starting material for the room-temperature form of hexagonal CuS.

The complex thermal behavior of Cu_2S is shown by the three reversible transitions in figure 2. Solid-solid transitions were found at 376 and 720 K with isothermal heat absorptions of 0.865 and 0.280 kcal/mole. Above each of these transitions, the heat capacity data of table 5 that were derived from enthalpies show the rather unusual behavior of decreasing values with

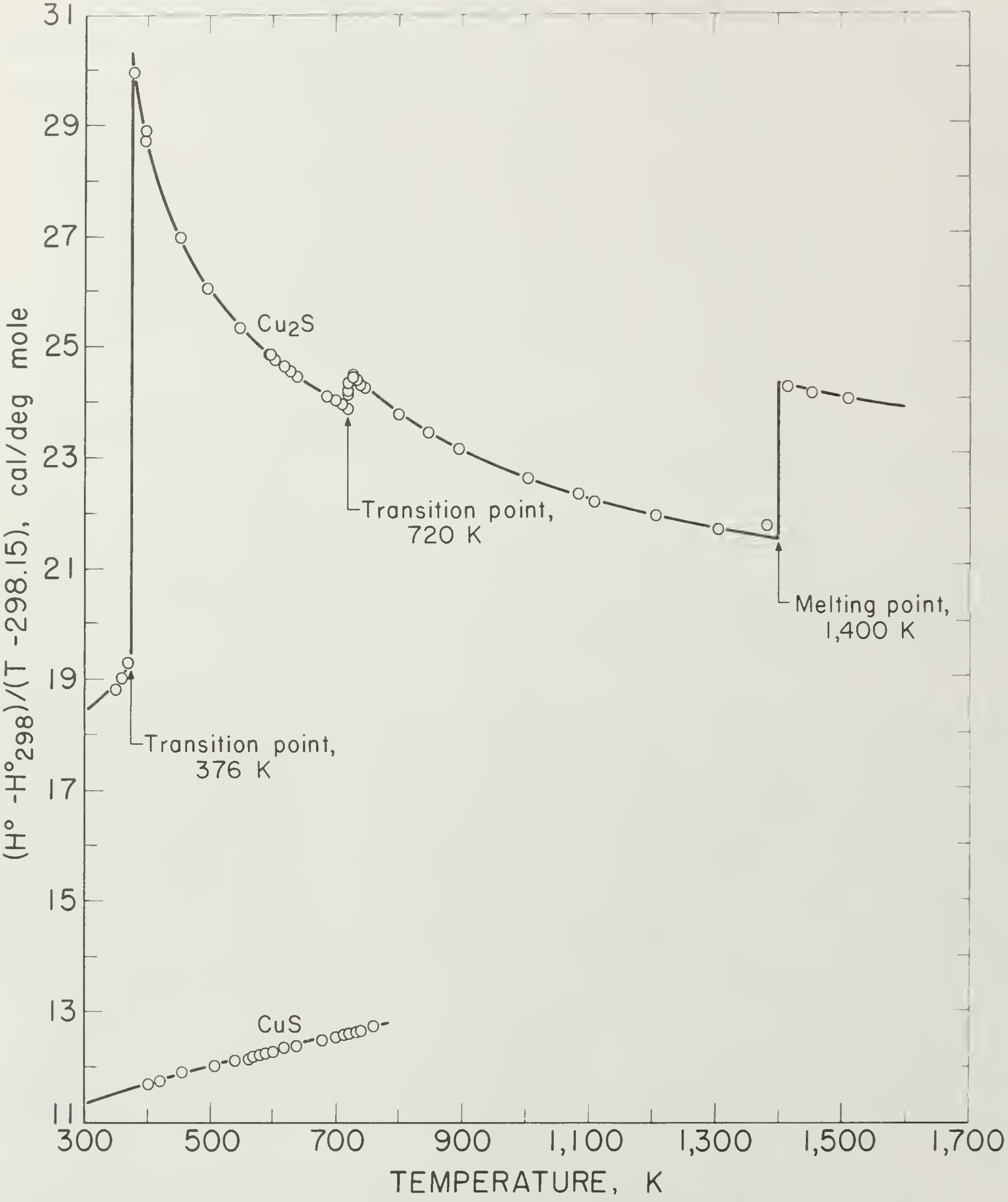

FIGURE 2. - High-temperature mean heat capacities.

increasing temperature. Enthalpy measurements made above and then below the transitions at 376 and 720 K verified reversibility of phase transitions by again being on the curve of the mean heat capacity. The third transition from solid to liquid was found at about 1,400 K with a heat of fusion of 3.070 kcal/mole. Rapid reversibility of phase transitions was confirmed by cooling separate samples from temperatures above the three transitions at 376, 720, and 1,400 K to 298 K in the calorimeter under the same conditions as for enthalpy measurements, and then within minutes subjecting these samples to X-ray diffraction analyses. Such tests were made at approximately 600, 1,000, and 1,500 K. An additional test was made at about 350 K to have a sample heated below the transition at 376 K. All samples reverted to the stable reference form of monoclinic Cu_2S, and no metastable form was detected by X-ray. Over 2 months later, reanalysis of the same samples detected no structural change. This meticulous program was followed to be sure that the room-temperature form was the same after quenching in the calorimeter from each form encountered in this investigation, and to insure that there were no very slow transitions at room temperature. The quench from the liquid state, in particular, was suspect, in view of the small measured heat of fusion of 3.070 kcal/mole. Only the room-temperature form of monoclinic Cu_2S was detected by X-ray diffraction analyses for samples used in enthalpy measurements.

The transition at 720 K for Cu_2S was established by 12 enthalpy measurements made within 34° of the transition temperature. Figure 2 and table 4 show the results of four measurements, all lying along the isothermal transition line within 1° of the 720 K transition. This transition temperature was initially determined from enthalpy measurements with a minimum furnace residence time of 1.5 hr. To confirm the transition temperature, additional measurements were made with residence times much longer than the minimum. Measurements with residence times 11 to 46 times longer than the minimum established enthalpies below, at, and above the transition point at temperatures of 700.5 (17 hr), 720.5 (19 hr), 720.9 (43 hr), 727.1 (69 hr), and 740.6 K (21 hr).

Enthalpy measurements of Cu_2S above the melting point of 1,400 K resulted in cracking of the silica-glass capsules. This cracking was caused by a slight visible devitrification of the silica-glass, and was probably aided either by a volume change of the sample upon rapid freezing in the calorimeter, or by the liquid wetting of the capsule wall with subsequent strain on the capsule upon freezing. The cracking of the glass capsule occurred inside of the calorimeter without loss of the sample, so that an adequate number of successful measurements were obtained for the liquid state before being discontinued at 1,509.3 K. X-ray diffraction analyses of the samples from the cracked capsules showed no differences from the starting material.

Smoothed enthalpy values for the sulfides from tables 5-6 were fitted with equations to better meet the needs of various users, particularly in engineering applications. Kelley described the method of derivation based on the equation first recommended by Maier and Kelley (30) and on the graphical procedure developed by Shomate (37). The derived equations follow, expressed in kcal/mole, together with the temperature ranges of validity and average deviations from the smooth data.

$\underline{Cu_2S(c,\ell)}$

Base $H^\circ_{298} = \alpha - Cu_2S$

α: $H^\circ - H^\circ_{298} = 5.24 \times 10^{-3}T + 17.72 \times 10^{-6}T^2 - 2.29 \times 10^2 T^{-1} - 2.369$

(298 - 376 K; 0.04 pct),

$\Delta H^\circ_{376}(\alpha-\beta) = 0.865$

β: $H^\circ - H^\circ_{298} = 25.24 \times 10^{-3}T - 3.12 \times 10^{-6}T^2 - 1.58 \times 10^2 T^{-1} - 6.267$

(376 - 720 K; 0.01 pct),

$\Delta H^\circ_{720}(\beta-\gamma) = 0.280$

γ: $H^\circ - H^\circ_{298} = 20.38 \times 10^{-3}T - 0.37 \times 10^{-6}T^2 + 0.15 \times 10^2 T^{-1} - 4.153$

(720 - 1,400 K; 0.01 pct),

$\Delta H^\circ_{1,400}(\gamma-\ell) = 3.070$

ℓ: $H^\circ - H^\circ_{298} = 21.43 \times 10^{-3}T - 3.266$

(1,400 - 1,600 K; < 0.01 pct),

$\underline{CuS(c)}$

$H^\circ - H^\circ_{298} = 10.29 \times 10^{-3}T + 2.42 \times 10^{-6}T^2 + 0.33 \times 10^2 T^{-1} - 3.394$

(298 - 780 K; 0.03 pct).

STANDARD ENTHALPIES AND GIBBS ENERGIES OF FORMATION

Standard enthalpies and Gibbs energies of formation were calculated as functions of temperature for Cu_2S and CuS by combining enthalpy and entropy increments of the present investigation with supplementary data from the literature. Calculations were also made for reactions of copper with S_2(g). The supplementary data needed for the calculations were obtained from various sources. The standard enthalpy of formation at 298.15 K for S_2(g) was taken from Wagman and others (43). King, Mah, and Pankratz was the source of enthalpies and entropies for Cu(s,l) and the standard enthalpies of formation for Cu_2S and CuS. Increments of the enthalpy and entropy above 298.15 K for S(c,l) were obtained from West (46), and were corrected to agree with International Practical Temperature Scale of 1968. The remaining thermodynamic properties for S(c,l) and S_2(g) were from the JANAF tables (10).

The results of the calculations are given in tables 7-10, which also list equilibrium constants in addition to enthalpies and Gibbs energies.

TABLE 7. - Formation data for $2Cu(c) + S(c,l) = Cu_2S(c)$

T, K	ΔHf°, kcal	ΔGf°, kcal	Log Kf	T, K	ΔHf°, kcal	ΔGf°, kcal	Log Kf
0	-19.73	-19.73	∞	376	-18.49	-21.02	12.218
100	-19.58	-19.91	43.513	[1]388.36	-18.42	-21.11	11.880
200	-19.52	-20.30	22.183	388.36	-18.83	-21.11	11.880
298.15	-19.40	-20.68	15.159	400	-18.79	-21.18	11.572
300	-19.40	-20.68	15.065	500	-18.62	-21.80	9.529
[1]368.54	-19.28	-20.99	12.447	600	-18.50	-22.44	8.174
368.54	-19.38	-20.99	12.447	700	-18.42	-23.11	7.215
[2]376	-19.36	-21.02	12.218	[3]717.8	-18.41	-23.22	7.070

[1] Transition point of S.
[2] Transition point of Cu_2S.
[3] Boiling point of S.

TABLE 8. - Thermodynamic data for the reaction $2Cu(c,l) + 1/2S_2(g) = Cu_2S(c,l)$

T, K	ΔHr°, kcal	ΔGr°, kcal	Log Kr	T, K	ΔHr°, kcal	ΔGr°, kcal	Log Kr
0	-35.05	-35.05	∞	800	-31.18	-24.96	6.819
100	-35.09	-33.38	72.952	900	-30.97	-24.20	5.877
200	-34.96	-31.72	34.662	1,000	-30.80	-23.45	5.125
298.15	-34.74	-30.17	22.115	1,100	-30.67	-22.73	4.516
300	-34.74	-30.14	21.957	1,200	-30.59	-22.01	4.009
[1]376	-34.47	-29.00	16.856	1,300	-30.58	-21.29	3.579
376	-33.61	-29.00	16.856	[2]1,357.6	-30.62	-20.88	3.361
400	-33.42	-28.71	15.686	1,357.6	-36.86	-20.88	3.361
500	-32.74	-27.62	12.073	[3]1,400	-36.89	-20.38	3.181
600	-32.18	-26.65	9.707	1,400	-33.82	-20.38	3.181
700	-31.73	-25.77	8.046	1,500	-33.69	-19.43	2.831
[1]720	-31.65	-25.59	7.768	1,600	-33.55	-18.48	2.524
720	-31.37	-25.59	7.768				

[1] Transition point of Cu_2S.
[2] Melting point of Cu.
[3] Melting point of Cu_2S.

TABLE 9. - Formation data for $Cu(c) + S(c,l) = CuS(c)$

T, K	ΔHf°, kcal	ΔGf°, kcal	Log Kf	T, K	ΔHf°, kcal	ΔGf°, kcal	Log Kf
0	-12.61	-12.61	∞	[1]388.36	-12.69	-12.79	7.198
100	-12.59	-12.65	27.647	388.36	-13.10	-12.79	7.198
200	-12.63	-12.73	13.911	400	-13.12	-12.78	6.983
298.15	-12.60	-12.75	9.346	500	-13.44	-12.66	5.534
300	-12.60	-12.75	9.288	600	-13.64	-12.48	4.546
[1]368.54	-12.59	-12.78	7.579	700	-13.74	-12.28	3.834
368.54	-12.69	-12.78	7.579	[2]717.8	-13.75	-12.24	3.727

[1] Transition point of S.
[2] Boiling point of S.

TABLE 10. - Thermodynamic data for the reaction $Cu(c) + 1/2S_2(g) = CuS(c)$

T, K	ΔHr°, kcal	ΔGr°, kcal	Log Kr	T, K	ΔHr°, kcal	ΔGr°, kcal	Log Kr
0	-27.93	-27.93	∞	400	-27.76	-20.32	11.102
100	-28.10	-26.12	57.085	500	-27.55	-18.48	8.078
200	-28.07	-24.14	26.379	600	-27.32	-16.69	6.079
298.15	-27.94	-22.24	16.302	700	-27.05	-14.93	4.661
300	-27.94	-22.20	16.173	780	-26.82	-13.56	3.799

DISCUSSION

King, Mah, and Pankratz compiled a monograph on the thermodynamic properties of substances important in the metallurgy of copper. This compilation was sponsored by the International Copper Research Association. At the time the compilation was to be published, the present investigation of high-temperature enthalpies for Cu_2S and CuS had been finished. Thus, the smoothed enthalpy values were included in the compilation to make it as complete as possible. These enthalpies were reported in the compilation with the low-temperature heat capacities measured by Anderson. After publication of the compilation, the heat capacities were remeasured, primarily to extend Anderson's data below 56 K. When the new heat capacities were combined with the same experimental enthalpies, the resulting smooth enthalpies reported herein were found to be the same as those given in the compilation for CuS, and slightly changed only between 298 and 376 K for Cu_2S. Consequently, enthalpies reported for Cu_2S in the compilation still fit reasonably well with the new heat capacities of the present investigation.

Low-temperature heat capacities of Cu_2S and CuS were measured by an adiabatic calorimeter in the present investigation and an isothermal-jacketed calorimeter in the studies of Anderson. His data averaged about 1 pct higher than heat capacities of this investigation, except near 295 K where the difference was closer to -0.5 pct for Cu_2S and 0.5 pct for CuS. Anderson derived the entropy increment for CuS as $S^\circ_{298}-S^\circ_{56}$ = 13.29 cal/deg mole, and estimated the portion below 56 K as 2.64 cal/deg mole. These values resulted in S°_{298} = 15.9±0.3 cal/deg mole, which compares well with S°_{298} = 16.05 cal/deg mole of this investigation. In the case of Cu_2S, Anderson reported S°_{298} = 28.9±0.5 cal/deg mole, which is in fair agreement with S°_{298} = 27.76 cal/deg mole of the present work. His estimation of the entropy below 56 K as 6.06 cal/deg mole is about 0.6 unit higher than determined in the present work.

No measurements of high-temperature enthalpies have been reported in the literature for CuS. An upper temperature limit of 780 K for the stability of CuS was adopted from the studies of Kullerud (27). This temperature is in agreement with results of the present investigation, which showed decomposition occurred at 779 K and may have started near 761 K.

Enthalpy measurements of Cu_2S showed three reversible transitions that were reported previously. For the first transition from the monoclinic to hexagonal stucture, temperatures from 364 to 388 K have been given in the literature. The present investigation established this transition between 370.2 and 380.2 K for an average temperature of 375 K. However, 376 K was adopted from Jost and Kubaschewski (20) and Kubaschewski (26) because their heat capacity measurements by adiabatic calorimetry below 400 K are more sensitive than enthalpy measurements by drop calorimetry. The isothermal heat of transition of 0.865 kcal/mole from the present work compares favorably with the value of about 0.920 kcal/mole reported by Jost and Kubaschewski, and 0.889 kcal/mole measured by Kubaschewski. Present results are also in good agreement with the transition temperature of 388 K and the heat absorption of 0.896 kcal/mole measured with a constant heating calorimeter by Ueda (42), and 376 K and 0.920 kcal/mole calculated by Kelley.

The second transition for Cu_2S was established at a temperature of 720 K. A spread in temperatures from about 678 to 743 K has been reported for the transition due to sluggish behavior. Barton (4) wrote, "The inversion is not well defined; it is subject to considerable hysteresis because the sulfur atoms must shift from the hexagonal- to the cubic-closest-packing on heating." Roseboom (35) stated, "Although this structure cannot be quenched to room temperature, inversion is slow near the transition temperature, and this fact accounts for the 20-degree uncertainty. However, the inversion occurs rapidly 50° above or below the transition." This sluggish behavior was not encountered in the present enthalpy measurements made with furnace residence times of 11 times longer than the minimum of 1.5 hr. The 720 K temperature and heat absorption of 0.280 kcal/mole determined for the transition from this investigation are in good agreement with 717 K and 0.287 kcal/mole reported by Jost and Kubaschewski, 708 K and 0.306 kcal/mole measured by Kubaschewski, 723 K and 0.090 kcal/mole given by Ueda, and 703 K and 0.110 kcal/mole reported by Wehefritz (44) from galvanic cell measurements. The transition temperature of the present investigation is in disagreement with 623 K calculated by Kelley, but in agreement with his transition heat of 0.200 kcal/mole.

The third transition of Cu_2S was the congruent melting at 1,400 K adopted from measurements made by Jensen (18) using differential thermal analysis. Present enthalpy measurements did not determine the melting point due to the premelting effect at 1,381.9 K, which showed an abnormally high thermal effect of 1.2 pct above the curve in figure 2. Consequently, the data were extrapolated to 1,400 K from the last valid experimental measurement at 1,304.4 K. Temperatures from 1,400 to 1,403 K are reported in the literature for the melting point. The present investigation determined the heat of fusion as 3.070 kcal/mole compared with 2.700 kcal/mole measured with a water calorimeter by Johannsen and Vollmer (19), 2,700 kcal/mole from differential thermal analysis measurements by Mendelevich, Krestovnikov, and Glazor (31), 2.300 kcal/mole from extrapolation of equilibrium data by Richardson and Antill (34), and values calculated by Kelley (23) resulting in either 2.900 kcal/mole from the study by Friedrich (15) or 5.500 kcal/mole by averaging the data of Truthe (41) and Friedrich (14).

High-temperature measurements of Cu_2S by others have been limited. Heat capacity measurements between 203 and 803 K were reported by Jost and Kubaschewski; however, their values were not tabulated and instead, were presented graphically. Their data differed from the present investigation by ±1 pct or less. Kubaschewski tabulated heat capacity values measured from 223 to 803 K. His values varied from the present investigation by ±0.03 pct or less. Kelley (22) calculated enthalpies between 350 and 1,400 K from the incomplete and scattered data of investigators given in the Introduction. Kelley's enthalpies were 1 to 2 pct higher than those of this investigation.

Enthalpy data expressed in equation form are commonly used by industrial scientists in engineering applications. Consequently, it should be noted that all of the standard-form equations given in this paper are an excellent fit to the smooth data with average deviations of 0.04 pct or less. Except for the equation representing the enthalpy data from 298 to 376 K for Cu_2S, all other equations are the same as given by King, Mah, and Pankratz in the Bureau of Mines compilation sponsored by the International Copper Research Association.

REFERENCES[4]

1. Adami, L. H., and E. G. King. Heats of Formation of Anhydrous Sulfates of Cadmium, Cobalt, Copper, Nickel, and Zinc. BuMines RI 6617, 1965, 10 pp.

2. Anderson, C. T. The Heat Capacities at Low Temperatures of the Sulfides of Copper and Lead. J. Am. Chem. Soc., v. 54, 1932, pp. 107-111.

3. Barany, R., L. B. Pankratz, and W. W. Weller. Thermodynamic Properties of Cuprous and Cupric Ferrites. BuMines RI 6513, 1964, 19 pp.

4. Barton, P. B., Jr. Solid Solutions in the System Cu-Fe-S. Part I: The Cu-S and CuF-S Joins. Econ. Geol., v. 68, 1973, pp. 455-465.

5. Bellati, M., and S. Lussana. Sui calori specifici e di trasformazione dei solfuri e seleniuri di argento e di rame Ag_2S; Cu_2S; Ag_2Se; Cu_2Se (The Specific Heats and Heats of Transformation of the Sulfides and Selenides of Silver and Copper Ag_2S; Cu_2S; Ag_2Se; Cu_2Se). Venezia Ist. Atti, v. 7, Series 6, 1888-1889, pp. 1051-1059.

6. Bornemann, K., and O. Hengstenberg. Uber die spezifischen Warmen einiger metallhuttenmannisch wichtiger Sulfide mit besonderer Berucksichtigung hoherer Temperaturen (The Specific Heats of Some Sulfides Used in Metallurgy, With Special Reference to High Temperatures). Metall u. Erz., v. 17, 1920, pp. 313-319, 339-349.

7. Comite International des Poids et Mesures (The International Committee on Weights and Measures). The International Practical Temperature Scale of 1968. Metrologia, v. 5, 1969, pp. 35-44.

8. Craig, J. R., and S. D. Scott. Sulfide Phase Equilibria. Ch. in Sulfide Mineralogy, Mineralogical Society of America, Short Course Notes, ed. by P. H. Ribbe. Washington, D.C., v. 1, 1974, vp.

9. Douglas, T. B., and E. G. King. High-Temperature Drop Calorimetry. Ch. 8 in Experimental Thermodynamics, v. 1. Calorimetry of Non-Reacting Systems, ed. by J. P. McCullough and D. W. Scott. Butterworths, London, 1968, pp. 293-331.

10. Dow Chemical Co., Thermal Research Laboratory. JANAF Thermochemical Tables, 2d ed. NSRDS-NBS-37, SN03030872, U.S. Government Printing Office, Washington, D.C., 1971, 1141 pp.

11. Elliot, R. P. Constitution of Binary Alloys, First Supplement. McGraw-Hill Book Co., Inc., New York, 1965, 877 pp.

12. Evans, H. T. Crystal Structure of Low Chalcocite. Nature Phys. Sci., v. 232, 1971, pp. 69-70.

---

[4] Titles enclosed in parentheses are translations from the language in which the item was published.

13. Ferrante, M. J. Enthalpies and Entropies Above 298.15° K for Copper Sulfate and Copper Oxysulfate. BuMines RI 7600, 1972, 8 pp.

14. Friedrich, K. Untersuchungen uber Schichten bildende Systeme. Die Systeme Cu_2S-Ni_3S_2 and Cu_2S-Ni_2S (Investigations of Layer-Forming Systems. The Systems Cu_2S-Ni_3S_2 and Cu_2S-Ni_2S). Metall u. Erz, v. 11, 1914, p. 160.

15. _____. Die Schmelzdiagramme der binaren Systeme Schwefelsilber-Kupfersulfur und Bleiglanz-Kupfersulfur (The Melting Point Curves of the Systems Argentite-Chalcocite and Galenite-Chalcocite). Metallurgie, v. 4, 1907, p. 671.

16. Hansen, M., and K. Anderko. Constitution of Binary Alloys. McGraw-Hill Book Co., Inc., New York, 1958, 1305 pp.

17. International Union of Pure and Applied Chemistry, Inorganic Chemistry Division, Commission on Atomic Weights. Atomic Weights of the Elements. Pure Appl. Chem., v. 37, 1974, pp. 591-603.

18. Jensen, E. Melting Relations of Chalcocite. Avhandl. Norske Videnskaps-Akad., Olso, Matematish-Naturvidenskapelig Klasse, No. 6, 1947, 14 pp.

19. Johannsen, F., and H. Vollmer. Untersuchungen im System Kupfer-Kupfersulfid (Investigations on the System Copper-Copper Sulfide). Z. Erz. u. Metallhuttenw., v. 13, 1960, pp. 313-322.

20. Jost, W., and P. Kubaschewski. Spezifische Warmen von Silber- und Kupfer (I) - Chalkogeniden von-70° C bis zu 550° C (Specific Heats of Silver and Copper (I) Chalcogenides From 70° C to 550° C). Z. Physika. Chem. (Frankfurt), v. 60, 1968, pp. 69-78.

21. Justice, B. H. Thermal Data Fitting With Orthogonal Functions and Combined Table Generation. The FITAB Program. Univ. Mich., Ann Arbor, Mich., COO-1149-143, 1969, 49 pp.

22. Kelley, K. K. Contributions to the Data on Theoretical Metallurgy. XIII. High-Temperature Heat-Content, Heat-Capacity, and Entropy Data for the Elements and Inorganic Compounds. BuMines Bull. 584, 1960, 232 pp.

23. _____. Contributions to the Data on Theoretical Metallurgy. V. Heats of Fusion of Inorganic Substances. BuMines Bull. 393, 1936, 166 pp.

24. King, E. G., A. D. Mah, and L. B. Pankratz. INCRA Series on the Metallurgy of Copper. Monograph II. Thermodynamic Properties of Copper and Its Inorganic Compounds. The International Copper Research Association, Inc., New York, 1973, 257 pp.

25. Ko, H-C., and D. W. Richardson. Enthalpies of Formation of Cupric and Cuprous Bromides. BuMines RI 8078, 1975, 9 pp.

26. Kubaschewski, P. Spezifische Wärmen und thermische Fehlordnung von Kupferchalkogeniden Teil II: Die Systeme Cu_2S-CuS und Cu_2Se-CuSe (Specific Heats and Thermal Disorder of Copper Chalcogenides. II. Cu_2S-CuS and Cu_2Se-CuSe Systems). Ber. Bunsenges. Physika. Chem., v. 77, 1973, pp. 74-80.

27. Kullerud, G. The Cu-S System. Carnegie Inst. Wash. Yearbook 56, Washington, D.C., 1957, pp. 195-197.

28. Mah, A. D., L. B. Pankratz, W. W. Weller, and E. G. King. Thermodynamic Data for Cuprous and Cupric Oxides. BuMines RI 7026, 1967, 20 pp.

29. Maier, C. G. Resistance Thermometers for Chemists. J. Phys. Chem., v. 34, 1930, pp. 2860-2868.

30. Maier, C. G., and K. K. Kelley. An Equation for the Representation of High-Temperature Heat Content Data. J. Am. Chem. Soc., v. 54, 1932, pp. 3243-3246.

31. Mendelevich, A. Y., A. N. Krestovnikov, and V. M. Glazov. Phase Equilibria of Pseudobinary Group I Chalcogenide Systems in the Regular Solution Approximation. Russ. J. Phys. Chem., London, v. 43, 1969, pp. 1723-1724.

32. Pankratz, L. B., and E. G. King. High-Temperature Enthalpies and Entropies of Chalcopyrite and Bornite. BuMines RI 7435, 1970, 10 pp.

33. Richardson, D. W., and R. R. Brown. Enthalpy of Formation of Malachite $[Cu_2(CO_3)(OH)_2]$. BuMines RI 7851, 1974, 5 pp.

34. Richardson, F. D., and J. E. Antill. Thermodynamic Properties of Cuprous Sulphide and Its Mixtures With Sodium Sulphide. Trans. Faraday Soc., v. 51, 1955, pp. 22-33.

35. Roseboom, E. H., Jr. High-Temperature X-Ray Studies in the System Cu-S (Abstract). Geol. Soc. Amer. Bull., v. 71, 1960, p. 1959.

36. _____. An Investigation of the System Cu-S and Some Natural Copper Sulfides Between 25° and 700° C. Econ. Geol., v. 61, 1966, pp. 641-672.

37. Shomate, C. H. High-Temperature Heat Contents of Magnesium Nitrate, Calcium Nitrate, and Barium Nitrate. J. Am. Chem. Soc., v. 66, 1944, pp. 928-929.

38. Shunk, F. A. Constitution of Binary Alloys, Second Supplement. McGraw-Hill Book Co., Inc., New York, 1969, 720 pp.

39. Stuve, J. M., D. W. Richardson, and E. G. King. Low-Temperature Heat Capacities and Enthalpy of Formation of Copper Oxysulfate. BuMines RI 8045, 1975, 18 pp.

40. Taylor, A. R., Jr., M. H. Brown, and E. G. Taylor. Heat of Formation of Cuprous Cyanide and Its Heat Capacity From 10° to 400° K. BuMines RI 7499, 1971, 12 pp.

41. Truthe, W. Uber das Verhalten der Sulfide von Pb, Cu, Ag und des Cu_2O in den Schmelzen der zugehorigen Chloride (The Behavior of the Sulfides of Lead, Copper and Silver and of Cuprous Oxide in the Fusions of the Corresponding Chlorides). Z. Anorg. Chem., v. 76, 1912, p. 161.

42. Ueda, R. X-Ray and Thermal Studies on the Phase Transitions of Cuprous Sulphide Cu_2S. J. Phys. Soc., Japan, v. 4, 1949, pp. 287-292.

43. Wagman, D. D., W. H. Evans, V. B. Parker, I. Halow, S. M. Bailey, and R. H. Schumm. Selected Values of Chemical Thermodynamic Properties. NBS Tech. Note 270-3, 1968, 264 pp.

44. Wehefritz, V. Untersuchungen am System Kupfer-Schwefel (Investigations on the System Copper-Sulfur). Z. Physika. Chem. (Frankfurt), v. 26, 1960, pp. 339-358.

45. Weller, W. W. Low-Temperature Heat Capacities and Entropies at 298.15° K of Anhydrous Sulfates of Cobalt, Copper, Nickel, and Zinc. BuMines RI 6669, 1965, 6 pp.

46. West, E. D. The Heat Capacity of Sulfur From 25 to 450°, the Heats and Temperatures of Transition and Fusion. J. Am. Chem. Soc., v. 81, 1959, pp. 29-37.

47. White, W. P. Extra Specific Heat in Cuprous Sulfide: Specific Heat of Ferrous Oxide. J. Am. Chem. Soc., v. 55, 1933, pp. 1047-1053.

48. Yund, R. A., and G. Kullerud. Thermal Stability of Assemblages in the Cu-Fe-S System. J. Petrol., v. 7, 1966, p. 458.

☆U.S. GOVERNMENT PRINTING OFFICE: 1978-703-103/65

INT.-BU.OF MINES,PGH.,PA. 23233

e22.09
Un3Qmo

RI 8306

Bureau of Mines Report of Investigations/1978

Extracting Uranium From Low-Grade Ore From the Coso Mountains, Calif.

DEPOSITORY
NOV 17 1978
UNIV. OF ILL. LIBRARY
AT URBANA-CHAMPAIGN

UNITED STATES DEPARTMENT OF THE INTERIOR

Report of Investigations 8306

Extracting Uranium From Low-Grade Ore From the Coso Mountains, Calif.

By J. H. Maysilles, I. L. Nichols, and D. C. Seidel

March 3, 1849

UNITED STATES DEPARTMENT OF THE INTERIOR
Cecil D. Andrus, Secretary

BUREAU OF MINES

This publication has been cataloged as follows:

Maysilles, James H

Extracting uranium from low-grade ore from the Coso Mountains, Calif. / by J. H. Maysilles, I. L. Nichols, and D. C. Seidel. [Washington] : U.S. Dept. of the Interior, Bureau of Mines, 1978.

14 p. : ill., diagr. ; 27 cm. (Report of investigations - Bureau of Mines ; 8306)

Bibliography: p. 14.

1. Uranium ores - California - Coso Mountains. 2. Leaching. I. Nichols, Ivan LeRoy, joint author. II. Seidel, Don C., joint author. III. United States. Bureau of Mines. IV. Title. V. Series: United States. Bureau of Mines. Report of investigations - Bureau of Mines ; 8306.

TN23.U7 no. 8306 622.06173

U.S. Dept. of the Int. Library

CONTENTS

Page

Abstract.. 1
Introduction.. 1
Description of the samples.. 2
Experimental studies.. 4
    Sulfuric acid leaching, yellow fraction....................... 4
        Reagent requirements...................................... 4
        Effect of leaching time................................... 5
    Acid leaching, red fraction................................... 5
        Sulfuric acid leaching.................................... 5
        Nitric and hydrochloric acid leaching..................... 6
        Effect of different preleaching treatments................ 6
    Percolation leaching with sulfuric acid....................... 7
    Percolation leaching in a 12-inch-diameter column............. 9
    Uranium recovery from leach solution.......................... 12
Conclusions and recommendations................................... 12
References.. 14

ILLUSTRATIONS

1. Laboratory flooded column for percolation leaching................ 8
2. Twelve-inch-diameter column for percolation leaching............... 11

TABLES

1. Analysis of Coso Range samples.................................... 3
2. Screen analysis and uranium content, sample 1..................... 3
3. Reagent requirements for acid leaching, sample 1.................. 4
4. Leaching time versus particle size, sample 1...................... 5
5. Leaching with H_2SO_4, sample 2R................................ 6
6. Results of using HNO_3 and HCl as leaching agents, sample 2R.... 6
7. Sulfuric acid leaching with different preleach treatments, sample 2R 7
8. Percolation with acid solution in a flooded column, sample 1...... 9
9. Stream data for percolation with acid solution in a flooded column, sample 1.......... 9
10. Stream data for percolation with acid solution in a 12-inch-diameter column, sample 2.......... 10
11. Washing data for percolation test in 12-inch-diameter column, sample 2.......... 10

EXTRACTING URANIUM FROM LOW-GRADE ORE FROM THE COSO MOUNTAINS, CALIF.

by

J. H. Maysilles,[1] I. L. Nichols,[2] and D. C. Seidel[3]

ABSTRACT

The Bureau of Mines, U.S. Department of the Interior, is investigating several types of low-grade uranium deposits. Projections indicate that an increased percentage of future production will be derived from such sources. One material studied was from the Coso Mountains of California; this material contained 0.04 to 0.12 percent U_3O_8. The deposit contains at least two distinct types of mineralization. The material representing the bulk of this deposit was amenable to acid leaching; 80 to 85 percent U_3O_8 extraction resulted from leaching with 20 to 40 pounds per ton of sulfuric acid. No oxidizing agent was required. This ore fraction could be treated by either agitation or percolation leaching. Uranium recovery and purification from the acid leach solution was accomplished using anion exchange followed by precipitation with hydrogen peroxide and ammonia. The second type of mineral was very refractory to acid leaching; a maximum extraction of only 44 percent was obtained with sulfuric acid. Nitric and hydrochloric acids were ineffective also.

INTRODUCTION

During the past 5 years, the feed grade to U.S. uranium mills has decreased steadily. In 1972 the average grade was approximately 0.21 percent U_3O_8; by 1976 the grade had dropped to 0.15 percent (1).[4]

More than 90 percent of the U.S. uranium mill feed has been produced from conventional ore deposits with uranium grades in the range 0.1 to 0.3 percent U_3O_8. The term "conventional uranium ore" has generally been used to designate sandstone-type materials containing at least 0.1 percent U_3O_8.

---

[1] Chemical engineer.

[2] Metallurgist.

[3] Research supervisor.

All authors are with the Salt Lake City Metallurgy Research Center, Bureau of Mines, Salt Lake City, Utah.

[4] Underlined numbers in parentheses refer to items in the list of references at the end of this report.

Unless large new deposits of these conventional uranium ores or other relatively good ores are discovered, uranium producers will have to depend on lower grade and refractory materials for an increasing percentage of their production. Increasing demand, rising prices, and the need for full utilization of uranium resources all indicate that the lower grade and refractory ores will have to be processed in the United States.

Current Bureau of Mines leaching studies are concentrating on systems for recovering uranium from ores containing 0.01 to 0.1 percent U_3O_8. Studies are in progress on several of these materials. Information is being developed on both the processing characteristics of individual materials and the variability between different materials. The objective of this effort is to develop a technology base for processing lower grade uranium ores which are not now being treated commercially.

This report presents the results of acid leaching and supporting characterization studies on a uranium-bearing arkosic sandstone from the Coso area west of Death Valley in California. The available samples of this material contained from 0.04 to 0.12 percent U_3O_8, and the limestone content was equivalent to less than 1 percent $CaCO_3$. Although the size of the deposit is not known, it does appear likely that significant amounts of uranium are present in the area. The potential for similar deposits in other areas also seems likely.

The Bureau of Mines characterization studies investigated the effect of acid leaching variables such as time, temperature, and reagent requirements. These tests were made to determine the amenability of this material to uranium extraction by conventional methods.

DESCRIPTION OF THE SAMPLES

Two different samples were made available to the Bureau for this investigation. These samples were considered to be generally representative of the types of materials found in this area but were not composites of any specific deposit.

Sample 1 weighed about 140 pounds and was used for initial laboratory evaluation. A microscopic examination showed that this sample, which contained 0.04 percent U_3O_8, consisted predominantly of quartz and feldspar (both microcline and plagioclase) grains up to 2 millimeters in the long dimension. The grains were poorly cemented by clay minerals and iron oxides. The cementing materials constituted only about 5 percent of the sample. Small amounts of hornblende, muscovite, and jarosite were also present. No uranium minerals could be identified.

Sample 2, which weighed approximately 1,500 pounds, was obtained later for larger scale tests. This sample was found to contain two petrologically distinct components. The bulk of the sample was composed of a yellowish material, most of which was finer than 1/2 inch in size, which contained 0.16 percent U_3O_8. The larger pieces appeared to be a friable conglomerate. A handpicked sample of this material is referred to as sample 2Y. This component of sample 2 was similar to sample 1.

The other component of sample 2 consisted of very hard pieces of a dark red material, most of which was greater than 1/2 inch in size. This is referred to as the "red" component. The amount of red material was small compared with the total sample. Petrographic examination of a handpicked sample (sample 2R) indicated that the general composition of the red fraction was also similar to that of sample 1, but that it also contained goethite ($\alpha FeO(OH)$). When the sink fraction from a heavy medium separation was passed through a Franz Isodynamic Separator,[5] the magnetic fraction was almost entirely goethite. The radioactivity of this magnetic fraction was approximately twice that of the nonmagnetic fraction. The goethite exhibited a concentric structure of radially fibrous crystals. Although the uranium mineral was not identified, it is probable that the uranium is enclosed in the concentric structure. Chemical analyses of all samples are given in table 1.

TABLE 1. - Analysis of Coso Range samples

Sample	Analyses, wt-pct							
	U_3O_8	V_2O_5	$CaCO_3$	Fe	Mo	P_2O_5	RSO_4	Organic C
1..........	0.040	0.007	0.5	2.1	0.004	0.19	1.2	0.2
2..........	.125	.006	.2	5.7	.001	.28	1.1	-
2Y.........	.16	.009	.6	1.4	<.005	.37	1.8	.1
2R.........	.18	.004	.6	12.8	<.005	.22	.8	.2

A wet screen analysis was made on sample 1 after it was crushed to minus 3 mesh. The results, which are given in table 2, showed concentration of uranium in the fine fractions.

TABLE 2. - Screen analysis and uranium content, sample 1

Particle size	Wt-pct	U_3O_8 content	
		Analysis, pct	Distribution, pct
Minus 3-mesh plus 10-mesh.........	17.9	0.0046	2.1
Minus 10-mesh plus 35-mesh........	29.8	.0046	3.4
Minus 35-mesh plus 65-mesh........	12.1	.0096	2.8
Minus 65-mesh plus 100-mesh.......	5.0	.0186	2.3
Minus 100-mesh plus 200-mesh......	9.2	.042	9.6
Minus 200-mesh plus 325-mesh......	4.7	.076	8.9
Minus 325-mesh....................	21.4	.134	70.9
Calculated head.............	100.0	.040	100.0
Assay head..................	-	.040	-

---

[5] Reference to specific equipment or manufacturers does not imply endorsement by the Bureau of Mines.

EXPERIMENTAL STUDIES

If significant amounts of acid-consuming components such as $CaCO_3$ are not present, then sulfuric acid solution is usually an effective leaching agent for uranium-bearing materials. Uranium in its oxidized (plus 6) state is easily dissolved by acidic solutions, and the reduced (plus 4) state can normally be oxidized to the hexavalent state by oxidizing agents such as $NaClO_3$ or MnO_2 (3, pp. 59-70). The uranium is present in solution mostly as anion complexes with sulfate, for example, $UO_2(SO_4)_3{}^{4-}$, and can be extracted and purified effectively by anion exchange.

Agitation leaching tests were made to determine the acid, oxidant, and time requirements for the amenable yellow fraction (samples 1 and 2Y). For the refractory red component (sample 2R), the effectiveness of different acids and different preleach treatments was studied. Percolation leaching tests were made to determine the solution flow rate through a packed bed, and ion exchange studies were made on the resulting leach solutions to determine if the uranium could be effectively removed and purified.

Sulfuric Acid Leaching, Yellow Fraction

The yellow fraction of the Coso Range material, as represented by sample 1, is very amenable to leaching with sulfuric acid at ambient temperature. To determine the reagent requirements, several series of batch agitation leaching tests were conducted in which 150 to 300 grams of crushed material were leached in a 1-liter beaker. The uranium extraction was calculated on the basis of the U_3O_8 content of the products.

Reagent Requirements

The acid and oxidant requirements for agitation leaching of sample 1 were determined by making a series of tests with 10- to 120-pound-per-ton additions of H_2SO_4 and 0- to 10-pound-per-ton additions of $NaClO_3$ as shown in table 3. This material was effectively leached by 20- to 40-pound-per-ton additions of H_2SO_4. The addition of $NaClO_3$ produced no increase in uranium extraction.

TABLE 3. - Reagent requirements for acid leaching, sample 1[1]

H_2SO_4, lb/ton	$NaClO_3$,[2] lb/ton	Final solution pH	U_3O_8 extraction, pct
10	0	2.4	56
20	0	1.4	80
40	0	1.1	82
80	0	.8	78
120	0	.6	81
40	5	1.2	83
40	10	1.0	81

[1] Leaching conditions: Ambient temperature (approximately 22° C), 18 hours duration, 50 percent solids, minus 10-mesh grind.

[2] $NaClO_3$ added 1 hour after start of test.

When $NaClO_3$ was used, it was added 1 hour after the start of the test. This procedure was used because the reaction of acid and gangue materials may produce reducing agents in the initial stages of the leaching which would tend to consume any oxidant present at that time. These agents can be oxidized by atmospheric oxygen before the $NaClO_3$ is added.

Effect of Leaching Time

Tests using leaching times of 1/2 to 4 hours were made on minus 3-mesh and minus 10-mesh material to determine the effect of time on extraction (table 4). When the amount of acid used was somewhat greater than the minimum required, 1/2 hour of leaching was sufficient for both grinds.

TABLE 4. - Leaching time versus particle size, sample 1[1]

Grind	Leaching time, hr	U_3O_8 extraction, pct
Minus 3-mesh..........	0.5	82
Do..................	1	82
Do..................	2	83
Do..................	4	83
Minus 10-mesh.........	.5	79
Do..................	1	82
Do..................	2	80
Do..................	4	82

[1] Conditions: Ambient temperature, 50 percent solids, 45 lb/ton H_2SO_4.

Acid Leaching, Red Fraction

The red component of the ore, as represented by sample 2R, was much less amenable to leaching than was the yellow fraction. Tests were made on this material using different acids as lixiviants. Also, a variety of preleach treatments was used in an attempt to improve the uranium extraction; these included roasting, roasting followed by fine grinding, leaching in sodium thiosulfate solution, and autoclave leaching with water.

Sulfuric Acid Leaching

The red fraction leached very poorly with H_2SO_4, as shown by the results given in table 5. Even when this material was ground to minus 200 mesh, the uranium extraction was only 44 percent.

The extraction results are somewhat anomalous but are felt to be within the experimental limitations imposed by the combination of test procedures, analytical precision, and composition variations in the red fraction.

TABLE 5. - Leaching with H_2SO_4, sample 2R[1]

Grind	H_2SO_4, lb/ton	$NaClO_3$, lb/ton	Solids, pct	Temperature, ° C	Final solution pH	U_3O_8 extraction, pct
Minus 3-mesh...	30	0	50	22	1.35	15
Do...........	40	0	50	22	1.05	13
Do...........	100	0	50	22	-	9
Minus 35-mesh..	40	0	50	22	1.15	4
Do...........	40	5	50	22	1.15	4
Minus 200-mesh.	400	0	33	85	.4	44

[1] Condition: 18 hours duration.

Nitric and Hydrochloric Acid Leaching

Table 6 shows the results of leaching with nitric and hydrochloric acids. The acid additions in each test were equivalent to 400 pounds per ton of ore. Even with this high acid addition, both acids were relatively ineffective.

TABLE 6. - Results of using HNO_3 and HCl as leaching agents, sample 2R[1]

Leaching solution	Temperature, ° C	Final solution pH	U_3O_8 extraction, pct
HNO_3........10 pct..	22	0.3	20
HCl.........10 pct..	22	.1	32

[1] Conditions: 33 percent solids, minus 200 mesh, 18 hours duration.

Effect of Different Preleaching Treatments

Several preleaching treatments were used in conjunction with acid leaching of the red fraction; these were a reducing leach with sodium thiosulfate solution, autoclave leaching with water, and several roasting and grinding procedures. The results are summarized in table 7. Roasting of the material before leaching increased the uranium extraction to more than 70 percent.

In other tests, the yellow fraction remained amenable after being roasted; 80 percent U_3O_8 extraction resulted from leaching with 40 pounds per ton addition of H_2SO_4 after this material had been roasted 4 hours at 550° C. Hence, sample 2 could be roasted before leaching if desired without first separating the red and yellow fractions.

TABLE 7. - Sulfuric acid leaching with different preleach treatments, sample 2R[1]

Preleach treatment	Grind	H_2SO_4, lb/ton	Final solution pH	U_3O_8 extraction, pct
None	Minus 200-mesh	400	0.4	44
Reducing preleach[2]	.....do	400	.45	38
Preleach 4 hours[3]	.....do	350	.25	[4]41
Roast at 400° C for 4 hours on minus 10-mesh material.	.....do	400	.55	67
Roast at 550° C for 4 hours on minus 10-mesh material.	.....do	400	.4	77
Roast at 550° C for 4 hours	Minus 10-mesh	400	.75	67
Roast at 600° C for 4 hours	.....do	400	.2	74
Roast at 650° C for 4 hours	.....do	400	.25	70

[1] Conditions: 33 percent solids, 85° C, 18 hours duration.

[2] Reducing preleach in 300 lb/ton $Na_2S_2O_3 \cdot 5H_2O$ solution, 33 percent solids, ambient temperature. Solution contained <0.001 g/l U_3O_8.

[3] Preleach 4 hours at 200° C, 210 lb/sq in gage steam. 2.4 percent U_3O_8 extracted.

[4] Includes extraction from preleach.

Percolation Leaching With Sulfuric Acid

Percolation leaching, in which the ore is placed in vats or open heaps, is an alternative to agitation leaching. The solution is distributed over the top of the ore, allowed to percolate through the bed, and collected at the bottom for recirculation. If this method is to be used, the ore must be coarse enough to permit the percolation of the solution, but the particle size must be small enough so that the uranium minerals are exposed to the solution.

To simulate heap leaching, small-scale percolation tests were made on sample 1 in 1-1/2-inch- and in 4-inch-diameter columns. The bed depth was from 1 to 2 feet. The solution was added at a rate which maintained a layer of about 1/4 inch of liquid on top of the bed. This procedure is termed a "flooded column" operation. Effluent was collected and recycled. Figure 1 shows the bench-scale column arrangement used in these tests.

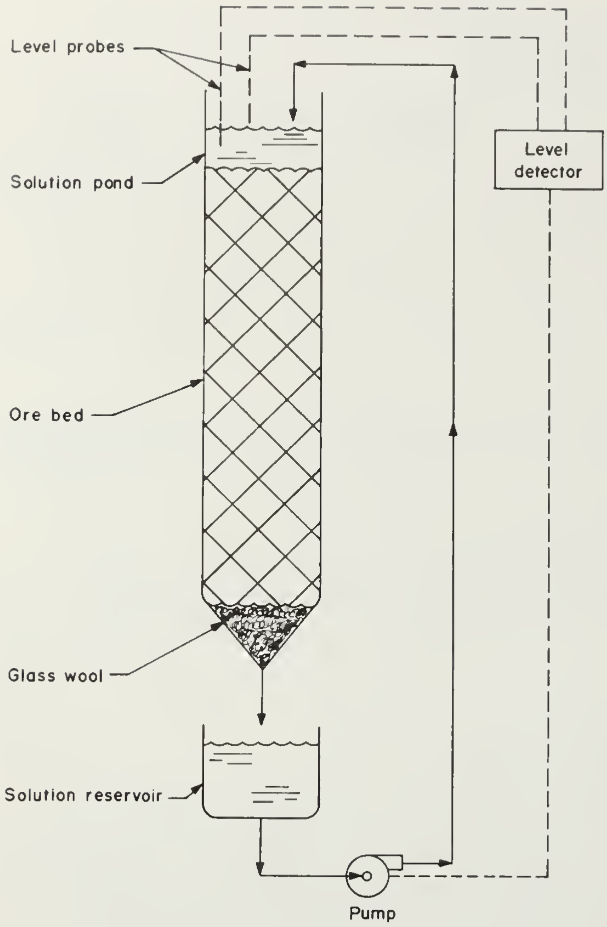

FIGURE 1. - Laboratory flooded column for percolation leaching.

The results of the small-scale percolation leaching tests are given in tables 8-9. Both total extractions and rate effects are shown. The total U_3O_8 extraction after completion of the test is given in table 8. The last column in table 9 gives the extraction percentage that is reached at various times. The acid requirement and uranium extraction were essentially the same as for batch agitation leaching (refer to table 3). The minus 3-mesh material gave slightly lower U_3O_8 extraction and also required a longer leaching time. The indicated flow rates would be adequate for heap leaching, which can be done with percolation rates as low as 2 gallons per square foot per day (2). The time needed for maximum uranium extraction by percolation leaching was much longer than for agitation leaching.

TABLE 8. - Percolation with acid solution in a flooded column, sample 1[1]

Test	Column diameter, in	Grind	H_2SO_4, lb/ton	Duration, hr	Final solution pH	U_3O_8 extraction, pct
1..........	1.5	Minus 10-mesh.....	10	75	1.6	42
2..........	1.5	.....do...........	20	74	1.1	83
3..........	1.5	.....do...........	40	74	.5	89
4..........	1.5	.....do...........	[2]40	24	-	88
5..........	4	Minus 3-mesh......	40	170	.7	84

[1] Conditions: ambient temperature; ore bed height 11 inches for 1-1/2-inch-diameter column, 25 inches for 4-inch-diameter column.

[2] Ore was wetted with water, then blended with concentrated H_2SO_4 and allowed to stand at ambient temperature for 145 hours before percolating with water.

TABLE 9. - Stream data for percolation with acid solution in a flooded column, sample 1

Test	Time after start of test, hr	Flow rate, gal/sq ft day	U_3O_8 extraction, pct
1................	21	16	-
	45	15	39
	73	10	42
2................	20	4	-
	45	3	-
	73	14	83
3................	21	6	-
	45	9	75
	73	8	89
4................	-	-	-
5................	74	6	50
	98	8	63
	123	10	71
	145	12	79

Percolation Leaching in a 12-Inch-Diameter Column

A larger scale percolation leaching test was made to examine further the feasibility of this method of extraction and also to provide enough pregnant solution for subsequent uranium purification by ion exchange and precipitation. Sample 2 was used to determine the behavior of the combined red and yellow fractions.

A 12-inch-diameter column was loaded with 240 pounds of sample 2, making an ore bed 3 feet deep. A photograph of the column is shown in figure 2. Except for the size of the apparatus, the setup was essentially the same as that used for the smaller columns. The procedure was the same except that a constant solution flow rate of 9.3 gallons per square foot per day was used instead of the flooded column technique. The ore bed accepted this flow rate, and no solution ponding on top of the bed was observed during the test. The solution was distributed over the bed surface by directing the flow onto a plastic screen covering the top of the bed. Upon completion of the test, the leach solution was allowed to drain, and three wash solutions were added at the same flow rate and collected separately. The wash solutions were adjusted to pH 1.5 to prevent possible precipitation of uranium from solution, which can occur if the pH becomes higher than 1.5 to 2.0. The data are summarized in tables 10-11.

TABLE 10. - Stream data for percolation with acid solution in a 12-inch-diameter column, sample 2[1]

Time, days	Solution				U_3O_8 extraction, pct
	pH	Emf, mv[2]	Assays, g/l		
			U_3O_8	Fe	
2..................	0.2	-660	2.76	2.6	39
14..................	.32	-	3.53	8.35	50
21..................	-	-	3.65	10.9	51
35..................	.42	-735	3.74	13.3	52
64..................	-	-710	3.84	15.2	54
77..................	.7	-700	3.92	15.4	55
139..................	.95	-625	4.35	17.3	61

[1] Conditions: 240-lb charge, minus 2-inch size, bed height 3 feet, 50 lb/ton H_2SO_4, 82 percent solids, solution flow rate 9.3 gal/sq ft day.

[2] Emf values are based on the sign convention that the more negative the value, the more oxidizing the conditions. Voltages measured in reference to a platinum-calomel electrode.

TABLE 11. - Washing data for percolation test in 12-inch-diameter column, sample 2

Solution	Volume added, liter	Volume out, liter	pH	Assays, g/l	
				U_3O_8	Fe
Leach liquor.........	24.3	5.6	0.95	4.35	17.3
Wash 1...............	18.7	18.8	1.05	2.89	11.4
Wash 2...............	18.7	18.0	1.35	.45	2.0
Wash 3...............	18.7	18.1	1.75	.10	-

Most of the uranium dissolution occurred within 14 days, and a significant amount was leached in only 2 days. This would be the expected result of preferential leaching of the yellow component, as predicted by the small column tests. The red fraction would be expected to leach very slowly by percolation and yield a low recovery even over a long period. If, for example, 75

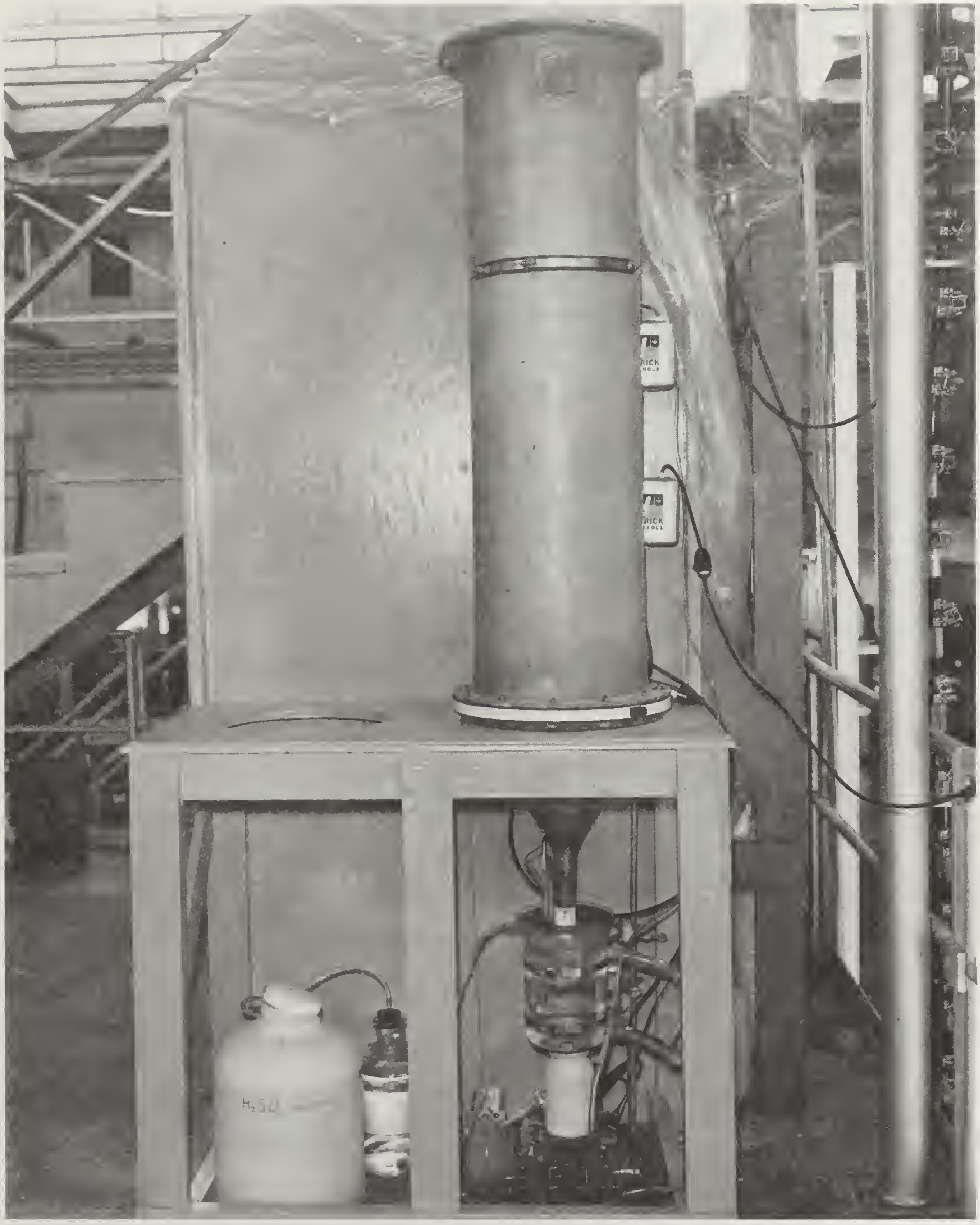

FIGURE 2. - Twelve-inch-diameter column for percolation leaching.

percent of the uranium were contained in the yellow material, then a recovery rate of 80 percent from the yellow fraction and zero from the red fraction would give an extraction of 60 percent for the entire sample; the actual recovery was 61 percent.

The data given in table 11 indicate that the washing procedure previously described was effective. Essentially all of the soluble uranium was removed by three washes.

It was expected that the larger pieces of yellow conglomerate would break down during the course of the leaching and that some fines would appear in the outflow of the column. In fact, no fines were observed, and screen analyses before and after leaching showed no such breakdown. The fractions of minus 4-mesh material before and after leaching were 65 and 67 percent, respectively.

Uranium Recovery From Leach Solution

The feasibility of the recovery and purification of uranium from acid leach solution by ion exchange extraction and precipitation was examined. The leach and wash solutions from the 12-inch column operation were composited resulting in a 1.15 pH solution containing 1.56 grams per liter U_3O_8 and 5.3 grams per liter Fe. This solution was put through a fixed bed of Amberlite IRA 430 resin. With a nominal solution residence time of 60 minutes (based on the volume of wet settled resin), the initial effluent contained 0.001 gram per liter U_3O_8. The loaded resin was eluted with 8 volumes of 1.5 $\underline{M}$ NaCl solution acidified to a pH of 1.0 with H_2SO_4 and then washed with 1 volume of water. The residence time of the eluant was 100 minutes. The eluate contained 6.5 grams per liter U_3O_8, and the eluted resin contained 0.42 gram per liter U_3O_8.

The final yellow cake product was made by precipitation with hydrogen peroxide and ammonia using a standard procedure (4). After drying, this product assayed 4.0 percent Fe and 2.2 percent sulfate; these are acceptable levels for these impurities. The precipitation filtrate contained 0.001 gram per liter U_3O_8. Hence, the ion exchange and precipitation steps recovered more than 99.9 percent of the U_3O_8 from the leach solution.

CONCLUSIONS AND RECOMMENDATIONS

1. The yellow component of the Coso Range material can be effectively agitation leached in 1/2 hour with a 20- to 40-pound-per-ton H_2SO_4 addition. The addition of an oxidant does not improve the leaching.

2. Leaching the red fraction of this material does not appear to be practical. Roasting before leaching is necessary. If the red and yellow fractions could be separated, unnecessary roasting of the yellow fraction, which is the bulk of the material, would be avoided.

3. The yellow fraction can be processed by percolation or heap leaching with H_2SO_4 solution. The reagent requirements are no greater than for agitation leaching, and the indicated percolation rates are high enough to make

these methods practicable. If the red fraction of the ore is present, the uranium extraction from this material is low, but the effectiveness of leaching the yellow fraction is not affected.

4. The yellow material responded to both agitation and percolation leaching. Cost studies would be required to determine which procedure is more advantageous for any specific application.

5. Uranium recovery from acid leach solution is effective. Anion exchange and precipitation steps give a high recovery and a good yellow cake product.

It is recommended that the yellow and red ore components be separated before this material is processed. Screening at approximately 1/2 inch should be considered as a method for making this separation.

REFERENCES

1. Facer, J. F., Jr. Production Statistics. Uranium Industry Seminar, Grand Junction, Colo., Oct. 19-20, 1976, GJO-108 (76), Energy Research and Development Administration, pp. 191-200.

2. Mashbir, D. Heap Leaching of Low Grade Uranium Ore. Min. Cong. J., December 1964, p. 50.

3. Merritt, R. C. The Extractive Metallurgy of Uranium. U.S. Atomic Energy Commission, Colorado School of Mines Research Institute, Golden, Colo., 1971, 576 pp.

4. Shabbir, M., and K. E. Tame. Hydrogen Peroxide Precipitation of Uranium. BuMines RI 7931, 1974, 13 pp.

☆U.S. GOVERNMENT PRINTING OFFICE: 1978-703-103/61

INT.-BU.OF MINES,PGH.,PA. 23234

622.07
Un32mo

RI 8307

Bureau of Mines Report of Investigations/1978

DEPOSITORY
NOV 27 1978
UNIV. OF ILL. LIBRARY
AT URBANA-CHAMPAIGN

Chemical Flame Inhibition Using Molecular Beam Mass Spectrometry

Reaction Rates and Mechanisms in a Methane Flame Inhibited With 1.1% CF_3Br

UNITED STATES DEPARTMENT OF THE INTERIOR

Report of Investigations 8307

Chemical Flame Inhibition Using Molecular Beam Mass Spectrometry

Reaction Rates and Mechanisms in a Methane Flame Inhibited With 1.1% CF_3Br

By Joan C. Biordi, Charles P. Lazzara, and John F. Papp

March 3 1849

UNITED STATES DEPARTMENT OF THE INTERIOR
Cecil D. Andrus, Secretary

BUREAU OF MINES

This publication has been cataloged as follows:

Biordi, Joan C

Chemical flame inhibition using molecular beam mass spectrometry; reaction rates and mechanisms in a methane flame inhibited with 1.1% CF_3Br / by Joan C. Biordi, Charles P. Lazzara, and John F. Papp. [Washington] : U.S. Dept. of the Interior, Bureau of Mines, 1978.

43 p. : ill., diagrs. ; 27 cm. (Report of investigations - Bureau of Mines ; 8307)

Bibliography: p. 31-34.

1. Flame - Analysis. 2. Flame spectroscopy. 3. Mass spectrometry. I. Lazzara, Charles P., joint author. II. Papp, John F., joint author. III. United States. Bureau of Mines. IV. Title. V. Series: United States. Bureau of Mines. Report of investigations - Bureau of Mines ; 8307.

TN23.U7 no. 8307 622.06173
U.S. Dept. of the Int. Library

CONTENTS

Page

Abstract 1
Introduction 1
Experimental work 2
Results and interpretation 6
Composition 6
Rate coefficients of elementary flame reactions 8
Comparisons among clean and inhibited flames 11
Disappearance of CF_3Br 15
Compositions and kinetic analyses of inhibitor-related species 17
Summary 29
References 31
Appendix A.--Flame species smoothed composition profiles 35
Appendix B.--Flame species net reaction rate profiles 39
Appendix C.--List of symbols 43

ILLUSTRATIONS

1. Element conservation for clean and inhibited flames 5
2. Temperature and composition profiles for the major stable species of the uninhibited flame III 6
3. Temperature and composition profiles for the major radical species and formaldehyde in the uninhibited flame III 6
4. Temperature and composition profiles for the major stable species unrelated to the inhibitor in flame IV 7
5. Temperature and composition profiles of principal unstable species (except H) and the inhibitor, flame IV 7
6. Temperature and composition profiles for the major stable species related to the inhibitor in flame IV 7
7. Composition profiles for minor intermediate species, both stable and unstable, and for H atom, flame IV 7
8. Net reaction rate profiles for the major species of the uninhibited flame III 9
9. Net reaction rate profiles for the major stable species unrelated to the inhibitor in the inhibited flame IV 9
10. Rate coefficients determined for elementary reactions occurring in methane flames 9
11. Net reaction rate as a function of distance from the burner surface for methane and oxygen in flames III and IV 11
12. Mole fraction of H, O, OH, and CH_3 as a function of temperature in the uninhibited flame III and the inhibited flame IV containing 1.1% CF_3Br 11
13. Net reaction rate for the inhibitor as a function of temperature for two nearly stoichiometric methane flames containing initially different amounts of CF_3Br 14
14. Rate coefficient for thermal decomposition of CF_3Br, expressed as first order, calculated assuming Br atom abstraction occurs with the rate constant previously determined 16

ILLUSTRATIONS--Continued

Page

15. Net reaction rate profiles for HF, CF_2, and CF_3Br in flame IV..... 18
16. Net reaction rate profiles for CH_3Br, CH_2CF_2, and HBr in flame IV. 18
17. Net reaction rate profiles for Br_2, CF_3H, and F_2CO in flame IV.... 19
18. Rate coefficient for the reaction $CH_3+CF_3Br \rightarrow CH_3Br+CF_3$ as a function of temperature as determined from analysis of flame II and flame IV.. 21

TABLES

1. Characteristics of flames examined at 0.042 atm.................. 3
2. Temperature for maximum rate of decay of fuel and inhibitor in 0.042 atm, nearly stoichiometric CH_4-O_2-Ar flames........... 15
3. Reactions of the principal fluorocarbon species in inhibited flames.. 23
4. Reactions responsible for the formation of fluorocarbons in CF_3Br-inhibited flames.................................... 30
5. Summary of rate coefficients determined from kinetic analysis of a methane-oxygen-argon flame containing 1.1% CF_3Br initially. 30
A-1. Characteristics of flames III and IV examined at 0.042 atm......... 35
A-2. Smoothed composition profiles for the species in flame III....... 36
A-3. Smoothed composition profiles for the species unrelated to the inhibitor in flame IV.. 37
A-4. Smoothed composition profiles for the species related to the inhibitor in flame IV.. 38
B-1. Net reaction rate profiles for the species in flame III.......... 40
B-2. Net reaction rate profiles for the species unrelated to the inhibitor in flame IV.. 41
B-3. Net reaction rate profiles for the species related to the inhibitor in flame IV.. 42

CHEMICAL FLAME INHIBITION USING MOLECULAR BEAM MASS SPECTROMETRY

Reaction Rates and Mechanisms in a Methane Flame Inhibited With 1.1% CF_3Br[1]

by

Joan C. Biordi,[2] Charles P. Lazzara,[3] and John F. Papp[4]

ABSTRACT

The Bureau of Mines used molecular beam-mass spectrometry to determine the microstructure of a 10.1% CH_4-21.2% O_2-67.6% Ar-1.1% CF_3Br inhibited flame and its uninhibited analog, both stabilized at 32 torr on a cooled flat-flame burner. Composition profiles of atomic, radical, and stable species and temperature profiles for both flames were obtained and compared. Kinetic analyses of the profiles yielded values for the rate coefficients of several elementary methane flame reactions and information on the reactions of formation and decay of the observed halocarbon species. CF_3Br is judged to decay by thermal decomposition as well as by abstraction reactions, and the fluorocarbon chemistry occurring in the inhibited flame is due primarily to CF_2 radical reactions. Rate coefficients and mechanisms for reactions of the inhibitor-related species are given.

INTRODUCTION

Chemical flame inhibitors are considered to act by interfering with the normal chemical reaction paths of flame propagation. This Bureau of Mines report is one of a series that documents an effort to provide the basic flame data required to understand the mechanisms by which flame inhibitors operate at the molecular level.

In the preceding papers (4, 7-8)[5] we have reported on the general character of the microstructure of low-pressure methane flames containing a small amount of CF_3Br and on the detailed kinetics and mechanisms for a flame containing 0.3% CF_3Br in comparison with its uninhibited analog. It was clear from examination of these flames that the fluorine part of the inhibitor molecule reacts rapidly in the flame, but it was not possible to detect the CF_3 radical despite the ability to detect and measure other flame radicals with mole fractions of 10^{-4} to 10^{-5}. It was found that although the H atom concentration was reduced at low temperatures in the inhibited flame relative to the clean flame, some manifestations of inhibition observed for other chemical inhibitors, such as HBr (52), were only marginally evident. We therefore chose to examine the detailed microstructure of a flame containing significantly more CF_3Br to improve our chances of observing the CF_3 radical, to look for more pronounced effects of the inhibitor, and to obtain more data for clarifying mechanisms in this complex reaction system.

---

[1] This report is a combined and expanded version of two articles published in the Journal of Physical Chemistry (12-13).

[2] Research chemist, Bureau of Mines, Washington, D.C., formerly with Pittsburgh Mining and Safety Research Center, Bureau of Mines, Bruceton, Pa.

[3] Research chemist, Pittsburgh Mining and Safety Research Center, Bureau of Mines, Bruceton, Pa.

[4] Research physicist, Pittsburgh Mining and Safety Research Center, Bureau of Mines, Bruceton, Pa.

[5] Underlined numbers in parentheses refer to items in the list of references preceding the appendixes.

EXPERIMENTAL WORK

Two flames were examined at 0.042 atm: an uninhibited, slightly lean CH_4-O_2-Ar flame, and a flame of similar stoichiometry containing initially 1.1% CF_3Br. These quenched, flat flames differ from those studied previously in initial mass flow rate and, therefore, in burning velocity. A burning velocity of about 48 cm sec^{-1} for the clean flame was found to give satisfactorily stable (for quantitative microstructure determinations) inhibited flames when the CF_3Br was added.

The molecular beam sampling mass spectrometric detection system was the same as described previously, as were the techniques for radical detection and measurement (4, 7-8). Only departures from previously described procedures will be given here.

The formaldehyde profiles, determined at 30 amu, were corrected for $C^{18}O$. The expression used for the correction is $I_{30(H_2CO)} = I_{30} - (^{18}O/^{16}O)\ I_{28}$, where $(^{18}O/^{16}O)$ is the ratio of the natural isotopic abundance of ^{18}O to ^{16}O and I is the measured mass spectral intensity of mass 30 and mass 28 ($C^{16}O$) as indicated. This correction was not made in previously reported profiles for H_2CO (7-8). The effect of this correction to flames I and II, the clean and 0.3% CF_3Br flames, respectively, was to reduce the maximum X_{H_2CO} by 15% in flame I and 25% in flame II and to eliminate the apparent residual H_2CO in the secondary reaction zone.

The change in initial mass flow rate (burning velocity) for the clean flame from that previously used resulted in a different final flame temperature. The area expansion ratio profile was also different at the lower linear flow velocity. The characteristics of the two flames studied here, flame III and flame IV, as well as the two flames examined previously, flame I and flame II, are given in table 1. Flame temperature profiles were measured using fine wire platinum versus platinum-10% rhodium thermocouples coated with silica to minimize surface radical recombination. A temperature correction was made for the radiant energy loss of the thermocouple.

TABLE 1. - Characteristics of flames examined at 0.042 atm

	Flame I	Flame II	Flame III	Flame IV
Flow, g sec^{-1}:				
CH_4	0.0182	0.0182	0.0107	0.0108
O_2	0.0763	0.0765	0.0456	0.0455
Ar	0.3005	0.3002	0.1811	0.1808
CF_3Br	0	0.0047	0	0.0110
CH_4 ... mole-pct	10.3	10.3	10.1	10.1
O_2 ... mole-pct	21.6	21.6	21.5	21.2
Ar ... mole-pct	68.1	67.8	68.4	67.6
CF_3Br ... mole-pct	0	0.3	0	1.1
V_o[1] ... cm sec^{-1}	79.3	79.5	47.6	48.0
T_{max}[2] ... K	1,868	1,911	1,781	1,966
T_{ad}[3] ... K	2,379	2,374	2,375	2,358
A[4]	1.0+0.13z	1.0+0.13z	1.0+0.35z	1.0+0.35z

[1] Calculated using $T_{initial}$ = 298 K.

[2] As determined in the absence of the sampling probe (5).

[3] Calculated adiabatic flame temperature.

[4] Area expansion ratio (dimensionless) expressed as a function of distance from the burner surface, z, in centimeters, for $0<z<1$ cm.

Mass spectral sensitivities for CH_3Br, CH_2CF_2, F_2CO, HF, and Br in the 1.1% CF_3Br flame were determined by direct comparison with the flame containing initially 0.3% CF_3Br. That is, the 0.3% CF_3Br flame served as the calibration standard for the named species in the 1.1% CF_3Br flame. For CH_3Br (±10%), CH_2CF_2 (±2%), and F_2CO (±18%), the relative ionization cross-section calculations were also performed in the manner previously described (7) and the percent variation between the two approaches is given in the parentheses. This agreement gives an indication of the precision of the cross-section calculations from one set of ionizer conditions to another. For HBr (±8%), Br (<1%), and HF (±6%) conservation of mass calculations showed good agreement, as noted parenthetically, with the 0.3% CF_3Br flame calibration procedure, and this is an indication of the precision with which these flames can be reproduced on the burner over extended periods of time.

For CF_3Br, the initial points of the profile were set equal to the known, initial CF_3Br concentration. This is a more reliable procedure for CF_3Br than calibration with the initial, cold gas mixture because of possibly different temperature dependencies in the scattering function for CF_3Br and Ar, and the possible temperature effects on the CF_3Br fragmentation pattern. Both of these effects are quantitatively unknown, but since the temperature over the initial portion of the profile reaches 900 K, the procedure adopted essentially corrects for them up to that temperature.

In addition to the CF_2 radical (11), two other previously unobserved species, CF_3H and Br_2, were observed and measured. CF_3H was monitored as CHF_2^+ at mass 51, corrected for ^{13}C contributions from CF_2^+ at mass 50. The latter ion is formed from several other inhibited flame species. At the position in the flame for which CF_3H is a maximum, these corrections amounted to 10% of the observed intensity at 51 amu. An ionization efficiency curve for 51 amu determined at the maximum yielded an appearance potential of 15.4±0.5 ev. The lowest reported appearance potential for CHF_2^+ from CF_3H is 15.75 ev (36). Other compounds (21) for which CHF_2^+ appearance potentials have been reported can be eliminated, either on the basis of their appearance potentials or because of lack of supporting mass spectral evidence for their existence in this flame. Lifshitz and Long (35) calculated a value of 15.7 ev for CHF_2^+ from CH_2CF_2, which is present in the flame, but consider that the rearrangement required to give this ion has a very low probability of occurrence. The profiles of mass 64 and mass 51, determined simultaneously in order to test this conclusion, are sufficiently different to insure that they derive from different species. The cross-section technique (11) was used to estimate the CF_3H concentration. Two calculations were made, one with the comparison ion CF_2^+ at 50 amu from CF_3Br, and one with FCO^+ at 47 amu from F_2CO. The results were the same to ±10%.

Br_2 was identified by its characteristic triplet at 158-160-162 amu, a feature not observed in the mass spectrum of CF_3Br or HBr. The uncertainty in the absolute concentration of Br_2 is large because of the need to estimate a partial ionization cross section for CF_3Br^+, the only possible comparison ion to minimize discrimination in the mass filter. The calculated value for $X_{Br_2}(\max)$, $\sim 3\times10^{-6}$, is probably good only to within an order of magnitude.

The physical model and computational techniques used to analyze the profile data as well as a program listing and output for one flame have been published (40). From the concentration profiles, profiles of fractional mass flux, G_i, are calculated for each species according to the equation

$$G_i = \left[\frac{M_i}{\Sigma X_i M_i}\right]\left\{X_i - \left(\frac{D_{i-Ar}}{v}\right)\left[\frac{dX_i}{dz} + k_{T_i}\frac{d\ \ln\ T}{dz}\right]\right\}, \tag{A}$$

where z is the perpendicular distance from the burner surface, X_i denotes mole fraction, M_i molecular weight, D_{i-Ar} the binary diffusion coefficient with argon, k_{T_i} the binary thermal diffusion ratio with argon, and v the average bulk flow velocity. Individual species net reaction rates, the sum of the rates of all reactions forming and all reactions consuming a given species, are calculated as

$$K_i = \frac{\rho_o v_o}{A\ M_i}\left(\frac{dG_i}{dz}\right), \tag{B}$$

where ρ_o and v_o are the cold gas density and velocity, respectively, and A is the area expansion ratio. These net reaction rates, together with the concentrations and temperatures at each position in the flame, are the starting point from which kinetic analyses and deductions about mechanisms are made.

Application of the requirements of conservation of matter at the atomic level provides a test of the internal consistency and accuracy of the concentration profiles and their reduction to flux profiles (22). At each point in the flame the deviation of the net flux of any atomic species from its known inlet flux should be zero. Figure 1 shows the deviation in percent for C, H, and O in flames III and IV, and for F and Br in flame IV. Figure 1D is the

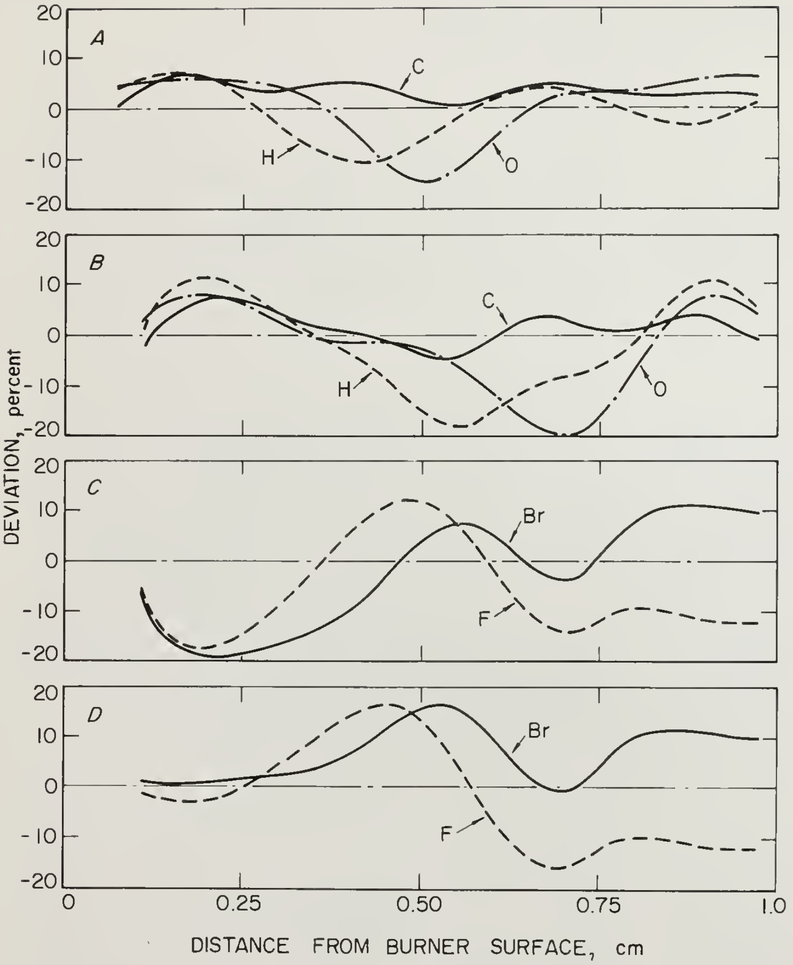

FIGURE 1. - Element conservation for clean and inhibited flames. *A*, Carbon, hydrogen, oxygen in flame III; *B*, carbon, hydrogen, oxygen in flame IV; *C*, bromine and fluorine in flame IV; *D*, same as in *C* except thermal diffusion is ignored.

result of a calculation for flame IV in which k_T was set equal to zero. This calculation suggests that part of the reason for the low F and Br flux at low values of z, where the CF_3Br profile is nearly flat, is an error in evaluation of the thermal diffusion flux for the inhibitor. Whether this is due primarily to the use of unrealistic molecular parameters (40) in calculating k_T for CF_3Br or in probe perturbation to the temperature gradient close to the burner surface is not known. In the region of the flame where the magnitude of the CF_3Br net reaction rate is near its maximum, T∼1,650 K, and at higher temperatures, the thermal diffusion term makes a negligible difference in K_{CF_3Br}. Thus, calculations of reaction rate coefficients involving CF_3Br in this part of the flame are not strongly affected by the modeling of thermal diffusion. At lower temperature--for example, at 1,400 K where $|K_{CF_3Br}| \sim 0.1 |K_{CF_3Br}|_{max}$--the magnitude of the net reaction rate is about 50% higher with $k_T = 0$.

The broad, qualitative description of the complex experimental and analytical procedures used to gather the data of this report is admittedly written for readers familiar with the conventional technique of flame microstructure and with our previous communications on this subject. Further information on conventional techniques is available elsewhere (22). The details of our experiments have been published with respect to construction of the burner, probe, and detector and their performance (4), temperature measurements (4), the problem of probe perturbation to the flame (5), the identification and measurement of radical species in the flame (34), data reduction techniques (40), and applicability of these techniques to the determination of rate coefficients for reactions occurring in flames (7, 10).

RESULTS AND INTERPRETATION

Composition

As before, the complete microstructure of a clean flame and its inhibited analog were determined. Figures 2 and 3 show the mole fraction species profiles measured for the uninhibited flame III, $z \leq 1$ cm. Figures 4 through 7 show the mole fraction species profiles measured for the inhibited flame IV containing 1.1% CF_3Br. The temperature profiles determined for these flames are also shown and they have been shifted to account for the probe cooling effect described previously (5).

In these figures, the symbols are the data points and the lines through them are the results of applying smoothing techniques (40) to the data points for the purpose of calculating smooth first and second derivatives. Profiles were actually measured, though with a smaller density of data points, as far as $z = 13$ cm, with smoothing techniques applied using data points out to 1.7 cm. The ostensibly too low, flat portion of the Br curve reflects the average of all these data points. The H, O, and OH profiles shown here appear to be inconveniently truncated at $z = 1$ cm. Extended profiles of these species are given in reference 9. No attempt was made to measure the radicals HCO and HO_2 in either flame, although both had been observed in earlier studies. Appendix A contains a partial computer listing (every fifth point) of the smoothed mole fraction profiles for flames III and IV.

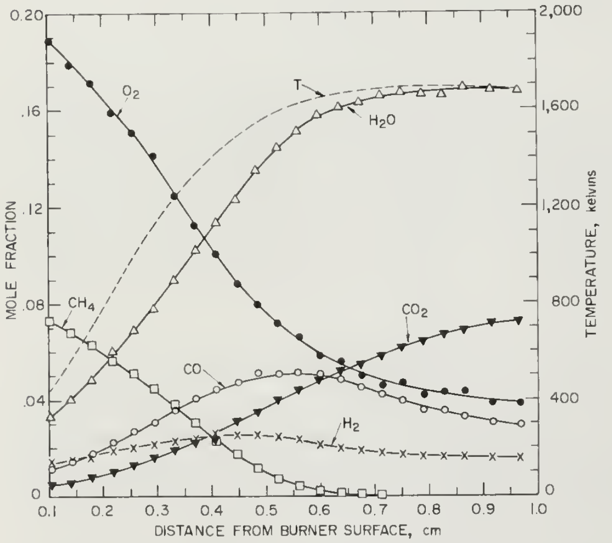

FIGURE 2. - Temperature and composition profiles for the major stable species of the uninhibited flame III.

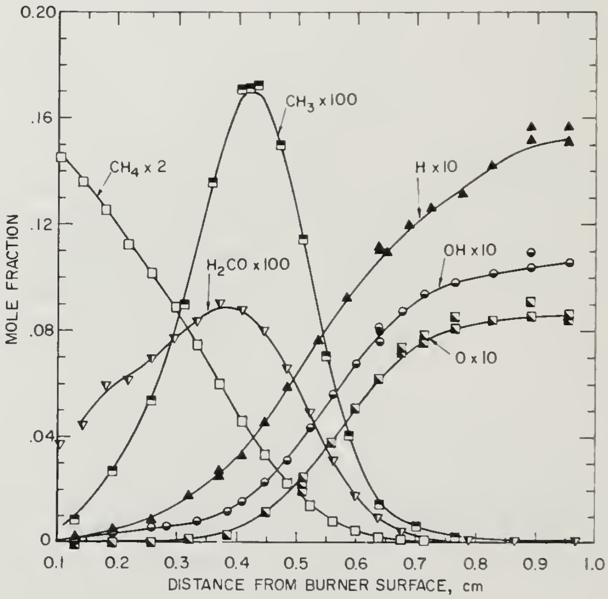

FIGURE 3. - Temperature and composition profiles for the major radical species and formaldehyde in the uninhibited flame III.

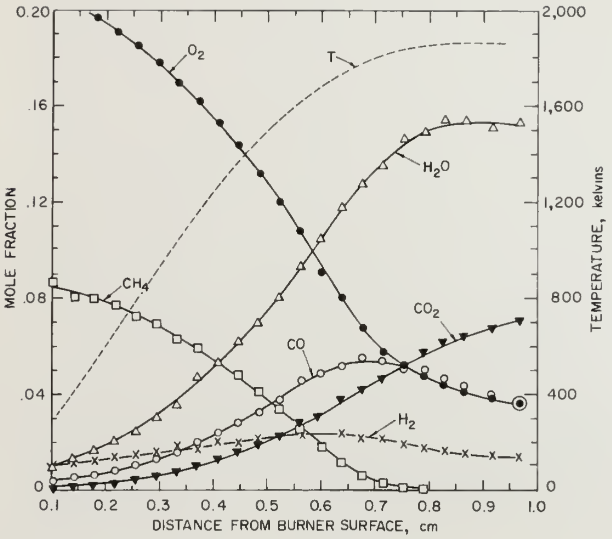

FIGURE 4. - Temperature and composition profiles for the major stable species unrelated to the inhibitor in flame IV.

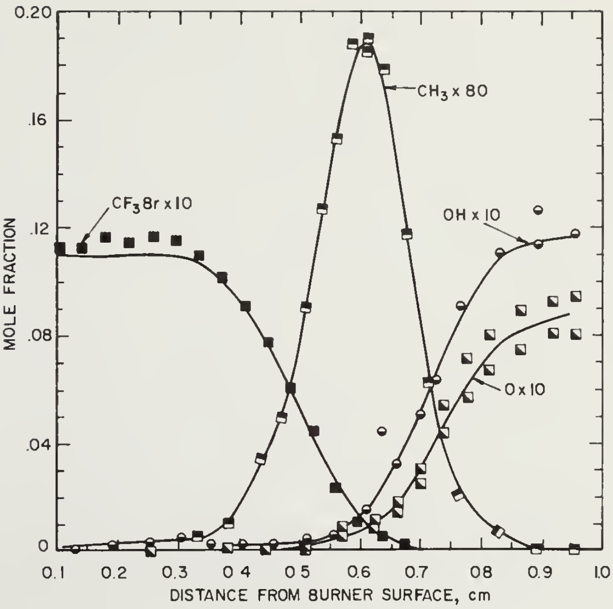

FIGURE 5. - Temperature and composition profiles of principal unstable species (except H) and the inhibitor, flame IV.

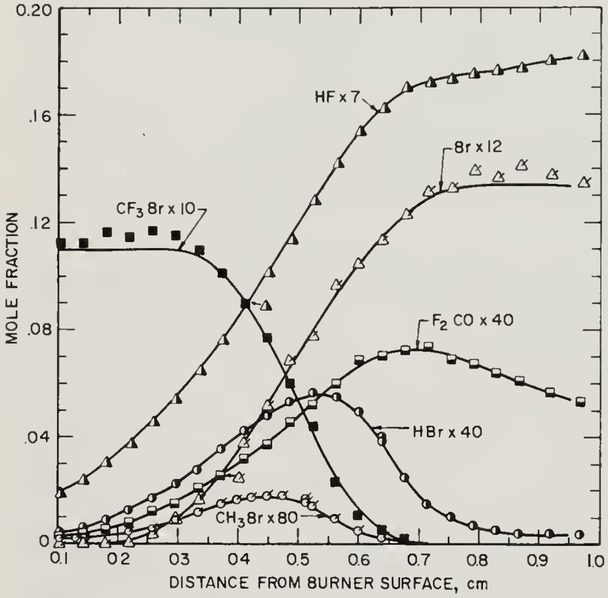

FIGURE 6. - Temperature and composition profiles for the major stable species related to the inhibitor in flame IV.

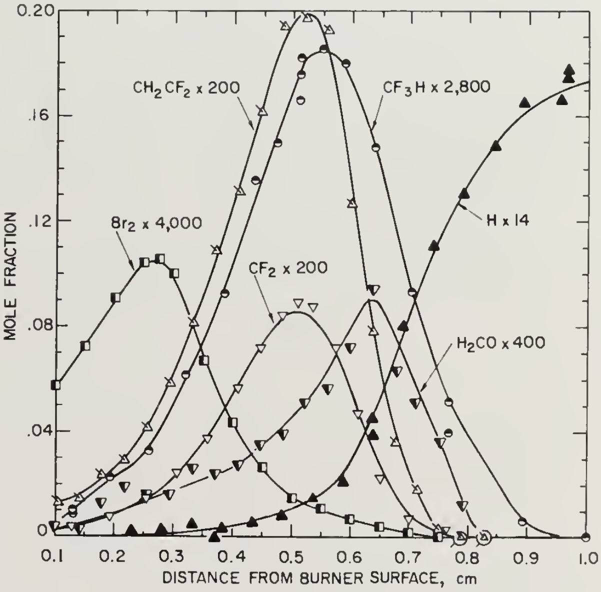

FIGURE 7. - Composition profiles for minor intermediate species, both stable and unstable, and for H atom, flame IV.

A comparison of the maximum concentrations of species related to the inhibitor in flames containing 0.3% and 1.1% CF_3Br initially shows them to be three to four times greater in the latter flame. This corresponds roughly to the ratio of initial CF_3Br concentrations and implies that there are no marked changes in the mechanism of formation and decay of these species between the two inhibited flames. In detail, of course, this must depend upon the relative temperature dependencies of the reactions involved. CF_3H and Br_2 have maximum mole fractions of 6.6×10^{-5} and 2.6×10^{-5}, respectively, in flame IV. They were not observed in the 0.3% CF_3Br flame, probably because one-third to one-fourth of these maxima is near the limit of detection for our apparatus as presently used. For the same reason, we could not unambiguously detect the CF_3 radical in either flame. However, the observation of CF_3H provides a route for calculating the concentration profile for CF_3 (11). This calculation gives a maximum mole fraction of CF_3 of about 3×10^{-5} occurring at $z = 0.52$ cm in flame IV. Because the appearance potential for CF_3^- from CF_3 is only 2 ev less than that from CF_3Br, and because of the relatively broad electron energy spread of the ionizer, it is not surprising that such a small contribution to the 69-amu intensity could not be identified in the "tail" of the relatively very strong signal from CF_3Br.

Rate Coefficients of Elementary Flame Reactions

The net reaction rate profiles calculated according to equations A and B are shown in figures 8 and 9 for all the stable species not related to the inhibitor in flames III and IV, respectively. The net reaction rate for each species, K_i (moles cm^{-3} sec^{-1}), is plotted versus z(cm), the distance of the sampling probe from the burner surface. The bumps and shoulders exhibited by several of the rate profiles in figures 8 and 9 are due to small local variations in the smoothed mole fraction data, and no attempt was made to eliminate them. Appendix B contains a partial computer listing (every fifth value) of the net reaction rates for all species observed in flames III and IV.

From the appropriate species net reaction rates, rate coefficients for the following four reactions were calculated over a 100 K range in each flame:

$$H + CH_4 \rightarrow H_2 + CH_3 \qquad (1)$$

$$H + O_2 \rightarrow OH + O \qquad (2)$$

$$CO + OH \rightarrow CO_2 + H \qquad (3)$$

$$CH_3 + O \rightarrow H_2CO + H \qquad (4)$$

The details of these calculations have been discussed elsewhere (8, 10). The results are shown in figure 10, where log k_j is plotted versus (1/T K) for each reaction. The broken lines are from flame III, 1,500-1,600 K, and the solid lines are from flame IV, 1,725-1,825 K. Individual data points are shown only at the beginning and end of the range.

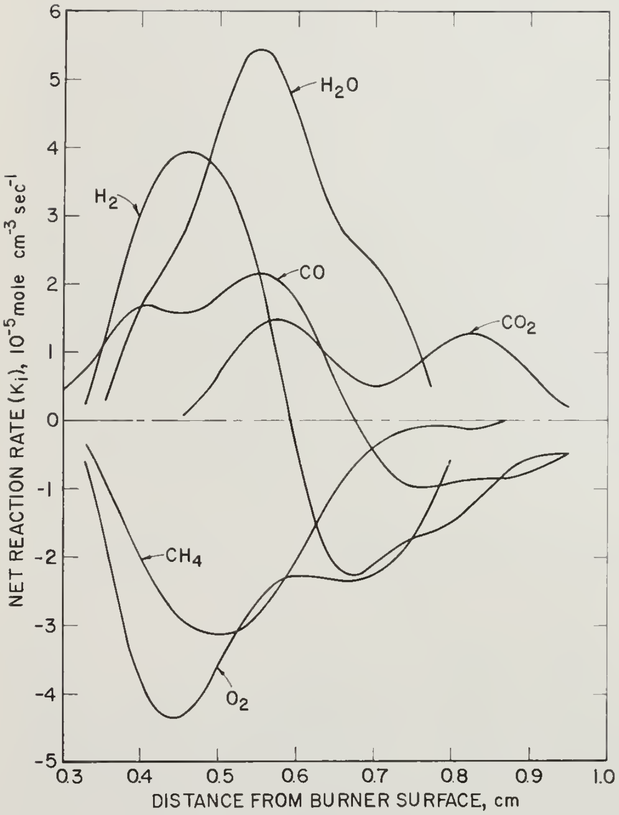

FIGURE 8. - Net reaction rate profiles for the major species of the uninhibited flame III.

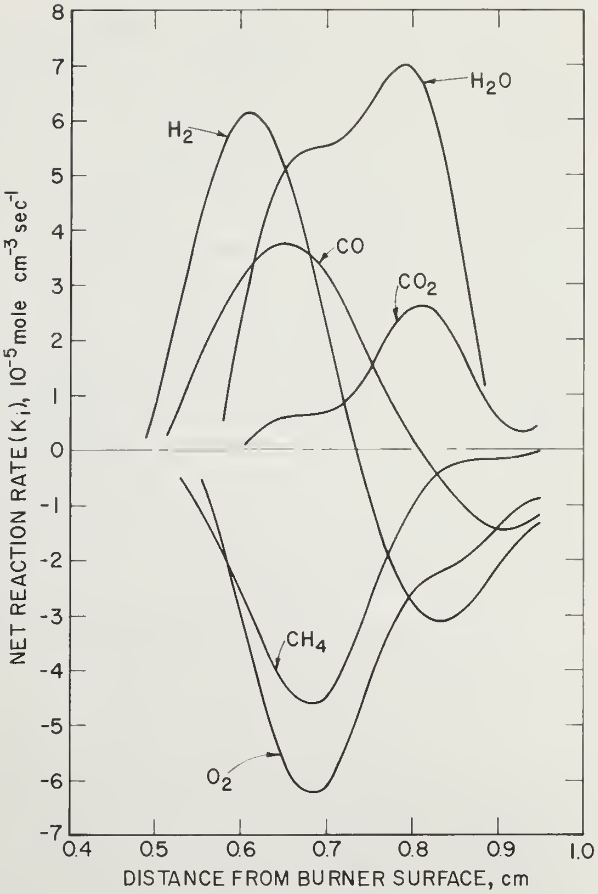

FIGURE 9. - Net reaction rate profiles for the major stable species unrelated to the inhibitor in the inhibited flame IV.

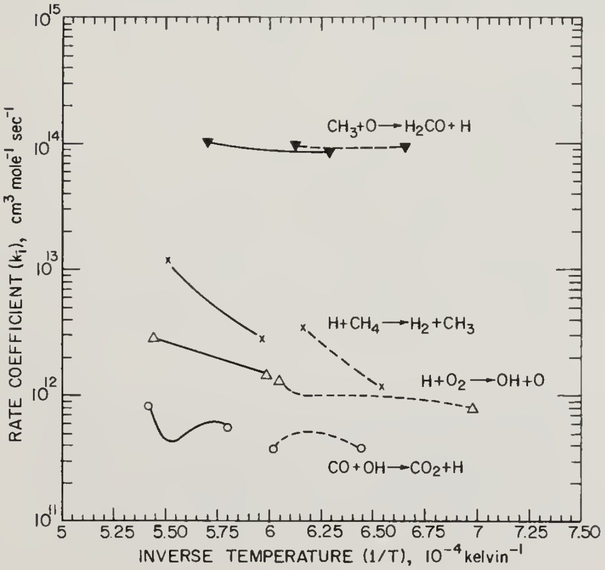

FIGURE 10. - Rate coefficients determined for elementary reactions occurring in methane flames. Dashed lines, results from uninhibited flame III; solid lines, results from inhibited flame IV.

The rate coefficients shown in figure 10 are similar in absolute value and temperature dependence to those obtained for the same reactions in earlier flame structure studies in our laboratory. There are several points to be made regarding these results. The first is in regard to observed temperature dependencies for $H+CH_4$ and $CO+OH$. It is the case that the rate coefficient for $H+CH_4$ exhibits curvature above 1,000 K (6, 15, 44). Thus, straight-line extrapolation of the rate coefficients in figure 10 to lower temperature will lead to erroneously low values of k for this reaction. A smooth extrapolation is not possible even over the 100 K gap that separates temperature ranges covered in these two flames. This reflects upon the precision with which the temperature dependence of a rate coefficient can be determined for a flame reaction when the calculation relies upon the net reaction rate for a species (CH_4) being consumed by other significant reactions ($CH_4 + OH \rightarrow H_2O + CH_3$). For the CO+OH reaction, we cannot discern any temperature dependence for the rate coefficient over the temperature range available in a single flame. However, the difference between the average values for k_3 in each flame gives an activation energy consistent with recent results for this reaction in this temperature range (50).

For flame IV, k_1 is calculated without consideration of the possible interfering reaction

$$Br + CH_4 \rightarrow HBr + CH_3 . \qquad (5)$$

This reaction has been proposed in some mechanisms of halocarbon inhibition as the source of regeneration of HBr, which is considered to be the principal radical scavenger. At the maximum rate of methane disappearance in flame IV, the temperature is 1,790 K, and reaction 5 can be calculated to account for about 6% of the observed net reaction rate for methane, using a rate coefficient determined in clean flames for k_1 (6) and extrapolating a value for k_5 from low-temperature studies (32). To the extent that this extrapolation is correct, reaction 5 is not important over the range of temperature for which k_1 is calculated in flame IV. Similar considerations apply to the calculation of k_4 in flame IV. If in the inhibited flame there are significant new routes for methyl radical disappearance, then k_4 will be lower than calculated here. One possible reaction is

$$CF_2 + CH_3 \rightarrow CH_2CF_2 + H, \qquad (6)$$

and consideration of this reaction would reduce k_4 by $\{k_6 (X_{CF_2}/X_0)\}$ at every point in flame IV. The ratio X_{CF_2}/X_0 is 1 at 1,600 K and ~0.02 at 1,800 K. A reasonable estimate for k_6 is 10^{13} cm^3 $mole^{-1}$ sec^{-1}, by analogy with a similar reaction involving methylene (33, 42), so k_4 might be lower than shown in figure 10 by as much as 12% at the low-temperature end of its range in the inhibited flame.

The relatively good temperature overlap of the rate coefficients shown in figure 10, reaction 1 notwithstanding, between clean and inhibited flames suggests that no significant changes in mechanism are occurring for the reaction of the species in question (CH_4, O_2, CO_2, CH_3) in the regions of the flame where they are reacting most rapidly. These reactions are simply delayed to higher temperatures when the inhibitor is present.

Comparisons Among Clean and Inhibited Flames

As with the flame containing 0.3% CF_3Br, the profiles shown in figures 4-7 are all shifted downstream relative to those of the clean flame (figs. 2-3). The shift is greater here, about 2 mm, than that observed in the 0.3% CF_3Br flame. The net reaction rate profiles for methane and oxygen (fig. 11) are also shifted to higher temperatures and are narrower in the inhibited flame. This effect was not as pronounced with the lower inhibitor concentration (7-8). These results are similar to those obtained by Wilson (52) for very lean CH_4-O_2 flames at 0.05 atm containing initially 1.88% HBr. Radicals could not be observed in that study, but a recent molecular beam investigation of a clean flame of similar composition and pressure (41) shows that OH and O are the dominant chain carriers and are first detected at about the same value of z. The concentration of hydrogen atom is at least four to five times smaller

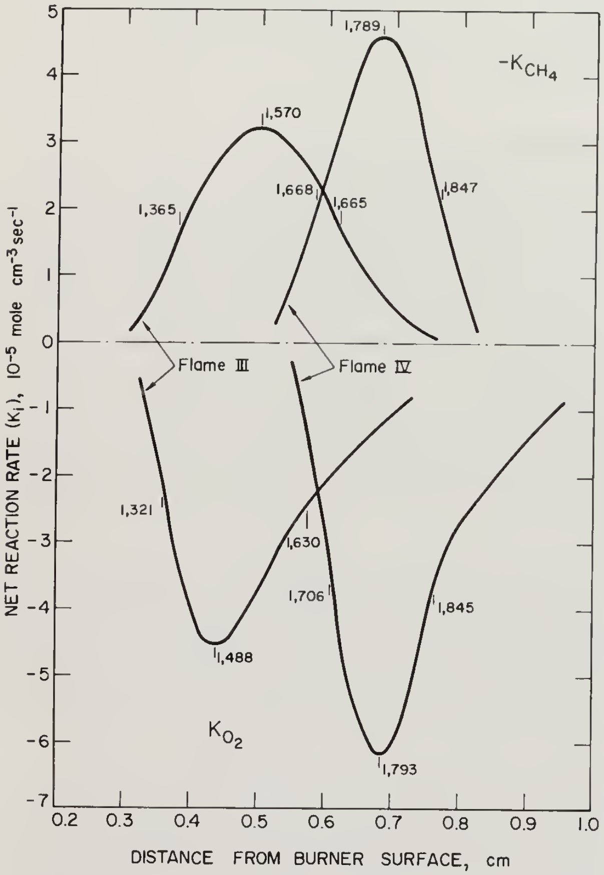

FIGURE 11. - Net reaction rate as a function of distance from the burner surface for methane and oxygen in flames III and IV. The temperature (K) is given at several values of z, cm.

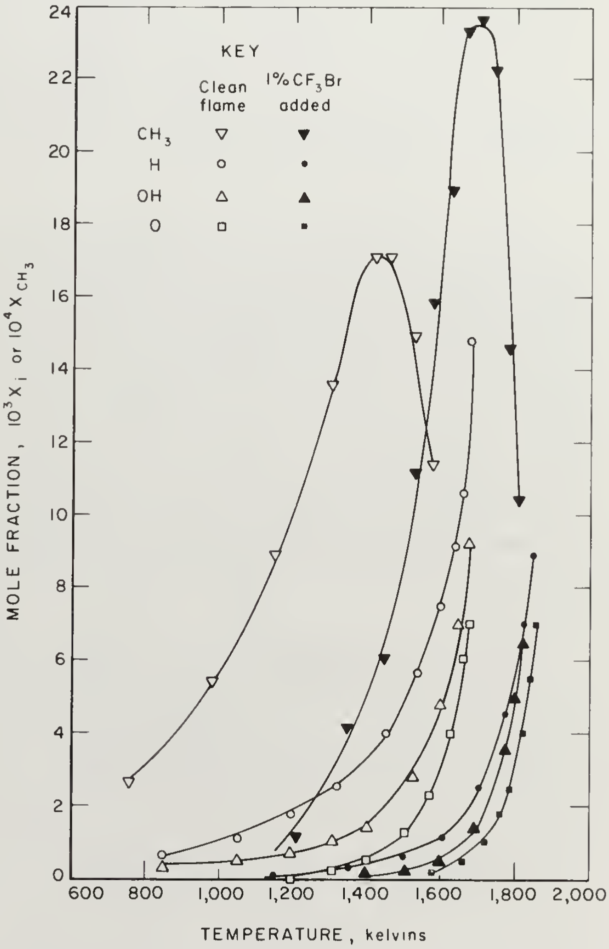

FIGURE 12. - Mole fraction of H, O, OH, and CH_3 as a function of temperature in the uninhibited flame III and the inhibited flame IV containing 1.1% CF_3Br. X_i is the mole fraction of H, O, or OH.

than [OH] and [O] in the lean flame.[6] In the nearly stoichiometric clean flames studied here, H is the chain carrier in greatest concentration everywhere in the flame, and it is observed earliest in the flame. The onset of OH and O is downstream of that for H, but the concentration differences among the three radicals are not as great in the stoichiometric as in the lean flame. Thus, even though different radical species predominate in the early part of these flames, the inhibitor has the same effect on the rates of disappearance of fuel and oxidant in each case. There are no data available that show directly the effect of CF_3Br or HBr on the radical species concentration in lean flames.

An examination (9) of the effect of CF_3Br on the concentrations of the principal radical species, H, O, and OH, reveals that, for flames containing 0.3% CF_3Br initially, only H atom concentrations are reduced at equivalent temperatures below ~1,600 K relative to the clean flame. At higher inhibitor concentration, 1.1% CF_3Br, all three radical concentrations are reduced in the low-temperature region of the flame, as shown in figure 12. The maximum radical concentrations are those expected assuming the characteristic H_2/O_2 reactions balanced at the final flame temperature. These maximum radical concentrations may increase or decrease (both were observed) when inhibitor is added to quenched flames.

The shifting of the primary reaction zone to higher temperature with the addition of inhibitor is responsible for the observed increase in peak methyl radical concentration in flame IV and also provides some insight into the nature of the reactions responsible for the decay of formaldehyde. The reactions forming methyl radical are reaction 1 and the analogous reaction of CH_4 with OH and, less importantly, with O. The rate coefficients for these reactions are temperature dependent. In the inhibited flame they occur at a higher temperature, and therefore CH_3 is formed at a faster rate than in the clean flames. The principal reaction removing CH_3, reaction 4, is not temperature dependent so its rate of decay is about the same in both flames. (At the peak X_{CH_3} in each flame, the concentration of O atoms is about the same.) The net effect is a higher peak concentration for CH_3 in the inhibited flame (fig. 12).

On the other hand, the product of reaction 4, formaldehyde, is reduced by nearly a factor of 4 in the 1.1% CF_3Br flame. A reduction of formaldehyde peak concentration was observed for the flame containing 0.3% CF_3Br (8) and in methane flames containing HBr (52). Since its formation rate is not substantially different between flames III and IV, the decrease in maximum $[H_2CO]$ must be caused by a greatly increased rate of decay in the inhibited flame. This implies a strongly temperature-dependent rate coefficient for the reactions responsible for that decay. It is possible to estimate that temperature dependence. At any given z, the net reaction rate for H_2CO is the difference between the overall rate of formation, K_f, and the overall rate of decay, K_d, of formaldehyde at that point in the flame

$$K_{H_2CO} = K_f - K_d .$$

---

[6] "Flame" in the context of this discussion refers to the preheat and primary reaction zones, to $0<z\lesssim1$ cm in the low-pressure studies.

If it is assumed that reaction 4 is the only significant process forming H_2CO, then

$$\begin{aligned} K_f &= k_4[CH_3][O] \\ K_d &= k_4[CH_3][O] - K_{H_2CO}\,. \end{aligned} \tag{C}$$

The decay processes are usually (22, 53) thought to be abstraction reactions

$$H(O,OH) + H_2CO \rightarrow H_2(OH,H_2O) + HCO, \tag{7}$$

and there is evidence (29) that thermal decomposition reactions may be particularly important; for example,

$$H_2CO + M \rightarrow H_2 + CO + M. \tag{8}$$

We can write

$$\left.\begin{array}{l} K_d = k_7[H_2CO]\Sigma[i] \quad i = H,\ O,\ OH \\ \\ \text{or} \\ \\ K_d = k_8[H_2CO][M] \end{array}\right\} \tag{D}$$

where approximation is made that all of the abstraction reactions represented by reaction 7 have the same magnitude and temperature dependence. Substituting one of the equations D into equation C, it is possible to solve for k_7 or k_8 at any point in either flame. These calculations were carried out for both flames and spanned a temperature range of over 500 K.

The activation energy calculated for reaction 7 was 26 kcal $mole^{-1}$; for reaction 8 it was 44 kcal $mole^{-1}$. Such high activation energies suggest that reaction 8 or a similar thermal decomposition reaction is responsible for a significant part of the decay of formaldehyde, since the abstraction reactions have characteristically $E_a \sim 2\text{-}4$ kcal $mole^{-1}$ (16, 51). This is not to say that abstraction reactions do not occur. Indeed, the fact that the activation energy calculated for reaction 8 is rather higher than previously measured suggests that attributing all the H_2CO decay to reaction 8, as is done in the calculation described here, overestimates k_8. Our observations are consistent with a distribution between abstraction and thermal decomposition reactions first suggested by Peeters and Mahnen in their studies of lean CH_4-O_2 flames (41).

One model of flame inhibition proposes a zone of inhibition between the transport zone and the primary reaction zone of the flame (52). In this region of the flame, the inhibitor and/or its products of decomposition are thought to scavenge radicals efficiently and to compete with the normal chain-propagating or branching reactions, delaying those reactions until the temperature has increased to a point where the inhibiting reactions can no longer compete. Much of the data we have obtained is consistent with this model. Examples are the directly observed reduction of chain carrier concentrations in the low-temperature region of inhibited relative to clean flames, the early reaction of the inhibitor molecule relative to fuel, and the shifting to

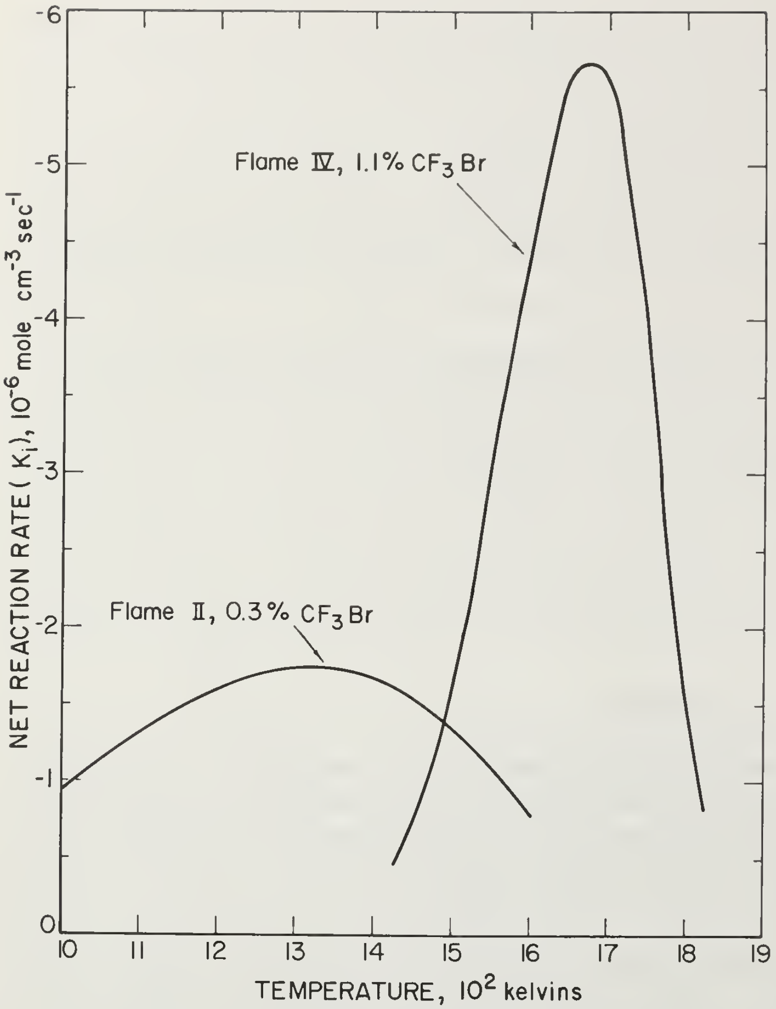

FIGURE 13. - Net reaction rate for the inhibitor as a function of temperature for two nearly stoichiometric methane flames containing initially different amounts of CF_3Br.

higher temperatures of the net reaction rate of fuel and oxidant in the presence of inhibitor. However, the behavior of the inhibitor in the 1.1% CF_3Br flame relative to the 0.3% flame is not similarly consistent. In each case, the inhibitor begins to react and achieves its maximum rate of decay earlier (at lower z and T) than methane, but the CF_3Br reacts more rapidly at significantly higher temperature in the 1.1% flame than in the 0.3% flame. Figure 13 shows K_{CF_3Br} as a function of temperature in flames II and IV. Table 2 lists the temperatures at which the maximum rates of decay occur for methane and CF_3Br in all four flames examined. Flames I and III differ initially in mass flow rate only and hence the difference in final flame temperature (28). The temperature at which CH_4 disappears most rapidly reflects the difference. Flames II and IV also differ in initial inhibitor concentration. The final flame temperature is 50 K higher for IV, but the maximum net reaction rate for CF_3Br occurs at a temperature 365 K higher in IV than II. The shift to higher temperature and narrowing of K_{CF_3Br} in flame IV relative to flame II (fig. 13) is like that of methane in the inhibited relative to the clean flames. The maximum rate of decay of CF_3Br in flame IV is greater than in flame II, owing to the greater initial CF_3Br concentration in the former.

TABLE 2. - Temperature for maximum rate of decay of fuel and inhibitor in 0.042 atm, nearly stoichiometric CH_4-O_2-Ar flames[1]

Flame	Initial $[CF_3Br]$, %	T_{final}	T at $\lvert K_{CH_4} \rvert_{max}$	T at $\lvert K_{CF_3Br} \rvert_{max}$
I.............	0	1,868	1,640	-
III............	0	1,781	1,570	-
II.............	0.3	1,911	1,660	1,310
IV.............	1.1	1,966	1,790	1,675

[1] All temperatures are in kelvins.

With increasing inhibitor concentration, the zone of inhibition, if that idea is at all applicable, is also shifted to higher temperature, and the reaction of the inhibitor itself is also delayed. At equivalent temperatures the concentrations of H, O, and OH are smaller than in flame II (9), and the observed delay in inhibitor decay seems to be a consequence of this reduction in radical concentration. The implication is that of the several possible reactions that can be written to account for the observed reduction of radical concentration in the low-temperature region of the flame, those between CF_3Br and radicals, for example,

$$H + CF_3Br \rightarrow HBr + CF_3 , \qquad (9)$$

are not the most important. Reaction 9 does occur and is still a significant reaction destroying CF_3Br in the flame, as will be discussed presently, but it is delayed to higher temperatures, just as reaction 1 is.

Disappearance of CF_3Br

In the 0.3% CF_3Br flame, it was found that at the maximum rate of disappearance of CF_3Br, thermal decomposition could account for, at most, 8% of the decay rate. The rate coefficient, k_{td}, given by Benson and O'Neal (3) was used. Reaction with H atom to give HBr and CF_3 was responsible for the disappearance of CF_3Br, and a rate coefficient could be calculated. The result was given by 2.2×10^{14} exp(-9,460/RT) for $700<T<1,550$ K. In the flame containing 1.1% CF_3Br initially, at the maximum decay rate for CF_3Br, the predicted rate of thermal decomposition, k_{td} (again using Benson and O'Neal's rate coefficient), is nearly 10 times greater than the observed net reaction rate, $\lvert K_{td} \rvert_{B\&O} = 10 \lvert K_{CF_3Br} \rvert_{max}$.

The value for the thermal decomposition rate coefficient recommended by Benson and O'Neal is from an RRK calculation and represents an attempt to calculate the limiting high-pressure value. The only experimental value for k_{td}, reported by Sehon and Szwarc (45), is more than a factor of 10 lower than Benson and O'Neal's. Thus, at the temperature of interest, using Sehon and Szwarc's number, we might conclude that CF_3Br disappears by thermal decomposition.

Hydrogen atoms are present in the region of flame IV over the temperature range in which CF_3Br disappears. Although the H atom concentration at any given temperature below the maximum temperature is lower than in flame III, these concentrations are not negligible. At the maximum CF_3Br decay rate, if we assume the abstraction reaction alone is responsible for the decay, we calculate a value of $k_9 = 1.6\times10^{13}$ cm^3 $mole^{-1}$ sec^{-1}, T = 1,666 K. The number agrees well with the value (1.3×10^{13}) extrapolated using the expression given earlier.

Thus assigning the decay of CF_3Br either to thermal decomposition or to H atom abstraction would yield values for the rate coefficients for these reactions that are consistent with what is known about either reaction. This holds over the range of CF_3Br decay for which $1,600\leq T<1,800$ K.

It is reasonable to suppose that, in this flame, CF_3Br is consumed by both abstraction and thermal decomposition reactions. If we assume that the abstraction reaction occurs with the rate coefficient measured in flame II, we can estimate a CF_3Br decay rate due to abstraction. Where the observed CF_3Br decay rate is greater than the calculated abstraction rate, we assign the difference to thermal decomposition. For $T\geq1,670$ K this difference is positive and the thermal decomposition rate constant, expressed as a first-order coefficient, is the solid line shown in figure 14. At temperatures lower than 1,670 K, the abstraction reaction predicts a greater rate of CF_3Br decay than observed, and so a meaningful k_{td} cannot be calculated. At 1,600 K, for example, the observed K_{CF_3Br} is 75% of that required if the abstraction and thermal decomposition were occurring, the latter proceeding at the rate required by extrapolating the solid line in figure 14 to 1,600 K. On the basis of this analysis, thermal decomposition accounts for about 50% of the CF_3Br disappearance rate at its maximum in flame IV and at higher temperature.

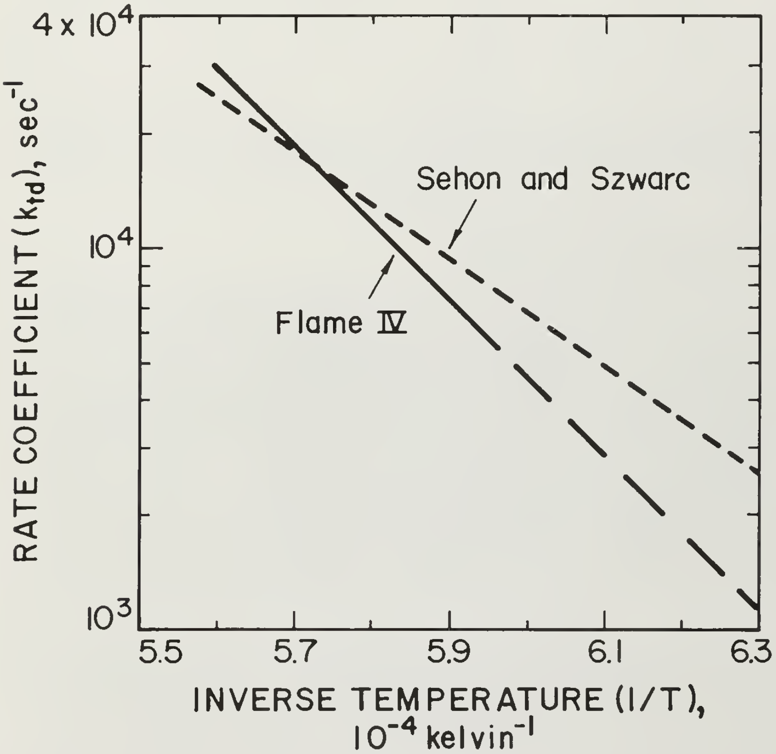

FIGURE 14. - Rate coefficient for thermal decomposition of CF_3Br, expressed as first order, calculated assuming Br atom abstraction occurs with the rate constant previously determined (8). Solid line, flame IV; dashed line from reference 45.

We expect (10) to be able to use net reaction rate curves (fig. 13) to about $1/2|K_{CF_3Br}|_{max}$, $1,550\leq T\leq1,780$ K. The fact that we cannot utilize the low-temperature portion of the K_{CF_3Br} is an inconsistency that is ultimately due to experimental limitations of these flame data, to the errors in modeling thermal diffusion noted earlier, to error in determining the absolute value of H atom concentration, particularly at low values of z, and to possible limitations in the curve-smoothing operation for reactant-type profiles at low z values. All of these possible sources of error diminish in magnitude with increasing values of z and T.

The dashed line in figure 14 is the expression for k_{td} of Sehon and Szwarc (45), extrapolated to flame temperature. The conditions of Sehon and Szwarc's experiment were 5-20 torr and 1,020-1,090 K. From Benson and O'Neal's calculations, it is likely that these conditions are well into the pressure-falloff region for CF_3Br decomposition. The pressure here is higher, 32 torr, but so is the temperature, and our conditions are also probably well into the pressure-falloff region. In absolute value, our calculated rate coefficient for thermal decomposition is not very different from extrapolation of Sehon and Szwarc's measurements, and both are at least an order of magnitude lower than the computed high-pressure limiting value.

As in previous work (7), reactions of CF_3Br with O and Br atoms were found to be negligibly important. Abstraction by methyl radical to give CH_3Br accounted for 10% to 30% of the decay rate of CF_3Br below 1,700 K. The reaction was considered, quantitatively, in making the calculations for the contribution of thermal decomposition. The reverse reactions, forming CF_3Br, are also unimportant in the flame.

Compositions and Kinetic Analyses of Inhibitor-Related Species

When 1.1% CF_3Br is added to a methane flame, a number of brominated and fluorinated species are observed. They are Br_2, CH_3Br, HBr, CH_2CF_2, CF_2, CF_3H, F_2CO, HF, and the Br atom. Figures 6 and 7 show the concentration profiles for these species. The first six are relatively short-lived intermediates, F_2CO is a long-lived intermediate, and HF and Br have the appearance of "products" in low-pressure flames. The net reaction rate profiles calculated according to equations A and B for all the inhibitor-related species except Br atom are illustrated in figures 15-17. The rate profiles shown are plots of the net reaction rates listed in appendix B with local variations removed. Some concepts that are important in understanding the flame as a chemically reacting system are illustrated by these figures. From figure 7 it appears that molecular Br_2 is formed at low values of z in the flame, and this is confirmed by its net reaction rate in figure 17. However, in general, it is not possible to deduce from the spatial order of observation of the species in the flame, the spatial order in which they are formed in the flame. For example, HF (fig. 7) is observed in appreciable amounts at z~0.4 cm, and its maximum rate of production is at z~0.6 cm (fig. 15). The HF observed at low z is due entirely to diffusion induced by the large concentration gradient of HF. This is true of all of the inhibitor-related species except Br_2 and may be observed by comparing the onset of the appropriate profiles of figures 6 and 7 with those of figures 15-17.

With the possible exception of Br_2 and CF_3H, the kinetic steady state approximation ($d[i]/dt \sim 0$ relative to some other rate process) does not apply

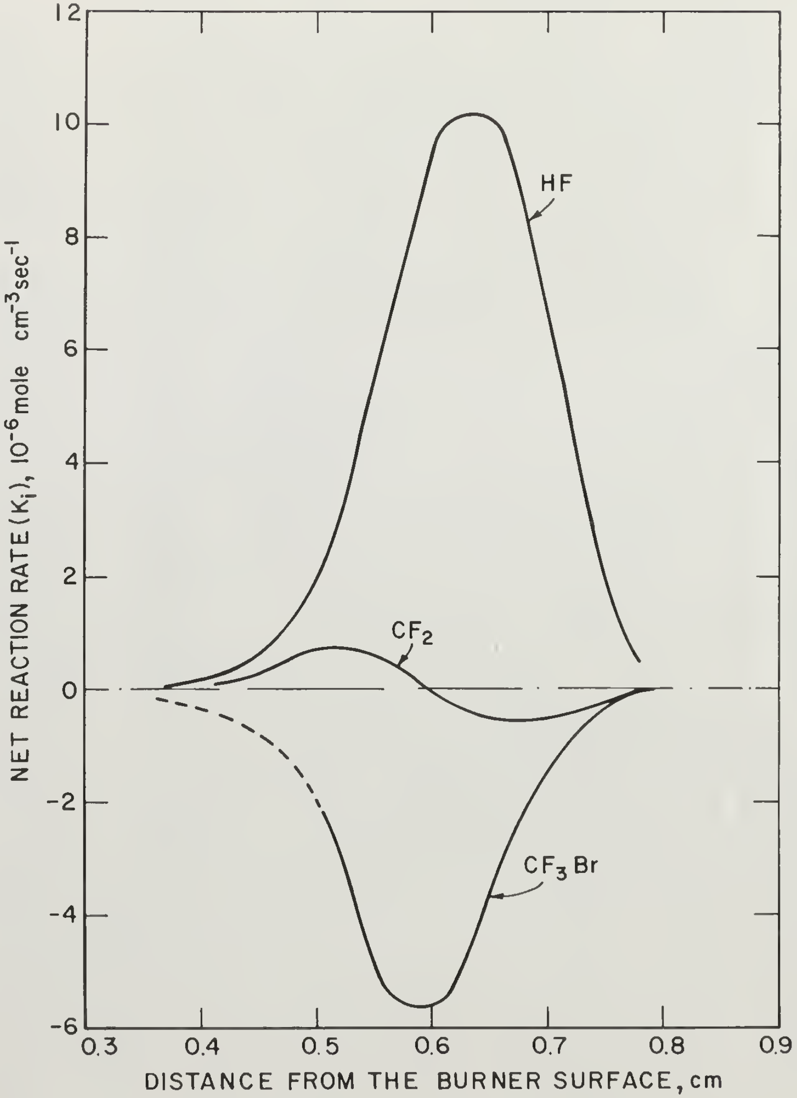

FIGURE 15. - Net reaction rate profiles for HF, CF_2, and CF_3Br in flame IV.

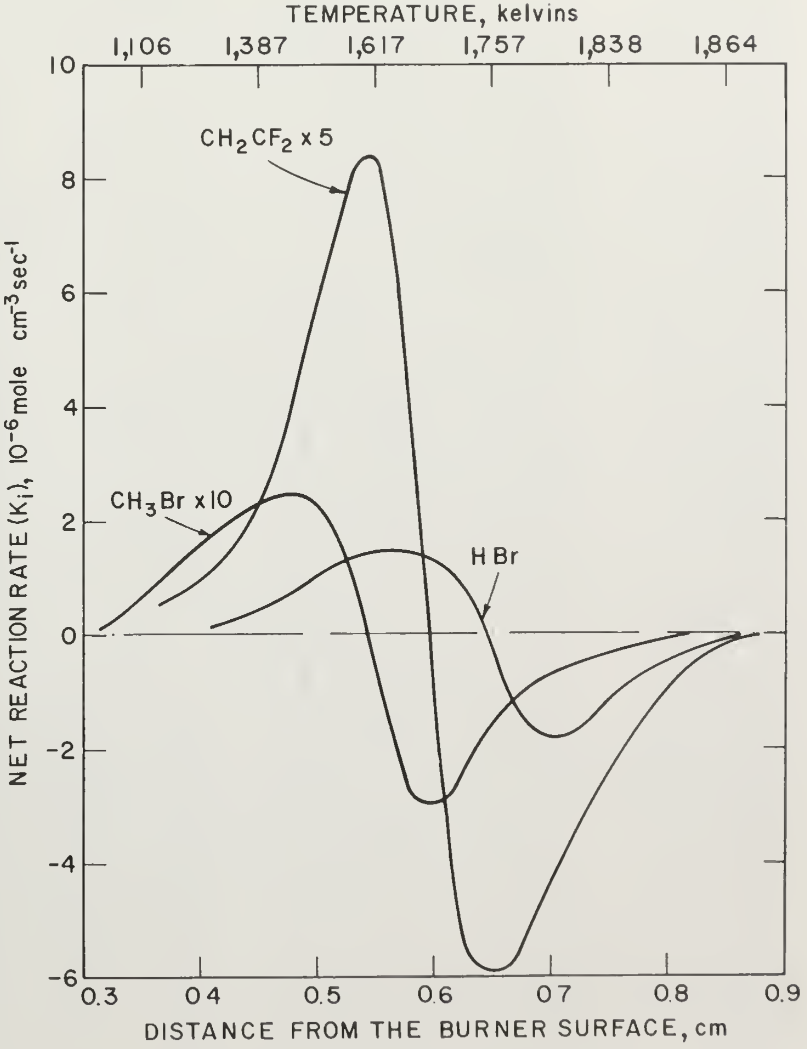

FIGURE 16. - Net reaction rate profiles for CH_3Br, CH_2CF_2, and HBr in flame IV.

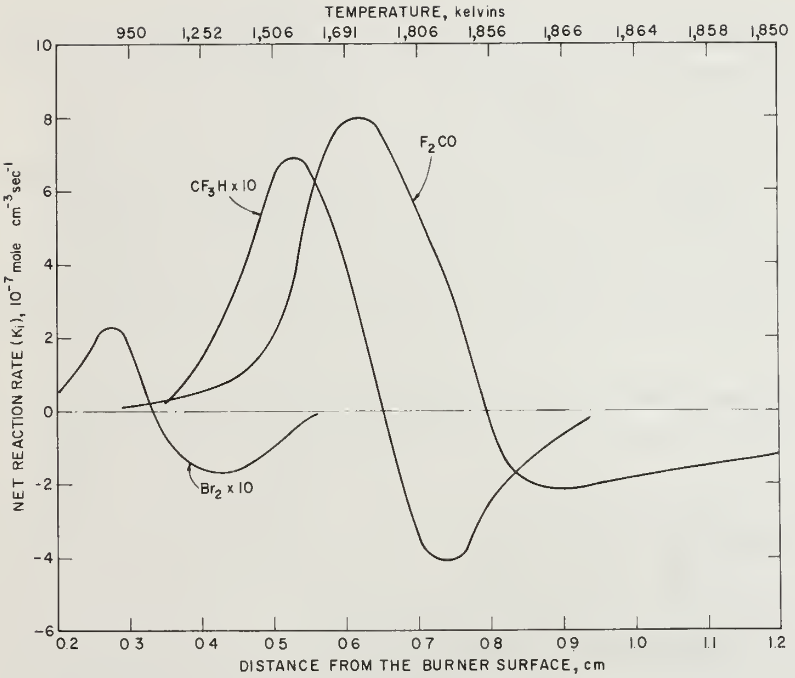

FIGURE 17. - Net reaction rate profiles for Br_2, CF_3H, and F_2CO in flame IV.

to any of the intermediate species related to the decay of CF_3Br. The simplification afforded by this approximation in other complex reaction systems is not generally available in flame analyses.

The species formed earliest in the flame are, in addition to Br_2 (870 K), CH_3Br (1,448 K) and CF_2 (1,538 K), followed by CF_3H (1,569 K), CH_2CF_2 (1,598 K), and HBr (1,634 K); the temperature at which the maximum net reaction rate is observed is given in parentheses. The F_2CO (1,720 K) and HF (1,731 K) are clearly later intermediates, well separated from the other species related to the decay of CF_3Br. The dashed part of the net reaction rate curve for CF_3Br (fig. 15) is calculated from the sum of the observed net reaction rates of species formed directly as a result of the reaction of CF_3Br.

There are some differences in the relative order of appearance of these species between flame IV and flame II, containing initially 0.3% CF_3Br (_7_). In that flame the maximum F_2CO appearance rate preceded that for HF, and both the HF and HBr maxima occurred at about the same value of z. The temperature profiles are different between these two flames, so that the place at which a given species reaches a maximum or a minimum in K_i will depend upon the temperatures and the temperature dependencies of all the reactions contributing to the formation and decay of the species. The difference in the relative position of HBr between flame II and flame IV may be a reflection of the differences in the decay mechanism for CF_3Br between the two flames. As previously noted, in flame II, decay is predominately via the abstraction reaction $H+CF_3Br \rightarrow HBr+CF_3$; in flame IV, the thermal decomposition reaction giving Br and CF_3 is also important. Thus the reaction $Br+H_2 \rightarrow HBr+H$ may be more important in the overall rate of formation of HBr at low temperature in flame IV than in flame II.

The individual net reaction rate, K_i, determined by equation B is the collective effect of all the reactions forming and all the reactions consuming the species i. When the reactions responsible for the production and decay of a given species are known, particularly when a single reaction path dominates, it is straightforward to calculate a rate coefficient for the dominant reaction from the complete microstructure data, as is done for reactions 1-4. When the mechanisms are only partially known, as is the case here, the procedure is to propose reactions that could explain the observation of a particular species. When rate coefficients for these reactions have been measured in other systems, or can be reasonably estimated, it is possible to calculate the value of K_1 to be associated with each reaction. Comparison with the observed K_1 gives an indication of the importance of the proposed reaction. Rate coefficients that are consistent with the proposed mechanism can be calculated for individual reactions if there is sufficient kinetic data available for most of the other reactions in the scheme. Rate coefficients so determined are frequently the only available quantitative data for the reactions at elevated temperature. The analyses that follow are the result of applying the procedure outlined above to inhibitor-related species in flame IV.

CH_3Br and CF_3H.--The reactions found to be significant in the formation and decay of CH_3Br in the inhibited flame over the temperature range 1,250-1,600 K follow:

Formation $$CH_3+CF_3Br \rightarrow CH_3Br+CF_3 \tag{10}$$

$$CH_3+Br_2 \rightarrow CH_3Br+Br \tag{11}$$

Decay $$CH_3Br+H(OH) \rightarrow HBr(HOBr)+CH_3 \tag{12-13}$$

$$CH_3Br+Br \rightarrow HBr+CH_2Br \tag{14}$$

$$CH_3Br \rightarrow CH_3+Br \tag{15}$$

Reactions 11 and 14 are relatively minor contributors to K_1, so that even if the absolute concentration of Br_2 is in error by an order of magnitude, the rate coefficient calculated for CH_3Br formation by reaction 10 would not be significantly different. Reactions of CH_3Br with O, CF_3, and CH_3 are negligibly slow here. To the extent that quantitative information is available for the reverse reaction, either from measurement of the reverse or from calculations using equilibrium constants and the rate coefficient of the forward reaction, the reverse reactions are also slow.

A rate coefficient, k_{10}, for reaction 10 over the temperature range cited may be calculated by quantitatively taking into account the contribution of the other reactions (7). The results are shown in figure 18. Shown also are the earlier results from the flame initially containing 0.3% CF_3Br. The temperature range over which this rate coefficient was determined in that flame was 650 to 1,250 K, and the values below 900 K depended importantly upon an estimated concentration of Br_2 in that flame. The points shown in figure 18 are for $900<T<1,600$ K, and the value $5.8\times10^{12}\ \exp(-4,200/RT)\ cm^3\ mole^{-1}\ sec^{-1}$ for k_{10} from both flames is a better estimate for this rate coefficient than that obtained from either flame separately.

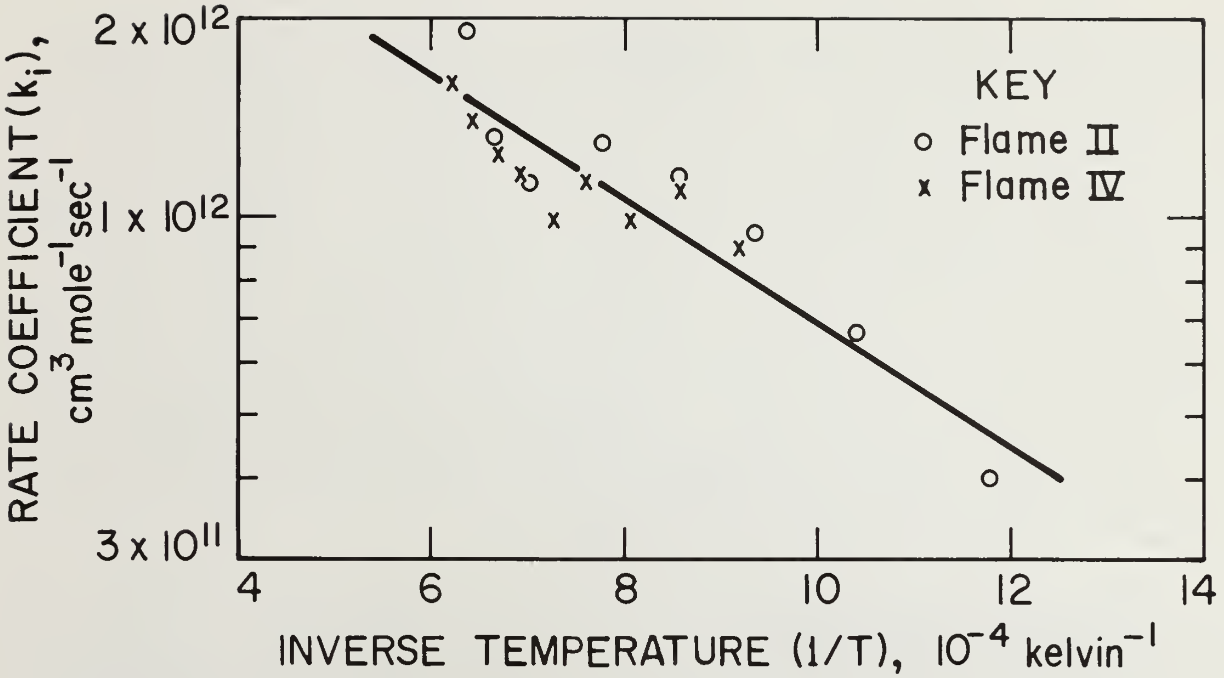

FIGURE 18. - Rate coefficient for the reaction $CH_3+CF_3Br \rightarrow CH_3Br+CF_3$ as a function of temperature as determined from analysis of flame II and flame IV. The Arrhenius expression for k is 5.8×10^{12} exp(-4,200/RT) $cm^3 mole^{-1} sec^{-1}$, 900<T<1,600 K.

CF_3H is the only observed inhibitor-related species that contains the CF_3 group intact. We use its net reaction rate, with the assumption that it is formed by H atom abstraction reactions between CF_3 and various hydrogen-containing species in the flame, to calculate a profile for CF_3 in the flame (11). A formation reaction not considered earlier, $CF_2+HF \rightarrow CF_3H$, is about two orders of magnitude slower than the observed rate of CF_3H formation and is therefore negligible. In the calculation a value for the rate coefficient analogous to that recommended for insertion by HBr and HCl was used (1, 17).

The decay reaction for CF_3H is relatively slow, since CF_3H is next to the last to disappear (F_2CO is last) of the intermediates associated with the inhibitor (fig. 17). Several reactions may be important in the decay:

$$CF_3H+H(O,OH) \rightarrow H_2(OH,H_2O)+CF_3 \quad (16)$$

$$CF_3H \rightarrow CF_2+HF \quad (17)$$

$$Br+CF_3H \rightarrow HBr+CF_3 \quad (18)$$

$$CH_3+CF_3H \rightarrow CH_4+CF_3 \quad (19)$$

Reactions 16, 18, and 19 are the reverse of important formation reactions, and using rate coefficients from standard sources (32, 48), reactions 18 and 19 are found to be too slow to be important sources of decay of CF_3H. At the position of maximum decay, reaction 16, with H atoms, accounts for only ~8% of the observed decay rate. Since [H]~[OH] here and [O] is about half that, at best, radical abstraction reactions, assuming them all to be equally fast, can account for only 20% of the observed net reaction rate. The thermal decomposition reaction 17 is of primary importance in the disappearance of CF_3H, and we calculate a value for k_{17}, expressed as a first-order rate constant, of $(6\pm1)\times10^3$ sec^{-1} at T = 1,845 K. This result is about seven times lower than suggested by the only other value reported in the literature (49). That datum was from a shock tube experiment in which the average conditions of measurement were 3,000 torr and 1,400 K. The authors considered the reaction to be into the falloff region under those conditions, and the flame conditions here are even farther from the high-pressure limit. Expressed as second order, $CF_3H+M \rightarrow CF_2+HF+M$, the rate coefficient is 2×10^{10} cm^3 $mole^{-1}$ sec^{-1} at 1,845 K, where M is any other molecule in the flame.

The CF_2,CH_2CF_2,F_2CO,HF Axis.--The four named species are linked together by the fact that reactions forming some of them consume others, and while we can estimate rate coefficients for these reactions based upon the behavior observed for the net reaction rate of individual species, their behavior is related. For this reason we discuss the kinetic analyses of these species together. Table 3 lists the reactions that are pertinent to their formation and decay in the flame, together with the literature rate coefficients and references to the literature on the reactions.

The reactions responsible for the formation and decay of CF_2, as determined from analyses of the net reaction rate profile for CF_2, have been published (11). Some new information from considerations of $K_{CH_2CF_2}$ has implications for the estimated rate coefficients of the CF_2 reactions and will now be discussed.

Observation of CF_2 in flame IV suggests for the formation of CF_2CH_2 the reaction

$$CF_2+CH_3 \rightleftarrows (CF_2CH_3)^* \rightarrow CF_2CH_2+H \qquad (20)$$

by analogy to the reaction between (triplet) methylene and methyl radical (33, 42). This is in addition to the reactions proposed earlier (7),

$$CF_3+CH_3 \underset{(-21)}{\overset{(21)}{\rightleftarrows}} (CF_3CH_3)^* \xrightarrow{(22)} CF_2CH_2+HF.$$

TABLE 3. - Reactions of the principal fluorocarbon species in inhibited flames

Reaction	Literature rate coefficient, cm^3 $mole^{-1}$ sec^{-1}	Reference	Remarks
(20) $CF_2+CH_3 \rightleftarrows (CF_2CH_3)^* \rightarrow CF_2CH_2+H$...	-	42	By analogy to $^3CH_2$ reaction for which k = $(3\text{-}6)\times10^{13}$ cm^3 $mole^{-1}$ sec^{-1}.
(21-22) $CF_3+CH_3 \rightleftarrows (CF_3CH_3)^* \rightarrow CF_2CH_2+HF$	$k_{13} = 6.8\times10^{13}$ (440 K)	31, 43, 47	-
(23) $CF_3+H \rightarrow CF_2+HF$	5×10^{13} (1,540 K) - 2×10^{14} (900-1,300 K)	11, 46	-
(24) $CF_3H \rightarrow CF_2+HF$	1.2×10^{12} exp(-63,000/RT) sec^{-1}	49	Reaction conditions likely to be in the pressure falloff region.
(25a) $CH_2CF_2+O \rightarrow F_2CO+CH_2$	4×10^{13} exp(-3,200/RT)	7, 27, 37, 38	-
(25b) $\rightarrow H_2CO+CF_2$			
(26) $CF_2+H \rightarrow CF+HF$	10^{13} (1,800 K)	11	-
(27a) $CF_2+O \rightarrow CO+F+F$	-	25, 39	A rate coefficient of $(1\text{-}5)\times10^{13}$ was estimated for these reactions collectively in reference 11.
(27b) $\rightarrow F_2CO$	-	2	
(27c) $\rightarrow FCO+F$	-	30	
(28a) $CF_2+OH \rightarrow CO+HF+F$	$(1\text{-}3)\times10^{13}$ (1,800 K)	11	-
(28b) $\rightarrow F_2CO+H$			
(29a) $CF_2+O_2 \rightarrow F_2CO+O$	2×10^{13} exp(-26,500/RT)	30	-
(29b) $\rightarrow CO+2F+O$	-	-	Endothermic.
(30) $CF_3+O_2 \rightarrow F_2CO+OF$	-	26	By analogy to CH_3 reaction for which k = 1.2×10^{12} exp(-12,500/RT) cm^3 $mole^{-1}$ sec^{-1}.
(31) $CF_3+O \rightarrow F_2CO+F$	-	7, 41	By analogy to CH_3 reaction for which $k{\sim}10^{14}$ cm^3 $mole^{-1}$ sec^{-1}.
(32) $CF_3+OH \rightarrow F_2CO+HF$	-	7, 19	By analogy to CH_3 reaction for which $k = 4\times10^{12}$ cm^3 $mole^{-1}$ sec^{-1}.

*Denotes a vibrationally excited molecule.

Reaction 20 was not considered in the analyses of flame II. In that flame it was estimated that $X_{CF_3} < 10^{-4}$, from our inability to detect this radical. From the current data, the maximum mole fraction of CF_3 in flame II was more like 10^{-5}, and a rate coefficient calculated for reaction 21 from that data is an order of magnitude higher than reported earlier. The rate coefficient from the present calculation is $>2 \times 10^{14}$ cm^3 $mole^{-1}$ sec^{-1}, and k_{21} would be greater to the extent that reactions 21, -21 are in the pressure falloff region for the conditions of that flame. A similar calculation, in which reaction 20 was ignored entirely, was performed for flame IV and gave $k_{21} > 5 \times 10^{14}$ cm^3 $mole^{-1}$ sec^{-1} at 1,435 K. A value of 6.8×10^{13} cm^3 $mole^{-1}$ sec^{-1} is recommended for k_{21} (24). Since this value is nearly gas kinetic, and if anything, likely to be smaller at high temperature, it is unreasonable to assign the formation of CH_2CF_2 solely to the sequence of reactions 21-22.

The literature value for the rate coefficient of reaction 21, the measured concentration of CF_2, and the calculated concentration of CF_3 were used to account for the contribution of the sequence of reactions 21-22 to the net rate of formation of CH_2CF_2. In the temperature range $1{,}300 < T < 1{,}600$ K, CH_2CF_2 is being formed (fig. 16), and decay reactions are assumed to be unimportant. A value for k_{20} was calculated over this temperature and found to be temperature insensitive at 2×10^{13} cm^3 $mole^{-1}$ sec^{-1}. Inclusion of the decay reactions for CH_2CF_2, to the extent that their rate coefficients are known (11), does not significantly change this number below 1,600 K. At the point in the flame where CH_2CF_2 is being formed at a maximum rate, reaction 20 accounts for ~80% of that formation rate; reactions 21-22 account for, at most, 20%. The same mechanism may be reasonably applied to flame II (7). Previously we supposed only reactions 21 and 22 were important in flame II (7). We did not look for the CF_2 radical in that flame and observed it for flame II subsequent to the experiments on flame IV (11).

In analyzing the net reaction rate profile for CF_2 (11), the reaction between CF_2 and CH_3 was considered to give HF and the $CFCH_2$ radical, an endothermic reaction that was neglected as slow. When reaction 20 is added to the decay scheme for CF_2 using the rate coefficient determined in the preceding analysis, we calculate rate coefficient for other reactions forming and consuming CF_2 that are higher than those reported earlier (11). The reactions (table 3) forming CF_2 are 23, 24, and 25b; the reactions consuming CF_2 are 20, 26, 27, and 28. A rate constant of 8×10^{14} cm^3 $mole^{-1}$ sec^{-1} for reaction 23 is consistent with this mechanism. This number is a factor of four greater than that calculated ignoring reaction 20 and corresponds to the reaction occurring essentially at every collision. Reactions 26-28 have rate coefficients two to three times greater than previously estimated, depending upon which radical is assumed to dominate the decay. If the reactions between CF_2 and H, O, and OH are equally fast, then the rate coefficient for those reactions at $1{,}800 \pm 30$ K is 3×10^{13} cm^3 $mole^{-1}$ sec^{-1}.

Carbonyl fluoride may be produced by several different reactions:

$$CF_2 + O \rightarrow F_2CO \tag{27b}$$

$$CF_2 + OH \rightarrow F_2CO + H \tag{28b}$$

$$CF_2+O_2 \rightarrow F_2CO+O \quad (29a)$$

$$CF_3+O_2 \rightarrow F_2CO+OF \quad (30)$$

$$CF_3+O \rightarrow F_2CO+F \quad (31)$$

$$CF_3+OH \rightarrow F_2CO+HF \quad (32)$$

$$CH_2CF_2+O \rightarrow F_2CO+CH_2 \quad (25a)$$

The net reaction rate profile for F_2CO (fig. 17) shows an unusually long upstream foot. Although most of the F_2CO is formed at higher temperatures, it is being formed even at temperatures as low as 1,100 K in the flame. K_{F_2CO} begins to increase rapidly where O atoms are observed in the flame, and the most important reactions forming F_2CO are those involving O atoms. Below about 1,375 K, the concentration of oxygen atoms is zero, and reactions 27b, 31, and 25a may be neglected. The contributions of reactions 30 and 32 were estimated by assigning to them the rate coefficients of analogous methyl radical reactions (7, 19) with the result that both reactions are negligibly slow here. Reaction 29a is of minor importance, contributing at most 20% of the observed net reaction rate of F_2CO at temperatures below 1,375 K. The reaction principally responsible for F_2CO formation in the absence of oxygen atoms is reaction 28b, $CF_2+OH \rightarrow F_2CO+H$. Using K_{F_2CO} for $1{,}090<T<1{,}375$ K, the rate coefficient for reaction 28b is calculated to be $(5\pm1)\times10^{12}$ cm^3 mole^{-1} sec^{-1}, where the limits show precision only.

Previously we calculated 3×10^{13} cm^3 mole^{-1} sec^{-1} for CF_2+(OH, O, or H), assuming equal rate coefficients for each radical (11). The present result is consistent in that several reactions for CF_2 with O and OH, including reaction 28b, were considered together in the CF_2 analysis.

For $1{,}495<T<1{,}780$ K, where F_2CO is being formed most rapidly and the oxygen atom concentration is not zero, the principal formation reactions are CF_2+O (27b) and CH_2CF_2+O (25a). The reactions involving CF_3, including reaction 31, together account for about 20% of the observed K_{F_2CO} over this temperature range. Reaction 29a, CF_2+O_2, diminishes in importance, contributing at most 5% to K_{F_2CO}. We account for reaction 28b using the rate coefficient determined at lower temperature. We cannot, from the F_2CO analysis, determine which of the two reactions, 27b or 25a, dominates. Assigning the formation to reaction 25a alone suggests a rate constant for this reaction of 1×10^{13} cm^3 mole^{-1} sec^{-1}, in agreement with a similar analysis for flame II (7). Assigning the formation to reaction 27b alone requires a rate coefficient of 2×10^{13} cm^3 mole^{-1} sec^{-1} for that reaction. This last number is consistent with the estimate made from the CF_2 net reaction rate analyses.

Reaction 27b, CF_2+O, is spin disallowed and, presumably, slow. Bauer (2), from shock tube studies of the oxidation of perfluoroethylene, suggests that this reaction has a rate constant very much larger than that for the reaction of CF_2 and molecular oxygen (reaction 29a). The rate coefficient for that reaction at the midpoint of the temperature range considered here, 1,635 K, is 5.7×10^9 cm^3 mole^{-1} sec^{-1} (30).

Reaction 25a, $CH_2CF_2+O \rightarrow F_2CO+CH_2$, is spin allowed and has been identified as occurring in the room temperature photolysis of NO_2 and $CF_2 = CXY$ mixtures, where X and Y are either F, H, Cl, or Br (37). Those results suggest, however, that reaction 25b (table 3) rather than reaction 25a is the dominant reaction path for the interaction of CH_2CF_2+O. If that is also true at flame temperatures (and we cannot distinguish directly between the two paths here), then not only is reaction 27b the most important F_2CO formation route in the flame, but the results of the reassessment of the K_{CF_2} analyses discussed earlier represent upper limit values for the rate coefficients involved. The latter follows from the fact that reaction 25b represents a formation reaction for CF_2 whose occurrence mitigates the effect of consumption reaction 20 to the extent that their rates are similar.

There are 10 reactions in table 3 that may lead either directly to HF or to F atoms which we assume rapidly abstract a hydrogen atom from other flame species to yield HF. These reactions are

$$CF_3+CH_3 \rightarrow \ldots \rightarrow CF_2CH_2+HF \tag{21-22}$$

$$CF_3+H \rightarrow CF_2+HF \tag{23}$$

$$CF_2+O \rightarrow CO+F+F \tag{27a}$$

$$\rightarrow FCO+F \tag{27c}$$

$$CF_2+OH \rightarrow CO+HF+F \tag{28a}$$

$$CF_3+O \rightarrow F_2CO+F \tag{31}$$

$$CF_3+OH \rightarrow F_2CO+HF \tag{32}$$

$$CF_2+H \rightarrow CF+HF \tag{26}$$

$$CF_3H \rightarrow CF_2+HF \tag{24}$$

$$CF_2+O_2 \rightarrow CO+2F+O \tag{29b}$$

Reaction 29b can be eliminated from consideration since it is endothermic and its rate will be slower than for exothermic reaction 29a (table 3). The rate coefficient for 29a has been determined (30), and the rate of this reaction is negligibly slow with respect to the observed K_{HF} everywhere in the flame.

Because of the number of reactions leading to HF and the paucity of literature rate data for these reactions, we cannot eliminate or account for enough of them to calculate independent rate constants for the others from the observed K_{HF}. We can, however, learn something about the magnitude of the rate coefficients for the reactions by comparison with the decay of CF_3Br. In this analysis, we can also use rate coefficients previously determined from the net reaction rates of other species to make decisions about which of these reactions are most important in producing HF in different regions of the flame.

If the reactions yielding HF from CF_3Br were very fast relative to the decay rate of CF_3Br, we would expect to observe three HF molecules produced rapidly for every CF_3Br molecule that decays and that

$$-(K_{HF})_{max} \sim 3\ (K_{CF_3Br})_{min}.$$

We find that

$$-(K_{HF})_{max} = 1.7\ (K_{CF_3Br})_{min}$$

in both inhibited flames, II and IV. The rates of the reactions occurring between the decay of CF_3Br and the production of HF are not, collectively, very much faster than the CF_3Br decay reactions in this flame.

At the maximum rate of production of HF, $z = 0.62$ cm and $T = 1{,}720$ K, the observed K_{HF} is 10.2×10^{-6} mole cm^{-3} sec^{-1}. A production rate for HF at this point in the flame can be calculated by assigning to the reactions listed earlier the upper limit rate coefficient determined from the analyses of other species involved in the reaction; for example, from the K_{CF_2} analysis for reaction 23. For reactions 31 and 32, the rate coefficient was assumed to be that of the analogous CH_3 reaction, although for reaction 32 a factor of 10 increase in the rate coefficient made no difference in the conclusion. The assumption was made that all of the reactions listed giving HF or F resulted in the maximum possible rate of HF production so that, for example, reaction 27a yielded a contribution to K_{HF} equal to twice the rate calculated for the rate of the reaction of CF_2+O. Each F atom produced is assumed to rapidly react to give HF. The maximum rate of HF production calculated in this manner was 13.3×10^{-6} mole cm^{-3} sec^{-1}. This value represents quite reasonable agreement with the observed K_{HF}(max), 10.2×10^{-6} mole cm^{-3} sec^{-1}, in view of the uncertainties in the rate data. Without the assumption of maximum HF production rate from each reaction or the use of lower limit rate coefficients, a calculated K_{HF} that is 2 to 2.5 times, respectively, lower than the observed K_{HF} is obtained.

From this type of calculation at various points in the flame, we identify the most important reactions for HF production. We find that for $z < 0.5$ cm, the low z foot of the K_{HF} profile is accounted for by the reactions (in order of importance)

$$CF_3+H \rightarrow CF_2+HF$$

$$CF_2+H \rightarrow CF+HF$$

$$CF_2+OH \rightarrow CO+HF+F$$

Near the maximum rate of production of HF, the reaction of CF_2+O joins these three reactions as a major contributor to HF production, but it does not dominate. Thus, although the net reaction rate profiles for both F_2CO and HF show an unusual low z foot and both begin to increase rapidly where the concentration of oxygen atoms in the flame begins to increase rapidly, the correlation is significant for F_2CO but not for HF.

Br_2.--Molecular bromine was not observed in the flame containing 0.3% CF_3Br initially (7). Analysis of the formation rate of CH_3Br at low temperature in that flame suggested that molecular bromine must occur in the flame at low values of z. Thus, the observation of Br_2 in the present flame was expected, and its maximum at very low z values provided gratifying confirmation of the earlier analysis. The maximum mole fraction observed for Br_2 is 2.6×10^{-5}, and this may be in error by an order of magnitude because of the uncertainties in the cross sections used to estimate the concentration of Br_2 relative to that of CF_3Br. The uncertainty in the net reaction rate for Br_2 will be about the same as the uncertainty in the mole fraction.

In spite of the large range of uncertainty we cannot account for the observed rate of formation of Br_2 in this flame. The reactions that may reasonably be expected to produce Br_2 in the flame are

$$Br + CF_3Br \rightarrow Br_2 + CF_3 \qquad (33)$$

$$Br + CH_3Br \rightarrow Br_2 + CH_3 \qquad (34)$$

$$Br + HBr \rightarrow Br_2 + H \qquad (35)$$

$$Br + Br + M \rightarrow Br_2 + M \qquad (36)$$

Assuming that the reverse reactions are not important, which provides for a maximum possible production rate for Br_2, we calculate a total net reaction rate for Br_2 at 850 K of $\sim 10^{-10}$ mole cm^{-3} sec^{-1}. This is more than two orders of magnitude lower than the observed maximum net reaction rate for Br_2. The rate coefficients used in these calculations were $8.13 \times 10^{13} \exp(-25{,}170/RT)$ for reaction 33 (20), $5 \times 10^{13} \exp(-22{,}900/RT)$ for reaction 34 (32), and $2.7 \times 10^{14} \exp(-22{,}200/T)$ for reaction 35 (18). For reaction 36 the rate coefficient was calculated from the recommended recombination rate coefficient for Ar as a third body, M: $\log k_{36-Ar} = 15.381 - 2.287 \log(T/300) + 1.154 \log^2(T/300)$ (14).

A possible additional source of Br_2 is recombination of Br at the burner surface. If this were the primary source of molecular bromine we would expect to observe a concentration profile for Br_2 having the appearance of reactant profiles with the maximum concentration at the burner surface. The net reaction rate profile would also have its maximum at the burner surface in that case. The concentration of Br_2 as close to the burner surface as we can reliably sample is about 1/3 of the maximum; surface recombination undoubtedly occurs, but it does not appear to be the principal source of Br_2.

Two modeling studies of H_2/O_2 flames inhibited with HBr predict molecular bromine with a concentration maximum occurring close to the cold gas boundary (18, 23). Galant attributes the Br_2 behavior to reaction 36 and the reverse of reaction 35 in the H_2/O_2 flame. From our observations either a Br_2-producing reaction different from reactions 33-36 is important in methane flames, or the recombination of Br atoms in these flames is, for reasons not known, anomalously fast.

SUMMARY

The microstructure, including radical species, of nearly stoichiometric CH_4-O_2-Ar flames containing initially 1.1% CF_3Br has been determined. These data are analyzed in light of previous microstructure studies of flames containing 0.3% CF_3Br initially and of the analogous clean flame.

Comparison of the maximum concentration of inhibitor-related species in flames initially containing 1.1% and 0.3% CF_3Br suggests that similar mechanisms for formation and decay of these species are operating in both flames. These reactions, as well as those responsible for the disappearance of the major reactants and production of the major products, are shifted to higher temperatures in the presence of 1.1% CF_3Br. The effects of this inhibitor on the net reaction rate curves for methane and oxygen, and on the maximum concentration of formaldehyde, are similar to effects observed with HBr in very lean flames where different chain carriers predominate in the preheat zone of the flame.

The different temperature regions for the primary reaction zones in the inhibited versus the analogous clean flame account for the greater maximum CH_3 concentration in the former. The difference in formaldehyde maxima between the inhibited and clean flames is consistent with a mechanism of decay for that species that includes a large contribution from thermal decomposition reactions.

The behavior of CF_3Br in the 1.1% flame is different from its behavior in the 0.3% flame. Its net reaction rate both is shifted to higher temperature and is narrower in the flame containing more inhibitor. By analogy to the major reactants, we conclude that the decay of CF_3Br is also delayed on account of the reduction of radicals at low temperature in the inhibited relative to the clean flame. This observation is inconsistent with the idea of a zone of inhibition just prior to the primary reaction zone in which the inhibitor and/or its decomposition products scavenge radicals in direct competition with chain-branching reactions.

Analysis of the decay of CF_3Br suggests that, in contrast to the earlier study, the inhibitor is consumed not only by reaction with H, but also by thermal decomposition. Each pathway is equally important at the maximum rate of decay of CF_3Br.

From analyses of the net reaction rate profiles of the bromine- and fluorine-containing species observed, mechanisms to account for the formation of these species in the primary reaction zone of the flame have been deduced. The observation of the CF_2 radical and of CF_3H, from which a profile for the CF_3 radical may be calculated, provided critically important information. The presence of molecular bromine, though anticipated, cannot be accounted for quantitatively. The reactions judged to be primarily responsible for the major stable species containing fluorine are collected in table 4. They are, for the most part, radical-radical reactions involving CF_2, and the fluorocarbon chemistry occurring in this flame is due primarily to the CF_2 and not the CF_3 radical, as originally postulated (7). Rate coefficients for these and the reactions of other species related to the presence of the inhibitor were determined, and the results are given in table 5.

TABLE 4. - Reactions responsible for the formation of fluorocarbons in CF_3Br-inhibited flames

CH_2CF_2	$CH_3+CF_2 \rightarrow (CF_2CH_3)^* \rightarrow CH_2CF_2+H$
F_2CO	$CF_2+OH \rightarrow F_2CO+H$ $CF_2+O \rightarrow F_2CO$ $CH_2CF_2+O \rightarrow F_2CO+CH_2$
HF	$CF_3+H \rightarrow HF+CF_2$ $CF_2+H \rightarrow HF+CF$ $CF_2+OH \rightarrow HF+CO+F$ $CF_2+O \rightarrow CO+\underbrace{F+F}$ $+2RH \rightarrow 2HF+2R$

*Denotes a vibrationally excited molecule.

TABLE 5. - Summary of rate coefficients determined from kinetic analysis of a methane-oxygen-argon flame containing 1.1% CF_3Br initially

Reaction	Temperature range, K	k, cm^3 $mole^{-1}$ sec^{-1}
$CH_3+CF_3Br \rightarrow CH_3Br+CF_3$	900-1,600	$5.8 \times 10^{12} \exp(-4{,}200/RT)$
$CF_3H+M \rightarrow CF_3+H+M$	1,845	2×10^{10}
$CH_3+CF_2 \rightarrow \ldots \rightarrow CF_2CH_2+H$	1,300-1,600	2×10^{13}
$CF_3+H \rightarrow HF+CF_2$	1,800	$\leq 8 \times 10^{14}$
$CF_2+(H,OH,O) \rightarrow$ product	1,800	3×10^{13}
$CF_2+OH \rightarrow F_2CO+H$	1,090-1,375	5×10^{12}
$CF_2+O \rightarrow F_2CO$	1,495-1,780	$\sim 10^{13}$
$CH_2CF_2+O \rightarrow F_2CO+CH_2$		

REFERENCES

1. Barnes, G. R., R. A. Cox, and R. F. Simmons. The Kinetics of the Gas-Phase Thermal Decomposition of Chlorodifluoromethane. J. Chem. Soc. (B), 1971, pp. 1176-1180.

2. Bauer, S. H., K. C. Hou, and E. L. Resler, Jr. Single-Pulse Shock-Tube Studies of the Pyrolysis of Fluorocarbons and of the Oxidation of Perfluoroethylene. Phys. Fluids Supplement I, 1969, pp. I-125-I-132.

3. Benson, S. W., and H. E. O'Neal. Kinetic Data on Gas Phase Unimolecular Reactions. NBS, Stand. Ref. Data Series, No. 21, 1970, p. 501.

4. Biordi, J. C., C. P. Lazzara, and J. F. Papp. Flame Structure Studies of CF_3Br Inhibited Methane Flames. Proc. 14th Internat. Symp. on Combustion, Combustion Institute, Pittsburgh, Pa., 1973, pp. 367-381.

5. _____. Molecular Beam Mass Spectrometry Applied to Determining the Kinetics of Reactions in Flames. I. Empirical Characterization of Flame Perturbation by Molecular Beam Sampling Probes. Combustion and Flame, v. 23, 1974, pp. 73-82.

6. _____. The Rate Coefficient for $H+CH_4 \rightarrow H_2+CH_3$ in the Temperature Range 1300-1700° K. J. Chem. Phys., v. 61, No. 2, 1974, pp. 741-742.

7. _____. Chemical Flame Inhibition Using Molecular Beam Mass Spectrometry. Reaction Rates and Mechanisms in a 0.3 Percent CF_3Br Inhibited Methane Flame. BuMines RI 8029, 1975, 42 pp.

8. _____. Flame Structure Studies of CF_3Br-Inhibited Methane Flames. II. Kinetics and Mechanisms. Proc. 15th Internat. Symp. on Combustion, Combustion Institute, Pittsburgh, Pa., 1975, pp. 917-932.

9. _____. The Effect of CF_3Br on Radical Concentration Profiles in Methane Flames. Ch. in Halogenated Fire Suppressants, ed. by R. G. Gann. ACS Symp. Series No. 16, 1975, pp. 256-294.

10. _____. Molecular Beam Mass Spectrometry Applied to Determining the Kinetics of Reactions in Flames. II. Critique of the Method for Rate Coefficient Determinations. Combustion and Flame, v. 26, 1976, pp. 57-76.

11. _____. Mass Spectrometric Observation of Difluorocarbene and Its Reactions in Inhibited Methane Flames. J. Phys. Chem., v. 80, 1976, pp. 1042-1048.

12. _____. Flame Structure Studies of CF_3Br Inhibited Methane Flames. 3. The Effect of 1% CF_3Br on Composition, Rate Constants, and Net Reaction Rates. J. Phys. Chem., v. 81, 1977, pp. 1139-1145.

13. _____. Flame Structure Studies of CF_3Br Inhibited Methane Flames. IV. Reactions of Inhibitor Related Species in Flames Containing Initially 1.1 Percent CF_3Br. J. Phys. Chem., v. 82, 1978, pp. 125-132.

14. Brown, N. J. Halogen Kinetics Pertinent to Flame Inhibition: A Review. Ch. in Halogenated Fire Suppressants, ed. by R. G. Gann. ACS Symp. Series No. 16, 1975, pp. 341-375.

15. Clark, T. C., and J. E. Dove. Examination of Possible Non-Arrhenius Behavior in the Reactions $H+C_2H_6 \rightarrow H_2+C_2H_5$, $H+CH_4 \rightarrow H_2+CH_3$, $CH_3+C_2H_6 \rightarrow CH_4+C_2H_5$. Can. J. Chem., v. 51, 1973, pp. 2147-2154.

16. Cordiero, A. A., P. M. Becker, and R. J. Heinsohn. Computer Simulations of Two Lean Premixed Methane-Oxygen Flames. Pennsylvania State University, University Park, Pa., 1972, 33 pp.

17. Cox, R. A., and R. F. Simmons. The Kinetics of the Gas-Phase Thermal Decomposition of Bromodifluoromethane. J. Chem. Soc. (B), 1971, pp. 1625-1631.

18. Day, J. J., D. V. Stamp, K. Thompson, and G. Dixon-Lewis. Inhibition of Hydrogen-Air and Hydrogen-Nitrous Oxide Flames by Halogen Compounds. Proc. 13th Internat. Symp. on Combustion, Combustion Institute, Pittsburgh, Pa., 1971, pp. 705-712.

19. Fenimore, C. P. Destruction of Methane in Water Gas by Reaction of CH_3 With OH Radicals. Proc. 12th Internat. Symp. on Combustion, Combustion Institute, Pittsburgh, Pa., 1969, pp. 463-467.

20. Ferguson, K. C., and E. Whittle. Kinetics of the Reaction Between HBr and CF_3Br. J. Chem. Soc., Faraday Trans., v. 68, No. 1, 1972, pp. 295-305.

21. Field, F. H., and J. F. Franklin. Electron Impact and Ionization Phenomena. Academic Press, New York, rev. ed., 1970, pp. 239-493.

22. Fristrom, R. M., and A. A. Westenberg. Flame Structure. McGraw-Hill Book Co., Inc., New York, 1965, 424 pp.

23. Galant, S., and J. P. Appleton. Theoretical Investigation of Inhibition Phenomena in Halogenated Flames. Ch. in Halogenated Fire Suppressants, ed. by R. G. Gann. ACS Symp. Series No. 16, 1975, pp. 406-427.

24. Giles, R. D., and E. Whittle. Photolysis of Mixtures of Acetone and Hexafluoroacetone. Trans. Faraday Soc., v. 61, 1965, pp. 1425-1436.

25. Hsu, D. S. Y., M. E. Umstead, and M. C. Lin. Kinetics and Mechanisms of Reactions of Fluoromethylidyne, Monofluoromethylene, and Difluoromethylene Radicals. In Fluorine-Containing Free Radicals. ACS Symp. Series No. 66, 1978, pp. 128-151.

26. Izod, T. P. J., G. B. Kistiakowsky, and S. Matsuda. Oxidation of Carbon Monoxide Mixtures With Added Ethane or Azomethane Studied in Incident Shock Waves. J. Chem. Phys., v. 55, 1971, pp. 4425-4432.

27. Jones, D. S., and S. J. Moss. Arrhenius Parameters for Reactions of Oxygen Atoms With the Fluorinated Ethylenes. Internat. J. Chem. Kinetics, v. 6, 1974, pp. 443-452.

28. Kaskan, W. E. The Dependence of Flame Temperature on Mass Burning Velocity. Proc. 6th Internat. Symp. on Combustion, Combustion Institute, Pittsburgh, Pa., 1957, pp. 134-143.

29. Kaskan, W. E., and J. J. Reuther. Limiting Equivalence Ratio, Dissociation, and Self-Inhibition in Premixed, Quenched, Fuel-Rich Hydrocarbon/Air Flames. Proc. 16th Internat. Symp. on Combustion, Combustion Institute, Pittsburgh, Pa., 1977, pp. 1083-1095.

30. Keating, E. L., and R. A. Matula. COF_2 Formation: The High Temperature C_2F_4-O_2 Reaction System. Pres. at the 1973 Fall Meeting of the Eastern States Section of the Combustion Institute, McGill University, Montreal, Quebec, Canada, Oct. 11-12, 1973, 18 pp.; available from Combustion Kinetics Lab., Dept. Mech. Eng. and Mechanics, Drexel Univ., Philadelphia, Pa.

31. Kobrinsky, P. C., G. O. Pritchard, and S. Toby. Pressure Dependence of the Cross-Combination Ratio for CF_3 and CH_3 Radicals. J. Phys. Chem., v. 75, 1971, pp. 2225-2226.

32. Kondratiev, V. N. Rate Constants of Gas Phase Reactions (trans. by L. J. Holtschlag and ed. by R. M. Fristrom). NBS, COM-72-10014, 1972, 428 pp.

33. Laufer, A. H., and A. M. Bass. Mechanism and Rate Constant of the Reaction Between Methylene and Methyl Radicals. J. Phys. Chem., v. 79, 1975, pp. 1635-1638.

34. Lazzara, C. P., J. C. Biordi, and J. F. Papp. Concentration Profiles for Radical Species in a Methane-Oxygen-Argon Flame. Combustion and Flame, v. 21, 1973, pp. 371-382.

35. Lifshitz, C., and F. A. Long. Appearance Potentials and Mass Spectra of Fluorinated Ethylenes. I. Decomposition Mechanisms and Their Energetics. J. Phys. Chem., v. 67, 1963, pp. 2463-2468.

36. _____. Appearance Potentials and Mass Spectra of Fluorinated Ethylenes. II. Heats of Formation of Fluorinated Species and Their Positive Ions. J. Phys. Chem., v. 69, 1965, pp. 3731-3736.

37. Mitchell, R. C., and J. P. Simons. The Reaction of $O(2^3P)$ Atoms With 1,1-Difluoro-olefins. J. Chem. Soc. (B), v. 80, 1968, pp. 1005-1007.

38. Mitsch, R. A., and A. S. Rogers. Reactivities in Olefin-Difluorocarbene Reactions. Internat. J. Chem. Kinetics, v. 1, 1969, pp. 439-450.

39. Modica, A. P., and J. E. LaGraff. Decomposition and Oxidation of C_2F_4 Behind Shock Waves. J. Chem. Phys., v. 43, 1965, pp. 3383-3392.

40. Papp, J. F., C. P. Lazzara, and J. C. Biordi. Chemical Flame Inhibition Using Molecular Beam Mass Spectrometry. Computational Methods for Analyzing Flame Microstructure. BuMines RI 8019, 1975, 90 pp.

41. Peeters, J., and G. Mahnen. Reaction Mechanisms and Rate Constants of Elementary Steps in Methane-Oxygen Flames. Proc. 14th Internat. Symp. on Combustion, Combustion Institute, Pittsburgh, Pa., 1973, pp. 133-146.

42. Pilling, M. J., and J. A. Robertson. A Rate Constant for $CH_2(^3B_1)+CH_3$. Chem. Phys. Letters, v. 33, 1975, pp. 336-339.

43. Pritchard, G. O., and M. J. Perona. The Elimination of HF From Vibrationally Excited Fluoroethanes. The Decomposition of 1,1,1-Trifluoroethane-d_0 and d_3. Internat. J. Chem. Kinetics, v. 2, 1970, pp. 281-297.

44. Roth, P., and Th. Just. Atom-Resonanzaborptionsmessungen beim thermischen Zerfall von Methon hinter Stosswellen (Atom Resonance Absorption Measurement of the Thermal Decomposition of Methane Behind a Shock Wave). Ber. Bunsenges. Phys. Chem., v. 79, No. 8, 1975, pp. 682-686.

45. Sehon, A. H., and M. Szwarc. The C-Br Bond Dissociation Energy in Halogenated Bromomethanes. Proc. Royal Soc. London, Ser. A, v. 209, 1951, pp. 110-131.

46. Skinner, G. B. Inhibition of the Hydrogen-Oxygen Reaction by CF_3Br and CF_2BrCF_2Br. Ch. in Halogenated Fire Suppressants, ed. by R. G. Gann. ACS Symp. Series No. 16, 1975, pp. 295-317.

47. Tedder, J. M., and J. C. Walton. Reactions of Halogenomethyl Radicals. Progress in Reaction Kinetics, v. 4, 1967, pp. 37-61.

48. Trotmann-Dickenson, A. F., and G. S. Milne. Tables of Bimolecular Gas Reactions. NBS, NSRDS-NBS 9, 1967, 129 pp.

49. Tschuikow-Roux, E., and J. E. Marte. Thermal Decomposition of Fluoroform in a Single-Pulse Shock Tube. I. J. Chem. Phys., v. 42, 1965, pp. 2049-2056.

50. Vandorren, J., J. Peeters, and P. J. Van Tiggelen. Rate Constants of the Elementary Reaction of Carbon Monoxide With Hydroxyl Radical. Proc. 15th Internat. Symp. on Combustion, Combustion Institute, Pittsburgh, Pa., 1975, pp. 745-753.

51. Westenberg, A. A., and N. deHaas. Measurement of the Rate Constant for $H+H_2CO \rightarrow H_2+HCO$ at 297-652° K. J. Phys. Chem., v. 76, No. 16, 1972, pp. 2213-2214.

52. Wilson, W. E., J. T. O'Donovan, and R. M. Fristrom. Flame Inhibition by Halogen Compounds. Proc. 12th Internat. Symp. on Combustion, Combustion Institute, Pittsburgh, Pa., 1969, pp. 929-942.

53. Wise, H., and W. A. Rosser. Homogeneous and Heterogeneous Reactions of Flame Intermediates. Proc. 9th Internat. Symp. on Combustion, Combustion Institute, Pittsburgh, Pa., 1963, pp. 733-746.

APPENDIX A.--FLAME SPECIES SMOOTHED COMPOSITION PROFILES

This appendix contains a partial listing (every fifth value) of the smoothed species composition profiles determined for the uninhibited flame III and the inhibited flame IV containing 1.1% CF_3Br. The characteristics of both flames are given in table A-1.

TABLE A-1. - Characteristics of flames III and IV examined at 0.042 atm

	Flame III	Flame IV
Flow, g sec^{-1}:		
CH_4	0.0107	0.0108
O_2	0.0456	0.0455
Ar	0.1811	0.1808
CF_3Br	0	0.0110
CH_4 ...mole-pct..	10.1	10.1
O_2 ...mole-pct..	21.5	21.2
Ar ...mole-pct..	68.4	67.6
CF_3Br ...mole-pct..	0	1.1
V_o[1] ...cm sec^{-1}..	47.6	48.0
T_{max}[2] ...K..	1,781	1,966
T_{ad}[3] ...K..	2,375	2,358

[1] Cold gas velocity calculated using $T_{initial}$ = 298 K.

[2] As determined in the absence of the sampling probe (5).

[3] Calculated adiabatic flame temperature.

These smoothed mole fraction profiles are obtained by applying various smoothing techniques to the mole fractions calculated from mass spectral intensities and calibration factors (7, 40).[1] The numbers under the column heading INDEX (tables A-2-A-4) are used in the computer program to identify each position. The numbers under the column heading Z are the distances, in centimeters, between the sampling probe tip and the burner surface. (Z = 0.0 is the burner surface.) The numbers in the column labeled TEMP are the smoothed temperature profiles in kelvins. The temperature profiles have been shifted to account for the probe "cooling" effect as described in reference 5. The temperatures given are those used in the kinetic analyses of the flames. The remaining columns are the mole fractions of the species listed at the head of the column. These smoothed mole fraction profiles appear as solid lines plotted through the data points in figures 2-7 of the text. The smoothed temperature profiles appear as the dashed line in the figures. The argon (column labeled A) mole fraction varies through the flame because it is defined to be the difference between 1 and the sum of all the other species mole fractions, $X_{Ar} = 1 - \sum_i X_i$, where $i \neq Ar$.

---

[1] Underlined numbers in parentheses refer to items in the list of references preceding the appendixes.

TABLE A-2. - Smoothed composition profiles for the species in flame III

			MOLE FRACTION										
INDEX	Z	TEMP	CH4	CO	CO2	H	H2O	OH	A	H2	O2	O	H2CO	CH3
5	.020	300.	.805E-01	.636E-02	.230E-02	0.	.207E-01	0.	.678E+00	.119E-01	.200E+00	0.	.170E-03	.940E-05
10	.045	300.	.791E-01	.732E-02	.267E-02	0.	.231E-01	0.	.677E+00	.125E-01	.198E+00	0.	.230E-03	.218E-04
15	.070	349.	.770E-01	.868E-02	.325E-02	.208E-04	.266E-01	.170E-04	.676E+00	.132E-01	.195E+00	0.	.293E-03	.356E-04
20	.095	418.	.742E-01	.104E-01	.403E-02	.764E-04	.310E-01	.615E-04	.676E+00	.140E-01	.190E+00	0.	.353E-03	.526E-04
25	.120	496.	.710E-01	.124E-01	.499E-02	.157E-03	.360E-01	.125E-03	.675E+00	.149E-01	.185E+00	0.	.407E-03	.804E-04
30	.145	579.	.676E-01	.147E-01	.612E-02	.253E-03	.415E-01	.197E-03	.674E+00	.158E-01	.179E+00	0.	.469E-03	.129E-03
35	.170	667.	.639E-01	.170E-01	.739E-02	.361E-03	.473E-01	.271E-03	.673E+00	.167E-01	.173E+00	0.	.539E-03	.198E-03
40	.195	758.	.602E-01	.195E-01	.881E-02	.487E-03	.533E-01	.344E-03	.672E+00	.177E-01	.167E+00	0.	.592E-03	.282E-03
45	.220	852.	.564E-01	.222E-01	.104E-01	.643E-03	.595E-01	.415E-03	.671E+00	.186E-01	.160E+00	0.	.627E-03	.378E-03
50	.245	946.	.525E-01	.250E-01	.120E-01	.844E-03	.658E-01	.484E-03	.669E+00	.196E-01	.154E+00	0.	.666E-03	.490E-03
55	.270	1037.	.484E-01	.280E-01	.139E-01	.110E-02	.722E-01	.554E-03	.668E+00	.205E-01	.146E+00	.149E-04	.716E-03	.631E-03
60	.295	1122.	.442E-01	.310E-01	.158E-01	.140E-02	.790E-01	.632E-03	.666E+00	.214E-01	.139E+00	.447E-04	.766E-03	.807E-03
65	.320	1200.	.397E-01	.340E-01	.179E-01	.175E-02	.862E-01	.731E-03	.665E+00	.224E-01	.130E+00	.935E-04	.812E-03	.101E-02
70	.345	1270.	.350E-01	.370E-01	.201E-01	.216E-02	.936E-01	.868E-03	.664E+00	.232E-01	.121E+00	.171E-03	.855E-03	.124E-02
75	.370	1333.	.302E-01	.398E-01	.224E-01	.262E-02	.101E+00	.106E-02	.663E+00	.240E-01	.113E+00	.294E-03	.883E-03	.145E-02
80	.395	1391.	.256E-01	.424E-01	.249E-01	.315E-02	.109E+00	.134E-02	.662E+00	.246E-01	.104E+00	.480E-03	.883E-03	.162E-02
85	.420	1442.	.211E-01	.446E-01	.274E-01	.378E-02	.116E+00	.171E-02	.660E+00	.250E-01	.964E-01	.744E-03	.851E-03	.170E-02
90	.445	1488.	.170E-01	.465E-01	.302E-01	.450E-02	.123E+00	.219E-02	.658E+00	.252E-01	.892E-01	.109E-02	.793E-03	.166E-02
95	.470	1526.	.134E-01	.480E-01	.330E-01	.531E-02	.130E+00	.278E-02	.655E+00	.252E-01	.828E-01	.153E-02	.710E-03	.151E-02
100	.495	1559.	.101E-01	.493E-01	.360E-01	.617E-02	.137E+00	.345E-02	.652E+00	.249E-01	.771E-01	.206E-02	.609E-03	.129E-02
105	.520	1586.	.744E-02	.501E-01	.390E-01	.704E-02	.143E+00	.420E-02	.649E+00	.243E-01	.721E-01	.268E-02	.496E-03	.103E-02
110	.545	1608.	.526E-02	.506E-01	.419E-01	.790E-02	.148E+00	.500E-02	.646E+00	.236E-01	.676E-01	.337E-02	.381E-03	.763E-03
115	.570	1627.	.358E-02	.505E-01	.447E-01	.872E-02	.153E+00	.580E-02	.643E+00	.227E-01	.634E-01	.411E-02	.275E-03	.534E-03
120	.595	1642.	.236E-02	.499E-01	.472E-01	.949E-02	.156E+00	.659E-02	.641E+00	.217E-01	.597E-01	.487E-02	.190E-03	.358E-03
125	.620	1654.	.151E-02	.488E-01	.496E-01	.102E-01	.159E+00	.733E-02	.641E+00	.207E-01	.563E-01	.561E-02	.127E-03	.227E-03
130	.645	1662.	.961E-03	.473E-01	.518E-01	.109E-01	.161E+00	.798E-02	.640E+00	.198E-01	.532E-01	.628E-02	.798E-04	.141E-03
135	.670	1667.	.616E-03	.455E-01	.539E-01	.114E-01	.163E+00	.854E-02	.641E+00	.190E-01	.506E-01	.685E-02	.450E-04	.934E-04
140	.695	1671.	.408E-03	.436E-01	.559E-01	.120E-01	.164E+00	.899E-02	.641E+00	.183E-01	.483E-01	.730E-02	.231E-04	.672E-04
145	.720	1674.	.279E-03	.417E-01	.580E-01	.124E-01	.165E+00	.934E-02	.641E+00	.176E-01	.465E-01	.763E-02	.124E-04	.475E-04
150	.745	1677.	.192E-03	.398E-01	.601E-01	.128E-01	.166E+00	.960E-02	.642E+00	.171E-01	.451E-01	.788E-02	.804E-05	.317E-04
155	.770	1679.	.123E-03	.380E-01	.621E-01	.132E-01	.166E+00	.980E-02	.642E+00	.167E-01	.440E-01	.805E-02	.560E-05	.215E-04
160	.795	1681.	.639E-04	.364E-01	.640E-01	.136E-01	.166E+00	.995E-02	.642E+00	.163E-01	.432E-01	.819E-02	.353E-05	.168E-04
165	.820	1681.	.202E-04	.349E-01	.657E-01	.140E-01	.167E+00	.101E-01	.642E+00	.160E-01	.425E-01	.829E-02	.194E-05	.149E-04
170	.845	1681.	0.	.335E-01	.672E-01	.144E-01	.167E+00	.102E-01	.642E+00	.158E-01	.418E-01	.836E-02	.755E-06	.132E-04
175	.870	1681.	0.	.323E-01	.685E-01	.147E-01	.167E+00	.103E-01	.642E+00	.156E-01	.410E-01	.841E-02	0.	.111E-04
180	.895	1680.	0.	.311E-01	.696E-01	.149E-01	.168E+00	.103E-01	.643E+00	.155E-01	.400E-01	.845E-02	0.	.894E-05
185	.920	1679.	0.	.301E-01	.706E-01	.151E-01	.168E+00	.104E-01	.643E+00	.154E-01	.390E-01	.849E-02	0.	.682E-05
190	.945	1678.	0.	.292E-01	.715E-01	.151E-01	.168E+00	.105E-01	.644E+00	.153E-01	.382E-01	.852E-02	0.	.463E-05
195	.970	1676.	0.	.284E-01	.724E-01	.152E-01	.168E+00	.105E-01	.644E+00	.152E-01	.377E-01	.856E-02	0.	.235E-05
200	.995	1674.	0.	.276E-01	.734E-01	.152E-01	.168E+00	.106E-01	.644E+00	.152E-01	.375E-01	.861E-02	0.	.459E-06

TABLE A-3. - Smoothed composition profiles for the species unrelated to the inhibitor in flame IV

MOLE FRACTION

INDEX	Z	TEMP	CH_4	CO	CO_2	H	H_2O	OH	A	H_2	O_2	O	H_2CO	CH_3
5	.020	300.	.854E-01	.156E-02	.324E-03	.129E-05	.503E-02	0.	.684E+00	.829E-02	.203E+00	0.	0.	.345E-05
10	.045	300.	.855E-01	.211E-02	.616E-03	.286E-05	.634E-02	0.	.679E+00	.883E-02	.205E+00	0.	0.	.776E-05
15	.070	300.	.854E-01	.273E-02	.889E-03	.425E-05	.783E-02	0.	.675E+00	.942E-02	.206E+00	0.	.523E-06	.121E-04
20	.095	300.	.847E-01	.343E-02	.117E-02	.515E-05	.954E-02	0.	.672E+00	.100E-01	.205E+00	0.	.362E-05	.164E-04
25	.120	349.	.835E-01	.423E-02	.147E-02	.539E-05	.115E-01	0.	.671E+00	.107E-01	.204E+00	0.	.735E-05	.207E-04
30	.145	427.	.820E-01	.513E-02	.184E-02	.530E-05	.136E-01	0.	.670E+00	.113E-01	.201E+00	0.	.121E-04	.250E-04
35	.170	510.	.802E-01	.613E-02	.227E-02	.609E-05	.158E-01	0.	.670E+00	.120E-01	.198E+00	0.	.174E-04	.293E-04
40	.195	597.	.783E-01	.724E-02	.278E-02	.979E-05	.182E-01	.293E-05	.670E+00	.127E-01	.195E+00	0.	.226E-04	.336E-04
45	.220	684.	.762E-01	.841E-02	.337E-02	.187E-04	.207E-01	.146E-04	.670E+00	.134E-01	.191E+00	0.	.279E-04	.380E-04
50	.245	769.	.740E-01	.976E-02	.406E-02	.344E-04	.235E-01	.361E-04	.669E+00	.141E-01	.187E+00	0.	.331E-04	.423E-04
55	.270	853.	.714E-01	.113E-01	.487E-02	.575E-04	.268E-01	.665E-04	.669E+00	.148E-01	.182E+00	0.	.383E-04	.463E-04
60	.295	934.	.685E-01	.130E-01	.585E-02	.871E-04	.306E-01	.103E-03	.667E+00	.156E-01	.178E+00	0.	.434E-04	.499E-04
65	.320	1014.	.654E-01	.150E-01	.704E-02	.122E-03	.351E-01	.139E-03	.666E+00	.163E-01	.173E+00	0.	.484E-04	.544E-04
70	.345	1090.	.622E-01	.172E-01	.843E-02	.163E-03	.400E-01	.172E-03	.663E+00	.170E-01	.168E+00	0.	.533E-04	.661E-04
75	.370	1165.	.588E-01	.197E-01	.100E-01	.212E-03	.453E-01	.197E-03	.660E+00	.177E-01	.162E+00	0.	.584E-04	.105E-03
80	.395	1238.	.553E-01	.223E-01	.118E-01	.273E-03	.507E-01	.214E-03	.657E+00	.185E-01	.156E+00	0.	.643E-04	.192E-03
85	.420	1307.	.516E-01	.250E-01	.136E-01	.348E-03	.561E-01	.226E-03	.654E+00	.193E-01	.150E+00	0.	.735E-04	.317E-03
90	.445	1374.	.477E-01	.279E-01	.155E-01	.439E-03	.615E-01	.235E-03	.652E+00	.201E-01	.144E+00	0.	.860E-04	.456E-03
95	.470	1436.	.435E-01	.310E-01	.175E-01	.544E-03	.671E-01	.248E-03	.650E+00	.210E-01	.137E+00	.350E-04	.992E-04	.636E-03
100	.495	1495.	.390E-01	.343E-01	.197E-01	.666E-03	.731E-01	.279E-03	.648E+00	.219E-01	.129E+00	.102E-03	.112E-03	.912E-03
105	.520	1549.	.342E-01	.379E-01	.220E-01	.819E-03	.798E-01	.350E-03	.646E+00	.228E-01	.121E+00	.202E-03	.127E-03	.128E-02
110	.545	1598.	.293E-01	.416E-01	.246E-01	.104E-02	.872E-01	.492E-03	.643E+00	.235E-01	.113E+00	.329E-03	.147E-03	.170E-02
115	.570	1643.	.244E-01	.450E-01	.275E-01	.139E-02	.951E-01	.746E-03	.640E+00	.240E-01	.104E+00	.477E-03	.171E-03	.208E-02
120	.595	1684.	.196E-01	.481E-01	.307E-01	.192E-02	.103E+00	.115E-02	.637E+00	.242E-01	.945E-01	.662E-03	.195E-03	.232E-02
125	.620	1720.	.151E-01	.507E-01	.340E-01	.266E-02	.111E+00	.175E-02	.635E+00	.241E-01	.856E-01	.930E-03	.220E-03	.233E-02
130	.645	1751.	.111E-01	.525E-01	.374E-01	.361E-02	.119E+00	.258E-02	.632E+00	.237E-01	.772E-01	.135E-02	.223E-03	.206E-02
135	.670	1779.	.762E-02	.536E-01	.408E-01	.471E-02	.126E+00	.362E-02	.630E+00	.230E-01	.697E-01	.197E-02	.196E-03	.160E-02
140	.695	1802.	.493E-02	.539E-01	.443E-01	.585E-02	.133E+00	.486E-02	.626E+00	.220E-01	.633E-01	.280E-02	.163E-03	.112E-02
145	.720	1821.	.299E-02	.535E-01	.477E-01	.695E-02	.138E+00	.621E-02	.623E+00	.210E-01	.580E-01	.379E-02	.132E-03	.727E-03
150	.745	1835.	.173E-02	.524E-01	.512E-01	.794E-02	.143E+00	.757E-02	.619E+00	.198E-01	.537E-01	.485E-02	.993E-04	.445E-03
155	.770	1847.	.976E-03	.509E-01	.546E-01	.879E-02	.147E+00	.881E-02	.615E+00	.187E-01	.501E-01	.585E-02	.617E-04	.265E-03
160	.795	1855.	.559E-03	.491E-01	.577E-01	.954E-02	.150E+00	.983E-02	.613E+00	.177E-01	.472E-01	.671E-02	.272E-04	.164E-03
165	.820	1860.	.328E-03	.471E-01	.604E-01	.102E-01	.152E+00	.106E-01	.612E+00	.168E-01	.447E-01	.738E-02	.445E-05	.106E-03
170	.845	1863.	.189E-03	.451E-01	.627E-01	.107E-01	.153E+00	.110E-01	.612E+00	.160E-01	.426E-01	.787E-02	0.	.618E-04
175	.870	1865.	.967E-04	.432E-01	.646E-01	.112E-01	.154E+00	.113E-01	.613E+00	.154E-01	.408E-01	.821E-02	0.	.239E-04
180	.895	1866.	.361E-04	.414E-01	.662E-01	.116E-01	.153E+00	.115E-01	.615E+00	.149E-01	.394E-01	.844E-02	0.	0.
185	.920	1866.	0.	.398E-01	.679E-01	.118E-01	.153E+00	.116E-01	.616E+00	.144E-01	.382E-01	.860E-02	0.	0.
190	.945	1866.	0.	.384E-01	.695E-01	.120E-01	.153E+00	.117E-01	.617E+00	.141E-01	.372E-01	.872E-02	0.	0.
195	.970	1865.	0.	.373E-01	.712E-01	.122E-01	.153E+00	.118E-01	.617E+00	.138E-01	.364E-01	.882E-02	0.	0.
200	.995	1864.	0.	.363E-01	.727E-01	.123E-01	.153E+00	.119E-01	.617E+00	.136E-01	.357E-01	.890E-02	0.	0.

TABLE A-4. - Smoothed composition profiles for the species related to the inhibitor in flame IV

			MOLE FRACTION											
INDEX	Z	TEMP	CF3BR	HF	HBR	BR	CH3BR	HCO	F2CO	CH2CF2	HO2	BR2	CF3H	CF2
5	.020	300.	.109E-01	.144E-02	.317E-04	0.	.797E-05	0.	.224E-04	.432E-04	0.	.915E-05	.191E-06	0.
10	.045	300.	.109E-01	.176E-02	.465E-04	0.	.938E-05	0.	.320E-04	.553E-04	0.	.106E-04	.677E-06	0.
15	.070	300.	.109E-01	.212E-02	.641E-04	0.	.115E-04	0.	.422E-04	.595E-04	0.	.122E-04	.139E-05	.241E-05
20	.095	300.	.109E-01	.253E-02	.870E-04	0.	.154E-04	0.	.546E-04	.627E-04	0.	.139E-04	.220E-05	.810E-05
25	.120	349.	.109E-01	.299E-02	.115E-03	0.	.211E-04	0.	.711E-04	.691E-04	0.	.157E-04	.319E-05	.155E-04
30	.145	427.	.109E-01	.351E-02	.150E-03	0.	.278E-04	0.	.934E-04	.825E-04	0.	.177E-04	.457E-05	.233E-04
35	.170	510.	.109E-01	.408E-02	.195E-03	0.	.353E-04	0.	.123E-03	.103E-03	0.	.199E-04	.629E-05	.314E-04
40	.195	597.	.109E-01	.471E-02	.253E-03	.284E-04	.443E-04	0.	.161E-03	.127E-03	0.	.221E-04	.791E-05	.403E-04
45	.220	684.	.109E-01	.540E-02	.324E-03	.107E-03	.558E-04	0.	.207E-03	.154E-03	0.	.241E-04	.928E-05	.514E-04
50	.245	769.	.110E-01	.614E-02	.400E-03	.250E-03	.707E-04	0.	.262E-03	.189E-03	0.	.257E-04	.110E-04	.657E-04
55	.270	853.	.110E-01	.694E-02	.476E-03	.466E-03	.890E-04	0.	.324E-03	.235E-03	0.	.262E-04	.137E-04	.843E-04
60	.295	934.	.110E-01	.781E-02	.557E-03	.760E-03	.110E-03	0.	.394E-03	.294E-03	0.	.249E-04	.176E-04	.108E-03
65	.320	1014.	.108E-01	.877E-02	.649E-03	.114E-02	.133E-03	0.	.470E-03	.367E-03	0.	.218E-04	.219E-04	.137E-03
70	.345	1090.	.105E-01	.979E-02	.760E-03	.160E-02	.158E-03	0.	.552E-03	.450E-03	0.	.179E-04	.260E-04	.173E-03
75	.370	1165.	.101E-01	.109E-01	.881E-03	.215E-02	.181E-03	0.	.639E-03	.534E-03	0.	.143E-04	.307E-04	.215E-03
80	.395	1238.	.946E-02	.120E-01	.996E-03	.278E-02	.202E-03	0.	.732E-03	.615E-03	0.	.114E-04	.368E-04	.262E-03
85	.420	1307.	.866E-02	.132E-01	.110E-02	.349E-02	.216E-03	0.	.832E-03	.704E-03	0.	.901E-05	.435E-04	.312E-03
90	.445	1374.	.772E-02	.144E-01	.119E-02	.425E-02	.222E-03	0.	.938E-03	.806E-03	0.	.701E-05	.493E-04	.361E-03
95	.470	1436.	.665E-02	.156E-01	.127E-02	.504E-02	.219E-03	0.	.105E-02	.903E-03	0.	.533E-05	.545E-04	.401E-03
100	.495	1495.	.551E-02	.169E-01	.134E-02	.583E-02	.204E-03	0.	.118E-02	.970E-03	0.	.404E-05	.601E-04	.425E-03
105	.520	1549.	.433E-02	.182E-01	.139E-02	.661E-02	.176E-03	0.	.130E-02	.997E-03	0.	.323E-05	.645E-04	.426E-03
110	.545	1598.	.321E-02	.194E-01	.139E-02	.734E-02	.139E-03	0.	.143E-02	.971E-03	0.	.273E-05	.662E-04	.401E-03
115	.570	1643.	.221E-02	.207E-01	.134E-02	.801E-02	.988E-04	0.	.154E-02	.865E-03	0.	.229E-05	.653E-04	.352E-03
120	.595	1684.	.140E-02	.217E-01	.124E-02	.863E-02	.647E-04	0.	.164E-02	.691E-03	0.	.183E-05	.622E-04	.287E-03
125	.620	1720.	.801E-03	.227E-01	.109E-02	.919E-02	.411E-04	0.	.172E-02	.506E-03	0.	.142E-05	.572E-04	.214E-03
130	.645	1751.	.412E-03	.234E-01	.893E-03	.969E-02	.266E-04	0.	.178E-02	.347E-03	0.	.107E-05	.505E-04	.146E-03
135	.670	1779.	.186E-03	.240E-01	.681E-03	.101E-01	.171E-04	0.	.181E-02	.222E-03	0.	.754E-06	.429E-04	.904E-04
140	.695	1802.	.703E-04	.244E-01	.495E-03	.105E-01	.104E-04	0.	.182E-02	.133E-03	0.	.468E-06	.354E-04	.505E-04
145	.720	1821.	.192E-04	.247E-01	.358E-03	.108E-01	.703E-05	0.	.181E-02	.728E-04	0.	.219E-06	.286E-04	.258E-04
150	.745	1835.	.152E-05	.248E-01	.266E-03	.110E-01	.603E-05	0.	.178E-02	.311E-04	0.	.404E-07	.227E-04	.126E-04
155	.770	1847.	0.	.250E-01	.206E-03	.111E-01	.509E-05	0.	.174E-02	.713E-05	0.	0.	.180E-04	.639E-05
160	.795	1855.	0.	.251E-01	.165E-03	.112E-01	.302E-05	0.	.168E-02	0.	0.	0.	.143E-04	.357E-05
165	.820	1860.	0.	.252E-01	.138E-03	.112E-01	.728E-06	0.	.163E-02	0.	0.	0.	.111E-04	.205E-05
170	.845	1863.	0.	.253E-01	.119E-03	.112E-01	0.	0.	.157E-02	0.	0.	0.	.794E-05	.103E-05
175	.870	1865.	0.	.255E-01	.108E-03	.112E-01	0.	0.	.151E-02	0.	0.	0.	.482E-05	.359E-06
180	.895	1866.	0.	.256E-01	.101E-03	.112E-01	0.	0.	.146E-02	0.	0.	0.	.243E-05	0.
185	.920	1866.	0.	.257E-01	.964E-04	.112E-01	0.	0.	.141E-02	0.	0.	0.	.105E-05	0.
190	.945	1866.	0.	.258E-01	.941E-04	.112E-01	0.	0.	.137E-02	0.	0.	0.	.308E-06	0.
195	.970	1865.	0.	.260E-01	.921E-04	.112E-01	0.	0.	.133E-02	0.	0.	0.	0.	0.
200	.995	1864.	0.	.260E-01	.898E-04	.112E-01	0.	0.	.129E-02	0.	0.	0.	0.	0.

APPENDIX B.--FLAME SPECIES NET REACTION RATE PROFILES

This appendix contains a partial listing (every fifth value) of the net reaction rate profiles determined for the species observed in the uninhibited flame III and the inhibited flame IV containing 1.1% CF_3Br. These net reaction rates were computed according to equations A and B. A description of the physical model for these computations, the method of computation, and a detailed listing of the computer program can be found in reference 40. The numbers under the column heading INDEX are used in the computer program to identify each position. The Z column numbers are the distances, in centimeters, between the sampling probe tip and the burner surface. The TEMP column numbers are a smoothed temperature profile, in kelvins, which has been shifted to account for the probe cooling effect (5).[1] The remaining columns list the net reaction rates, in units of mole cm^{-3} sec^{-1}, for the species at the head of the column. The values of the net reaction rates listed under the argon column, A, are meaningless. These individual net reaction rates, K_i, are the starting point for the kinetic analyses of the flame.

The net reaction rate profiles are very sensitive to small local variations in the smoothed mole fraction profiles. While the order of magnitude and the global variation of the net reaction rates are an accurate representation of the flame system chemistry, the local variations (bumps, glitches, and shoulders) which appear in these rate profiles result from deviations in the smoothed mole fraction profiles. When considered necessary, an effort has been made to minimize local variations in the net reaction rates in the region of the flame where they are used to compute reaction rate coefficients or deduce mechanisms. Figures 8 and 9 in the text are plots of the reaction rate profiles of the species indicated as obtained from this compilation. Certain regions, for example, where the net reaction rate for CH_4 is positive close to the burner, are not shown in the figures. Figures 11, 13, 15, 16, and 17 in the text are plots based on these net reaction rates with local variations removed. The flame region or temperature range over which a particular reaction rate profile can be utilized is limited by the experimental data and the curve-smoothing operation (5).

---

[1] Underlined numbers in parentheses refer to items in the list of references preceding the appendixes.

TABLE B-1. - Net reaction rate profiles for the species in flame III

NET REACTION RATE

INDEX	Z	TEMP	CH4	CO	CO2	H	H2O	OH	A	H2	O2	O	H2CO	CH3
5	.070	349.	.221E-04	-.241E-05	-.167E-05	-.310E-05	-.126E-04	-.433E-06	.659E-06	.462E-05	.211E-04	0.	.136E-06	-.470E-07
10	.095	418.	.128E-04	-.235E-05	-.190E-05	-.251E-05	-.106E-04	-.293E-06	.166E-05	-.181E-05	.134E-04	0.	.109E-06	-.193E-06
15	.120	496.	.851E-05	-.137E-05	-.205E-05	-.216E-05	-.714E-05	-.164E-06	.414E-05	-.210E-05	.820E-05	0.	-.191E-07	-.366E-06
20	.145	579.	.484E-05	-.166E-06	-.219E-05	-.215E-05	-.370E-05	-.199E-07	.650E-05	-.251E-05	.282E-05	0.	.444E-07	-.401E-06
25	.170	667.	.215E-05	-.159E-05	-.235E-05	-.320E-05	-.847E-06	.746E-07	.942E-05	-.311E-05	-.592E-06	0.	.340E-06	-.302E-06
30	.195	758.	.602E-06	-.102E-05	-.255E-05	-.536E-05	.517E-06	.111E-06	.783E-05	-.363E-05	-.606E-06	0.	.345E-06	-.266E-06
35	.220	852.	.509E-06	-.307E-06	-.263E-05	-.800E-05	-.779E-06	.846E-07	.388E-05	-.501E-05	.228E-05	-.105E-06	-.257E-08	-.444E-06
40	.245	946.	.757E-06	-.747E-06	-.261E-05	-.102E-04	-.430E-05	-.433E-07	.486E-06	-.638E-05	.665E-05	-.550E-06	-.129E-06	-.787E-06
45	.270	1037.	.115E-05	.100E-05	-.239E-05	-.112E-04	-.866E-05	-.342E-06	-.330E-05	-.709E-05	.889E-05	-.750E-06	.485E-07	-.101E-05
50	.295	1122.	.724E-06	.367E-05	-.198E-05	-.115E-04	-.108E-04	-.886E-06	-.398E-05	-.564E-05	.638E-05	-.944E-06	.152E-06	-.834E-06
55	.320	1200.	-.179E-05	.641E-05	-.144E-05	-.122E-04	-.801E-05	-.169E-05	-.530E-06	-.687E-06	-.158E-05	-.151E-05	.274E-06	-.197E-06
60	.345	1270.	-.638E-05	.969E-05	-.100E-05	-.146E-04	-.589E-06	-.268E-05	.499E-05	.794E-05	-.133E-04	-.237E-05	.519E-06	.761E-06
65	.370	1333.	-.124E-04	.137E-04	-.842E-06	-.187E-04	.790E-05	-.368E-05	.105E-04	.185E-04	-.257E-04	-.333E-05	.854E-06	.215E-05
70	.395	1391.	-.187E-04	.165E-04	-.962E-06	-.228E-04	.152E-04	-.445E-05	.158E-04	.284E-04	-.359E-04	-.414E-05	.918E-06	.399E-05
75	.420	1442.	-.241E-04	.166E-04	-.947E-06	-.243E-04	.202E-04	-.482E-05	.208E-04	.353E-04	-.419E-04	-.463E-05	.789E-06	.514E-05
80	.445	1488.	-.280E-04	.157E-04	-.103E-06	-.216E-04	.249E-04	-.465E-05	.219E-04	.387E-04	-.436E-04	-.480E-05	.631E-06	.449E-05
85	.470	1526.	-.304E-04	.160E-04	.210E-05	-.148E-04	.317E-04	-.393E-05	.152E-04	.392E-04	-.416E-04	-.470E-05	.422E-06	.283E-05
90	.495	1559.	-.315E-04	.176E-04	.560E-05	-.604E-05	.407E-04	-.270E-05	.999E-06	.374E-04	-.372E-04	-.431E-05	.150E-06	.126E-05
95	.520	1586.	-.312E-04	.199E-04	.960E-05	.216E-05	.493E-04	-.107E-05	-.159E-04	.328E-04	-.320E-04	-.345E-05	-.193E-06	-.440E-06
100	.545	1608.	-.294E-04	.215E-04	.129E-04	.788E-05	.542E-04	.795E-06	-.293E-04	.246E-04	-.274E-04	-.191E-05	-.609E-06	-.211E-05
105	.570	1627.	-.261E-04	.211E-04	.146E-04	.109E-04	.532E-04	.273E-05	-.355E-04	.129E-04	-.244E-04	.347E-06	-.908E-06	-.281E-05
110	.595	1642.	-.216E-04	.185E-04	.142E-04	.126E-04	.470E-04	.454E-05	-.338E-04	-.579E-06	-.230E-04	.308E-05	-.904E-06	-.264E-05
115	.620	1654.	-.167E-04	.138E-04	.120E-04	.144E-04	.385E-04	.600E-05	-.261E-04	-.125E-04	-.230E-04	.576E-05	-.713E-06	-.238E-05
120	.645	1662.	-.119E-04	.790E-05	.906E-05	.165E-04	.311E-04	.689E-05	-.163E-04	-.201E-04	-.234E-04	.774E-05	-.574E-06	-.196E-05
125	.670	1667.	-.779E-05	.180E-05	.646E-05	.175E-04	.265E-04	.708E-05	-.799E-05	-.226E-04	-.236E-04	.852E-05	-.520E-06	-.115E-05
130	.695	1671.	-.465E-05	-.351E-05	.513E-05	.154E-04	.236E-04	.659E-05	-.197E-05	-.217E-04	-.230E-04	.803E-05	-.424E-06	-.470E-06
135	.720	1674.	-.250E-05	-.734E-05	.546E-05	.993E-05	.199E-04	.560E-05	.249E-05	-.195E-04	-.213E-04	.661E-05	-.249E-06	-.263E-06
140	.745	1677.	-.125E-05	-.937E-05	.716E-05	.321E-05	.138E-04	.436E-05	.550E-05	-.178E-04	-.182E-04	.486E-05	-.933E-07	-.292E-06
145	.770	1679.	-.769E-06	-.982E-05	.949E-05	-.748E-06	.635E-05	.314E-05	.588E-05	-.167E-04	-.132E-04	.335E-05	-.281E-07	-.268E-06
150	.795	1681.	-.862E-06	-.935E-05	.116E-04	.102E-05	.402E-06	.210E-05	.243E-05	-.154E-04	-.689E-05	.235E-05	-.201E-07	-.146E-06
155	.820	1681.	-.130E-05	-.878E-05	.126E-04	.807E-05	-.165E-05	.129E-05	-.384E-05	-.132E-04	-.579E-06	.181E-05	-.186E-07	-.292E-07
160	.845	1681.	-.940E-06	-.855E-05	.123E-04	.165E-04	-.410E-07	.737E-06	-.987E-05	-.104E-04	.328E-05	.144E-05	-.209E-07	.852E-08
165	.870	1681.	-.114E-06	-.852E-05	.105E-04	.214E-04	.282E-05	.467E-06	-.110E-04	-.773E-05	.267E-05	.100E-05	-.196E-07	.138E-09
170	.895	1680.	0.	-.812E-05	.773E-05	.202E-04	.470E-05	.500E-06	-.508E-05	-.592E-05	-.238E-05	.462E-06	-.542E-08	-.533E-08
175	.920	1679.	0.	-.692E-05	.462E-05	.140E-04	.540E-05	.796E-06	.371E-05	-.511E-05	-.913E-05	-.148E-07	0.	-.218E-08
180	.945	1678.	0.	-.507E-05	.220E-05	.651E-05	.631E-05	.120E-05	.898E-05	-.483E-05	-.134E-04	-.204E-06	0.	-.436E-08

TABLE B-2. - Net reaction rate profiles for the species unrelated to the inhibitor in flame IV

INDEX	Z	TEMP	NET REACTION RATE											
			CH4	CO	CO2	H	H2O	OH	A	H2	O2	O	H2CO	CH3
5	.070	300.	.943E-05	.100E-05	.815E-06	.389E-07	.132E-05	0.	-.244E-04	.295E-05	.221E-04	0.	-.117E-07	.143E-07
10	.095	300.	.235E-04	.909E-06	.331E-06	.459E-07	.620E-06	0.	-.167E-04	.124E-04	.259E-04	0.	-.202E-08	.148E-07
15	.120	349.	.237E-04	-.969E-07	-.414E-06	.127E-07	-.172E-05	0.	-.916E-05	.882E-05	.220E-04	0.	-.390E-08	.932E-08
20	.145	427.	.109E-04	-.724E-06	-.813E-06	-.110E-06	-.181E-05	-.360E-08	-.449E-05	-.266E-08	.113E-04	0.	-.109E-08	.608E-08
25	.170	510.	.617E-05	-.683E-06	-.109E-05	-.362E-06	-.179E-05	-.927E-07	-.890E-06	-.250E-05	.681E-05	0.	.517E-08	.523E-08
30	.195	597.	.423E-05	-.853E-06	-.135E-05	-.654E-06	-.330E-05	-.225E-06	.170E-05	-.399E-05	.394E-05	0.	.653E-08	.430E-08
35	.220	684.	.405E-05	-.226E-05	-.178E-05	-.973E-06	-.719E-05	-.267E-06	.510E-05	-.463E-05	.259E-05	0.	.653E-08	.666E-08
40	.245	769.	.476E-05	-.291E-05	-.256E-05	-.116E-05	-.130E-04	-.260E-06	.883E-05	-.467E-05	.205E-05	0.	.805E-08	.136E-07
45	.270	853.	.498E-05	-.409E-05	-.359E-05	-.117E-05	-.185E-04	-.160E-06	.141E-04	-.456E-05	.161E-05	0.	.100E-07	.846E-08
50	.295	934.	.343E-05	-.549E-05	-.454E-05	-.114E-05	-.203E-04	.954E-08	.188E-04	-.410E-05	.139E-05	0.	.974E-08	-.513E-07
55	.320	1014.	.114E-05	-.521E-05	-.488E-05	-.129E-05	-.167E-04	.193E-06	.185E-04	-.399E-05	.108E-05	0.	.788E-08	-.327E-06
60	.345	1090.	-.290E-06	-.339E-05	-.432E-05	-.177E-05	-.854E-05	.321E-06	.119E-04	-.486E-05	.127E-05	0.	.245E-08	-.996E-06
65	.370	1165.	-.104E-06	-.139E-05	-.300E-05	-.255E-05	.393E-06	.354E-06	.182E-05	-.705E-05	.248E-05	0.	-.242E-07	-.157E-05
70	.395	1238.	.179E-05	-.718E-06	-.152E-05	-.328E-05	.573E-05	.284E-06	-.699E-05	-.999E-05	.457E-05	0.	-.724E-07	-.123E-05
75	.420	1307.	.447E-05	-.157E-05	-.608E-06	-.360E-05	.396E-05	.997E-07	-.984E-05	-.122E-04	.702E-05	-.426E-06	-.675E-07	-.729E-06
80	.445	1374.	.618E-05	-.305E-05	-.824E-06	-.368E-05	-.443E-05	-.274E-06	-.457E-05	-.115E-04	.899E-05	-.145E-05	-.475E-08	-.175E-05
85	.470	1436.	.560E-05	-.433E-05	-.228E-05	-.473E-05	-.158E-04	-.982E-06	.625E-05	-.611E-05	.994E-05	-.194E-05	.217E-07	-.349E-05
90	.495	1495.	.253E-05	-.249E-05	-.444E-05	-.891E-05	-.251E-04	-.217E-05	.153E-04	.474E-05	.926E-05	-.188E-05	-.508E-07	-.338E-05
95	.520	1549.	-.247E-05	.435E-05	-.624E-05	-.181E-04	-.271E-04	-.389E-05	.166E-04	.199E-04	.602E-05	-.147E-05	-.131E-06	-.105E-05
100	.545	1598.	-.864E-05	.138E-04	-.647E-05	-.318E-04	-.194E-04	-.603E-05	.108E-04	.365E-04	-.996E-06	-.136E-05	-.594E-07	.253E-05
105	.570	1643.	-.157E-04	.226E-04	-.446E-05	-.464E-04	-.275E-05	-.831E-05	.296E-05	.509E-04	-.121E-04	-.250E-05	.114E-07	.721E-05
110	.595	1684.	-.238E-04	.298E-04	-.736E-06	-.555E-04	.180E-04	-.104E-04	-.272E-05	.596E-04	-.263E-04	-.535E-05	.173E-06	.116E-04
115	.620	1720.	-.326E-04	.348E-04	.314E-05	-.533E-04	.368E-04	-.116E-04	-.254E-05	.605E-04	-.413E-04	-.924E-05	.746E-06	.124E-04
120	.645	1751.	-.408E-04	.372E-04	.556E-05	-.382E-04	.489E-04	-.115E-04	.574E-05	.537E-04	-.539E-04	-.124E-04	.896E-06	.789E-05
125	.670	1779.	-.458E-04	.366E-04	.621E-05	-.143E-04	.539E-04	-.911E-05	.164E-04	.408E-04	-.613E-04	-.126E-04	.269E-06	.646E-06
130	.695	1802.	-.456E-04	.330E-04	.651E-05	.100E-04	.550E-04	-.425E-05	.172E-04	.249E-04	-.617E-04	-.897E-05	-.935E-07	-.470E-05
135	.720	1821.	-.398E-04	.266E-04	.860E-05	.268E-04	.569E-04	.262E-05	.236E-05	.853E-05	-.554E-04	-.214E-05	-.190E-07	-.635E-05
140	.745	1835.	-.303E-04	.185E-04	.135E-04	.329E-04	.617E-04	.100E-04	-.232E-04	-.609E-05	-.451E-04	.558E-05	.361E-07	-.579E-05
145	.770	1847.	-.200E-04	.102E-04	.201E-04	.309E-04	.676E-04	.158E-04	-.487E-04	-.179E-04	-.347E-04	.116E-04	-.207E-06	-.436E-05
150	.795	1855.	-.115E-04	.284E-05	.252E-04	.264E-04	.698E-04	.184E-04	-.629E-04	-.262E-04	-.273E-04	.143E-04	-.520E-06	-.250E-05
155	.820	1860.	-.593E-05	-.319E-05	.258E-04	.242E-04	.632E-04	.173E-04	-.591E-04	-.306E-04	-.235E-04	.138E-04	-.595E-06	-.103E-05
160	.845	1863.	-.313E-05	-.798E-05	.214E-04	.252E-04	.468E-04	.133E-04	-.389E-04	-.308E-04	-.215E-04	.112E-04	-.257E-06	-.547E-06
165	.870	1865.	-.206E-05	-.117E-04	.138E-04	.266E-04	.244E-04	.826E-05	-.111E-04	-.275E-04	-.189E-04	.804E-05	-.152E-07	-.877E-06
170	.895	1866.	-.172E-05	-.140E-04	.684E-05	.254E-04	.350E-05	.388E-05	.124E-04	-.223E-04	-.150E-04	.536E-05	0.	-.905E-06
175	.920	1866.	-.138E-05	-.144E-04	.343E-05	.205E-04	-.953E-05	.102E-05	.237E-04	-.172E-04	-.111E-04	.344E-05	0.	-.248E-06
180	.945	1866.	-.452E-06	-.124E-04	.411E-05	.133E-04	-.126E-04	-.315E-06	.230E-04	-.137E-04	-.906E-05	.216E-05	0.	0.

TABLE B-3. - Net reaction rate profiles for the species related to the inhibitor in flame IV

NET REACTION RATE

INDEX	Z	TEMP	CF3BR	HF	HBR	BR	CH3BR	HCO	F2CO	CH2CF2	HO2	BR2	CF3H	CF2
5	.070	300.	-.372E-06	.598E-06	.219E-07	0.	-.136E-08	0.	.181E-07	.207E-07	0.	.435E-08	.148E-08	-.192E-07
10	.095	300.	-.215E-05	.568E-06	.898E-08	0.	-.473E-09	0.	-.281E-09	-.196E-07	0.	.229E-08	.812E-09	.100E-08
15	.120	349.	-.237E-05	-.768E-07	-.390E-07	0.	-.103E-08	0.	-.279E-07	-.472E-07	0.	-.477E-09	-.975E-09	.328E-08
20	.145	427.	-.108E-05	-.427E-06	-.402E-07	-.552E-07	-.103E-08	0.	-.415E-07	-.420E-07	0.	-.998E-10	-.376E-10	.382E-08
25	.170	510.	-.593E-06	-.543E-06	-.132E-06	-.374E-06	-.765E-08	0.	-.498E-07	-.114E-07	0.	.156E-08	.350E-08	-.597E-08
30	.195	597.	-.286E-06	-.645E-06	-.107E-06	-.697E-06	-.186E-07	0.	-.499E-07	-.143E-07	0.	.417E-08	.421E-08	-.235E-07
35	.220	684.	.177E-07	-.781E-06	-.201E-07	-.913E-06	-.264E-07	0.	-.422E-07	-.632E-07	0.	.814E-08	-.472E-08	-.429E-07
40	.245	769.	.361E-06	-.101E-05	.473E-07	-.109E-05	-.250E-07	0.	-.298E-07	-.103E-06	0.	.154E-07	-.139E-07	-.604E-07
45	.270	853.	.878E-06	-.127E-05	.802E-08	-.119E-05	-.146E-07	0.	-.136E-07	-.120E-06	0.	.230E-07	-.111E-07	-.750E-07
50	.295	934.	.144E-05	-.142E-05	-.141E-06	-.124E-05	.120E-08	0.	.494E-08	-.114E-06	0.	.210E-07	-.379E-09	-.871E-07
55	.320	1014.	.191E-05	-.132E-05	-.223E-06	-.126E-05	.226E-07	0.	.236E-07	-.266E-07	0.	.651E-08	.526E-08	-.952E-07
60	.345	1090.	.213E-05	-.900E-06	-.313E-07	-.122E-05	.558E-07	0.	.400E-07	.122E-06	0.	-.909E-08	-.407E-08	-.917E-07
65	.370	1165.	.207E-05	-.316E-05	.321E-06	-.105E-05	.103E-06	0.	.498E-07	.158E-06	0.	-.152E-07	-.130E-07	-.616E-07
70	.395	1238.	.175E-05	.180E-06	.490E-06	-.703E-06	.151E-06	0.	.498E-07	.157E-07	0.	-.114E-07	.200E-08	.135E-07
75	.420	1307.	.120E-05	.417E-06	.412E-06	-.145E-06	.192E-06	0.	.443E-07	-.153E-07	0.	-.910E-08	.245E-07	.147E-06
80	.445	1374.	.491E-06	.490E-06	.369E-06	.580E-06	.224E-06	0.	.494E-07	.342E-06	0.	-.103E-07	.212E-07	.333E-06
85	.470	1436.	-.432E-06	.739E-06	.584E-06	.139E-05	.247E-06	0.	.882E-07	.820E-06	0.	-.111E-07	.142E-07	.541E-06
90	.495	1495.	-.164E-05	.153E-05	.980E-06	.218E-05	.239E-06	0.	.181E-06	.107E-05	0.	-.112E-07	.393E-07	.708E-06
95	.520	1549.	-.307E-05	.303E-05	.130E-05	.282E-05	.156E-06	0.	.330E-06	.136E-05	0.	-.759E-08	.683E-07	.767E-06
100	.545	1598.	-.447E-05	.506E-05	.145E-05	.319E-05	-.176E-07	0.	.510E-06	.168E-05	0.	-.285E-08	.680E-07	.669E-06
105	.570	1643.	-.545E-05	.724E-05	.151E-05	.326E-05	-.206E-06	0.	.676E-06	.121E-05	0.	-.115E-08	.545E-07	.416E-06
110	.595	1684.	-.569E-05	.911E-05	.145E-05	.313E-05	-.298E-06	0.	.782E-06	-.196E-07	0.	-.185E-08	.437E-07	.682E-07
115	.620	1720.	-.512E-05	.102E-04	.984E-06	.302E-05	-.258E-06	0.	.808E-06	-.931E-06	0.	-.214E-08	.297E-07	-.277E-06
120	.645	1751.	-.399E-05	.103E-04	-.358E-07	.314E-05	-.160E-06	0.	.765E-06	-.118E-05	0.	-.169E-08	.806E-08	-.526E-06
125	.670	1779.	-.269E-05	.933E-05	-.120E-05	.348E-05	-.104E-06	0.	.684E-06	-.114E-05	0.	-.143E-08	-.171E-07	-.624E-06
130	.695	1802.	-.154E-05	.737E-05	-.182E-05	.380E-05	-.908E-07	0.	.583E-06	-.916E-06	0.	-.159E-08	-.347E-07	-.575E-06
135	.720	1821.	-.826E-06	.493E-05	-.171E-05	.377E-05	-.610E-07	0.	.463E-06	-.657E-06	0.	-.233E-08	-.404E-07	-.434E-06
140	.745	1835.	-.363E-06	.258E-05	-.124E-05	.322E-05	-.825E-08	0.	.318E-06	-.554E-06	0.	-.283E-08	-.417E-07	-.269E-06
145	.770	1847.	-.825E-07	.782E-06	-.796E-06	.229E-05	.172E-07	0.	.154E-06	-.451E-06	0.	-.130E-08	-.375E-07	-.137E-06
150	.795	1855.	-.199E-08	-.257E-06	-.529E-06	.128E-05	-.320E-08	0.	-.459E-08	-.208E-06	0.	-.890E-10	-.230E-07	-.573E-07
155	.820	1860.	0.	-.597E-06	-.379E-06	.506E-06	-.341E-07	0.	-.126E-06	-.309E-07	0.	0.	-.965E-08	-.238E-07
160	.845	1863.	0.	-.430E-06	-.268E-06	.960E-07	-.222E-07	0.	-.194E-06	0.	0.	0.	-.126E-07	-.152E-07
165	.870	1865.	0.	.233E-07	-.177E-06	-.141E-07	-.192E-08	0.	-.216E-06	0.	0.	0.	-.258E-07	-.131E-07
170	.895	1866.	0.	.536E-06	-.115E-06	.193E-07	0.	0.	-.211E-06	0.	0.	0.	-.300E-07	-.935E-08
175	.920	1866.	0.	.885E-06	-.687E-07	.632E-07	0.	0.	-.196E-06	0.	0.	0.	-.212E-07	-.273E-08
180	.945	1866.	0.	.909E-06	-.212E-07	.631E-07	0.	0.	-.174E-06	0.	0.	0.	-.140E-07	0.

APPENDIX C.--LIST OF SYMBOLS

Symbol	Units	Definition
A	-	Area expansion ratio.
amu	-	Atomic mass units.
D_{i-Ar}	$cm^2\ sec^{-1}$	Binary diffusion coefficient of species i with argon.
G_i	-	Fractional mass flux of species i.
I_m	-	Mass spectral intensity at mass m.
K	-	Degrees kelvin.
K_i	moles $cm^{-3}\ sec^{-1}$	Net reaction rate of species i.
k_j	sec^{-1} (1st order) $cm^3\ mole^{-1}\ sec^{-1}$ (2d order) $cm^6\ mole^{-2}\ sec^{-1}$ (3d order)	Chemical reaction rate coefficient of reaction j.
k_{T_i}	-	Thermal diffusion ratio of species i.
M_i	$g\ mole^{-1}$	Gram molecular weight of species i.
RRK	-	Rice-Ramsperger-Kassel theory of unimolecular reactions.
T	K	Temperature.
v	$cm\ sec^{-1}$	Bulk flow velocity.
X_i	-	Mole fraction of species i.
z	cm	Perpendicular distance from the burner surface to sampling probe tip.
ρ	$g\ cm^{-3}$	Mean mass density.

☆U.S. GOVERNMENT PRINTING OFFICE: 1978-703-103/70

INT.-BU.OF MINES,PGH.,PA. 23235

622.09
Un32mo

RI 8308

Bureau of Mines Report of Investigations/1978

Linear Polarization Measurements at High Temperatures in Hypersaline Geothermal Brines

DEPOSITORY
NOV 17 1978
UNIV. OF ILL. LIBRARY
AT URBANA-CHAMPAIGN

UNITED STATES DEPARTMENT OF THE INTERIOR

Report of Investigations 8308

Linear Polarization Measurements at High Temperatures in Hypersaline Geothermal Brines

By Stephen D. Cramer and Paul B. Needham, Jr.

March 3, 1849

UNITED STATES DEPARTMENT OF THE INTERIOR
Cecil D. Andrus, Secretary

BUREAU OF MINES

This publication has been cataloged as follows:

Cramer, Stephen D

Linear polarization measurements at high temperatures in hypersaline geothermal brines / by S. D. Cramer and P. B. Needham. [Washington] : U.S. Dept. of the Interior, Bureau of Mines, 1978.

15 p. ; 27 cm. (Report of investigations - Bureau of Mines ; 8308)

Bibliography: p. 14-15.

1. Geothermal engineering. 2. Incrustations. 3. Corrosion and anticorrosives. I. Needham, Paul B., joint author. II. United States. Bureau of Mines. III. Title. IV. Series: United States. Bureau of Mines. Report of investigations - Bureau of Mines ; 8308.

TN23.U7 no. 8308 622.06173

U.S. Dept. of the Int. Library

CONTENTS

Page

Abstract.... 1
Introduction.... 1
Acknowledgment.... 4
Experimental procedures.... 4
  Polarization measurements.... 5
  Electrode preparation.... 5
Results and discussion.... 6
Conclusions.... 12
References.... 14

ILLUSTRATIONS

1. Bureau of Mines Geothermal Test Facility located at the Salton Sea Known Geothermal Resource Area (KGRA) near Calipatria, Calif.... 2
2. Schematic diagram of electrochemical test package mounted on in situ corrosion test package.... 4
3. Electrodes exposed to unflashed input brine.... 7
4. Galena-based scale formed on weight-loss coupons exposed to unflashed input brine for 15 days.... 7
5. Potentiostatic polarization curve for 430 stainless steel exposed to unflashed input brine.... 8
6. Scaling characteristics of three process streams.... 10
7. Corrosion of 1020 carbon steel measured by linear polarization during a period when scale was depositing on the electrode surfaces.... 11

TABLES

1. Chemical analysis of brines in three process streams of the Bureau of Mines Geothermal Test Facility.... 3
2. Corrosion rates in Magmamax 1 brine obtained by linear polarization and weight-loss techniques.... 12

LINEAR POLARIZATION MEASUREMENTS AT HIGH TEMPERATURES IN HYPERSALINE GEOTHERMAL BRINES

by

Stephen D. Cramer[1] and Paul B. Needham, Jr.[2]

ABSTRACT

The Bureau of Mines conducted a series of in situ linear polarization measurements in high-temperature, high-pressure hypersaline geothermal brines at the Bureau of Mines Geothermal Test Facility in the Imperial Valley of California. The measurements represented an evaluation of the linear polarization technique for obtaining instantaneous corrosion rates of materials of construction in flowing hypersaline hydrothermal fluids that rapidly form scales on exposed surfaces. A special method was devised for use with the linear polarization technique that resulted in obtaining corrosion rates for 1020 carbon steel, 316 and 430 stainless steel, titanium, various nickel-based alloys, and aluminum 6061 under strong scale-forming conditions. The measurements also provided information on scale-deposition rates in various geothermal environments. Exploratory in situ potentiostatic polarization measurements were made in the flowing brines to qualitatively determine scale-deposition effects on the electrochemical measurements.

INTRODUCTION

Corrosion is one of the major problems that must be solved in order to fully develop the Nation's geothermal resources. The determination of materials needed for constructing geothermal resource recovery plants, including those for minerals recovery, power generation, and secondary process facilities, requires the recognition of the special needs of the industry. Recent development of geothermal resources, found mainly in the Western United States, is focusing on liquid-dominated geothermal reservoirs in which the working fluids are highly corrosive, high-temperature brines. Located in the Imperial Valley of southern California are six large and distinct liquid-dominated known geothermal resource areas (KGRA). Of particular interest to the Bureau of Mines is the Salton Sea KGRA containing hypersaline brines, which offer a high potential for the recovery of valuable mineral and metal products (3).[3]

---

[1] Chemical research engineer.
[2] Research physicist.
Both authors are with the Avondale Metallurgy Research Center, Bureau of Mines, College Park, Md.

The brines from the Salton Sea KGRA are, typically, discharged from the wellhead at temperatures in excess of 200° C; downhole brine temperatures of 350° C have been reported (13). Total dissolved solids, largely as chlorides of the alkali and alkaline earth metals, are in the range of 20 to 30 wt-pct. In addition, the brines contain heavy-metal ions, dissolved gases including carbon dioxide with lesser amounts of hydrogen sulfide, ammonia, methane, and hydrogen, and may be saturated with silica. These constituents result in the formation of complex scales on metal surfaces exposed to the brine.

In the present work, brine was used from geothermal well Magmamax 1, located on the Salton Sea KGRA, which flowed into the Bureau of Mines Geothermal Test Facility (fig. 1). The facility was designed for testing materials to provide several of the important process steps that will be found in

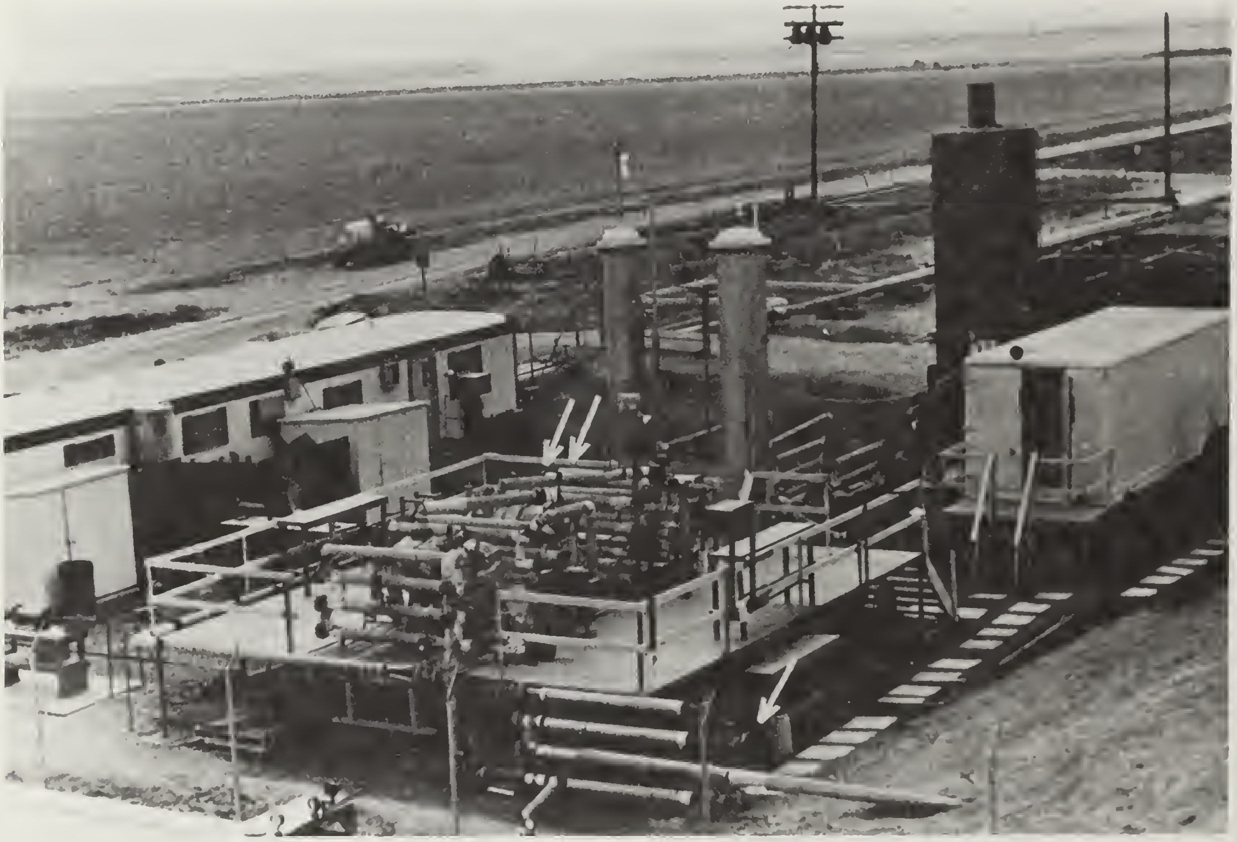

FIGURE 1. - Bureau of Mines Geothermal Test Facility located on the Salton Sea Known Geothermal Resource Area (KGRA) near Calipatria, Calif. (Arrows show the approximate locations of the electrochemical test packages.)

---

[3] Underlined numbers in parentheses refer to items in the list of references at the end of this report.

a geothermal resource recovery plant. It incorporates two stages of steam separation that allow the brines to flash-evaporate at successively lower pressures and temperatures. A representative analysis for the major constituents of the unflashed input brine from Magmamax 1, together with wellhead temperature, pressure, and pH, is shown in table 1. Typical values of the chloride content, temperature, pressure, and pH are also given in table 1 for the concentrated brine following two stages of steam separation and for the steam condensate. Dissolved gases, particularly carbon dioxide, are stripped from the brine at each stage of steam separation. This results in the higher values of pH observed for the concentrated brine compared with those of the unflashed input brine.

TABLE 1. - Chemical analysis of brines in three process streams of the Bureau of Mines Geothermal Test Facility

Constituent concentration	Input brine	Concentrated brine (second stage)[1]	Steam condensate[1]
Na....................ppm..	46,900	-	-
Ca....................ppm..	22,700	-	-
K.....................ppm..	7,870	-	-
Mn....................ppm..	603	-	-
Sr....................ppm..	558	-	-
Fe....................ppm..	477	-	-
Li....................ppm..	148	-	-
Pb....................ppm..	36	-	-
Cl....................ppm..	118,200	128,000	8,620
Temperature.........° C..	229	178	~100
Pressure...........psig..	302	140	0
pH........................	5.1	5.7	6.7

[1] Dashes indicate no measurement taken.

The present work describes our initial experience in applying the linear polarization technique to in situ corrosion measurements in high-temperature, high-pressure geothermal environments. Originally developed by Stern and Geary (15), the technique is widely used to study corroding systems (4-9, 11, 14). Commercial instrumentation based on the technique relies on the fact that, for many corroding systems, the corrosion kinetics in a narrow region around the corrosion potential are nearly linear. It is assumed that the reversible potentials of competing oxidation-reduction reactions are sufficiently far removed from the corrosion potential that the corrosion reaction is dominant and that ohmic and concentration effects are minimal. Since electrochemical measurements in complex, high-temperature geothermal brines have not been made before, the present application may raise questions that can only be answered by further study in the laboratory and the field. However, at the time the polarization measurements were made, a 30-day weight-loss corrosion test involving 6,400 corrosion test coupons was in progress at the Geothermal Test Facility (2), and there was a unique opportunity to compare and evaluate measurements using the two techniques.

ACKNOWLEDGMENT

The authors wish to acknowledge the assistance of Roger J. Dexter, Western Region Marketing Coordinator, Petrolite Corp., Stafford, Tex., for use of the M-103 corrosion rate instrument, M511-E industrial probes, and electrode materials at the Geothermal Test Facility, Imperial Valley, Calif.

EXPERIMENTAL PROCEDURES

Linear polarization measurements were made with the Petrolite M-103E portable corrosion rate instrument.[4] The three-electrode technique (4-9, 11, 14) was employed using cylindrical electrodes of identical material for the working, counter, and reference electrodes. All measurements were made with respect to the potential of the freely corroding electrode by superimposing a signal of ±10 mv dc. Given the assumptions inherent in the instrumentation, the measured current was converted directly into a corrosion rate for the test material, expressed as mils per year (mils/yr) of surface thickness lost.

Because of the high temperature and pressure of the brine, the electrodes were mounted on Petrolite M-511E industrial probes designed for pressures up to 600 lb/sq in and temperatures up to 260° C. The electrode assemblies were exposed to the brine and condensate environments through a specially designed electrochemical test package (fig. 2) that was, in turn, mounted on one of seven in situ corrosion test packages. Mounted in this way, the electrode assembly could be inserted directly into the corrosion test package for optimum exposure of the electrodes to the flowing brine.

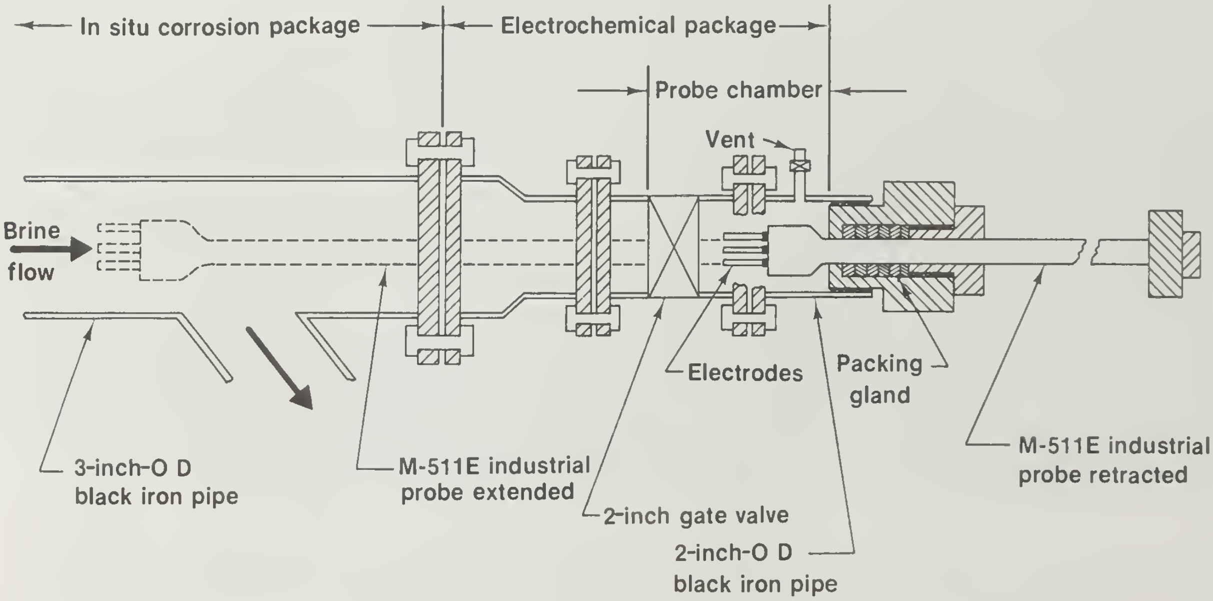
In situ corrosion package
Electrochemical package
Probe chamber
Vent
Brine flow
Electrodes
Packing gland
M-511E industrial probe retracted
3-inch-O D black iron pipe
M-511E industrial probe extended
2-inch gate valve
2-inch-O D black iron pipe

FIGURE 2. - Schematic diagram of electrochemical test package mounted on in situ corrosion test package.

---

[4] Use of specific trade names does not imply endorsement by the Bureau of Mines.

The electrochemical package served three functions: (1) to isolate the probe during installation, (2) to provide access to the highly turbulent brine flowing through the corrosion test package, and (3) as a containment vessel that allowed hot brine to slowly circulate through the probe chamber and around the electrodes. Before making the polarization measurements, the gate valve was opened, filling the probe chamber with brine, and the vent (fig. 2) was opened for 1 to 2 min, purging the probe chamber of trapped air. The probe was then extended through the gate valve into the flowing brine or retained in the retracted position exposed to the brine inside the probe chamber. Purging of the probe chamber and the circulation of the brine removed air from the electrode surroundings.

Polarization Measurements

Linear polarization measurements were made in each of the three process streams listed in table 1: (1) the unflashed input brine, (2) the concentrated brine following two stages of steam separation, and (3) the steam condensate. Measurements were begun immediately following the insertion of the electrodes into the brine and were repeated periodically for times up to 40 hours after the initial exposure. The measurements were made in pairs by polarizing the working electrode first cathodically and then anodically. The reported corrosion rates were the average of the consecutive cathodic and anodic values. The electrodes were at their "open-circuit" or corrosion potential between measurements.

Electrode Preparation

Sets of electrodes were made from eight metals and alloys chosen for their widely differing compositions and resistances to corrosion. These were 1020 carbon steel, 316 and 430 stainless steel, Monel 400, aluminum 6061, Inconel 625, Hastelloy C-276, and titanium. The dimensions of the electrodes were selected to compensate for chemical and physical differences between the metals and alloys so that the measurements could be made without further calibration. Measurements were made with each set of electrodes in the input brine, and further measurements were made with the 1020 carbon steel electrodes in the concentrated brine and steam condensate.

The electrodes were mechanically polished to a 240-grit finish using silicon carbide abrasive, washed with water, rinsed with methanol, and air dried. They were weighed before each test to within ±0.5 mg, and threaded onto glass-insulated mounting pins on the M-511E probes. These mounting pins were isolated from the brine using flat sealing gaskets of Viton A rubber or Teflon.

At the end of each test, the probe-electrode assembly was washed with water, rinsed with methanol, and dried with forced air. On removal of the electrodes, the mounting pins were immediately examined for any fluid leakage around the gasket. (Tests were repeated if leakage was observed at either the working or reference electrodes.) The electrodes were rinsed with methanol, dried a second time, and reweighed to determine the weight change of the electrode resulting from either corrosion or scaling. The electrodes were then examined with a microscope for localized corrosion.

Used electrodes were reconditioned by repeating the surface-grinding technique to remove corrosion products and scale accumulation. Dimensional changes in the electrodes were checked with a micrometer. In all other respects, the reconditioned and new electrodes were treated identically.

Potentiostatic polarization measurements, to qualitatively determine the effect of scale deposition on the corrosion kinetics, were made using a Wenking 66TA potentiostat.

RESULTS AND DISCUSSION

Chemical, fluid dynamic, and thermodynamic properties of the geothermal brine delivered to the Bureau's Geothermal Test Facility varied because of fluctuations in the operation of Magmamax 1. Consequently, the initial experiments were directed toward identifying the properties of the brine and/or the test facility that would affect the polarization measurements.

Brines from the Salton Sea KGRA readily form scales on exposed metal surfaces. These scales range in composition from amorphous silica and silicates to heavy-metal sulfides and calcite (1-2, 10), depending upon the processing of the brine. Two sets of electrodes, exposed for 3 hours to the input brine, are shown in figure 3 with the resulting layers of scale, consisting predominantly of galena. (A third set of clean, unexposed electrodes is shown for comparison.) The typical structure of the predominant galena scale is illustrated by the scanning electron micrograph in figure 4 using scale formed on 15-day weight-loss coupons exposed to input brine.

Exploratory potentiostatic polarization measurements were made in unflashed input brine to qualitatively determine the effect of scale on the observed electrode kinetics. Type 430 stainless steel electrodes in the retracted position were used for the measurements. Beginning at a potential 100-mv cathodic to the open-circuit potential, the potential was swept at a rate of 20 mv/min in the anodic direction (fig. 5). Curve A corresponds to electrodes that were initially free of scale when the potential sweep began. Curve B corresponds to electrodes that were extended into the flowing input brine for 3 hours to allow the scale to form, but it was retracted prior to the potential sweep measurements. The currents observed for the initially scale-free electrodes were suppressed by several orders of magnitude when the galena-based scale was present. The initially scale-free electrodes exhibited a region of current instability in the potential range of +200 to +500 mv, which essentially disappeared when the electrodes were covered with scale. The small negative potentials at the crossover between cathodic and anodic kinetics were probably due to slight differences in the surface condition of the working and reference electrodes.

Preliminary linear polarization measurements were made using carbon steel electrodes in the concentrated brine. The measured currents became increasingly unstable as the electrodes were positioned further into the flowing brine. With the electrodes fully inserted into the brine, the currents were extremely difficult to measure. Reynolds number calculations indicate the brine is highly turbulent in the vicinity of the electrodes when they are in the extended position. Turbulence produces erosive conditions that can delay

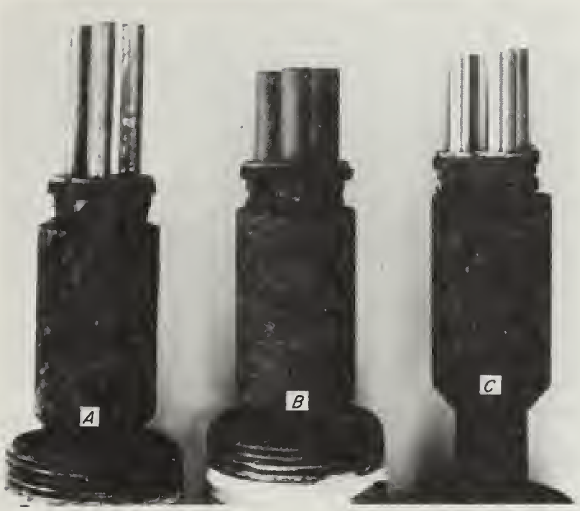

FIGURE 3. - Electrodes exposed to unflashed input brine. *A*, 430 stainless steel, before exposure; *B*, titanium, 3.2-hour exposure; *C*, 316 stainless steel, 3.4-hour exposure.

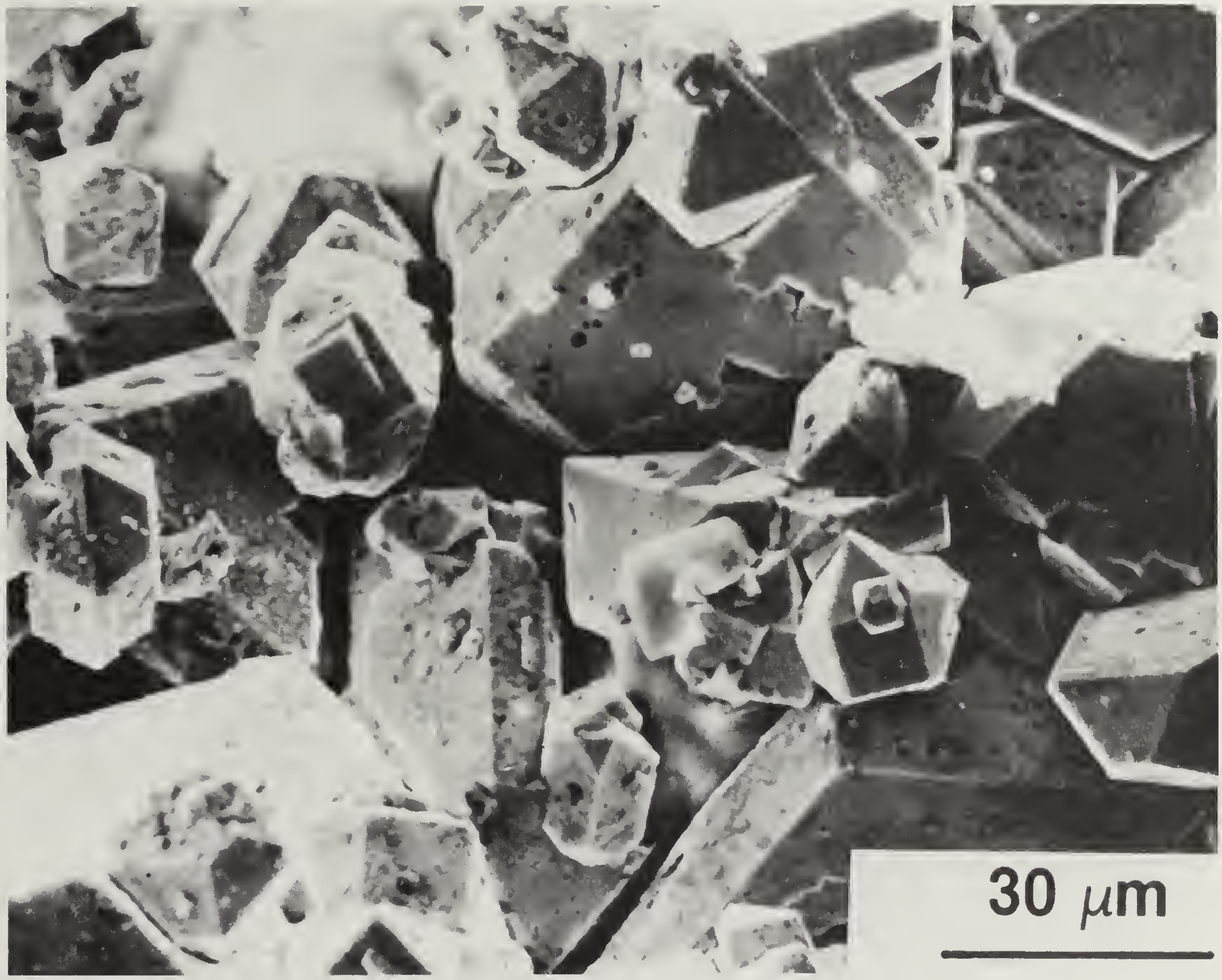

FIGURE 4. - Galena-based scale formed on weight-loss coupons exposed to unflashed input brine for 15 days.

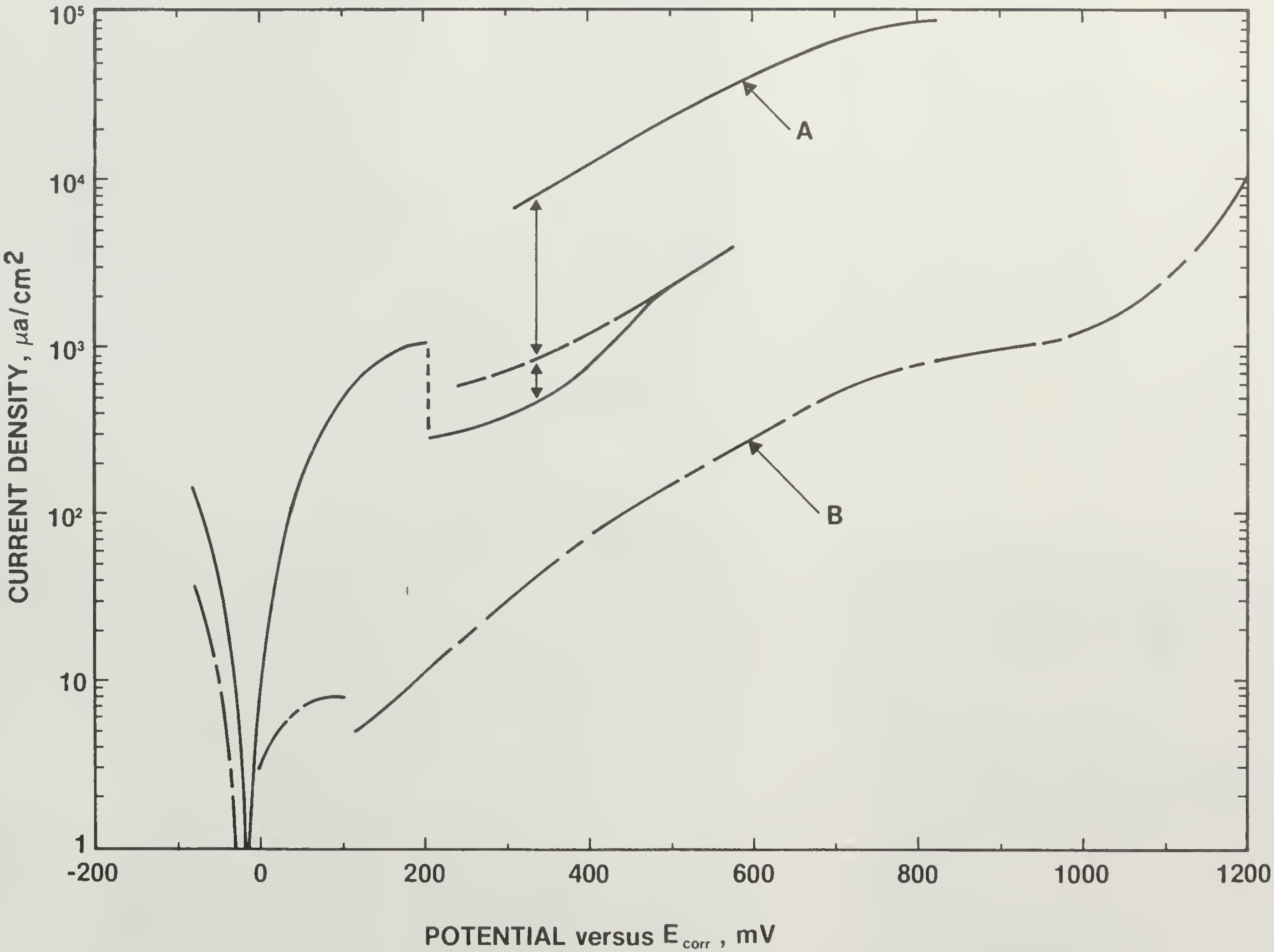

FIGURE 5. - Potentiostatic polarization curves for 430 stainless steel exposed to unflashed input brine. A, initially scale-free electrodes; B, electrodes exposed 3 hours to flowing brine. Potentials measured with respect to the corrosion potential, E_{corr}, of 430 stainless steel.

or disrupt the deposition of scale on the corroding surface. These changes in the condition of the scale on the corroding surface can lead to current fluctuation of one order of magnitude or more, as the potentiostatic polarization measurements indicated. Consequently, all subsequent linear polarization measurements were made with the probe in the retracted position and the electrodes exposed to brine slowly circulating within the probe chamber, which resulted in experimentally more reproducible conditions.

Even with the probe in the retracted position, however, current instabilities were observed at periodic intervals during linear polarization measurements. These instabilities correlated precisely with the operation of certain automatic pressure and flow-rate control valves in the Geothermal Test Facility. The functioning of these valves produced local changes in pressure within the corrosion test packages. Analysis of the pressure variations showed that at certain times the pressure in the vicinity of the electrode assembly dropped below the saturation pressure of the brine, and boiling occurred in the fluid surrounding the electrodes. Consequently, for all subsequent linear polarization measurements, the procedure was to close the 2-inch gate valve on the electrochemical package before each measurement, temporarily isolating the probe chamber from the flowing brine and possible transient pressure effects. Immediately following the measurement, the gate valve was reopened. This procedure yielded a consistent set of measurements that was relatively free of distortions produced by the control functions of the Geothermal Test Facility.

The scaling rates for the three process streams were determined by weight-gain measurements of electrodes exposed for times ranging from several hours up to 40 hours. These measurements were made with the probes in the retracted position so that the results could be used to interpret the subsequent linear polarization measurements. The weight-gain results are shown in figure 6, expressed in mg/cm^2 based on the nominal exposed electrode surface areas. Carbon steel electrodes were used in the concentrated brine and steam condensate, and all of the electrode materials except aluminum 6061 were used for measurements in the input brine. The scale deposition rates, obtained as the slope of the curves, were 0.31 mg/cm^2/hr for the input brine, 0.094 mg/cm^2/hr for the concentrated brine, and 0.032 mg/cm^2/hr for the steam condensate. The scale from the input brine was hard and adherent, scale from the concentrated brine was hard and moderately adherent, and scale from the steam condensate was soft and poorly adherent.

Instantaneous corrosion rates for 1020 carbon steel were determined periodically by the linear polarization technique in the input brine, concentrated brine, and steam condensate for exposures up to 14 hours. During this time, as shown by figure 6, scale steadily accumulated on the surface of the electrodes. The corrosion results (fig. 7) were strongly dependent upon the type of scale formed and the scale deposition rate. In the steam condensate, where the scaling rate was low and the scale was relatively nonadherent, the corrosion rate was independent of the exposure time. In the concentrated brine, where the scale depositon rate was more rapid and the scale was moderately adherent, the corrosion rate declined gradually owing to the increasing thickness of the scale. In the input brine, where the scaling rate was triple that

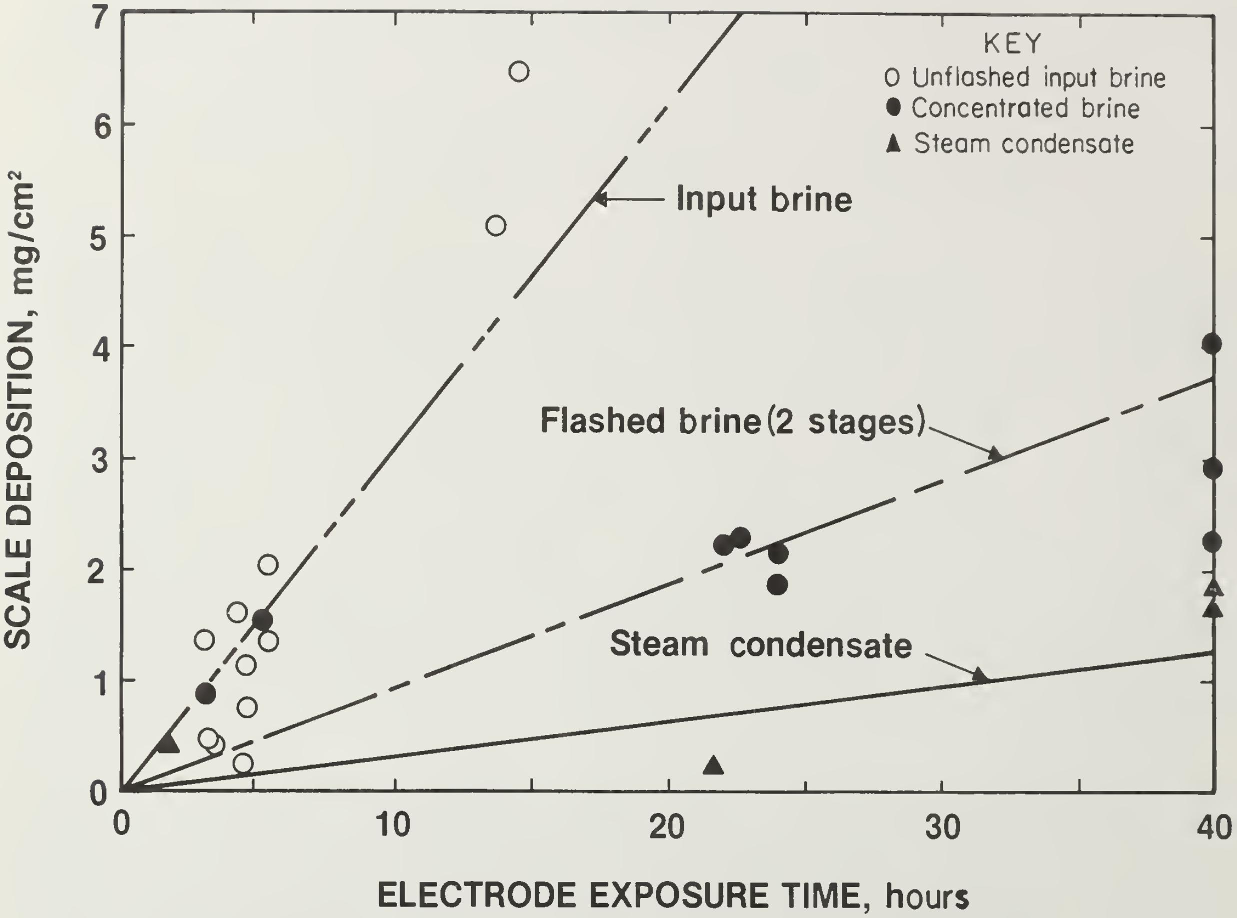

FIGURE 6. - Scaling characteristics of three process streams.

in the concentrated brine, the corrosion rate dropped even more sharply because of the rapid growth of the scale layer. The area of the metal exposed to the brine is known only for times that are short relative to the scale deposition rate, that is, at the beginning of the exposure when scale formation is slight. The strong correlation between scale deposition rate, scale adhesion, and declining corrosion rate suggests the results observed for the input and concentrated brines occurred primarily because scale growth reduced the area of metal exposed to the brine, not because the actual corrosion rate was changing.

Actual corrosion rates based on the known surface area were obtained from the linear polarization measurements by extrapolating time-dependent data, illustrated by figure 7, to zero exposure time, corresponding to the condition where the electrode surface was free of scale. Under these conditions, the corroding surface (assuming uniform general corrosion) and the nominal surface area of the electrode were equivalent. As a practical matter, the data in figure 7 suggest that the corrosion measurements obtained in the first 15 min for the input brine and in the first 30 to 40 min for the concentrated brine provide a reasonable estimate of the actual corrosion rate. In any case, the

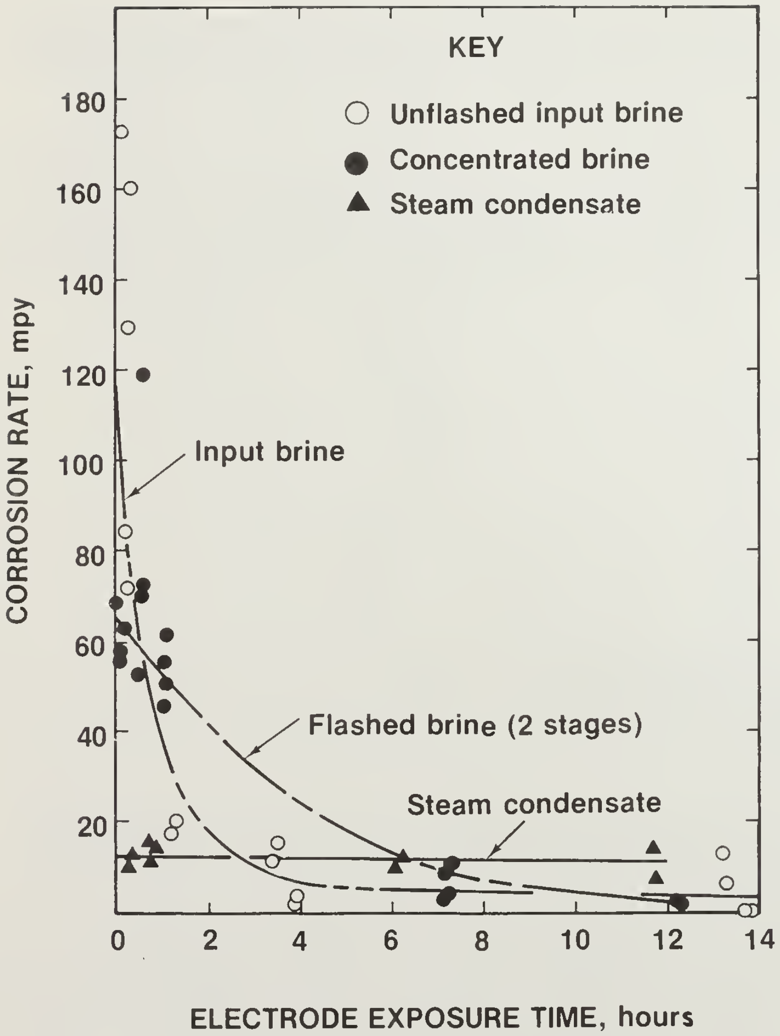

FIGURE 7. - Corrosion of 1020 carbon steel measured by linear polarization during a period when scale was depositing on the electrode surfaces.

actual corrosion rate will be referred to here as the scale-free corrosion rate, emphasizing that the observed decline in the corrosion rate was the result of scale deposition, which reduced the area of metal exposed to the brine. Subsequent corrosion measurements were made by plotting time-dependent linear polarization data obtained over a 3-hour period and then extrapolating to zero-exposure time. The results of the measurements for the eight alloys are given in table 2. Carbon steel corroded at rates ranging from 12 mils/yr in the steam condensate to 145 mils/yr in the input brine. Corrosion rates in the input brine ranged from 0.2 mil/yr for titanium to 610 mils/yr for aluminum 6061. The aluminum 6061 electrodes were the only ones to experience observable localized corrosion during the 3-hour test exposures. Microscopic examination showed that they had pitted severely.

Included in table 2 are the results of the 15-day in situ weight-loss measurements (2) that were run concurrently with the linear polarization measurements in the same three process steps at the Geothermal Test Facility. At the end of the 15-day weight-loss tests, examination of the test coupons showed that they were thickly coated with scale. Although these coupons had been exposed for much longer times, the scales had compositions and properties similar to those observed on the linear polarization electrodes. In view of the persistant growth of scales in the input and concentrated brines, the corrosion of the weight-loss samples was probably retarded by the scales in a manner similar to that shown by the linear polarization measurements (fig. 7). Consequently, the measured corrosion rate for the weight-loss coupons could be interpreted as the time-averaged value of the instantaneous corrosion rate or, equivalently, as the area-averaged value, where scale coverage is considered a function of time. In this model, the upper limit of the corrosion rate for the weight-loss samples would be, by definition, the scale-free value obtained by linear polarization. For extended exposures, the observed corrosion rate for the weight-loss samples should be equal to or less than that obtained by linear polarization. (See table 2.)

TABLE 2. - Corrosion rates in Magmamax 1 brine obtained by linear polarization and weight-loss techniques

Alloy	Test environment	Linear polarization results, mils/yr	Weight-loss results,[1] mils/yr
Aluminum 6061.......	Input brine........	610	([2])
1020 carbon steel...	.....do............	145	67
Monel 400...........	.....do............	62	([2])
316 stainless steel.	.....do............	5.6	.7
430 stainless steel.	.....do............	3.1	.6-2.2
Inconel 625.........	.....do............	.8	0
Hastelloy C-276.....	.....do............	.4	.1
Titanium............	.....do............	.2	([2])
1020 carbon steel...	Concentrated brine.	62	48
Do................	Steam condensate...	12	([2])

[1] Fifteen-day exposure (2).

[2] Corrosion rate not measured.

The placement and method of using the polarization electrodes described represents a departure from typical field polarization applications in which the electrodes are continuously exposed to the working system for long, unattended periods. However, such a departure may be necessary in high-temperature, hypersaline geothermal brines because of unstable conditions linked with variations in the chemistry, fluid dynamics, and thermodynamics of the brine, and because of the massive scaling associated with the brine (1, 10). Until techniques for scale control have been developed (1, 13), the best approach for making corrosion measurements by the linear polarization technique would appear to involve measurements on initially scale-free electrodes in exposures of short duration. This, however, need not detract from either the potential usefulness of the technique for measuring corrosion rates in such environments, or its importance for monitoring changes in the corrosiveness of specific process steps.

CONCLUSIONS

These studies have shown that the linear polarization technique is applicable to corrosion measurements in high-temperature, hypersaline geothermal brines as long as the following essential modifications of the method are made: (1) The electrodes must be isolated from highly turbulent brine flows to give experimentally reproducible conditions, (2) the electrodes must be isolated from nonsteady conditions related to the control functions of facility equipment, particularly those that may reduce the pressure below the saturation pressure of the brine and cause boiling and two-phase flow around the electrodes, and (3) the corrosion rate must be obtained for electrodes free of scale, which can be obtained by extrapolating the time-dependent corrosion data to zero-exposure time.

The corrosion rates for scale-free electrodes were shown to represent the upper limit for the corrosion of extended exposure weight-loss coupons. In this model, the deposition of scale reduced the area of the corroding surface. Consequently, the observed corrosion rates for weight-loss coupons in exposures of 15 days were substantially less than values obtained for scale-free electrodes by the linear polarization technique.

REFERENCES

1. Barnes, H. L., W. F. Downs, J. D. Rimstidt, and D. O. Hayba. Control of Silica Deposition in Geothermal Systems. Annual Report on Grant G0-155140-1 to U.S. Bureau of Mines, July 1977, 42 pp.; available upon request from S. D. Cramer, Avondale Metallurgy Research Center, Bureau of Mines, Avondale, Md.

2. Carter, J. P., and F. X. McCawley. In Situ Corrosion Tests in Salton Sea Geothermal Brine Environments. J. Metals, v. 30, No. 3, March 1978, pp. 11-15.

3. Hornburg, C. D. Geothermal Development of the Salton Sea. Chem. Eng. Prog., v. 73, July 1977, pp. 89-94.

4. Leroy, R. L. The Range of Validity of the Linear Polarization Method for Measurement of Corrosion Rates. Corrosion, v. 29, July 1973, pp. 272-275.

5. _____. Evaluation of Corrosion Rates From Polarization Measurements. Corrosion, v. 31, May 1975, pp. 173-177.

6. _____. Evaluation of Corrosion Rates From Nonlinear Polarization Data. J. Electrochem. Soc., v. 124, July 1977, pp. 1006-1012.

7. Mansfeld, F. Some Errors in Linear Polarization Measurements and Their Correction. Corrosion, v. 30, March 1974, pp. 92-96.

8. _____. On the Shape of Some Polarization Curves in the Vicinity of the Corrosion Potential. Corrosion, v. 30, September 1974, pp. 320-323.

9. Mansfeld, F. and K. B. Oldham. A Modification of the Stern-Geary Linear Polarization Equation. Corr. Sci., v. 11, 1971, pp. 787-796.

10. Miller, D. G., A. J. Piwinskii, and R. Yamauchi. The Use of Geochemical-Equilibrium Calculations To Estimate Precipitation From Geothermal Brines. Lawrence Livermore Laboratory, Univ. Calif., Livermore, Calif., UCRL-52197, January 1977, 35 pp.

11. Oldham, K. B., and F. Mansfeld. On the So-Called Linear Polarization Method for Measurement of Corrosion Rates. Corrosion, v. 27, October 1971, pp. 434-435.

12. Owen, L. B. Precipitation of Amorphous Silica From High-Temperature Hypersaline Geothermal Brines. Lawrence Livermore Laboratory, Univ. Calif., Livermore, Calif., UCRL-51866, June 1975, 20 pp.

13. Palmer, T. D. Characteristics of Geothermal Wells Located in the Salton Sea Geothermal Field, Imperial County, California. Univ. Calif., Livermore, Calif., UCRL-51976, December 1975, 54 pp.

14. Palombarini, G., L. Felloni, and G. P. Cammarota. On the Shape of Some Polarization Curves in the Vicinity of the Corrosion Potential. Corrosion, v. 29, June 1973, pp. 245-250.

15. Stern, M., and A. L. Geary. Electrochemical Polarization: A Theoretical Analysis of the Shape of Polarization Curves. J. Electrochem. Soc., v. 104, January 1957, pp. 56-63.

☆U.S. GOVERNMENT PRINTING OFFICE: 1978-703-103/66

622.09
Un32mo

RI 8309

Bureau of Mines Report of Investigations/1978

Improved Methods for Monitoring Production From Vertical Degasification Wells

DEPOSITORY
NOV 2[illegible] 197[illegible]
UNIV. OF ILL. LIBRARY
[illegible] CHAMPAIGN

UNITED STATES DEPARTMENT OF THE INTERIOR

Report of Investigations 8309

Improved Methods for Monitoring Production From Vertical Degasification Wells

By S. W. Lambert and M. A. Trevits

March 3 1849

UNITED STATES DEPARTMENT OF THE INTERIOR
Cecil D. Andrus, Secretary

BUREAU OF MINES

This publication has been cataloged as follows:

Lambert, S W

Improved methods for monitoring production from vertical degasification wells / by S. W. Lambert and M. A. Trevits. [Washington] : U.S. Dept. of the Interior, Bureau of Mines, 1978.

14 p. : ill., diagrs. ; 27 cm. (Report of investigations - Bureau of Mines ; 8309)

Includes bibliographies.

1. Mine gases. 2. Gas wells. 3. Coal mines and mining. I. Trevits, M. A., joint author. II. United States. Bureau of Mines. III. Title. IV. Series: United States. Bureau of Mines. Report of investigations - Bureau of Mines ; 8309.

TN23.U7 no. 8309 622.06173

U.S. Dept. of the Int. Library

CONTENTS

Page

Abstract... 1
Introduction... 1
Acknowledgments.. 2
General well completion.. 2
Methods of removing and measuring water........................ 2
Problems of monitoring water production........................ 2
    Solids in waterlines....................................... 4
    Freezing... 4
    Improper pumping interval.................................. 4
    Gas in waterlines.. 5
Improved methods for monitoring water production............... 5
Methods of removing and measuring gas.......................... 8
Problems of monitoring gas production.......................... 9
    Water in gaslines.. 9
    Freezing... 9
    Sudden pressure release.................................... 9
    Solids in gaslines... 10
Improved methods for monitoring gas production................. 10
Conclusion... 12
Appendix A.--Proper pump-cycling procedures.................... 13
Appendix B.--Methods to prevent and control well unloading..... 14

ILLUSTRATIONS

1. Single-horizon (open hole) completion....................... 3
2. Multiple-horizon completion................................. 3
3. Downhole water-production equipment......................... 6
4. Surface water-monitoring equipment.......................... 7
5. Gas-production and monitoring equipment..................... 8

IMPROVED METHODS FOR MONITORING PRODUCTION FROM VERTICAL DEGASIFICATION WELLS[1]

by

S. W. Lambert[2] and M. A. Trevits[2]

ABSTRACT

In this Bureau of Mines investigation, production was monitored for 1 year at over 30 coalbed gas-drainage boreholes located in Alabama, Pennsylvania, and West Virginia. Results indicate that the quality of data gathered from such wells can be improved greatly if potential problems are anticipated and prevented in the early stages of well production.

Major water-monitoring problems include solids buildup, freezing, the presence of gas in surface waterlines, and improper pumping interval settings. Such problems may be avoided by incorporating in the original well design waterline filters, sand screens, separator tanks, and systems to automatically control pumping intervals.

Problems related to measurement of coalbed gas flow include large quantities of water vapor contained in the gas, especially during winter months; freezing and subsequent obstruction of flow; sudden, uncontrolled release of gas pressure; and solids buildup in metering equipment. The installation of commercially available items, such as filters, separators, and insulation, and the thoughtful application of a basic knowledge of coalbed gas reservoir characteristics will prevent most production-monitoring problems.

INTRODUCTION

In July 1974, a project was initiated to establish optimum well density for coalbed gas-drainage boreholes. Project design called for degasification of large tracts of land with possible eventual expansion to an entire coal basin. An early phase of project development was to design and implement an accurate means of measuring production from drainage boreholes.

---

[1] The work described in this report was performed by a component of the Bureau of Mines that was transferred to the Department of Energy on October 1, 1977.

[2] Geologist.

Both authors are now with Pittsburgh Mining Operations, Department of Energy, Pittsburgh, Pa. (formerly with Pittsburgh Mining and Safety Research Center, Bureau of Mines, Pittsburgh, Pa.).

Calculations of the effectiveness of any degasification program depend upon the quality of data collected as mining approaches and intercepts a borehole. Correlation of borehole production to reductions in face emissions and the derivation of coalbed reservoir parameters can be provided if sound information is available for analysis.

ACKNOWLEDGMENTS

The authors thank Leon DeBardelaben, drilling superintendent, and L. Graves, president, both of Graves Well Drilling Co., Inc., for their technical assistance in the field and helpful comments regarding pump design.

GENERAL WELL COMPLETION

Coalbed gas wells may be drilled or cored through one or several gas-producing coalbed horizons. An additional length of borehole is drilled below the lowest coalbed to allow water to drain from producing zones and provide a collecting pool from which water is pumped to the surface.

Boreholes that produce gas from a single horizon are typically cased and cemented from immediately above the coalbed to the surface, blocking excessive drainage from upper water-bearing formations (fig. 1). Casing may also be set through several coalbeds along the full depth of the borehole. Gas is produced through openings which are either cut or pierced into the casing at each coalbed horizon. This manner of completion allows simultaneous production of gas and water from any number of selected horizons (fig. 2).

METHODS OF REMOVING AND MEASURING WATER

Water produced from exposed formations collects in the sump and is removed by means of a sucker-rod pump. Water is pumped up through 4- to 8-inch-diameter cased holes via production tubing, which is normally 1-1/2 to 2-3/8 inches in diameter. The water is then piped through a positive-displacement meter and measured. The mechanical configuration used to drain water from coal gas wells was adapted from oilfield applications and has proved to be effective when water production is less than 100 bpd.

A timing mechanism installed within the electric power circuit to the pump motor automatically controls pumping intervals. In this manner, a pump may be preset to operate only during designated intervals of each 24-hour period.

PROBLEMS OF MONITORING WATER PRODUCTION

Solids in waterlines have caused significant meter inaccuracies and pump malfunctions. Subfreezing temperatures have resulted in loss of water production data and permanent damage to wellhead equipment, pipes, and meters. Improper pumping intervals have allowed water to rise in boreholes to levels above the coalbed, thereby reducing gas production; or have allowed water to fall to the pump horizon, resulting in excessive wear of equipment. Such water-related problems can result in higher maintenance costs in terms of

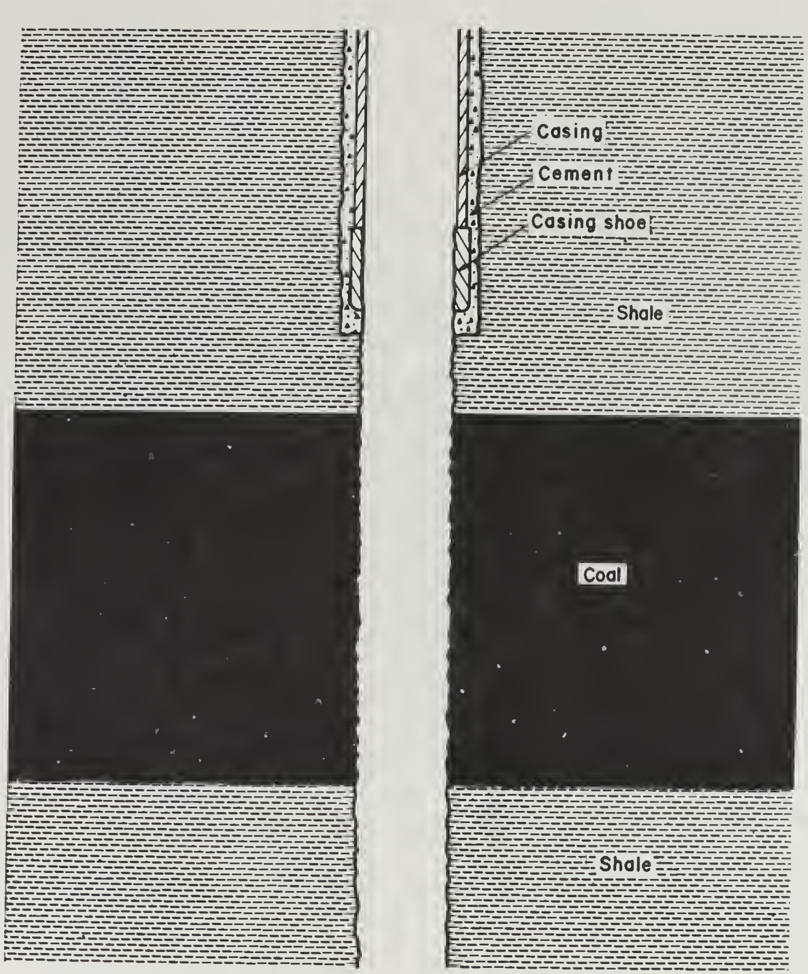
Casing
Cement
Casing shoe
Shale
Coal
Shale

FIGURE 1. - Single-horizon (open hole) completion.

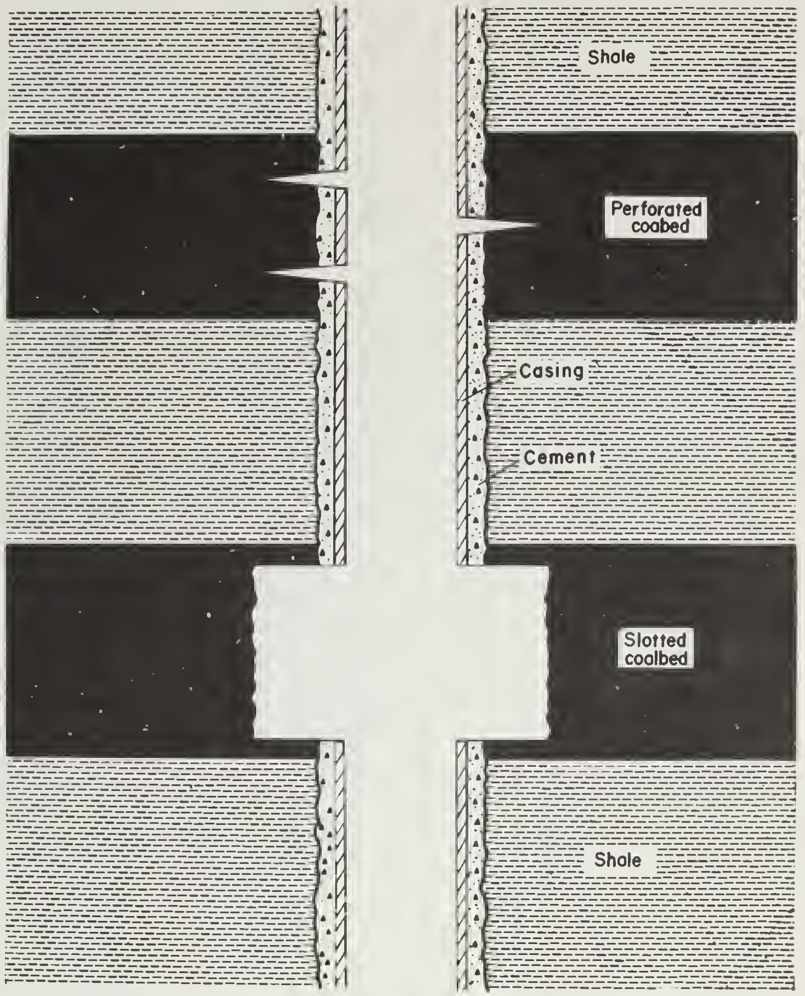
Shale
Perforated coalbed
Casing
Cement
Slotted coalbed
Shale

FIGURE 2. - Multiple-horizon completion.

meter repair, rig time, and number of man-hours prescribed to insure proper well operation.

Solids in Waterlines

Water produced from coal gas wells, especially during early stages of production, normally contains small amounts of coal or other rock fines. Scale resulting from oxidation of casing and tubing is another common ingredient of the water produced. If formation waters contain large percentages of salts, precipitates may enter surface flow lines, thus adding to the total solids content of the water.

Except for very large particles, most solids pass through the water-production-and-monitoring system without difficulty. The small percentage of solids remaining in the system usually accumulates in the housing chamber of the water meter, impairing and eventually stopping the measuring mechanism. At some wells, water meters have performed several months without clogging; at many wells, however, meters have repeatedly clogged within 1 week.

Rock material sometimes becomes lodged in valve openings in the downhole pump mechanism. Usually, this material is coal or shale that has sloughed off formations exposed in the wellbore. Pump stoppage due to lodging of rock material is most likely to occur during the first few days of production and especially after the well has been stimulated.

Freezing

In low temperatures, wellbore water sometimes freezes inside surface lines, restricting flow and causing leakage. Extended subfreezing conditions result in permanent damage to wellhead equipment, pipes, and meters.

Gas-producing coals are normally several hundred feet deep, and the water drained is usually quite warm compared with winter surface temperatures. If pumping is controlled by a timing mechanism, there are periods when no water moves through surface lines. Water remaining in the lines during these periods cools rapidly and may freeze.

Improper Pumping Interval

To achieve maximum gas production from coalbed gas wells, borehole water levels must be kept below the lowest producing coalbed. This is accomplished by either operating pumps continuously, or time-cycling pumps to operate for certain intervals each day.

Continuous pump operation over extended periods (months) may result in excessive wear of moving parts within the motor and the pump jack. Downhole pump components may also be worn quickly, especially when borehole water has been lowered to the pump horizon. Large volumes of gas are drawn into the pump causing dry to semidry conditions, which increase frictional wear.

Several wells were equipped with a timing mechanism to control pumping intervals. Ideally, the mechanism is set to pump continuously when flow to the wellbore is high, and then adjusted as prescribed by changes in flow. At all sites, it was found that pumping intervals were improperly set. In some cases, the interval was too long, causing excessive pump wear and significant volumes of gas in the waterlines. Where the interval was too short, the fluid level was constantly above the coalbed, thus limiting gas and water production.

Gas in Waterlines

Gas passing through positive-displacement water meters is measured as water and may account for significant errors in production records. Such errors were found to be common, occurring to varying degrees at all wells examined. In some cases, gas accounted for up to 75 percent of the metered water volume. Gas may enter waterflow lines in the dissolved state (as minute bubbles of gas coming out of solution) or as free gas drawn directly into lines by the downhole pump.

The solubility of coalbed gas increases directly as pressure increases, and diminishes as temperature increases. As much as 4 cubic feet of gas can be dissolved in 1 barrel of water at a depth of 1,000 feet, based on a hydrostatic pressure of 433 psig and a formation temperature of 100° F.[3] As pressure gradient is reduced around the wellbore, some of the dissolved gas comes out of solution and is produced through gas flow lines; however, a percentage of the dissolved gas remains in the water as it is pumped. As a result, gas comes out of solution while being brought to the surface and is measured through the water meter. Field tests to determine the degree of meter error resulting from such dissolved gases were conducted at several wells. At the start of the tests, borehole water levels were known to be at a static level well above the downhole pump horizon, which prevents large quantities of undissolved gas from entering waterlines. The meters used were checked for accuracy prior to and subsequent to the field tests. Results indicate that dissolved gases may account for 10- to 23-percent errors in measurements of water production.

Improper cycle settings or continuous pump operation may lower water level in a borehole to the downhole pump horizon. If this occurs, gas is drawn directly into waterlines and pumped to the surface, causing large errors in metered water measurements. Tests conducted at wells where fluid levels were known to be at or near the base of the downhole pump show meter readings to be from 20 to 75 percent greater than the actual volume of water removed during testing.

IMPROVED METHODS FOR MONITORING WATER PRODUCTION

The gas contained in waterlines can be removed before the water is metered by incorporating a 30- to 50-gallon-capacity, vented separation tank in the surface waterflow system. Such tanks have been field tested at four producing wells where gas in waterlines had severely decreased meter accuracy. After the tanks were installed, meter accuracies increased to over 98 percent in all cases. The suggested position and installation design suitable for use at coalbed gas wells are shown in figure 3.

---

[3] Uren, L. C. Water in Oil and Gas Reservoirs. Petrol. Production Eng., 3d ed., 1953, pp. 30-32.

Most large pieces of solid debris carried through waterlines settle in the separation tank. The remaining solids, suspended in the flow system, can be taken out of the water with a dirt-and-rust water filter installed downstream from the separation tank (fig. 3). The type of filter used at test well sites was a small plastic unit with a 3/4-inch-diameter connection and a replaceable filter cartridge.

Downhole pump stoppage owing to lodging of large pieces of coal or other rock material can be averted by installation of a screen (12 openings per inch to 4 openings per inch) at the lower end of the water-production tubing (fig. 4). Stainless steel screens identical to those used in the water-well industry have been used successfully at three of the four wells tested. The failure at the fourth test site was due to the extremely small size of openings in the screen used.

Cycled pumping, if properly controlled, is effective in controlling borehole water levels without causing unnecessary wear of equipment. Pump cycles must, therefore, be checked frequently and reset with every significant change in water production if optimum benefits are to be realized. (See appendix A.)

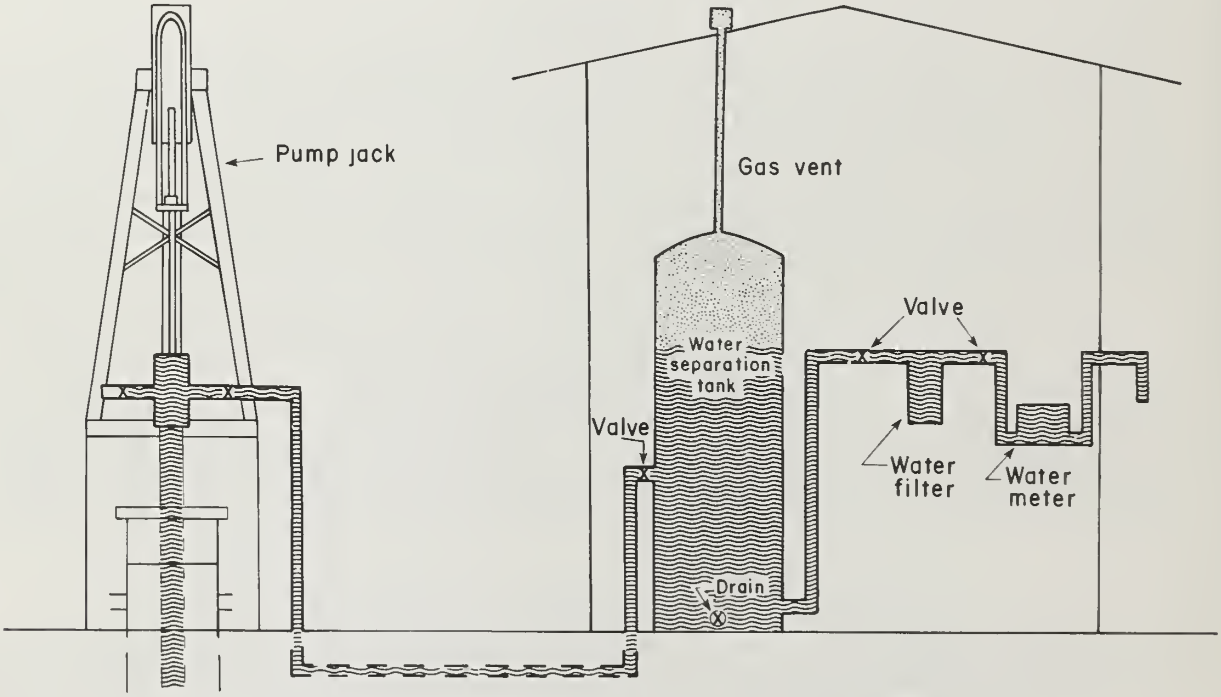

FIGURE 3. - Downhole water-production equipment.

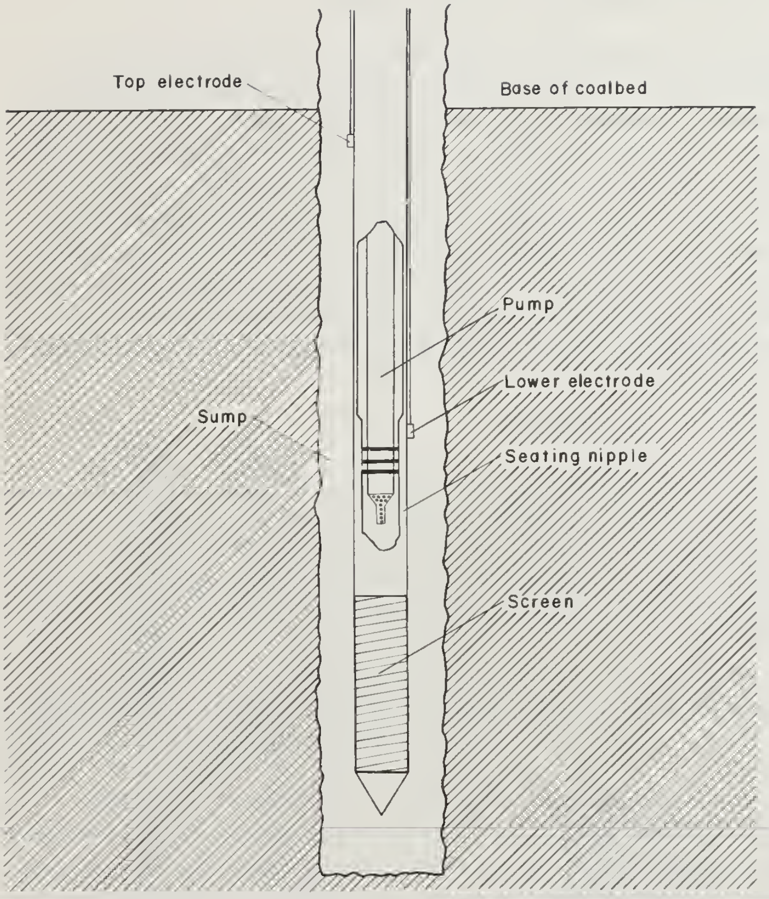

FIGURE 4. - Surface water-monitoring equipment.

A system that automatically controls pumping intervals to maintain water level below the coalbed is being tested at several well sites. Two electrode wires are fastened to water-production tubing as the tubing is lowered in the hole. One electrode is positioned near the bottom of the tubing and the other is placed just below the base of the coalbed. When the borehole water level rises to the top electrode, a circuit is completed that activates the pump jack motor (fig. 4). Water continues to be pumped from the well until the fluid level drops below the lower electrode. This system is expected to eliminate the frequent need to monitor fill-up rates (appendix A) and the possibility of drawing large volumes of gas through waterlines because the downhole pump is always submerged in fluid.

An alternative method to cycled pumping is the use of a variable-speed control on the pump. After the borehole water has been lowered to the pump horizon or near the intake, pump speed is reduced so the fluid level is held constant. Periodic checks for changes in the well's productivity might indicate a need to change the pumping interval. After shut-in periods or maintenance, the pump is adjusted to full capacity to dewater the wellbore rapidly. Conditions favorable for unloading may be created; therefore, adequate precautions should be taken (appendix B).

To prevent freezing, surface waterlines are wrapped with heat tape and then covered with fiberglass insulation. In areas where severe and prolonged low temperatures are common, waterlines are buried below the frostline. In addition, meters, water filter, and separator tank should be contained in small, insulated meter houses. Heat lamps installed in meter houses have proved to be a simple, effective, and inexpensive preventative against freezing. (All houses should be ventilated to some degree, especially those in which heat lamps are employed.)

METHODS OF REMOVING AND MEASURING GAS

Gas from coalbeds is produced through the annular space between water-production tubing and borehole casing. Wells produce under no-back-pressure conditions to optimize coalbed gas desorption and formation-water drainage. Once the gas reaches the surface, it is piped through a positive-displacement meter where it is measured (fig. 5). Three types of meters have been used to measure coalbed gas production, depending on the volumes of gas produced. Diaphragm meters are normally used on nonstimulated wells that produce less than 10,000 cfd. The most common kind of meter used to monitor gas flow from stimulated wells is the rotary meter with a measuring capacity of up to 84,000 cfd. Four-inch turbine meters have been used to monitor flows of over 84,000 cfd.

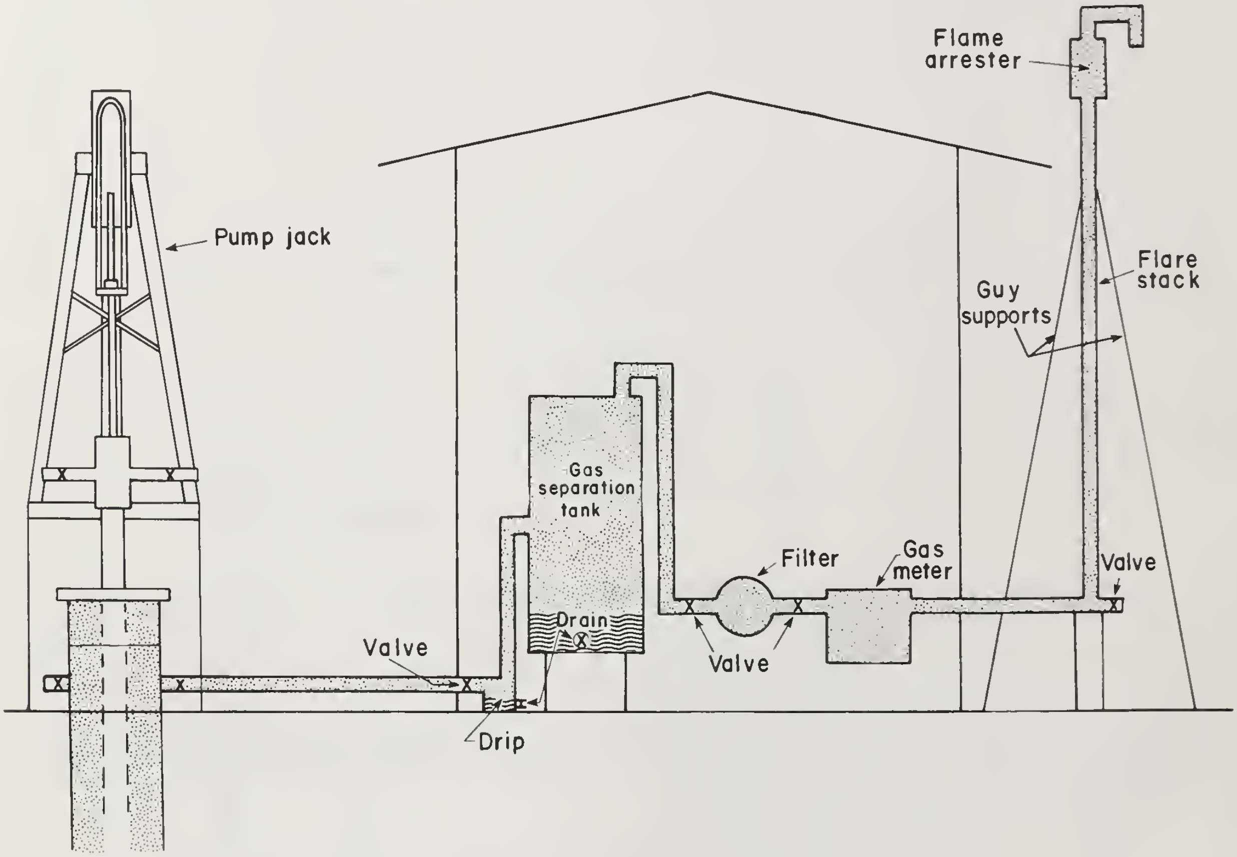
Flame arrester
Pump jack
Flare stack
Guy supports
Gas separation tank
Filter
Gas meter
Valve
Drain
Valve
Valve
Drip

FIGURE 5. - Gas-production and monitoring equipment.

PROBLEMS OF MONITORING GAS PRODUCTION

Gas produced from coalbeds contains water vapor that condenses and collects along various points in the gasline, including the meter. Field studies indicate that water buildup decreases meter accuracy and, in many cases, permanently damages working components. The effects of even small quantities of water in gaslines are most pronounced during periods of subfreezing weather conditions. Sudden pressure release after wells have been shut in results in temporary, large-volume gas flows, which are usually greater than can be accurately measured by the gas meter. Rock fines normally accumulate within the gas meter over a period of time, but solids buildup may accelerate if excessively high gas volumes are allowed to flow through lines.

Water in Gaslines

As warm coalbed gas is subjected to cooler surface temperatures, some of its ability to carry moisture is lost; therefore, condensation occurs. The water condensate accumulates at low points along the pipeline and in metering devices. The problem occurs frequently during winter months, when differences between gas temperature and surface temperature are the greatest.

Reduction of gas flow velocity also causes water to separate from gas; this occurs in areas where pipe diameter increases, thus providing favorable sites for liquid accumulation.

Finally, water is stripped from the gas stream at angled sections along surface flow lines and meter locations where temporary turbulent flow occurs; this results from the collision or impingement of gas against pipe walls or meter chamber, causing some moisture to be extracted from the flow.

Freezing

The problem of water in gaslines is greater during periods of low temperature because conditions for condensation are intensified. The problem becomes acute when temperatures drop to below freezing. Even small amounts of ice in gas flow lines cause back pressure, resulting in apparent low coalbed gas production. Formation of ice in gas meters has damaged many of the instruments since the Bureau first began its coalbed gas-drainage program several years ago.

Sudden Pressure Release

Sudden, uncontrolled release of gas pressure has been a major cause of meter inaccuracies and has resulted in severe meter damage on many occasions.

Gas flow from the well is shut off routinely for pipe or meter maintenance, or to test for pressure buildup. During the shut-in period, gas continues to flow from the coalbed, building pressure in the wellbore. When the pressure is released quickly, a sudden surge of gas, or pressure wave, strikes the meter. Diaphragm meters are especially vulnerable to this surge and are almost always damaged. Rotary and turbine meters, although not damaged as easily, have been rendered inoperable by sudden surges of pressure.

Although damage to the meter may not occur, significant errors have resulted from recording measured gas volumes during a period of gas-pressure release. When gas is moving under pressure, more volume (at standard temperature and pressure) passes through the meter than is actually indicated on the meter index. If the necessary correction multipliers for gas flow under pressure are not applied, incorrect volume measurements may result.

Sudden pressure release has occurred at several wells because water was allowed to build up in the wellbore. Normal pumping operations may be temporarily interrupted for a number of reasons, such as electric power failure, mechanical malfunction, or general maintenance. As the fluid level rises, gas production to the surface decreases in proportion to the increasing hydraulic pressure exerted on the coalbed. Field studies indicate, however, that gas continues to accumulate around the wellbore periphery, building pressures similar to those exerted by the increasing hydraulic head. Once pumping is resumed and the borehole water level is lowered, disequilibrium is created in which gas pressure in the coalbed exceeds hydraulic head. As a result, violent eruptions occur at the surface as large volumes of expanding gas travel up the wellbore to reestablish pressure equilibrium. Sudden gas-pressure release of this nature is referred to as "unloading."

Solids in Gaslines

Particles of rock or other solid material accumulate in most gas meters over extended periods of time under normal flowing conditions. If left unchecked, solids cause malfunctions in all types of meters used. Field experience indicates that rotary meters are the most susceptible to malfunction caused by solids because of the close clearance between components of the inner rotating cartridge. Diaphragm meters usually do not stop functioning with small amounts of solids buildup, but meter accuracy diminishes as a portion of the measuring reservoir is filled with solids. Turbine meters will normally allow very small (less than 1 millimeter in diameter) material to pass through inner mechanisms.

Larger solids are normally carried through gaslines when well pressure is suddenly released, especially when unloading occurs. Such solids almost invariably clog and usually damage inner meter components.

IMPROVED METHODS FOR MONITORING GAS PRODUCTION

Commercially available filters have been designed to remove fine solid particles with very little pressure drop (0.5 psig or less), which makes them suitable for use on coalbed gas wells. Filters have been tested only on gaslines equipped with rotary meters, but they are adaptable to other meter types. Fiberglass is normally the filtering element used. At one test well equipped with such a filter, the gas meter operated for over 1 year without malfunctioning or losing accuracy. Suggested in-line placement of gas filters is indicated in figure 5.

The moisture content of coalbed gas has to be sufficiently low to assure accurate measurement of gas flow. In addition, coalbed gas sold commercially must meet requirements specifically noted in purchase agreements which normally limit the water content to approximately 7 pounds of water per million cubic feet of gas measured at standard temperature and pressure. During cold weather periods, test wells (ranging from 1,053 to 1,076 feet deep) have been found to contain from 31 to 103 pounds of water per million cubic feet of gas produced.[4] Although gasline condensate buildup has been a chronic problem at many Bureau vertical test wells, experimentation with water-gas separation devices has been limited because most of the gas produced is not sold.

The basic means used to remove moisture from coalbed gaslines are cooling, absorption, and impingement.[5] Devices used to remove liquid impurities are drips and separators.

The basic function of a drip is to remove liquid from the gas stream or liquid that has accumulated within the pipeline. A drip catches liquid in a gas stream by reducing the velocity of the gas stream, which causes the liquid to drop out. Liquid that has accumulated at low points within the pipeline is removed by use of a drip equipped with a drain which operates automatically or manually.

The primary function of a separator is to remove entrained fluids from the gas stream. Baffles, deflectors, tubes, rare elements, and gravity separation chambers are some of the mechanisms used within a separator device to remove moisture. There are several commercially designed separators that meet requirements for a single well or for several wells in the same pipeline system.

Meter inaccuracy and possible meter damage caused by sudden pressure release can be avoided by allowing gas pressure to bleed off gradually while maintaining flow pressures within the given meter range. To do this, a pressure gage is installed in the gas flow line near the meter. Flow pressures are periodically recorded and are then calculated into a standard equation solving for actual flow.

Sudden pressure release that results in unloading can be avoided if a few precautionary steps are taken, such as gasline shut-in, resumption of pumping, and subsequent slow bleedoff. Detailed description of actions to be taken if unloading is anticipated is included in appendix B. These methods have been field tested on several occasions and have proved to be very effective.

Ice formation in gaslines near the wellhead is prevented by properly insulating and heating meters and other points favorable to water accumulation (fig. 5). The number of routine field inspections of wells should be increased during especially cold periods to assure minimum condensate buildup. At the test wells examined, gaslines that had been wrapped with electric heat tape and covered with fiberglass insulation were rarely found to contain sufficient amounts of ice to cause significant back pressure. In addition, well sites equipped with insulated meter houses containing heat lamps yielded accurate, uninterrupted production information, even during prolonged subfreezing weather conditions.

---

[4] Based on volumes of condensate accumulated in a flare stack similar to that shown in figure 5.

[5] Rumbaugh, J. R. Gas Conditioning Before Measurement. Pres. at 36th Appalachian Gas Measurement Seminar, Pittsburgh, Pa., Aug. 10-12, 1976; available for consultation at Department of Energy Mining Operations, Pittsburgh, Pa.

CONCLUSION

Results of this study indicate that the quality of data gathered from degasification wells can be significantly improved if potential problems are anticipated and prevented during the early stages of well production. Problems related to the measurements of both gas and water can generally be avoided by equipping wells with commercially available items and by applying a basic knowledge of the coalbed reservoir throughout the productive life of the well.

APPENDIX A.--PROPER PUMP-CYCLING PROCEDURES

1. Pump the well continuously until a marked decrease in water production (compared with specified pump capacity) is observed. At new wells, it may take several weeks for this decrease to occur. At wells that have been pumped regularly, the decrease in water production rate may be observed in a few hours. At wells where pumping has been continuous, no decrease will be observed.

2. Measure and record the continuous, low-volume flow, using a device *other than the water meter*. A 5- or 10-gallon container and a stopwatch are sufficient to record such flow rates.

3. Turn off the pump jack and allow fluid to rise above the position of the downhole pumping mechanism. This usually takes less than a few hours. (The rate of waterflow into the well is known from item 2. The approximate volume of water and the time necessary to raise the level of water above the downhole pump is calculated from the known dimensions of the borehole and the production tubing within.) Unnecessarily long periods (days) of nonpumping should be avoided (appendix B).

4. Resume pumping and monitor flow as specified in item 2. Waterflow will increase rapidly to the current maximum pump capacity and remain at this high flow rate until the water level in the borehole is lowered to the downhole pump horizon. Once this occurs, water flow rate falls quickly (within 5 to 10 minutes) and is usually accompanied by an increase in gas flow through the waterlines.

5. Allow the pump to operate continuously until water flow rate is similar to that measured in item 2.

6. Given the rate of waterflow into the borehole (measured in items 2 and 5) and the dimensions of the wellbore and production tubing, the time (pump "off" cycle) required to fill the sump below the coalbed is calculated. Given the current real pump capacity (measured in item 4), the time (pump "on" cycle) required to remove water from the sump can also be calculated. Pump cycles are set accordingly and rechecked periodically to assure proper coalbed water drainage.

APPENDIX B.--METHODS TO PREVENT AND CONTROL WELL UNLOADING

1. In most cases, gaslines should be closed as soon as possible after pumping has been interrupted. The objective is to build gas pressure in upper portions of the borehole above the water column. However, if well maintenance requires gaslines to remain open, the borehole should be filled with water before work begins.

2. Once pumping is resumed, water production should be monitored closely at the wellhead (not through the water meter) for one of the following indications that the borehole water level has been lowered to or near the downhole pump horizon:

a. Sharp reduction of water production rate (compared with pump capacity).

b. Sharp increase in the quantity of gas coming through waterlines.[1]

3. Gaslines may be opened as soon as borehole water level is determined to be at or near downhole pump horizon. Gas valves should be opened very slowly to allow *gradual* bleedoff of gas pressure.

4. If well has shown a tendency to unload, allow pump to operate continuously until initial high formation pressures are reduced. Several months of continuous pumping may be required.

---

[1] Because the borehole is under pressure, large volumes of water (several times pump capacity) sometimes accompany gas through waterlines. If this should occur, pumping should be discontinued until pressure in the wellbore is reduced.

INT.-BU.OF MINES,PGH.,PA. 23250

☆U.S. GOVERNMENT PRINTING OFFICE: 1978-703-103/67

622.06
Un32mo

RI 8310

Bureau of Mines Report of Investigations/1978

Jet Fan Effectiveness as Measured With SF_6 Tracer Gas

DEPOSITORY
NOV [illegible] 1978
UNIV. OF ILL. LIBRARY
[illegible]

UNITED STATES DEPARTMENT OF THE INTERIOR

Report of Investigations 8310

Jet Fan Effectiveness as Measured With SF_6 Tracer Gas

By Joseph E. Matta, Edward D. Thimons, and Fred N. Kissell

March 3 1849

UNITED STATES DEPARTMENT OF THE INTERIOR
Cecil D. Andrus, Secretary

BUREAU OF MINES

This publication has been cataloged as follows:

Matta, Joseph E
Jet fan effectiveness as measured with SF_6 tracer gas / by J. E. Matta, Edward D. Thimons, and Fred N. Kissell. [Washington] : U.S. Dept. of the Interior, Bureau of Mines, 1978.

14 p. : ill., diagrs. ; 27 cm. (Report of investigations - Bureau of Mines ; 8310)

Bibliography: p. 14.

1. Mine ventilation. 2. Fans (Machinery). I. Thimons, Edward D., joint author. II. Kissell, Fred N., joint author. III. United States. Bureau of Mines. IV. Title. V. Series: United States. Bureau of Mines. Report of investigations - Bureau of Mines ; 8310.
TN23.U7 no. 8310 622.06173
U.S. Dept. of the Int. Library

CONTENTS

Page

Abstract.. 1
Introduction.. 1
Test procedure.. 2
Dead-heading tests using SF_6.................................. 3
    Test site... 3
    Baseline ventilation test (no fan)...................... 3
    Test using a 29-inch fan at L1 location................. 4
    Test using a 25-inch fan at L1 location................. 6
    Test using Venturi air mover at L1 location............. 7
    Test using a 29-inch fan at L2 location................. 7
Jet fan tests using SF_6 at a location with an inadequate fresh air source 9
Summary... 13
References.. 14

ILLUSTRATIONS

1. Diagram of the expansion of a "free" jet and "half" jet............ 2
2. Dead-heading test site... 4
3. SF_6 decay curve for baseline ventilation and 29-inch fan test....... 5
4. Measuring jet expansion angle using a dry-chemical fire extinguisher... 6
5. SF_6 decay curve for 25-inch fan test............................... 8
6. SF_6 decay curve for air mover test................................. 8
7. SF_6 decay curve for 29-inch fan blowing across airway.............. 9
8. Test area with an inadequate source of fresh air.................. 10
9. Test area ventilated by jet fan-anemometer measurements............ 10
10. Test area ventilated by jet fan-baseline and SF_6 measurements....... 11
11. SF_6 decay curve for large section using no jet fan................. 11
12. SF_6 decay curve for section using 30-inch fan...................... 12

JET FAN EFFECTIVENESS AS MEASURED WITH SF_6 TRACER GAS

by

Joseph E. Matta,[1] Edward D. Thimons,[2] and Fred N. Kissell[3]

ABSTRACT

The Bureau of Mines conducted tests using a tracer-gas technique to measure the effectiveness of the jet fan, which is often employed in mines to ventilate dead headings.

Results of these tests show that jet fans can (1) ventilate dead headings beyond the maximum penetration distance indicated by smoke-tube detection of air movement, and (2) redistribute available fresh air through larger working areas. However, if the fresh air base is insufficient, the fan will merely recirculate the contaminated air and disperse it over a larger volume.

INTRODUCTION

Underground mines generally circulate large quantities of fresh air. Although the overall ventilation volume is usually sufficient, distribution of the available air is often inadequate. In working areas where mining is in progress, large quantities of fresh air are needed to dilute and remove contaminating gases; inactive mine areas require lesser amounts of fresh air. Auxiliary fans are often used to distribute air so that fresh air can be supplied to the working areas without increasing the total amount of fresh air entering the mine.

One auxiliary ventilation technique is to place a fan in an airway or work area, without the use of a bulkhead or tubing. This is commonly referred to as jet or impulse ventilation. The principal action of the fan is the entrainment of air by the fan jet (5).[4] Then, by suitable placement of the fan, air may be moved to the desired locations.

---

[1] Research physicist.

[2] Supervisory physicist.

[3] Physical research scientist.

All authors are with Pittsburgh Mining and Safety Research Center, Bureau of Mines, Pittsburgh, Pa.

[4] Underlined numbers in parentheses refer to items in the list of references at the end of this report.

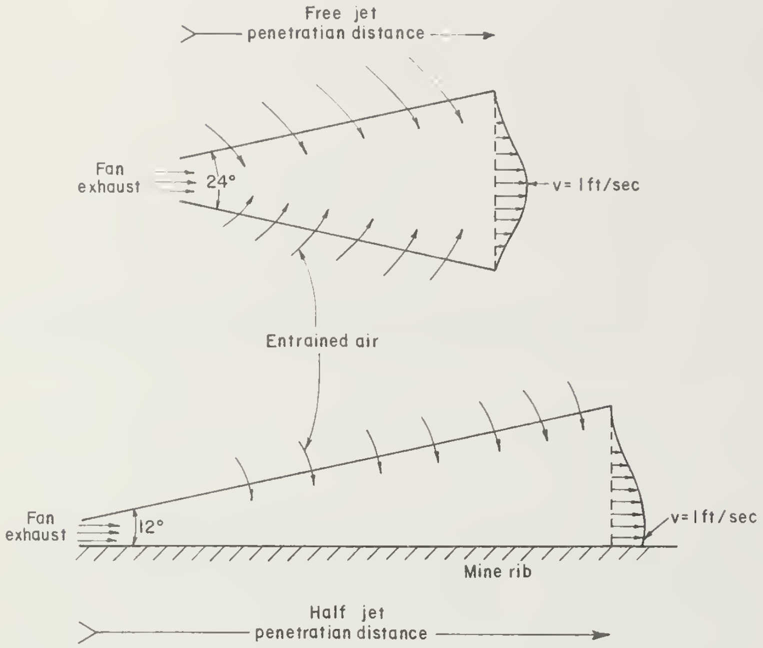

FIGURE 1. - Diagram of the expansion of a "free" jet and "half" jet.

Jet fans have been tested in dead headings that had no through ventilation (3-4). Fan effectiveness was determined from air velocity measurements using various heading and fan configurations. For example, Krause (3) has shown that the penetration distance of a free jet is doubled by placing the fan outlet along the rib (fig. 1). The penetration was measured as the distance from the fan to where the jet velocity dropped to 1 ft/sec. Since the air is entrained only along one side of the jet a "half jet" is formed. Also, results of computer studies and mine surveys indicate that jet ventilation systems can considerably improve the distribution of air currents in mines with large cross-sectional areas (2). The ventilation current propagated by a jet fan along a longwall face has also been investigated (6).

Although the tests indicate that jet fans can move large quantities of entrained air, some recirculation occurs; therefore, it is difficult to determine what fraction of the air being moved is fresh air. Accordingly, the Bureau of Mines has used sulfur hexafluoride (SF_6) tracer-gas dilution measurements to determine the effectiveness of a jet fan in bringing in fresh air.

Sulfur hexafluoride has been used in metal (7) mines to measure the amount of return air being recirculated into the intake air owing to leakage through stoped areas. Drivas (1) has used SF_6 as a tracer gas to study ventilation systems in buildings. From the decay curve of the tracer gas, the effective ventilation purging of various rooms was determined. In the present study, the Drivas method was used in a dead heading to evaluate the effectiveness of various fans and their positioning. The ability of a jet fan to redistribute fresh air was also studied.

TEST PROCEDURE

To study the effectiveness of jet fans in purging a fixed volume, V, SF_6 was released uniformly throughout the volume. The SF_6 concentration, C, at any time, t, can be shown to decay exponentially as

$$C = C_0 \; e^{-(Q/V)\;t}, \qquad (1)$$

where Q is the effective[5] amount of fresh air purging the volume, and C_o is the initial SF_6 concentration. A semilog plot of the concentration versus time yields a straight line with a slope equal to -Q/V. The slope can be written as

$$-\frac{Q}{V} = \frac{\ln {}^{C_1}/C_2}{t_1 - t_2}, \tag{2}$$

where C_1 and C_2 are any two concentrations along the straight line at time t_1 and t_2, respectively. Therefore, knowing the volume, V, of the heading, which can be measured, one can obtain the fresh air quantity, Q.

The SF_6 was released directly from a SF_6 lecture bottle through a 0.006-inch hole. The smallness of the hole resulted in a fine spray of SF_6, which was further mixed by moving the lecture bottle throughout the volume during release. The amount of tracer gas emitted was calculated from the weight loss of the lecture bottle. The gas samples were taken in the mine at fixed time intervals, using 10-ml glass syringe bottles, tightly closed with rubber stoppers. The samples were analyzed later with a portable electron-capture chromatograph (7).

DEAD-HEADING MEASUREMENTS USING SF_6

Test Site

In order to determine the effectiveness of jet fans, four dead-heading tests using SF_6 as a tracer gas were carried out in the W-104 heading of the U-32 section of the White Pine Copper mine in Michigan (fig. 2).

The jet fan was usually positioned at L1 along the right rib, near the entrance to the heading. In one test, the fan was located across the crosscut at L2. The fans were blowing into the heading, and no tubing was used. The two sampling positions were 60 feet and 150 feet from the crosscut (location L1). The height of the 165-foot-long, 28-foot-wide heading ranged from 17 feet at the crosscut to almost 9 feet at the face. The test-section volume, as determined from various tape measurements along the heading, was approximately 50,500 ft^3. The airflow in the crosscut was 57,000 cfm.

Baseline Ventilation Test (No Fan)

To measure baseline ventilation in the heading, a 90-min test was made with no fan. To insure uniform mixing, the SF_6 lecture bottle was moved back and forth along the entire heading while the gas (0.37 ft^3) was being

---

[5] Drivas used a mixing factor, k, for rooms not well mixed to obtain a $C = C_o e^{-k(Q/V)t}$ decay curve. Since k is a constant, the Q in equation 1 incorporates this factor to obtain an effective purging air quantity.

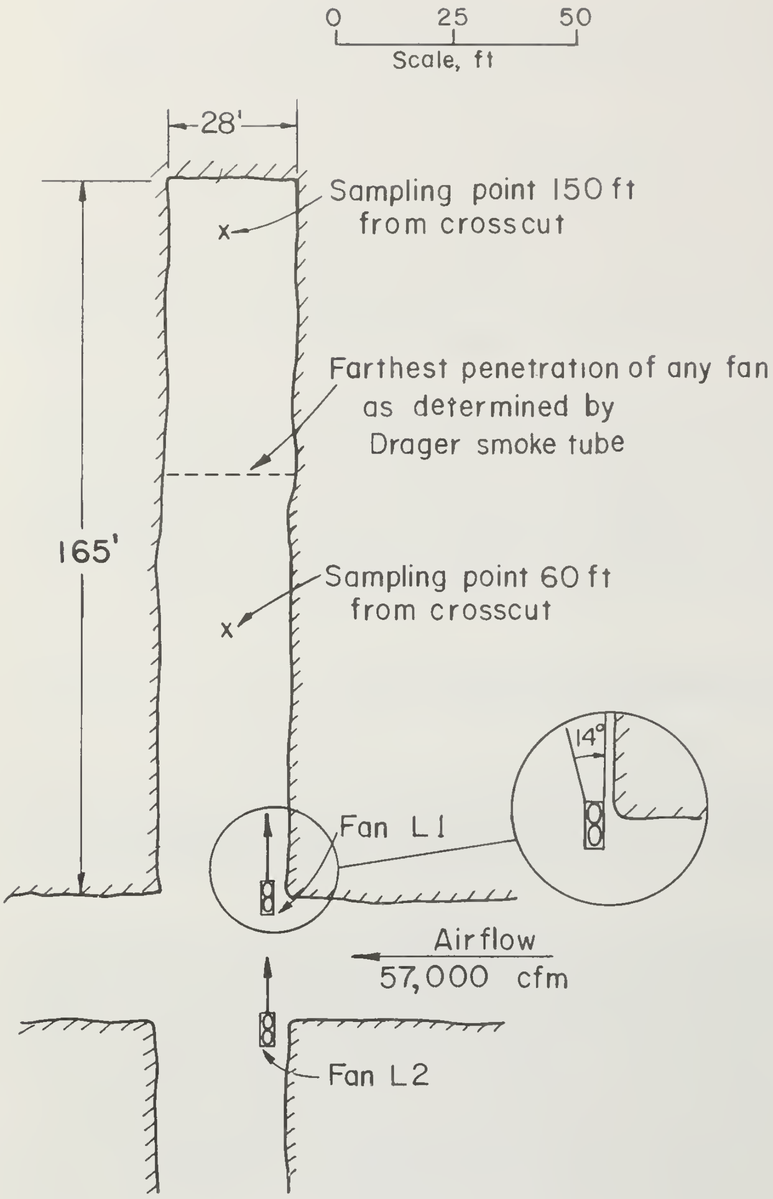
0
25
50
Scale, ft
28'
Sampling point 150 ft from crosscut
Farthest penetration of any fan as determined by Drager smoke tube
165'
Sampling point 60 ft from crosscut
14°
Fan L1
Airflow
57,000 cfm
Fan L2

FIGURE 2. - Dead-heading test site.

released.[6] The SF_6 concentrations were then measured periodically at the two sampling locations. Figure 3 shows that without an auxiliary fan, the SF_6 concentration at the 150-foot sampling location is nearly constant for the 90-min period. This indicates that no fresh air is reaching the face; however, the other sampling location shows that approximately 1,350 cfm of the air moving in the crosscut penetrates 60 feet into the heading. As shown by the dilution equation, the air quantity, Q, is determined by multiplying the slope, -Q/V, of the concentration versus time relationship by the volume of the heading. Since 0.37 ft^3 of SF_6 was released in a volume of 50,500 ft^3, the initial SF_6 concentration then should be approximately 7.3 ppm. This is consistent with the initial measured concentrations as indicated in figure 3.

Test Using a 29-Inch Fan at L1 Location

After the 90-min baseline ventilation test, a 29-inch fan blowing about 20,000 ft^3/min was turned on. No ejector nozzle or tubing was used. The fan was located at the L1 position and did not interfere with the airflow through the crosscut, which remained about 57,000 cfm. Since the fan exhausted near the right rib, a half jet was formed with an expansion

---

[6] It is important to release the SF_6 uniformly throughout the heading being tested. If SF_6 is released in one portion of the heading, it will spread by convective currents throughout the entire heading. This spreading of SF_6 will result in a concentration drop if the sampling location is near the release location. This concentration drop could erroneously be interpreted as fresh air being brought into the heading.

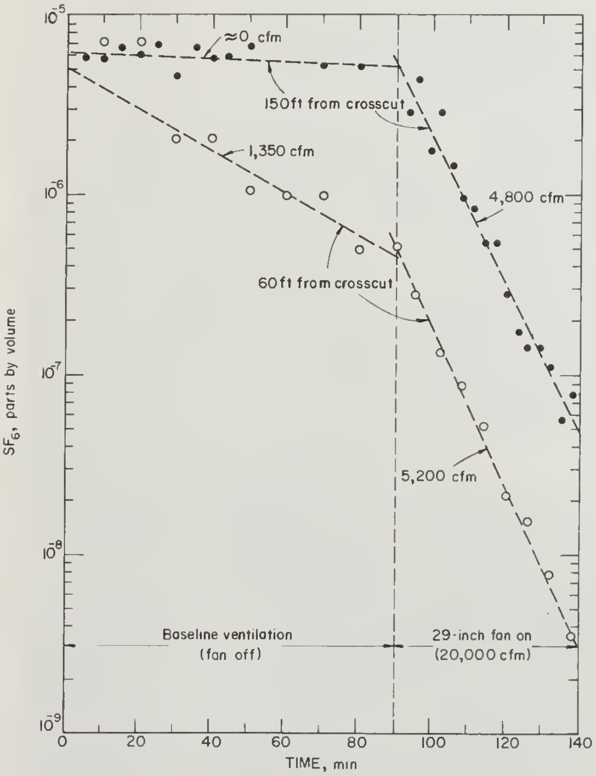

FIGURE 3. - SF_6 decay curve for baseline ventilation and 29-inch fan test.

angle of 14°±1° (fig. 2). This angle was determined by releasing the contents of a dry-chemical fire extinguisher into the intake of the fan and then marking the location over which the smoke passed (fig. 4). The dry-chemical extinguisher was also used to verify that there was no recirculation back into the intake of the fan. This was done by releasing some smoke slightly downstream of the fan in the crosscut. The fresh air purging both the 60-foot and 150-foot sampling positions as determined from the 90- to 140-min "fan-on" portion of figure 3 was approximately 5,000 cfm.

A Drager[7] smoke tube was also used to obtain an estimate of the jet penetration distance. Smoke was released at various distances from the face until some noticeable circulation from the fan was observed. This distance to the fan is then an approximate estimate of the fan penetration. For the 29-inch fan test, the penetration distance appeared to be 60 to 65 feet into the heading.

---

[7] Reference to specific trade names does not imply endorsement by the Bureau of Mines.

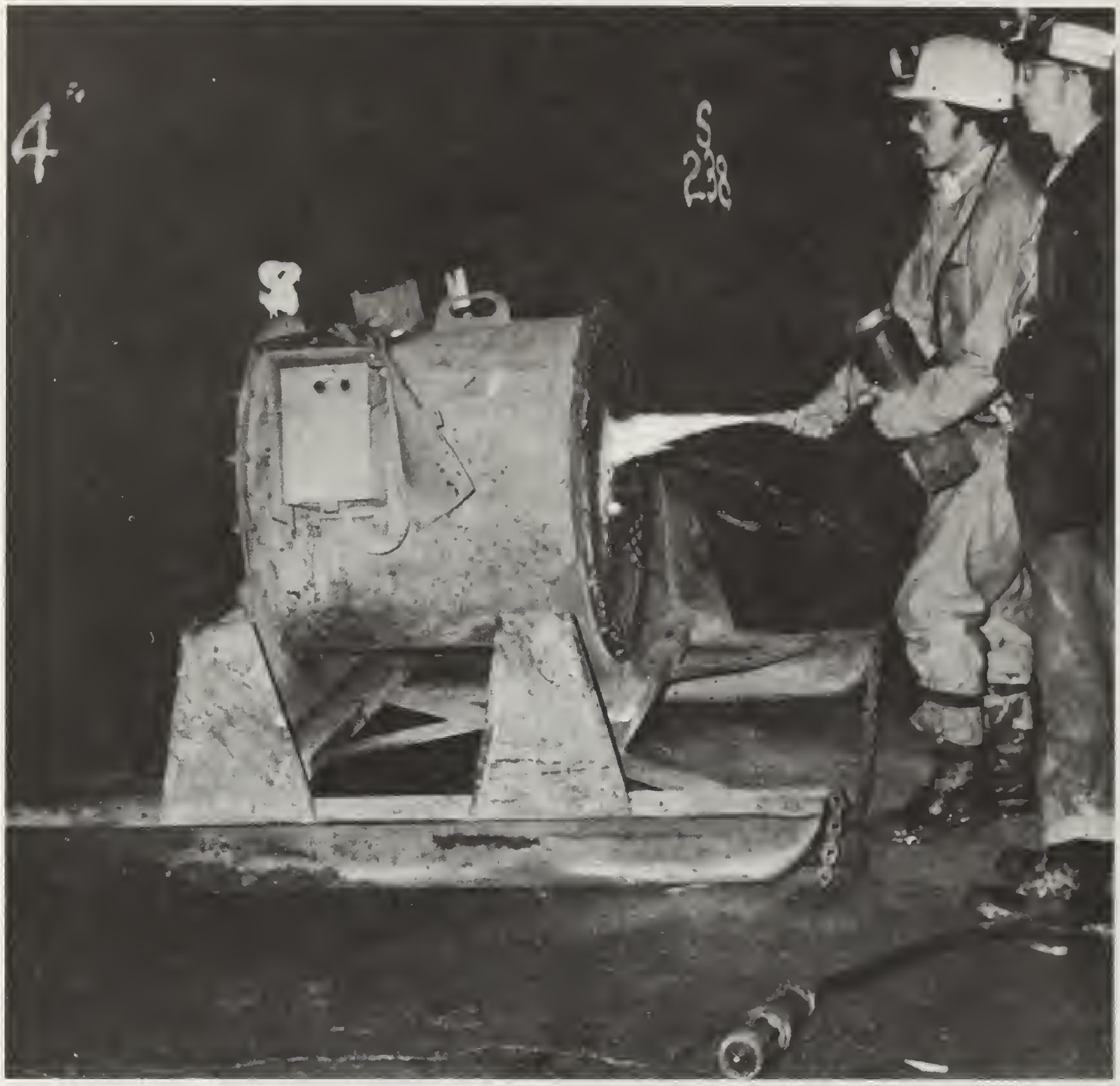

FIGURE 4. - Measuring jet expansion angle using a dry-chemical fire extinguisher.

Test Using a 25-Inch Fan at L1 Location

A similar test was performed at the same L1 location using a 25-inch fan blowing 12,000 cfm. A 3-foot section of rigid duct was attached to the exhaust end of the fan. This section, which is slightly tapered to a 24-in diam, is ordinarily used as a union between the 24-inch tubing and the 25-inch fan. Smoke-tube penetration measurements indicated that the 25-inch fan at this location penetrated a slightly greater distance into the heading (80 to 90 feet). The expansion angle of the half jet formed (13°±1°) was similar to the jet angle formed by the prior 29-inch fan test. The fan was turned on after the SF_6 was released. The first concentration measurements were made 1 min after turning on the fan. The effect of purging the heading appears more pronounced with this fan. About 6,000 cfm of fresh air penetrates to the 150-foot sampling location, but more than 10,000 cfm of fresh air reaches the 60-foot sampling location (fig. 5). This is a significant improvement over the 29-inch fan.

Test Using Venturi Air Mover at L1 Location

A test was then made at the same L1 location with a Venturi-type air mover. Operating on compressed air at 100 psi, it exhausted approximately 10,000 ft^3/min of air, which contained about 9,000 cfm of entrained air. The air mover was positioned 3 feet off the ground along the right rib just inside the crosscut (location L1). The air jet appeared to penetrate 60 to 65 feet into the heading. Results of the test (fig. 6) indicate that 3,500 and 5,000 cfm of air penetrates 150 and 60 feet, respectively, into the heading. The airflow purging the heading in this test was slightly less than that generated by the 29-inch fan at the same location. Although both jet fans purged the heading more effectively, the air mover could be advantageous in certain situations owing to its portability.

Test Using a 29-Inch Fan at L2 Location

The 29-inch fan was also tested at L2 (fig. 2) behind the crosscut along the right rib. This location was selected because Krause had suggested (3) that if the jet expands in the fresh air, better ventilation could be expected. The theory is that if a jet expands in fresh air, it does not entrain as much contaminated air; thus recirculation of contaminated air is reduced. However, the jet of the fan and the airflow through the crosscut interfered. The high airflow in the crosscut forced the jet to expand and diffuse rapidly toward the left rib; a few feet into the heading, no well-defined jet could be observed. The penetration was less than 20 feet into the heading, and airflow in the crosscut was reduced 30%. Compared with the two prior fan tests, the airflow (fig. 7) purging the heading was considerably reduced.

These tests demonstrate that a tracer gas can be used to assess the effectiveness of a jet ventilation system in a dead heading. In the tests conducted, the purging action improves as the penetration distance of the jet fan increases. The tracer technique also shows that air can effectively purge beyond the penetration distance measured by a smoke tube, and that the fan position can significantly alter the purging effect.

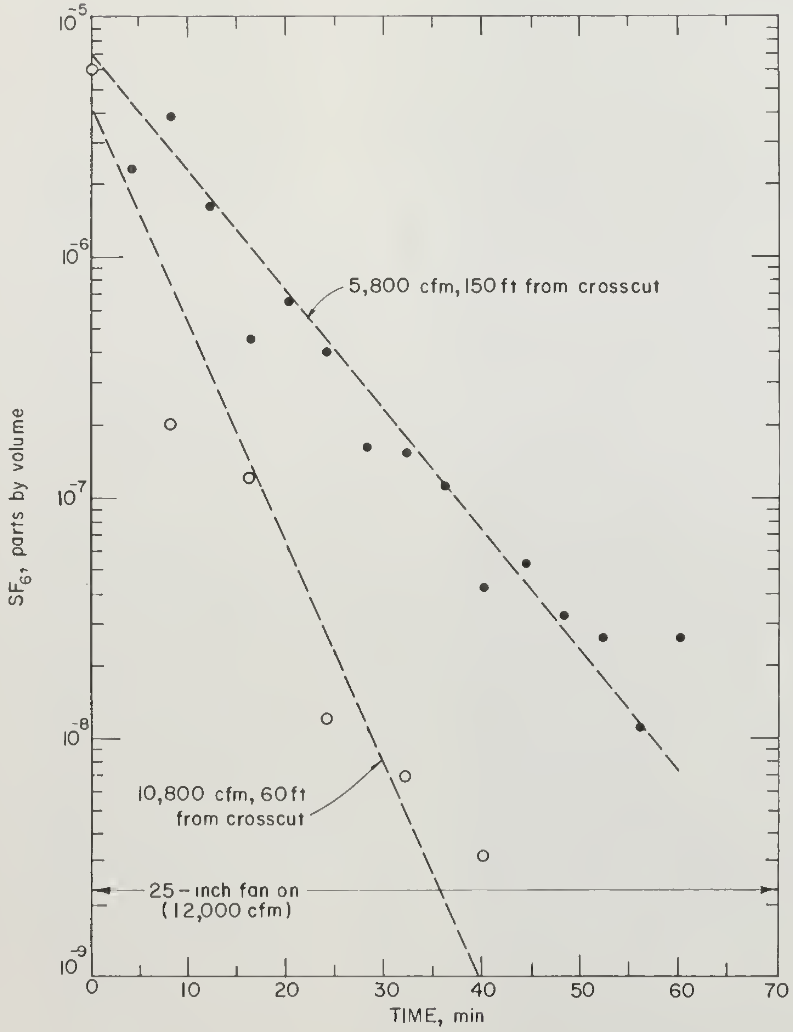

FIGURE 5. - SF$_6$ decay curve for 25-inch fan test.

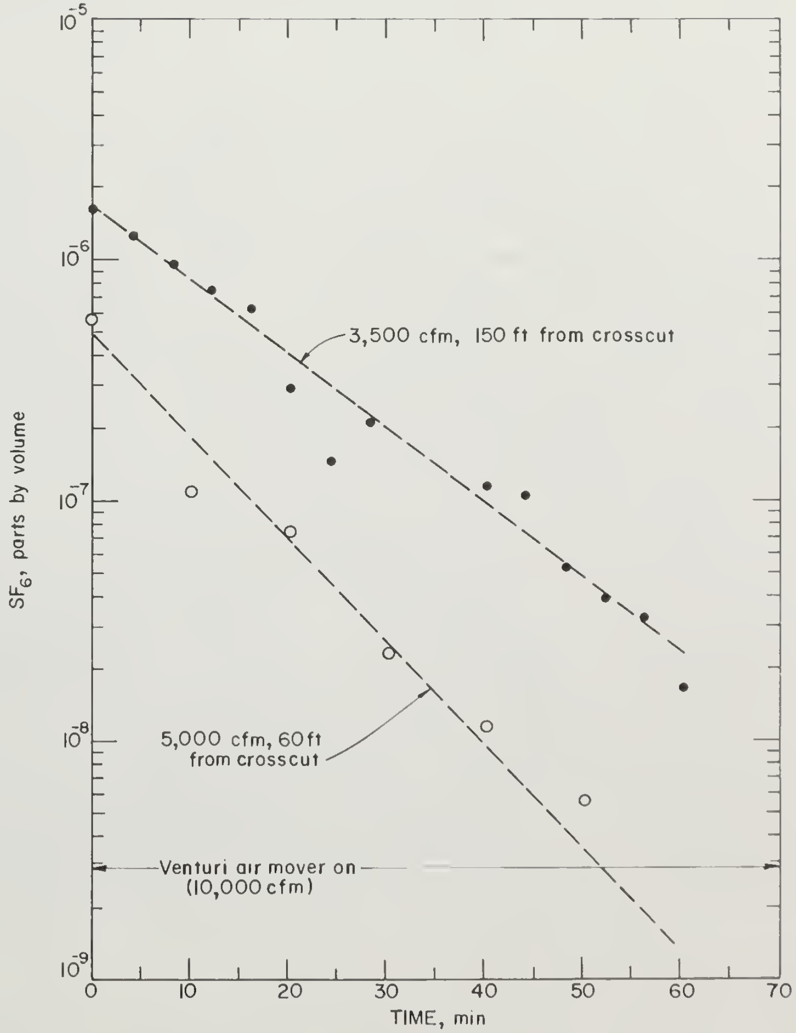

FIGURE 6. - SF$_6$ decay curve for air mover test.

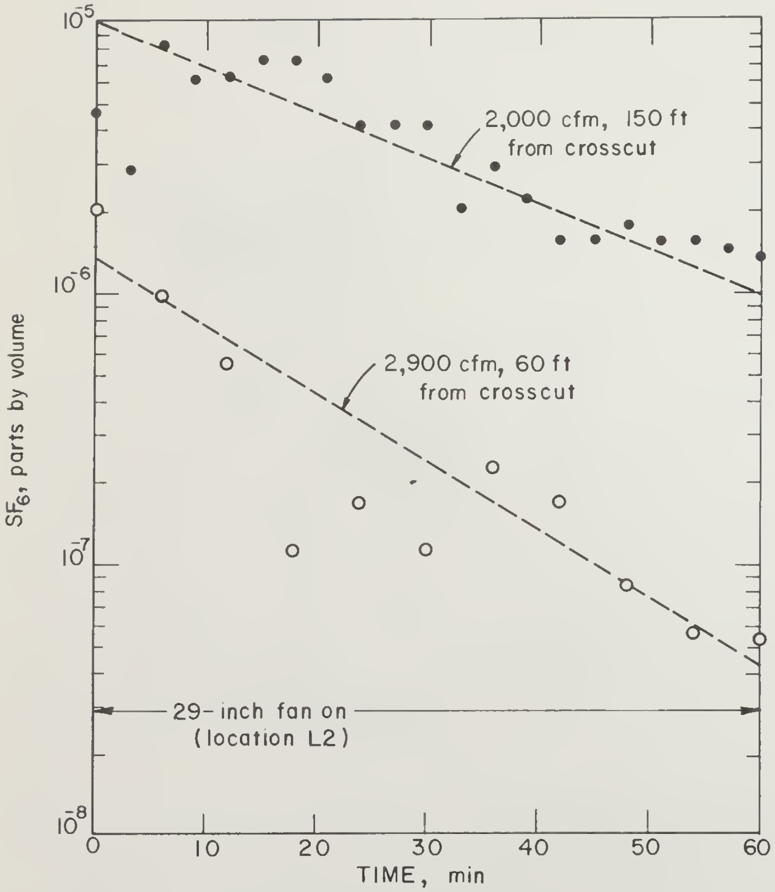

FIGURE 7. - SF_6 decay curve for 29-inch fan blowing across airway.

JET FAN TESTS USING SF_6 AT A LOCATION WITH AN INADEQUATE FRESH AIR SOURCE

In the White Pine tests, the jet fan always had an adequate source of fresh air. The amount of air flowing in the crosscut was always greater than that moving through the fan, and smoke-release tests with the dry-powder fire extinguisher indicated that contaminated air from the heading was moving away from the fan and not back toward its intake.

Where fresh air is not plentiful, the jet fan is likely to be much less effective. To see how this lack of fresh air would affect the SF_6 tracer-gas results, another series of tests was conducted in a single-level inactive limestone mine in western Pennsylvania. The general ventilation system of the mine was simple; about 140,000 cfm of air enters the mine through vertical intakes from the surface and exits through an exhaust fan in a drift entry. Due to the large cross sections (averaging 600 to 700 ft^2), the number of intake and exhaust airways, and the condition of the stoppings, the level of airflow reaching the test site (fig. 8) was quite low. It was impossible to estimate the amount of fresh air passing through the area because smoke clouds dissipated before traveling far enough to permit velocity estimates. No air motion was detected across the gob pile, which extended two-thirds of the way to the roof located in the last crosscut between the 6 and 7 butt.

To ventilate the region inby the last crosscut between 6 and 7 butt (area outlined by heavy dashes in fig. 8), a 30-in-diam, 14,000-cfm jet fan was placed as shown in figure 9. The fan location was selected so that the fan jet would entrain additional air from the test area. With the fan turned on, a series of anemometer traverses showed that 60,000 cfm of air was being drawn over the gob pile and split around the center pillar adjacent to the fan. The fan entrainment ratio was about 4:1. The superficial indication was that the test area was well ventilated; however, results of subsequent SF_6 dilution tests indicated otherwise.

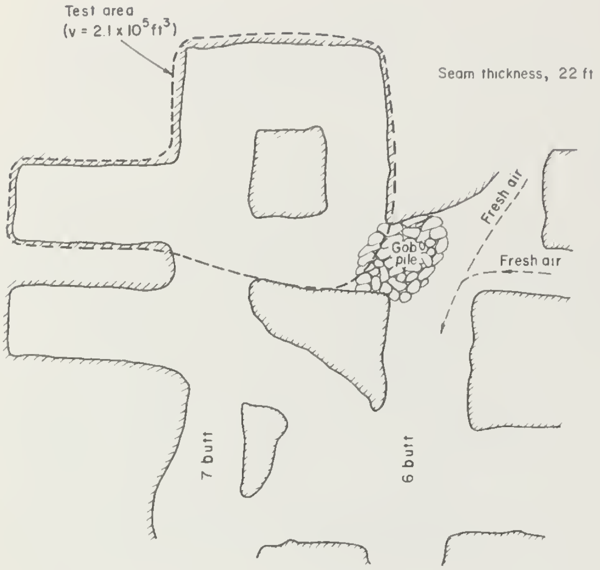
Test area
(v = 2.1 x 10⁵ ft³)
Seam thickness, 22 ft
Fresh air
Gob pile
Fresh air
7 butt
6 butt

FIGURE 8. - Test area with an inadequate source of fresh air.

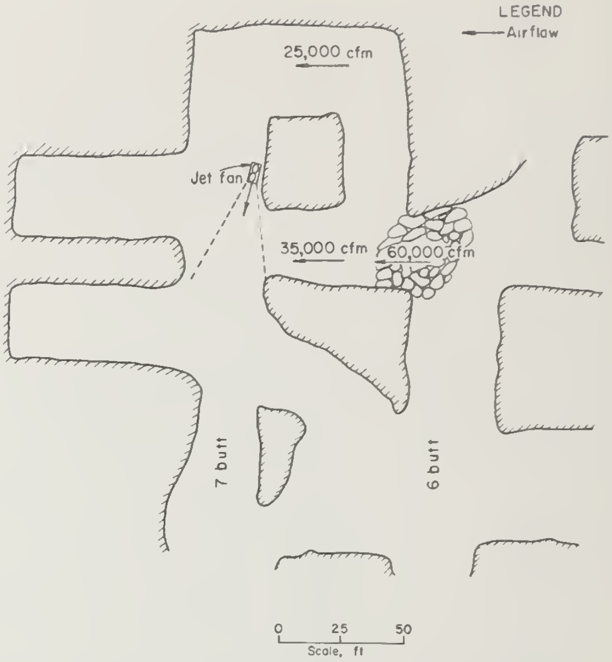
LEGEND
Airflow
25,000 cfm
Jet fan
35,000 cfm
60,000 cfm
7 butt
6 butt
0
25
50
Scale, ft

FIGURE 9. - Test area ventilated by jet fan-anemometer measurements.

A fan-off baseline test was first attempted. The SF_6 was released in the small area shown in figure 10, and sampling was conducted at the face location S1. The resulting concentration-time decay curve is shown in figure 11. It is not smooth, but the general trend of the decay curve indicates a value of 32,000 cfm of fresh air. However, this was an impossible value because the fan was off; no air movement in the test area could be detected. It was evident that this was due to our failure to spread the SF_6 uniformly throughout the test area. As the small SF_6 cloud naturally diffused and spread throughout the test area, the concentration decline was being interpreted as a fresh-air influx. Therefore, a new baseline test was designed to insure that the SF_6 was evenly spread throughout the test area.

In the new baseline test conducted several weeks later, 0.44 ft^3 of SF_6 was released from the lecture bottle while the bottle was carried in a circle around the central pillar. The fan was then employed at location F1 for 10 min to insure more even mixing, and then the fan was off for the next 90 min to determine the baseline. Both the face area S1 and the reputed source of fresh air at intake S2 were sampled. The results are shown in figure 12.

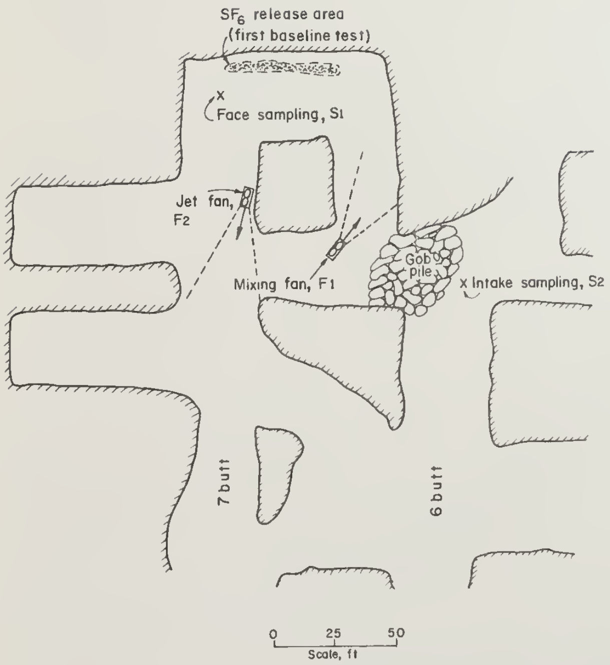
SF_6 release area
(first baseline test)
Face sampling, S1
Jet fan,
F2
Mixing fan, F1
Gob pile
Intake sampling, S2
7 butt
6 butt
0
25
50
Scale, ft

FIGURE 10. - Test area ventilated by jet fan-baseline and SF_6 measurements.

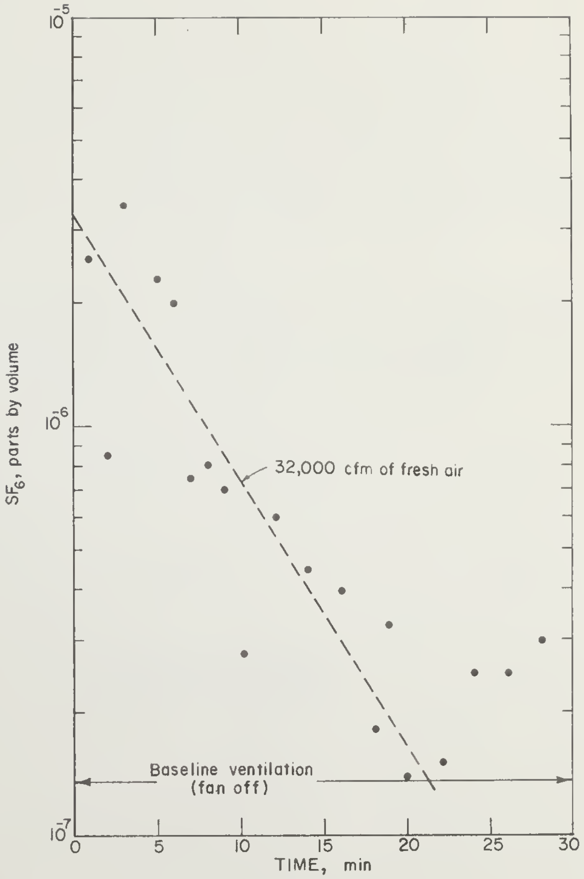

FIGURE 11. - SF_6 decay curve for large section using no jet fan.

Figure 12 indicates that the mixing fan caused an initial decline in SF_6 concentration. SF_6 also appeared at S2, indicating that the mixing fan was also spreading SF_6 outside of the test area. When the fan was turned off, the concentration at both locations stabilized, indicating that neither was receiving any fresh air.

At the end of the 90-min baseline period, the fan was moved to F2 and turned on. Both of the sampling locations showed a decline in SF_6 concentration, and a decline curve drawn through the first 30 min of data (elapsed time of 100 to 130 min in fig. 12) indicates that 6,400 cfm of fresh air is reaching both locations. However, as the test continues, the concentration at both locations levels off and becomes stable. Neither S1 nor S2 was receiving much fresh air, and the concentration decline at both locations was due to the fan action spreading the SF_6 cloud throughout larger and larger portions of the mine. Such a spreading out cannot produce a concentration decline for very long, which causes the concentrations in figure 12 to level off.

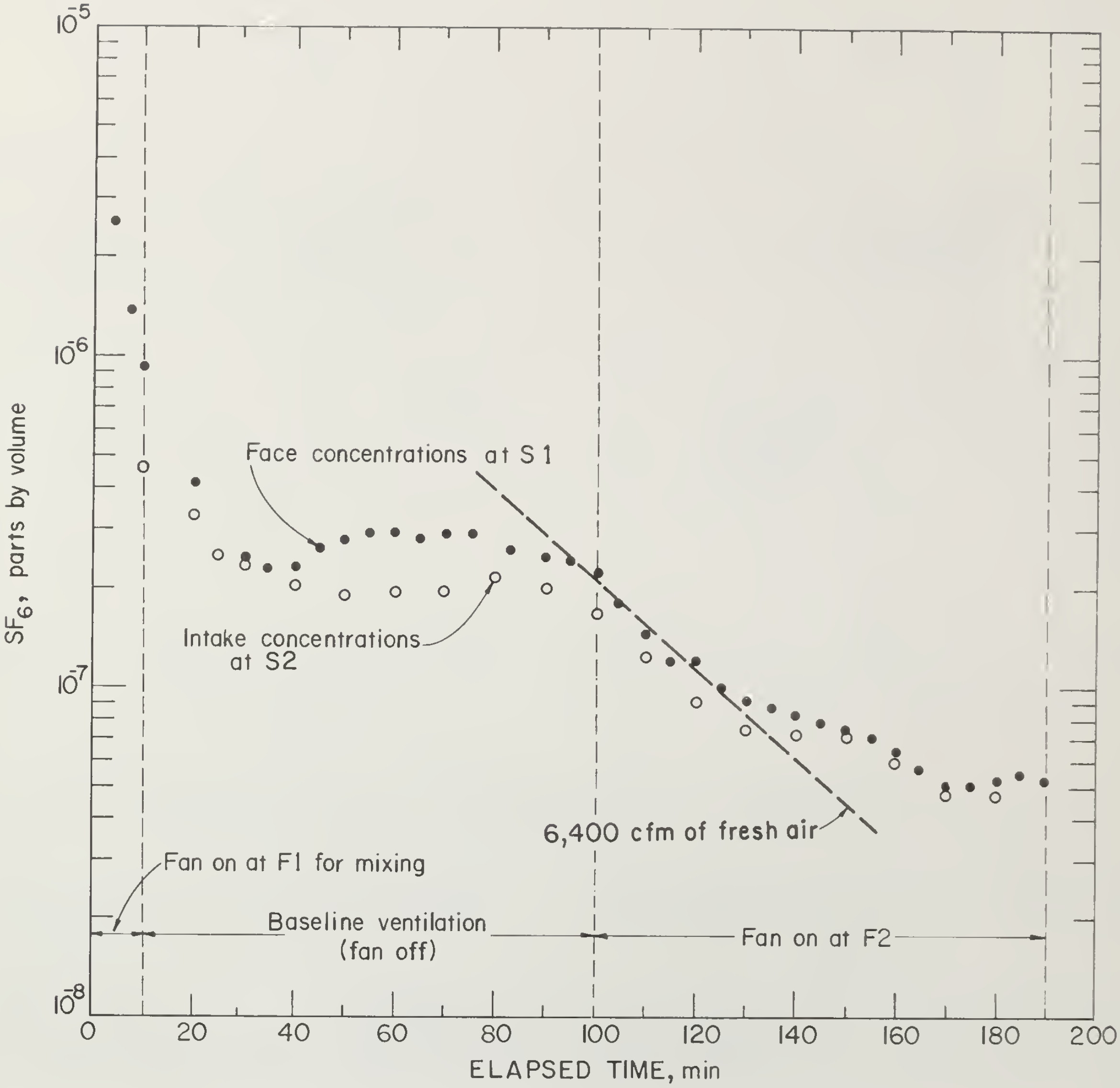

FIGURE 12. - SF_6 decay curve for section using 30-inch fan.

Subsequent to this test, several other tests were conducted with the fan at positions other than F2. The results were virtually the same in every instance.

The tests indicated that a concentration decline cannot always be interpreted as an influx of fresh air. At the start of the test, it is necessary to release the SF_6 uniformly throughout the test area. During the test, it is necessary to monitor the fresh-air source to insure that it does not become as contaminated as the test area. If SF_6 spreading is suspected, one test should be conducted for a period sufficient to insure that the decay curve does not level off.

SUMMARY

Tracer gas can be used to study the effectiveness of jet fans if some care is taken in conducting the experiments and analyzing the results. It is important to clearly define a test area, and to disperse the tracer gas uniformly throughout the test area. A concentration decline in the test area can then be interpreted as an influx of fresh air if it can be shown that there is a continuous source of fresh air outside of the test area.

In the dead-heading tests, which were conducted at White Pine, effective ventilation occurred at twice the greatest distance at which the jet from the fan could be detected with the smoke tube. The best fan position was on the heading side of the crosscut rather than the opposite side.

REFERENCES[8]

1. Drivas, P. J., P. G. Simmonds, and F. H. Shair. Experimental Characterization of Ventilation Systems in Buildings. Environ. Sci. Technol., v. 6, No. 7, 1972, pp. 609-614.

2. Frycz, A., and K. Biernacki. Application of Induction Ventilation Systems for the Improvement of Climatic Conditions in Metal Mines. Proc. First Internat. Mine Vent. Cong., Johannesburg, 1975, 495 pp.

3. Krause, D. Freistrahlen bei der Sonderbewetterung (Free Jets in Auxiliary Ventilation). Neue Bergbautechnik, v. 2, No. 1, January 1972, pp. 44-52.

4. _____. Impulsbewetterung im Bergbau (Impulse Ventilation in Mines). Neue Bergbautechnik, No. 3, March 1975, pp. 195-200 (part 1); No. 6, June 1975, pp. 457-462 (part 2).

5. McElroy, G. E. Role of Air Jets in Mine Ventilation. Trans. AIME, v. 163, 1945, pp. 399-414.

6. Radchenko, G. A., E. A. Mailybaev, and V. F. Slepykh. (Practical Investigations at a Ventilation Current Propagated Along the Wall of a Longwall Face.) Fiz. Tekhn., Probl. Razrabotki Polezn. Iskop., No. 3, May-June 1965, pp. 118-123.

7. Thimons, E. D., R. J. Bielicki, and F. N. Kissell. Using Sulfur Hexafluoride as a Gaseous Tracer To Study Ventilation Systems in Mines. BuMines RI 7916, 1974, 22 pp.

---

[8] Titles enclosed in parentheses are translations from the language in which the item was originally published.

☆U.S. GOVERNMENT PRINTING OFFICE: 1978-703-103/69

INT.-BU.OF MINES,PGH.,PA. 23254

UNIVERSITY OF ILLINOIS – URBANA
N30112028089693A